Imperial College London

DINITROGEN ACTIVATION AND REDUCTION WITH IRON PHOSPHINE COMPLEXES

by

Laurence Robertson Doyle

A dissertation submitted to the

Department of Chemistry of Imperial College London

for the degree of

Doctor of Philosophy

April 2015

Abstract

The conversion of dinitrogen to ammonia is a fundamental process for sustaining life on our planet. Ammonia provides a source of fixed nitrogen for nitrification and assimilation into plants, and is the ultimate source of almost all nitrogenated compounds. Synthetic ammonia is produced on a colossal scale by the Haber Bosch process, with an annual ammonia output exceeding 130 million tonnes. However, the intensive operating conditions of this process require a staggering energy cost; hence, the development of a lower energy solution is recognised as one of the major challenges of modern chemistry.

This dissertation explores the chemistry of homogeneous systems based on iron diphosphine complexes that are able to transform coordinated dinitrogen into ammonia. A greater understanding of these systems may provide insight into the iron-based catalysts utilised in both biological nitrogen fixation and the industrial Haber Bosch process. Ultimately, this could lead to a more sustainable process for meeting the global requirement for fixed nitrogen.

Chapter 1 provides a general introduction into dinitrogen fixation chemistry, with a particular focus on homogeneous systems involving iron.

Chapter 2 describes a convenient synthetic protocol to 1,2-bis(dialkylphosphino)ethanes. These are among the most versatile ligands used in inorganic chemistry, although issues with prior syntheses, often involving extremely hazardous phosphine precursors, has limited their accessibility.

Chapter 3 is an exploration of a seminal work on dinitrogen fixation involving iron complexes, which facilitate the conversion of coordinated dinitrogen to ammonia in what is known as the Leigh cycle. Mechanistic understanding of the key ammonia producing step has provided the focus of considerable interest and speculation for over a decade.

Chapter 4 provides insight into the dinitrogen and dihydrogen affinity of an iron(I) complex.

Chapter 5 details the experimental procedures performed in this work.

Declaration

The work described in this thesis was carried out by myself, except where noted otherwise, between October 2011 and April 2015, and under the supervision of Dr Andrew Ashley and Dr George Britovsek.

Copyright

The copyright of this thesis rests with the author and is made available under a Creative Commons Attribution Non-Commercial No Derivatives licence. Researchers are free to copy, distribute or transmit the thesis on the condition that they attribute it, that they do not use it for commercial purposes and that they do not alter, transform or build upon it. For any reuse or redistribution, researchers must make clear to others the licence terms of this work.

Acknowledgements

Firstly, I'd like to express my gratitude to Dr Andrew Ashley for the opportunity to study in his group. Your continual input and enthusiasm have contributed enormously to this research, and the experience of working with you has been enriching. I am also grateful to my co-supervisor Dr George Britovsek for his advice and support throughout my PhD studies.

My sincere thanks also to the following people who have contributed to this work. Dr Andrew White for his dedicated crystallography, and for his assistance and perseverance in disentangling my own crystallographic endeavours. Dr Will Myers and Dr Jeff Harmer, who performed the EPR measurements. Dr Alex Thom for offering his insight through discussion and theoretical calculations. Dr Greg Wildgoose, who assisted with the electrochemistry. Pete Haycock for his NMR expertise, and Dr Lisa Haigh for mass spectrometry analysis. Prof. Quentin Pankhurst and Lara Bogart for Mössbauer measurements. Prof. Andy Weller and Dr Mark Chadwick for their assistance with the solid-state UV-vis experiments. Prof. Dermot O'Hare for kindly offering the use of his lab on several occasions; also, many thanks to the rest of his group, in particular, Samantha Binding for her help with collecting and analysing the SQUID data. I am also very grateful for the efforts of the past MSci students who have worked on related projects, particularly Caroline Wood, Corin Briault-Hutter, and Duncan Fraser. I am glad none of you were seriously maimed by the experience.

A special thanks to Dr Thomas Herrington; your absence from the group is still felt, and your legacy/reputation has not been forgotten. In all seriousness, many thanks for your advice and friendship, it was immensely enjoyable working with you. To the rest of the group, you are a uniquely talented bunch and it has been a pleasure to know you all. Sarah Gates, your punting skills are otherworldly, I can only aspire to such mastery. Peter Hill, your affinity with vacuum pumps is uncanny. Andrew Crawford and Dr Nicholas Phillips, the inexplicable graffiti artists. Daniel Scott, your origami talents are truly undeniable, and Florian Langmann, you bring a whole new cultural experience to the group. Above all else, I am grateful for your friendship.

Thanks also to Anita Toscani, Dr Maria Gragert and Dr Matt Morton for their camaraderie. And to Dr Atanas Tomov; your approachability, chemical knowledge, and unconventional choice in music for the lab have been much appreciated.

A final thank you to my family.

I wish all of you the very best.

Abbreviations

Numerical abbreviations for complexes discussed in Chapters 3 and 4 are provided at the end of this thesis (cut out if desired).

δ	chemical shift
ε	extinction coefficient
λ	wavelength
μ	magnetic moment
ν	stretching frequency
$\nu_{1/2}$	full width at half maximum
χ_m	molar magnetic susceptibility
ADP	adenosine diphosphate
AES	Auger electron spectroscopy
ATP	adenosine triphosphate
Ar	aryl
BDE	bond dissociation energy
br	broad
$BArF_{24}^-$	$[B\{3,5\text{-}(CF_3)_2C_6H_3\}_4]^-$
Cp	cyclopentadienyl
Cp*	pentamethylcyclopentadienyl
CT	charge transfer
CV	cyclic voltammogram
CW	continuous wave
d	doublet
DABCO	1,4-diazabicyclo[2.2.2]octane
DCM	dichloromethane
DFB	difluorobenzene
depe	1,2-bis(diethylphosphino)ethane
DFT	density functional theory
DMeOPrPE	$[\{MeO(CH_2)_3\}_2PCH_2]_2$
DME	1,2-dimethoxyethane
dmpe	1,2-bis(dimethylphosphino)ethane
DMSO	dimethylsulfoxide
dppe	1,2-bis(diphenylphosphino)ethane
ENDOR	electron nuclear double resonance
E_a	activation energy

ESEEM	electron spin echo envelope modulation
Et	ethyl
EPR	electron paramagnetic resonance
FC	field cooled
FeMoco	Fe-Mo cofactor
Fp*	$Cp^*Fe(CO)_2$
HIPT	3,5-{2,4,6-$^{i}Pr_3C_6H_2$}$_2C_6H_3$
HOMO	highest occupied molecular orbital
HS	high spin
HYSCORE	hyperfine sublevel correlation
^{i}Bu	*iso*-butyl
^{i}Pr	*iso*-propyl
IR	infrared
IVCT	intervalence charge transfer
LS	low spin
LUMO	lowest unoccupied molecular orbital
Lut	lutidinium (2,6-dimethylpyridinium)
Me	methyl
Nap	naphthalimide
^{n}Bu	n-butyl
NMP	*N*-Methyl-2-pyrrolidone
NMR	nuclear magnetic resonance
Ph	phenyl
PMHS	polymethylhydrosiloxane
^{R}PNP	2,6-$(R_2PCH_2)_2C_5H_3N$
p	pentet
pdmab	*p*-(dimethylamino)benzaldehyde
PP	diphosphine
ppm	parts per million
proton sponge	1,8-bis(dimethylamino)naphthalene
q	quartet
R	alkyl
RT	room temperature
s	singlet
t	triplet
$t_{½}$	half-life
^{t}Bu	*tert*-butyl

TBME	*tert*-butyl methyl ether
Tf	trifluoromethanesulfonyl
TMDS	tetramethyldisiloxane
TMS	trimethylsilyl
THF	tetrahydrofuran
TMP	2,2,6,6-tetramethylpiperidine
TPB	tris(phosphino)borane
TPP	tetraphenylporphyrin
UV-Vis	ultraviolet-visible
XRD	X-ray diffraction
VT	variable temperature
ZFC	zero-field cooled

Units

°C	degree Celsius
μ_B	Bohr magneton
A	amps
Å	ångström
atm	atmosphere
cal	calorie
deg	degree
eV	electron volt
g	gram
G	gauss
h	hour
J	joule
K	Kelvin
L	litre
m	metre
M	molar
mol	mole
Oe	Oersted
s	second
T	tesla

Contents

Chapter 1: Introduction

1.0 Overview.....11

1.1 The Haber-Bosch process.....12

1.2 Biological N_2 fixation.....14

1.3 N_2 coordination to transition metals.....16

1.4 Homogeneous N_2 fixation 18

1.4.1 Early Mo systems.....20

1.4.2 Fe systems.....23

1.4.3 Hydrogenation of transition metal coordinated N_2.....29

1.5 Summary.....31

1.6 Thesis aims.....32

1.7 References.....33

Chapter 2: A convenient synthetic protocol to 1,2-bis(dialkylphosphino)ethanes

2.1 Introduction.....36

2.2 Synthesis of bidentate alkyl phosphine ligands.....37

2.3 Diphosphine pincer ligands.....43

2.4 Conclusions.....45

2.5 References.....46

Chapter 3: N_2 activation with Fe diphosphine complexes

3.0.1 Introduction.....49

3.0.2 Preliminary spectroscopic studies of the Leigh deprotonation reaction.....56

Part 1: Fe complexes of dmpe.....61

3.1.1 Introduction.....61

3.1.2 Isolating Fe(0) species.....61

3.1.3 Diamagnetic-paramagentic transition in the Leigh deprotonation step....68

3.1.4 Isolating Fe(I) species.....73

3.1.5 Electrochemistry of Fe(0) and Fe(I) species.....85

3.1.6 Cooperative activation of N_2 with Fe(0) and K^+ salts.....91

3.1.7 H_2 experiments.....113

Part 2: Fe complexes of depe.....120

3.2.1 Introduction.....120

3.2.2 Synthesis of Fe(0).....120

3.2.3 Diamagnetic-paramagnetic transition in the Leigh deprotonation step...122

3.2.4 Isolating Fe(I) species.....124

3.2.5 Electrochemistry of Fe(0) and Fe(I) species.....131

3.2.6 Cooperative activation of N_2 with Fe(0) and K^+ salts.....134

3.2.7 H_2 experiments.....143

Part 3: Quantification of NH_3 and N_2H_4 from acidification experiments.....148

3.3.1 Introduction.....148

3.3.2 Comparison of literature procedures.....150

3.3.3 Acidification experiments.....152

Part 4: Concluding remarks.....156

References.....158

Chapter 4: N_2 and H_2 binding to the S = ½ Fe(I) complex $[Fe(depe)_2][BArF_{24}]$

4.1 Introduction.....162

4.2 Reversible N_2 binding to 13.....165

4.3 Reversible H_2 binding to 13.....169

4.4 Solid-state reactions of 13 with H_2.....174

4.5 Concluding remarks.....176

4.6 References.....176

Chapter 5: Experimental

5.1 General procedures.....178

5.2 Experimental details for Chapter 2.....180

5.3.1 Experimental details for Chapter 3, Part 1.....189

5.3.2 Experimental details for Chapter 3, Part 2.....194

5.3.3 Experimental details for Chapter 3, Part 3.....197

5.4 Experimental details for Chapter 4.....198

5.5 References.....198

Appendix.....200

Chapter 1: Introduction

1.0 Overview

N_2 fixation is the conversion of atmospheric N_2 to NH_3, a fundamental process upon which all life is dependent. Although N_2 accounts for 78% of our atmosphere, its extreme inertness makes it chemically inaccessible to most biological organisms, in which N is an essential element found in proteins and nucleic acids. The "fixing" of N_2 to NH_3, or NH_4^+, provides a chemically accessible form of N, which is the ultimate source of almost all nitrogenated compounds found in Nature and produced industrially.[1]

Biological N_2 fixation is performed by diazotrophs containing the nitrogenase family of enzymes,[2-4] whilst synthetic NH_3 is produced by the Haber-Bosch process from the reaction of N_2 and H_2 gas over an Fe catalyst (Figure 1.1).[5] The Haber-Bosch process has become one of the largest scale industrial processes with a global output of 130 million tonnes of NH_3 *per annum*.[6] The majority of this is used in the agricultural industry as a feedstock for ammonium fertilisers, which are estimated to be responsible for sustaining ca. 40% of the world's population.[7] NH_3 is also used in the production of nitric acid, plastics, fibres, explosives, dyes, and pharmaceuticals. Although modern plants are very efficient, energy demanding operating conditions are required, with temperatures in excess of 300 °C and pressures of between 100–300 atm.[8] As a consequence, this process is responsible for ca. 1-2% of total global energy consumption, with a correspondingly high share of greenhouse gas emissions.[9] Thus, a lower energy solution to N_2 fixation is recognised as one of the major challenges of modern chemistry.[10, 11]

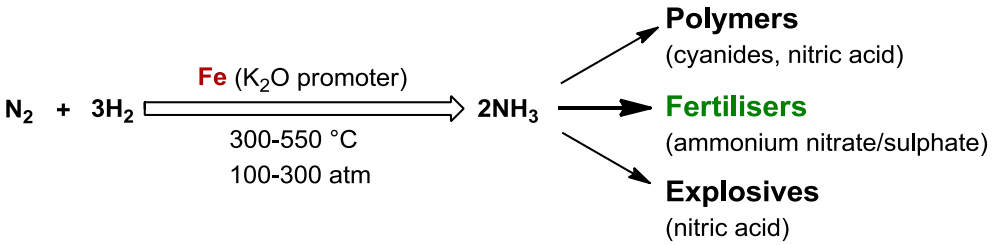


Figure 1.1 N_2 fixation by the Haber-Bosch process and the industrial uses of NH_3.

The chemical inertness of N_2 is due to several factors, the most significant arguably being the high bond dissociation energy (BDE) of the N≡N triple bond (941 kJ mol^{-1}), and in particular the first BDE (410 kJ mol^{-1}), which accounts for almost half of this value.[12] Hence, whilst acetylene (H-C≡C-H) contains a similarly strong triple bond (BDE = 962 kJ mol^{-1}), it is

considerably more reactive under ambient conditions since initial cleavage of the first bond (BDE = 222 kJ mol^{-1}) is much easier than for N_2.[12] Thus, although formation of NH_3 from N_2 and H_2 is thermodynamically favourable overall ($\Delta H^{\ominus}$ = –92.22 kJ mol^{-1}, $\Delta G^{\ominus}_f$ = –16.48 kJ mol^{-1}), there is a considerable initial activation barrier to overcome.[13] Further kinetic stability is rendered by a large energy gap between the highest occupied molecular orbital and lowest unoccupied molecular orbital (HOMO-LUMO, 10.82 eV) and the non-polar nature of the N_2 molecule.[14] Additionally, N_2 has a high ionization potential (15.841 eV), a negative electron affinity (–1.903 eV), and whilst the proton affinity is positive (493.8 kJ mol^{-1}), it is lower than for other small molecules such as acetylene, CO, or even methane, meaning that N_2 remains resistant to protonation by strong acids under normal conditions.[14] Given these limitations, the transformation of N_2 performed under ambient conditions by Nature is remarkable, whilst man's own catalytic process represents one of the most significant technological achievements of the 20th century.

1.1 The Haber-Bosch process

The Haber-Bosch process, developed in the early part of the 20th century by Fritz Haber and later Carl Bosch and Alwin Mittasch, produces NH_3 from N_2 and H_2 gas using a heterogeneous Fe catalyst.[15] Other more expensive transition metal catalysts have since been developed, such as Ru in the Kellog process (KAAP), although Fe is the most commonly employed, and the process has remained relatively unchanged over its 100 year history.[5] The Fe catalyst is typically obtained from partial H_2 reduction of magnetite (Fe_3O_4) fused with various K, Ca, Al, and Si oxide promoters.[16] Surface composition can be determined through the use of surface spectroscopic techniques.[17] For example, Auger electron spectroscopy (AES) performed on a 10^{-4} cm^2 area of a sample industrial catalyst (BASF-S6-10) prepared from Fe_3O_4 fused with K_2O, Al_2O_3, and CaO, reveals considerable enrichment of the promoters at the surface (Table 1.1).[18] Under the reaction conditions, Fe in Fe_3O_4 is reduced by H_2 to the metallic state, whilst the oxidation states of the additives are unchanged. Since the catalyst particulate volume remains fairly constant, this results in a highly porous structure with a high surface area, in which the Al and Ca oxides provide structural support. The K(I) oxide, which is typically found to have a surface coverage of between 20-50%, is thought to act as an "electronic" promoter by improving the specific activity of the Fe surface.[19]

The mechanism of this heterogeneous chemistry has been the focus of intense research; elucidation of the catalyst enabled kinetic pathway, by which this otherwise inaccessible chemistry is realised, could enable the potential for energetic optimisation through rational

catalyst design.[20] The main steps of the process are understood to be: (i) chemisorption of N_2 and H_2 onto the catalyst surface with subsequent dissociation to form surface metal nitrides and hydrides; (ii) recombination to form surface metal bound NH, NH_2, and NH_3; and (iii) desorption of NH_3 (Figure 1.2). Theoretical models indicate dissociation of H_2 on the metal surface is barrierless, whereas dissociation of adsorbed N_2 is the rate determining step, likely as a consequence of its high first BDE.[18] The surface activity is also variable, for instance the Fe(111) surface exhibits higher activity than either Fe(100) or Fe(110), and similarly local concentrations of K(I) oxide promoter improve the rate of N_2 dissociation.[21] However, the nature of these interactions between Fe, K^+, and N_2 in this key dissociative step and subsequent N–H bond forming steps remain obscured to investigation by surface science techniques.[11] Thus, one key area of focus is the study of homogeneous model complexes (*vide infra*) which enable the use of solution phase spectroscopic techniques to gain further insight.

Table 1.1 Percentage composition of a promoted Fe catalyst (%), values from ref. 18.

	Fe	**K**	**Al**	**Ca**	**O**
Bulk composition	40.5	0.35	2.0	1.7	53.2
Surface (before reduction)*	8.6	36.1	10.7	4.7	40.0
Surface (after reduction*	11.0	27.0	17.0	4.0	41.0

*determined by Auger electron spectroscopy (AES); reduction conditions: ca. 400 °C treatment in a N_2/H_2 mix.

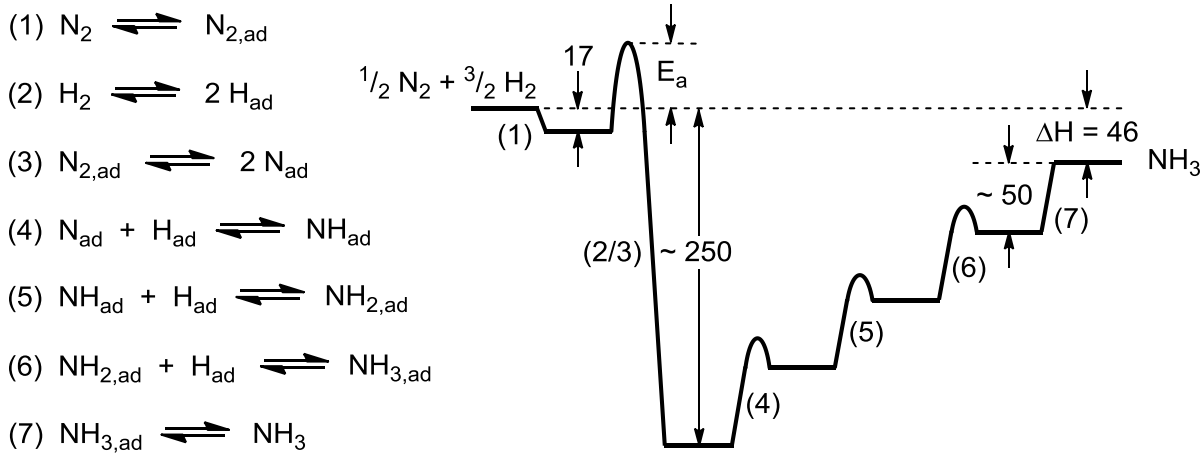


Figure 1.2 Potential energy diagram for the reaction of reactants N_2 and H_2 to form NH_3; the activation energy (E_a) depends on surface structure and composition; energies in kJ mol^{-1}; figure adapted from ref. 18.

1.2 Biological N_2 fixation

In Nature, diazotrophs are bacterial or archaeal organisms that are able to perform N_2 fixation and can thus survive without an external source of fixed N.[22] All diazotrophs contain nitrogenases, which are the single known family of enzymes capable of performing this fundamental process. The most efficient nitrogenase, and therefore the most widespread, contains an Fe-Mo cofactor (FeMoco, Figure 1.3) incorporating a Fe_7MoS_9C cluster, which is generally agreed to be the active site of N_2 binding and fixation; a second component of nitrogenase is the electron-transfer Fe protein (dinitrogenase reductase), which delivers the reducing electrons for this process.[1, 2] Less common "alternative nitrogenases" are also known with related Fe-V and Fe-Fe cofactors in which V or Fe is substituted at the Mo site.[23] Whilst notable that all nitrogenases are able to fix N_2 under biological conditions, it remains an energy intensive process, requiring 16 equivalents of adenosine triphosphate (ATP) per fixed N_2 molecule.[4] Anaerobic conditions are also essential due to poisoning from O_2, and a total of eight protons and electrons are required, rather than the expected six, since an additional two of each are redirected into producing an equivalent of waste H_2.

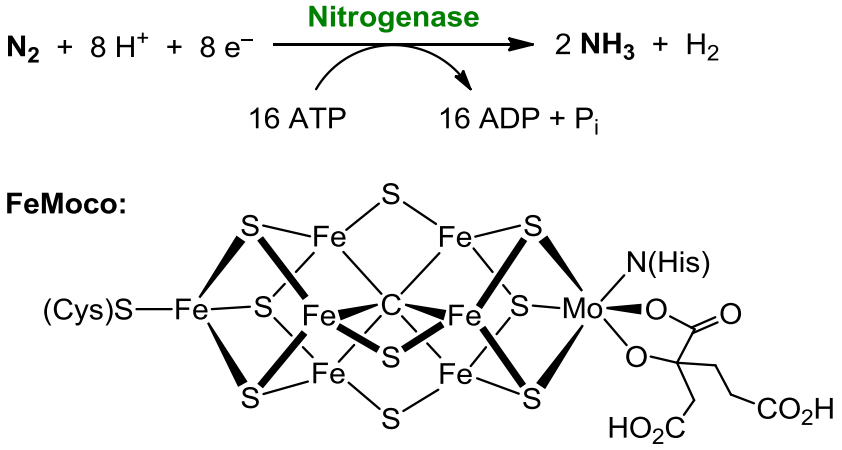


Figure 1.3 N_2 fixation performed by nitrogenase enzymes and the structure of the FeMo cofactor.

The mechanism of biological fixation has also been the source of much speculation over the last half century, with considerable debate centred on whether Fe or Mo is the active site, as well as the identity of an interstitial light atom (C, N, or O) at its centre. This was first revealed in a 1.16 Å resolution crystal structure, and was recently shown to be C through a combination of X-ray emission spectroscopy, higher-resolution (1.0 Å) crystallography, and electron spin echo envelope modulation (ESEEM) experiments.[24] Recent work by Hoffman *et al.* has made significant advancement through characterisation of freeze-trapped intermediates using a suite of electron nuclear double resonance (ENDOR), ESEEM, and hyperfine sublevel correlation (HYSCORE) techniques.[25] On the basis of these experiments,

a viable mechanism has been proposed involving eight sequential protonation and reduction steps and their corresponding intermediate states, E_n (n = 0–8; Figure 1.4).

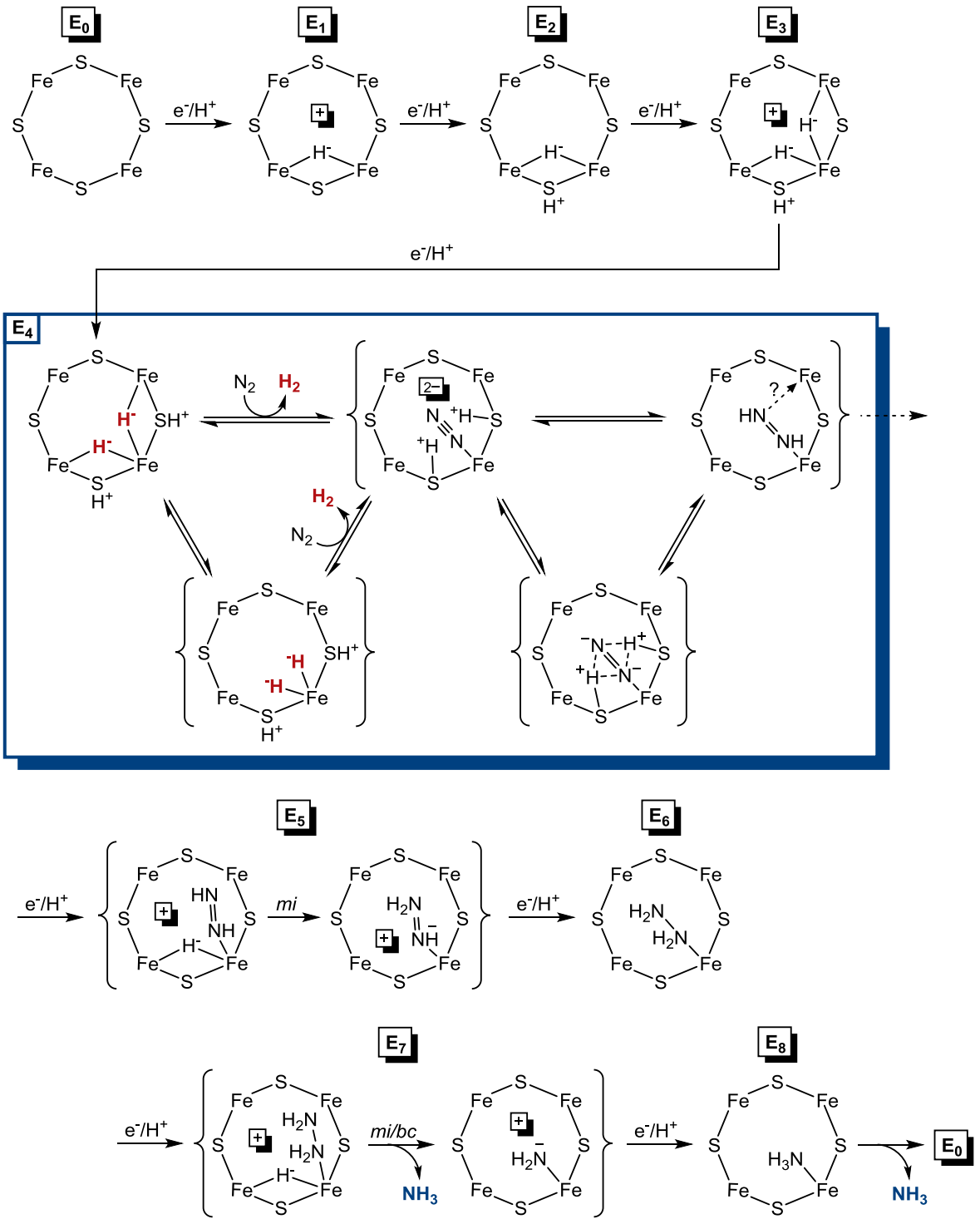


Figure 1.4 The mechanism of N_2 fixation proposed by Hoffman *et al.* to occur at the FeMoco in nitrogenase involving eight sequential protonation and reduction steps and the corresponding E_n (n = 0-8) states; hydrides in E_5-E_8 are presented as bridging, without evidence for or against terminal hydrides; N_2H_2 may similarly be end-on or side-on bound; mi = migratory insertion; bc = bond cleavage; figure adapted from ref. 25.

The first part of the mechanism ($E_{1–4}$) involves the accumulation of multiple reducing equivalents on the Fe_4 face of FeMoco through the formation of metal hydrides. This is followed by reductive elimination of H_2 and binding of N_2 (E_4), which undergoes symmetric reduction/protonation proceeding through diazene (N_2H_2) and hydrazene (N_2H_4) intermediates ($E_{4–7}$); the terminal N is then protonated to liberate NH_3 (E_7), and a second equivalent of NH_3 is produced after the final protonation/reduction step (E_8). This contrasts to an alternative asymmetric pathway, for example the hypothetical Chatt cycle (*vide infra*).[26] Interestingly, an explanation for the generation of H_2, which wastes four ATP and two [e^-/H^+], is suggested by the formation of two metal hydride bonds, amounting to four reducing equivalents, with loss of only two reducing equivalents upon reductive elimination of H_2.[25] Thus resulting in the reduction of a formally Fe(II) centre to a more electron rich Fe(0) centre, which enables binding of N_2 and subsequent transfer of two electrons onto the N_2 molecule. In addition, the bound N_2 may be activated by electrostatic interaction with two S-bound protons to provide a FeMoco bound N_2H_2 intermediate. This ability of metal hydride bonds to store reducing electrons also features in the homogeneous N_2 fixation chemistry of Fe discussed in section 1.4.2.

1.3 N_2 coordination to transition metals

The dissociation of N_2 is a key step in both biological and industrial N_2 fixation and can only be realised through coordination to one or more metal centres with subsequent activation of the strong N–N triple bond. Thus, insight into the bonding interaction between transition metals and N_2, as well as its reduced species such as N_2H_2 and N_2H_4, is crucial for understanding the functionalisation of N_2.

The first discovered transition metal complex incorporating a N_2 ligand was $[Ru(NH_3)_5(N_2)]^{2+}$, reported by Allen and Senoff in 1965.[27] Since then, numerous N_2 complexes have been prepared for almost every transition metal element, featuring a myriad of ancillary ligands. These have been prepared by several general methods: (i) substitution by N_2 of a weakly bound ligand; (ii) coordination to the vacant site of an unsaturated complex; and (iii) reduction of a metal complex to a low-valent species which binds N_2.

Monomeric complexes almost exclusively involve coordination of weakly activated N_2 in an η^1 end-on binding mode, whilst both η^1, η^1 end-on and η^2 side-on binding modes are found in dimeric species, typically exhibiting more pronounced N_2 activation; a combination of the two has also been observed (Figure 1.5).[28]

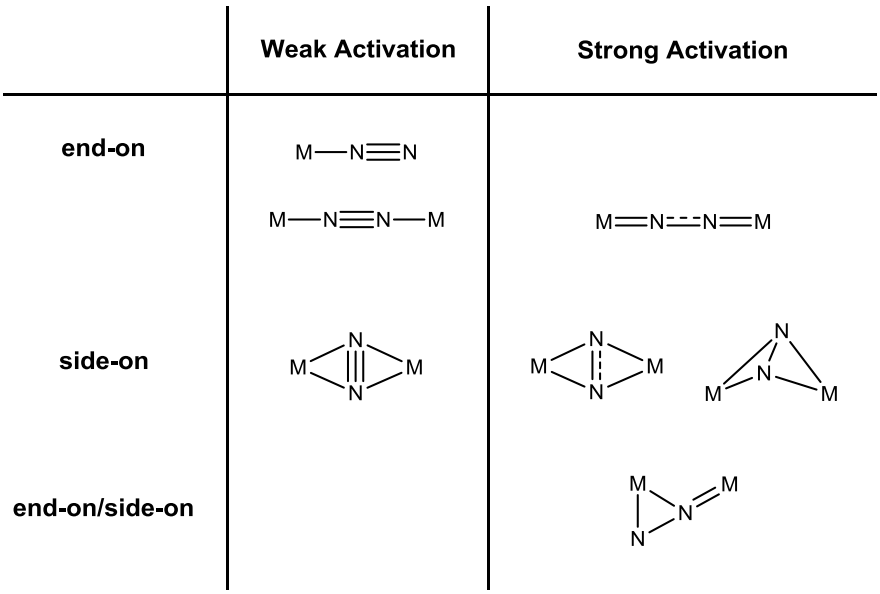


Figure 1.5 The known binding modes of N_2 in mono- and bi-metallic complexes.

The bonding interaction in these complexes involves both σ- and π- components as described by the Dewar–Chatt–Duncanson bonding model (Figure 1.6).[29] N_2 binds as a Lewis base through σ-donation from the HOMO ($3\sigma_g$) into an empty metal d-orbital (d_{z^2} or $d_{x^2-y^2}$) to form a σ-bond. In addition, N_2 is rendered Lewis acidic through π-backdonation from a filled metal d-orbital (d_{xz}, d_{yz}, or d_{xy}) into the LUMO ($1\pi^*g$) forming a π back-bond. The former σ-component dominates the M–N bonding in transition metal N_2 complexes, however, π-backdonation into the antibonding $1\pi^*g$ LUMO of N_2 is mainly responsible for weakening of the N–N triple bond.[30] Thus, an important distinction must be made between the lability of N_2 and the extent of N_2 activation in a transition metal N_2 complex. The former is dependent on the M–N bond strength, and therefore largely dominated by σ-effects, whilst the latter is a reflection of π-electron richness of the metal and its propensity to donate electron density onto the N_2 ligand.

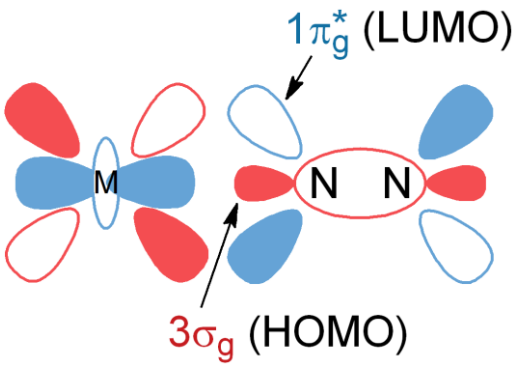


Figure 1.6 Coordination of N_2 to a transition metal centre described by the Dewar–Chatt–Duncanson bonding model; occupied orbitals are shown in red, unoccupied in blue.

Thus, strong N_2 activation manifests in low oxidation state transition metal complexes which may however contain relatively weak M–N bonds. Hence, although the Dewar–Chatt–Duncanson σ/π bonding is often labelled synergistic, this is perhaps a misleading description.[31] In addition, the number and type of ancillary ligands has a pronounced influence on the character of the metal and its coordination geometry, which both contribute to the resultant N_2 bonding and activation.

The extent of N_2 activation is typically inferred from the *ν*(N–N) stretching frequency in comparison to the value for free N_2 (IR: 2331 cm^{-1}); the crystallographically determined d(N–N) atomic separation is generally considered a less reliable measure, due to error in the solution model from disorder or unmodelled trace impurities, as well as discrepancies in locating nuclei from an electron density map. *ν*(N–N) and d(N–N) values for Fe N_2 complexes pertinent to this work are tabulated in Table 1.2; Fe(II) exhibits fairly weak activation of N_2 (2008–2145 cm^{-1}), with fairly modest improvement for more electron-rich Fe(0) (1891–2068 cm^{-1}). Notably, the extent to which the degree of N_2 activation determines reactivity, in particular towards protonation, is complex and a correlation is not necessarily assured. For instance, the reducing ability of the metal may also be expected to play an important role, and the outcome of protonation reactions can vary considerably with reaction temperature, choice of counteranion(s), and concentration/identity of the acid employed. In addition, side reactions may be anticipated from protonation at the ancillary ligands or the metal centre, thus presenting a considerable challenge to overall understanding of the complex mechanisms involved.

1.4 Homogeneous N_2 fixation

With the advent of isolable transition metal N_2 complexes, investigation into their protonation and reduction chemistry began apace, with a focus on providing a homogeneous model to mimic the biological N_2 fixation performed by nitrogenases. Pioneering work in this field was particularly focussed on the chemistry of Mo (along with related W), since oxidation of Mo(0) to Mo(VI) could feasibly provide all six of the electrons required to fully reduce N_2 coordinated at a single Mo site. Of particular importance are two related N_2 fixing cycles developed by the groups of Joseph Chatt and Richard Shrock, which will be briefly discussed to provide comparison with the later work on Fe that will be the focus of this work.

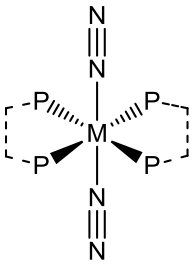
Table 1.2 *v*(N–N) and d(N–N) values for various N_2 complexes of Fe.

Compound	Fe ox. state	v(N–N)[a] (cm^{-1})	d(N–N)[b] (Å)	Ref.
N_2	–	2331	1.098	32
$[Fe(H)(N_2)(dmpe)_2][BPh_4]$	2	2094	1.112(9)	33
$[Fe(H)(N_2)(depe)_2[BPh_4]$	2	2091	1.070(12)	34
$[Fe(H)(N_2)(dppe)_2][BPh_4]$	2	2120, 2145[c]		35
$[Fe(H)(N_2)(DMeOPrPE)_2][BPh_4]$	2	2093	1.112(3)	36, 37
$[Fe(H)(N_2)\{P(CH_2CH_2PPh_2)_3\}][BPh_4]$	2	2100		38
$[Fe(H)(N_2)\{N(CH_2CH_2PPh_2)_3\}][BPh_4]$	2	2090	1.102(13)	39
$Fe(H)_2(N_2)(PMePh_2)_3$	2	2058		40
$Fe(H)_2(N_2)(PEtPh_2)_3$	2	2055	1.136(7)	40, 41
$Fe(H)_2(N_2)(PBuPh_2)_3$	2	2074		40, 42
$Fe(H)_2(N_2)(PPh_3)_3$	2	2008		43
$[Fe(\eta^5\text{-}C_5H_5)(N_2)(dippe)][BPh_4]$	2	2112	1.13(1)	44
$[Fe\{C(2\text{-}P^iPr_2C_6H_4)_3\}_3(N_2)][BArF_{24}]$	2	2128		45
$[Fe\{Si(2\text{-}P^iPr_2C_6H_4)_3\}_3(N_2)][BArF_{24}]$	2	2143	1.091(3)	46
$[\{Fe(\eta^5\text{-}C_5H_5)(dmpe)\}_2(\mu\text{-}N_2)][BF_4]_2{\cdot}2H_2O$	2, 2	2054[d]		47
$[\{Fe(\eta^5\text{-}C_5H_5)(dppe)\}_2(\mu\text{-}N_2)][PF_6]_2$	2, 2	2040[d]		48
$[(Fe(H)\{P(CH_2CH_2PMe_2)_3\})_2(\mu\text{-}N_2)][BPh_4]_2$	2, 2	2054[d], 2064[d]		49
$Fe\{C(2\text{-}P^iPr_2C_6H_4)_3\}(N_2)$	1	1992	1.134(4)	45
$Fe\{Si(2\text{-}P^iPr_2C_6H_4)_3\}(N_2)$	1	2003	1.1245(2)	46
$Fe\{Si(2\text{-}PPh_2C_6H_4)_3\}(N_2)$	1	2041	1.106(3)	50
$[\{Fe(\beta\text{-diketiminate-1})\}_2(\mu\text{-}N_2)]$	1	1778	1.182(5)	51
$Fe(N_2)(dmpe)_2$	0	1975		33
$Fe(N_2)(depe)_2$	0	1955	1.142(7)	52
$Fe(N_2)(dppe)_2$	0	2068		53
$Fe(N_2)(DMeOPrPE)_2$	0	1966		36
$Fe(N_2)\{P(CH_2CH_2PMe_2)_3\}$	0	2013		49
$Fe(N_2)\{P(CH_2CH_2P^iPr_2)_3\}$	0	1985		54
$Fe(N_2)\{N(CH_2CH_2PPh_2)_3\}$	0	1967		39
$[Fe\{Si(2\text{-}P^iPr_2C_6H_4)_3\}(N_2)][Na(THF)_3]$	0	1891	1.147(4)	46
$[Fe\{Si(2\text{-}P^iPr_2C_6H_4)_3\}(N_2)][Na(12\text{-}c\text{-}4)_2]$	0	1920	1.132(4)	46
$[Fe\{Si(2\text{-}PPh_2C_6H_4)_3\}(N_2)][Na(12\text{-}c\text{-}4)_2]$	0	1967		50
$Fe\{B(2\text{-}P^iPr_2C_6H_4)_3\}(N_2)$	0	2011		45
$[\{Fe(\beta\text{-diketiminate-1})\}_2(\mu\text{-}N_2)][K]_2$	0	1589	1.233(6)	51
$[Fe\{B(2\text{-}P^iPr_2C_6H_4)_3\}(N_2)][Na(12\text{-}c\text{-}4)_2]$	–1	1918	1.144(3)	55

[a] IR bands except where noted. [b] Determined by single-crystal X-ray diffraction. [c] Both singlet and triplet states are resolved by IR. [d] Raman bands. dmpe = $[Me_2PCH_2]_2$; depe = $[Et_2PCH_2]_2$; dppe = $[Ph_2PCH_2]_2$; DMeOPrPE = $[\{MeO(CH_2)_3\}_2PCH_2]_2$; dippe = $[^iPr_2PCH_2]_2$; 12-c-4 = $[C_2H_4O]_4$; $BArF_{24}^-$ = $[B\{3,5\text{-}(CF_3)_2C_6H_3\}_4]^-$; β-diketiminate-1 = $\{(2,6\text{-}(^iPr)_2C_6H_3)NC(^tBu)\}_2CH$.

1.4.1 Early Mo systems

Seminal work by Chatt,[56, 57] Hidai,[58] Van Tamelen,[59, 60] and their colleagues, established the ability of Mo and W phosphine complexes to fix coordinated N_2 to NH_3/NH_4^+ in a protic medium. In the earliest example, the Mo(0) complex $[Mo(N_2)_2(dppe)_2]$ (dppe = $[Ph_2PCH_2]_2$) produced NH_4^+ in up to 27% yield (per Mo) through protonation with HCl coupled with Na naphthalenide (NaNap) reduction in tetrahydrofuran (THF).[59] It was subsequently found that yields of up to 37% could be achieved using HBr in *N*-Methyl-2-pyrrolidone (NMP) without the use of an external reductant (Figure 1.7).[60] Furthermore, this reactivity was extended to the related phosphine complexes [*cis/trans*-$M(N_2)_2(PMe_2Ph)_4$] (M = Mo, W), for which the configurationally *cis* W complex converted 0.89 equivalents of coordinated N_2 to NH_4^+, implicating oxidation of W(0) to W(VI).[56, 57] Whilst this extreme range of oxidation states is improbable for an enzymatic catalytic cycle, it does provide evidence that a single metal site is capable of providing all of the six electrons required to fully reduce N_2. This forms the basis of the hypothetical Chatt cycle (Figure 1.8), which proceeds *via* sequential addition of six protons and electrons in an asymmetric pathway.[61]



cis/trans
M = Mo, W
P = PR_3, $\{R_2PCH_2\}$
R = alkyl, aryl

(i) [*trans*-$Mo(N_2)_2(dppe)_2$] —xs HBr, NMP→ Mo products + NH_4^+ (0.37 per Mo)

(ii) [*cis*-$W(N_2)_2(PMe_2Ph)_4$] —xs H_2SO_4, MeOH→ W(VI) products + N_2 + 2 NH_4^+ (1.78 per Mo)

—xs HX, MeOH→ $[W(X)_2(NNH_2)(PMe_2Ph)_4]$ + N_2
X = Cl, Br, I

Figure 1.7 Early Mo and W phosphine N_2 complexes.[26, 56, 60]

Using various ancillary ligands it has been possible to isolate examples of most of the proposed intermediate complexes, but not all, and a catalytic cycle based on these Mo(0) or W(0) species remains elusive.[62] However, this work provided the basis for the closely related Mo(III)–Mo(VI) system developed by Schrock *et al.*, which was the first well-defined homogeneous system capable of catalytic NH_3 production.[63]

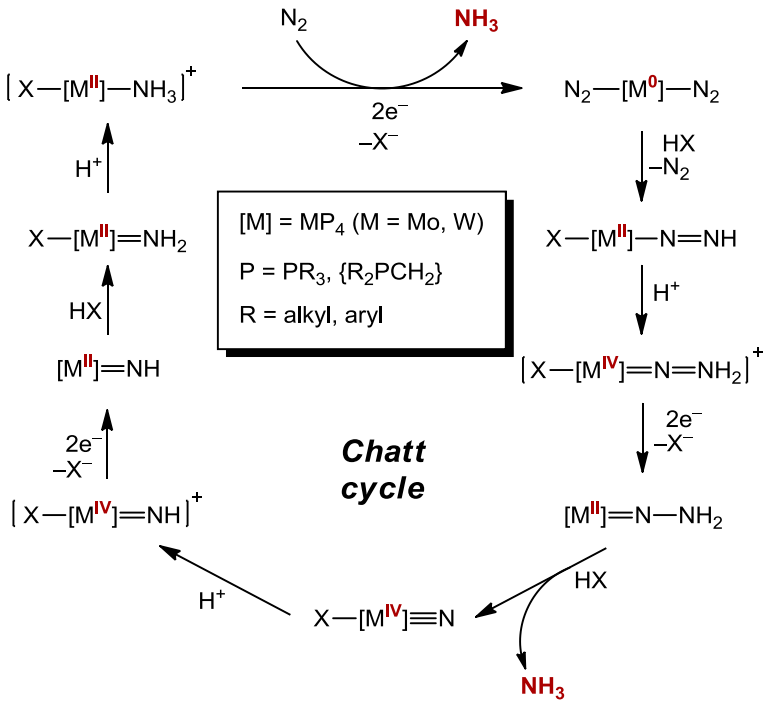


Figure 1.8 The Chatt cycle, involving M(0)–M(IV) (M = Mo, W).[61]

In the proposed cycle (Figures 1.9-1.10), the Mo(III) starting N_2 species incorporates a triamidoamine ($[\{ArNCH_2CH_2\}_3N]^{3-}$, Ar = HIPT = 3,5-$\{2,4,6\text{-}^iPr_3C_6H_2\}_2C_6H_3$) tripodal ligand that forces the complex to adopt a trigonal bipyramidal geometry in which the N_2 and subsequent reduced N fragments are coordinated in the apical site.[64] Protection from the surrounding bulky HIPT groups has aided isolation of eight of the intermediates proposed to be involved in this reaction, which are highlighted in Figure 1.10 (protonation is expected to be the initial step, hence $[Mo(II)]N_2^-$ is omitted from the cycle). Catalytic experiments employing [LutH][$BArF_{24}$] (LutH = 2,6-lutidinium; $BArF_{24}^-$ = $[B\{3,5\text{-}(CF_3)_2C_6H_3\}_4]^-$) as a proton source and Cp^*_2Cr as a reductant were performed for several of these intermediates, achieving approximately four turnovers in 63–66% efficiency (based on Cp^*_2Cr reducing equivalents) in each case (Figure 1.9).[63] The highest efficiency was obtained for the Mo(VI) nitride species, which marks the halfway intermediate in the Schrock cycle, generated from asymmetric protonation of the distal N and release of the first equivalent of NH_3. Although a remarkable achievement and a milestone for abiological homogeneous N_2 fixation, this remains a fairly modest performance compared to the FeMoco in nitrogenase, which achieves a 75% efficiency (only 4 out of 16 ATP are used to produce H_2) in effectively unlimited turnover. Furthermore, whilst the Schrock system operates at room temperature, the reaction is slow (ca. 4 turnovers per hour) due to the requirement for dropwise addition of the strong external reductant.

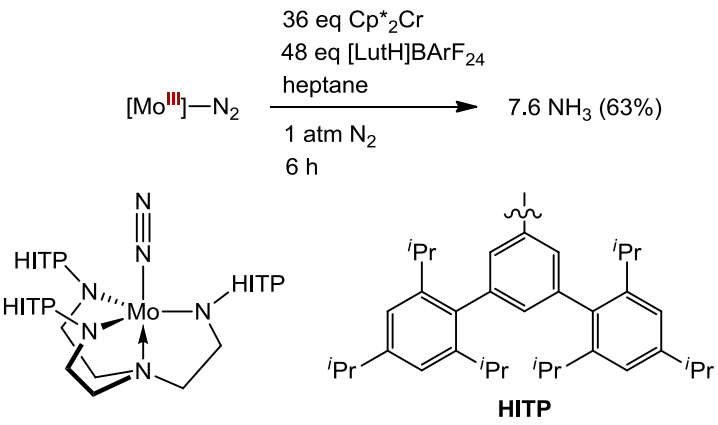


Figure 1.9 Catalytic NH_3 production using a homogeneous Mo catalyst, reported by Schrock *et al.*.[63]

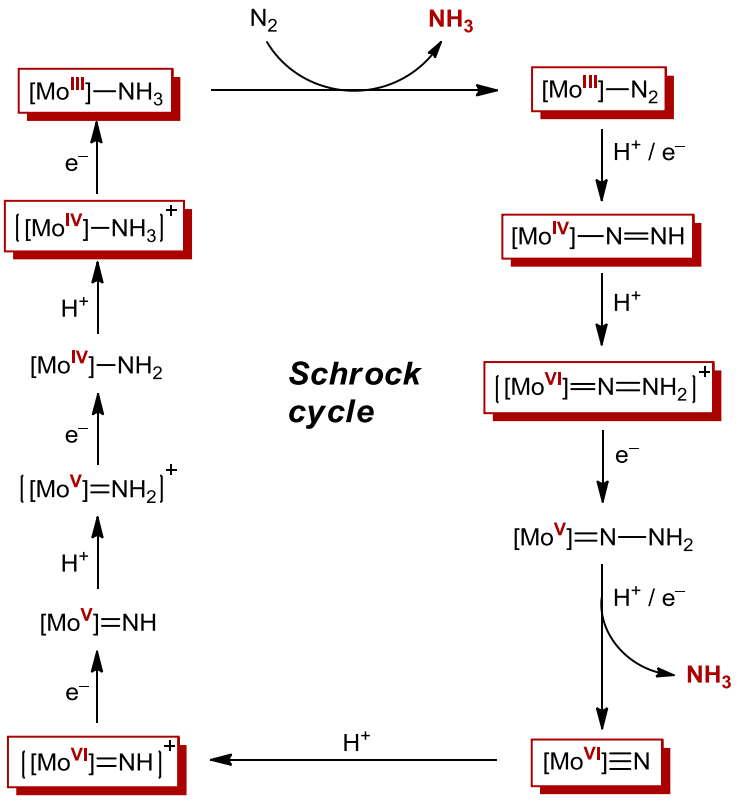


Figure 1.10 The Schrock cycle, involving M(III)–M(VI); [Mo] defined in Figure 1.9.[63]

A second catalytic Mo system was reported more recently by Nishibayashi *et al.* based on the dimeric Mo(0) complex [{Mo($^{t\text{Bu}}$PNP)$(N_2)_2$}$_2$(μ-N_2)] ($^{t\text{Bu}}$PNP = 2,6-(^{t}Bu$_2$PCH$_2$)$_2$C$_5$H$_3$N; Figure 1.11).[65] The active species is believed to be the monomeric complex [Mo($^{t\text{Bu}}$PNP)$(N_2)_3$] generated from initial protonation of the dimer, which subsequently undergoes essentially the same sequence of reaction steps as described in the Chatt cycle. Catalytic experiments utilised a vast excess of Cp_2Co and [LutH][OTf] (OTf = OSO_2CF_3) as a reductant and proton source, respectively, obtaining 11.8 equivalents of NH_3 in 49 % yield (based on reducing equivalents). However, yields were reduced with fewer proton/reductant

equivalents, whilst using the weaker reductant Cp_2Cr, resulted in no NH_3 being produced at all. Furthermore, the nature of the proton source had a pronounced effect, for instance substituting other lutidinium salts, [LutH][X] (X = $BArF_{24}^-$, Cl^-), resulted in dramatically reduced yields, thus further demonstrating the sensitivity of these systems to steric, electronic, and solubility factors.

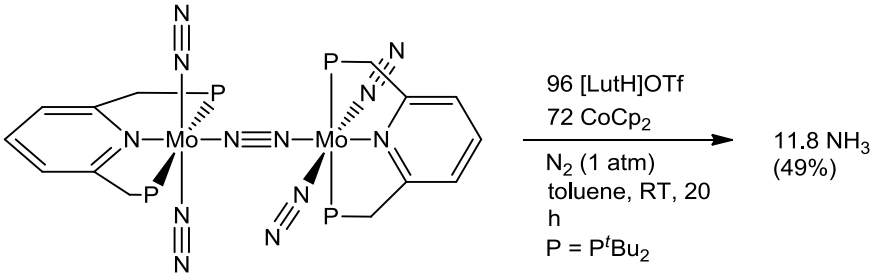


Figure 1.11 Catalytic NH_3 production using a homogeneous Mo catalyst, reported by Nishibayashi *et al.*.[65]

1.4.2 Fe systems

For many years, interest in Fe was overshadowed by the initial success of early transition metal model systems, in particular Mo and W, which were perceived to activate N_2 more strongly than Fe. However, since the crystallographic determination of seven Fe sites in the FeMoco cluster,[66] research into Fe systems continues to gain momentum, culminating in the recent report of the first catalytic system by Peters *et al.* (*vide infra*).[45]

The first major breakthrough in N_2 fixation using Fe was a reaction cycle reported by Leigh *et al.* in 1991, in which NH_3 was produced from N_2 coordinated to an Fe complex supported by chelating diphosphine ligands (Figure 1.12).[67] Sub-stoichiometric yields of NH_3 (up to 13% per Fe) are obtained in the acidification step, which is proposed to involve an Fe(0) complex, $Fe(N_2)(dmpe)_2$.[68] This species is generated *in situ* from reductive deprotonation of an Fe(II) hydrido N_2 complex, which may be considered to mimic the chemistry described by Hoffman *et al.* to occur at the active site of nitrogenase (*vide supra*), wherein reducing equivalents are stored in an Fe–H bond and subsequently transferred onto Fe. Ultimately, these electrons are sourced from the hydride reagent $NaBH_4$, which is incompatible with the base and acid employed, preventing the cycle being performed catalytically. In further contrast to the Mo and W systems, Fe is expected to undergo two-electron redox chemistry, cycling between Fe(0) and Fe(II) states. Accordingly, Leigh *et al.* proposed that three Fe(0) centres are required to reduce a single N_2 molecule, necessitating two of these Fe(0) centres to act as sacrificial reductants.

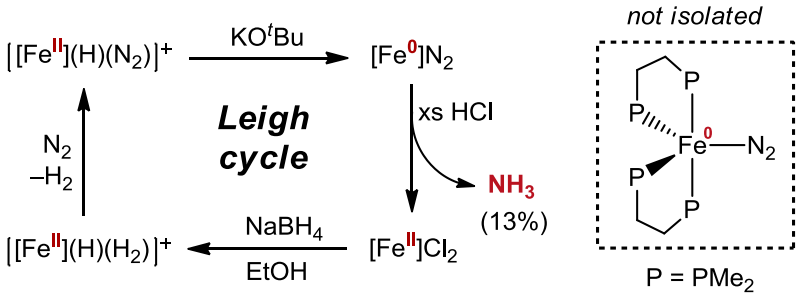


Figure 1.12 The Leigh cycle, involving Fe(0)-Fe(II); 13% yield of NH_3 per Fe; proposed active Fe(0) species highlighted on the right; [Fe] = [Fe(dmpe)$_2$]; BPh_4^- counteranion omitted.[67]

Several related systems involving deprotonation/reprotonation chemistry of Fe(II) hydrido N_2 complexes have been studied which yield similar quantities of NH_3. However, in almost all cases, the instability of Fe(0) intermediates has prevented their isolation and structural characterisation, casting uncertainty on the identities of the active species and limiting mechanistic understanding of the chemistry involved. A more comprehensive discussion of this seminal work on Fe and related research from the groups of Leslie Field and David Tyler is provided in the introduction to Chapter 3.

An approach more closely resembling Schrock's Mo system has been pursued by Peters *et al.*, pertaining to N_2 and reduced N_2 coordinated to Fe complexes of the tris(phosphino)borane (TPB = B{2-P^{i}Pr$_2$C$_6$H$_4$}$_3$) ligand scaffold (Figure 1.13), along with related systems with Si, C, and N substituted for B at the apical site.[45, 50, 69] The approximately trigonal bipyramidal geometries of these complexes were proposed to crudely mimic a plausible geometry of a single Fe in the FeMoco, whereby the interstitial C atom within the cluster is represented by the apical B/Si/C/N group. The parent [(TPB)Fe(N$_2$)][Na(THF)$_3$] complex (formally Fe(–I)) is prepared from Na/Hg reduction of (TPB)FeBr under N_2, and can be functionalised at the distal/β-N by trapping with electrophilic Me_3SiCl to form (TPB)Fe(NNSiMe$_3$; Figure 1.13).[70] Further reduction with Na/Hg yields the corresponding Na^+ bound anion [(TPB)Fe(NNSiMe$_3$)][Na(THF)], whilst performing the Na/Hg reduction of (TPB)FeBr in the presence of excess $Me_2Si(Cl)CH_2CH_2Si(Cl)Me_2$ provides access to the related disilylhydrazido(2–) complex. These transformations may be considered to mimic the first asymmetric protonation steps in an Fe-based Chatt cycle ([Fe]N$_2$ → [Fe]–N=NH → [Fe]≡N–NH$_2$) whereby silylium acts as a reductively stable proton surrogate.

The hemi-lability of the apical B group in these complexes *trans* to the N_2 or reduced N_2 ligand is proposed to account for its ability to stabilise both π-acidic N_2 and π-basic disilylhydrazido(2–) ligands. Accordingly, by adopting coordination modes between a zero-

electron donating neutral ligand (Z-type)[71] and a two-electron dianionic ligand (X_2-type), TPB is suggested to be able to stabilise the increasing Fe–N bond order arising from population of π*(N–N).[55]

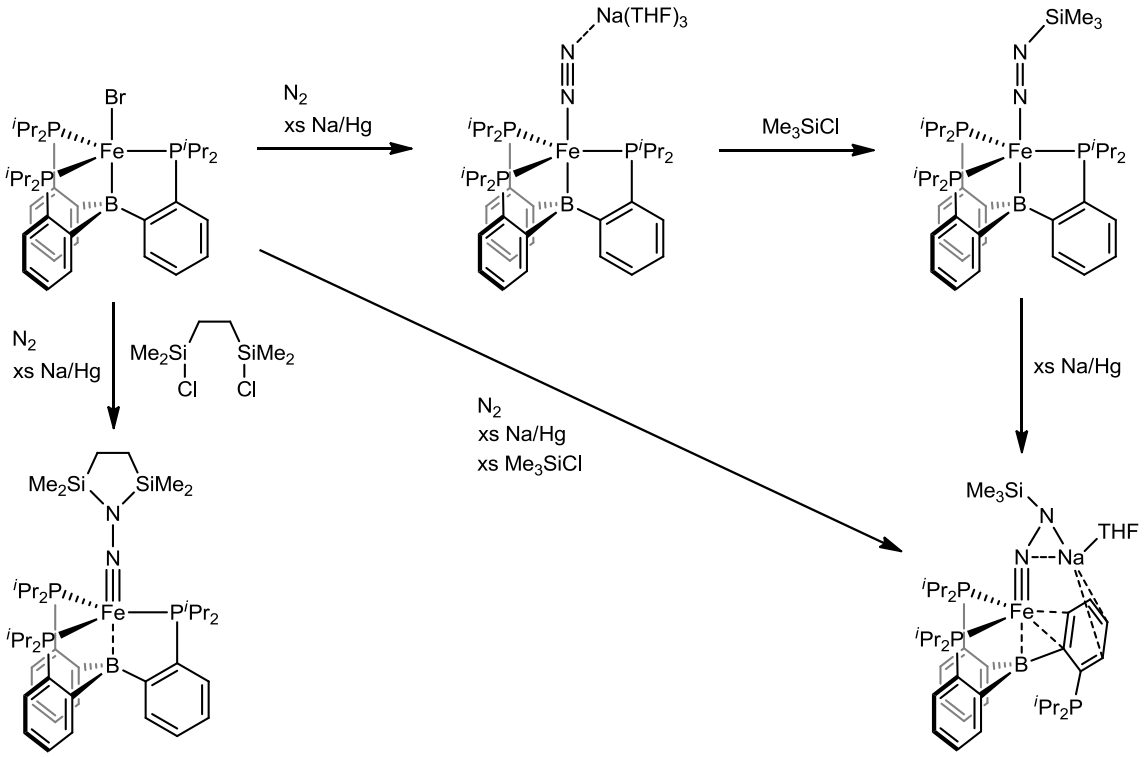


Figure 1.13 Transformations involving reduced N_2 coordinated to Fe complexes with a tris(phosphino)borane (TPB) ligand scaffold, reported by Peters *et al.*.[70]

The related Fe(0) complex [Fe(Si{2-P^{i}Pr$_2$C$_6$H$_4$}$_3$)(N$_2$)][Na(THF)$_3$] has also been prepared by Na naphthalenide reduction of the Fe(I) precursor Fe(Si{2-P^{i}Pr$_2$C$_6$H$_4$}$_3$)(N$_2$), and similarly reacts with Me_3SiCl to afford Fe(Si{2-P^{i}Pr$_2$C$_6$H$_4$}$_3$)(NNSiMe$_3$).[46] However, further reduction to the disilylhydrazido(2–) complex is thought to be inaccessible due to the lack of coordinative flexibility conferred by the anionic silyl ligand in contrast to neutral TPB.[70]

This work led the way towards achieving the first example of a homogeneous Fe system able to catalyse the fixation of N_2 to NH_3.[72] This was realised for [(TPB)FeN$_2$][Na(12-c-4)$_2$]] under a N_2 atmosphere at –78 °C, using an excess of HBArF$_{24}$·2Et$_2$O and KC_8 as a proton and electron source, respectively (Figure 1.14). 7.0 equivalents of NH_3 were produced per Fe in 44% efficiency (on the basis of reducing equivalents), whilst a similar yield of 6.2 equivalents was obtained for the Fe(I) precursor [(TPB)FeN$_2$][BArF$_{24}$]. Although less active than the Mo examples discussed earlier, this nevertheless indicates that a single Fe site may also be capable of stabilising all of the various intermediates of N_2 fixation and achieving catalytic turnover. Interestingly, under the same conditions the related tris(phosphino)silyl

complex $[(Si\{2\text{-}P^iPr_2C_6H_4\}_3)FeN_2][Na(12\text{-}c\text{-}4)_2]$ produces only sub-stoichiometric NH_3, whilst the tris(phosphino)alkyl complex $[(C\{2\text{-}P^iPr_2C_6H_4\}_3)FeN_2][K(Et_2O)_{0.5}]$ produced 4.6 equivalents of NH_3.[45] Thus, the performance of these complexes follows the trend in increasing flexibility of the apical donor group, Si < C < B; the greater flexibility for C relative to Si is proposed to be due to its enhanced ability to accommodate ionic charge. Although far from conclusive, this may bear relevance to the hypothesised role of the interstitial C atom in FeMoco in stabilising various N_xH_y reduction states through coordinative and redox flexibility.

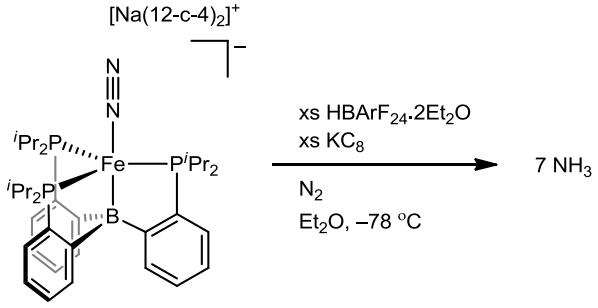


Figure 1.14 Catalytic NH_3 production using a homogeneous Fe catalyst, reported by Peters *et al.*.[72]

Of further interest is the effect of the Na^+ cation in $[Fe\{Si(2\text{-}P^iPr_2C_6H_4)_3\}(N_2)][Na(THF)_3]$, which is directly bound to the N_2 ligand (Figure 1.13). Upon exchanging the solvating THF ligands with 12-crown-4, Na^+ is sequestered and removed from the N_2 ligand, concomitant with an increase in the ν(N–N) stretch from 1891 to 1920 cm^{-1}.[46] Thus, it appears that the more Lewis acidic $[Na(THF)_3]^+$ cation provides additional activation of N_2, possibly by stabilising electron transfer from Fe into π*(N–N). A similar effect may be observed in the bimetallic Fe(0) complex $[\{Fe(\beta\text{-diketiminate-1})\}_2(\mu\text{-}N_2)][K]_2$ (β-diketiminate-1 = $\{(2,6\text{-}(^iPr)_2C_6H_3)NC(^tBu)\}_2CH$; Figure 1.15) reported by Holland *et al.*, in which two K^+ ions may contribute to the strong activation of the bridging N_2 ligand (ν(N–N) = 1589 cm^{-1}).[51]

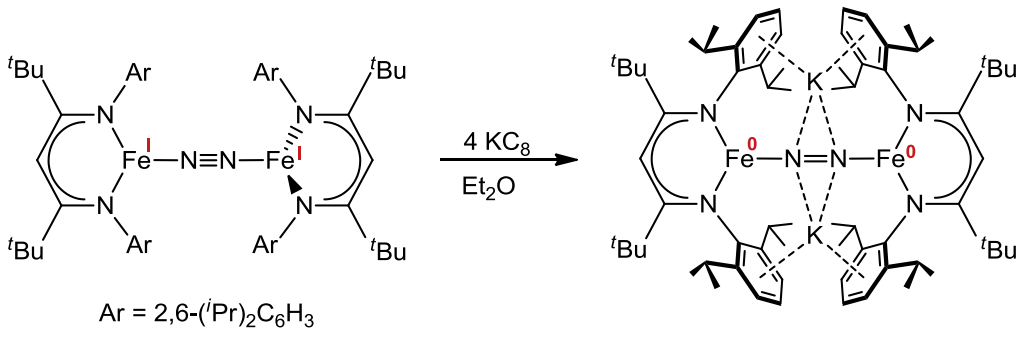


Figure 1.15 Increased activation of a bridging N_2 ligand in a bimetallic Fe(I) complex upon reduction to Fe(0), reported by Holland *et al.*.[51]

Notably, the Fe(I) precursor also exhibits strongly activated N_2 (ν(N–N) = 1778 cm^{-1}), which the authors suggest arises from the promotion of π-backdonation in these low-coordinate Fe complexes. Thus, upon reduction to the bimetallic Fe(0) complex, occupancy of π*(N–N) is further induced and additionally stabilised by K^+, resulting in an overall reduction in the N–N bond order. Although the resultant complex is reminiscent of the incorporation of K(I) oxide in the Fe Haber-Bosch catalyst, it nevertheless results from a K (KC_8) mediated reduction.

KC_8 reduction under N_2 of a related Fe(II) precursor incorporating less bulky aryl groups, [Fe(β-diketiminate-2)(μ-Cl)]$_2$ (β-diketiminate-2 = {(2,6-$(Me)_2C_6H_3$)NC(Me)}$_2$CMe), resulted in an unusual N–N cleavage reaction rather than expected formation of a bimetallic Fe(I) N_2 complex (Figure 1.16).[73]

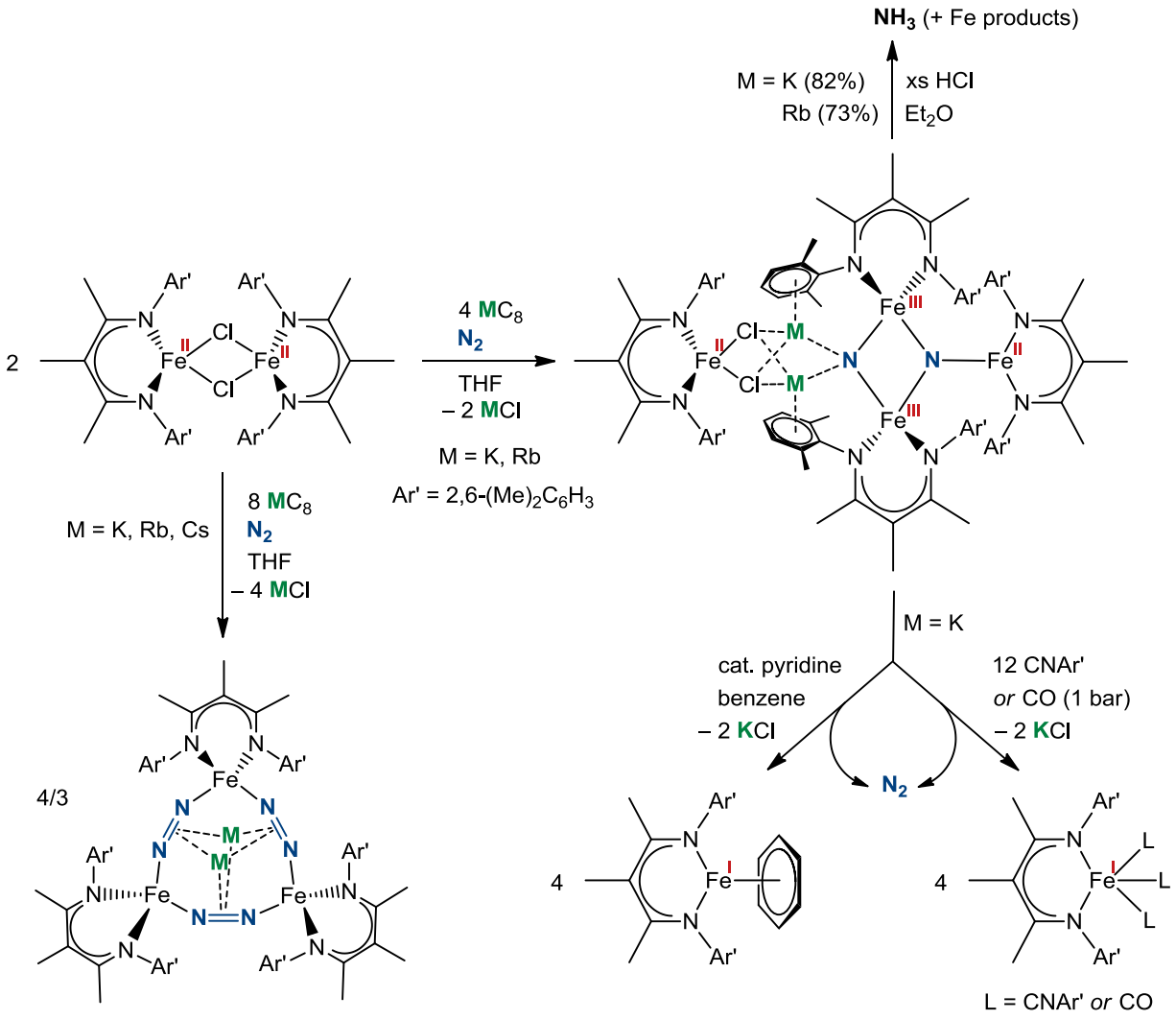


Figure 1.16 N_2 activation or cleavage from the MC_8 (M = K, Rb, Cs) reduction of a bimetallic Fe(II) β-diketiminate complex under N_2, reported by Holland *et al.*.[73, 74]

In the mixed valent Fe(II)/Fe(III) nitride product, one of the N^{3-} ligands appears to be similarly stabilised by two tightly bound K^+ ions, which are encapsulated by the π-system of the surrounding aryl groups. The dissociative reduction of N_2 in this reaction is further demonstrated upon acidification by the formation of NH_3 in 82% yield from protonation of the N^{3-} ligands. This represents an alternative strategy to the previous systems in that all of the reducing equivalents are delivered to N_2 prior to N–H bond forming steps, which mimics formation of nitrides on the Fe surface of the Haber-Bosch catalyst from dissociation of adsorbed N_2. Interestingly, N_2 can be reformed by the addition of Lewis bases (pyridine, CO, CN-2,6-$(Me)_2C_6H_3$) *via* coupling of the two nitride ligands.[74] This is thought to be driven by precipitation of KCl by-product and stabilisation of Fe(I) by the π-accepting β-diketiminate ligands; since the process began with an Fe(II) complex, the bond dissociation/reforming of N_2 is not truly reversible, although use of one equivalent of KC_8 per initial Fe(II) may implicate a transient Fe(I) intermediate.

The reduction of [Fe(β-diketiminate-2)(μ-Cl)]$_2$ with RbC_8 (two equivalents) provided the analogous Fe(II)/Fe(III) nitride complex.[75] Interestingly, when the number of reducing equivalents was increased from one to two MC_8 (M = K, Rb, Cs) per Fe(II) centre, trimetallic Fe(0–I) complexes M_2[(β-diketiminate-2)Fe(μ-N_2)]$_3$ (M = K, Rb, Cs) were formed, in which the three bridging N_2 ligands are activated but are not cleaved. This suggests that the degree of N_2 activation is not solely dependent on the number of external reducing equivalents; the reducing power of these graphite intercalation compounds of K, Rb and Cs metal are not expected to vary significantly since the reducing electrons are on the graphite layers. Holland *et al.* have performed computational work indicating that N_2 cleavage is only thermodynamically favourable when at least three β-diketiminate ($C_3N_2H_5^-$) Fe(I) fragments, an additional electron, and a K^+ ion are present.[76] Thus, the authors suggest that in the case of over-reduction, the cation–π interactions in the resultant structures prevent the approach of a third Fe centre, limiting the degree of N_2 activation. Furthermore, this may explain why the N_2 ligand is not cleaved in the previously discussed bimetallic Fe(I) N_2 complex with bulkier β-diketiminate ligands (Figure 1.15).

The Fe(II)/Fe(III) nitride complexes discussed above are the only examples of strong activation of Fe-bound N_2 resulting in complete N_2 bond cleavage. In contrast, this chemistry has been established for a number of N_2 complexes of early-transition metals (V, Nb, Ta, Mo), typically driven by oxidation of the metal centre and formation of strong, multiple M–N bonds.[77] For example, Cloke *et al.* reported the reduction of a bimetallic V(III) diamidoamine complex [V($Me_3SiN\{CH_2CH_2NSiMe_3\}_2$)(μ-Cl)]$_2$ under N_2 forms a V(V)/V(V) complex [V($Me_3SiN\{CH_2CH_2NSiMe_3\}_2$)(μ-N)]$_2$ in which a cleaved N_2 forms two bridging nitrido ligands (Figure 1.17).[78] Theoretical studies have indicated that an intermediate V(II) complex may

coordinate N_2 side-on prior to reaction with a second V(II) centre, resulting in concomitant N_2 reduction and V oxidation.[79] Further reduction of $[V(Me_3SiN\{CH_2CH_2NSiMe_3\}_2)(\mu\text{-}N)]_2$ affords the anionic V(V)/V(IV) dimer $K[V(Me_3SiN\{CH_2CH_2NSiMe_3\}_2)(\mu\text{-}N)]_2$, which exhibits tighter bonding within the V_2N_2 core and a dissociated amine group.

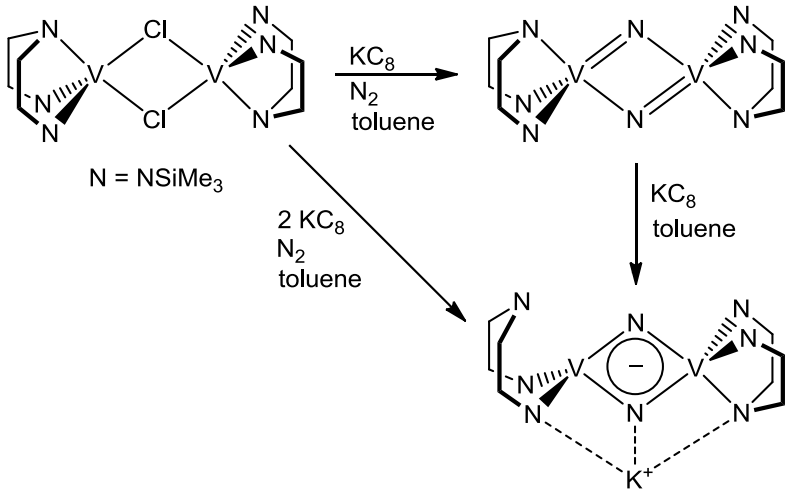


Figure 1.17 Reductive N_2 cleavage by a V(III) diamidoamine complex.[78]

1.4.3 Hydrogenation of transition metal coordinated N_2

Research into homogeneous N_2 fixation has mainly focused on a biomimetic approach involving the use of strong chemical reductants and acids. Despite H_2 being the only industrially viable reductant and proton source for N_2 fixation, to date few homogeneous examples have been reported which utilise H_2 for both these roles, and none involving Fe.

For the Leigh-type system reported by Tyler *et al.* based on the deprotonation/reprotonation of $[$*trans*-$Fe(H)(N_2)(DMeOPrPE)]^+$ (DMeOPrPE = $[\{MeO(CH_2)_3\}_2PCH_2]_2$), it is possible to substitute H_2 for the hydride reagent ($NaBH_4$) in the original cycle since the intermediate complex *trans*-$Fe(H)(H_2)(DMeOPrPE)]^+$ can be accessed directly from *trans*-$Fe(Cl)_2(DMeOPrPE)_2$ and H_2 (Figure 1.18).[37] Thus, the reduction of N_2 is ultimately performed by H_2 coupled with base, although protonation to NH_3 and N_2H_4 still requires the use of excess acid.

Of particular relevance to the Haber Bosch process is the production of NH_3 from the direct reaction of strongly activated nitride complexes with H_2. H_2 heterolysis across the Fe–N bonds of the highly reduced Fe(II)/Fe(III) nitride complex reported by Holland *et al.* (*vide supra*) could potentially yield NH_3; however, this was only detected upon subsequent acid work-up.[73] Thus, whilst partial protonation may occur from H_2, the only characterised product

of this reaction was the bimetallic Fe(II) bis(μ-hydride) complex [{Fe(β-diketiminate-2)}$_2$(μ-H)$_2$].

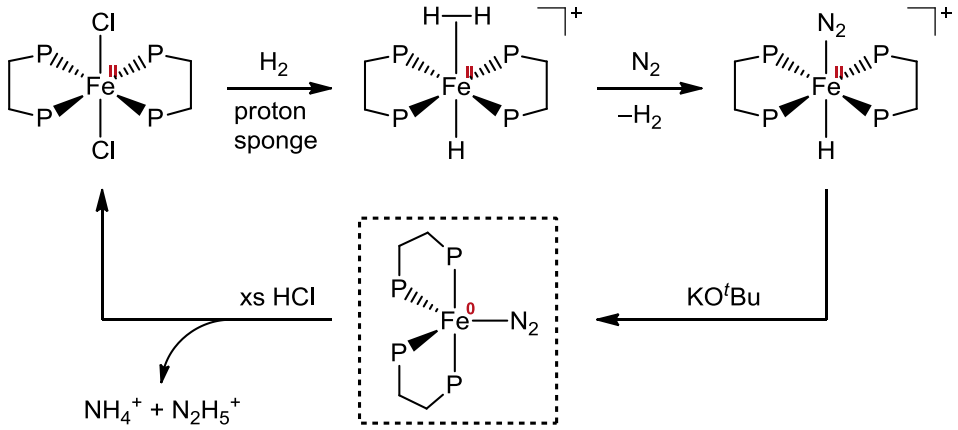


Figure 1.18 Modification of the Leigh cycle reported by Tyler *et al.*; P = P{(CH$_2$)$_3$OMe}$_2$; proton sponge = 1,8-bis(dimethylamino)naphthalene.[37]

Although several early transition metals have been shown to cleave N_2 to form nitrides, subsequent reactivity with H_2 is rare. Of such examples, the most successful is the bimetallic Zr(IV) complex [{(η^5-C$_5$HMe$_4$)$_2$Zr}$_2${μ$_2$, η^2, η^2-N$_2$}] (prepared from Na/Hg reduction of (η^5-C$_5$HMe$_4$)$_2$ZrCl$_2$ under N_2), which formally contains two Zr(IV) centres and N_2^{4-} (Figure 1.19).[80] Reaction with H_2 forms the diazinido species [{(η^5-C$_5$HMe$_4$)$_2$Zr}$_2${N$_2$H$_2$}], which subsequently liberates NH_3 (10–15% yield) upon warming to 85 °C under a H_2 atmosphere. In the absence of H_2, thermal decomposition results in a nitrido (μ-N^{3-}) and amido (μ-NH$_2^-$) bridged complex in which the Zr–N bonds remain intact. Whilst the reduction mechanism is uncertain and may possibly involve disproportionation of hydrazine, protonation at N is believed to occur *via* H_2 heterolysis across the Zr–N bonds.

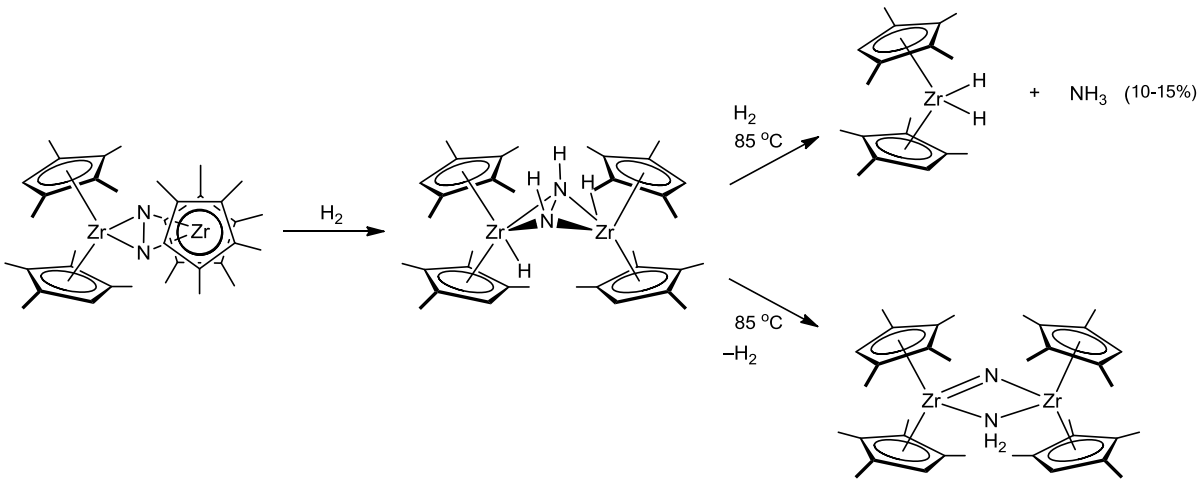


Figure 1.19 Hydrogenation and N_2 cleaving reactions of a bimetallic Zr(IV) complex reported by Chirik *et al.*.[80]

Similar nitride hydrogenolysis has been observed for a Ru(IV) nitride complex, although notably the nitride moiety was accessed from an azide rather than N_2 (Figure 1.20).[81]

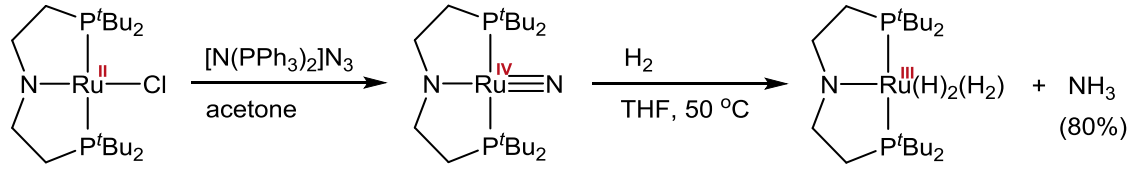


Figure 1.20 Hydrogenation of a Ru nitride complex reported by Schneider *et al.*.[81]

An alternative strategy employed by Hidai *et al.* is to activate N_2 and H_2 on separate complexes.[82] Accordingly, N_2 coordinated to W(0) in *cis*-W$(N_2)_2$(PMe$_2$Ph)$_4$ is successively protonated by the Ru(II) complex [Ru(Cl)(η^2-H_2)$(PP)_2$]$^+$ (PP = dppe, dppp; Figure 1.21) in which the σ-H_2 ligand is acidic (pseudo-aqueous pK_a = 6.0 {dppe}, 4.4 {dppp}). Unfortunately, heterolysis of σ-H_2 only delivers one proton, with the resulting Ru–H bond inaccessible as either a source of H^+ or electrons. Thus, six equivalents of [Ru(Cl)(η^2-H_2)$(PP)_2$]$^+$ are required, and all of the reducing electrons must be provided by W(0), preventing catalytic production of NH_3 (79% yield based on W).

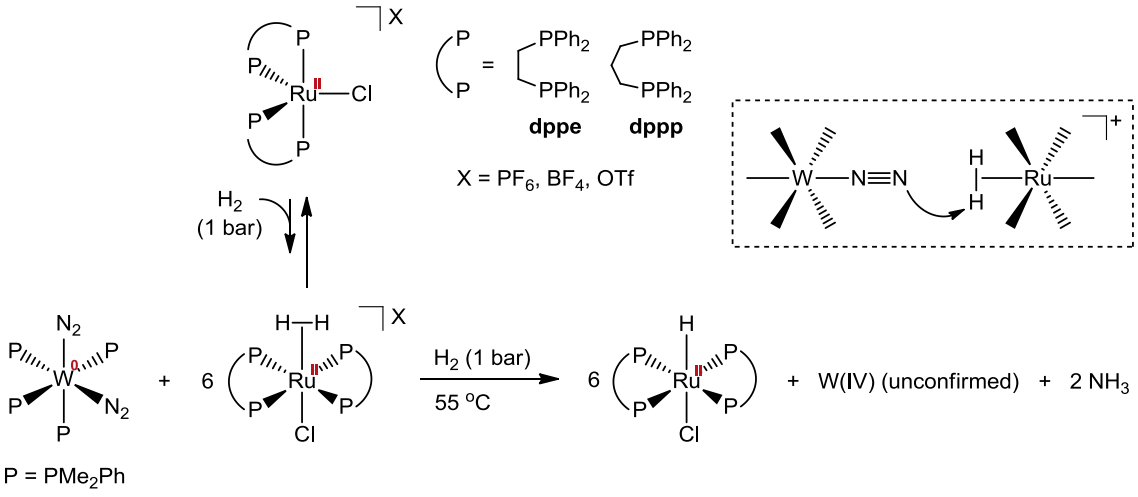


Figure 1.21 Hydrogenation of W-activated N_2 by a Ru σ-H_2 complex, reported by Hidai *et al.*.[82]

1.5 Summary

Improving our understanding of the fundamental chemistry performed by nitrogenases has proved to be a formidable challenge. Recent successes in developing homogeneous models provide increasing incentive to pursue this chemistry, and whilst a homogeneous replacement for the Haber Bosch process remains a distant prospect for the moment, these

systems may provide mechanistic insight that is not easily accessible for heterogeneous catalysts. Furthermore, N_2 fixation represents a benchmark of catalysis, enabling an otherwise kinetically unfeasible reaction to be performed as one of the largest scale industrial processes on the planet.

The homogeneous systems discussed are typically most closely related to biological nitrogen fixation, involving weak activation of N_2, with sequential delivery of protons and electrons to afford NH_3. These systems show considerable dependence on the choice of reductant and proton source, which are invariably more potent than those biologically accessible. However, the coordination environments of the simple model complexes employed are fairly crude in comparison to nitrogenase, which is one of the most complex enzymes known.[83] Nevertheless, catalytic N_2 fixation has now been shown to be possible for monomeric complexes of both Fe and Mo, although it still remains uncertain whether biological fixation occurs at a single or multiple metal site(s).

In contrast, strong activation of N_2 typically requires coordination of N_2 to at least two metal centres, possibly reflecting a multi-metallic approach occurring at the surface of the Haber Bosch catalyst. Several examples of reductive dissociation of N_2 to form nitride complexes have been established, whilst subsequent reactivity with H_2 is limited to only a few examples and yields of NH_3 remain low. Protonation at N is thought to occur *via* H_2 heterolysis across the M–N bond, with concurrent formation of metal hydrides. Thus the challenge will be to access the remaining two electrons and proton within the M–H bond in order to fully utilise H_2 as both a reductant and proton source. In this manner, it may be possible to perform homogeneous catalytic N_2 fixation using H_2. Although it is perhaps unrealistic to expect a homogeneous system to replace the Haber Bosch in this century, research into homogenous systems may provide the key to unlocking lower energy pathways that ultimately provide a sustainable method for meeting the global requirement for fixed N_2.

1.6 Thesis aims

The reaction cycle reported by Leigh *et al.* remains a seminal work on homogeneous N_2 fixation performed at Fe; however, the mechanism by which protonation and reduction of N_2 occurs in this system is still unresolved. Thus, the aim of this work was to identify, isolate and characterise the key reaction intermediates, utilising a suite of spectroscopic techniques (NMR, UV-vis, EPR, IR, and Raman, *inter alia*). Greater understanding of these species may provide a more general insight into kinetically feasible pathways through which N_2 may be

converted into NH_3, with the ultimate aim to develop a more energy efficient solution to current industrial methods.

1.7 References

1. Howard, J. B.; Rees, D. C., *Chem. Rev.*, **1996**, *96* (7), 2965-2982.
2. Burgess, B. K.; Lowe, D. J., *Chem. Rev.*, **1996**, *96* (7), 2983-3011.
3. Seefeldt, L. C.; Hoffman, B. M.; Dean, D. R., *Annu. Rev. Biochem.*, **2009**, *78*, 701-722.
4. Hoffman, B. M.; Dean, D. R.; Seefeldt, L. C., *Acc. Chem. Res.*, **2009**, *42* (5), 609-619.
5. Nielsen, A., *Ammonia: Catalysis and Manufacture*, Springer-Verlag Berlin and Heidelberg GmbH & Co. K, **1995**.
6. Smil, V., *Nature*, **1999**, *400* (6743), 415-415.
7. Fryzuk, M. D., *Nature* **2004**, *427* (6974), 498-499.
8. Appl, M., *Ammonia: Principles and Industrial Practice*, Wiley-VCH, Weinheim, **1999**.
9. Smith, B. E., *Science*, **2002**, *297* (5587), 1654-1655.
10. Hazari, N., *Chem. Soc. Rev.*, **2010**, *39* (11), 4044-4056.
11. MacLeod, K. C.; Holland, P. L., *Nat. Chem.*, **2013**, *5* (7), 559-565.
12. Shilov, A. E., *Russ. Chem. B+,* **2003**, *52* (12), 2555-2562.
13. Jia, H-P.; Quadrelli, E. A., *Chem. Soc. Rev.*, **2014**, *43* (2), 547-564.
14. Zhan, C. G.; Nichols, J. A.; Dixon, D. A., *J. Phys. Chem. A*, **2003**, *107* (20), 4184-4195.
15. Mittasch, A., *Geschichte der Ammoniaksynthese (History of the synthesis of ammonia)*, Verlag Chemie, Weinheim, **1951**.
16. Vancini, C. A., *Synthesis of Ammonia*, Macmillan Press, London, **1971**.
17. Ertl, G.; Thiele, N., *Appl. Surf. Sci.*, **1979**, *3* (1), 99-112.
18. Ertl, G., *J. Vac. Sci. Technol., A*, **1983**, *1* (2), 1247-1253.
19. Ertl, G.; Weiss, M.; Lee, S. B., *Chem. Phys. Lett.*, **1979**, *60* (3), 391-394.
20. Ertl, G., *Angew. Chem. Int. Ed.*, **2008**, *47* (19), 3524-3535.
21. Spencer, N. D.; Schoonmaker, R. C.; Somorjai, G. A., *J. Catal.*, **1982**, *74* (1), 129-135.
22. Postgate, J., *Nitrogen Fixation, 3rd Edition*, Cambridge University Press, Cambridge, **1998**.
23. Hu, Y.; Ribbe, M. W., *J. Biol. Inorg. Chem.*, **2015**, *20* (2), 435-445.
24. a) Einsle, O.; Tezcan, F. A.; Andrade, S. L. A.; Schmid, B.; Yoshida, M.; Howard, J. B.; Rees, D. C., *Science*, **2002**, *297* (5587), 1696-1700; b) Spatzal, T.; Aksoyoglu, M.; Zhang, L.; Andrade, S. L. A.; Schleicher, E.; Weber, S.; Rees, D. C.; Einsle, O., *Science*, **2011**, *334* (6058), 940-940; c) Lancaster, K. M.; Roemelt, M.; Ettenhuber, P.; Hu, Y.; Ribbe, M. W.; Neese, F.; Bergmann, U.; DeBeer, S., *Science*, **2011**, *334* (6058), 974-977.
25. Hoffman, B. M.; Lukoyanov, D.; Yang, Z.-Y.; Dean, D. R.; Seefeldt, L. C., *Chem. Rev.*, **2014**, *114* (8), 4041-4062.
26. Chatt, J.; Dilworth, J. R.; Richards, R. L., *Chem. Rev.*, **1978**, *78* (6), 589-625.
27. Allen, A. D.; Senoff, C. V., *Chem. Commun.*, **1965**, (24), 621-622.

28. Fryzuk, M. D., *Acc. Chem. Res.*, **2009**, *42* (1), 127-133.
29. a) Dewar, M., *Bull. Soc. Chim. Fr.*, **1951**, *1* (8), C71-79; b) Chatt, J.; Duncanson, L. A., *J. Chem. Soc.*, **1953**, (0), 2939-2947.
30. Shaver, M. P.; Fryzuk, M. D., *Adv. Synth. Catal.*, **2003**, *345* (9-10), 1061-1076.
31. Deeth, R. J.; Field, C. N., *J. Chem. Soc., Dalton Trans.*, **1994**, (13), 1943-1948.
32. Postgate, J., *The Chemistry and Biochemistry of Nitrogen Fixation*, Springer, US, **1971**.
33. Hills, A.; Hughes, D. L.; Jimenez-Tenorio, M.; Leigh, G. J.; Rowley, A. T., *J. Chem. Soc., Dalton Trans.*, **1993**, (20), 3041-3049.
34. a) Buys, I. E.; Field, L. D.; Hambley, T. W.; McQueen, A. E. D., *Acta Crystallogr., Sect. C: Cryst. Struct. Commun.*, **1993**, *49*, 1056-1059; b) Franke, O.; Wiesler, B. E.; Lehnert, N.; Tuczek, F., *Z. Anorg. Allg. Chem.*, **2002**, *628* (11), 2395-2402.
35. Franke, O.; Wiesler, B. E.; Lehnert, N.; Peters, G.; Burger, P.; Tuczek, F., *Z. Anorg. Allg. Chem.*, **2006**, *632* (7), 1247-1256.
36. Gilbertson, J. D.; Szymczak, N. K.; Tyler, D. R., *J. Am. Chem. Soc.*, **2005**, *127* (29), 10184-10185.
37. Crossland, J. L.; Young, D. M.; Zakharov, L. N.; Tyler, D. R., *J. Chem. Soc., Dalton Trans.* **2009**, (42), 9253-9259.
38. Stoppion, P.; Mani, F.; Sacconi, L., *Inorg. Chim. Acta*, **1974**, *11* (3), 227-230.
39. George, T. A.; Rose, D. J.; Chang, Y. D.; Chen, Q.; Zubieta, J., *Inorg. Chem.*, **1995**, *34* (5), 1295-1298.
40. Aresta, M.; Giannoccaro, P.; Rossi, M.; Sacco, A., *Inorg. Chim. Acta*, **1971**, *5* (0), 203-206.
41. Sacco, A.; Aresta, M., *Chem. Commun.* **1968**, (20), 1223-1224.
42. Vandersluys, L. S.; Eckert, J.; Eisenstein, O.; Hall, J. H.; Huffman, J. C.; Jackson, S. A.; Koetzle, T. F.; Kubas, G. J.; Vergamini, P. J.; Caulton, K. G., *J. Am. Chem. Soc.*, **1990**, *112* (12), 4831-4841.
43. Borodko, Y. G.; Broitman; Kachapin.Lm; Shilova, A. K.; Shilov, A. E., *Zh. Strukt. Khim.*, **1971**, *12* (3), 545-&.
44. Leal, A. D.; Tenorio, M. J.; Puerta, M. C.; Valerga, P., *Organometallics*, **1995**, *14* (8), 3839-3847.
45. Creutz, S. E.; Peters, J. C., *J. Am. Chem. Soc.*, **2014**, *136* (3), 1105-1115.
46. Lee, Y.; Mankad, N. P.; Peters, J. C., *Nature Chem.*, **2010**, *2* (7), 558-565.
47. Silverthorn, W. E., *J. Chem. Soc., Chem. Commun.*, **1971**, (20), 1310-1311.
48. Huttner, G.; Müller, H-D., *Angew. Chem. Int. Ed.*, **1975**, *14* (8), 571-572.
49. Field, L. D.; Messerle, B. A.; Smernik, R. J., *Inorg. Chem.*, **1997**, *36* (26), 5984-5990.
50. Mankad, N. P.; Whited, M. T.; Peters, J. C., *Angew. Chem. Int. Ed.*, **2007**, *46* (30), 5768-5771.
51. Smith, J. M.; Lachicotte, R. J.; Pittard, K. A.; Cundari, T. R.; Lukat-Rodgers, G.; Rodgers, K. R.; Holland, P. L., *J. Am. Chem. Soc.*, **2001**, *123* (37), 9222-9223.
52. a) Komiya, S.; Akita, M.; Yoza, A.; Kasuga, N.; Fukuoka, A.; Kai, Y., *J. Chem. Soc., Chem. Commun.*, **1993**, (9), 787-788; b) Perthuisot, C.; Jones, W. D., *New J. Chem.*, **1994**, *18* (5), 621-628.
53. Cable, R. A.; Green, M.; Mackenzie, R. E.; Timms, P. L.; Turney, T. W., *J. Chem. Soc., Chem. Commun.*, **1976**, (7), 270-271.
54. Field, L. D.; Guest, R. W.; Vuong, K. Q.; Dalgarno, S. J.; Jensen, P., *Inorg. Chem.*, **2009**, *48* (5), 2246-2253.
55. Moret, M-E.; Peters, J. C., *Angew. Chem. Int. Ed.*, **2011**, *50* (9), 2063-2067.

56. Chatt, J.; Pearman, A. J.; Richards, R. L., *Nature*, **1975**, *253* (5486), 39-40.
57. Chatt, J.; Pearman, A. J.; Richards, R. L., *J. Chem. Soc., Dalton Trans.*, **1977**, (19), 1852-1860.
58. Hidai, M., *Coord. Chem. Rev.*, **1999**, *185-6*, 99-108.
59. Van Tamelen, E. E.; Gladysz, J. A.; Miller, J. S., *J. Am. Chem. Soc.*, **1973**, *95* (4), 1347-1348.
60. Brulet, C. R.; Van Tamelen, E. E., *J. Am. Chem. Soc.*, **1975**, *97* (4), 911-912.
61. Pickett, C. J., *J. Biol. Inorg. Chem.*, **1996**, *1* (6), 601-606.
62. Schrock, R. R., *Philos. Trans. R. Soc. London, Ser. A*, **2005**, *363* (1829), 959-969.
63. Yandulov, D. V.; Schrock, R. R., *Science*, **2003**, *301* (5629), 76-78.
64. Schrock, R. R., *Acc. Chem. Res.* **2005**, *38* (12), 955-962.
65. Arashiba, K.; Miyake, Y.; Nishibayashi, Y., *Nature Chem.*, **2011**, *3* (2), 120-125.
66. Chan, M. K.; Kim, J. S.; Rees, D. C., *Science*, **1993**, *260* (5109), 792-794.
67. Leigh, G. J.; Jimenez-Tenorio, M., *J. Am. Chem. Soc.*, **1991**, *113* (15), 5862-5863.
68. Hall, D. A.; Leigh, G. J., *J. Chem. Soc., Dalton Trans.*, **1996**, (17), 3539-3541.
69. a) Betley, T. A.; Peters, J. C., *J. Am. Chem. Soc.*, **2003**, *125* (36), 10782-10783; b) MacBeth, C. E.; Harkins, S. B.; Peters, J. C., *Can. J. Chem.*, **2005**, *83* (4), 332-340.
70. Moret, M-E.; Peters, J. C., *J. Am. Chem. Soc.*, **2011**, *133* (45), 18118-18121.
71. Green, M. L. H., *J. Organomet. Chem.*, **1995**, *500* (1–2), 127-148.
72. Anderson, J. S.; Rittle, J.; Peters, J. C., *Nature*, **2013**, *501* (7465), 84-87.
73. Rodriguez, M. M.; Bill, E.; Brennessel, W. W.; Holland, P. L., *Science*, **2011**, *334* (6057), 780-783.
74. MacLeod, K. C.; Vinyard, D. J.; Holland, P. L., *J. Am. Chem. Soc.*, **2014**, *136* (29), 10226-10229.
75. Grubel, K.; Brennessel, W. W.; Mercado, B. Q.; Holland, P. L., *J. Am. Chem. Soc.*, **2014**, *136* (48), 16807-16816.
76. Figg, T. M.; Holland, P. L.; Cundari, T. R., *Inorg. Chem.*, **2012**, *51* (14), 7546-7550.
77. Fryzuk, M. D.; Johnson, S. A., *Coord. Chem. Rev.*, **2000**, *200*, 379-409.
78. Clentsmith, G. K. B.; Bates, V. M. E.; Hitchcock, P. B.; Cloke, F. G. N., *J. Am. Chem. Soc.*, **1999**, *121* (44), 10444-10445.
79. Bates, V. M. E.; Clentsmith, G. K. B.; Cloke, F. G. N.; Green, J. C.; Jenkin, H. D. L., *Chem. Commun.*, **2000**, (11), 927-928.
80. Pool, J. A.; Lobkovsky, E.; Chirik, P. J., *Nature*, **2004**, *427* (6974), 527-530.
81. Askevold, B.; Nieto, J. T.; Tussupbayev, S.; Diefenbach, M.; Herdtweck, E.; Holthausen, M. C.; Schneider, S., *Nature Chem.*, **2011**, *3* (7), 532-537.
82. Nishibayashi, Y.; Takemoto, S.; Iwai, S.; Hidai, M., *Inorg. Chem.*, **2000**, *39* (26), 5946-5957.
83. Rubio, L. M.; Ludden, P. W., *Annu. Rev. Microbiol.*, **2008**, *62*, 93-111.

Chapter 2: A convenient synthetic protocol to 1,2-bis(dialkylphosphino)ethanes

2.1 Introduction

Organophosphines (R_3P) are prime candidates for use as ancillary ligands in many transition metal catalysed transformations, and are arguably the most important class of spectator ligand in organometallic chemistry.[1] Analogous to the lighter group 15 element, nitrogen, trivalent phosphorus(III) forms comparatively softer Lewis bases (σ-donors) with a less tightly bound lone pair due to the lower electronegativity and larger atomic radii of phosphorus. In addition, vacant 3d and σ*(P–C) orbitals facilitate a π-backbonding mode with transition metals, conferring the ligand with additional Lewis acidic character. Hence, substitution at the phosphorus atom has a considerable effect on both the steric and electronic influence of the ligand over the metal centre, which enables fine tuning of catalyst reactivity and stability.[2]

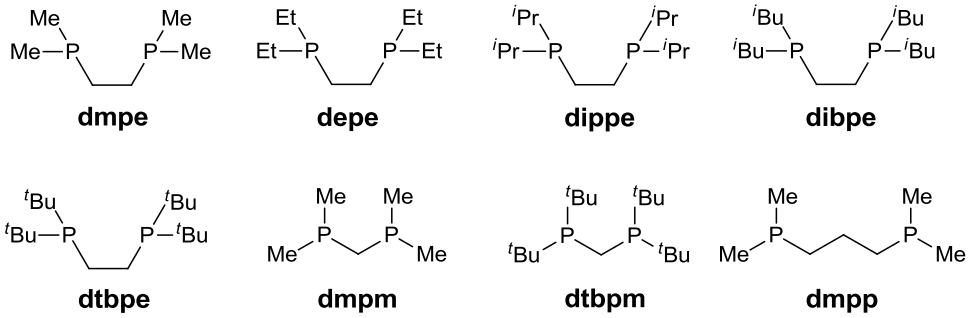


Figure 2.1 Common bidentate tertiary alkyl *bis*phosphine ligands with their abbreviations.

Although less common, alkyl phosphines are more electron-donating than their aryl phosphine counterparts and can therefore be more effective in promoting key oxidative addition steps common to catalytic cycles (e.g. alkene hydrogenation, hydroformylation).[3] In particular, 1,2-bis(dialkylphosphino)ethanes ($R_2PCH_2CH_2PR_2$; Figure 2.1) have found myriad applications in a number of important transformations as electron-rich chelating ligands. These include heterolytic H_2 activation (Co, Rh, Group 10 triad; Figure 2.2(a)),[4] C–H bond activation (Pt),[5] CO_2 reduction (Fe, Ni, Pt),[6] and N_2 fixation (Fe, Mo).[7] They have also facilitated the isolation of structurally interesting molecules incorporating ligand C–H agostic interactions (Ti)[8] and recently a σ-alkane complex (Rh; Figure 2.2(b)).[9]

Despite their utility, the syntheses of these simple yet versatile ligands can be lengthy and involve dangerous (highly toxic and pyrophoric) or costly reagents; consequently, related aryl

phosphine ligands that are far less air-sensitive and more readily prepared have hitherto been utilised to a greater extent. Although commercially available, both dmpe and depe are prohibitively expensive (Sigma Aldrich, April 2015: £113 and £93 per gram, respectively) and in order to investigate N_2 activation of Fe complexes bearing these ligands it was therefore necessary to evaluate their syntheses.

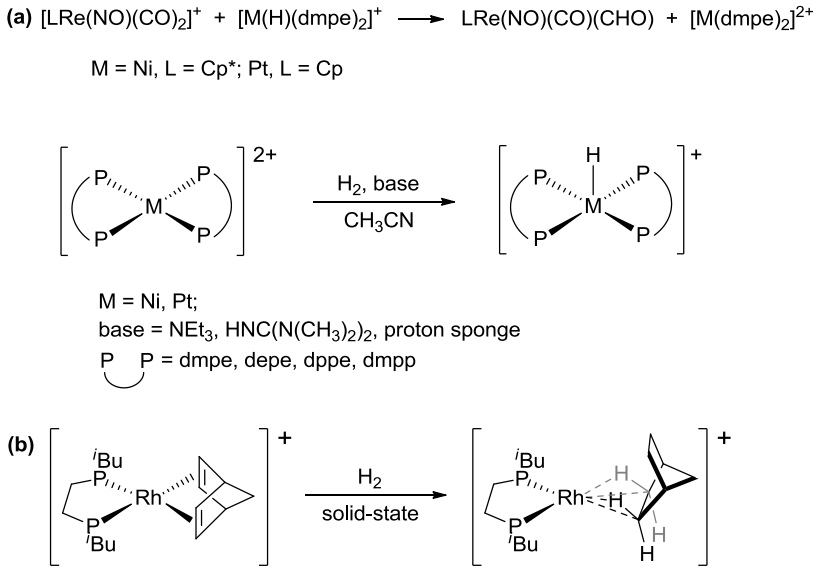


Figure 2.2 Alkyl bisphosphine complexes: (a) heterolytic cleavage of H_2 to form strong hydride donors for CO reduction; proton sponge = 1,8-bis(dimethylamino)naphthalene (b) solid-state H_2 heterolysis to form a σ-alkane Rh(I) complex.

2.2 Synthesis of bidentate alkyl phosphine ligands

The difficulty in preparing alkyl bisphosphines is conveniently illustrated by the synthetic protocols reported for 1,2-bis(dimethylphosphino)ethane ($Me_2PCH_2CH_2PMe_2$, dmpe; Figure 2.3). Generation of a phosphide precursor involves either $NaNH_2/NH_{3(l)}$ deprotonation of pyrophoric Me_2PH (from PH_3),[10] or Na reduction of $Me_2PCl/Me_2P\text{-}PMe_2$.[11] Other modifications have utilised $Me_2P(S)\text{-}P(S)Me_2$,[12,13] a precursor to $Me_2P\text{-}PMe_2$, which is prepared *via* a dangerous reaction of MeMgI with $P(=S)Cl_3$, that has in one case led to a severe accident.[14] Alkylation of $Cl_2PCH_2CH_2PCl_2$ affords $R_2PCH_2CH_2PR_2$ species in moderate yields, yet synthesis of the precursor requires specialised autoclave apparatus ($P/PCl_3/CH_2{=}CH_2$; 200°C, 70 atm)[15] or chlorination of highly pyrophoric $H_2PCH_2CH_2PH_2$.[16] Whilst $Cl_2PCH_2CH_2PCl_2$ is commercially available, its expense limits large-scale syntheses of $R_2PCH_2CH_2PR_2$.

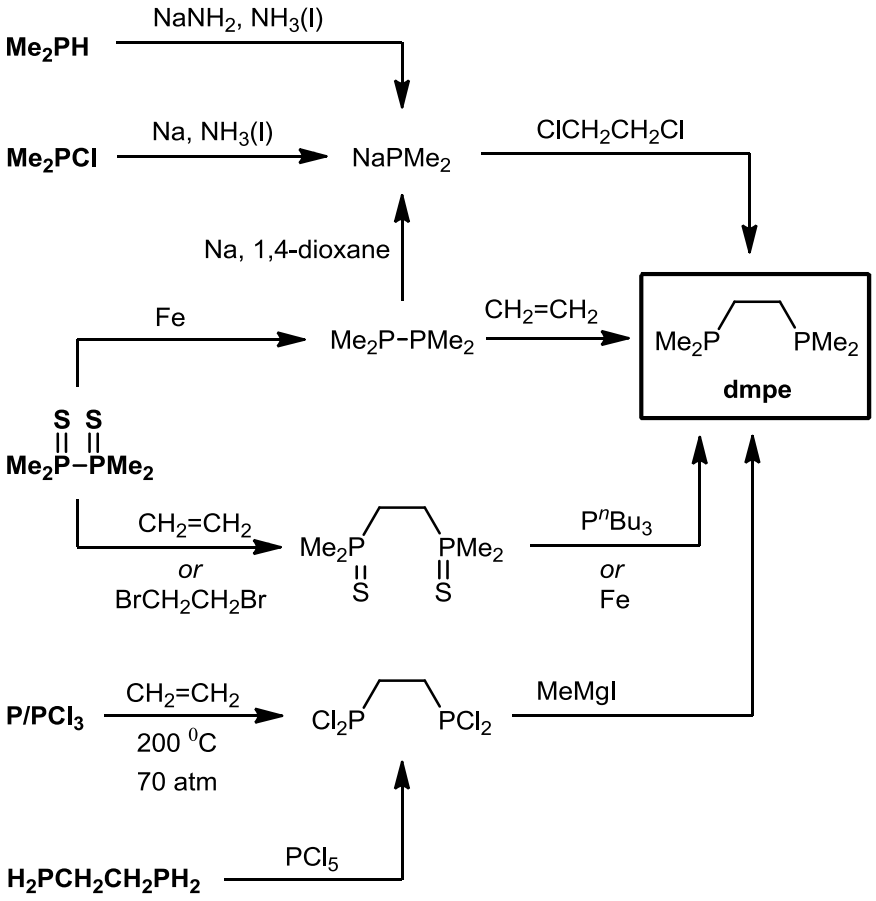


Figure 2.3 Previous synthetic routes to $Me_2PCH_2CH_2PMe_2$ (dmpe; **3a**).

Since we required multi-gram quantities of dmpe (and related alkyl phosphines), a route *via* the reduction of the bisphosphine oxide $Me_2P(=O)CH_2CH_2P(=O)Me_2$ (**1a**) was attractive since phosphine oxides are air stable, and more easily stored and manipulated than the alternative phosphine precursors. However, common strategies used for the deoxygenation of phosphine oxides (e.g. electrophilic aluminium hydrides,[17] hydrosilanes)[18] require aqueous work-ups that can result in considerable by-product waste, separation and purification issues on scale-up, and accordingly we wished to devise a novel reduction strategy which would avoid an aqueous work-up in the final step.

$^{n}Bu_2P(=O)CH_2CH_2P(=O)^{n}Bu_2$ has previously been prepared by Tsvetkov *et al.* from the condensation of $^{n}Bu_2P(=O)H$ with XCH_2CH_2X (X = Cl, Br) using concentrated $KOH_{(aq)}$ in DMSO.[19] Hays *et al.* documented the synthesis of secondary phosphine oxides ($R_2P(=O)H$; R = Me, Et)[20] from the reaction of RMgCl and inexpensive diethyl phosphite ($HP(=O)(OEt)_2$), postulating formation of a solution-phase active intermediate of the form $R_2P(=O)MgCl$ (Figure 2.4). This reactivity has now been explored by our group for R = ^{i}Pr, ^{i}Bu, and ^{t}Bu, which upon quenching with D_2O form $R_2P(=O)D$ (R = ^{i}Pr, ^{i}Bu, and ^{t}Bu; Figure 2.4). Notably, however, the reaction with ^{t}BuMgCl proceeds slowly with poor conversion and thus more

reactive ^{t}BuLi is required. Hays *et al.* also reported the use of *in-situ* $R_2P(=O)MgCl$ as a P-centred nucleophilic synthon $[R_2P(=O)]^-$ in $R_2P(=O)$-C bond formation, yet very few examples of direct tertiary phosphine oxide production using this method have been documented.[21]

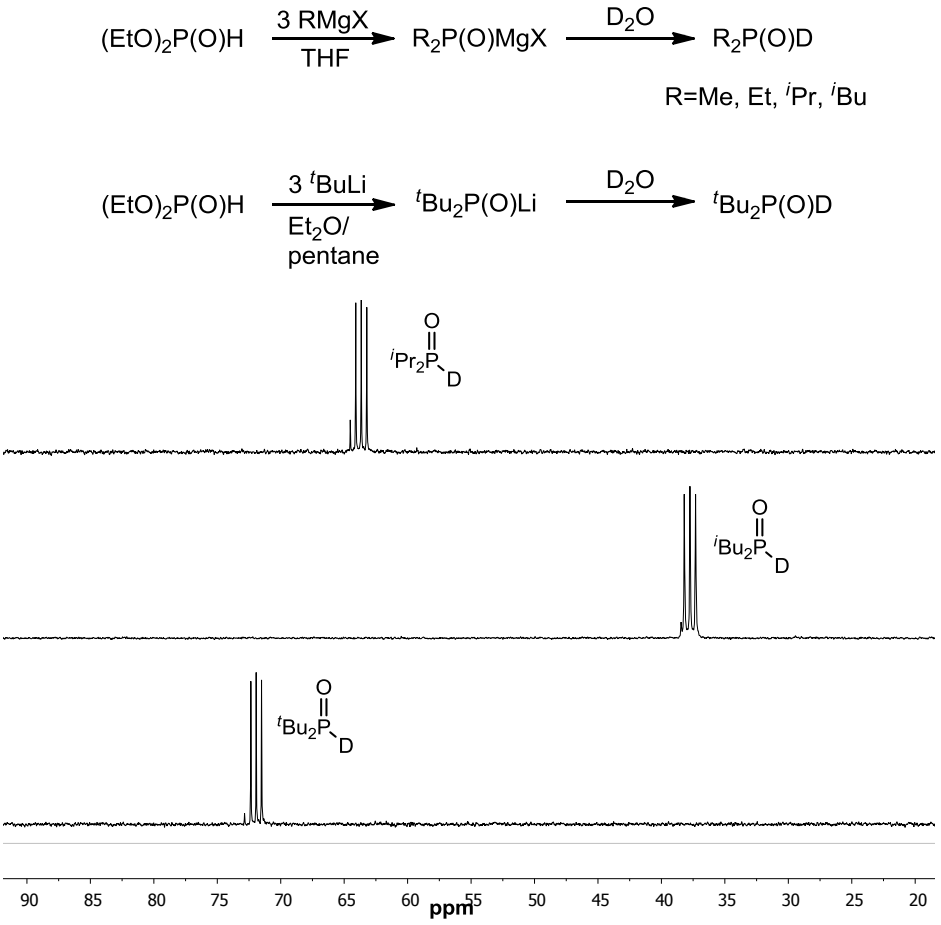


Figure 2.4 ^{31}P NMR spectra of secondary phosphine oxides generated *via* solution-phase active intermediates of the form $[R_2P(=O)M]$; M = MgX, Li; X = Cl, Br.

In order to avoid the prior synthesis of $Me_2P(=O)H$, we reacted MeMgCl and $HP(=O)(OEt)_2$ (3:1) in THF, which led to evolution of CH_4 and proposed *in situ* formation of $Me_2P(=O)MgCl$. Electrophilic trapping of the latter with $ClCH_2CH_2Cl$ and subsequent $K_2CO_{3(aq)}$ work-up precipitated $MgCO_3$ and afforded the target $Me_2P(=O)CH_2CH_2P(=O)Me_2$ (**1a**) in excellent yield (Figure 2.5). In this manner the entire carbon-phosphorus skeleton of the target phosphine can be conveniently assembled in a one-pot protocol.

Direct deoxygenation of **1a** was attempted using a variety of standard protocols: $LiAlH_4$ and MeOTf/MeI/Me_3SiCl,[22] DIBAL-H,[23] AlH_3,[24] $Ti(O^iPr)_4$ and PMHS,[25] $Cu(OTf)_2$ and TMDS;[18i] in each case poor conversions (< 10 %) and product separation difficulties were encountered. This latter effect is attributed to the strongly electron-donating character of the chelating

alkylphosphine. Rajendran and Gilheany recently reduced a variety of phosphine(V) oxides to their corresponding phosphine(III) boranes using $NaBH_4$, *via* their chlorophosphonium(V) chlorides.[26] Accordingly, reaction of **1a** with $(COCl)_2$ in CH_2Cl_2 rapidly affords $[Me_2P(Cl)CH_2CH_2P(Cl)Me_2][Cl]_2$ (**2a**) as a poorly soluble moisture-sensitive solid (along with CO_2 and CO), in almost quantitative yield (Figure 2.5). Whilst $NaBH_4$ reduction of **2a** reaction did cleanly form $(dmpe)\cdot(BH_3)_2$ (^{31}P NMR δ = 8.52 ppm; THF), dissociation of this strong adduct could be achieved neither by heating *in vacuo* (150°C, 10^{-3} mbar), nor using DABCO deprotection.[27] Other methods for deboronation of electron-rich phosphines using strong acids (e.g. $HBF_4.OMe_2$, CF_3SO_3H) and subsequent alkaline hydrolysis[28] were deemed incommensurate with the goals of our synthetic methodology.

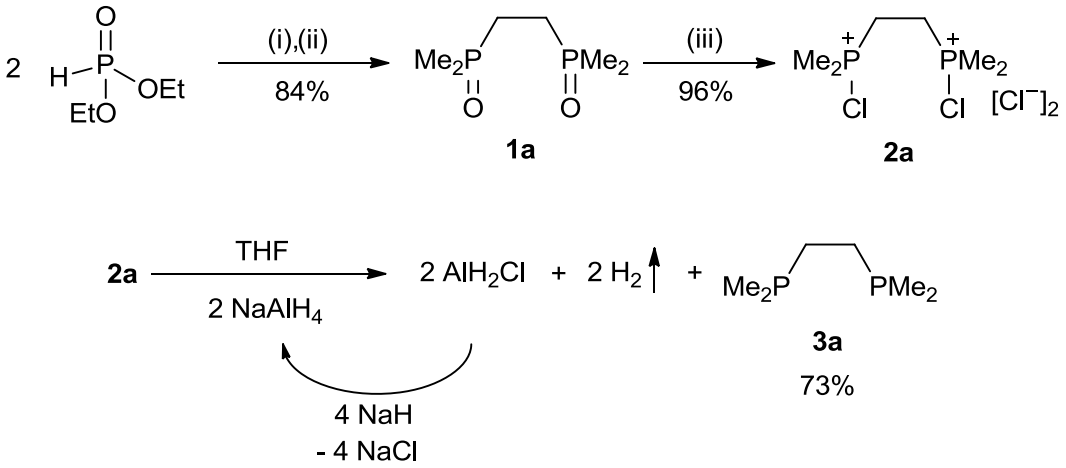


Figure 2.5 Synthesis of $Me_2PCH_2CH_2PMe_2$ (dmpe; **3a**): (i) 6 equiv. MeMgCl/THF; (ii) 0.5 equiv. $ClCH_2CH_2Cl$, reflux then K_2CO_3(aq); (iii) 2.1 equiv. $(COCl)_2/CH_2Cl_2$.

Recognising that the soft-soft interaction between BH_3 and a tertiary alkyl phosphine might be too strong to permit isolation of our target phosphines, our attention turned to the use of $NaAlH_4$ whereby the harder AlH_3 by-product should lead to weaker donor-acceptor adducts. Gratifyingly, NMR-scale reaction of **2a** with $NaAlH_4$ in THF afforded uncoordinated dmpe (**3a**) in quantitative yield (calibrated PPh_3 insert), as ascertained by the strongly shielded ^{31}P NMR resonance (δ = –48.3 ppm). 2 equivalents of $NaAlH_4$ are necessary to effect full conversion of **2a** to **3a**, implying that AlH_2Cl is the end-product after hydride transfer under this stoichiometry. Although **3a** is hydrocarbon-soluble, it could not be isolated from NaCl and $AlH_2Cl\cdot$THF by pentane extraction of the residue obtained upon removal of THF solvent. However, upon re-addition of THF to the solids, free **3a** was again observed by ^{31}P NMR spectroscopy. Thus, it appears that the Lewis acidic AlH_2Cl preferentially binds the harder O-donor THF when it is in excess, but upon solvent removal it binds the softer phosphine,

rendering it a hydrocarbon-insoluble strongly bound adduct and inhibiting mechanical separation.

In order to solve this predicament, we adapted the known reaction of $AlCl_3$ and MH (M = Li, Na, K) to form MCl and $MAlH_4$ salts,[29] recognising that incipiently formed AlH_2Cl or AlH_3 could regenerate AlH_4^-, thus blocking Al Lewis acids from binding **3a**. Satisfyingly, addition of activated NaH[30] to the reaction mixture of **3a** formed from $2NaAlH_4$/**2a** resulted in immediate appearance of the AlH_4^- resonance in the ^{27}Al NMR spectrum (δ = 98.7 ppm, quintet, $^1J_{Al\text{-}H}$ = 174 Hz), demonstrating that regeneration of $NaAlH_4$ by NaH is facile under these conditions (Figure 2.6).

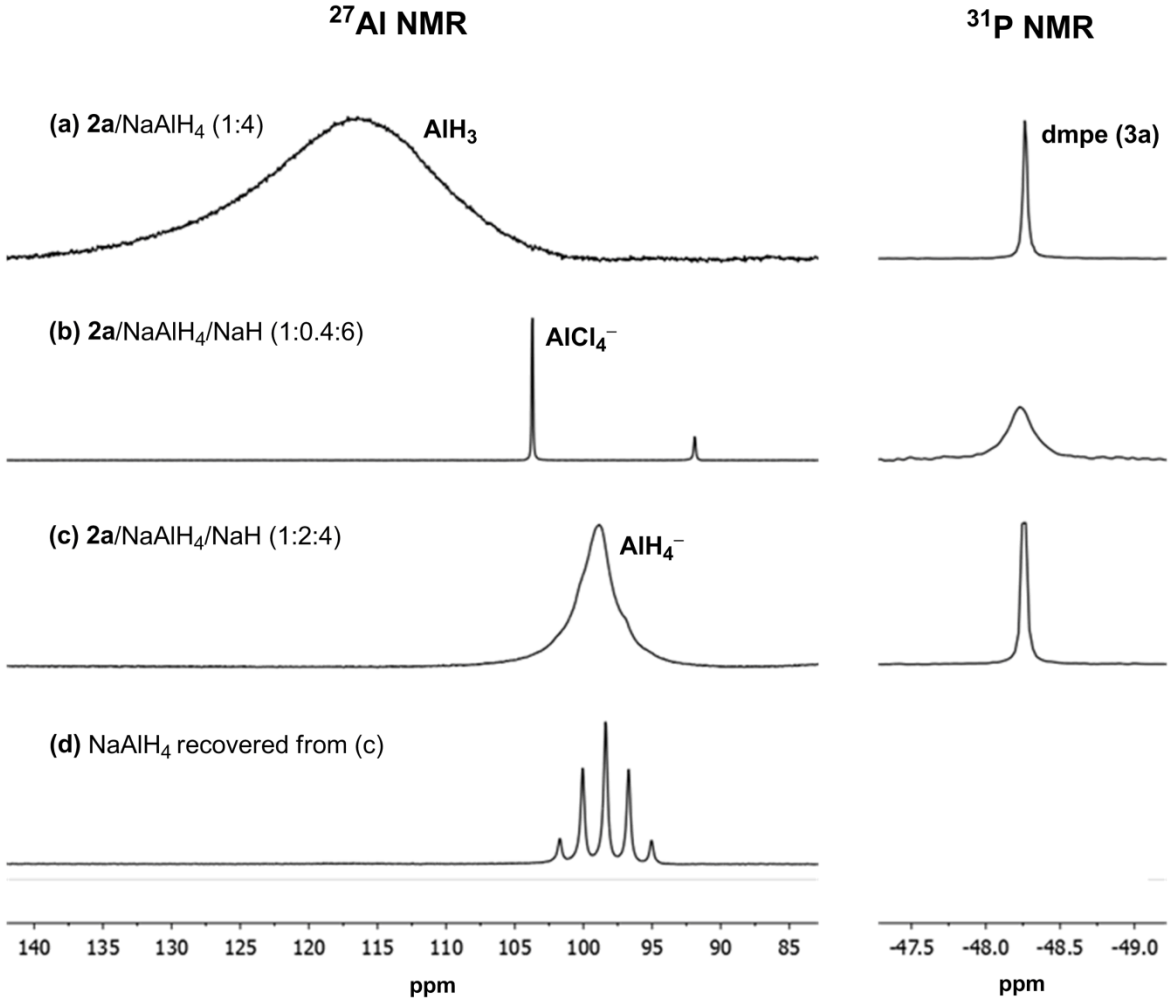


Figure 2.6 ^{27}Al and ^{31}P NMR spectra of NMR scale reductions of **2a** using $NaAlH_4$ and $NaAlH_4$/NaH.

Attempts to reduce **2a** with excess NaH and catalytic $NaAlH_4$ (10-20 mol%) resulted in severely diminished yields and insoluble precipitates. Furthermore, AlH_4^- was not observed in the reaction mixture by ^{27}Al NMR, whilst $AlCl_4^-$ could be identified (Figure 2.6(b)). The use of $NaBEt_3H$, which is similarly regenerated from BEt_3 with NaH or KH, was also investigated

as a potential catalyst. With 20 mol% $NaBEt_3H$, conversion to **2a** was achieved in only 13% yield and furthermore required the use of more reactive KH as the sacrificial reducing agent. P(III) and P(V) halide mixtures are known to comproportionate and give P-P bonded products;[31] we postulate that **3a** is unstable in the presence of cationic electrophilic **2a**, resulting in copolymerisation of the bifunctional moieties and precipitating insoluble phosphine polymers (Figure 2.7).

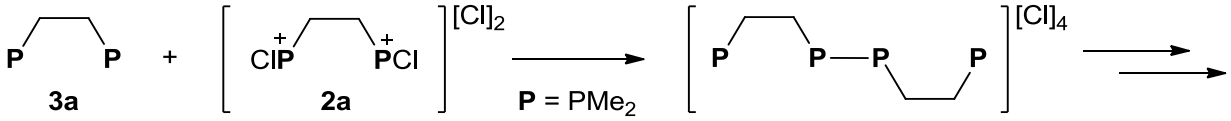
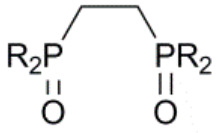
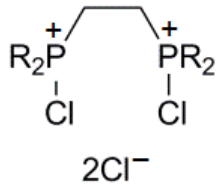


Figure 2.7 Proposed copolymerisation of **2a** and **3a**.

Fortunately, when stoichiometric $NaAlH_4$ and NaH are used it appears that the rate of comproportionation is not competitive, since under these conditions conversion to the phosphine is both rapid and quantitative by ^{31}P NMR (calibrated PPh_3 insert). Hence, **2a** could be reacted on a 5-20 gram scale with $NaAlH_4$/activated NaH (1:2:4 ratio) to afford **3a** in high yield (Figure 2.5), which was purified by vacuum distillation. Work-up is facile and consists of simple filtration from NaCl, pentane extraction, and removal of volatiles. $NaAlH_4$ was used in place of $LiAlH_4$ since it is considerably less hazardous[32] due to its greater thermal stability, and because the poorly soluble NaCl by-product precipitates from THF solution, thus simplifying the extraction process. Advantageously, $NaAlH_4$ was readily recovered in near quantitative yield (> 95%), and could be used in further reactions with no loss of reactivity.

In order to test the scope of our reaction sequence, we synthesised the corresponding $R_2P(=O)CH_2CH_2P(=O)R_2$ (**1b**-**e**) from RMgCl (R = Et, ^{i}Pr, ^{i}Bu) or RLi (R = ^{t}Bu),[33] $HP(=O)(OEt)_2$, and $ClCH_2CH_2Cl$, and reduced these to $R_2PCH_2CH_2PR_2$ (**3b**-**e**) *via* **2b**-**e** respectively; comparable yields are obtained in each case (Table 1). Particularly noteworthy is that all reactions scale-up linearly with no ensuing complications, even for sterically bulky substrates (R = ^{i}Pr, ^{t}Bu), and the syntheses have frequently been performed on a 5-30 gram scale.

Table 1. ^{31}P NMR spectral data and yields for compounds.

Compound		R	^{31}P (δ/ppm)[a]	Yield (%)[c]
	**1a**	Me	42.05	84
	1b	Et	51.21	78
	1c	^{i}Pr	56.07	76
	1d	^{i}Bu	46.43	92
	1e	^{t}Bu	60.09	85
	**2a**	Me	[b]	96
	2b	Et	107.21	97
	2c	^{i}Pr	114.47	94
	2d	^{i}Bu	99.03	96
	2e	^{t}Bu	120.01	96
	**3a**	Me	–48.79	73
	3b	Et	–18.77	84
	3c	^{i}Pr	9.12	85
	3d	^{i}Bu	–35.96	73
	3e	^{t}Bu	35.72	85

[a] NMR spectra for compounds **1a**-**e**, **2b**-**e** were recorded in $CDCl_3$; **3a**-**e** were recorded in C_6D_6.

[b] Compound insoluble in all common solvents attempted.[c] Purified yields (distillation/sublimation).

2.3 Diphosphine pincer ligands

To investigate the possibility of extending the protocol to bisphosphines with greater functionality we targeted the tridentate 'pincer' ligand 1,2-bis(di-*tert*-butylphosphinomethyl)pyridine (**^{tBu}PNP**). **^{tBu}PNP** has shown itself to be a strongly electron donating framework which forms structurally interesting and catalytically active complexes with an extensive range of transition metals.[34] Furthermore, in view of the ability of $LiAlH_4$ to attack pyridine and form lithium tetrakis(*N*-dihydropyridyl)aluminate isomers,[35] we considered **^{tBu}PNP** to be a viable target for testing the selectivity of our reductive step. Currently, **^{tBu}PNP** is synthesised from expensive phosphorous starting reagents either by lithiation of 2,6-lutidine (2,6-dimethylpyridine) followed by addition of $ClP^{t}Bu_2$; or an alternative two-step procedure involving a quarternisation reaction between 2,6-bis(chloromethyl)pyridine and $HP^{t}Bu_2$, followed by deprotonation using NEt_3 (Figure 2.8).

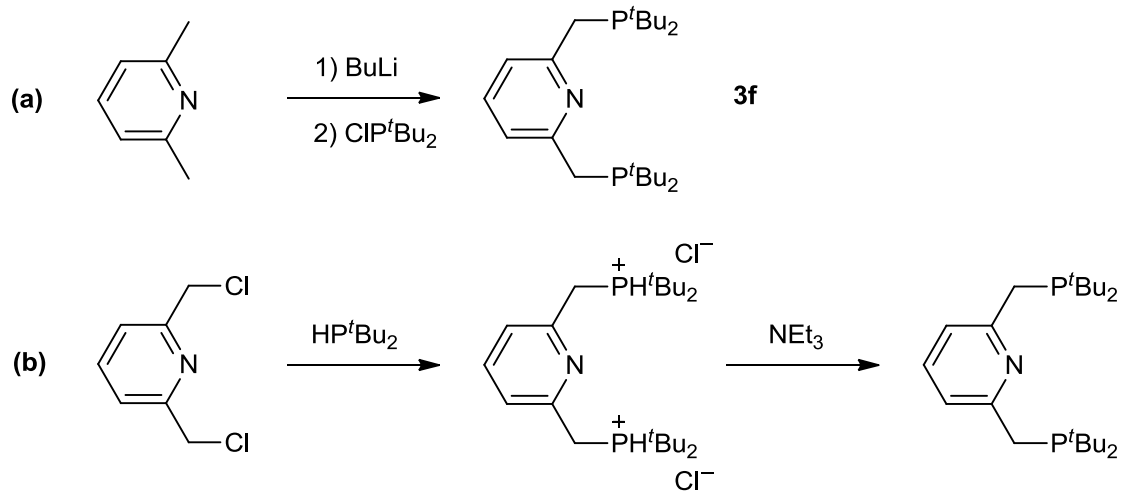
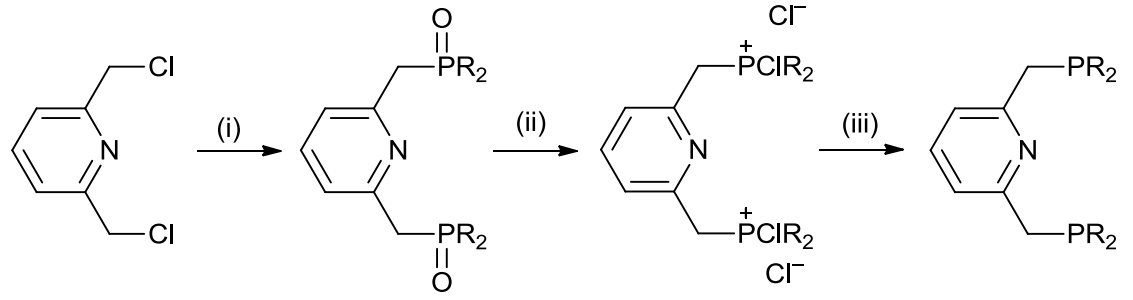


Figure 2.8 Literature methods for preparing **3f**; a) Kawatsura and Hartwig;[15] b) Milstein.[16]

Gratifyingly, 2,6-bis(chloromethyl)pyridine was phosphorylated with the [^{t}Bu$_2$P(=O)Li] reagent to provide 1,2-bis(di-*tert*-butylphosphinomethyl)pyridine P,P'-dioxide (**^{tBu}PNP(O)$_2$**; 72% yield from diethyl phosphite), which was successfully converted (*via* **^{tBu}PNP(Cl)$_4$**) to **^{tBu}PNP** in 79% yield on a multi-gram scale using our protocol (Figure 2.9). A catalytic reduction of **^{tBu}PNP(Cl)$_4$** was attempted using 10 mol% $NaAlH_4$ and excess NaH in THF, which resulted in a mixture of species containing phosphorus, as shown by ^{31}P NMR. However, substituting $NaAlH_4$ for $NaBEt_3H$ (5 mol%), led to good conversion to **^{tBu}PNP** and regeneration of BEt_3H^- (^{11}B NMR δ = –12.3 ppm). Subsequently, **^{tBu}PNP(Cl)$_4$** was reduced on a multi-gram scale to **^{tBu}PNP** in 69% yield, following extraction with pentane, filtration through silica, and recrystallisation from C_6H_6.



		^{R}PNP(O)$_2$	**^{R}PNP(Cl)$_4$**	**^{R}PNP**
Yield (%)	**R=Me**	**85** (40.57)[a]	**97** (–)[c]	**37** (–44.88)[b]
(^{31}P NMR; δ/ppm)	**Et**	**76** (49.49)[a]	**98** (105.27)[a]	**29** (–15.67)[b]
	^{t}Bu	**72** (58.19)[a]	**97** (114.75)[a]	**81** (35.05)[b]

Figure 2.9 Novel synthesis of 1,2-bis(dialkylphosphinomethyl)pyridine (^{R}PNP; R = Me, Et, ^{t}Bu); (i) 6 equiv. ^{t}BuLi/Et_2O/2equiv. $HP(=O)(OEt)_2$; (ii) excess $(COCl)_2/CH_2Cl_2$; (iii) 2-4 equiv. $NaAlH_4$/4 equiv. NaH/THF. [a] In $CDCl_3$; [b] in C_6D_6 ; [c] compound insoluble in all common solvents attempted.

Despite the high utility and popularity of **^{tBu}PNP** as a ligand, other electron-rich alkyl analogues are rare; so far, only the ^{i}Pr-, ^{t}Bu- and Np-substituted ligands have been reported.[36] The success of **^{tBu}PNP** may be attributed to an optimal balance between the electronic and steric properties of its complexes arising from the electron donating and shielding abilities of ^{t}Bu groups. Nevertheless, the less protecting Me- and Et- analogues could allow access to less hindered pincer complexes of greater reactivity. Hence, the phosphine oxide and chlorophosphonium salt precursors were prepared analogously to **^{tBu}PNP(O)$_2$** and **^{tBu}PNP(Cl)$_4$** in good to excellent yields (Figure 2.8). Although NMR scale reductions of ^{R}PNP(Cl)$_4$ (R = Me, Et) using $NaAlH_4$/NaH (1:4:6) indicated good conversion to the phosphines, extraction of the crude products with toluene or pentane resulted in poor yields. This may be due to stronger binding of the P- or N- donor sites to Al salts in the crude mixture upon removal of THF solvent prior to extraction. Since complexes of the simple $R_2PCH_2CH_2PR_2$ ligands were to be the focus of subsequent investigation into Fe-mediated N_2 fixation, optimisation of the syntheses of ^{R}PNP (R = Me, Et) were not investigated further.

2.4 Conclusions

A new, high yielding and facile synthetic route to 1,2-bis(dialkylphosphino)ethanes has been developed, which uses inexpensive reagents[37] and mild conditions, and demonstrates versatility for modulation of the alkyl groups and ligand backbone. Advantageously, the phosphine oxide and chlorophosphonium chloride precursors are readily handled solids, and amenable to large scale syntheses. The novel $NaAlH_4$/NaH reductive protocol is highly economical, and avoids issues encountered with other common reduction methods (boranes and silanes), for a convenient extraction process that obviates the need for an aqueous work-up. We anticipate the improved availability of these desirable alkylated bisphosphines will stimulate an enhanced interest in the study of their diverse and effectual coordination chemistry, which can be extended to other substrates incorporating dialkylphosphine moieties. In particular, this work has enabled exploration of the N_2 fixation chemistry of Fe complexes incorporating dmpe and depe ligands discussed herein, which would have otherwise been inhibited by the poor availability of these important ligands.

This work was published in *Advanced Synthesis & Catalysis*[38] and is reproduced here with permission from John Wiley & Sons.

2.5 References

1 a) *A Guide to Organophosphorus Chemistry*, John Wiley & Sons, New York, **2000**; b) B. F. Straub, *Angew. Chem., Int. Ed.*, **2010**, *49*, 7622-7622.

2 a) C. A. Tolman, *Chem. Rev.*, **1977**, *77*, 313-348; b) O. Kuhl, *Coord. Chem. Rev.*, **2005**, *249*, 693-704; c) C. A. Tolman, *J. Am. Chem. Soc.*, **1970**, *92*, 2953-2956.

3 J. Chatt, S. A. Butter, *Chem. Commun.*, **1967**, 501-502.

4 a) A. Miedaner, R. C. Haltiwanger, D. L. Dubois, *Inorg. Chem.*, **1991**, *30*, 417-427; b) D. E. Berning, B. C. Noll, D. L. DuBois, *J. Am. Chem. Soc.*, **1999**, *121*, 11432-11447; c) R. Ciancanelli, B. C. Noll, D. L. DuBois, M. R. DuBois, *J. Am. Chem. Soc.*, **2002**, *124*, 2984-2992; d) C. J. Curtis, A. Miedaner, W. W. Ellis, D. L. DuBois, *J. Am. Chem. Soc.*, **2002**, *124*, 1918-1925; e) D. L. DuBois, D. M. Blake, A. Miedaner, C. J. Curtis, M. R. DuBois, J. A. Franz, J. C. Linehan, *Organometallics*, **2006**, *25*, 4414-4419.

5 R. G. Peters, S. White, D. M. Roddick, *Organometallics*, **1998**, *17*, 4493-4499.

6 a) M. Hirano, M. Akita, K. Tani, K. Kumagai, N. C. Kasuga, A. Fukuoka, S. Komiya, *Organometallics*, **1997**, *16*, 4206-4213; b) L. Gonzalez-Sebastian, M. Flores-Alamo, J. J. Garcia, *Dalton Trans.*, **2011**, *40*, 9116-9122.

7 a) A. Hills, D. L. Hughes, M. Jimenez-Tenorio, G. J. Leigh, A. T. Rowley, *J. Chem. Soc., Dalton Trans.*, **1993**, 3041-3049; b) B. A. MacKay, M. D. Fryzuk, *Chem. Rev.*, **2004**, *104*, 385-401.

8 a) Z. Dawoodi, M. L. H. Green, V. S. B. Mtetwa, K. Prout, A. J. Schultz, J. M. Williams, T. F. Koetzle, *J. Chem. Soc., Dalton Trans.*, **1986**, 1629-1637; b) W. Scherer, T. Priermeier, A. Haaland, H. V. Volden, G. S. McGrady, A. J. Downs, R. Boese, D. Blaser, *Organometallics*, **1998**, *17*, 4406-4412.

9 S. D. Pike, A. L. Thompson, A. G. Algarra, D. C. Apperley, S. A. Macgregor, A. S. Weller, *Science*, **2012**, *337*, 1648-1651.

10 J. Chatt, R. G. Hayter, *J. Chem. Soc.*, **1961**, 896-904.

11 a) Y. Kiso, M. Kumada, K. Tamao, M. Umeno, *J. Organomet. Chem.*, **1973**, *50*, 297-310; b) S. A. Butter, J. Chatt, E. R. Wonchoba, G. W. Parshall, *Inorg. Synth.*, **1974**, pp. 185-191.

12 A. B. Burg, *J. Am. Chem. Soc.*, **1961**, *83*, 2226-2231.

13 a) G. W. Parshall, *J. Inorg. Nucl. Chem.*, **1960**, *14*, 291-292; b) P. Mäding, *Z. Chem.*, **1986**, *26*, 408-409.

14 a) J. E. Bercaw, G. W. Parshall, *Inorg. Synth.*, **1985**, *23*, 199-200; b) J. E. Bercaw, *Chem. Eng. News*, **1984**, *62*, 4.

15 R. J. Burt, J. Chatt, W. Hussain, G. J. Leigh, *J. Organomet. Chem.*, **1979**, *182*, 203-206.

16 A. N. Tavtorkin, S. A. Toloraya, E. E. Nifant'ev, I. E. Nifant'ev, *Tetrahedron Lett.*, **2011**, *52*, 824-825.

17 a) S. Griffin, L. Heath, P. Wyatt, *Tetrahedron Lett.*, **1998**, *39*, 4405-4406; b) C. A. Busacca, R. Raju, N. Grinberg, N. Haddad, P. James-Jones, H. Lee, J. C. Lorenz, A. Saha, C. H. Senanayake, *J. Org. Chem.*, **2008**, *73*, 1524-1531.

18 a) K. L. Marsi, *J. Org. Chem.*, **1974**, *39*, 265-267; b) J. C. Briggs, C. A. McAuliffe, W. E. Hill, D. M. A. Minahan, J. G. Taylor, G. Dyer, *Inorg. Chem.*, **1982**, *21*, 4204-4210; c) T. Coumbe, N. J. Lawrence, F. Muhammad, *Tetrahedron Lett.*, **1994**, *35*, 625-628; d) N. J. Lawrence, M. D. Drew, S. M. Bushell, *J. Chem. Soc., Perkin Trans. 1*, **1999**, 3381-3391; e) A. Allen, L. Ma, W. B. Lin, *Tetrahedron Lett.*, **2002**, *43*, 3707-3710; f) H. C. Wu, J. Q. Yu, J. B. Spencer, *Org. Lett.*, **2004**, *6*, 4675-4678; g) M. Berthod, A.

Favre-Reguillon, J. Mohamad, G. Mignani, G. Docherty, M. Lemaire, *Synlett*, **2007**, 1545-1548; h) C. Petit, A. Favre-Reguillon, B. Albela, L. Bonneviot, G. Mignani, M. Lemaire, *Organometallics*, **2009**, *28*, 6379-6382; i) Y. H. Li, S. Das, S. L. Zhou, K. Junge, M. Beller, *J. Am. Chem. Soc.*, **2012**, *134*, 9727-9732; j) Y. Li, L.-Q. Lu, S. Das, S. Pisiewicz, K. Junge, M. Beller, *J. Am. Chem. Soc.*, **2012**, *134*, 18325-18329.

19 E. N. Tsvetkov, N. A. Bondarenko, I. G. Malakhova, M. I. Kabachnik, *Synthesis* **1986**, *3*, 198-208.

20 H. R. Hays, *J. Org. Chem.*, **1968**, *33*, 3690-3694.

21 X. M. Gan, E. N. Duesler, R. T. Paine, *Inorg. Chem.*, **2001**, *40*, 4420-4427.

22 a) T. Imamoto, S. Kikuchi, T. Miura, Y. Wada, *Org. Lett.* **2001**, *3*, 87-90; b) L. H. Davies, B. Stewart, R. W. Harrington, W. Clegg, L. J. Higham, *Angew. Chem., Int. Ed.*, **2012**, *51*, 4921-4924.

23 C. A. Busacca, R. Raju, N. Grinberg, N. Haddad, P. James-Jones, H. Lee, J. C. Lorenz, A. Saha, C. H. Senanayake, *J. Org. Chem.* **2008**, *73*, 1524-153.

24 S. Griffin, L. Heath, P. Wyatt, *Tetrahedron Lett.* **1998**, *39*, 4405-4406.

25 T. Coumhe, N. J. Lawrence, F. Muhammad, *Tetrahedron Lett.*, **1994**, *35*, 625-628.

26 K. V. Rajendran, D. G. Gilheany, *Chem. Commun.*, **2012**, *48*, 817-819.

27 a) H. Brisset, Y. Gourdel, P. Pellon, M. Le Corre, *Tetrahedron Lett.*, **1993**, *34*, 4523-4526; b) J. M. Brunel, B. Faure, M. Maffei, *Coord. Chem. Rev.*, **1998**, *178*, 665-698.

28 a) D. B. G. Williams, H. Lombard, M. van Niekerk, P. P. Coetzee, C. W. Holzapfel, *Phosphorus, Sulfur Silicon Relat. Elem.*, **2002**, *177*, 2799-2803; b) L. McKinstry, T. Livinghouse, *Tetrahedron Lett.*, **1994**, *35*, 9319-9322.

29 A. E. Finholt, A. C. Bond, H. I. Schlesinger, *J. Am. Chem. Soc.*, **1947**, *69*, 1199-1203.

30 J. L. Hubbard, *Tetrahedron Lett.*, **1988**, *29*, 3197-3200. *(Use of unactivated NaH led to inconsistent reactivity, and results varied according to the batch used. To ensure reproducibility, the simple activation of NaH using $LiAlH_4$ solution was found to be essential.)*

31 P. Wawrzyniak, A. L. Fuller, A. M. Z. Slawin, P. Kilian, *Inorg. Chem.*, **2009**, *48*, 2500-2506.

32 A. E. Finholt, G. D. Barbaras, G. K. Barbaras, G. Urry, T. Wartik, H. I. Schlesinger, *J. Inorg. Nucl. Chem.* **1955**, *1*, 317-325.

33 T. Achard, L. Giordano, A. Tenaglia, Y. Gimbert, G. Buono, *Organometallics*, **2010**, *29*, 3936-3950

34 a) M. Kawatsura, J. F. Hartwig, *Organometallics*, **2001**, *20*, 1960-1964; b) J. P. Stambuli, S. R. Stauffer, K. H. Shaughnessy, J. F. Hartwig, *J. Am. Chem. Soc.*, **2001**, *123*, 2677-2678; c) D. Hermann, M. Gandelman, H. Rozenberg, L. J. W. Shimon, D. Milstein, *Organometallics*, **2002**, *21*, 812-818; d) E. Ben-Ari, M. Gandelman, H. Rozenberg, L. J. W. Shimon, D. Milstein, *J. Am. Chem. Soc.*, **2003**, *125*, 4714-4715; e) J. Zhang, M. Gandelman, L. J. W. Shimon, H. Rozenberg, D. Milstein, *Organometallics*, **2004**, *23*, 4026-4033; f) J. Zhang, M. Gandelman, D. Herrman, G. Leitus, L. J. W. Shimon, Y. Ben-David, D. Milstein, *Inorg. Chim. Acta*, **2006**, *359*, 1955-1960; g) J. I. van der Vlugt, M. Lutz, E. A. Pidko, D. Vogt, A. L. Spek, *Dalton Trans.*, **2009**, 1016-1023; h) J. I. van der Vlugt, E. A. Pidko, D. Vogt, M. Lutz, A. L. Spek, *Inorg. Chem.*, **2009**, *48*, 7513-7515; i) J. I. van der Vlugt, M. A. Siegler, M. I. Janssen, D. Vogt, A. L. Spek, *Organometallics*, **2009**, *28*, 7025-7032; j) R. Tanaka, M. Yamashita, K. Nozaki, *J. Am. Chem. Soc.*, **2009**, *131*, 14168-14169; k) M. Feller, E. Ben-Ari, M. A. Iron, Y. Diskin-Posner, G. Leitus, L. J. W. Shimon, L. Konstantinovski, D. Milstein, *Inorg. Chem.*, **2010**, *49*, 1615-1625; l) B. Gnanaprakasam, J. Zhang, D.

Milstein, *Angew. Chem., Int. Ed.*, **2010**, *49*, 1468-1471; m) K. Arashiba, Y. Miyake, Y. Nishibayashi, *Nature Chem.*, **2011**, *3*, 120-125; n) K. Arashiba, K. Sasaki, S. Kuriyama, Y. Miyake, H. Nakanishi, Y. Nishibayashi, *Organometallics*, **2012**, *31*, 2035-2041; o) R. Langer, Y. Diskin-Posner, G. Leitus, L. J. W. Shimon, Y. Ben-David, D. Milstein, *Angew. Chem., Int. Ed.*, **2011**, *50*, 9948-9952.

35 K. Hensen, A. Lemke, T. Stumpf, M. Bolte, H. Fleischer, C. R. Pulham, R. O. Gould, S. Harris, *Inorg. Chem.*, **1999**, *38*, 4700-4704.

36 a) A. Jansen, S. Pitter, *Monatsh. Chem.*, **1999**, *130*, 783-794; b) T. Yano, Y. Moroe, M. Yamashita, K. Nozaki, *Chem. Lett.*, **2008**, *37*, 1300-1301.

37 Total cost of reagents for preparing **3a** is *ca.* £7/g (*cf.* Sigma-Aldrich: £113 for 1g; April 2015)

38 L. R. Doyle, A. Heath, C. H. Low, A. E. Ashley, *Adv. Synth. Catal.*, **2014**, *356*, 603-608.

Chapter 3: N_2 activation with Fe diphosphine complexes

3.0.1 Introduction

The conversion of N_2 to NH_3 in the Leigh cycle (Figure 3.1) marked a milestone in N_2 fixation performed on Fe, generating considerable interest in the "simple" Fe diphosphine complexes on which it is based.[1] The key steps are: (i) deprotonation of [*trans*-Fe(H)(N_2)(dmpe)$_2$][BPh_4] to generate Fe(N_2)(dmpe)$_2$ (**4**) *in situ*; (ii) acidification of **4** with HCl producing NH_3 (up to 13% per Fe) and $FeCl_2$(dmpe)$_2$; (iii) conversion of the chloride complex to *cis*-Fe(H)$_2$(dmpe)$_2$, which undergoes protonation in alcohol solvent to form [*trans*-Fe(η^2-H_2)(H)(dmpe)$_2$]$^+$; and (iv) displacement of the coordinatively labile σ-H_2 ligand under N_2 to regenerate the starting N_2 complex. The cycle is notable for its use of a hydride reagent and a base - rather than the conventional single electron-based reducing agents used by Schrock[2] and Peters[3] (e.g. Cp^*_2Cr, KC_8) - to deliver reducing electrons to the metal centre through reductive deprotonation of an Fe–H bond, reverting Fe(II) to the active electron-rich Fe(0) species.[4] Notably, the hydride employed ($NaBH_4$) cannot be regenerated from H_2, preventing use of the latter as a more economical reductant. In addition, incompatibility of the acid, base, and hydride reagents prevent the cycle being performed catalytically in this form.

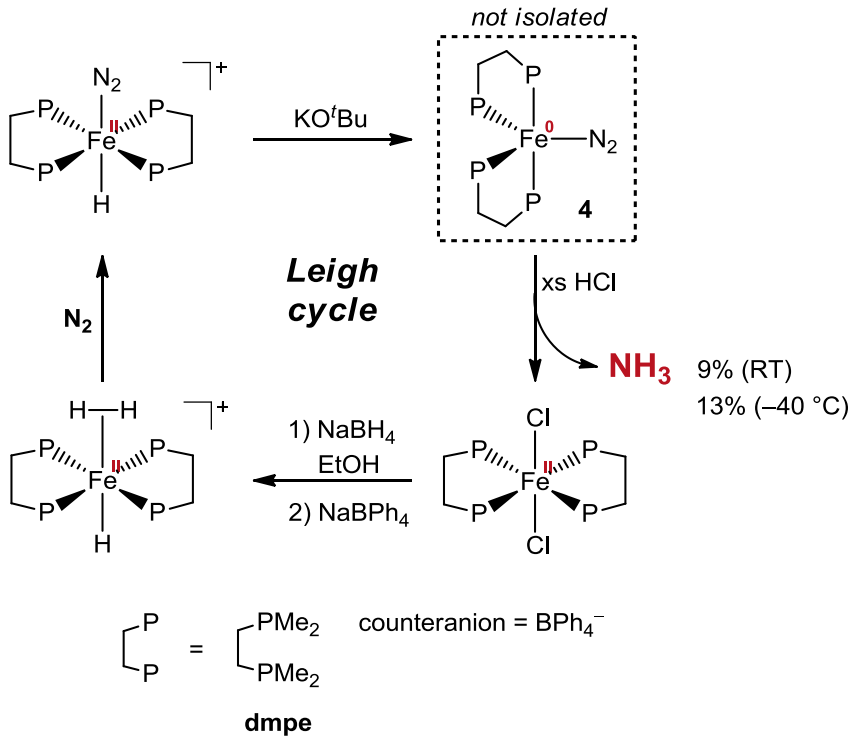


Figure 3.1. The Leigh cycle; the yield of NH_3 is given per Fe.[1]

Whilst Leigh was unable to establish a mechanism for NH_3 formation in the acidification step, the recovery of predominantly Fe(II) suggested that reduction of each molecule of N_2 to two equivalents of NH_3 required concomitant oxidation of three Fe(0) centres to Fe(II) in order to account for the six electrons required.[1] Hence, the maximum yield of NH_3 would be 67% per Fe. The comparably low yields obtained could suggest the main reaction pathway to be protonation at the Fe centre to reform [*trans*-Fe(H)(N_2)(dmpe)$_2$]$^+$, which was tested separately and shown not to produce NH_3 upon acidification with HCl. However, whilst this shows that the deprotonation step is crucial to NH_3 formation in the Leigh cycle, the role of **4** as the active species responsible for NH_3 production has been questioned.[5] Unfortunately, **4** was reported to be unstable with respect to dissociation of N_2 *in vacuo*, forming an oil which was presumed to be [Fe(dmpe)$_2$] and its known decomposition products, [{Fe(dmpe)$_2$}$_2$(μ-dmpe)][6] and Fe metal (Figure 3.2);[7] thus, separation from the reaction mixture and subsequent acidification of isolated **4** was not possible. The highly unstable 16 valence electron (VE) complex [Fe(dmpe)$_2$] has been generated by laser flash photolysis of *cis*-Fe(H)$_2$(dmpe)$_2$ either in alkane solvents or an Ar matrix at 12 K;[8] in the absence of other quenchers (e.g. CO, N_2, C_2H_4) this species undergoes oxidative addition with the alkane solvent to form *cis*-Fe(H)(alkyl)(dmpe)$_2$. In contrast, the related depe complex [Fe(depe)$_2$] undergoes cyclometallation *via* reversible oxidative addition of a methylene C–H bond on one of the depe ligands (Figure 3.3).[9, 10]

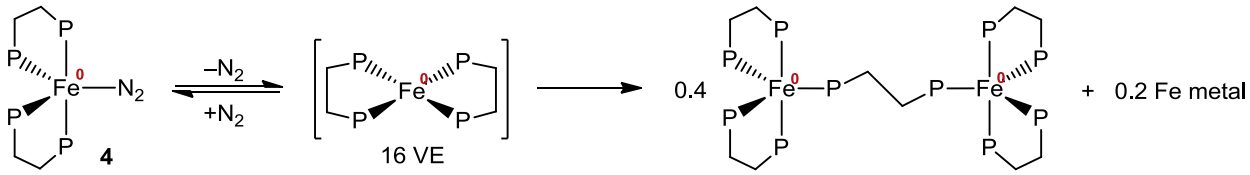


Figure 3.2 Decomposition of FeN$_2$(dmpe)$_2$ *via* dissociation of N_2; P = PMe$_2$.[4, 6]

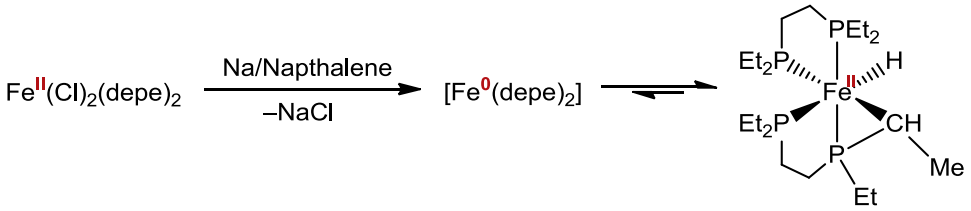


Figure 3.3 Formation of [Fe(depe)$_2$] and subsequent cyclometallation.[9, 10]

As Leigh has remarked, the uncertainty concerning the key intermediates involved produces an unsatisfactory situation, which has been mirrored in the investigations of related systems. Thus, deprotonation of Fe(II) hydrido N_2 complexes [*trans*-Fe(H)(N_2)(depe)$_2$]$^+$,[4] [*cis*-Fe(H)(N_2){P(CH$_2$CH$_2$PPh$_2$)$_3$}]$^+$,[4] and [*trans*-Fe(H)(N_2)(DMeOPrPE)]$^+$ (DMeOPrPE =

$[MeOCH_2CH_2CH_2)_2PCH_2]_2)$[11] with KO^{t}Bu base all produce mixtures that upon acidification (HCl, H_2SO_4, HBF_4, TfOH) generate similar yields of NH_3 (≤ 15% per Fe), whilst N_2H_4 is only detected in trace quantities (≤ 2% per Fe). However, only in the case of [*trans*-$Fe(H)(N_2)(depe)_2]^+$ has the Fe(0) product of the deprotonation reaction been isolated. This was achieved by Komiya *et al.* who prepared $Fe(N_2)(depe)_2$ *via* direct reduction of the $FeCl_2(depe)_2$ precursor with Na-naphthalenide under N_2 atmosphere (Figure 3.4); its trigonal bipyramidal structure was confirmed by single crystal X-ray crystallography (*vide infra*).[12] However, when the isolated compound was acidified and tested for NH_3 production by an analogous procedure to Leigh, no NH_3 was detected; instead quantitative liberation of N_2 and H_2 gas was recorded along with trace amounts of N_2H_4 (≤ 0.3%). Furthermore, stoichiometric HCl experiments indicated two stepwise protonations, forming initially $Fe(H)(Cl)(depe)_2$ and liberating N_2, with a second proton equivalent producing $Fe(Cl)_2(depe)_2$ and H_2.[10] This would indicate that, at least for the depe ligand system, the conditions resulting from the deprotonation reaction in the Leigh cycle are crucial for NH_3 formation, suggesting either reaction by-products or unknown side reactions could play a significant role. In related chemistry, George *et al.* have reported that the deprotonation of [*cis*-$Fe(H)(N_2)\{N(CH_2CH_2PPh_2)_3\}][BPh_4]$ with ^{n}BuLi generates $[Fe(N_2)\{N(CH_2CH_2PPh_2)_3\}]$, which was isolated as a solid admixed with $LiBPh_4$; subsequent acidification with HBr produced N_2H_4 and NH_3 in maximum yields of 11 and 3%, respectively.[13] The preference for N_2H_4 formation for this system is not well understood, one possibility is that the incomplete reduction of N_2 to N_2H_4 may reflect inefficiency of electron transfer from Fe.

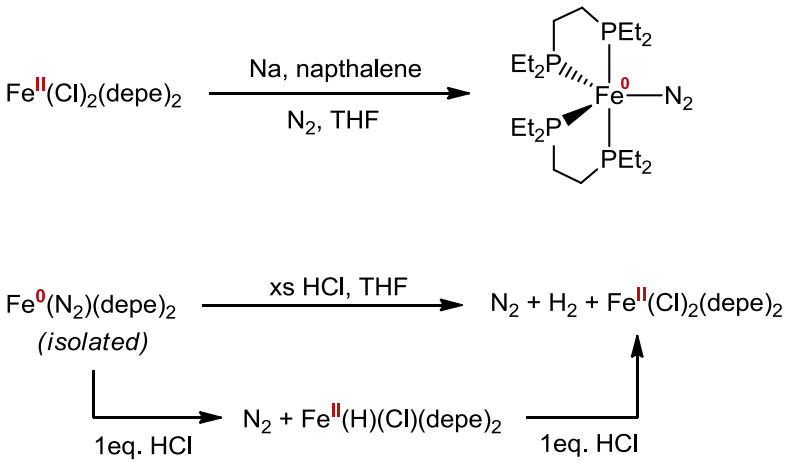


Figure 3.4 Synthesis of $Fe(N_2)(depe)_2$ and acidification with HCl, reported by Komiya *et al.*[10]

Computational studies by Tyler and co-workers have attempted to elucidate the mechanism of N_2 fixation in these systems by calculating the relative free energies of hypothetical intermediates (but no transition states) starting from **4**.[14] Since Fe(0) typically acts as a two-electron reductant,[5] a Chatt-type mechanism, in which three sequential protons and

electrons are transferred to the terminal N atom, was considered unlikely. Instead, two stepwise mechanisms were considered in which initial transfer of the first proton onto the terminal N and a second proton to either the distal (symmetric monomer) or proximal N (asymmetric monomer), is followed by a two-electron reduction (outer-sphere transfer) by sacrificial **4** (Figure 3.5). Additional protonation yields either NH_3 (asymmetric monomer) or hydrazine (symmetric monomer), with the latter shown experimentally to undergo Fe-mediated disproportionation in the presence of 1 M TfOH acid to NH_3 (Figure 3.6).[15]

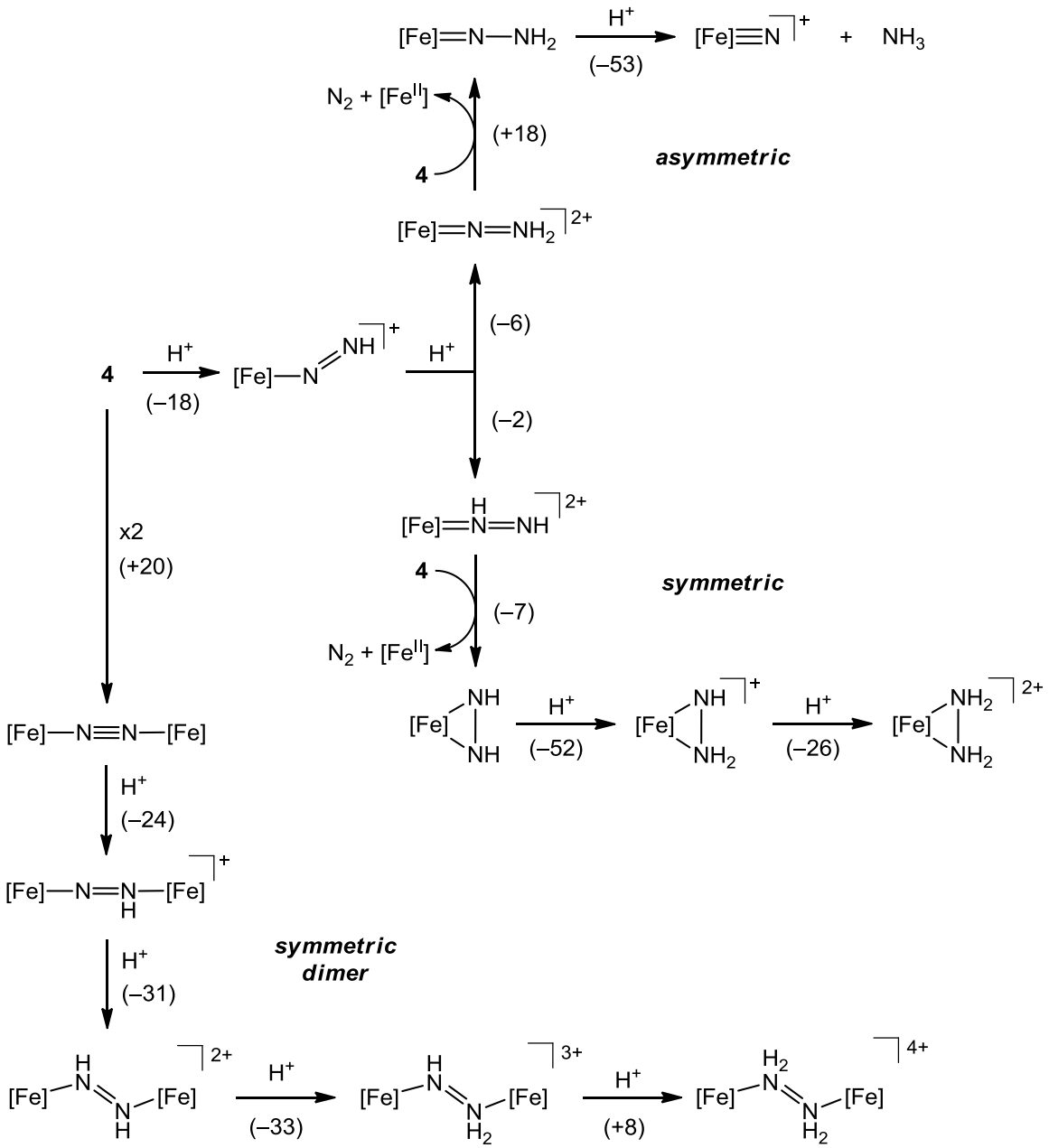


Figure 3.5 Hypothetical intermediates and DFT computed reaction energies (kcal mol^{-1}) for the acidification of **4** *via* symmetric monomer, asymmetric monomer, and symmetric dimer mechanisms proposed by Tyler *et al.* ; [Fe] = $[Fe(dmpe)_2]$.[14]

Although the second initial protonation is slightly more favoured for the asymmetric monomer pathway, further protonation or electron reduction is highly unfavourable, and therefore the symmetric monomer mechanism was considered preferable.

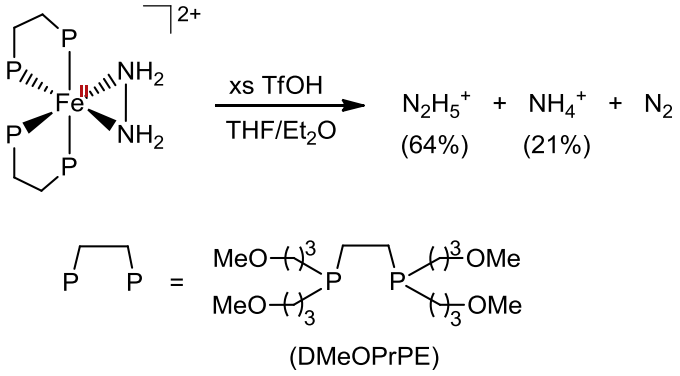


Figure 3.6 Fe-mediated disproportionation of N_2H_4, reported by Tyler *et al.*.[15]

A third mechanism was also considered involving dimerisation of **4** *via* a bridging N_2 ligand, with loss of the second N_2, prior to four successive protonations. The optimised geometries (B3LYP density functional/6-31G* basis set) of monomeric **4** and its dimeric complex indicated elongation of both N–N and Fe–N bonds in the latter by 0.015 Å and 0.08 Å, respectively (Table 3.1). In addition, Mulliken population analysis revealed a greater overall negative charge on the bridging N_2 ligand in the dimeric species compared to the terminal N_2 ligand in monomeric **4** (Table 3.2), suggesting the degree of N_2 activation increases upon dimerisation. However, whilst the first three protonation steps in this dimeric pathway are more energetically favourable than in either monomer pathways, the initial dimerisation is unfavourable by 20 kcal mol^{-1} such that competitive protonation (–18 kcal mol^{-1}) would likely prevent dimerisation from occurring. It should be noted however that transition state energies were not considered in this study, and therefore energy barriers between intermediates remain ambiguous. For instance, initial protonation of the Fe centre was calculated to be favoured by 40 kcal mol^{-1} indicating that the Fe(II) hydrido N_2 complex is the thermodynamic product (Figure 3.7). Whether proton transfer to N_2 is kinetically favoured is uncertain, but it seems plausible since the terminal N is more exposed to proton transfer than the Fe centre, especially when using bulky H^+ donors (e.g. TfOH vs HCl/Et_2O). Furthermore, the dipole of the complex is aligned such that the terminal N (N_β) has a partial negative charge whilst the Fe has a partial positive charge, attracting and repelling the proton, respectively. Notably, Leigh *et al.* reported that the maximum yield of NH_3 of 13 % (per Fe) was obtained when the acidification was performed at –40 °C, which may suggest a kinetic preference for protonation of the N_2 ligand.[4]

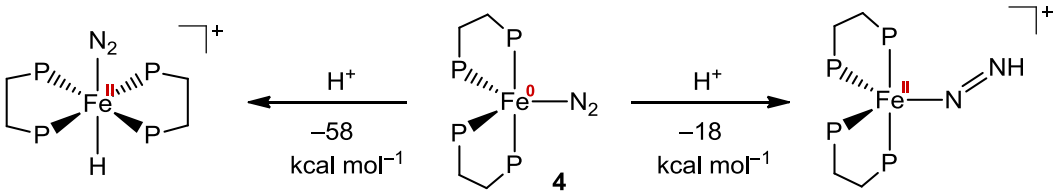


Figure 3.7 DFT computed reaction energies for protonation of **4** at either Fe or terminal N sites taken from ref 14; P = PMe_2.

Table 3.1 Bond lengths (Å) of **4** and its dimeric complex determined by geometry optimisations (B3LYP/6-31G*), reported by Tyler *et al.*.[14]

	Fe–P	**Fe–N**	**N–N**
$Fe(N_2)(dmpe)_2$ (**4**)	2.194–2.238	1.777	1.138
$[\{Fe(dmpe)_2\}_2(\mu\text{-}N_2)]$	2.191–2.245	1.856	1.153

Table 3.2 Atomic charges of **4** and its dimeric complex from Mulliken population analysis, reported by Tyler *et al.*.[14]

	Fe	**P**	**N_α**	**N_β**
$Fe(N_2)(dmpe)_2$ (**4**)	+0.04	+0.47–0.54	–0.09	–0.22
$[\{Fe(dmpe)_2\}_2(\mu\text{-}N_2)]$	0.27, 0.27	0.46–0.48	–0.20	–0.20

A further complication for the proposed monomer pathways is the availability of sacrificial **4**; initial proton transfer to either the Fe centre or the terminal N is considerably energetically favourable, such that there is unlikely to be an appreciable concentration of **4** remaining after the second protonation to perform outer-sphere electron transfer. The authors suggest that other intermediates, such as $[Fe(N_2H)(dmpe)_2]^+$ and $Fe(\mu\text{-}N_2H_4)(dmpe)_2$, could substitute as sacrificial reductants but discount an alternative mechanism whereby diazene in the symmetric pathway intermediate $Fe(N_2H_2)(dmpe)_2$ disproportionates to N_2 and N_2H_4, and subsequently N_2 and NH_3. Finally, they conclude that the symmetric monomer pathway proceeding through diazene and hydrazine intermediates is the most favourable of the mechanisms studied.

The groups of David Tyler and Leslie Field have sought to establish an experimental basis for these interconversions of diazene and hydrazine complexes of Fe. Using ^{15}N NMR spectroscopy, Field *et al.* have performed several mechanistically pertinent protonation and reprotonation reactions involving isolated ^{15}N labelled intermediates (Figure 3.8).[16, 17] The reaction of $Fe(Cl)_2(dmpe)_2$ with N_2H_4 afforded the side-on bound hydrazine complex $[cis\text{-}Fe(N_2H_4)(dmpe)_2][Cl]_2$, which was isolated as the BPh_4^- salt after salt metathesis with $NaBPh_4$. Subsequent deprotonation using KO^tBu produced $cis\text{-}Fe(N_2H_2)(dmpe)_2$, reported as

an Fe(0) diazene π-complex, whilst Tyler *et al.* have suggested this species is better described as an Fe(II) hydrazido(–2) complex.[14, 18] **4** could also be accessed from the hydrazine complex by employing a stronger base mixture of KO^{t}Bu and ^{t}BuLi (Schlosser base).[16] Remarkably, despite the known instability of diazene and its complexes, the reaction was shown to be reversible through protonation with weak acid 2,6-lutidinium triflate, which also led to eventual formation of NH_4^+ and the amine complex [*cis*-Fe(Cl)(NH_3)(dmpe)$_2$]$^+$. Tyler *et al.* have similarly prepared the related hydrazine complex [*cis*-Fe(N_2H_4)(DMeOPrPE)$_2$]$^{2+}$ (DMeOPrPE = [{MeO(CH_2)$_3$}$_2$PCH_2]$_2$) for which they were able to demonstrate reversible stepwise deprotonations to the corresponding hydrazido(1–) and diazene complexes.[19]

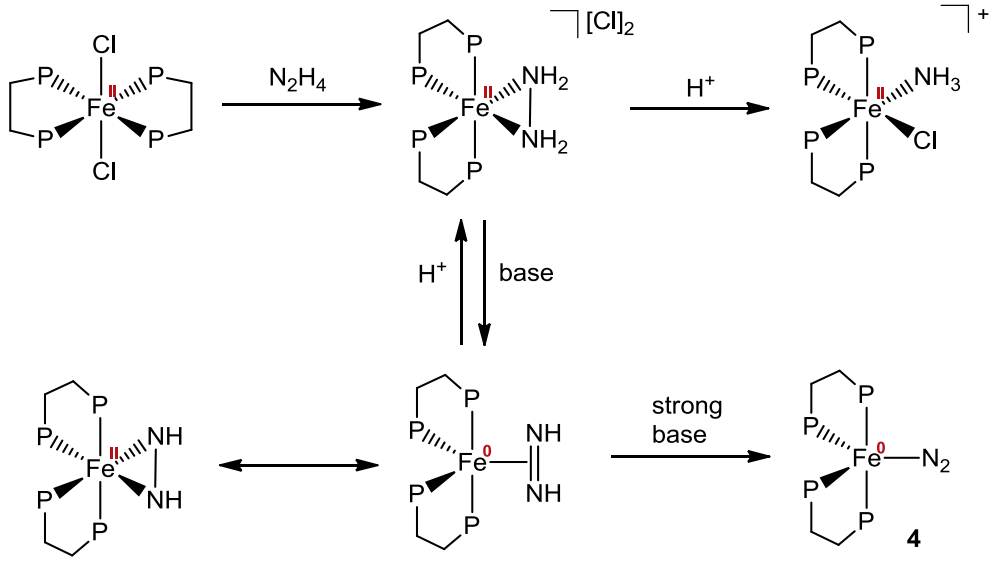


Figure 3.8 Acid and base mediated interconversion of diazene and hydrazene intermediates reported by Field *et al*.; P = PMe_2.[16]

Whilst plausible diazene intermediates have been prepared and acidified to generate NH_3 and N_2H_4, they have yet to be accessed from protonation of coordinated N_2. Recently, Tyler *et al.* reported a short lived purple species observed upon sub-stoichiometric acidification of Fe(N_2)(DMeOPrPE)$_2$ with TfOH (1 M in Et_2O).[20] Spectroscopic and reactivity studies suggested this to be the N_2-bridged Fe(I)/Fe(I) dimer [{Fe(DMeOPrPE)$_2$}$_2$(μ-N_2)]$^{2+}$, which it was hoped might be one of the elusive intermediates in the formation of NH_3 *via* the mechanism shown in Figure 3.9. Its independent synthesis could be achieved *via* several routes involving halide abstractions and reduction from Fe(Cl)$_2$(DMeOPrPE)$_2$; however, neither NH_3 or N_2H_4 were detected upon subsequent acidification. A possible indirect route to these products *via* disproportionation of diazene could not be confirmed due to experimental incompatibility with the diazene traps tested (phenylacetylene, norbornene, and azobenzene). Hence, no complete map for the reduction of coordinated N_2 to NH_3 has been

established for these Leigh-type systems, nor have any of the proposed intermediates, besides the Fe(0) N_2 complexes, been observed spectroscopically either prior to or during acidification.

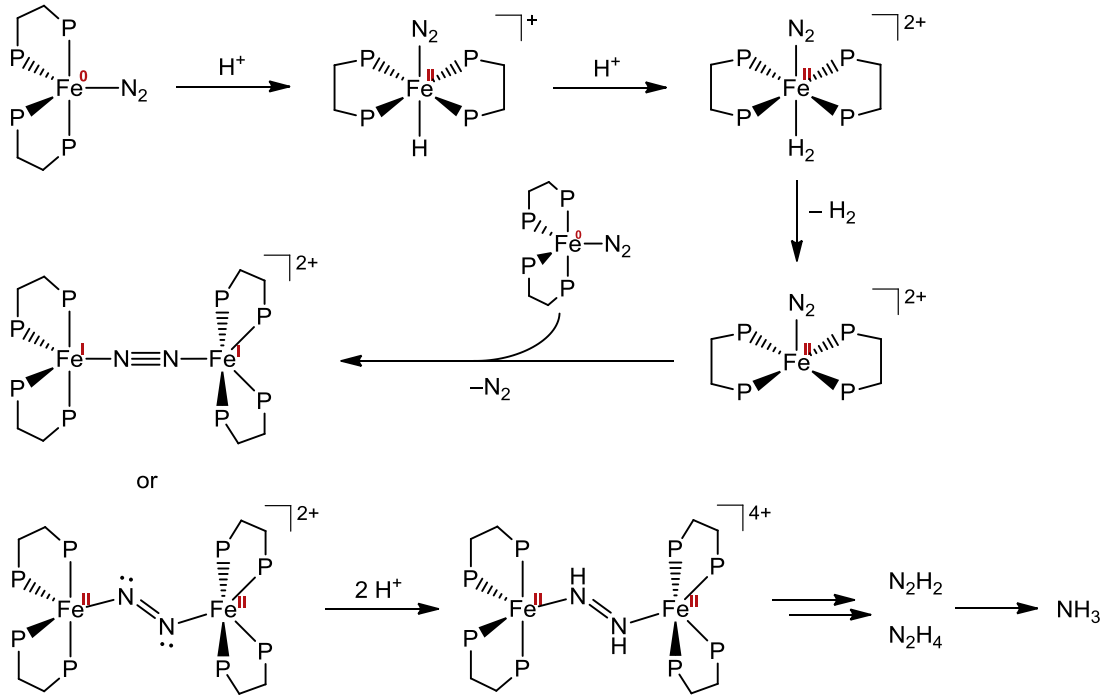


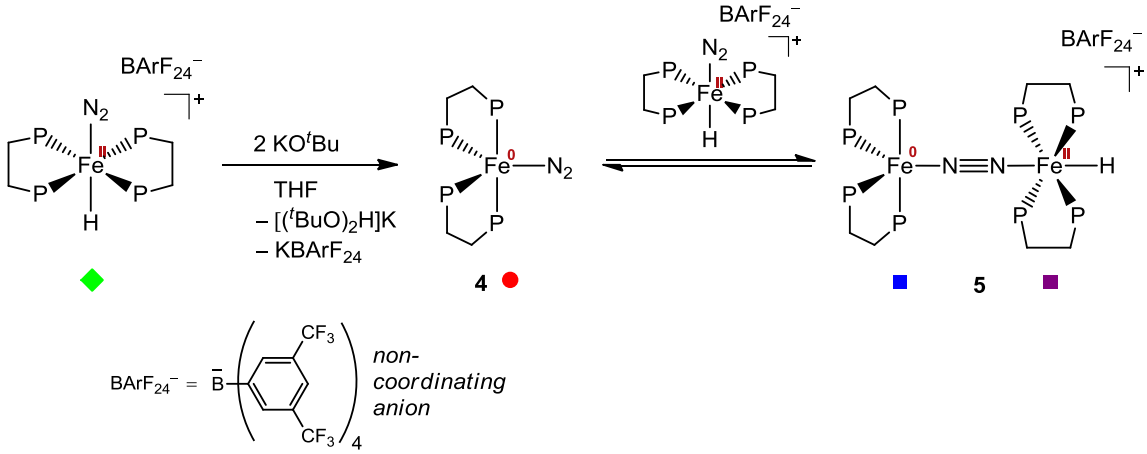
Figure 3.9 Formation of an N_2-bridged dimer during acidification as proposed by Tyler *et al.*; P = $P\{(CH_2)_3OMe\}_2$.[20]

3.0.2 Preliminary spectroscopic studies of the Leigh deprotonation reaction

The pioneering work of Leigh *et al.* employed mainly solution IR spectroscopy to follow the deprotonation of [*trans*-Fe(H)(N_2)(dmpe)$_2$][BPh_4], whereby a strong ν(N–N) band at 2093 cm^{-1} disappeared and was replaced by a ν(N–N) band at 1967 cm^{-1}, proposed to correspond to **4**.[1] Leigh initially assigned two ^{31}P NMR resonances (A_2B_2 triplets) to **4**, although this was revised 5 years later when it was realised that these were due to contaminating *cis*-Fe(H)$_2$(dmpe)$_2$.[4] More rigorous NMR experiments revealed a singlet resonance for **4** (δ = 59.9 ppm; THF), indicating rapid fluxional exchange of axial and equatorial phosphorus in solution congruous with the singlet observed by Komiya *et al.* for Fe(N_2)(depe)$_2$ (δ = 89.3 ppm, toluene-d_8);[12] in both cases fluxionality remained unresolved upon cooling. Prompted by a lack of supporting NMR spectroscopic data, initial research within our group was focused on using both NMR and EPR spectroscopy to elucidate species formed besides **4** in this crucial step of the Leigh cycle; some of this work was carried out by the MSci students Louis Oscroft, Mark Driver, and Corin Briault-Hutter.[21]

Since the starting complex [*trans*-Fe(H)(N_2)(dmpe)$_2$][BPh_4] is poorly soluble even in THF, it may be inferred that its concentration, as well as that of any other possible charged species formed during the deprotonation, may not be fully accounted for by NMR spectroscopy. To circumvent this issue, the non-coordinating counteranion [B{3,5-$(CF_3)_2C_6H_3$}$_4$]$^-$ ($BArF_{24}^-$) was used, which has the general ability to form salts with greatly improved solubility.[22] Accordingly, [*trans*-Fe(H)(N_2)(dmpe)$_2$][$BArF_{24}$] was deprotonated with KO^{t}Bu in THF in a reaction that proceeded entirely homogeneously. In the ^{31}P NMR spectrum (Figure 3.10), disappearance of [*trans*-Fe(H)(N_2)(dmpe)$_2$][$BArF_{24}$] (δ = 64.8 ppm, d, $^2J_{P-H}$ = 41 Hz) and formation of **4** (at a slightly different shift to that reported by Leigh *et al.*; 63.0 ppm, s) was observed, along with two additional resonances of equal intensity (δ = 69.5 and 61.6 ppm).

(a)



(b)

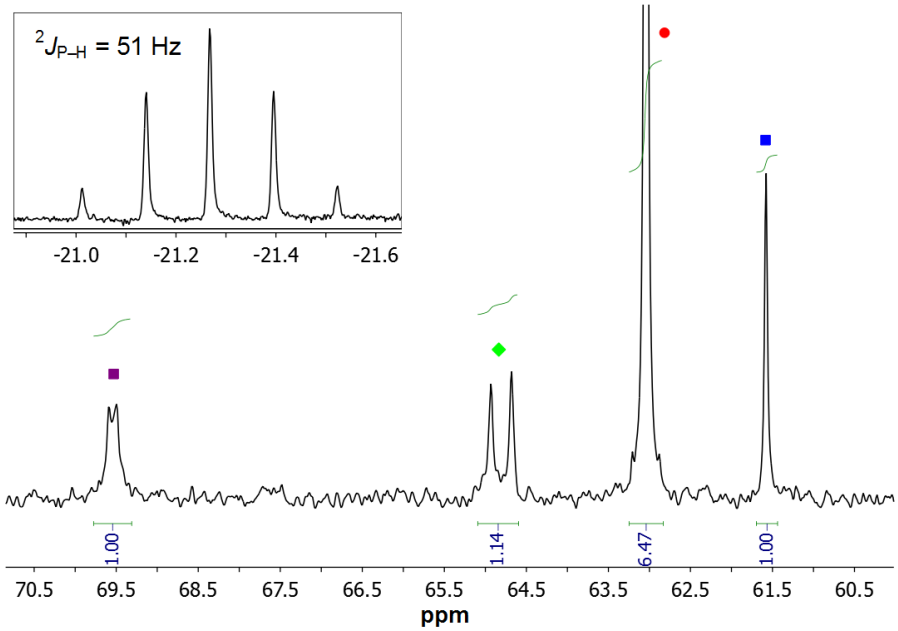


Figure 3.10 (a) Deprotonation of [Fe(H)(N_2)(dmpe)$_2$][$BArF_{24}$] with KO^{t}Bu (1:2, THF) and proposed formation of [*trans*-Fe(H)(dmpe)$_2$(μ-N_2)Fe(dmpe)$_2$][$BArF_{24}$] (**5**); (b) ^{31}P NMR spectrum after ca. 20 min; P = PMe_2.

The more downfield shifted resonance partially resolved as a doublet and was shown by $^{1}H/^{31}P$ HSQC NMR spectroscopy to be coupled to a pentet in the hydride region of the ^{1}H NMR spectrum (δ = –21.27 ppm, p, $^{2}J_{P\text{-}H}$ = 51 Hz). These additional resonances were assigned to the mixed valence Fe(II)/Fe(0) dimer [*trans*-$Fe(H)(dmpe)_2(\mu\text{-}N_2)Fe(dmpe)_2][BArF_{24}]$ (**5**), which could be independently generated as an equilibrium mixture by combining solutions of **4** (*vide infra*) and [*trans*-$Fe(H)(N_2)(dmpe)_2][BArF_{24}]$ in a 1:1 ratio.

It was hoped that deprotonation of **5** might allow access to the neutral dimer as an alternative route to dimerisation of **4** (Figure 3.11), the latter computed to be unfavourable by Tyler *et al.* (*vide supra*).[14] However, addition of either KO^{t}Bu or KCH_2Ph base to the above mixture afforded only **4**, suggesting a dimeric species may be formed transiently but undergoes rapid dissociation. Perhaps unsurprisingly, close examination of the ^{31}P NMR spectrum recorded for the archetypal deprotonation of [*trans*-$Fe(H)(N_2)(dmpe)_2][BPh_4]$ revealed the corresponding BPh_4^- salt of **5** to be present in low concentrations. Notably, solutions of **4** were also found to react with ^{t}BuOH (the conjugate acid of the KO^{t}Bu base) to form an equilibrium mixture with [*trans*-$Fe(H)(N_2)(dmpe)_2]^+$ and [*trans*-$Fe(H)(dmpe)_2(\mu\text{-}N_2)Fe(dmpe)_2]^+$, suggesting the deprotonation reaction is partly reversible. However, under the conditions reported by Leigh *et al.*, use of excess KO^{t}Bu (two equivalents) drives the reaction to almost complete conversion by sequestering ^{t}BuOH product as the adduct [($^{t}BuO)_2H]K$ (^{1}H NMR, THF, δ = 10.49 ppm, br s).

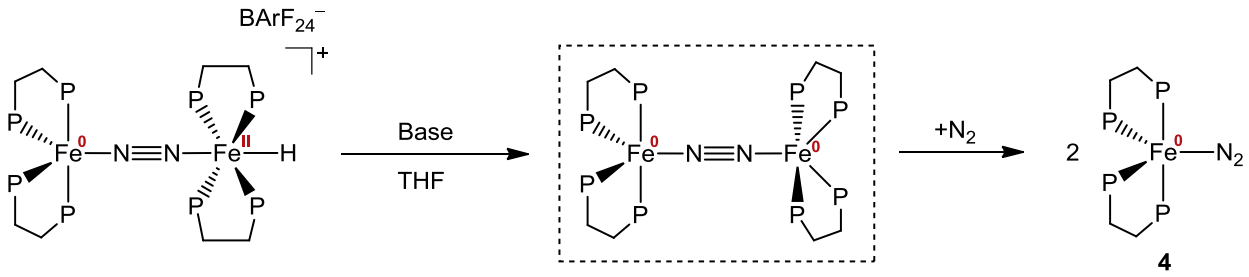


Figure 3.11 Deprotonation of [*trans*-$Fe(H)(dmpe)_2(\mu\text{-}N_2)Fe(dmpe)_2][BArF_{24}]$; P = PMe_2.

Another benefit of ensuring complete solubility of the deprotonation mixture was the ability to monitor the relative intensities of species formed by ^{31}P NMR spectroscopy. Since [*trans*-$Fe(H)(N_2)(dmpe)_2][BArF_{24}]$, **4** and **5** all contain either low-spin (LS) Fe(II) or Fe(0), these species are expected to be diamagnetic and thus, provided an appropriate pulse delay is used, the overall ^{31}P intensity should be conserved. However, it was found that over the course of the reaction, despite no observable precipitation, a significant loss of ca. 20% of the overall ^{31}P intensity occurred, indicating formation of an unknown paramagnetic species.

This was confirmed by recording the X-band CW-EPR spectrum of the mixture (Figure 3.12(a)), which exhibited a pseudo-isotropic Fe(I) (S = ½) signal; this was reproducible for both Fe(II) hydrido N_2 complexes [*trans*-Fe(H)(N_2)(dmpe)$_2$][X] (X = BPh_4^- , $BArF_{24}^-$) with either KO^{t}Bu or KCH_2Ph base. The KO^{t}Bu deprotonation reaction of the related depe complex [*trans*-Fe(H)(N_2)(depe)$_2$][BPh_4] was also analysed by CW-EPR, in which a similar axial signal was resolved (Figure 3.12(b)), although HYSCORE measurements performed on these samples indicated a strong hyperfine coupling interaction to a metal bound hydride ligand in the case of depe only (Figure 3.13).

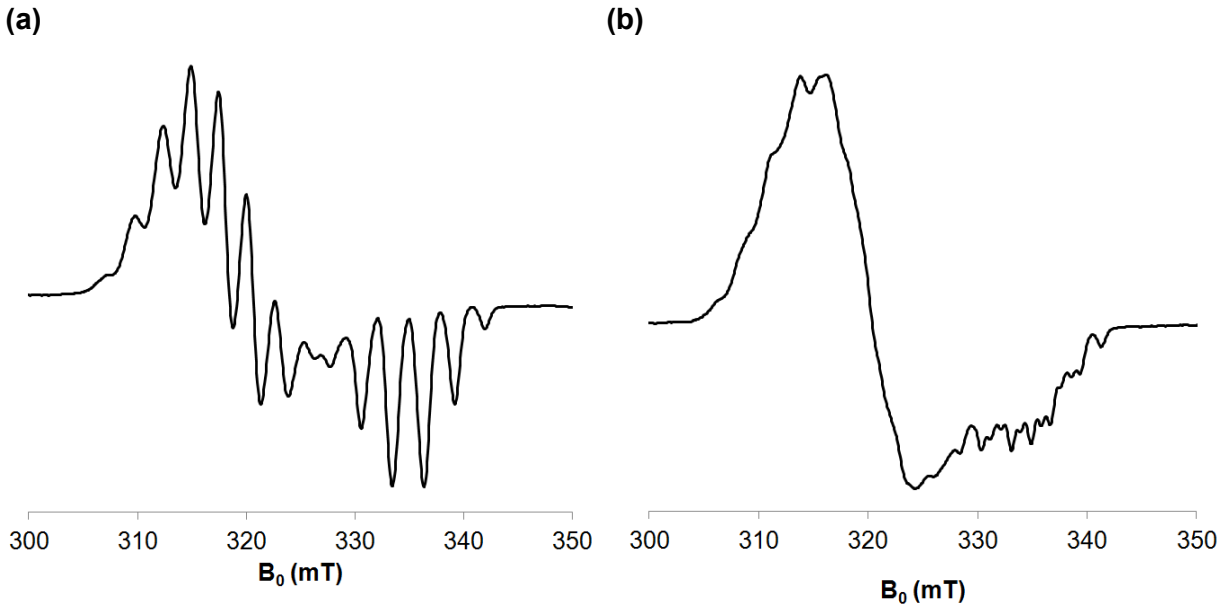
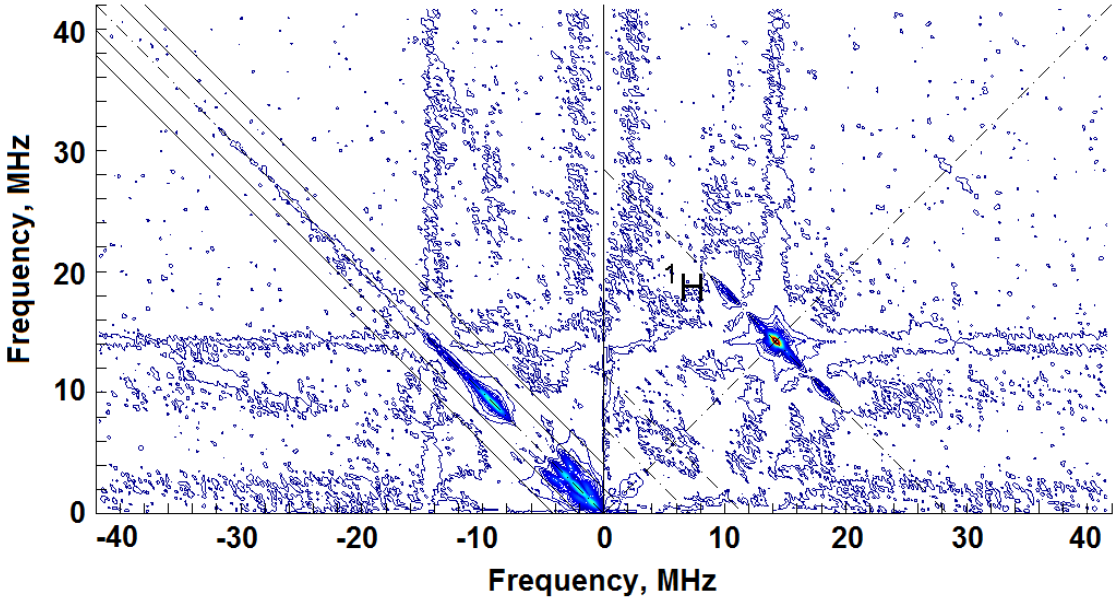


Figure 3.12 CW EPR spectra of the KO^{t}Bu deprotonation reaction of [*trans*-Fe(H)(N_2)(dmpe)$_2$][BPh_4] (a), and [*trans*-Fe(H)(N_2)(depe)$_2$][BPh_4] (b), recorded as THF glasses at 40 K.

Thus, in both cases, an unknown Fe(I) species was found to be present in significant concentration prior to acidification, consistent with electron transfer from Fe(0) prior to acidification in the Leigh system. However, the role of the Fe(0) and Fe(I) species in subsequent NH_3 formation remained ambiguous.

(a)



(b)

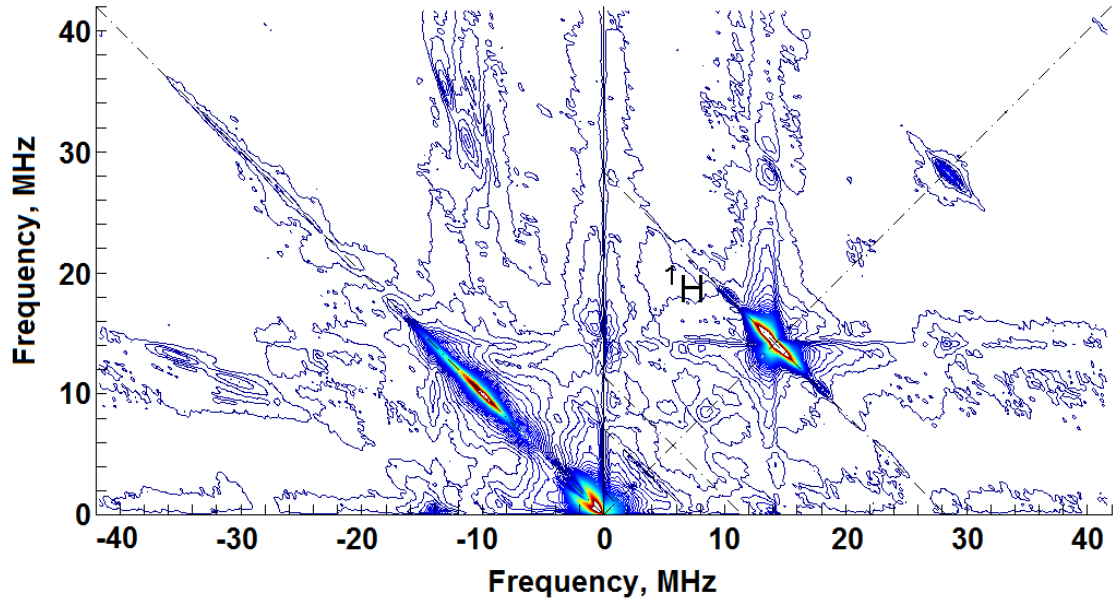


Figure 3.13 X-band HYSCORE spectra of the KO^{t}Bu deprotonation reaction of (a) [*trans*-Fe(H)(N_2)(dmpe)$_2$][BPh_4] (333mT, τ = 120 ns), and (b) [*trans*-Fe(H)(N_2)(depe)$_2$][BPh_4] (331.5 mT, 124 ns); recorded as THF glasses at 25 K.

Part 1: Fe complexes of dmpe

3.1.1 Introduction

Since the instability of the Fe(0) complex **4** had thus far prevented controlled acidification of isolated samples, its role as the active species responsible for NH_3 production in the Leigh cycle remained uncertain.[4] Although **4** appears to be the major component of the mixture formed prior to acidification, the influence of the remaining species, now known to include an EPR-active Fe(I) species, had yet to be verified. If **4** does not produce NH_3 with acid, as has been shown for the analogous $Fe(N_2)(depe)_2$ complex, two further possibilities are apparent: either another species directly responsible for NH_3 formation is generated in the deprotonation reaction, or a combination of **4** with one or more other species present is required. Thus, isolation of a stable form of **4** was targeted, such that its reactivity could be examined in order to test this hypothesis.

3.1.2 Isolating Fe(0) species

In the Leigh cycle, **4** is generated *in-situ via* reductive deprotonation of [*trans*-Fe(H)(N_2)(dmpe)$_2$][BPh_4] with excess KO^{t}Bu base (^{t}BuOH conjugate acid p$K_{a,DMSO}$ = 32.2),[23] additionally forming the adduct [(^{t}BuO)$_2$H]K in solution and precipitating $KBPh_4$.[1] KCH_2Ph (toluene conjugate acid p$K_{a,DMSO}$ = ~42)[24] has also been investigated as a stronger alternative base (Figure 3.14), anticipating faster consumption of starting material to prevent possible side-reactivity with **4**, and to benefit from the relatively more innocent conjugate acid toluene compared to [(^{t}BuO)$_2$H]K. Accordingly, the ^{31}P NMR spectrum (Figure 3.15) of this reaction mixture in Et_2O reveals almost exclusively **4** (δ = 63.4 ppm, s), with only a trace amount of a second species (δ = 66.1 ppm, s). However, EPR spectroscopy on the reaction mixture also revealed the same paramagnetic Fe(I) (S = ½) signal encountered using KO^{t}Bu base.

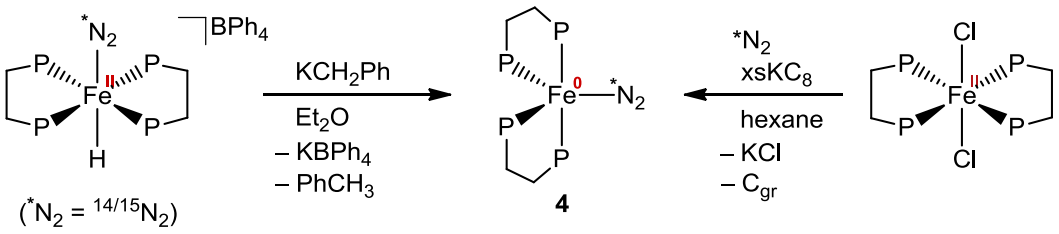


Figure 3.14 Preparation of $FeN_2(dmpe)_2$ (**4**) *in situ*; P = PMe_2.

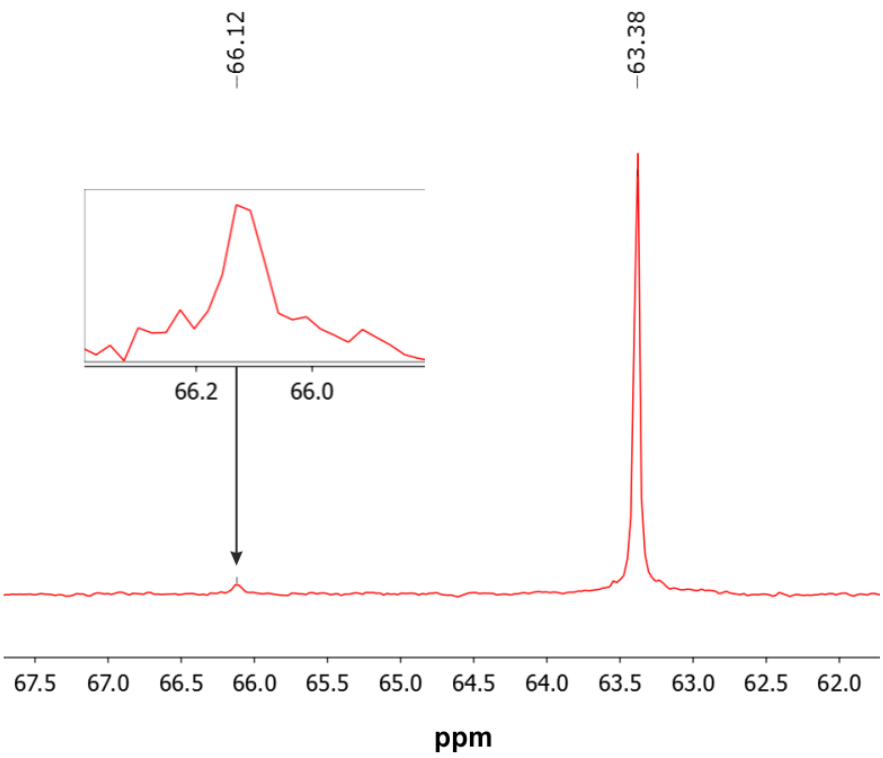


Figure 3.15 (a) ^{31}P NMR spectrum of the reductive deprotonation of [*trans*-Fe(H)(N_2)(dmpe)$_2$][BPh_4] with KCH_2Ph in Et_2O.

An alternative route to prepare **4** *in situ* has been reported by Field *et al. via* reduction of Fe(Cl)$_2$(dmpe)$_2$ in hexane under N_2 using excess KC_8.[16] Although they likewise never isolated **4**, this route was attractive to us since the KCl by-product is completely insoluble in the reaction medium; furthermore, performing the reaction under $^{15}N_2$ gas enables convenient ^{15}N labelling of **4**. However, in contrast to the reductive deprotonation reaction, a much stronger singlet resonance was observed at 66.0 ppm in the ^{31}P NMR spectrum for this reaction (Figure 3.16). In addition, a small amount of the known Fe(0) complex [{Fe(dmpe)$_2$}$_2$(μ-dmpe)] was identified, appearing at 61.4 (d) and 8.2 ppm (p), which is a known decomposition product of the coordinatively unsaturated complex [Fe(dmpe)$_2$] expected to be formed either as an intermediate prior to N_2 coordination or resulting from N_2 dissociation.[6] When performed under a $^{15}N_2$ atmosphere, two coupled doublets at 47.1 and 48.9 ppm ($^1J_{N\alpha\text{-}N\beta}$ = 5.9 Hz) were observed in the ^{15}N NMR spectrum (Figure 3.17) corresponding to the N_β and N_α shifts of **4**,[16] respectively, along with an upfield shifted singlet resonance at –54.9 ppm.

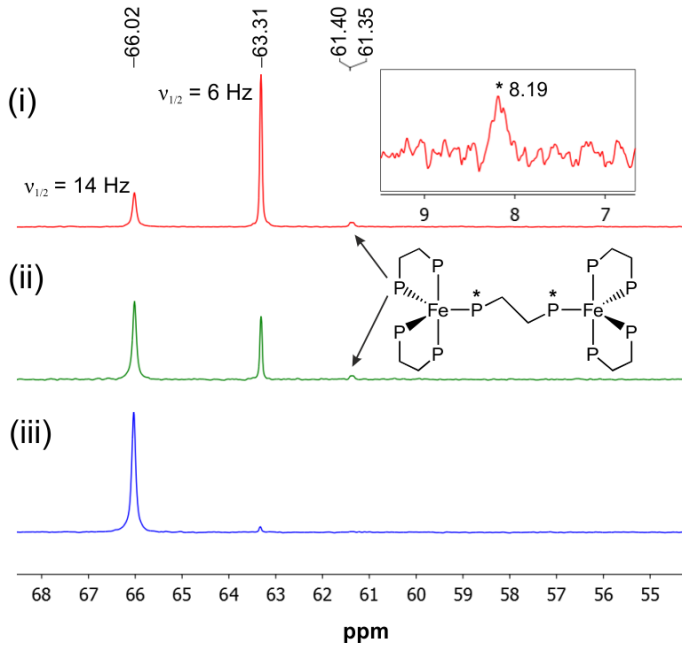


Figure 3.16 ^{31}P NMR spectra of the reduction of $Fe(Cl)_2(dmpe)_2$ under N_2 with xs KC_8 in hexane: (i) reaction mixture after 3 days; (ii) redissolved in hexane after removal of volatiles and drying *in vacuo*; (iii) recrystalised from hexane under argon; P = PMe_2.

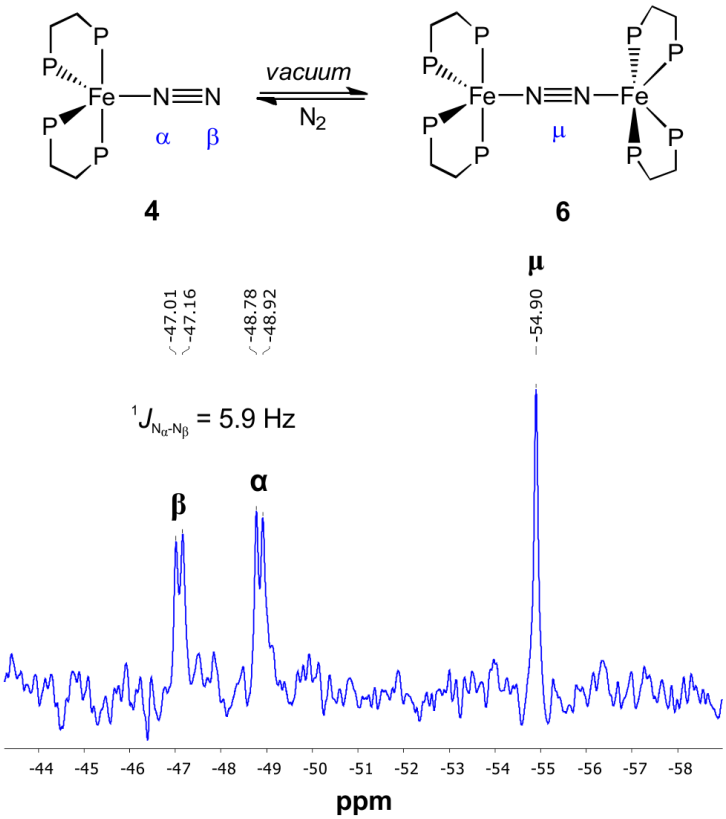
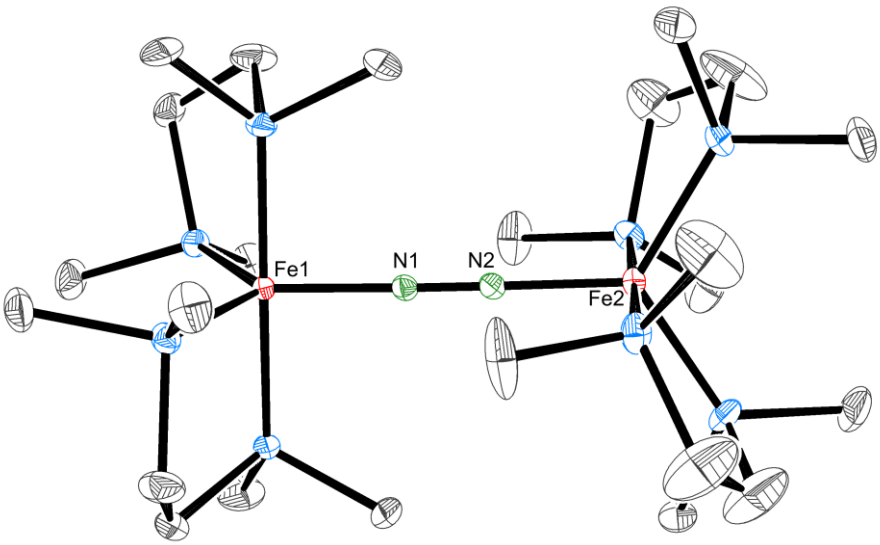


Figure 3.17 ^{15}N NMR spectrum of the reduction of $Fe(Cl)_2(dmpe)_2$ under $^{15}N_2$ with xs KC_8 in hexane overlaid with the equilibrium between species **4** and $[\{Fe(dmpe)_2\}_2(\mu\text{-}N_2)]$ (**6**); P = PMe_2.

To assess the reported instability of **4** *in vacuo*, hexane solvent was removed and the remaining oily solid dried for several hours at ca. 10^{-3} mbar pressure. Subsequent ^{31}P NMR analysis of this solid redissolved in hexane under Ar (Figure 3.16(b,ii) revealed **4** to still be present, albeit in a lower ratio to the unknown species at 66.0 ppm than previously observed. By slow evaporation of this mixture under Ar, deep red crystalline plates were grown which were suitable for single crystal X-ray diffraction; these solved as the novel Fe(0)/Fe(0) dimeric species [{Fe(dmpe)$_2$}$_2$(μ-N$_2$)] (**6**, Figure 3.18).

(a)

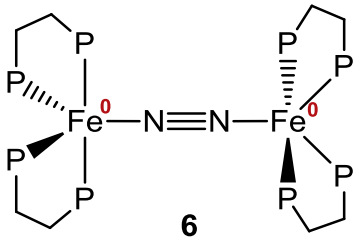


(b) **Bond lengths (Å):**

N1–N	1.144(3)	[1.153][a]
Fe1–N1	1.854(2)	
Fe2–N2	1.850(2)	[1.856][a]
[Fe1–P$_{eq}$]$_{av}$	2.1708(8)	
[Fe1–P$_{ax}$]$_{av}$	2.1684(8)	
[Fe1–P$_{eq}$]$_{av}$	2.1680(14)	
[Fe1–P$_{ax}$]$_{av}$	2.1761(17)	

Bond Angles (deg):

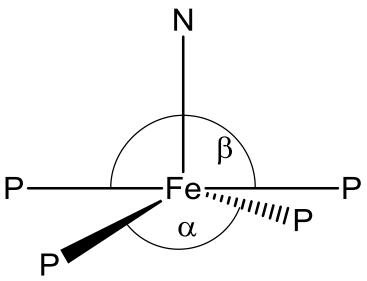
Fe1–N1–N2	178.7(2)
Fe2–N2–N1	179.1(2)



6

P = PMe$_2$

Fe coordination geometry:



τ = (β–α)/60

≈ 1 (trig. bipyr.)

≈ 0 (sq. pl.)

τ(Fe1) = 0.987

τ(Fe2) = 1.050

Figure 3.18 Solid-state structure of [{Fe(dmpe)$_2$}$_2$(μ-N$_2$)] (**6**); H atoms omitted for clarity, C atoms grey, Fe atom red, N atoms green, P atoms blue; anisotropic displacement ellipsoids shown at 30% probability; selected bond metric data, [a]DFT predicted values from ref. 14.

The recrystallised sample provided combustion analysis (CHN) consistent with this formulation and the corresponding ^{31}P NMR analysis (Figure 3.16(b,iii)) confirmed **6** to be responsible for the resonance at 66.0 ppm. Selected bond metric data for the dimeric complex **6** are displayed in Figure 3.18(b); a geometric parameter (τ;[25] defined in Figure 3.18(b)) can be used to systematically index the geometry of five-coordinate systems between either ideal trigonal bipyramidal (τ = 1) or square based pyramidal (τ = 0). The {Fe(dmpe)$_2$N} fragments have a near ideal trigonal bipyramidal coordination (τ_1 = 0.987, τ_2 = 1.050), whilst the equatorial planes about each Fe bisect one another close to perpendicular (82.08(4)°). The bridging N_2 ligand is approximately linear, exhibiting typical Fe–N single and N–N triple bond lengths, with values in close agreement with those predicted by Tyler *et al.* in the previously discussed computational study (see Figure 3.18(b)).[14]

6 can be prepared *via* **4** on a multi-gram scale by reduction of *trans*-Fe(Cl)$_2$(dmpe)$_2$ with excess KC_8 in hexane under N_2 (1-2 bar; Figure 3.19); higher pressures of N_2 inhibit N_2 dissociation and subsequent decomposition of [Fe(dmpe)$_2$] to [{Fe(dmpe)$_2$}$_2$(μ-dmpe)] and Fe metal. After filtering through Celite®, hexane solvent is mostly removed *in vacuo* and the remaining mixture of **4** and **6** is slurried for several days under Ar to selectively precipitate/crystallise less soluble **6**; any residual **4** or decomposition product [{Fe(dmpe)$_2$}$_2$(μ-dmpe)] is subsequently removed by decanting the supernatant and rinsing with additional cold hexane. The resulting microcrystalline sample is then rapidly recrystallised from hexane to remove any contaminating Fe metal; in this manner, samples of > 98% purity (by ^{31}P NMR) are obtained, which provide satisfactory combustion analysis (CHN).

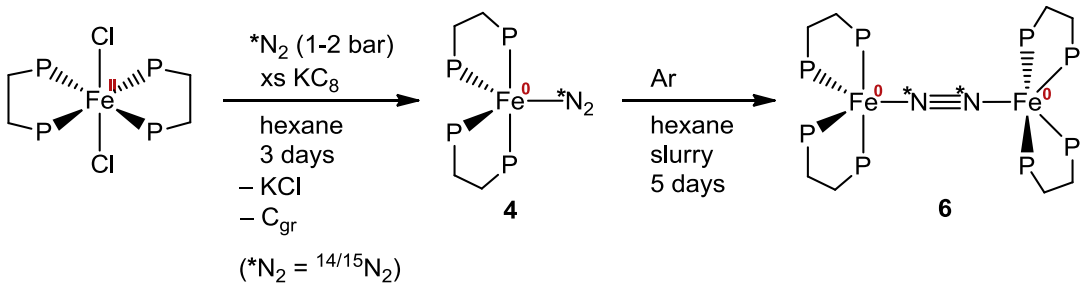


Figure 3.19 Multi-gram scale preparation of [{Fe(dmpe)$_2$}$_2$(μ-N$_2$)] (**6**); 93% yield; P = PMe$_2$.

As noted earlier, activation of the N_2 ligand through coordination to a metal centre with concomitant weakening of the N–N triple bond is most accurately correlated to the decrease in the stretching frequency, *v*(N–N), rather than changes in the N–N bond distance from single crystal X-ray crystallography.[5] Accordingly, *v*(N–N) was measured to be 1933 cm^{-1} for **6** by Raman spectroscopy (Figure 3.20) indicating increased activation of the N_2 ligand compared to the monomeric complex **4** (IR(KBr), *v*(N–N) = 1979 cm^{-1})[1] whilst still

corresponding to an N–N triple bond in line with other N_2 complexes of Fe (see Chapter 1, Table 1.2). Assignment of the Raman resonance to *ν*(N–N) was confirmed through comparison to the shifted resonance for the ^{15}N isotopically labelled compound, assuming simple harmonic vibration and an equivalent force constant k(N–N):

$$\nu = \frac{1}{2\pi}\sqrt{\frac{k}{\mu}} \quad , \quad \mu = \frac{m_A m_B}{m_A \times m_B} \quad \Rightarrow \quad \frac{\nu(^{14}N\text{-}^{14}N)}{\nu(^{15}N\text{-}^{15}N)} = \sqrt{\frac{\mu(^{15}N_2)}{\mu(^{14}N_2)}} = 1.035$$

$$\frac{\nu(^{14}N\text{-}^{14}N)}{\nu(^{15}N\text{-}^{15}N)} = \frac{1933\ cm^{-1}}{1870\ cm^{-1}} = 1.034$$

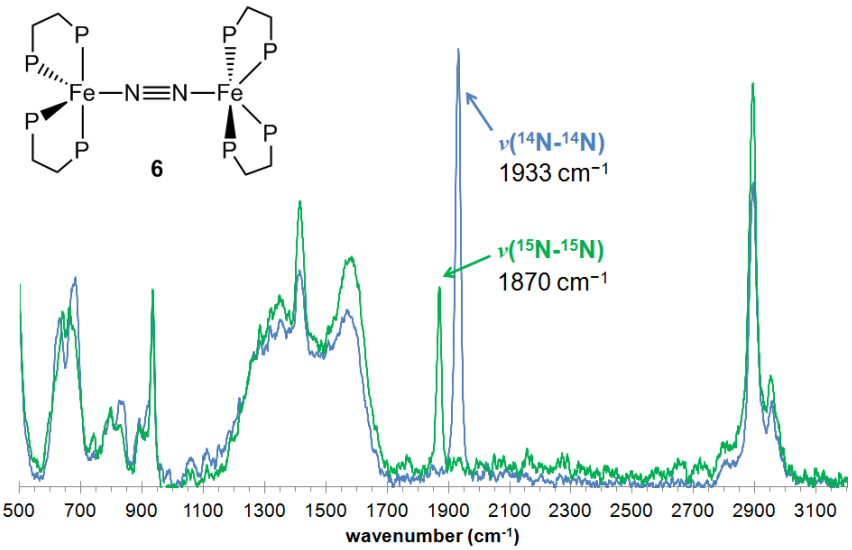
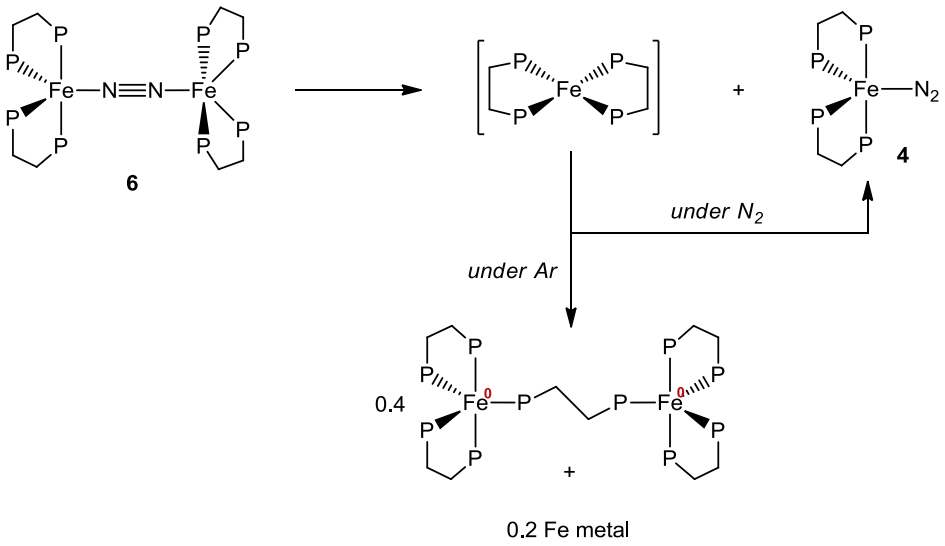


Figure 3.20 Raman spectra of [{Fe(dmpe)$_2$}$_2$(μ-$^{14}N_2$)] (**6**, blue) and [{Fe(dmpe)$_2$}$_2$(μ-$^{15}N_2$)] (green) recorded on powdered samples using a He-Ne (red) 633nm laser; P = PMe_2.

The increased degree of N_2 activation in the dimer relative to the monomer is presumed to be the result of additional π-backbonding into π*(N–N) from coordination to two Fe centres.

Although **6** has limited stability in donor solvents, as predicted by Tyler *et al.* on the basis of a low energy barrier for dissociation to **4** and [Fe(dmpe)$_2$] of only +6 kcal mol^{-1} (B3LYP, ε = 7.52 (THF)),[14] alkane solutions are relatively stable ($t_{½}$ = 21 days in hexane, pseudo-zero-order *k* = 5.3x10^{-9} M s^{-1}; Figure 3.21). This is thought to be due to the absence of donor solvents to perform nucleophilic attack on one of the Fe centres to displace **4** and generate the solvent stabilised (although metastable) complex [Fe(dmpe)$_2$]·THF (18 VE), which subsequently decomposes to [{Fe(dmpe)$_2$}$_2$(μ-dmpe)] and Fe metal (*vide supra*).

(a)



(b)

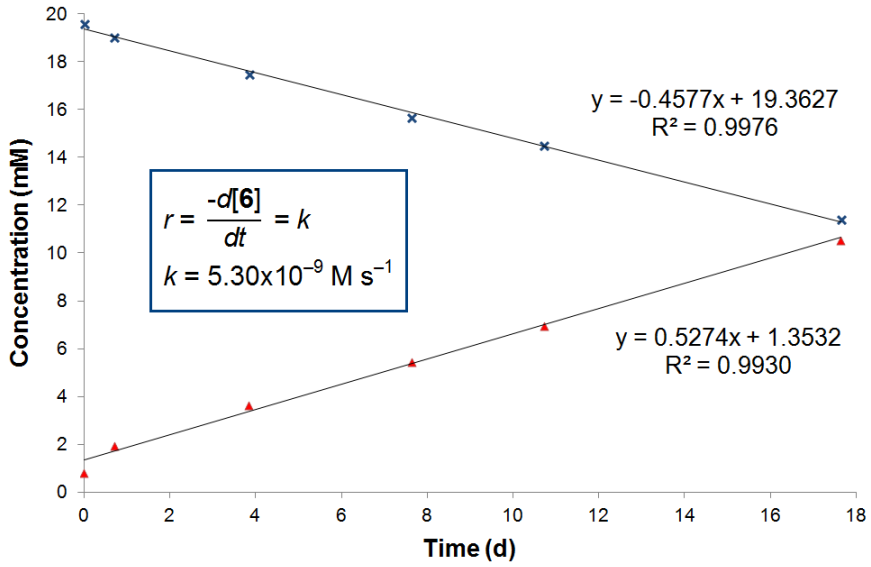


Figure 3.21 (a) Decomposition pathways for **6** under Ar and N_2; P = PMe_2; (b) pseudo-zero-order rate constant calculated from ^{31}P NMR determined concentrations of **6** (x) and **4** (▲) over time from a 20 mM hexane solution of **6** under Ar.

The vivid red colour of solutions of **6** corresponds to a strong electronic absorbance at 357 nm (3442 m^2 mol^{-1}; Figure 3.22). Under N_2 atmosphere, dissociation readily occurs to cleanly afford **4**, which exhibits a weaker broad band at ~340 nm (~1708 m^2 mol^{-1}). Thus, **4** is accessible for the first time from its dimeric solid-state form rather than as a reaction mixture with unknown contaminants.

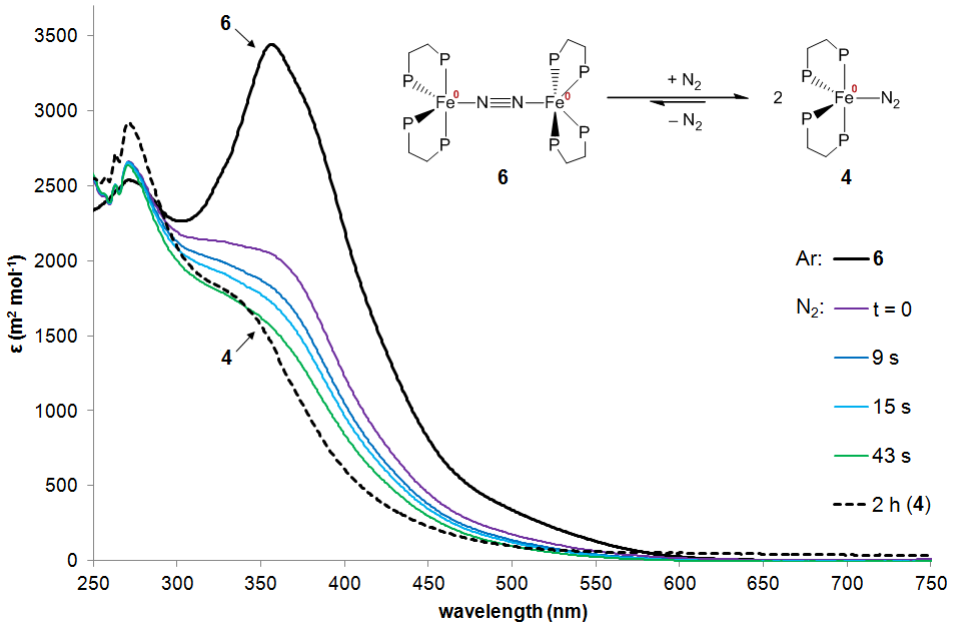


Figure 3.22 UV-vis spectra of **6** (Et_2O, Ar and N_2) showing dissociation to **4** under N_2 over time; time values are relative to initial measurement; P = PMe_2.

3.1.3 Diamagnetic-paramagentic transition in the Leigh deprotonation step

In the Leigh cycle, deprotonation of [*trans*-Fe(H)(N_2)(dmpe)$_2$][BPh_4] prior to acidification is essential for producing NH_3, however the roles of the various components of this mixture remain ambiguous. The NMR active (diamagnetic) products of the deprotonation step are: **4**; ^{t}BuOH, the conjugate acid of KO^{t}Bu, which reacts with excess KO^{t}Bu to form the adduct [(^{t}BuO)$_2$H]K (^{1}H NMR, δ = 8-10 ppm); and $KBPh_4$, which has limited solubility in THF and mostly precipitates from solution (Figure 3.23). It was hypothesised that a combination of **4** with one or more of the other species present in solution may generate the species responsible for the EPR (S = ½) signal characteristic of Fe(I).

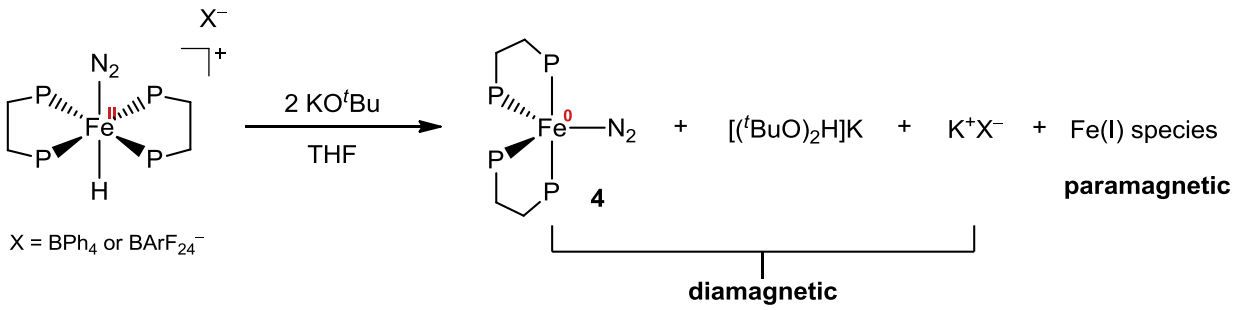


Figure 3.23 Species formed in the Leigh deprotonation reaction; P = PMe_2.

As discussed in Section 3.02, addition of ^{t}BuOH to the deprotonation mixture reforms [*trans*-Fe(H)(N_2)(dmpe)$_2$]$^+$ along with the dimeric species [*trans*-Fe(H)(dmpe)$_2$(μ-N_2)Fe(dmpe)$_2$]$^+$. However, both species are diamagnetic and regardless, are consumed by excess KO^{t}Bu to form **4** and [(^{t}BuO)$_2$H]K. Thus we turned our attention to the effect of K^+ salts in solution; $KBArF_{24}$ was employed due to the poor solubility of $KBPh_4$ in THF and furthermore, the non-coordinating $BArF_{24}^-$ counter anion ensures the K^+ ions are bound only by the weak interactions with the solvent. Accordingly, the addition of $KBArF_{24}$ to a solution of **4**, which was generated from **6** dissolved in THF under N_2, was monitored by NMR and EPR spectroscopy. Gratifyingly, the ^{31}P NMR resonance for **4** decreased by almost 50% (Figure 3.25), indicating consumption of diamagnetic Fe(0), whilst the X-band CW-EPR spectrum revealed the same Fe(I) near isotropic signal as that observed in the Leigh deprotonation step (Figure 3.24(a)).

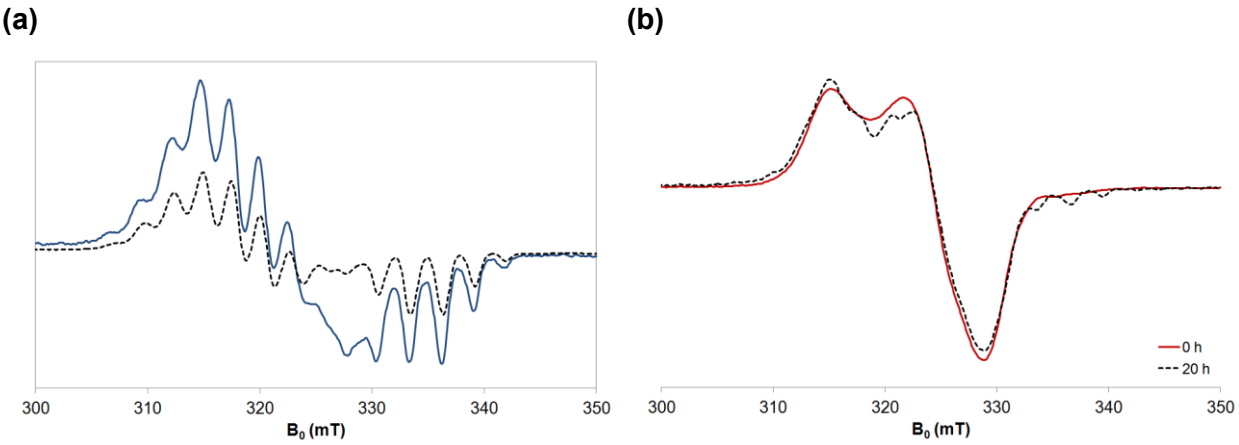


Figure 3.24 X-band CW-EPR spectra of (a) **4** with $KBArF_{24}$ (1:1) under N_2 (blue) and the Leigh deprotonation reaction mixture under N_2 ([*trans*-Fe(H)(N_2)(dmpe)$_2$][BPh_4]/KO^{t}Bu(1:2); dashed black); (b) **6** with $KBArF_{24}$ (1:2) under Ar (initial, red; and after 20 h at RT, dashed black); recorded at 40 K as THF glasses.

Hence, K^+ salts appear to be responsible for a diamagnetic-paramagnetic transition in the Leigh cycle, which was previously thought to only involve Fe(0)-Fe(II) redox processes. The effect of $KBArF_{24}$ additive was even more dramatic for solutions of the dimeric species **6** in THF under Ar, resulting in a decrease in the overall ^{31}P NMR intensity of 87% (Figure 3.26). Prior to addition of $KBArF_{24}$, the solution contained **6** (95%) and **4** (5%) by ^{31}P NMR spectroscopy; after addition, the resonance for **6** disappeared entirely, with only a slight increase in **4** (9%, likely from further dissociation of **6**) and formation of a small amount (4%) of the protonated dimeric species **5**. Interestingly, a different, near axial Fe(I) (S = ½) EPR signal was observed (Figure 3.24(b)). However, the characteristic hyperfine coupling of the near isotopic signal began to appear when this sample was left at RT for 20 h. Thus, it would

appear that **6** reacts with K^+ ions faster than **4**, which may shift the equilibrium between **4** and **6** in favour of the latter (Figure 3.27).

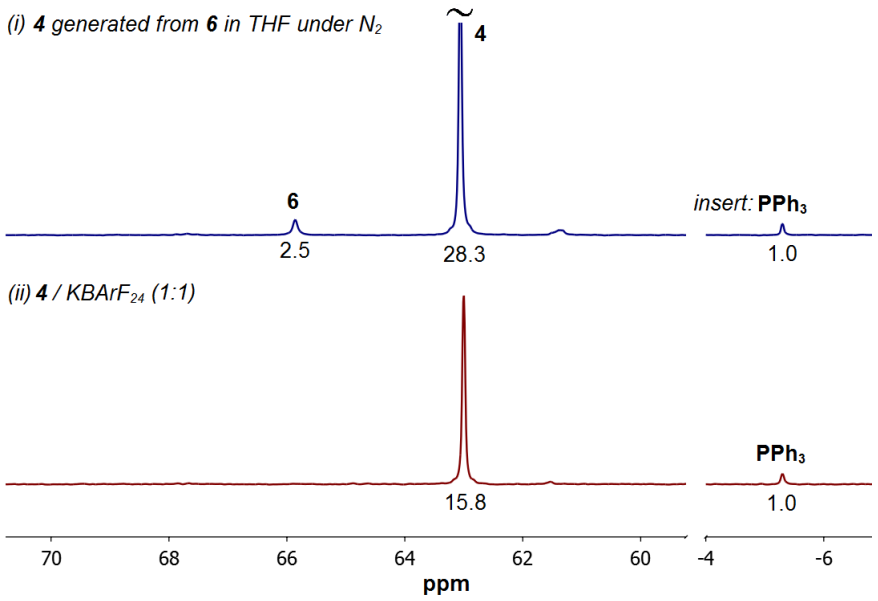


Figure 3.25 ^{31}P NMR spectrum of **4** in THF under N_2 before (top) and after (bottom) addition of $KBArF_{24}$ (1:1).

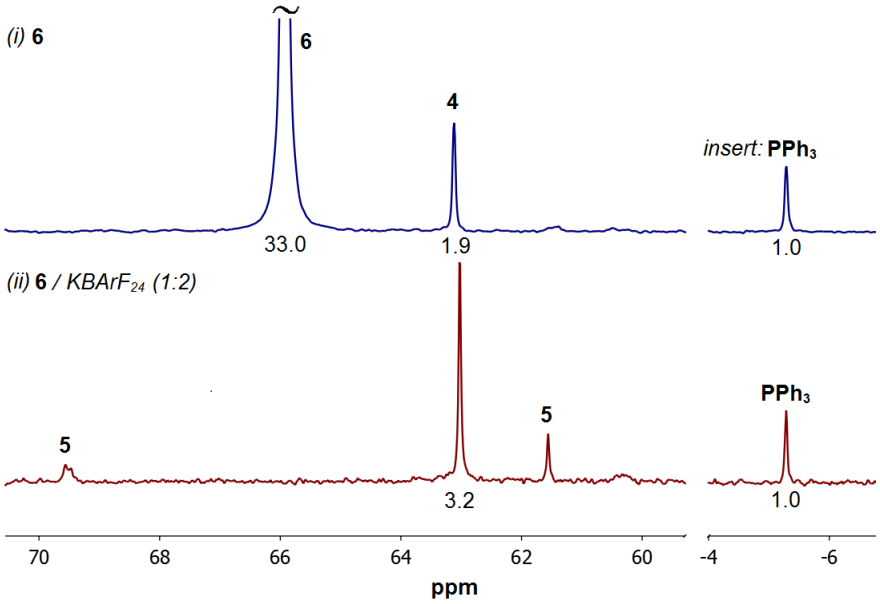


Figure 3.26 ^{31}P NMR spectrum of **6** in THF under Ar before (top) and after (bottom) addition of $KBArF_{24}$ (1:2).

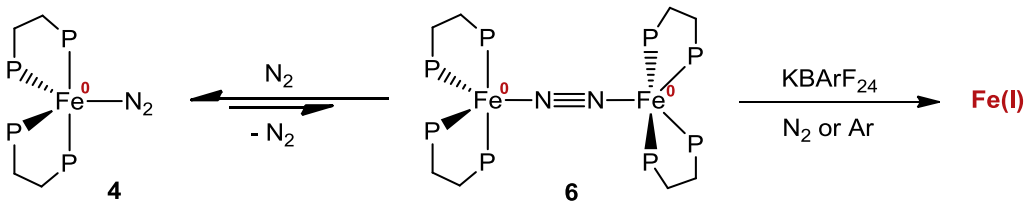


Figure 3.27 Proposed reaction of **4** with $KBArF_{24}$ *via* **6** to form an Fe(I) species; P = PMe_2.

Attempts to isolate crystalline products from this reaction in THF often yielded crystals of **6** along with $KBArF_{24}$, indicating a highly reversible process. A further issue was encountered with gradual formation of the protonated species **5** by ^{31}P NMR, suggesting adventitious H_2O was introduced upon addition of $KBArF_{24}$. However, rigorous drying of $KBArF_{24}$ prior to use gave no improvement, indicating an inherent instability of species in solution with respect to deprotonation or radical H· abstraction of the THF solvent. Accordingly, the more stable, albeit poorer donor solvents Et_2O and ^{t}BuOMe (TBME) have often been used preferentially in this work; notably, Leigh *et al.* also reported use of Et_2O solvent generates NH_3 in similar yields to THF.[1] Performing the reaction of **6** with $KBArF_{24}$ in these solvents, and also under an Ar atmosphere, appeared to shift the equilibrium further in favour of the Fe(I) species, as demonstrated by the resolution of broad resonances in the ^1H NMR spectra (Figure 3.28) and a noticeable change in the colour of the solution to a greenish brown. Remarkably, **6** also reacted instantaneously with $KBArF_{24}$ in pentane solvent, in which the latter is not expected to be soluble, resulting in a green precipitate and decolourisation of the initial red solution.

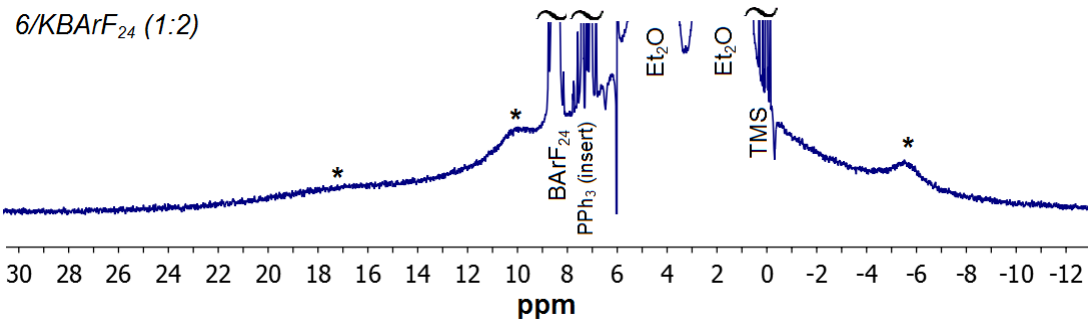
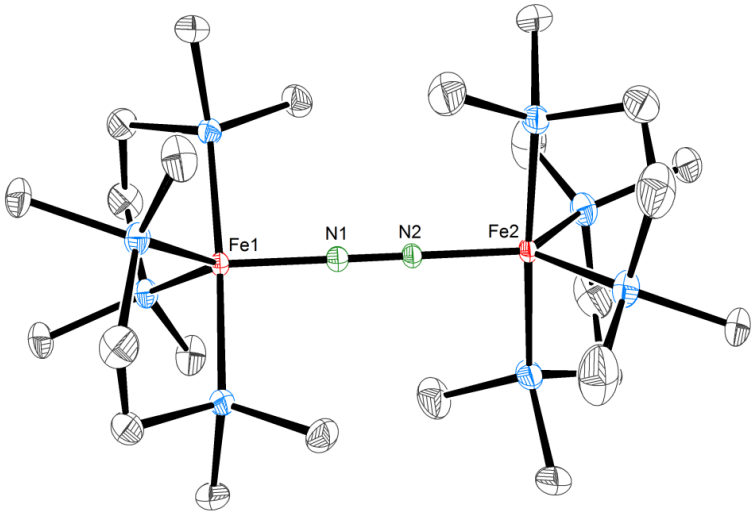


Figure 3.28 ^1H NMR spectra of the reaction of **6** with $KBArF_{24}$ (1:2, Et_2O, Ar); *broad resonances corresponding to a paramagnetic species.

Dark green crystals were grown by slow diffusion of pentane into a TBME solution of **6**/$KBArF_{24}$ (1:2), which were suitable for single crystal X-ray diffraction, solving as the dimer $[\{Fe(dmpe)_2\}_2(\mu\text{-}N_2)][BArF_{24}]$ (**7**, Figure 3.29). The unit cell of **7** incorporates a single $BArF_{24}^-$ counteranion per two very similar independent half molecules of $[\{Fe(dmpe)_2\}_2(\mu\text{-}N_2)]^+$, indicating a mixed valence Fe(0)/Fe(I) complex; selected bond metric data is presented in

Figure 3.29. Both independent dimer molecules have C_2 symmetry about axes that pass through the two Fe atoms and the bridging nitrogen centres and as a consequence the Fe–N-N-Fe units are perfectly linear. The N–N atomic separations in the crystal structures of **6** and **7** are the same within error, whilst the Fe–N bond distances are also very similar. However, whereas the two trigonal bipyramidal [Fe(dmpe)$_2$N] fragments in **6** are nearly perpendicular, in **7** these are staggered such that the equatorial planes bisect one another at either 33.35(5)° or 46.18(16)° for the two independent dimer molecules (Figure 3.30).

(a)

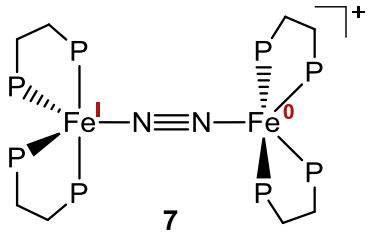


(b) **Bond lengths (Å):**

N1–N2	1.155(6)
Fe1–N1	1.820(4)
Fe2–N2	1.816(4)
[Fe1–P_{eq}]$_{av}$	2.1924(11)
[Fe1–P_{ax}]$_{av}$	2.2067(11)
[Fe2–P_{eq}]$_{av}$	2.191(2)
[Fe2–P_{ax}]$_{av}$	2.207(2)

Bond Angles (deg):

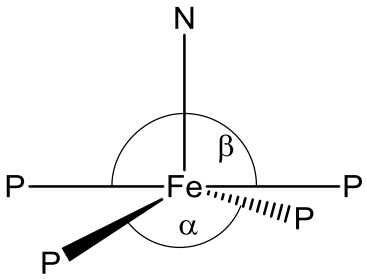
Fe1–N1–N2	180[a]
Fe2–N2–N1	180[a]



7

P = PMe_2

Fe coordination geometry:



τ = (β–α)/60

≈ 1 (trig. bipyr.)

≈ 0 (sq. pl.)

τ(Fe1) = 1.062

τ(Fe2) = 1.064

Figure 3.29 (a) Solid-state structure of [{Fe(dmpe)$_2$}$_2$(μ-N_2)][$BArF_{24}$] (**7**); $BArF_{24}^-$ counter anion and H atoms omitted for clarity, C atoms grey, Fe atom red, N atoms green, P atoms blue; anisotropic displacement ellipsoids shown at 30% probability; the unit cell contains two very similar independent dimer molecules of which only one is shown; (b) selected bond metric data are averaged for the two independent molecules; [a]the Fe-N-N-Fe unit lies along a C2 symmetry axis and as a consequence is perfectly linear.

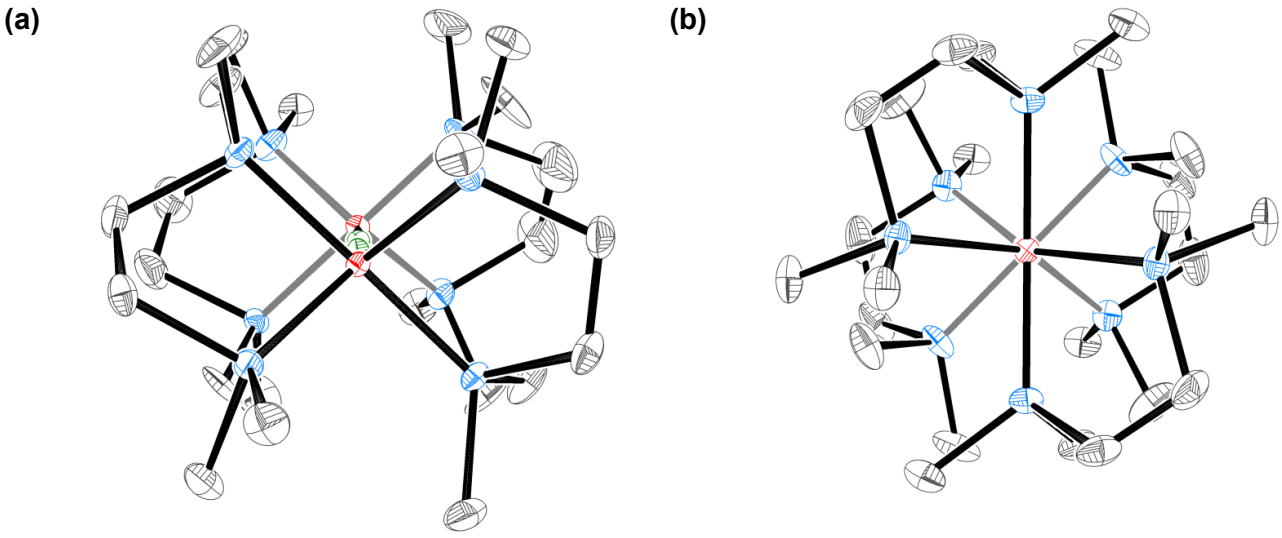


Figure 3.30 Comparison of the solid-state structures of **6** (a) and **7** (b) viewed along the Fe1-N1-N2-Fe2 axis (rear Fe–P bonds coloured grey).

Since **7** is related to **6** *via* a single electron oxidation, a concomitant reduction process must also have occurred. The presence of the $BArF_{24}^-$ anion in the oxidised species **7** necessarily implicates involvement of the K^+ cation in the formulation of the corresponding reduced species, which will be explored in section 3.1.6.

3.1.4 Isolating Fe(I) species

In order to further elucidate this reactivity with K^+ salts, the independent synthesis of **7** from **4** or **6** was performed using the ferrocenium oxidant $[Cp_2Fe][BArF_{24}]$ (Figure 3.31). Addition of $[Cp_2Fe][BArF_{24}]$ to a solution of **6** in Et_2O (1:1) resulted in a rapid colour change to a dark green solution, which was evaporated and rinsed with hexane to remove Cp_2Fe. The crude solid was recrystallised from a Et_2O solution layered with pentane, yielding dark green crystals of **7**. Alternatively, **7** can be accessed *via* addition of $[Cp_2Fe][BArF_{24}]$ (0.5 equivalents) to **4**. Complete oxidation of all Fe(0) centres to Fe(I) in **4** and **6** was also performed by analogous oxidation reactions with $[Cp_2Fe][BArF_{24}]$ (1 and 2 equivalents, respectively), which in both cases produced a paramagnetic green solid. After numerous attempts to grow a crystal suitable for single crystal X-ray diffraction - mostly yielding amorphous material - slow diffusion of pentane into a Et_2O solution finally provided a crystal which solved as the dicationic complex $[\{Fe(dmpe)_2\}_2(\mu\text{-}N_2)][BArF_{24}]_2$ (**8**; Figure 3.32(a)). However, the solution is poor (R1 = 15.4 %) due to considerable disorder within the $[Fe(dmpe)_2]$ fragment as a consequence of rotation along the Fe–N–N–Fe axis, clearly apparent in the residual electron density map (Figure 3.32(b)). Hence, whilst the structural composition of **8** can be determined with certainty, a bond metric analysis has not been

attempted. Subsequent characterisation of **7** and **8** was performed on samples providing consistent combustion analysis (CHN) with the crystallographically determined formulations.

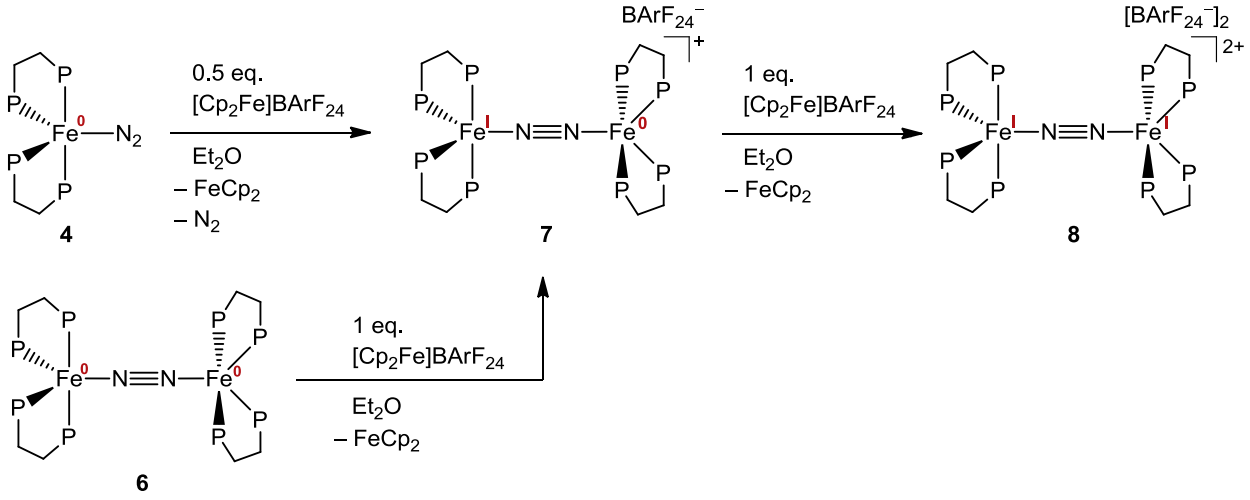


Figure 3.31 Synthesis of **7** and **8** *via* oxidation of either **4** or **6** in 82-86% yields; P = PMe_2.

(a) **(b)**

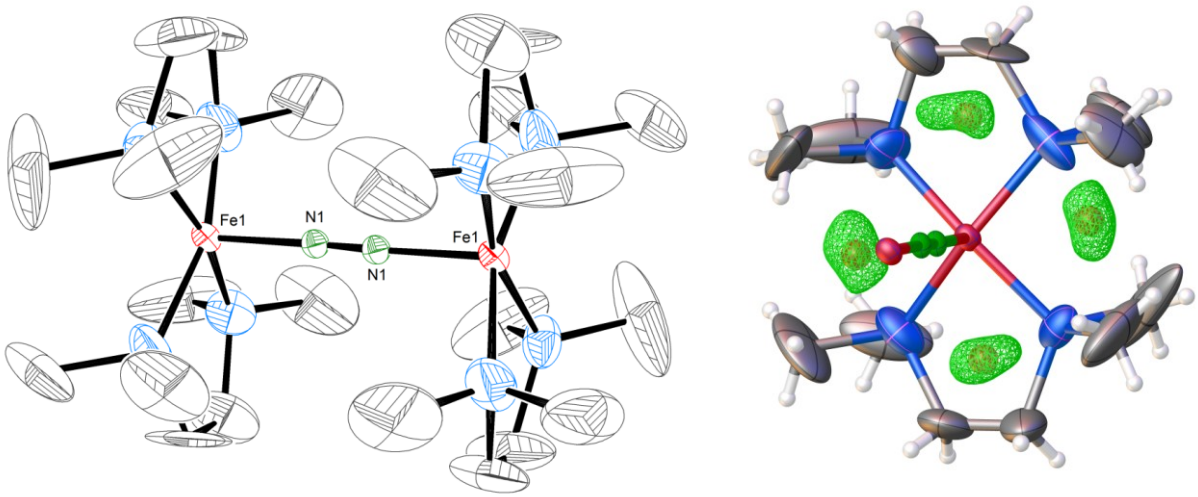


Figure 3.32 (a) Partial solution of the solid-state structure of $[\{Fe(dmpe)_2\}_2(\mu\text{-}N_2)][BArF_{24}]_2$ (**8**); $BArF_{24}^-$ counter anion and H atoms omitted for clarity, C atoms grey, Fe atom red, N atoms green, P atoms blue; anisotropic displacement ellipsoids shown at 30% probability; (b) electron density map and the first four Q-peaks (Q1–4) projected onto the asymmetric unit cell (plus second Fe1 and N1 atoms generated by inversion).

Both **7** and **8** are silent by ^{31}P NMR spectroscopy, although four broad resonances are resolved in the ^{1}H NMR spectra of **7** (THF, Figure 3.33) within the measured range (55 to –45 ppm); relative integrations of these broad resonances are approximate preventing unambiguous assignment.

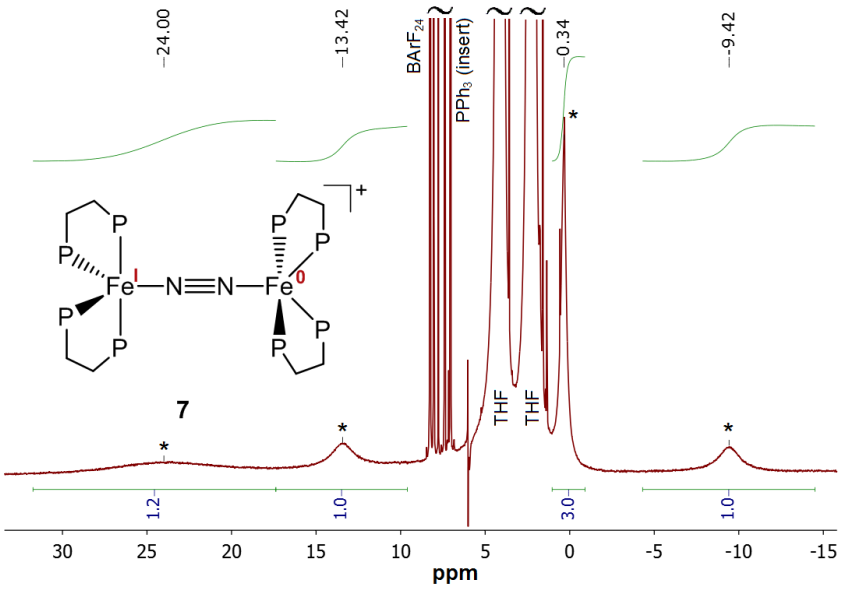


Figure 3.33 ^{1}H NMR spectra of [{Fe(dmpe)$_2$}$_2$(μ-N$_2$)][BArF$_{24}$] (**7**, THF, Ar); P = PMe$_2$.

Conversely to **6**, the N–N stretch of **7** is IR active (ν(N–N) = 1894 cm^{-1} (KBr pellet), 1885 cm^{-1} (Et$_2$O, Ar); Figure 3.34) and Raman inactive; this is possibly due to the lower symmetry in **7** either from partial localisation of the unpaired electron, or as a consequence of the two opposing [Fe(dmpe)$_2$N] fragments being staggered. The assignment of ν(N–N) to a dimeric form of **7**, as determined crystallographically in the solid-state, is supported by the close agreement between solid-state and solution measurements, and is further corroborated by UV-vis and EPR spectroscopic measurements of **7** under similar conditions (*vide infra*).

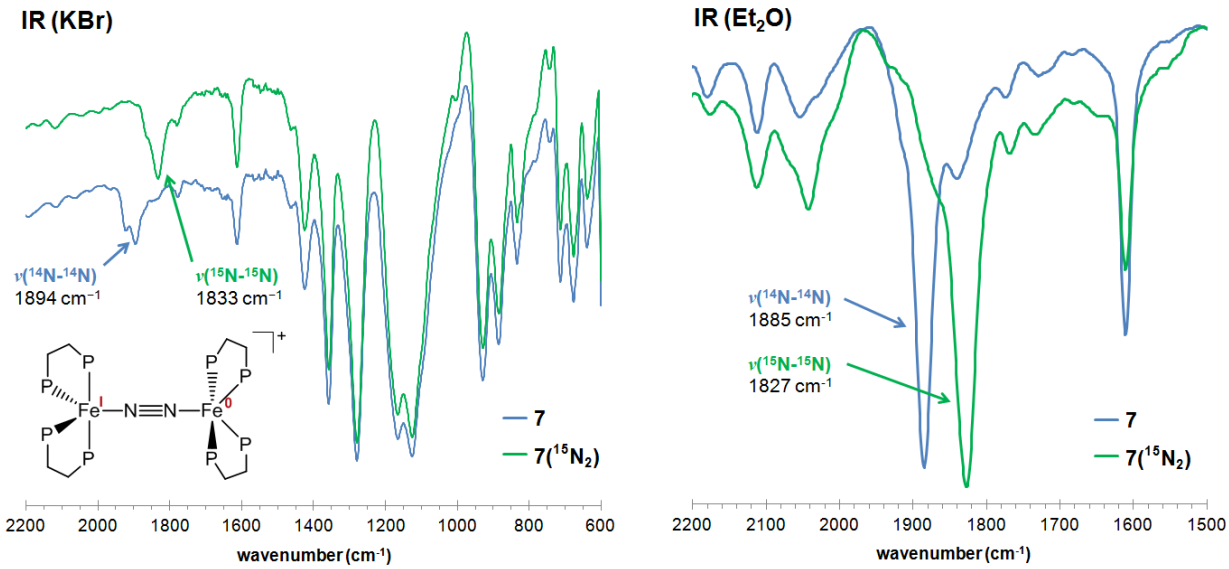


Figure 3.34 IR spectra of [{Fe(dmpe)$_2$}$_2$(μ-^{14}N$_2$)]BArF$_{24}$ (**7**, blue) and [{Fe(dmpe)$_2$}$_2$(μ-^{15}N$_2$)]BArF$_{24}$ (green) recorded as either a pressed solid KBr pellet (left) or a ~1 M Et$_2$O solution under Ar (right, solvent subtracted); P = PMe$_2$.

The N–N stretch of **8** is Raman active and IR inactive in the solid state, which is consistent with two opposing Fe(I) centres rather than an alternative mixed valence Fe(0)/Fe(II) assignment. However, the Raman spectra reveals three distinct bands very close in energy (ν(N–N) = 1929, 1946, 1963 cm^{-1}, Figure 3.35), which may reflect slight variations in coordination geometry for different polymorphs of **8**, or the rotational freedom about the Fe–N–N–Fe axis apparent in the partial structure solution (X-ray crystallography). In solution, a significantly stronger ν(N–N) stretch is observed by IR (ν(N–N) = 2081 cm^{-1}, Figure 3.35), which is thought to correspond to a monomeric Fe(I) species $[Fe(N_2)(dmpe)_2][BArF_{24}]$ formed upon dissociation of dimeric **8** (*vide infra*). Hence, the degree of N_2 activation appears to be considerably reduced in the monomeric species, consistent with less π-backdonation into π*(N–N) from a single Fe(I) centre. For comparison, solution IR spectra of **4**, **7**, and **8**, along with the protonated species [*trans*-$Fe(H)(N_2)(dmpe)_2][BArF_{24}]$ and **5**, are presented together in Figure 3.36; ν(N–N) values are provided in table 3.3.

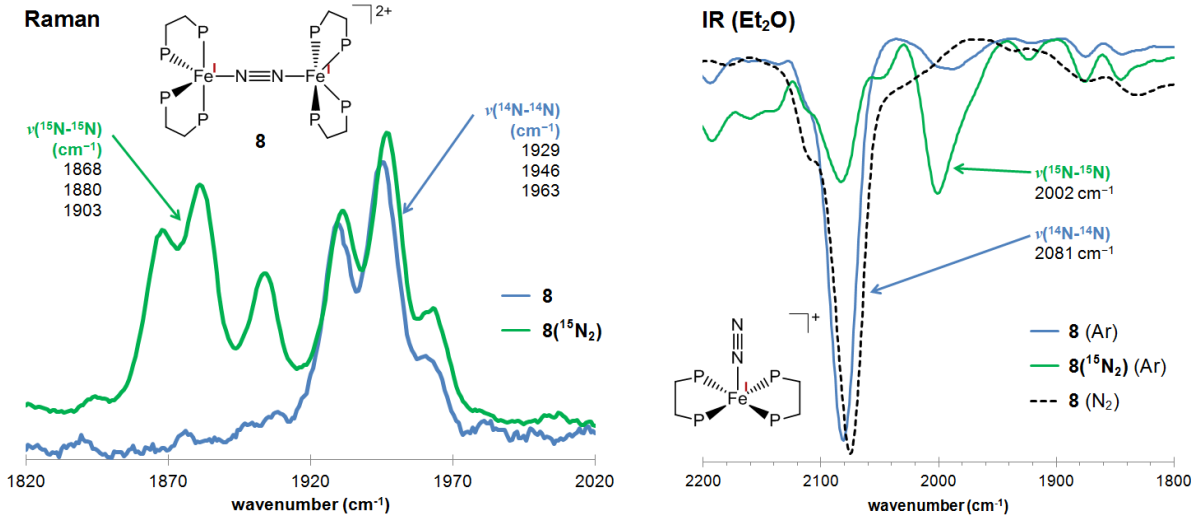


Figure 3.35 (left) Raman spectra of $[\{Fe(dmpe)_2\}_2(\mu\text{-}^{14}N_2)][BArF_{24}]_2$ (**8**, blue) and $[\{Fe(dmpe)_2\}_2(\mu\text{-}^{15}N_2)][BArF_{24}]_2$ (green), recorded on powdered samples using a He-Ne (red) 633 nm laser; (right) solution IR spectra (solvent subtracted) of $[\{Fe(dmpe)_2\}_2(\mu\text{-}^{14}N_2)][BArF_{24}]_2$ (**8**, 1,2-DFB, Ar blue), $[\{Fe(dmpe)_2\}_2(\mu\text{-}^{15}N_2)][BArF_{24}]_2$ (1,2-DFB, Ar green), and **8** (Et_2O, N_2, dashed black); IR measured ν(N-N) stretches are presumed to correspond to $[Fe(^{14/15}N_2)(dmpe)_2][BArF_{24}]$ generated *via* dissociation of **8**; P = PMe_2.

It may be inferred that the degree of N_2 activation reflects the electron availability for metal π-backbonding since ν(N–N) decreases with decreasing oxidation state of Fe, or with coordination to a second Fe centre. On this basis, a greater degree of N_2 activation is expected for the Fe(0)/Fe(0) dimer **6** relative to the Fe(0)/Fe(I) dimer **7**; however, the lower ν(N–N) stretch measured for the latter contradicts this. Alternatively, an enhanced Lewis

acidity for the cationic Fe(I) centre in **7** may promote π-backdonation from the Fe(0) centre by stabilising the resultant partial negative charge on the N_2 bridge (Figure 3.37); this is further supported by the observation of an intervalence charge transfer band (IVCT)[26] in the UV-vis spectra (*vide infra*). Accordingly, the N_2 bond order in **7** may be considered to be between 2.5 (N_2^-) and 3 (N_2); notably, **7** has the lowest *v*(N–N) stretch out of all the complexes incorporating a neutral ligand scaffold that are tabulated in section 1.4.

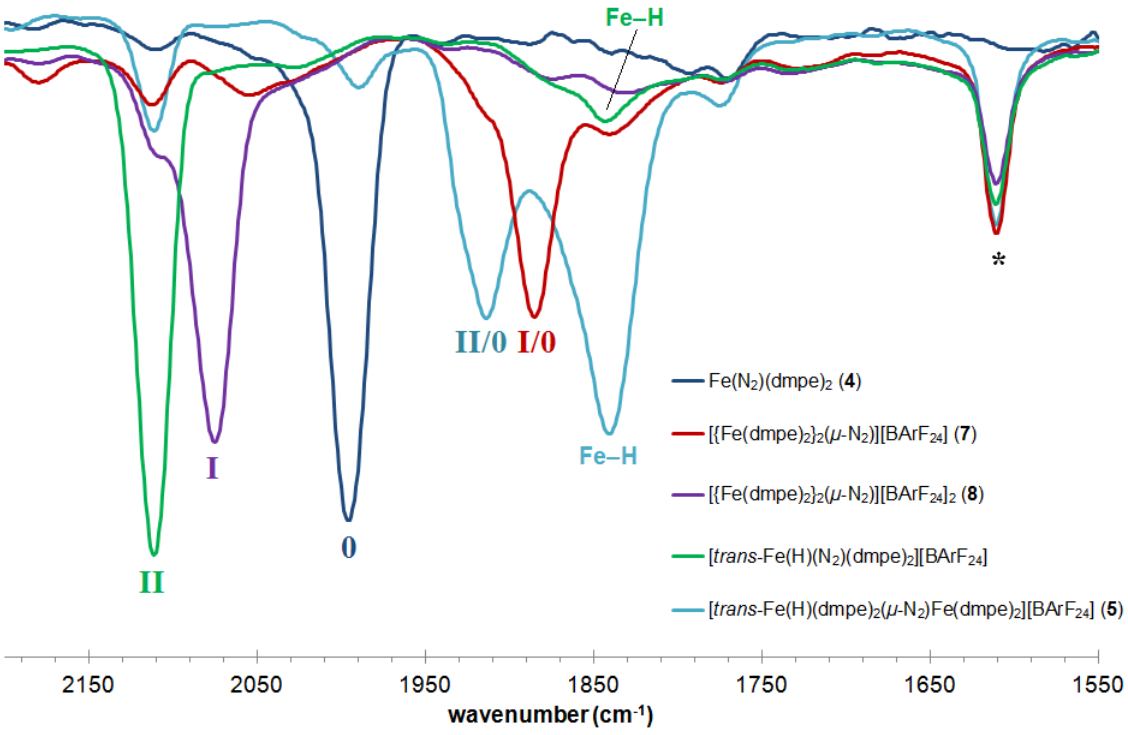


Figure 3.36 Solution IR spectra (Et_2O, solvent subtracted) of various $^{14}N_2$ complexes incorporating the [Fe(dmpe)$_2$] scaffold with their corresponding Fe oxidation states labelled; solutions measured under an Ar atmosphere; *corresponds to the $BArF_{24}^-$ counteranion *v*(C=C) stretch.

Table 3.3 *v*(N–N) stretches for compounds **4**–**8** in cm^{-1}.

Complex	Fe ox. state	IR (KBr)	IR (Et_2O)	Raman[a]
$FeN_2(dmpe)_2$ (**4**)	0	1979	1996	b
$[Fe(H)(dmpe)_2(\mu\text{-}N_2)Fe(dmpe)_2][BArF_{24}]$ (**5**)	2, 0	b	1914	b
$[\{Fe(dmpe)_2\}_2(\mu\text{-}N_2)]$ (**6**)	0, 0	c	c	1933
$[\{Fe(dmpe)_2\}_2(\mu\text{-}N_2)][BArF_{24}]$ (**7**)	1, 0[d]	1894	1885	c
$[\{Fe(dmpe)_2\}_2(\mu\text{-}N_2)][BArF_{24}]_2$ (**8**)	1, 1	c	2081	1929, 1946, 1963

[a] measured on a fine powder; [b] not measured; [c] no *v*(N–N) band; [d] see text.

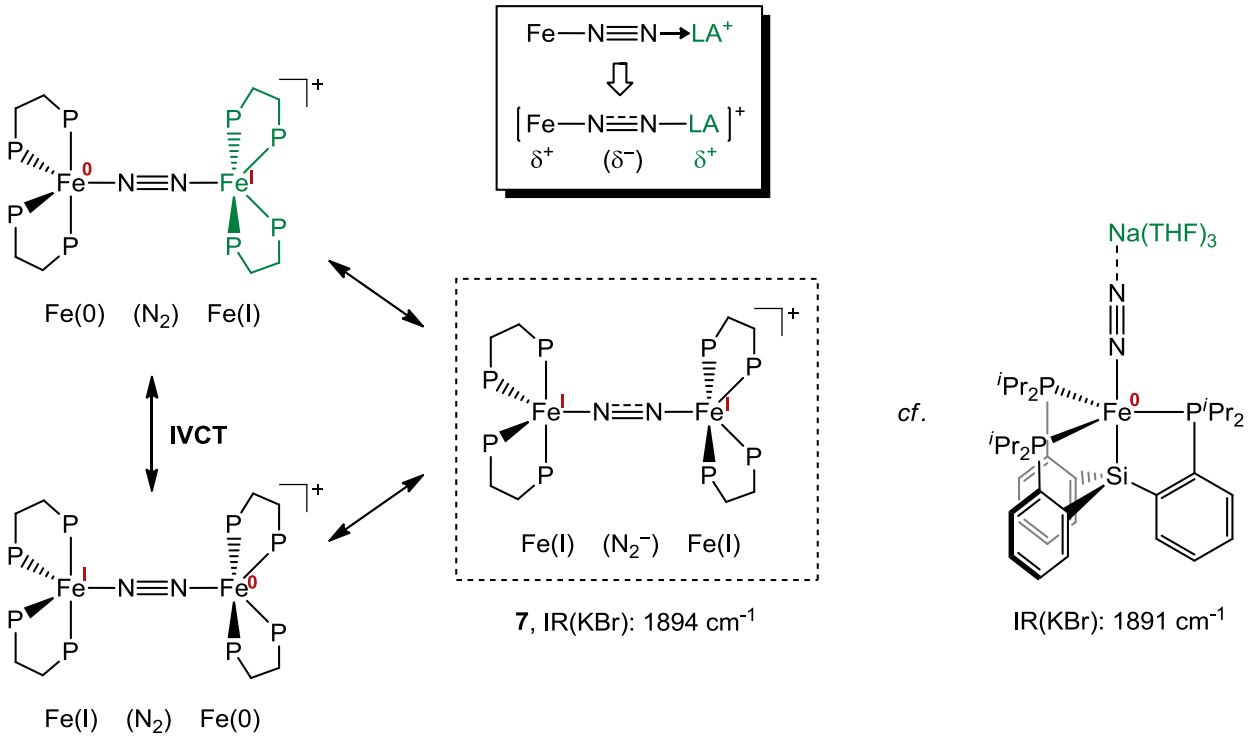


Figure 3.37 Hypothetical influence of a Lewis acidic Fe(I) fragment in **7** to promote electron transfer from the Fe(0) centre onto the N_2 ligand; IVCT = intervalence charge transfer; P = PMe_2; the complex on the right, reported by Peters *et al.*, is provided for comparison due to the incorporation of a Lewis acidic Na^+ cation bound to the N_2 ligand (see discussion in section 1.4.2).

The interconversions of monomeric and dimeric components of **7** and **8** (Figure 3.38) are manifested in their UV-vis spectra. Dissociation of **7** in donor Et_2O solvent under a N_2 atmosphere is observed by the disappearance of two distinct bands at λ_{max} = 470 (404 m^2 mol^{-1}) and 810 nm (274 m^2 mol^{-1}; Figure 3.39). Analysis of the latter band at λ_{max} = 810 nm, which is characteristic of an IVCT band,[26] has been described previously by the MSci student Caroline Wood.[27] The interaction energy (H_{ab}) between the donor and acceptor sites can be determined experimentally by UV-vis spectroscopy using the following Hush formula:[28]

$$H_{ab} = \frac{0.0205}{r} (\varepsilon_{max} \nu_{max} \Delta\nu_{½})^{½}$$

$$\alpha = \left(\frac{H_{ab}^{\,2}}{\nu_{max}^{\,2}} \right)^{½}$$

where r is the distance between Fe centres (4.79 Å, determined crystallographically), ν_{max} is the transition energy (12,346 cm^{-1}), $\Delta\nu_{½}$ is the full width at half maximum (62,893 cm^{-1}), and α is the delocalisation parameter. Mixed valence complexes may be categorised by the

Robin and Day classification according to the extent of electronic interaction between the two metal centres.[29] The three classifications describe either: no delocalisation of charge (class I, $\alpha \sim 0$); partial delocalisation of charge and therefore possible interconversion of oxidation states (class II, $0 < \alpha < 1/\sqrt{2} = 0.707$); and strong delocalisation of charge such that the oxidation states of the two metal centres may be considered equivalent (class III, $\alpha > 1/\sqrt{2} = 0.707$). The values of H_{ab} and α for **7** are calculated to be 6481.7 cm^{-1} and 0.53, respectively, which would describe **7** as a class II complex, with partial delocalisation across the Fe(0) and Fe(I) centres. This corroborates the unexpected degree of N_2 activation indicated by IR (*vide supra*) and is consistent with the crystallographically determined structure, in which the Fe coordination geometry and the Fe–N and Fe–P bond distances are essentially equivalent for the two metal centres.

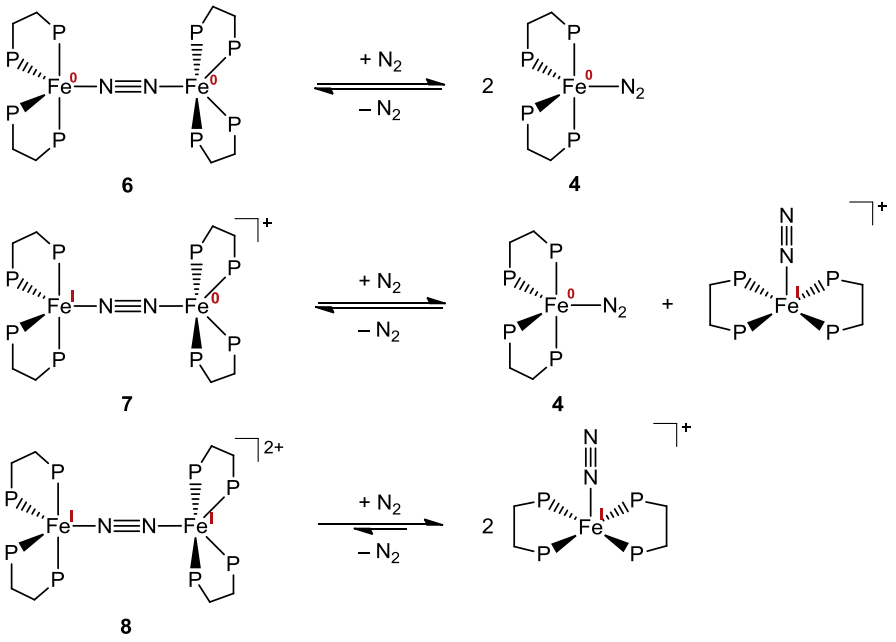


Figure 3.38 Dynamic interconversion of monomer and dimer species; P = PMe_2.

A reversible colour change was observed upon dissolution of **8** either to a vivid blue (under Ar) or a pale yellow (under N_2). UV-vis spectra of these solutions (Figure 3.40) are consistent with dissociation of **8** to the 15 VE species $[Fe(dmpe)_2][BArF_{24}]$ and the 17 VE species $[Fe(N_2)(dmpe)_2][BArF_{24}]$, respectively; the former exhibits hypsochromically shifted absorption features to the analogous Fe(I) depe complex $[Fe(depe)_2][BArF_{24}]$ (**13**, *vide infra*). Low temperature measurements of **8** conducted in Et_2O under an Ar atmosphere (therefore limiting the Fe:N_2 ratio to 2:1; Figure 3.40) appear to indicate the N_2 coordinated complex is favoured as the temperature is decreased. Attempts to isolate $[Fe(dmpe)_2][BArF_{24}]$ from **8** by removal of N_2 from solid or solution samples *in vacuo* have only resulted in regeneration of **8** and/or gradual sample decomposition.

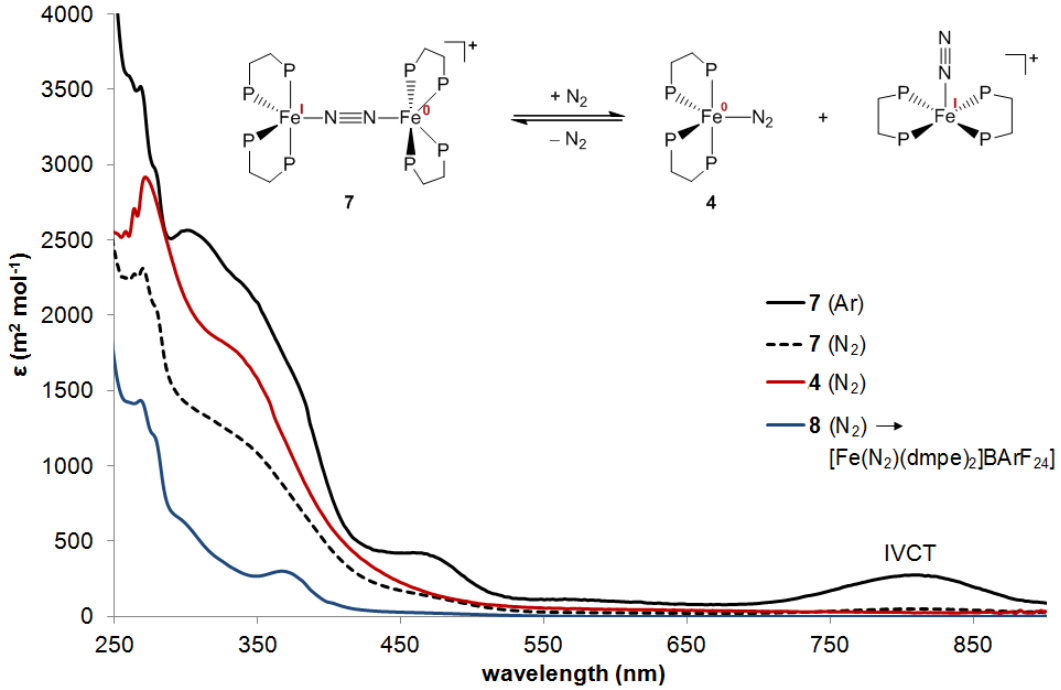


Figure 3.39 UV-vis spectra of **7** (Ar/N_2), **4** (N_2), and **8** (N_2) in Et_2O (0.125 mM, RT); P = PMe_2.

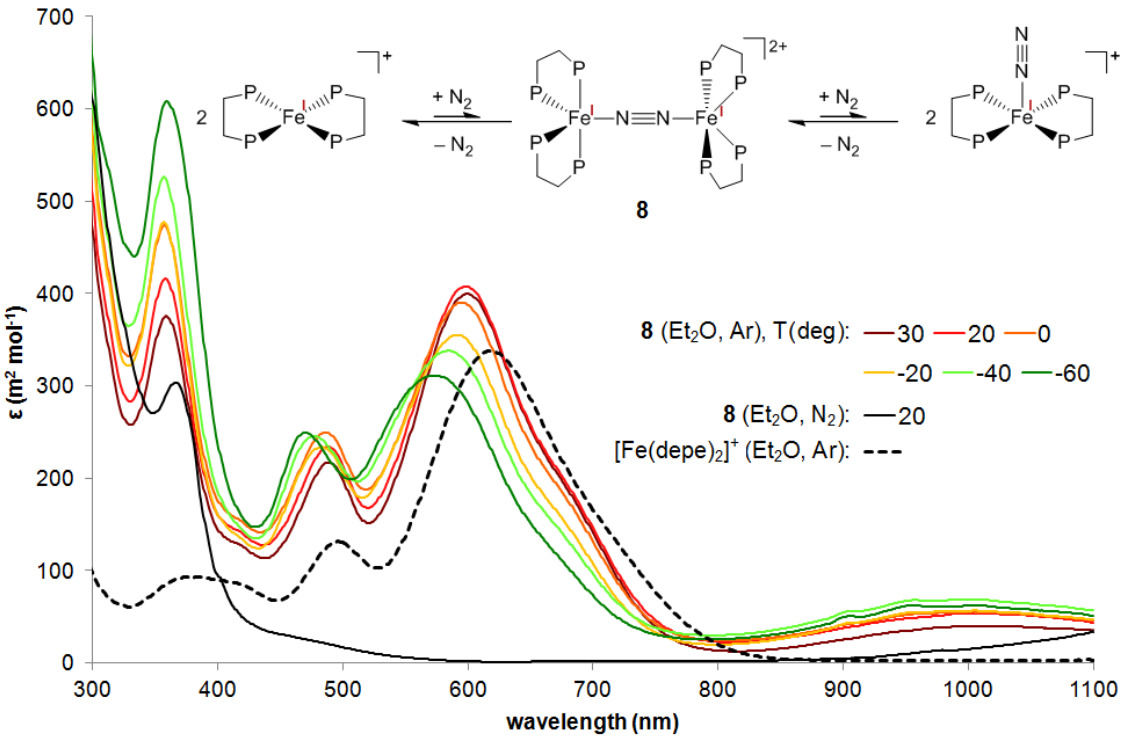


Figure 3.40 UV-vis spectra of **8** (Et_2O, Ar) between 30 and –60 °C; **8** (Et_2O, N_2, 20 °C); and $[Fe(depe)_2][BArF_{24}]$ (**13**, Et_2O, Ar, RT) for comparison; P = PMe_2.

The X-band CW EPR spectrum of **7** in THF initially revealed a pseudo axial signal which converted under a N_2 atmosphere over the course of 20 h to a near isotropic signal exhibiting strong hyperfine coupling to ^{31}P (Figure 3.41). Thus it appears that N_2 facilitates

dissociation of dimeric **7** to its Fe(I) and Fe(0) components, $[Fe(N_2)(dmpe)_2][BArF_{24}]$ (near isotropic signal) and **4** (EPR silent), respectively. Consequently, within this mixture a further possibility is the recombination of Fe(I) monomers *via* a bridging N_2 ligand - analogous to the dimerisation of **4** - to form the triplet (S = 1) dimer **8**. For an S = 1 system, it should be possible to resolve a very weak signal at half-field due to a formally forbidden $\Delta M_s = 2$ transition (Figure 3.42).[30] Indeed, a half-field signal was initially observed in this experiment, suggesting generation of **8**; however, this half-field signal disappears with formation of the near isotropic signal, consistent with the latter corresponding to the N_2-saturated monomeric complex $[Fe(N_2)(dmpe)_2][BArF_{24}]$.

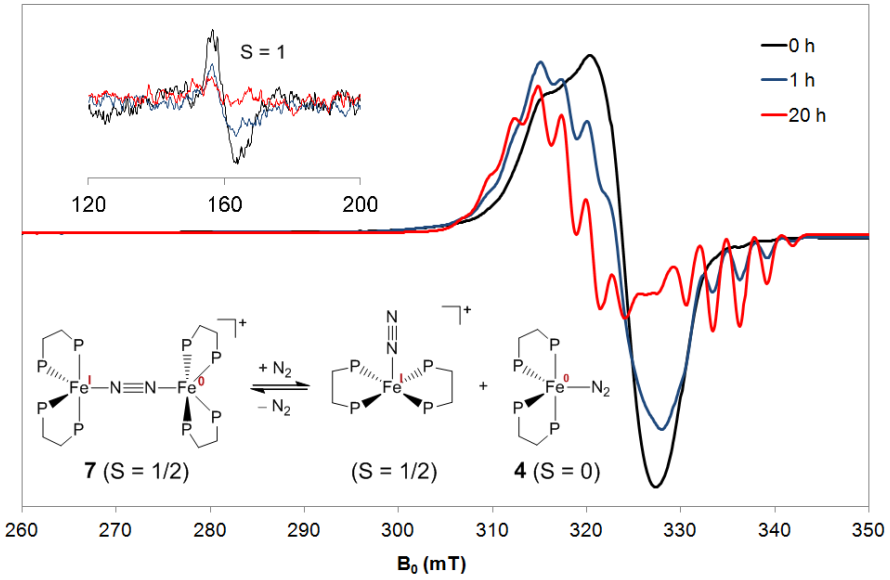


Figure 3.41 X-band CW EPR spectra of **7** (THF, N_2, black) and the same sample after 1 h at RT (blue) and after 20 h at RT (red); the inset shows the half-field region; recorded as a glass at 40 K; P = PMe_2.

Similarly, the EPR spectra of the isolated compound **8** reveals both dimer and monomer components. As a powder or a TBME (Ar) glass (Figure 3.43-3.44), a weak half-field signal is observed along with broad features centred at 320 mT characteristic of a triplet (S = 1) dimer. However, partial dissociation to $[Fe(N_2)(dmpe)_2][BArF_{24}]$ is apparent in the TBME spectra by the appearance of the near isotropic signal. Since the TBME glass was prepared under an Ar atmosphere, N_2 is limited to the initial one equivalent per **8**; thus dissociation is expected to result in both $[Fe(N_2)(dmpe)_2][BArF_{24}]$ and the N_2-free complex $[Fe(dmpe)_2][BArF_{24}]$. However, an appreciable concentration of N_2 relative to **8** (2.5 mM) may be available due to any adventitious N_2 not removed in the freeze-pump-thaw degassing of the solvent. Hence, whilst additional signals at ca. 280 and 290 mT were observed which could correspond to the N_2-free complex, their intensity is relatively low. The

corresponding spectra of **8** recorded as a THF glass under N_2 exhibits a much weaker S = 1 component, indicating almost complete dissociation of **8** to $[Fe(N_2)(dmpe)_2][BArF_{24}]$ (Figure 3.45-46).

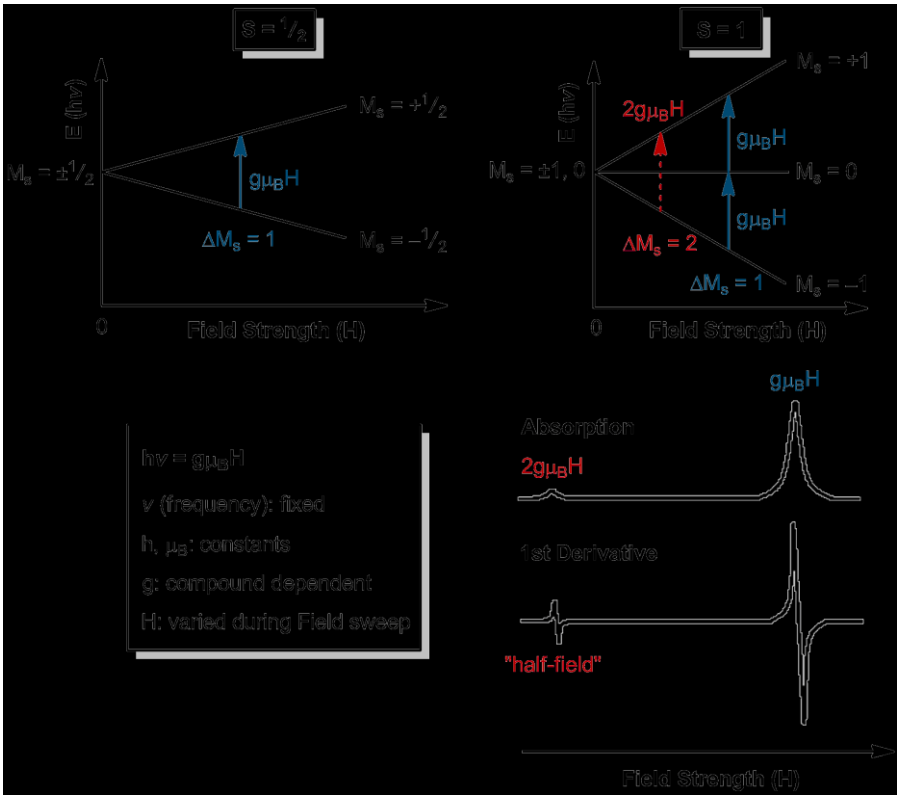


Figure 3.42 Manifestation of the formally forbidden $\Delta M_s = 2$ "half-field" signal for an S = 1 triplet spin state.

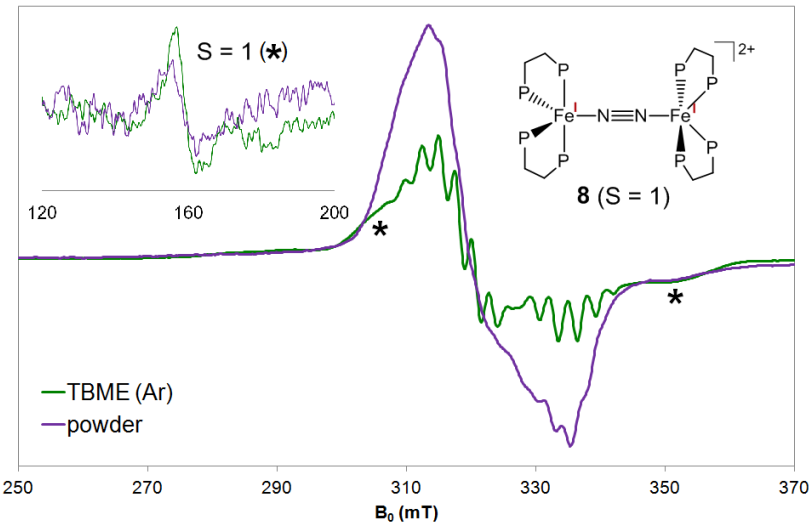


Figure 3.43 X-band CW EPR spectra of **8** as a TBME glass (green) and as a powder (purple) with inset showing half-field region; *marks broad S = 1 dimer features; recorded under Ar at 40 K; P = PMe_2.

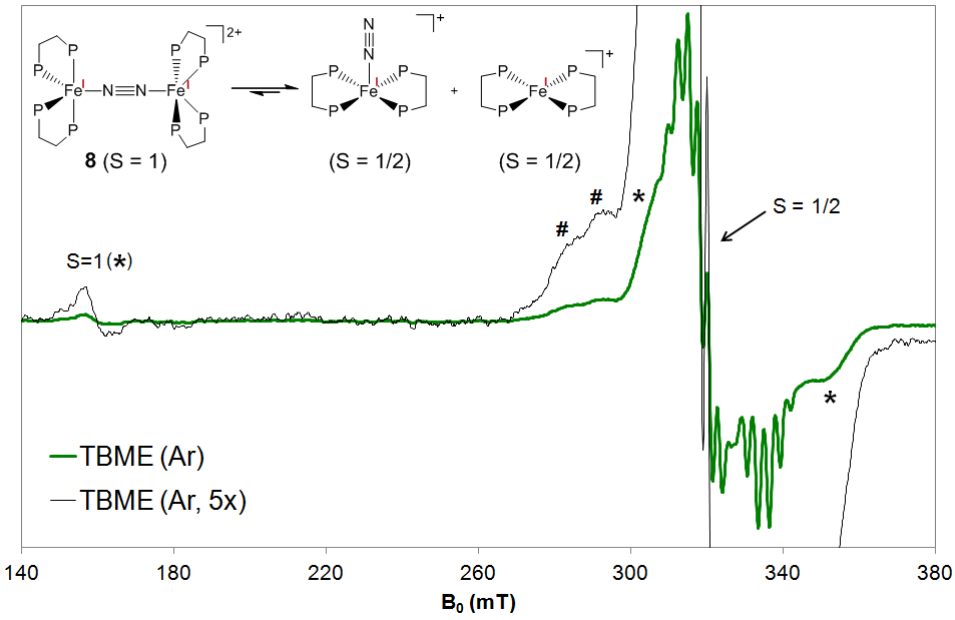


Figure 3.44 X-band CW EPR spectra of **8** (TBME, Ar, green) and with 20x magnification (black); *marks broad S = 1 dimer features; #marks underlying signals which may correspond to S = 1 or $[Fe(dmpe)_2][BArF_{24}]$ (S = ½); recorded as a glass at 40 K; P = PMe_2.

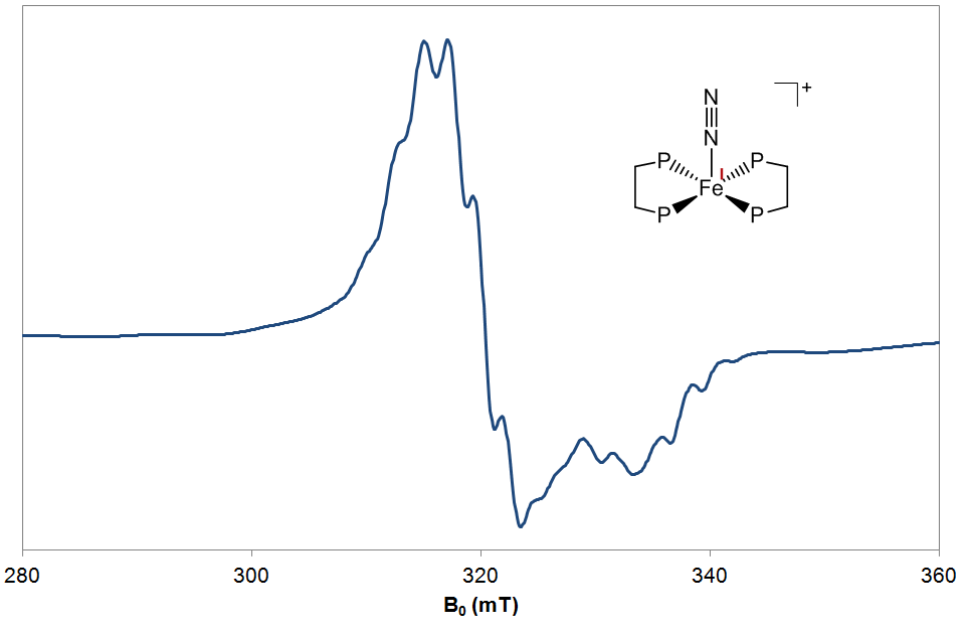


Figure 3.45 X-band CW EPR spectra of **8** (THF, N_2); recorded as a glass at 40 K; P = PMe_2.

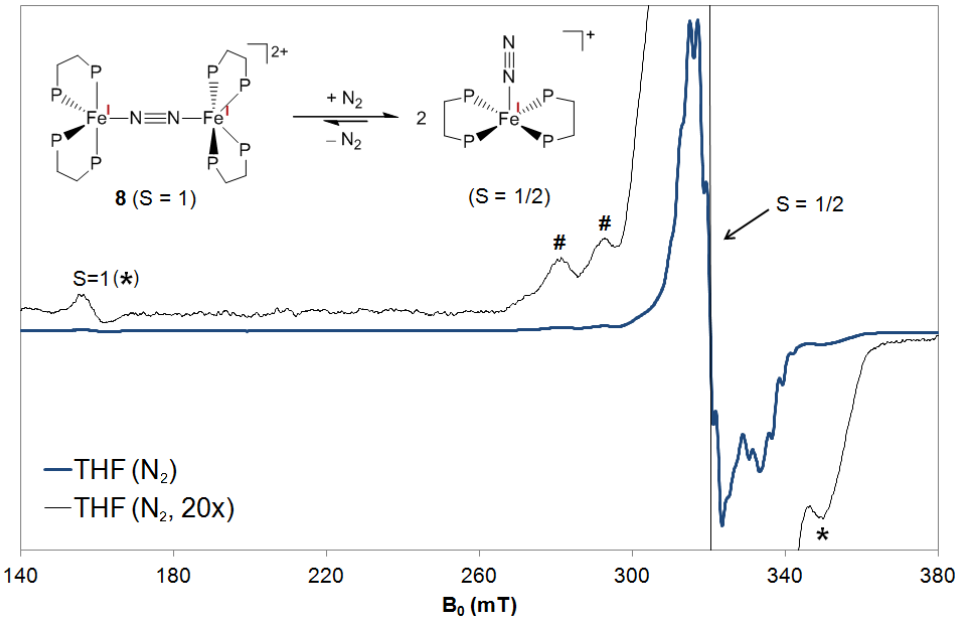


Figure 3.46 X-band CW EPR spectra of **8** (THF, N_2, blue) and with 20x magnification (black); *marks broad S = 1 dimer features; #marks underlying signal which may correspond to S = 1 or $[Fe(dmpe)_2][BArF_{24}]$ (S = ½); recorded as a glass at 40 K; P = PMe_2.

SQUID magnetrometry measurements performed on **7** demonstrated approximately Curie-Weiss paramagnetism within the range 150-300 K by a near linear relationship between the inverse molar susceptibility (χ_m^{-1}) and temperature (C = 1.03 emu K mol^{-1}; θ = 8.53 K; Figure 3.47); a diamagnetic correction was applied using Pascal's constants.[31] The average effective magnetic moment (μ_{eff}) within this range is 2.88 μ_B, whilst below 150 K, μ_{eff} decreases to 1.71 μ_B at 2 K.

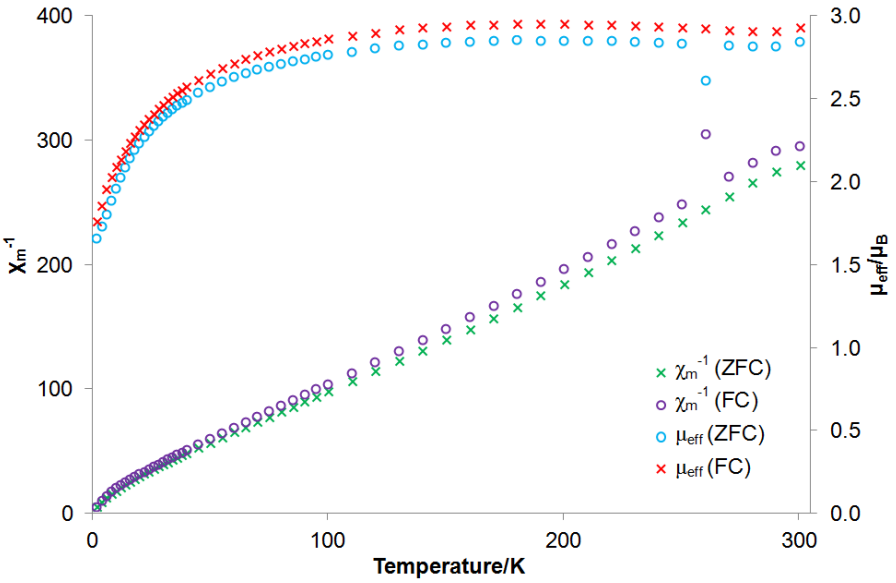


Figure 3.47 SQUID measured temperature dependence of μ_{eff} and χ_m^{-1} for **7**; zero-field cooled (ZFC) and field cooled (FC) measurements were recorded with an applied field of 1000 Oe.

Although a drop in paramagnetism is expected at very low temperature due to intermolecular exchange phenomena, this usually occurs over a much smaller temperature range, whereas the gradual decrease in μ_{eff} indicates a spin state transition occurring below 150 K. For a mixed valent Fe(0)/Fe(I) system, the spin magnetic moment contribution to μ_{eff} would be 1.73 μ_B for LS Fe(I) (S = ½) or 3.87 μ_B for high-spin (HS) Fe(I) (S = $^3/_2$), assuming no contribution from Fe(0) (LS, S = 0). Thus, it is difficult to rationalise the temperature dependence of μ_{eff} in terms of a LS to HS transition, noting that the low and high temperature limits appear to correspond to an S = ½ (μ_{so} = 1.73 μ_B) and S = 1 system (μ_{so} = 2.83 μ_B), respectively. Alternatively, the solid state complex may be considered to be an Fe(I)/Fe(I) system with a negatively charged bridging N_2^- ligand (S = $^3/_2$; Figure 3.48). This would imply a formal N–N bond order of 2.5, which is corroborated by the unexpectedly low *v*(N-N) stretching frequency of **7** (*vide supra*). The measured μ_{eff} is lower than the μ_{so} value for a S = $^3/_2$ system (3.87 μ_B), although antiferromagentic coupling along the Fe(I)–(N^{2-})–Fe(I) unit may significantly reduce μ_{eff}. In contrast, a 1,2-DFB solution magnetic moment was calculated by the Evans NMR method to be 1.78 μ_B (298 K),[32] corresponding to a LS Fe(0)/Fe(I) system. Further investigation into the unusual solid-state magnetism exhibited by **7** is unfortunately beyond the scope of this work, but may be investigated by DFT.

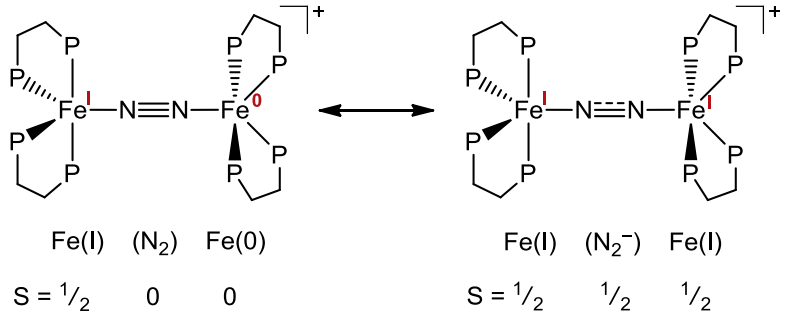


Figure 3.48 Hypothetical doublet (S = $^1/_2$) and quartet (S = $^3/_2$) states of **7**; P = PMe_2.

3.1.5 Electrochemistry of Fe(0) and Fe(I) species

Contrary to the simple Fe(0)-Fe(II) chemistry proposed in the original Leigh cycle, it is evident that this system involves single electron redox chemistry, in which Fe(I) is prominent. The ability of a metal complex to activate and fix coordinated N_2 is dependent on many factors, and interestingly, several controlled studies have shown that a greater degree of N_2 activation is often less conducive towards protonation.[33] Thus, considering the ultimate role of the metal is to provide electrons, its reducing ability may be crucial. To further investigate this, cyclic voltammetry was performed on **4**, **6**, **7**, and **8** in Et_2O with [$^nBu_4N$][$BArF_{24}$] electrolyte under either an Ar or N_2 atmosphere; redox couples are reported versus the

$Cp_2Fe^{+/0}$ couple. The proposed chemical and electrochemical transformations are outlined in Figure 3.49.

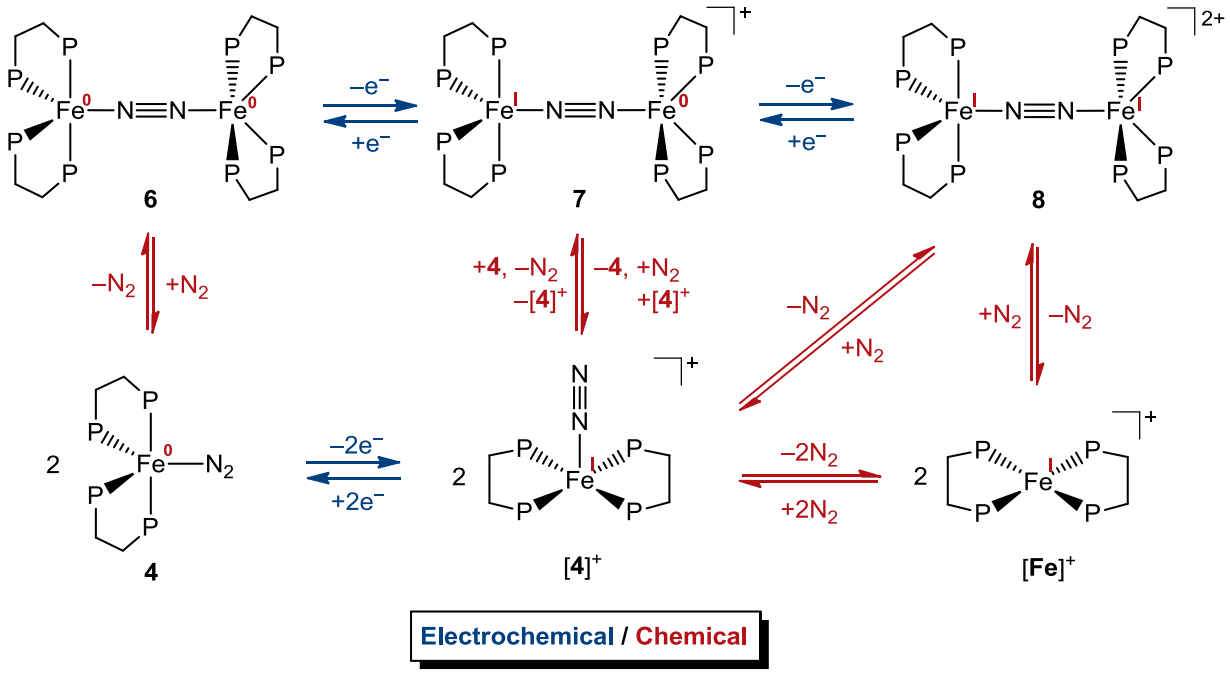


Figure 3.49 Chemical and electrochemical transformations of **4**, **6**, **7**, and **8**; P = PMe_2.

The cyclic voltammogram (CV) of **6** under Ar (Figure 3.50(a)) reveals a reversible electrochemical process centred at –2.2 V over all scan rates (100-2000 mV s^{-1}) corresponding to the single electron oxidation of **6** to **7**. A second wave commencing at –1.9 V is thought to correspond to oxidation of **4** to $[\mathbf{4}]^+$, since the former is generated by dissociation of either **6** or **7** in solution. Accordingly, since **6** appears to be the stronger reductant, $[\mathbf{4}]^+$ is likely reduced by **6** (from the bulk solution) to produce **4** and **7**, which would account for the relatively weak reduction wave of $[\mathbf{4}]^+$ (Figure 3.50(b)). Sweeping further oxidatively is thus expected to oxidise **7** to **8** (Figure 3.51(a)), which would be similarly susceptible to reduction from **6** to regenerate **7**. Consistently, reduction of **7** to **6** appears to be the only electrochemical process on the reductive sweep. The CV of **4** (generated from **6** under N_2 atmosphere; Figure 3.51(b)) reveals an irreversible wave at a similar potential to that assigned to oxidation of **4** to $[\mathbf{4}]^+$ in the CV of **6**. In this case, $[\mathbf{4}]^+$ may be expected to react with **4** to generate **7** by analogy to the synthesis of the latter *via* chemical oxidation of **4** with 0.5 equivalents of $[Cp_2Fe][BArF_{24}]$ (*vide supra*). Thus, **4** and **6** are remarkably strong reducing agents, even more potent than commonly employed reductants Cp_2Co and Cp_2^*Co (–1.33 and –1.84 V vs $Cp_2Fe^{+/0}$ in dimethoxyethane (DME)).[34]

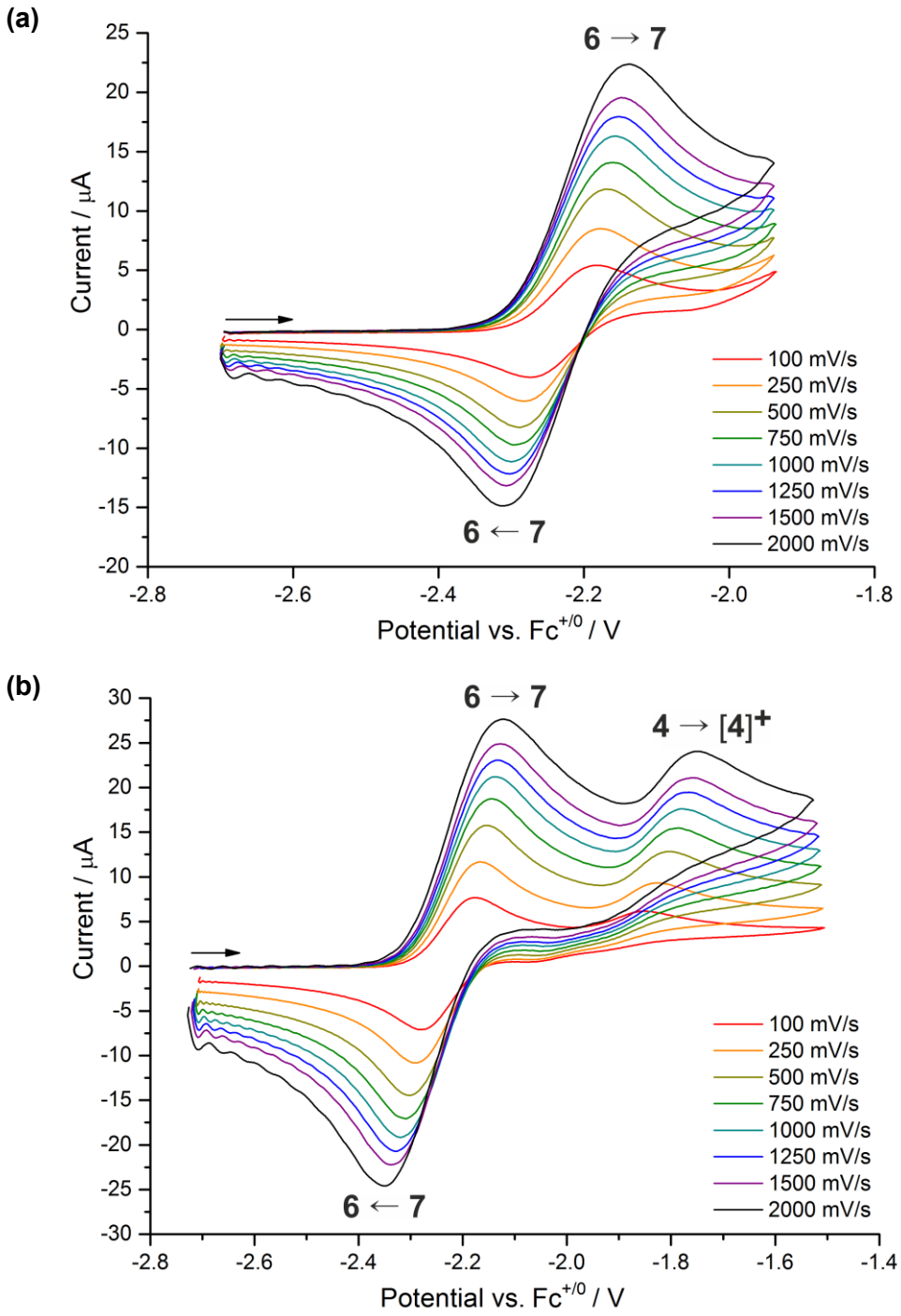


Figure 3.50 Cyclic voltammetry measurements of **6** (Et_2O, Ar); [^{n}Bu$_4$N][BArF$_{24}$] electrolyte; potential plotted relative to the $Cp_2Fe^{+/0}$ couple; arrow indicates direction of scan.

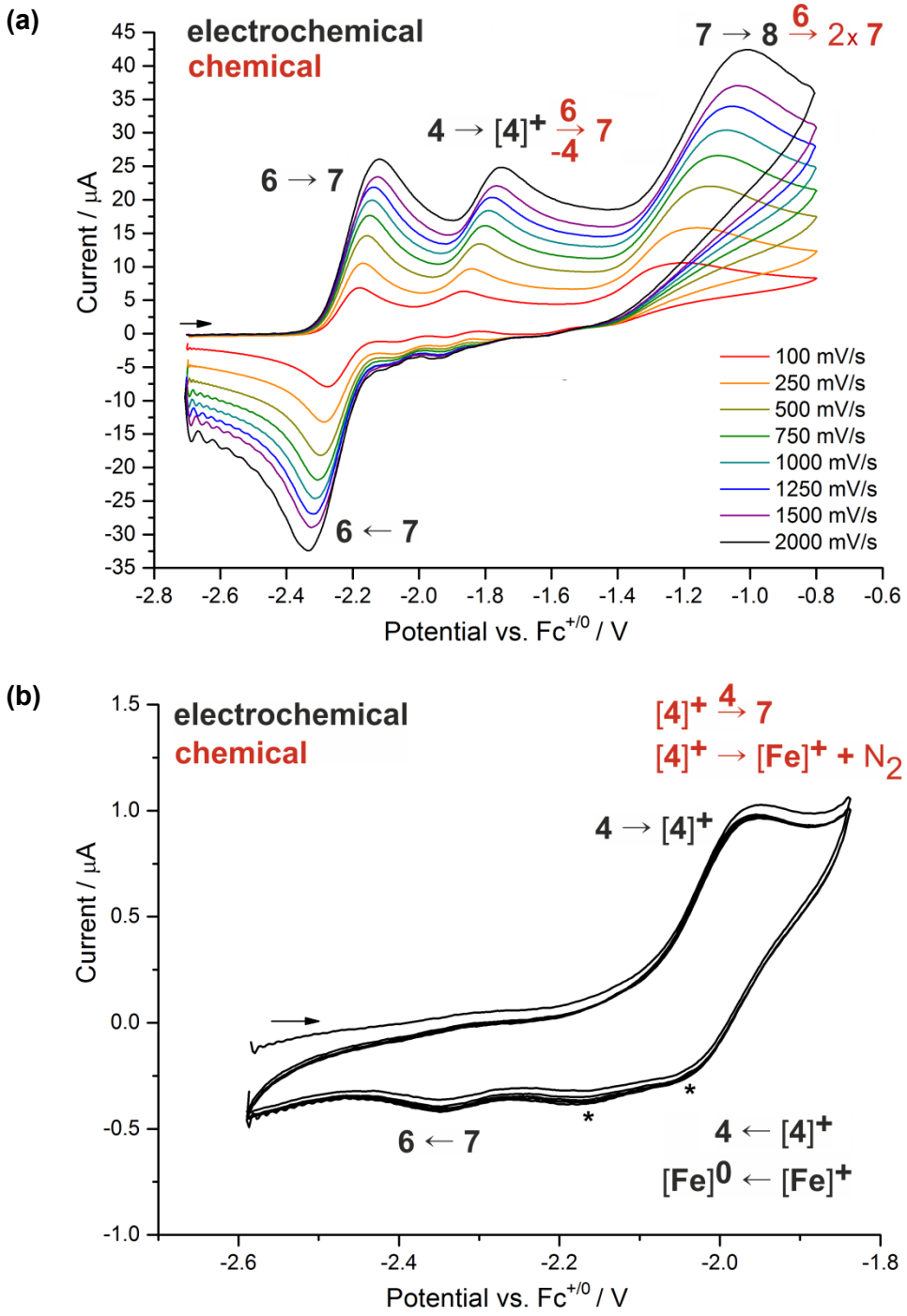


Figure 3.51 Cyclic voltammetry measurements of (a) **6** (Et_2O, Ar); (b) **4** (Et_2O, N_2); [$^nBu_4N$][$BArF_{24}$] electrolyte; potential plotted relative to the $Cp_2Fe^{+/0}$ couple; arrow indicates direction of scan.

Consistent with measurements of **6**, the CV of **7** under Ar (Figure 3.52(a)) reveals a reversible electrochemical event centred at –2.2 V corresponding to single electron reduction of **7** to **6**. Sweeping further oxidatively reveals a second wave commencing at –1.4 V (Figure 3.52(b)) which may be assigned to oxidation of **7** to **8**; hence, the corresponding reduction wave is only observed upon prior electrochemical oxidation (Figure 3.53(a), or Figure 3.53(b) second scan). This quasi-reversible wave along with the reversible **6**/**7** couple was also

measured in the CV of **8** under Ar (Figure 3.54(a)), along with additional electrochemical features at higher potentials (Figure 3.54(b)) which are likely attributable to the Fe(I)/Fe(II) couples of $[Fe]^+$ and/or $[\mathbf{4}]^+$.

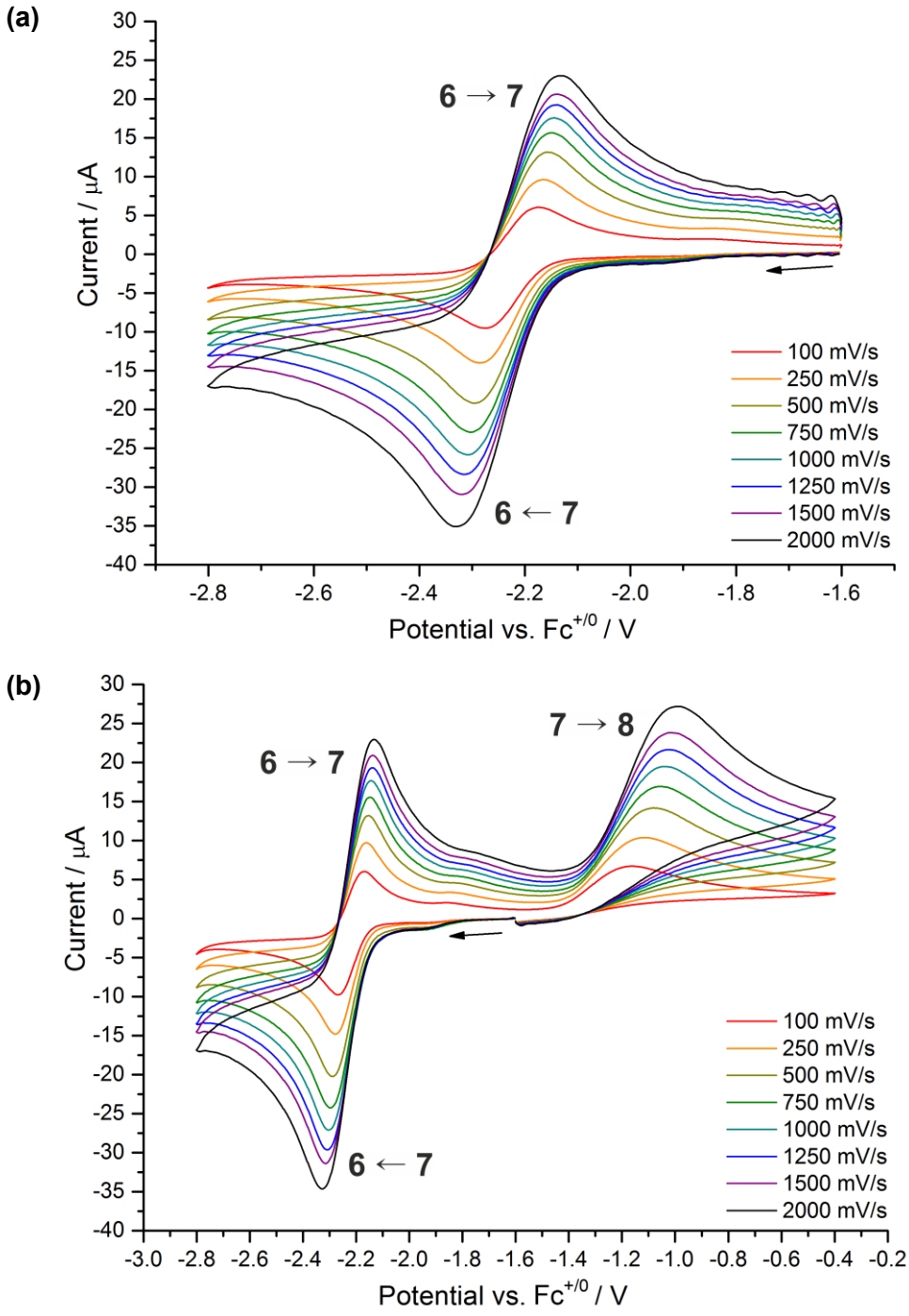


Figure 3.52 Cyclic voltammetry measurements of **7** (Et_2O, Ar); [^{n}Bu$_4$N][BArF$_{24}$] electrolyte; potential plotted relative to the $Cp_2Fe^{+/0}$ couple; arrow indicates direction of scan.

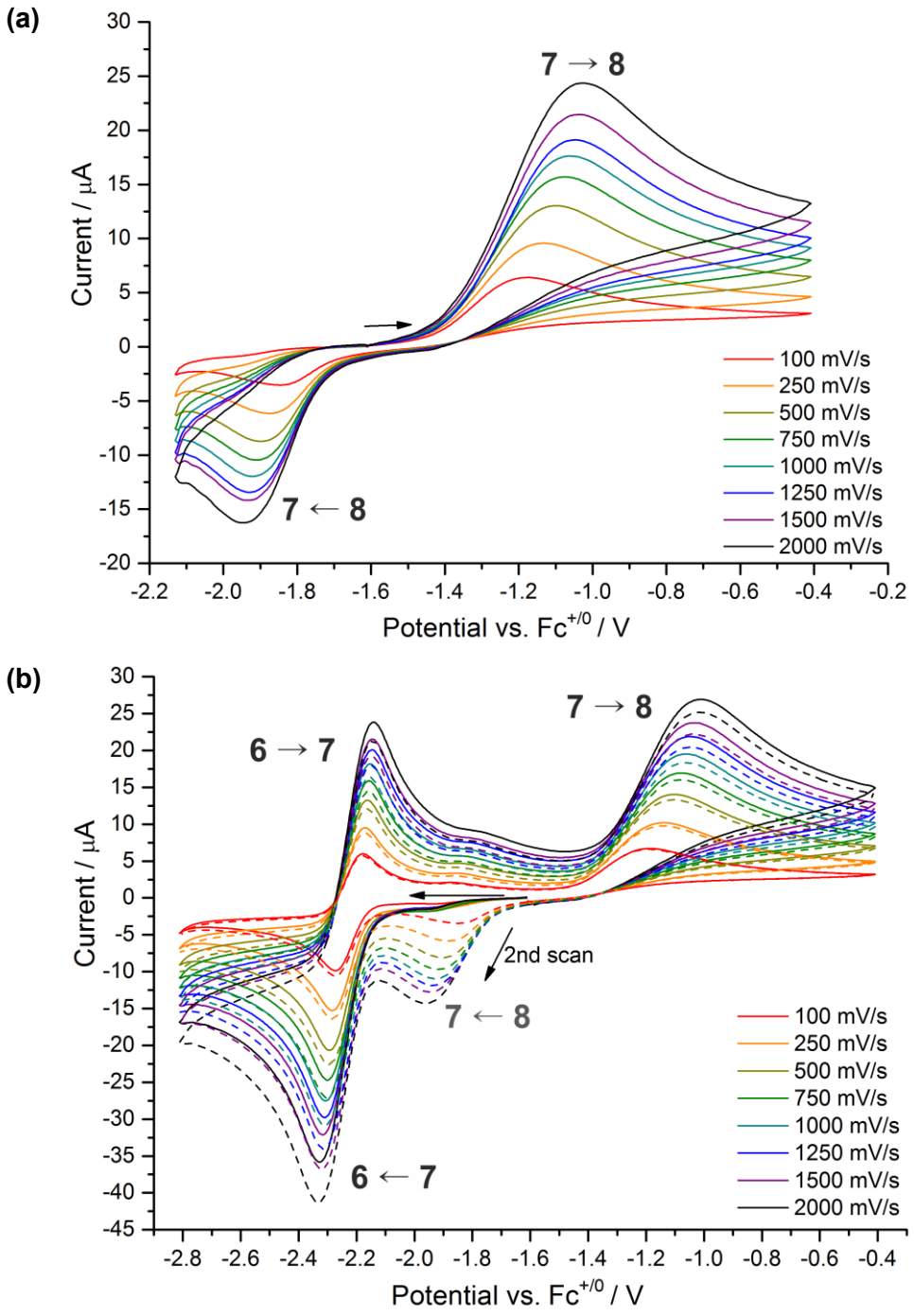


Figure 3.53 Cyclic voltammetry measurements of **7** (Et_2O, Ar); [$^nBu_4N$][$BArF_{24}$] electrolyte; potential plotted relative to the $Cp_2Fe^{+/0}$ couple; arrow indicates direction of scan.

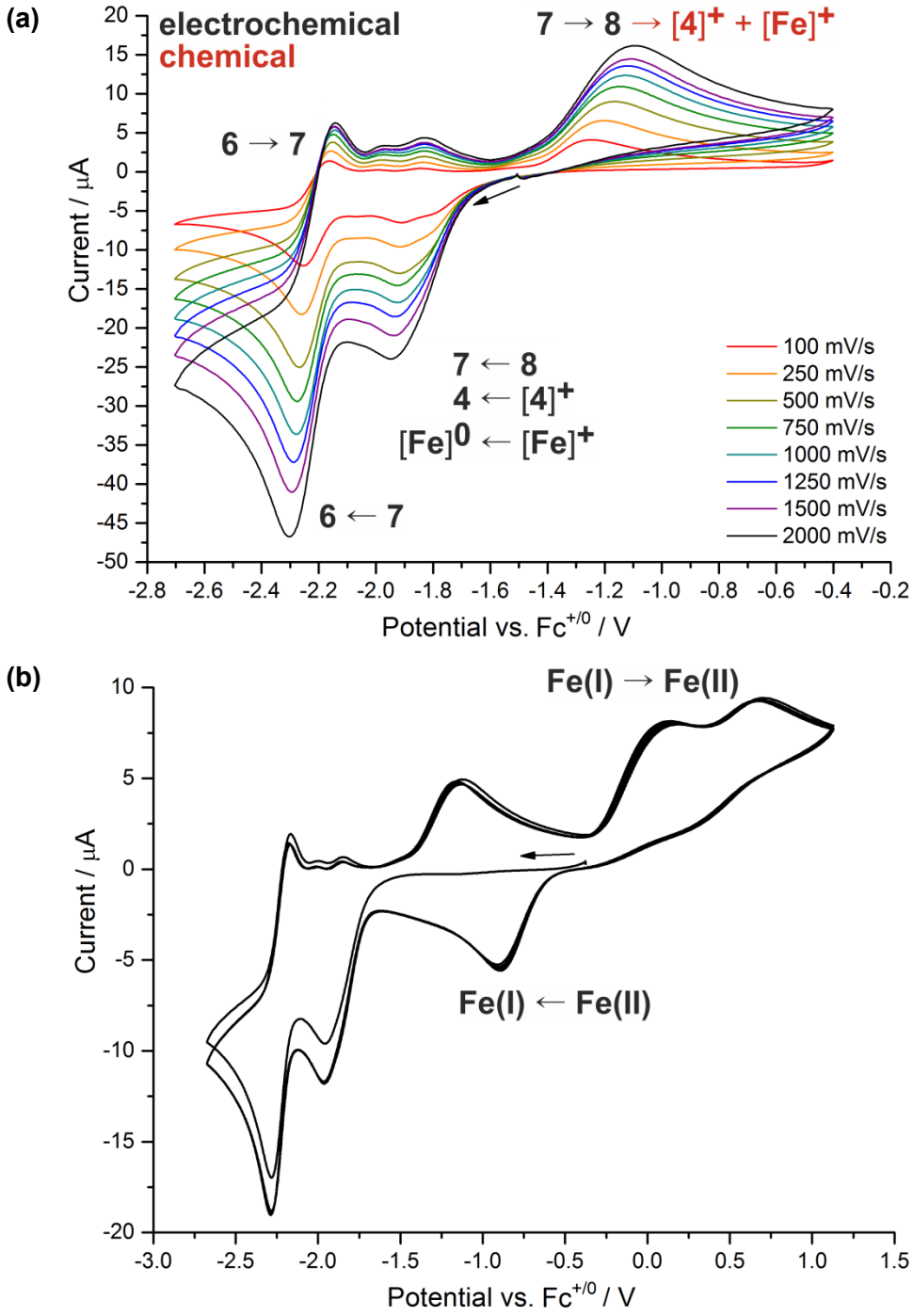


Figure 3.54 Cyclic voltammetry measurements of **8** (Et_2O, Ar); (a) variable scan rates (b) repeat scans; [$^nBu_4N$][$BArF_{24}$] electrolyte; potential plotted relative to the $Cp_2Fe^{+/0}$ couple; arrow indicates direction of scan.

3.1.6 Cooperative activation of N_2 with Fe(0) and K^+ salts

The EPR spectra recorded for the Leigh deprotonation mixture and the reaction of **4**/**6** with $KBArF_{24}$ (Section 3.1.4) clearly indicate formation of the same Fe(I) species, which can now

be unambiguously assigned to $[Fe(N_2)(dmpe)_2][BArF_{24}]$ generated by dissociation of **7** under N_2 (Figure 3.55). Since addition of $KBArF_{24}$ to either Fe(0) species **4** or **6** generates Fe(I) (within **7**), which is an oxidation process, a concomitant reduction process must also have occurred. Furthermore, whilst the $BArF_{24}^-$ anion is incorporated into the oxidised species (**7**), the K^+ cation is unaccounted for and is thus expected to be involved in the formation of a reduced species.

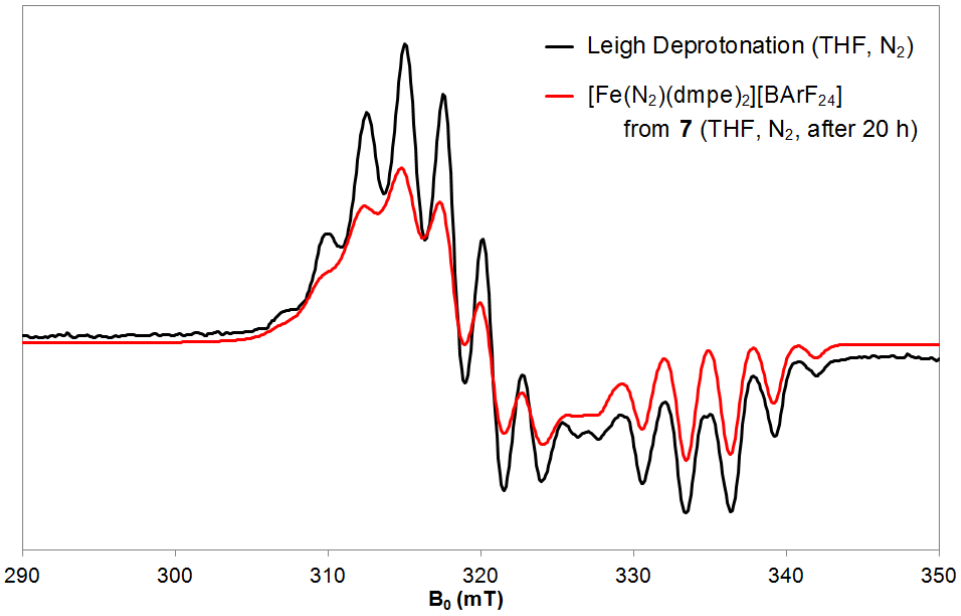


Figure 3.55 X-band CW EPR spectra of the Leigh deprotonation reaction ([*trans*-$Fe(H)(N_2)(dmpe)_2][BPh_4]$/$KO^tBu$ (1:2), THF, N_2, black), and **7** (THF, N_2, after 20 h, red); recorded as glasses at 40 K.

Similar reactivity is also apparent with Li^+ and Na^+ salts, which generate the same Fe(I) EPR signals corresponding to **7** and monomeric $[Fe(N_2)(dmpe)_2][BArF_{24}]$ (Figure 3.56). Notably, use of $NaBArF_{24}$ resulted in immediate formation of $[Fe(N_2)(dmpe)_2][BArF_{24}]$ only, and in significantly greater concentration than the equivalent reaction with $KBArF_{24}$, in which mainly **7** was initially observed. With $LiBArF_{20}$, a mixture of **7** and $[Fe(N_2)(dmpe)_2][BArF_{24}]$ was formed in an intermediate concentration. Corresponding NMR reactions were all initially ^{31}P NMR silent, however, for $NaBArF_{24}$ and $LiBArF_{24}$, the protonated species **5** was observed to grow in much faster, which likely forms as a result of THF deprotonation/H· abstraction. This increased rate of decomposition may correlate with the concentration and/or reactivity of a reduced component in this mixture, in which incorporation of the alkali metal is expected. Alternatively, Na^+ and Li^+ ions may activate THF more strongly. For this reason, and since specifically KO^tBu is employed in the Leigh cycle, our investigations have thus far focussed on potassium.

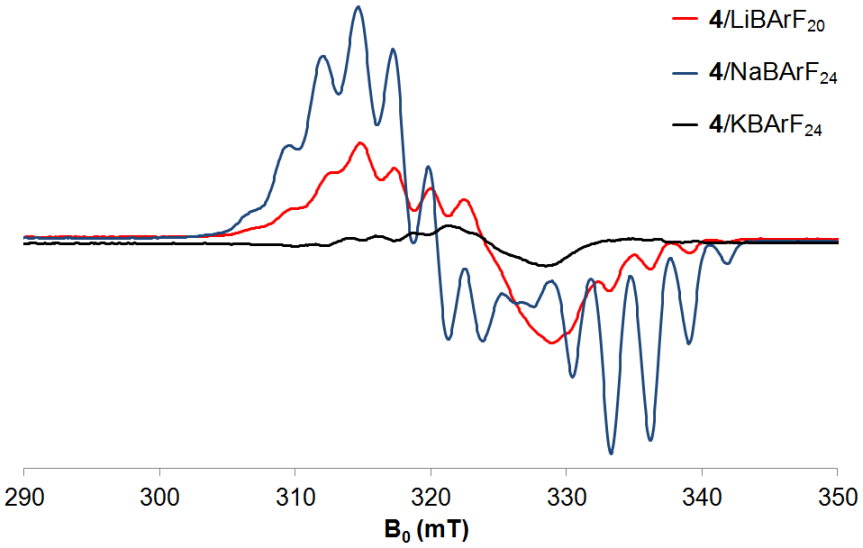


Figure 3.56 X-band EPR spectra of equivalent reactions of **4** with $LiBArF_{20}$, $NaBArF_{24}$, and $KBArF_{24}$ (1:1, 5mM, THF, N_2) recorded as glasses at 40 K.

Consistent with the previous EPR experiment, UV-vis spectroscopic analysis of the reaction of **6** with $KBArF_{24}$ (Et_2O, Ar; Figure 3.57) revealed characteristic bands at 470 and 810 nm corresponding to the formation of **7**. In addition, a strong charge transfer (CT) band at 309 nm was also resolved, which has not been observed in spectra recorded for either the component species ($KBArF_{24}$, **4** and **6**), or known products (**7** and **8** measured with and without $KBArF_{24}$).

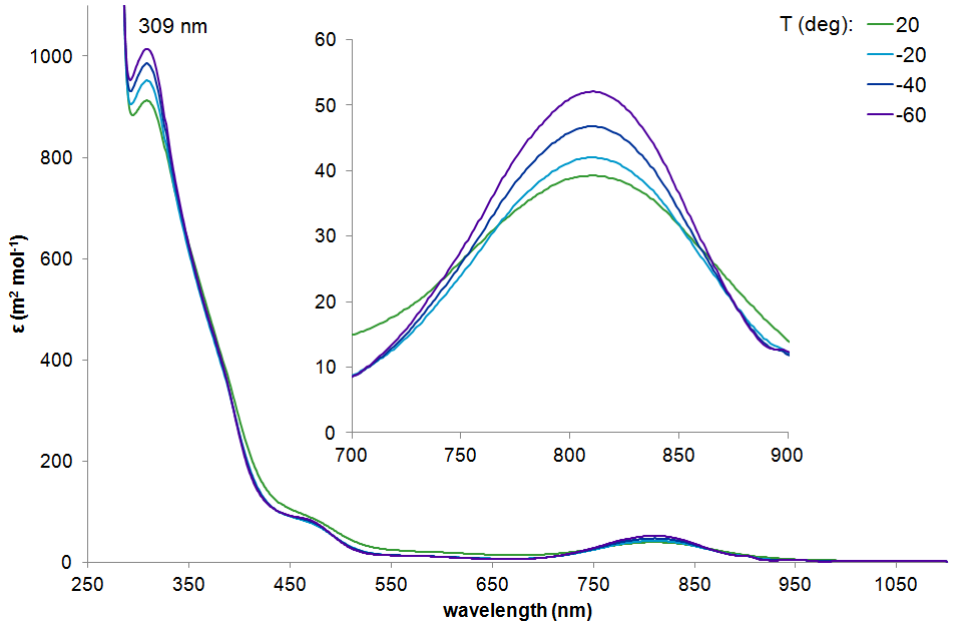


Figure 3.57 UV-vis spectra of **6** with $KBArF_{24}$ (1:4, Et_2O, Ar) recorded at temperatures between 20 and –60°; inset shows an IVCT band of **7**.

Hence, a new species is thought to be responsible for this CT band, which is generated in a reduction process concomitant with the oxidation of **6** to **7**. The temperature dependence of this band may indicate that the electron transfer is favoured at lower temperatures, consistent with the higher yield of NH_3 obtained by Leigh *et al.* when the acidification step was performed at –40 °C.

Importantly, the solvent is an unlikely candidate for reduction since the reaction proceeds in Et_2O or pentane solvent, which are both unreactive towards highly reducing KC_8; $KBArF_{24}$ also does not react with KC_8. Therefore, it would appear that Fe(0) is both the oxidant and the reductant in this reaction. In the simplest case, this would generate Fe(I) and Fe(–I), i.e. a disproportionation reaction. However, given the rarity of compounds containing Fe(–I),[35] it is perhaps more likely that a higher oxidation state of Fe is involved. This may be rationalised by prior transfer of one or more electrons from Fe(0) to a coordinated N_2 ligand, oxidising the Fe(0) centre and thus increasing its susceptibility towards reduction from another Fe(0) centre (Figure 3.58). Hence, the net effect would be oxidation of Fe(0) and reduction of N_2, which importantly is the necessary outcome of N_2 fixation.

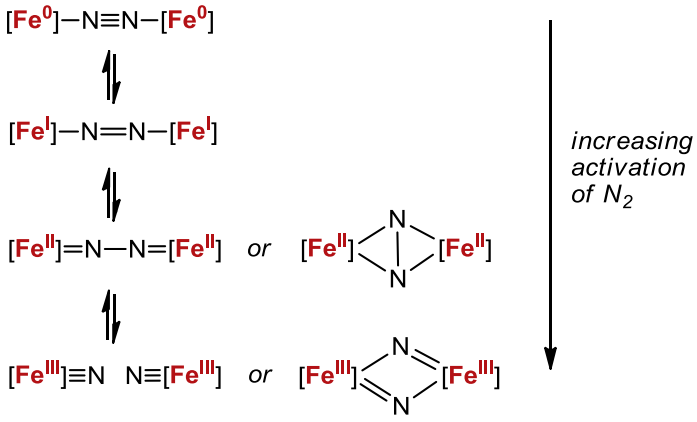


Figure 3.58 Increasing activation of N_2 resulting from electron transfer from Fe to N_2.

A similar effect may explain a reaction reported by Holland *et al.* in which an Fe(II) chloride complex was reduced with KC_8 under N_2 to form a mixed valence Fe(II)/Fe(III) nitride complex (Figure 3.59).[36] Reduction of N_2 to two nitrides requires six electrons; however, since only four equivalents of KC_8 were supplied, the remaining two electrons must necessarily come from oxidation of two Fe(II) centres to Fe(III). Interestingly, the crystallographically confirmed structure revealed coordination of two K^+ ions to one of the N^{3-} ligands, which was indicated in a subsequent DFT study to have a stabilising effect, making the activated Fe nitride complex more energetically accessible.[37] By analogy, a similar process is proposed in Figure 3.61, in which electron transfer from the Fe(0) centres in **6** onto the bridging N_2 ligand is stabilised through coordination of the latter to K^+ ions.

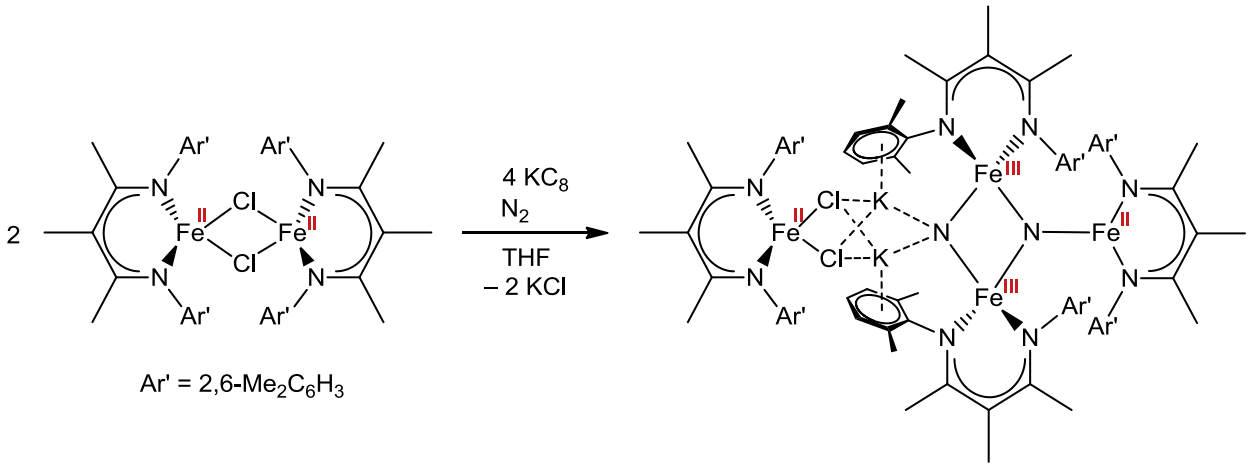


Figure 3.59 Reduction of an Fe(II) chloride complex with KC_8 reported by Holland *et al.*. The produced mixed valence Fe(II)/Fe(III) nitride complex incorporates two K^+ ions stabilising one of the nitride ligands.[36]

In this manner, K^+ ions may be comparable to protons since initial protonation at N_2 is similarly expected to induce electron transfer from Fe to ultimately produce NH_3. Furthermore, whilst protonation at the Fe centre is thermodynamically favoured (and presumed kinetically unfavoured) compared to protonation at N, the larger K^+ ion can be expected to show a much greater preference for coordination at the N_2 ligand. Hence, K^+ ions, which are present in the Leigh deprotonation mixture, may be involved in directing protonation towards the N_2 ligand through simple substitution of N–K bonds with N–H bonds (Figure 3.60). Thus, the CT band at 309 nm may be diagnostic of a π–π* transition from a reduced N ligand (imido, diazinido, or hydrazinido) to an Fe centre.

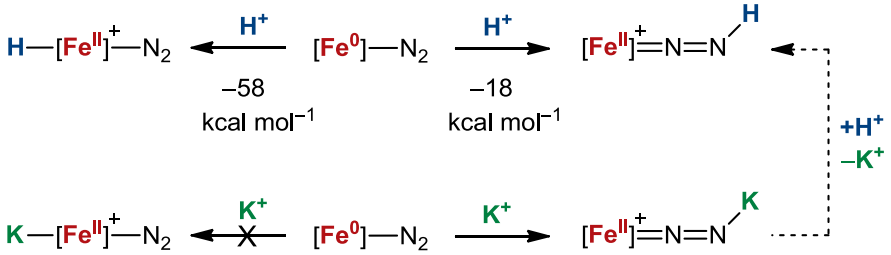


Figure 3.60 Proposed preference of K^+ ions to coordinate to N_β, contrasting the thermodynamic preference for protonation at Fe; energies calculated in ref. 14.

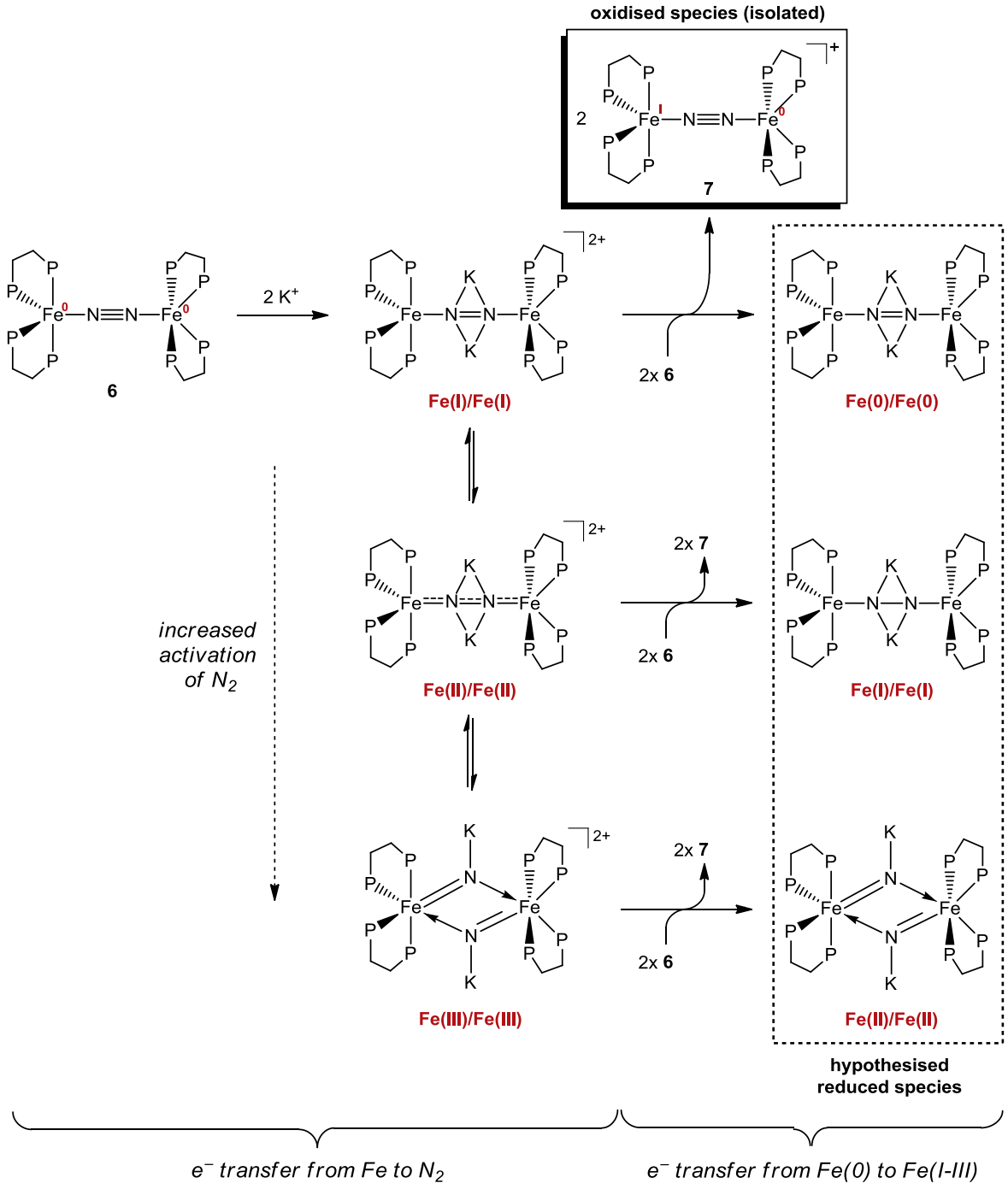


Figure 3.61 Hypothetical pathways for the reaction of **6** with $KBArF_{24}$ wherein K^+ ions facilitate electron transfer from Fe(0) to activated N_2, with subsequent reduction by additional **6**; P = PMe_2.

Obtaining experimental evidence for a reduced species formed concurrently with **7** in the reaction of **6** with $KBArF_{24}$ has thus far proved extremely challenging. Whilst **7** is clearly observed by EPR and UV-vis spectroscopy, only the latter technique has indicated conclusively that an additional species is present. As noted previously, attempts to selectively crystallise the products of this reaction have often yielded **6** and $KBArF_{24}$, indicating a reversible reaction. By ^{1}H NMR spectroscopy, broad resonances are observed

at ca. 18, 10, and –6 ppm (Figure 3.62). These resonances appear similar albeit chemically shifted to those of **7**; however, concentration effects, interaction with **4**, **6**, and $KBArF_{24}$, and the reversibility of this reaction, may all be expected to significantly perturb *δ*.[38] This highlights some of the inherent limitations of NMR spectroscopy for studying such reactions, particularly when both diamagnetic and paramagnetic species may be in rapid equilibria (e.g. a reversible electron transfer), resulting in poor resolution and signal averaging.

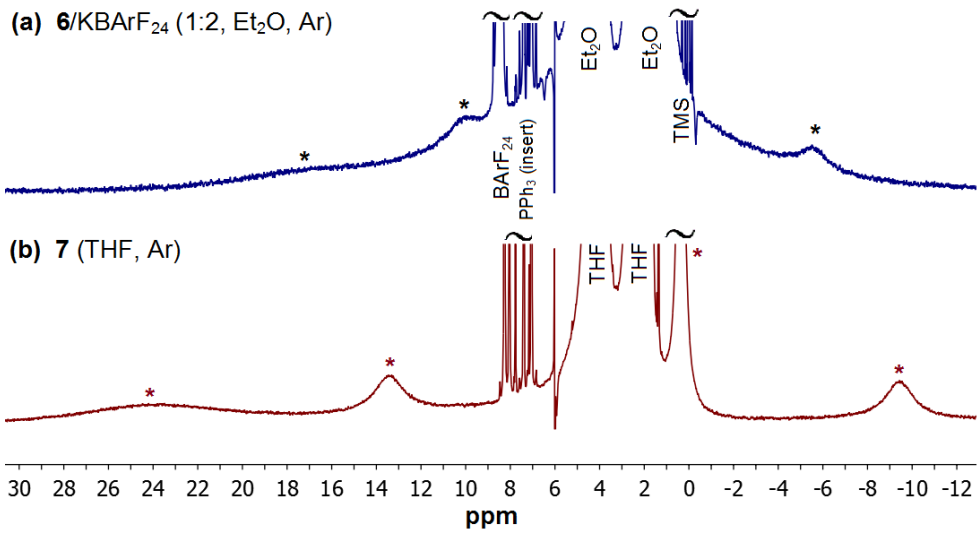


Figure 3.62 ^{1}H NMR spectra of the reaction of **6** with $KBArF_{24}$ (1:2,Et_2O, Ar) and **7** (THF, Ar); *marks broad Fe(I) features.

Furthermore, no additional paramagnetic or diamagnetic signals were resolved upon cooling to –80 °C. Hence, whilst other paramagnetic Fe species may remain NMR silent, the presence of additional diamagnetic LS Fe(0) or LS Fe(II) appears to be unlikely. X-band CW-EPR experiments should be able to detect any Kramer's ions (non-integer spin, i.e., Fe(I) or Fe(III), S = $^1/_2$, $^3/_2$, or $^5/_2$), however, no additional signals to those resulting from **7** or **8** were resolved. HS Fe(II) is a non-Kramer's ion (S = 1, 2), which typically experiences a large zero-field splitting such that allowed EPR transitions only appear at high magnetic fields and/or high frequencies.[39] Unfortunately, since this requires a more elaborate experimental setup, it has not been possible to perform such measurements to enable detection of HS Fe(II).

As with UV-vis spectroscopy, Raman and IR spectroscopy should be able to analyse for all Fe species irrespective of oxidation states. Within a sealable quartz cuvette, an Et_2O solution of **6** with $KBArF_{24}$ (1:2) was evaporated to dryness and the resulting thin film analysed by Raman spectroscopy. No *ν*(N–N) stretch was detected, including the previously measured *ν*(N–N) stretch of **6** at 1933 cm^{-1}. This absence indicates either: that the *ν*(N–N) stretch is Raman inactive; complete scission of the N–N bond; or decomposition due to laser irradiation, which has been encountered for related Fe diphosphine complexes incorporating

an Fe–N–N–Fe unit.[20] Solution IR measurements, performed using a sealable cell with a NaCl window, were complicated by protonation reactions that appeared to be as a consequence of atmospheric exposure from imperfect sealing of the cell. As a result, analysis for *ν*(N–N) stretches corresponding to reduced N_2 fragments was inconclusive.

It was hoped that cyclic voltammmetry might provide further insight through direct measurement of the reaction of **6** with $KBArF_{24}$. Unfortunately, whilst the measured CVs (Figure 3.64) differed noticeably to those of **6** in isolation, poor resolution was encountered, which may have been the result of chemical interference with the Pt electrodes. Thus, sweeping reductively (Figure 3.64(a)) appears to reveal waves corresponding to the reduction of **7** and [**4**]$^+$ which are shifted by approximately +0.5 V relative to the previous measurements. Additional quasi-reversible waves were partially resolved at ca. –2.0 and –2.3 V (or –2.5 and –2.8 V when referenced according to a **6**/**7** couple of –2.2 V), which may tentatively be attributed to highly reduced species generated in the reaction.

Thus, we attempted to use electrophilic reagents (EX) to trap any activated $[N_2]K_x$ fragments and facilitate their isolation in a stable form (Figure 3.63). Precipitation of KX and irreversible N–E bond formation could also be expected to drive the equilibrium reaction. Accordingly, after addition of Me_3SiCl to a mixture of **6** and $KBArF_{24}$ (2:1:2, Et_2O), broad resonances were observed in the ^{1}H NMR spectra corresponding to **7**. However, closer inspection revealed formation of $Me_3SiSiMe_3$ (^{1}H NMR, Et_2O, δ = –0.4 ppm), indicating reduction of Me_3SiCl by **6**, which was subsequently found to also occur in the absence of $KBArF_{24}$. The highly reactive nature of species in this mixture was further demonstrated with MeOTf, which led to immediate precipitation upon addition to either **4**, **6**, or **7**, likely as a result of methylation at the Fe centres (^{1}H NMR, Et_2O, δ = –0.95 ppm, p, J_{PH} = 8.9 Hz, Fe–CH_3; ^{31}P NMR, Et_2O, δ = 63.7 ppm, s, $\nu_{1/2}$ = 7.7 Hz).

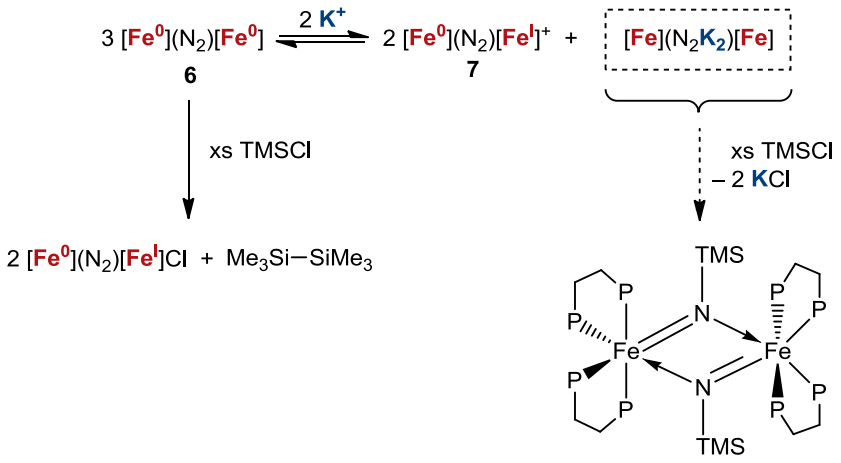


Figure 3.63 Attempted use of TMSCl to trap the proposed reduced N_2 species formed in the reaction of **6** with $KBArF_{24}$; TMS = $SiMe_3$; [Fe] = $[Fe(dmpe)_2]$; P = PMe_2.

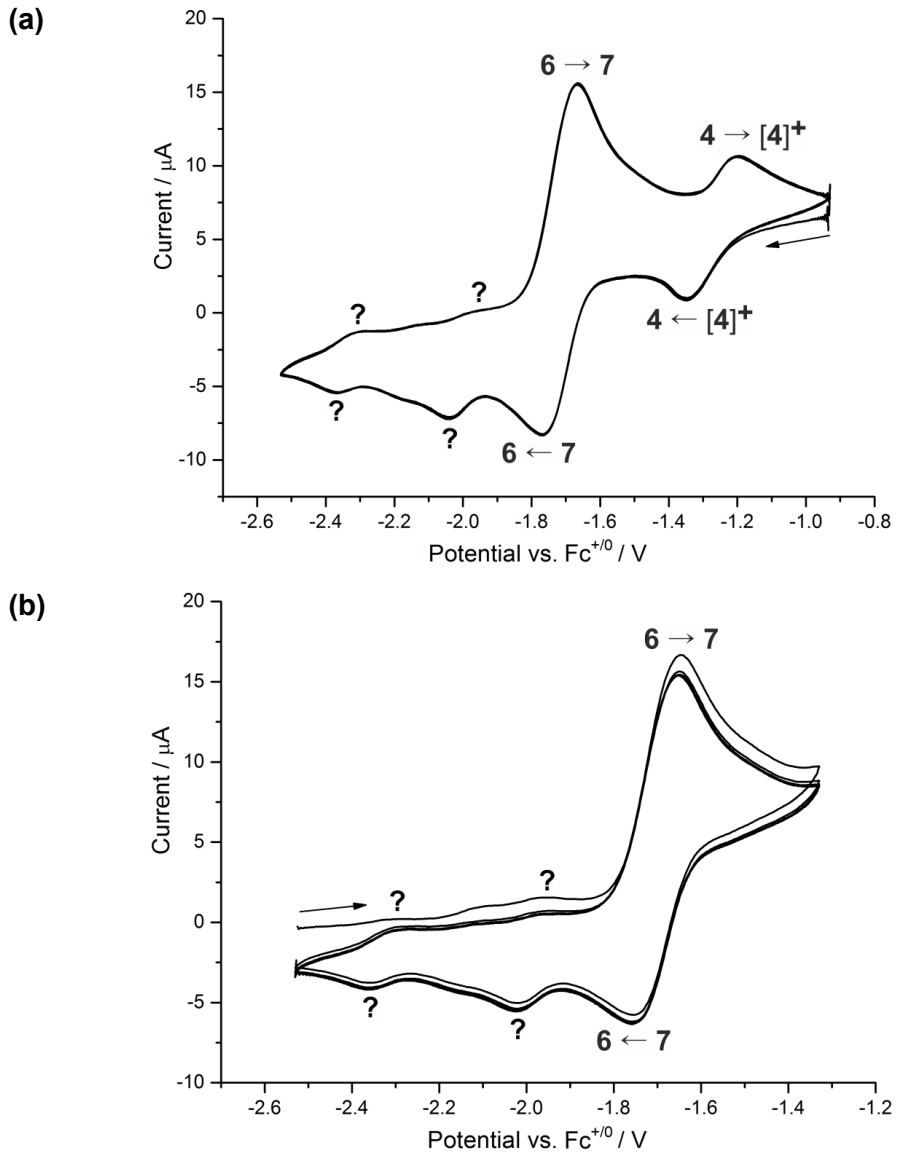


Figure 3.64 Cyclic voltammetry measurements of **6** with $KBArF_{24}$ (1:2, Et_2O, Ar); [^{n}Bu_4N][$BArF_{24}$] electrolyte; potential plotted relative to the Cp_2Fe/Cp_2Fe^+ couple; arrow indicates direction of scan.

Therefore, an alternative strategy was devised whereby the hypothesised reduced species would be targeted directly, circumventing undesired reaction pathways and the resulting complex reaction mixtures. For this purpose, the Fe(II) hydrido azide complex *trans*-$Fe(H)(N_3)(dmpe)_2$ (**9**) was targeted as a source of reduced N accessible from the azide ligand, which may be considered a composite of N^- and an N_2 leaving group. The synthesis of **9** was achieved *via* a substitution reaction of [*trans*-$Fe(H)(N_2)(dmpe)_2$][BPh_4] with [^{n}Bu_4N][N_3] in THF, which is driven by the precipitation of [^{n}Bu_4N][BPh_4] (Figure 3.65). Alternatively, **9** was synthesised from *cis*-$Fe(H)_2(dmpe)_2$ and NaN_3 (1:2) in MeOH in a similar method to that reported by Field *et al.* for the synthesis of *trans*-$Fe(N_3)_2(dmpe)_2$.[40]

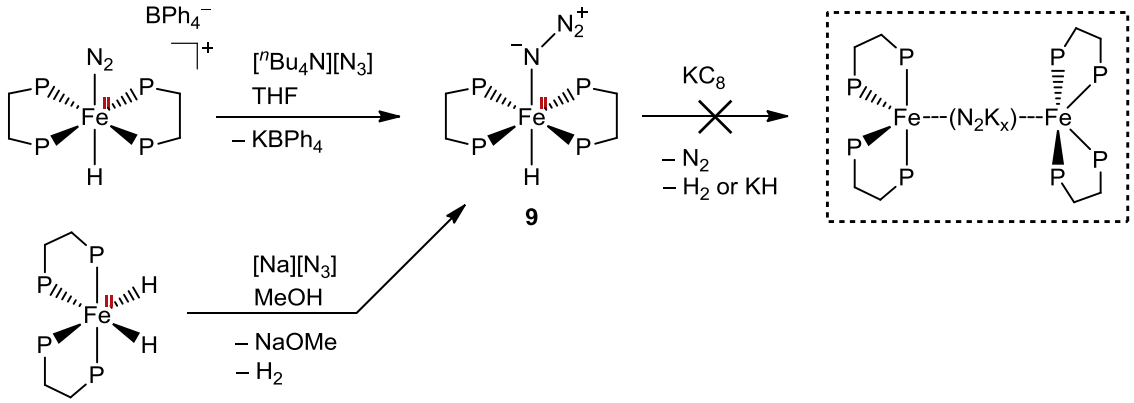
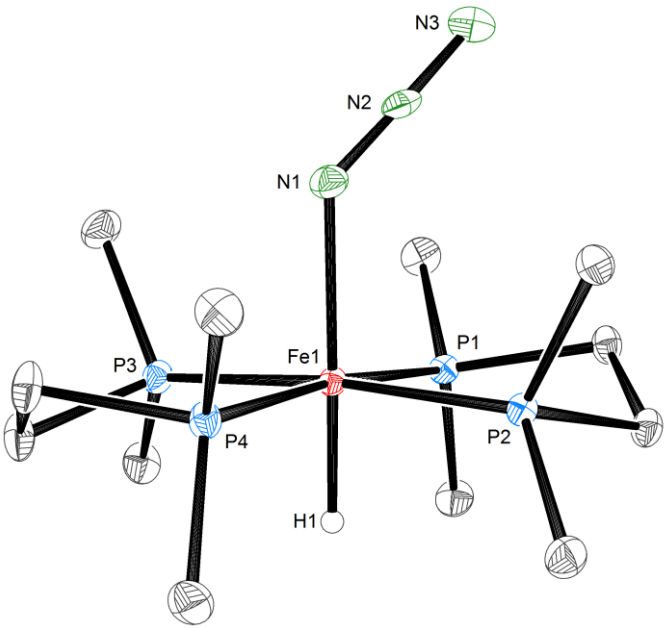


Figure 3.65 Attempted synthesis of a K-stabilised reduced N fragment *via* reduction of *trans*-Fe(H)(N_3)(dmpe)$_2$ (**9**); P = PMe_2.

NMR spectroscopy revealed **9** to be a diamagnetic LS Fe(II) complex (^{31}P NMR, Et_2O, δ = 73.1 ppm, d; ^{1}H NMR, Et_2O, δ = –30.76 ppm (Fe–H), q, $^2J_{PH}$ = 48.4 Hz). The solid state structure (Figure 3.66) was solved by single crystal X-ray crystallography to reveal a near linear N_3^- ligand, which coordinates to Fe in a bent, end-on binding mode (Fe1–N1–N2 = 130.48(19)°). The solid state IR spectrum (KBr pellet; Figure 3.67) exhibits a diagnostic asymmetric N=N=N stretch at 2026 cm^{-1}.[41] A comparison of selected bond metric data and $\nu_{asymm}(N_3)$ for **9** and related Fe azide complexes are tabulated in Table 3.4; all of these complexes contain weakly activated, near linear azide ligands which coordinate Fe in a bent, end-on binding mode.



Bond lengths (Å):

Fe1–N1	2.077(2)
N1–N2	1.169(3)
N2–N3	1.185(3)
Fe1–H1	1.48(3)
[Fe1–P]$_{av}$	2.1902(8)

Bond Angles (deg):

Fe1 N1 N2	130.48(19)
N1 N2 N3	178.0(3)

Figure 3.66 Solid-state structure of *trans*-Fe(H)(N_3)(dmpe)$_2$ (**9**); H1 atom white, all other H atoms omitted for clarity, C atoms grey, Fe atom red, N atoms green, P atoms blue; anisotropic displacement ellipsoids shown at 30% probability.

Table 3.4 Selected bond metric data and $\nu_{asymm}(N_3)$ for **9** and related azide compounds

Compound (E–N1–N2–N3)	**N1–N2** (Å)	**N2–N3** (Å)	**E–N1–N2** (deg)	**N1–N2–N3** (deg)	**$\nu_{asymm}(N_3)$** (cm^{-1})	**Ref.**
HN_3	1.24	1.13	108.8	171.3	2140	42
$Fe(H)(N_3)(dmpe)_2$ (**9**)	1.169(3)	1.185(3)	130.48(19)	178.0(3)	2026[a]	tw
$Fe(H)(N_3)(depe)_2$ (**14**)	1.181(2)	1.175(2)	131.07(10)	178.12(16)	2029[a]	tw
trans-$Fe(N_3)_2(dmpe)_2$	1.162(5)	1.179(5)	132.4(3)	176.6(4)	2029[b]	40
trans-$Fe(N_3)_2(depe)_2$					2037[b]	40
$Fe(N_3)(TPP)$	1.186(6)	1.192(8)	121.8(4)	178.1(7)	2055[a]	43

TPP = tetraphenylporphyrin; [a]KBr pellet; [b]Nujol mull; tw = this work.

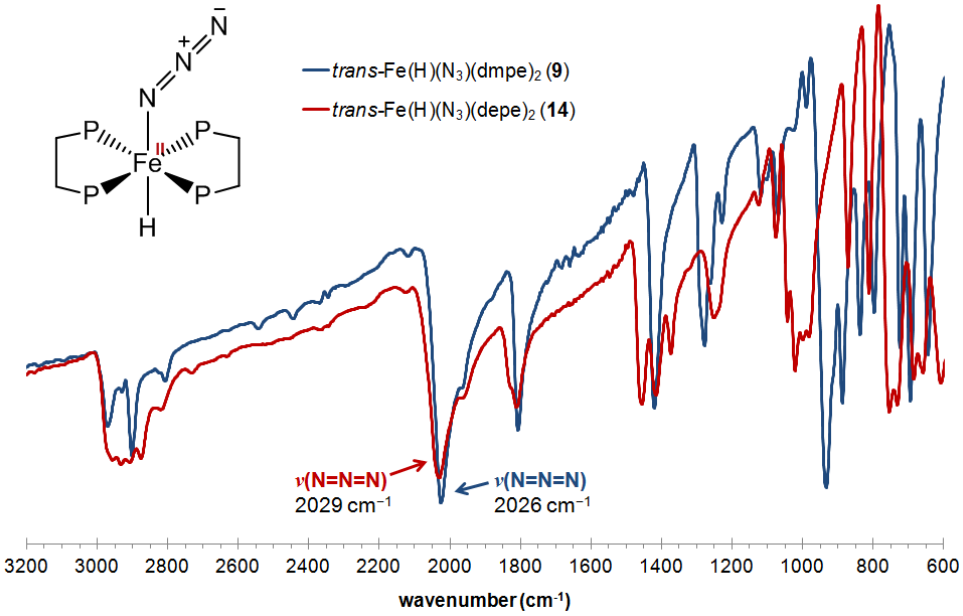
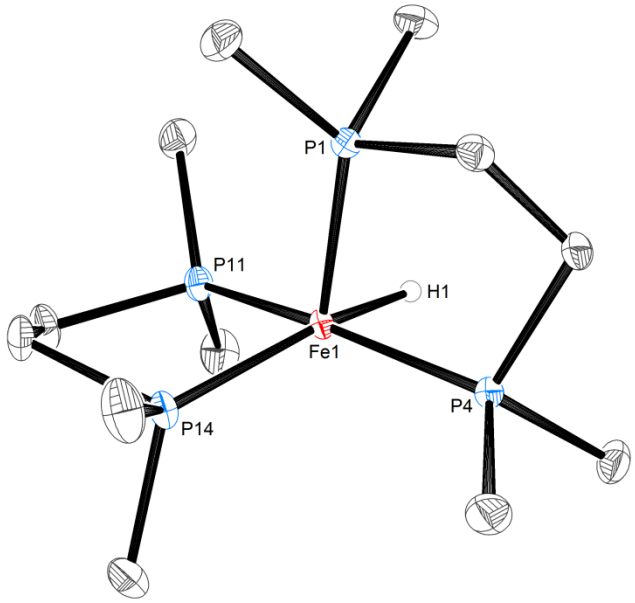


Figure 3.67 IR spectra of *trans*-$Fe(H)(N_3)(dmpe)_2$ (**9**, blue) and *trans*-$Fe(H)(N_3)(depe)_2$ (**14**, red) recorded as pressed solid KBr disks; the diagnostic asymmetric ν(N–N) stretch is labelled; the corresponding symmetric stretches are likely those at 1279 and 1252 cm^{-1} for **9** and **14**, respectively; P = PMe_2, PEt_2.

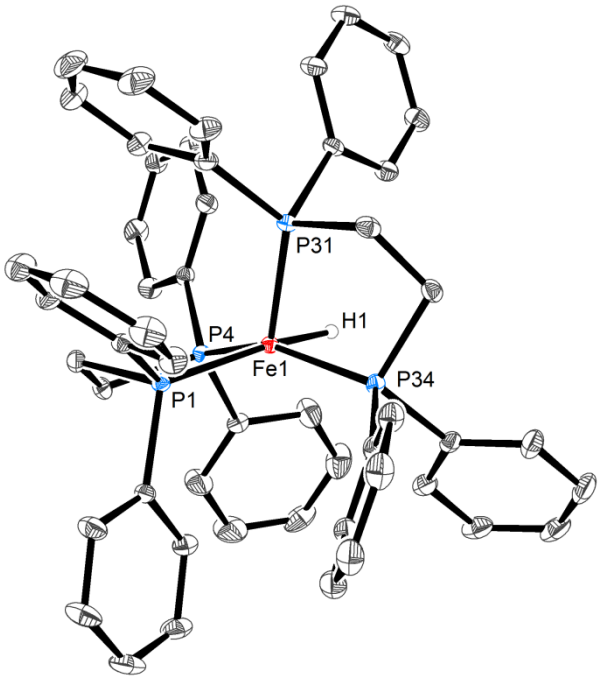
Upon reduction with KC_8 (1–2 equivalents) in hexane, the diamagnetic ^{31}P and ^{1}H NMR resonances of **9** disappeared and the solution turned an intense yellow colour, or alternatively, an intense red colour with excess KC_8 (> 2 equivalents). In contrast to poorly soluble **9**, the products of these reactions were extremely soluble in organic solvents. This led us, in the former case, to employ $SiMe_4$ as an unusual crystallisation solvent, from which yellow crystals were grown that were solved by single crystal X-ray diffraction as $Fe(H)(dmpe)_2$ (**10**, Figure 3.68(a)). To date, only two other Fe(I) hydride complexes (Figure 3.69) have been crystallographically characterised, reflecting the low oxidation state of Fe(I) and the reactivity of its hydrides.[44] Highly disordered dark green crystals were grown from

the red hexane solution. However, due to incorporation of solvent molecules, only when the more symmetric cyclopentane solvent was substituted was it possible to grow a single crystal suitable for X-ray diffraction measurements. This was solved as [*cis*-Fe(dmpe)$_2$(μ-K)]$_4$·2(cyclopentane) (**11**·2(cyclopentane); Figure 3.70).

(a)



(b)



(c) **Bond Lengths/Angles;**

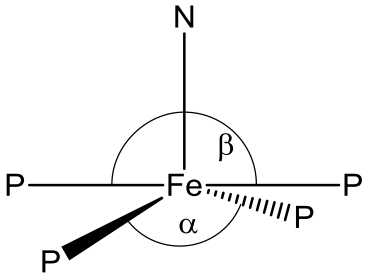
10:

Fe1–H1	1.49(3) Å
[Fe1–P]$_{av}$	2.1646(6) Å
P14–Fe1–H1	164.2(10)°
P11–Fe1–P4	163.22(2)°

Fe(H)(dppe)$_2$:

Fe1–H1	1.46(2) Å
[Fe1–P]$_{av}$	2.1857(4) Å
P1–Fe1–H1	165.8(3)°
P34–Fe1–P4	148.743(16)°

Fe coordination geometry:



$\tau = (\beta - \alpha)/60$

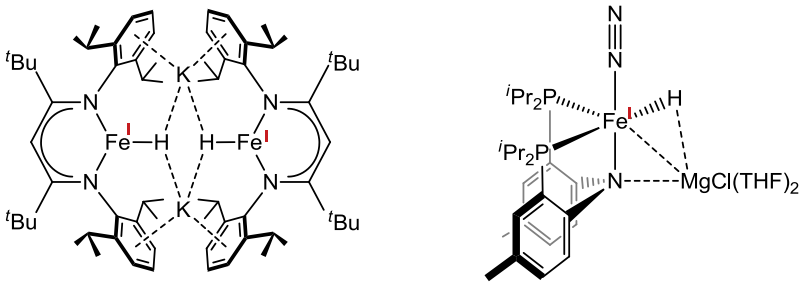
≈ 1 (trig. bipyr.)

≈ 0 (sq. pl.)

10: τ(Fe1) = 0.0163

Fe(H)(dppe)$_2$: τ(Fe1) = 0.275

Figure 3.68 Solid-state structures of (a) Fe(H)(dmpe)$_2$ (**10**); and (b) Fe(H)(dppe)$_2$; H1 atom white, all other H atoms omitted for clarity, C atoms grey, Fe atom red, P atoms blue; anisotropic displacement ellipsoids shown at 30% probability; (c) selected bond metric data.



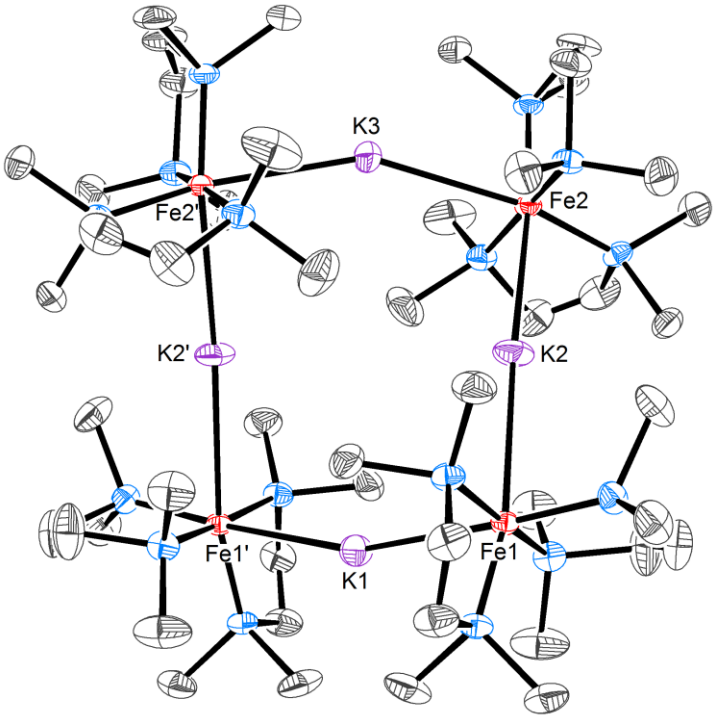
2x {HS Fe(**I**), S = 3/2} LS Fe(**I**), S = 1/2

Figure 3.69 The only crystallographically characterised Fe(I) hydrides to date: Holland *et al.* (2012, left); Mindiola *et al.* (2015, right).[44]

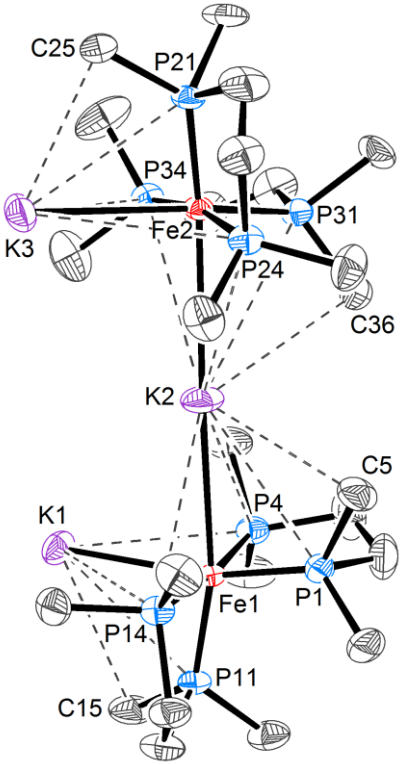
A single hydride ligand in **10** could be clearly located in the electron density map at one of the base vertices of the pseudo-square based pyramidal coordination geometry about Fe (τ(Fe1) = 0.0163; ideal τ = 0). The solid state structure of **10**, a 17 VE complex, can also be expected to be similar to the related but crystallographically uncharacterised 18 VE Fe(II) hydride *cis*-Fe(H)$_2$(dmpe)$_2$, in which a second hydride ligand would occupy the sixth vertex of an octahedral coordination geometry. The related complex Fe(H)(dppe)$_2$, one of very few examples of Fe(I) hydride complexes, has been prepared by Sacco *et al. via* Na reduction of *trans*-Fe(H)(Cl)(dmpe)$_2$,[45] and has since been crystallographically characterised in the Ashley group (Figure 3.65(b)). A more pronounced distortion from square based pyramidal coordination is observed for Fe(H)(dppe)$_2$ (τ(Fe1) = 0.275), presumably to optimally balance the steric demand of the bulky Ph groups with an electronic preference for square based pyramidal geometry.

11, a formally Fe(–I) 17 VE complex, exhibits an unusual tetrameric structure incorporating four distorted [Fe(dmpe)$_2$(K)$_2$] octahedrons, with each K bridging two Fe centres. The ring is conformationally twisted, which in addition to an inward distortion of peripheral P donor atoms appears to suggest steric shielding and/or electronic stabilisation of K. The average Fe–K bond distance of 3.4324(24) Å is comparable to the sum of the Fe and K covalent radii (3.35(12) Å; r(Fe, LS) = 1.32(3) Å; r(K) = 2.03(12) Å; deduced from crystallographic data)[46] and well within the sum of the Fe and K van der Waals radii (values obtained by various approaches are compiled in ref. 47). This would suggest a largely covalent Fe–K bond, rather than an ionic bond between discreet charges, which is further supported by the inherent solubility of **11** in non-polar hydrocarbon solvents. Possible dissociation of the tetrameric structure to lower polymeric forms may occur upon solvation, which could account for the difference in colour between the intense red of the hydrocarbon solutions of **11** and the dark green of its crystalline form. However full dissociation to a monomeric form is perhaps unlikely since this would necessarily expose the K^+ ions, and thus precipitation would be expected.

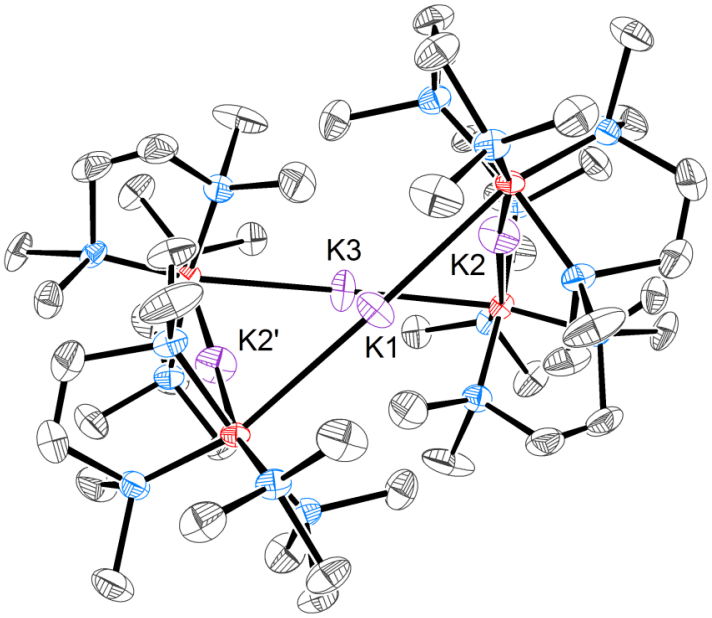
(a)



(b)



(c)



(d) **Bond lengths (Å):**

Fe1–K1	3.4224(8)
Fe1–K2	3.4562(15)
Fe2–K2	3.4933(15)
Fe2–K3	3.3576(9)
$[Fe1–P]_{av}$	2.1305(16)
$[Fe2–P]_{av}$	2.142(3)
$[K]\cdots[P_3]_{av}$	3.884(3)
$[K]\cdots[C_1]_{av}$	3.383(10)

Bond Angles (deg):

Fe1–K1–Fe1	162.63(7)
Fe1–K2–Fe2	169.97(6)
Fe2–K3–Fe2'	153.70(8)
K1–K2–K3	103.21(4)
K2–K1–K2'	77.14(5)
K2–K3–K2'	76.45(5)

Figure 3.70 Solid-state structure of [*cis*-Fe(dmpe)$_2$(μ-K)]$_4$ (**11**); two cyclopentane solvent molecules and all H atoms omitted for clarity, C atoms grey, Fe atom red, N atoms green, P atoms blue; K atoms purple; anisotropic displacement ellipsoids shown at 30% probability; (a) grown structure; (b) asymmetric unit cell with long distance K–P and K–C interactions indicated by dashed bonds; (c) grown structure viewed along K1–K3 axis revealing twisted ring conformation; (d) selected bond metric data; $[K]\cdots[P_3]_{av}$ and $[K]\cdots[C_1]_{av}$ are the averaged distances between K1–K3 and their respective three closest neighbouring P atoms and closest neighbouring C atom, respectively.

The failure of the above synthetic strategy towards a reduced N fragment would appear to suggest that N_3^- is a better leaving group than N_2 under these reductive conditions, reflecting the comparably weak Fe–N bond and the large lattice enthalpy of precipitated KN_3 (Figure 3.71). UV irradiation of azide metal complexes has been reported in some cases to generate nitride complexes through loss of N_2, however this has not been observed for **9** (λ= 365 nm, THF).

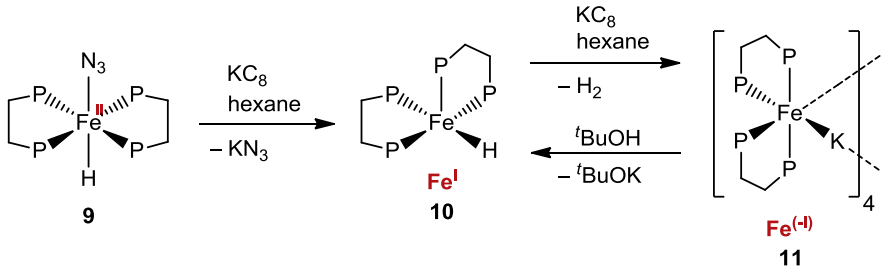


Figure 3.71 Reduction of *trans*-Fe(H)(N_3)(dmpe)$_2$ (**9**) to form Fe(H)(dmpe)$_2$ (**10**) and [*cis*-Fe(dmpe)$_2$(μ-K)]$_4$ (**11**); P = PMe_2.

The intense red colour of **11** arises from broad absorption features at ca. 410 (191 m^2 mol^{-1}) and 555 nm (40 m^2 mol^{-1}) in the UV-vis spectrum, whilst yellow **10** exhibits a band at ca. 400 nm (258 m^2 mol^{-1}; Figure 3.72(a)). The X-band CW-EPR spectra of **10** revealed an axial Fe(I) (S = ½) signal with some partially resolved hyperfine coupling to P nuclei (Figure 3.72(b)). A very similar signal was observed for **11**, which may be the result of decomposition to **10** upon dilution to a suitable concentration for EPR spectroscopy. Similarly, whilst considerable effort was made to ensure rigorously dry conditions, the molar absorption coefficient values from UV-vis spectroscopy may be underestimated as a consequence of decomposition of **10** and **11** to weakly absorbing *cis*-Fe(H)$_2$(dmpe)$_2$.

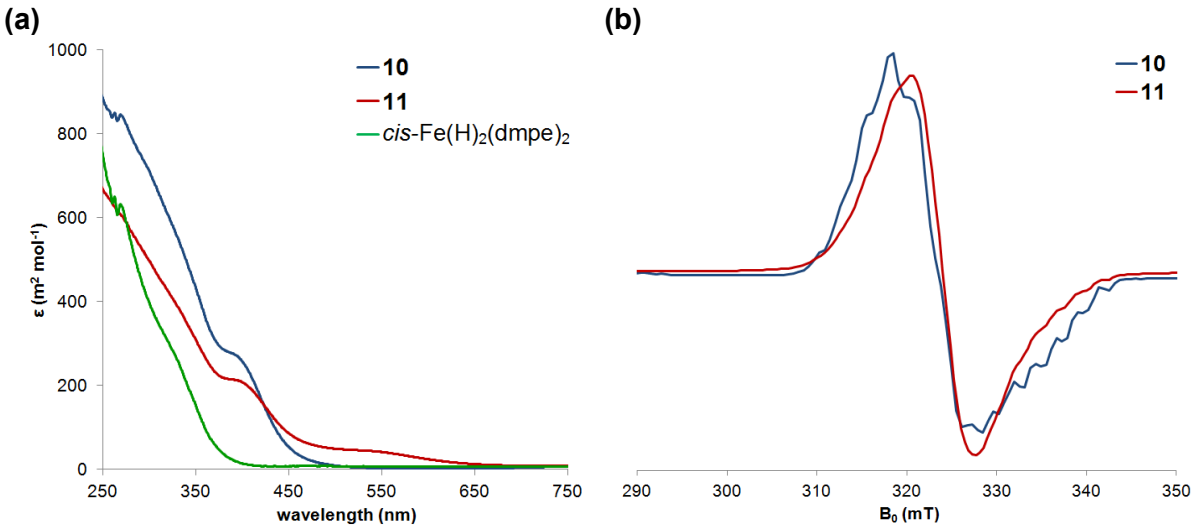


Figure 3.72 (a) UV-vis spectra of **10** (Et_2O, Ar), **11** (pentane, Ar), and *cis*-Fe(H)$_2$(dmpe)$_2$ (Et_2O, Ar); (b) X-band EPR spectrum of **10** and **11** (hexane, Ar) recorded as a glasses at 40 K.

Conversion of **10** to **11** with excess KC_8 could follow several possible mechanisms, likely involving either single electron reduction of Fe(I) followed by loss of H_2, or two electron reduction of Fe(I) from heterolytic cleavage of the Fe–H bond *via* deprotonation (Figure 3.73). When the reduction of **9** was performed in Et_2O solvent a short-lived diamagnetic intermediate was initially observed (^{31}P NMR, Et_2O, δ = 59.8 ppm, s(br), $\nu_{½}$ = 18 Hz; ^{1}H NMR, Et_2O, δ = –15.96 ppm (Fe–H), q, $^2J_{PH}$ = 35.4 Hz; Figure 3.74), which would appear to implicate initial reduction to a Fe(0) hydride complex.

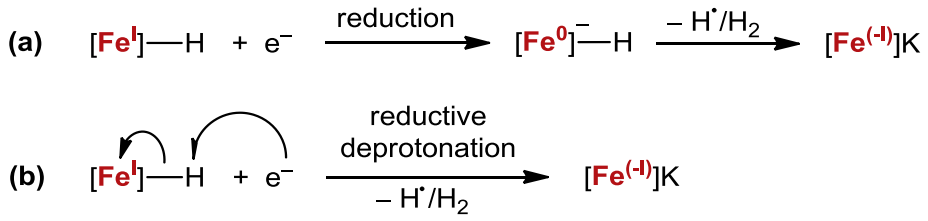


Figure 3.73 Hypothesised mechanisms for the reduction of $Fe(H)(dmpe)_2$ (**10**) to [*cis*-$Fe(dmpe)_2(\mu\text{-}K)]_4$ (**11**) with KC_8; [Fe] = $Fe(dmpe)_2$.

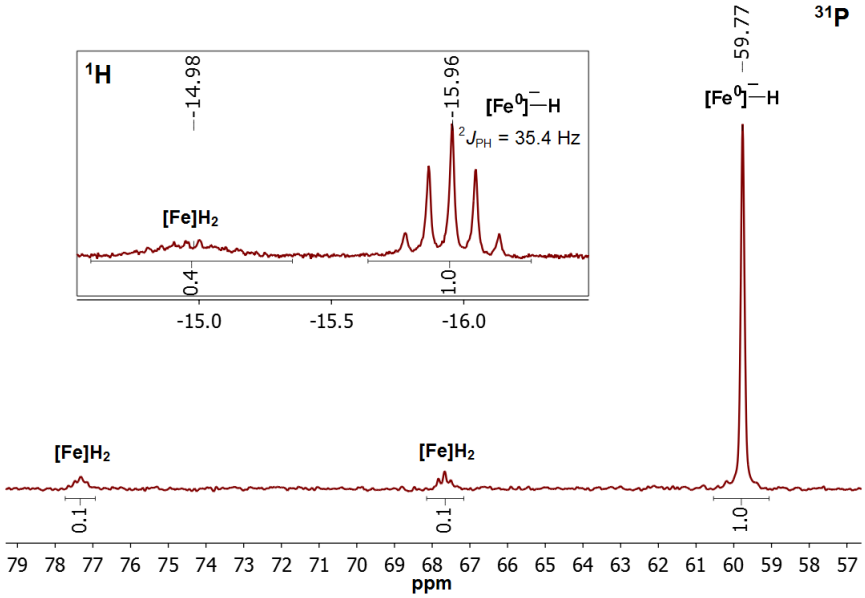


Figure 3.74 ^{31}P NMR spectra of the reduction of **9** with excess KC_8 (Et_2O, Ar) after ca. 5 min which reveals the formation of an intermediate hydride species proposed to be $[Fe(H)(dmpe)_2]K$; inset shows the hydride region in the corresponding ^{1}H NMR spectra; *cis*-$Fe(H)_2(dmpe)_2$ is formed as a by-product.

Unfortunately, *cis*-$Fe(H)_2(dmpe)_2$, which is unreactive towards KC_8, is always formed in these reactions in varying amounts, possibly as a result of H· transfer (a disproportionation reaction) or as a consequence of the extreme sensitivity of both **10** and **11** towards adventitious H_2O. Notably, the presence or absence of a N_2 atmosphere does not appear to

affect the reaction other than the trace amount of **4** detected by NMR spectroscopy. **11** appears to be stable in hydrocarbon solvents, remaining vivid red and NMR silent over several days at RT. In donor solvents, however, solutions appear darker and gradual decomposition to *cis*-$Fe(H)_2(dmpe)_2$ is observed by NMR spectroscopy, indicating deprotonation of the solvent. Similarly, *cis*-$Fe(H)_2(dmpe)_2$ is generated in toluene or benzene solvent. However, since **11** is appreciably less soluble than *cis*-$Fe(H)_2(dmpe)_2$ in hydrocarbon solvents it is possible to remove the latter contaminant through careful recrystallisation, although syntheses have thus far been limited to small scale reactions (< 0.1 mmol). Unfortunately, the hydride complexes have very similar solubilities and consequently it has not been possible to isolate pure samples of **10**.

Analogous reduction reactions of *trans*-Fe(H)(Cl)$(dmpe)_2$, *trans*-Fe(H)(CN)$(dmpe)_2$, and [*trans*-Fe(H)$(N_2)(dmpe)_2$][X] (X = BPh_4 or $BArF_{24}$), all containing a hydride ligand and a leaving group, were also investigated as more conveniently synthesised precursors to **9**. However, reduction of *trans*-Fe(H)(Cl)$(dmpe)_2$ was much slower in hexane than **9** and *cis*-$Fe(H)_2(dmpe)_2$ clearly grew in over the course of the reaction. Substituting TBME or Et_2O solvent resulted in much faster consumption of starting material and appeared to significantly reduce *cis*-$Fe(H)_2(dmpe)_2$ formation to the trace amounts generated from **9**. In contrast, *trans*-Fe(H)(CN)$(dmpe)_2$ reacted much more slowly with KC_8 to generate *cis*-$Fe(H)_2(dmpe)_2$ over the course of several days, reflecting the strong coordination of the CN^- ligands. Reduction of [*trans*-Fe(H)$(N_2)(dmpe)_2$][X] (X = BPh_4 or $BArF_{24}$) was expected to be comparably faster since the anions are non-coordinating and the N_2 ligand is coordinatively labile. However, reduction of [*trans*-Fe(H)$(N_2)(dmpe)_2$][BPh_4] appeared to suffer from decomposition of the BPh_4^- anion, whilst a significant amount of **4** was generated from the reduction of [*trans*-Fe(H)$(N_2)(dmpe)_2$][$BArF_{24}$]. In all these attempts, it was necessary to use a slight excess of KC_8 to ensure complete conversion of starting material, followed by addition of substoichiometric ^{t}BuOH acid to protonate any contaminating **11**. Accordingly, **10** could be accessed from either **11** or a mixture of **10** and **11** *via* protonation with ^{t}BuOH in hexane. However, this second step also produces trace *cis*-$Fe(H)_2(dmpe)_2$, which in contrast to **10** does not react with KC_8 preventing recovery of **11**. Heterolytic activation of H_2 by **11** was also envisaged as a route to preparing **10**, along with innocuous KH by-product. Admission of H_2 to a pentane solution of **11** immediately formed a grey precipitate (KH) along with *cis*-$Fe(H)_2(dmpe)_2$; the latter may be generated from disproportionation of **10** under H_2. Unfortunately, this cannot be easily verified using samples of isolated **10** due to its extreme sensitivity to trace H_2O, which is almost certainly introduced upon addition of H_2 gas, despite prior drying with a purifying column (NANOCHEM® WA-500 OMX™), storage over molecular sieves (4 Å), and stoichiometric delivery with a Toepler pump. The inevitable

formation of *cis*-Fe(H)$_2$(dmpe)$_2$ thus led us to examine possible synthetic routes to **10** and **11** *via cis*-Fe(H)$_2$(dmpe)$_2$. No reaction resulted from attempted H· abstraction with Gomberg's dimer (a source of Ph_3C·) or comproportionation with **4** (Figure 3.75(a-b)). Oxidation to a hypothesised Fe(III) species [Fe(H)$_2$(dmpe)$_2$]$^+$ with ferrocenium salts and subsequent reductive deprotonation with base (KO^{t}Bu or NEt_3; Figure 3.75(c)) produced contaminating [*trans*-Fe(H)(σ-H$_2$)(dmpe)$_2$]$^+$, which subsequently forms *cis*-Fe(H)$_2$(dmpe)$_2$ in the presence of base. Protonation with MeOH to this Fe(II) hydrido dihydrogen complex was also attempted with the possibility that subsequent reduction would form an Fe(I) hydrido dihydrogen species that could dissociate H_2 (Figure 3.75(d)); however *cis*-Fe(H)$_2$(dmpe)$_2$ was ultimately regenerated. Thus, the optimal synthesis of **10** and **11** remains the reduction of either *trans*-Fe(H)(Cl)(dmpe)$_2$ or **9**.

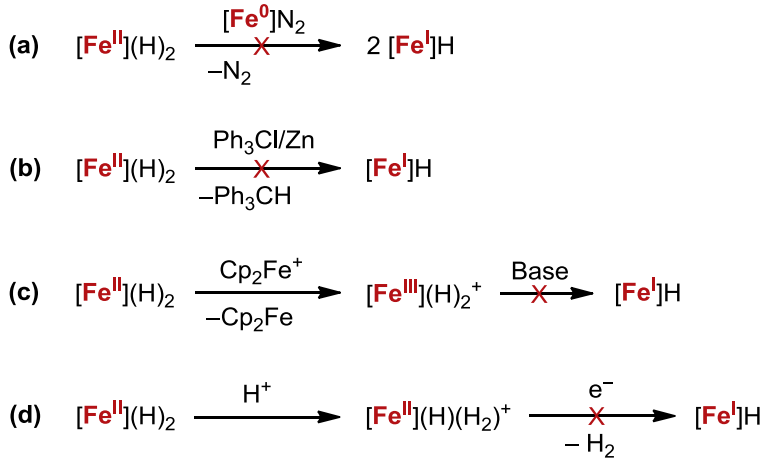


Figure 3.75 Attempted synthesis of Fe(H)(dmpe)$_2$ (**10**) *via cis*-Fe(H)$_2$(dmpe)$_2$.

Although neither **10** or **11** were initial synthetic targets, their accessibility from Fe(II) monohydride complexes may be significant. Whilst KC_8 reduction of [*trans*-Fe(H)(N_2)(dmpe)$_2$]$^+$ did not prove to be a viable method for generating **10**, the axial EPR signal of the latter was nevertheless observed in reaction aliquots. Hence, it is hypothetically possible that **4** or **6** generated from deprotonation of [*trans*-Fe(H)(N_2)(dmpe)$_2$]$^+$ in the Leigh cycle, may be sufficiently reducing to act as the reductant in a comproportionation reaction with [*trans*-Fe(H)(N_2)(dmpe)$_2$]$^+$ to generate **10** with loss of N_2 (Figure 3.76). Unfortunately, it was not possible to source a suitable electrode to measure the reduction potential of this Fe(II) hydrido N_2 complex since Pt, used previously, is incompatible with these hydridic species. However, whilst more sensitive EPR experiments have yet to be conducted, the NMR study discussed in section 3.0.2 indicates **4** and [*trans*-Fe(H)(N_2)(dmpe)$_2$]$^+$ preferentially undergo an association reaction to form **5**. Alternatively, in view of the apparent accessibility of Fe(–I), the possibility of a disproportionation reaction should also be considered, in which **7** and **11** could be generated from Fe(0) (Figure 3.76). If formed in the

Leigh deprotonation reaction, **11** would almost certainly react with $[(^tBuO)_2H]K$ or [*trans*-$Fe(H)(N_2)(dmpe)_2]^+$ to form **10**, which is also likely to be unstable under these protic conditions (*vide supra*). Notably, the only EPR active species observed in the Leigh deprotonation step or the reaction of **4**/**6** with $KBArF_{24}$ are those corresponding to or derived from **7** and/or **8**. Interestingly, for the analogous deprotonation reaction of [*trans*-$Fe(H)(N_2)(depe)_2]^+$, there is both EPR and NMR spectroscopic evidence for the formation of the related species $Fe(H)(depe)_2$ (**15**; *vide infra*).

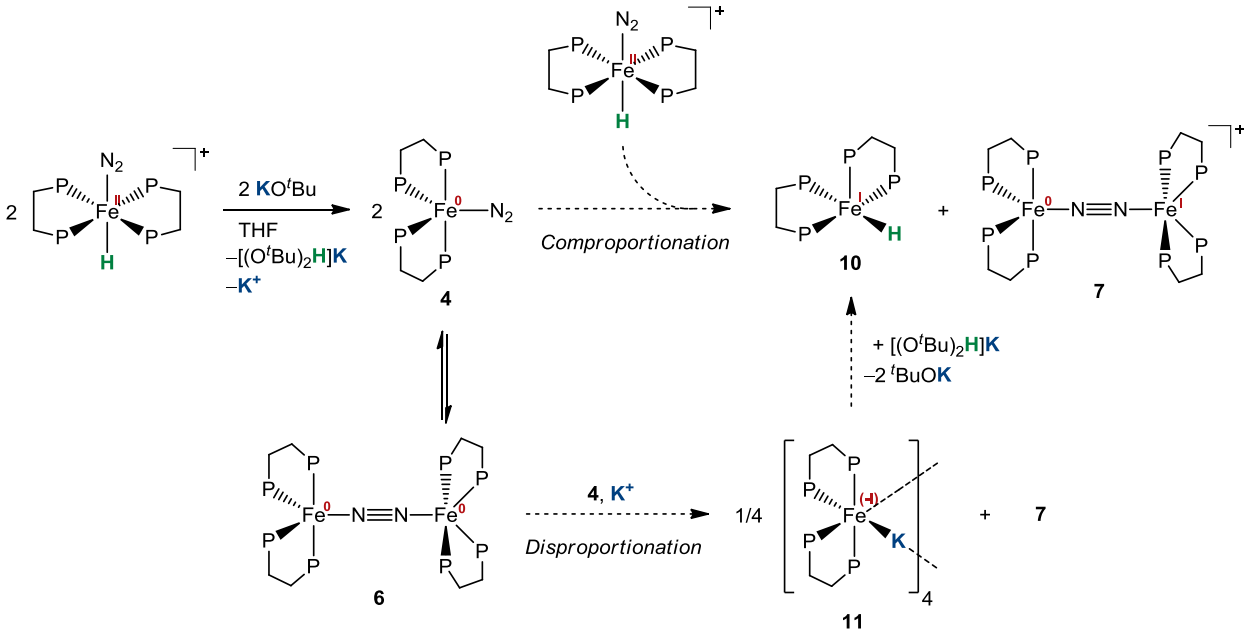


Figure 3.76 Hypothetical involvement of $Fe(H)(dmpe)_2$ (**10**) and [*cis*-$Fe(dmpe)_2(\mu\text{-}K)]_4$ (**11**) in the Leigh deprotonation reaction; P = PMe_2.

The chemistry of simple Fe(I) hydrides remains relatively unexplored and mostly limited to a few acidification/oxidation reactions of $FeH(dppe)_2$ (Figure 3.77).[48] Due to unresolved issues with the preparation of highly sensitive **10**, only preliminary investigation into its reactivity has been undertaken. As an Fe(I) hydride, it may be expected to undergo single electron chemistry to form more stable Fe(0) and/or Fe(II) compounds. One such transformation of particular interest to N_2 fixation chemistry would be H· atom transfer to N_2 since H· incorporates both an H^+ and an e^- for concomitant protonation and reduction; furthermore, it may be possible to generate **4** from the Fe(0) by-product under N_2. Thus far, NMR and EPR experiments have indicated that the triply bonded N_2 moiety in **4** is unreactive towards **10**, such that prior activation of N_2 is likely necessary. Holland *et al.* have recently demonstrated 1,2-insertion of an Fe–H bond in the HS Fe(II) complex LFeH (L = 1,3-bis(tertbutyl)-1,3-bis(2,6-diisopropylphenylimido)-propyl; Figure 3.78) across the N=N double bond of azobenzene (*trans*-PhN=NPh) to form the hydrazido complex LFe(NPhNHPh).[49] Subsequent

Fe(I) species generated from Fe–N bond homolysis are thought to facilitate N–N bond cleaving reactions *via* a radical chain mechanism.

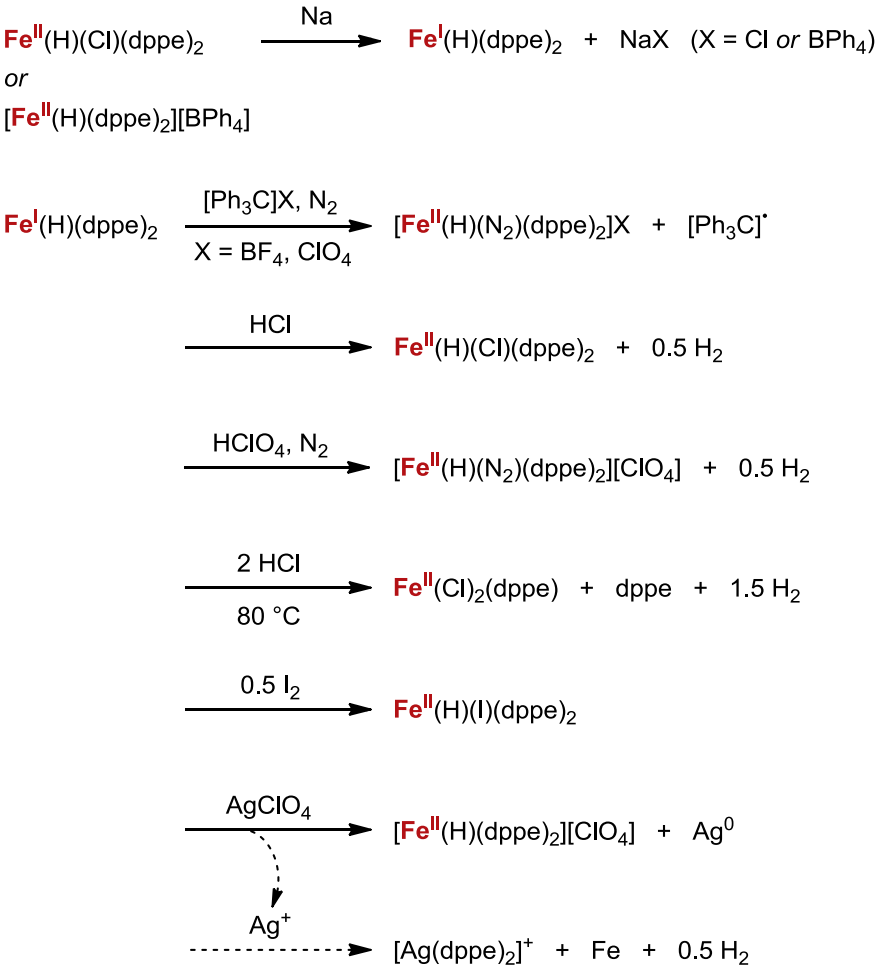


Figure 3.77 Synthesis of $Fe(H)(dppe)_2$ and its reactions with $[Ph_3C]^+$, acids, and oxidants, reported by Sacco *et al.*; notably, transformations result in oxidation of Fe(I) to Fe(II), and $[Ph_3C]^+$ acts as an oxidant rather than a hydride abstractor.[45, 48]

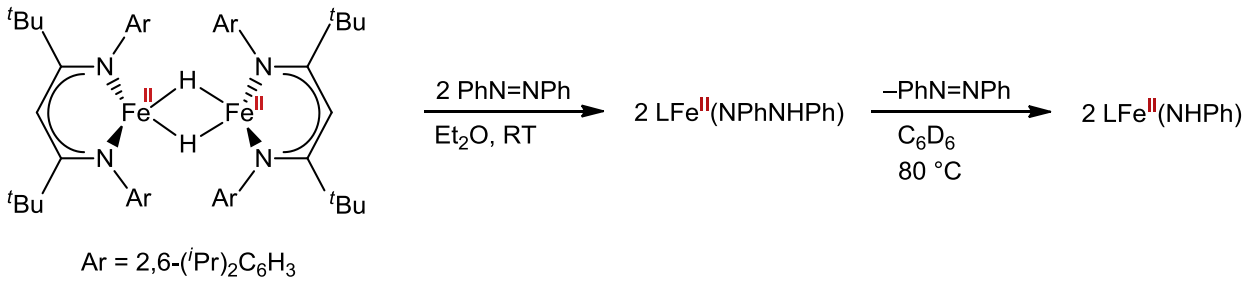


Figure 3.78 N=N bond cleavage by a HS Fe(II) hydride complex, reported by *Holland et al.*.[49]

Hence, we decided to perform a similar reaction of **10** with azobenzene (1:1) in Et_2O, which resulted in an immediate colour change from yellow/orange to a dark green colour, arising

from an electronic absorption feature at 463 nm (Figure 3.79). Over the course of 24 h, ^{31}P NMR spectroscopy revealed formation of the known azobenzene complex Fe(NPh=NPh)(dmpe)$_2$ (^{31}P NMR, Et_2O, δ = 64.8 ppm (t) and 57.3 ppm (t), $^2J_{PP}$ = 34 Hz),[17] which mostly precipitated, along with *cis*-Fe(H)$_2$(dmpe)$_2$. A similar green coloured solution was obtained when the reaction was performed in pentane, from which it was possible to grow green crystals by cooling to –30 °C. A suitable crystal was solved by single crystal X-ray diffraction as *trans*-Fe(H)$_x$(NPhNPh)(dmpe)$_2$ (x = 0–1, Figure 3.80).

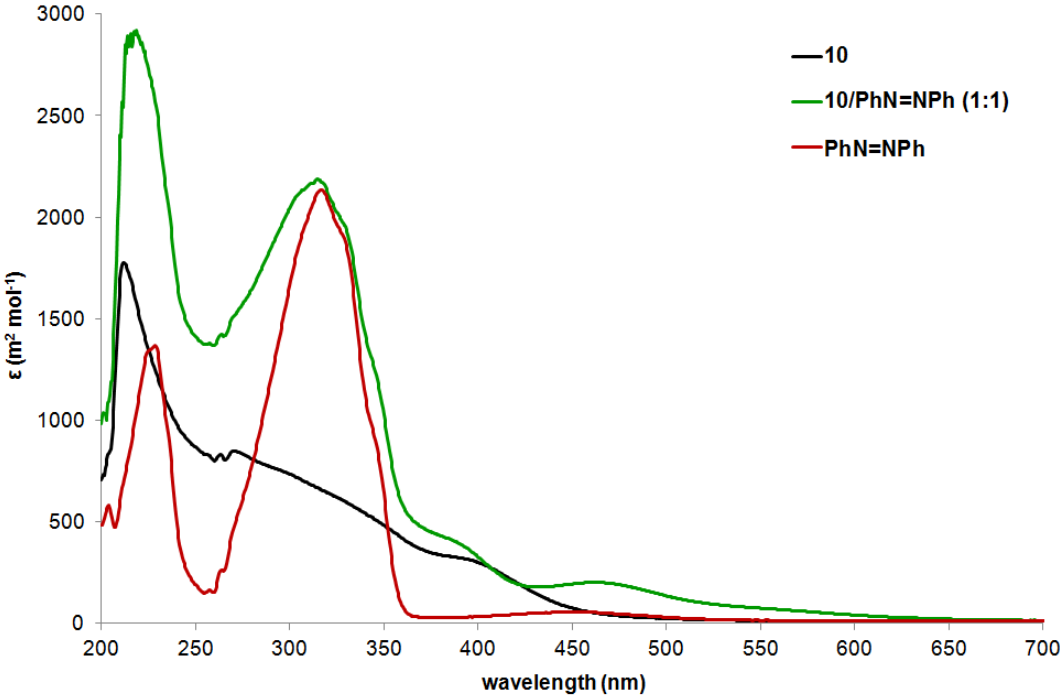
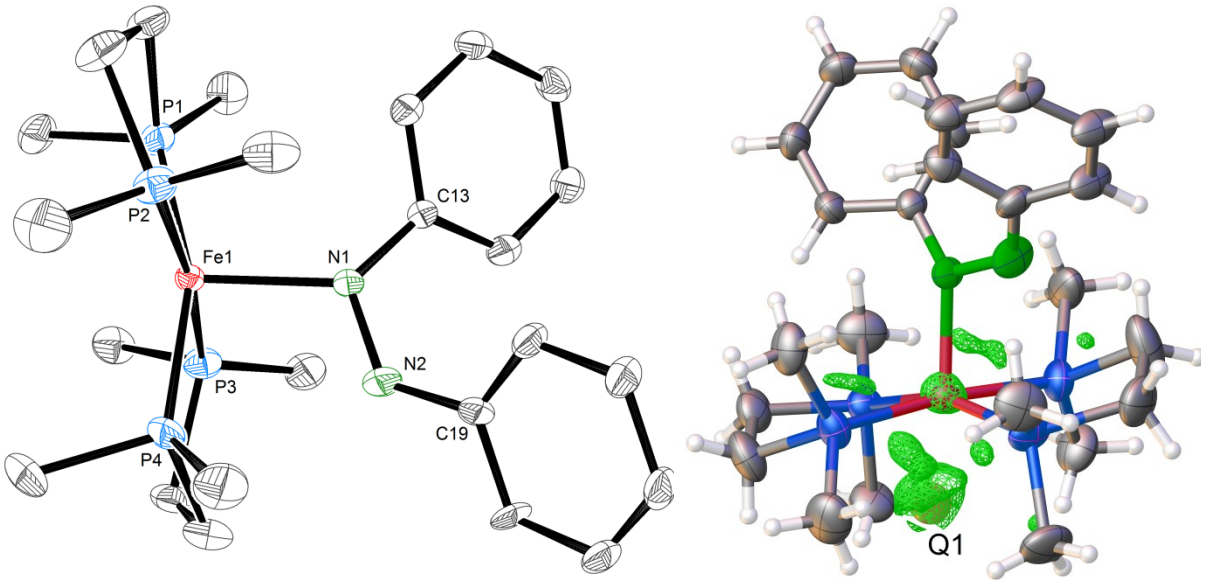


Figure 3.79 UV-vis spectra of **10** (Et_2O, Ar) before (black) and after addition of PhN=NPh (green), and PhN=NPh (Et_2O, Ar, red).

It is unclear whether there is a H atom bonded to the metal *trans* to the "NPhNPh" ligand, although a residual electron density peak (Q1, 1.53 e$^-$/Å^3) is located at ca. 1.99 Å from the Fe centre and off-axis (Q1–Fe–N1 = 165.11(8)°); whereas no residual electron density was located at the uncoordinated N atom, arguing against 1,2-insertion of Fe–H across the N=N bond. The N=N bond length of 1.368(4) Å is significantly shorter than in the π-complex Fe(NPh=NPh)(dmpe)$_2$ (1.412(4) Å),[17] or in other side-on bound azobenzene complexes of Fe (1.398–1.441 Å)[49, 50] indicating a reduced degree of activation (cf. *trans*-azobenzene,[51] 1.247(2) Å, and *cis*-azobenzene,[52] 1.253(4) Å). However, the Ph rings of the coordinated azobenzene have clearly rotated along the N–N axis with a resultant dihedral angle of 46.8(5)° (cf. *trans*-azobenzene, 180.0° and *cis*-azobenzene, 8.0°). This would suggest that the green species is an intermediate to Fe(NPh=NPh)(dmpe)$_2$ in which azobenzene binds to Fe end-on and the double bond is partially broken; subsequent loss of the hydride ligand is

proposed to occur *via* H· abstraction by a second equivalent of **10**, producing *cis*-$Fe(H)_2(dmpe)_2$ by-product (Figure 3.81). Hence, this would avoid the unfavourable 19 VE configuration of an intermediate π-complex *trans*-$Fe(H)(NPh{=}NPh)(dmpe)_2$. Unfortunately due to the sensitivity of the green species it was not possible to analyse for a *v*(Fe–H) stretch by IR spectroscopy and thus unambiguously determine whether this species contains a hydride ligand. Notably, *cis*-$Fe(H)_2(dmpe)_2$ was found not to react with azobenzene, demonstrating the greater reactivity of **10**, whilst azobenzene was found to readily displace N_2 in **6** to generate $Fe(NPh{=}NPh)(dmpe)_2$ (Figure 3.81).

(a) **(b)**



(c)

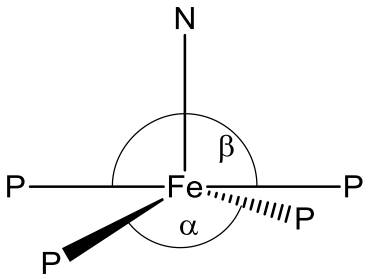
Bond lengths (Å):

Fe1–N1	2.079(3)
Fe1···N2	2.868(4)
N1–N2	1.368(4)
$[Fe–P]_{av}$	2.2003(11)

Bond Angles (deg):

Fe1–N1–N2	111.0(2)
C13–N1–N2–C19	46.8(5)

Fe coordination geometry:



$\tau = (\beta–\alpha)/60$

≈ 1 (trig. bipyr.)

≈ 0 (sq. pl.)

$\tau(Fe1) = 0.212$

Figure 3.80 (a) Solid-state structure of *trans*-$Fe(H)_x(NPhNPh)(dmpe)_2$; x = 0-1; C atoms grey, Fe atom red, N atoms green, P atoms blue; anisotropic displacement ellipsoids shown at 30% probability; (b) electron density map and the first Q-peak (Q1) projected onto the asymmetric unit cell; (c) selected bond metric data.

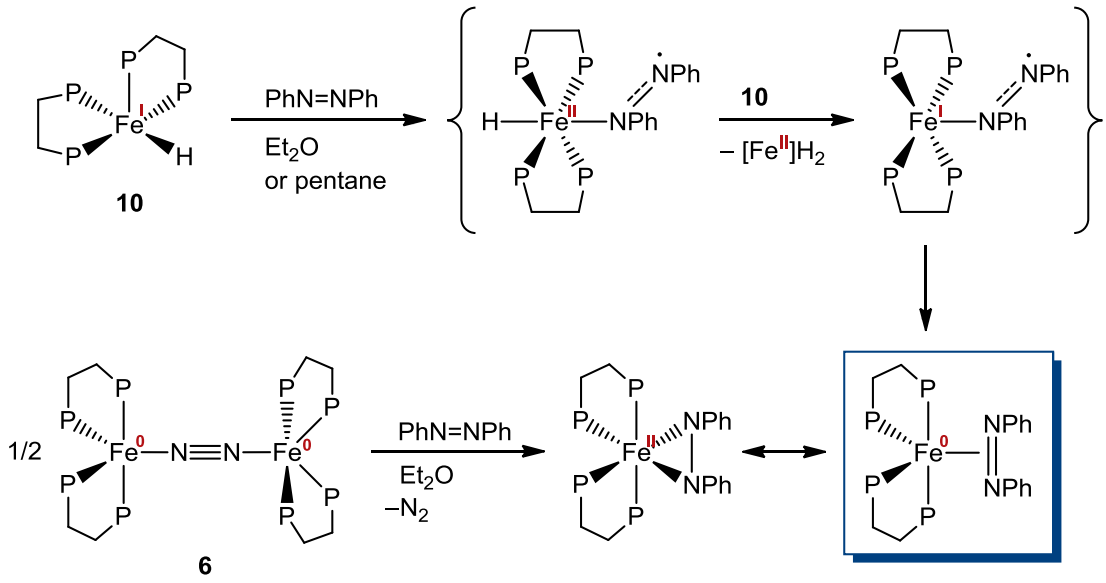


Figure 3.81 Reaction of Fe(H)(dmpe)$_2$ (**10**) with PhN=NPh to form Fe(NPh=NPh)(dmpe)$_2$; and an alternative synthesis of Fe(NPh=NPh)(dmpe)$_2$ from **6**; P = PMe$_2$.

3.1.7 H_2 experiments

As discussed in Chapter 1, only a few examples of homogeneous systems that utilise H_2 as a source of electrons or protons for N_2 fixation have been reported. In the case of Fe, H_2 has been employed in Leigh-type chemistry to generate [*trans*-Fe(H)(η^2-H_2)(DMeOPrPE)$_2$]$^+$ along with a proton, from the reaction of *trans*-Fe(Cl)$_2$(DMeOPrPE)$_2$ with H_2 and a proton sponge (Figure 3.82).[11] Conversion under N_2 provides the Fe(II) hydrido N_2 complex for subsequent deprotonation/reprotonation chemistry in which the Fe–H bond is a source of two electrons. The proton generated from the H_2 reaction is not utilised however, and additional acid is required to liberate NH_3.

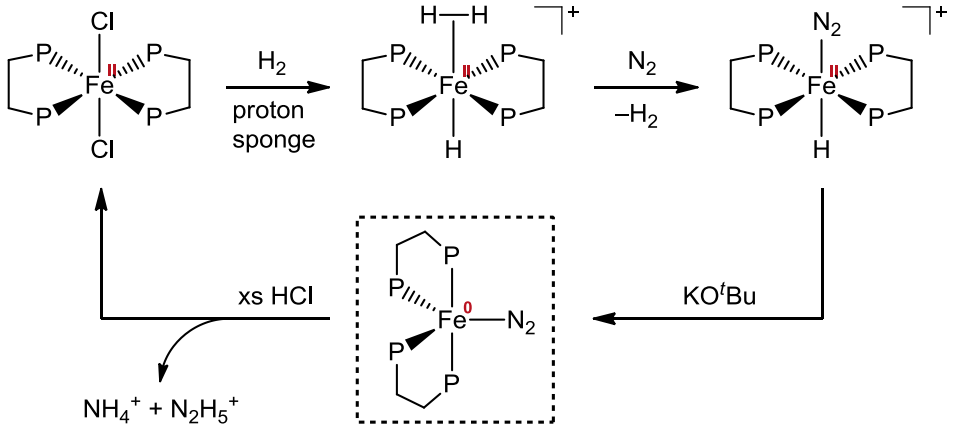


Figure 3.82 Modification of the Leigh cycle reported by Tyler *et al.*; P = P{(CH$_2$)$_3$OMe}$_2$.[11]

The archetypal Fe(II) *tris*-hydride complex [*trans*-Fe(H)(η^2-H_2)(dmpe)$_2$]$^+$ incorporates H ligated as both a classical hydride (H^-) and as a non-classical σ-H_2 ligand.[53] Field *et al.* have estimated the pK_a of this complex to be around that of EtOH (p$K_{a,DMSO}$ = 29.8), in which solvent it is formed reversibly from *cis*-Fe(H)$_2$(dmpe)$_2$; whereas *cis*-Fe(H)$_2$(dmpe)$_2$ is fully protonated in MeOH (p$K_{a,DMSO}$ = 29.0) and not protonated to a detectable degree in ^{i}PrOH (p$K_{a,DMSO}$ = 30.2).[23, 54] The acidic nature of the σ-H_2 ligand in Fe(II) non-classical hydride complexes is well documented;[55] this is ascribed to the activation of the H–H bond to heterolysis through a combination of σ-coordination from σ(H–H) into an empty σ(M) orbital, and π-backdonation from an occupied π(M) orbital into σ*(H–H). In addition, a positive charge on the metal centre will further increase the acidity of H_2 by stabilising the conjugate base (H^-). Thus, heterolytic cleavage of the H–H bond upon deprotonation yields a classical hydride (M–H) with loss of H^+, whereas a highly π-basic metal centre will destabilise the σ-H_2 complex resulting in H–H bond homolysis to form the oxidative addition product (Figure 3.83).

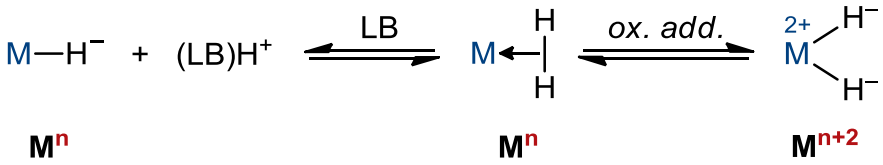


Figure 3.83 Interconversion between non-classical dihydrogen (σ-H_2) and classical hydride (H^-) transition metals complexes *via* either reversible oxidative addition, or deprotonation with a Lewis base.

Since the N_2 ligand in **4** and **6** is only relatively weakly activated, H_2 is unable to react directly with coordinated N_2, instead the N_2 ligand is displaced to form the oxidative addition product *cis*-Fe(H)$_2$(dmpe)$_2$. Analogous to the dissociation of **6** to **4** under a N_2 atmosphere, *cis*-Fe(H)$_2$(dmpe)$_2$ and **4** are generated from **6** under a H_2 atmosphere (Figure 3.84). Subsequent reaction of **4** with additional H_2 occurs at a much slower rate to form exclusively *cis*-Fe(H)$_2$(dmpe)$_2$.

The mixed valence dimer **7** is fully converted under H_2 (1 bar, THF or Et_2O) to form a 1:1 mixture of *cis*-Fe(H)$_2$(dmpe)$_2$ and [*trans*-Fe(H)(η^2-H_2)(dmpe)$_2$][$BArF_{24}$] (Figure 3.85); the latter complex incorporates hydrogen ligated as both a classical hydride and as a non-classical σ-H_2 ligand, and importantly is related to *cis*-Fe(H)$_2$(dmpe)$_2$ by a single protonation step. The reaction appears instantaneous even at low temperatures and no other species besides a small amount of [*trans*-Fe(H)(N_2)(dmpe)$_2$][$BArF_{24}$] were spectroscopically observed; the N_2 ligand in this Fe(II) complex is labile and expected to be in rapid exchange with H_2.[7]

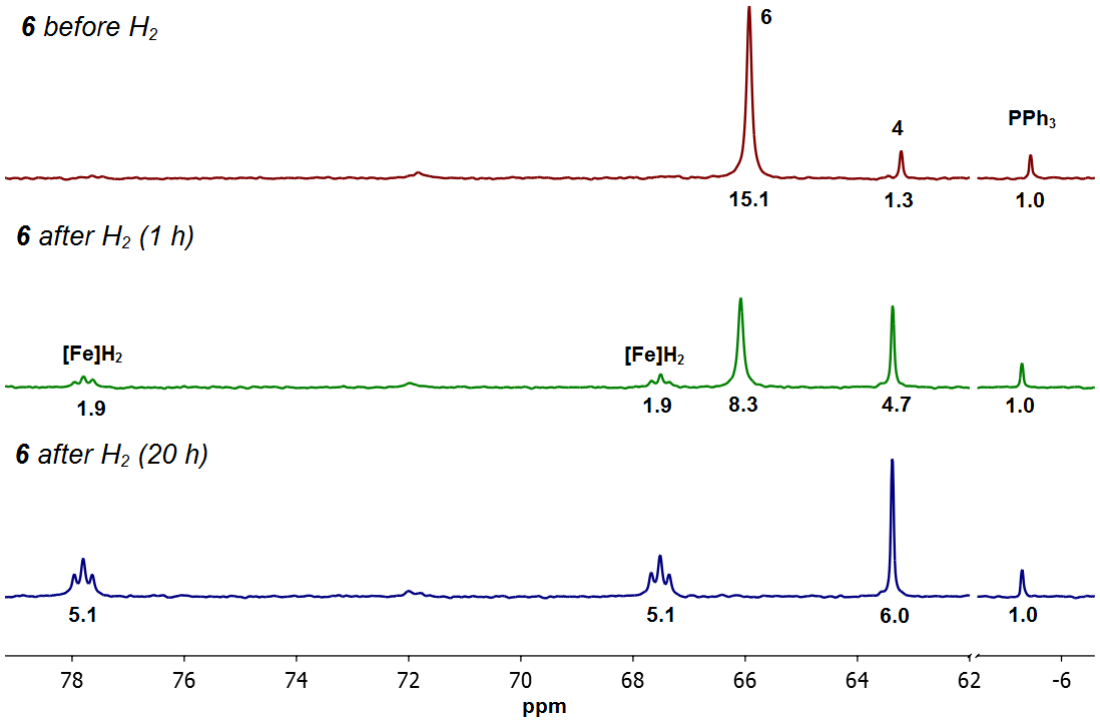


Figure 3.84 ^{31}P NMR spectra of the reaction of **6** with H_2 (1 bar) in pentane; integrated relative to PPh_3 within a capillary insert.

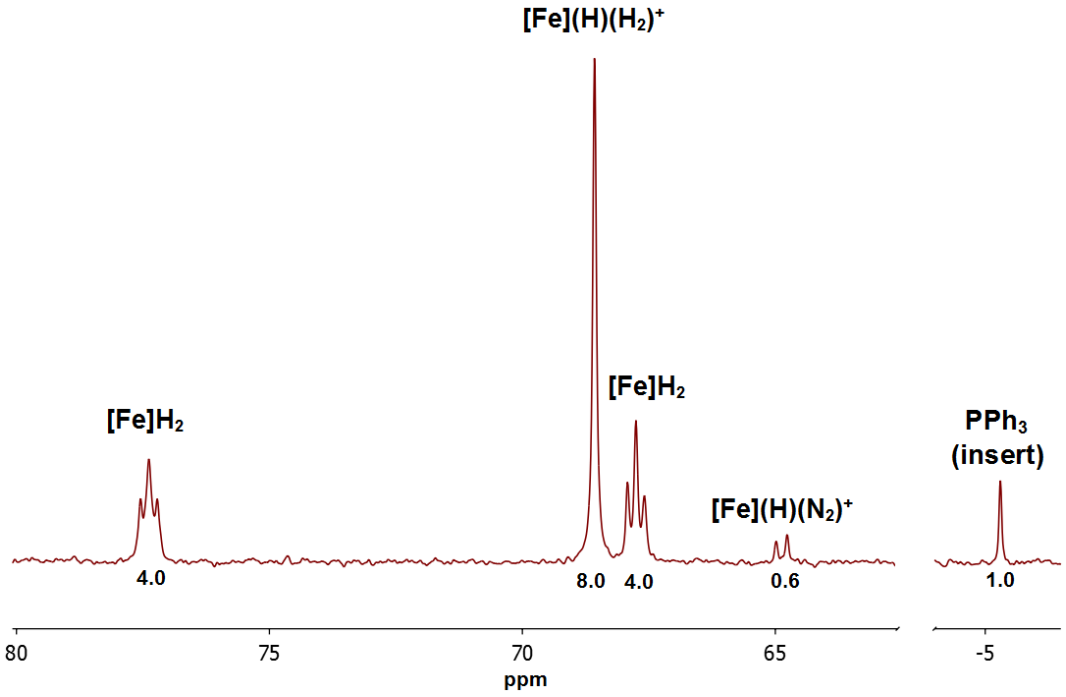


Figure 3.85 ^{31}P NMR spectrum of the reaction of **7** (0.008 mmol) with H_2 (1 bar) in THF; the amount of [Fe] (= $[Fe(dmpe)_2]$) was calculated to be 0.017 mmol by integration against PPh_3 within a capillary insert; P = PMe_2.

Hence, the mechanism is obscured, however by analogy to **6**, **7** can be expected to undergo dissociation to Fe(I) and Fe(0) fragments (Figure 3.86). The binding affinity of N_2 is reduced in Fe(I) relative to **4**, as demonstrated by VT UV-vis measurements on **8** (*vide supra*), and thus formation of **4** is anticipated from this initial dissociation. However, the slow displacement of N_2 in **4** with H_2 would appear to be incongruous with the observed rapid reaction of **7** with H_2. In contrast, coordination of H_2 (in excess) to Fe(I) can be expected to be fast, forming either a non-classical Fe(I) σ-H_2 complex, or the Fe(III) oxidative addition product. Thus, it is possible that displacement of N_2 in **4** proceeds *via* the protonated species [*trans*-Fe(H)(N_2)(dmpe)$_2$][$BArF_{24}$], which may be generated from deprotonation of either non-classical Fe(I) or classical Fe(III) hydride complexes. This would produce [*trans*-Fe(H)(η^2-H_2)(dmpe)$_2$][$BArF_{24}$] along with **10**; the latter can be expected to readily convert to *cis*-Fe(H)$_2$(dmpe)$_2$, likely proceeding *via* disproportionation and subsequent oxidative addition under H_2 (Figure 3.86(b)). Irrespective of the mechanism, the outcome of this reaction is the activation of H_2 by **7** to form three hydride ligands and an acidic σ-H_2 ligand, which effectively translates to four hydrides and a proton.

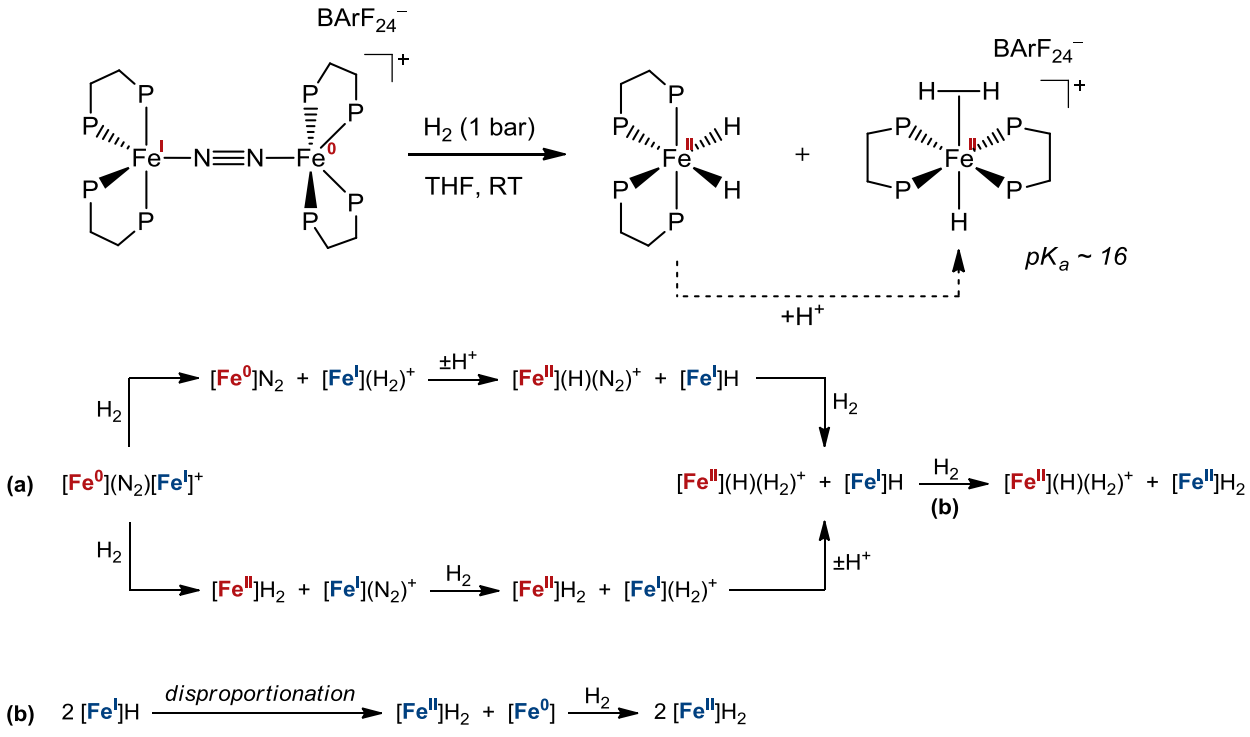


Figure 3.86 (a) Hypothetical pathways for the reaction of **7** with H_2 involving dissociation to Fe(I) and Fe(0) monomers; (b) Conversion of **10** to *cis*-Fe(H)$_2$(dmpe)$_2$ under H_2; [Fe] = [Fe(dmpe)$_2$].

The reaction of **6** with $KBArF_{24}$, in which **7** is generated, has also been performed under a H_2 atmosphere. Significantly, the oxidation of **6**, and subsequent reaction of **7** with H_2, provides a single electron and proton equivalent per starting molecule of **6**, such that fixation of N_2 by

H_2 could be achieved by these transformations. Thus, coordination of K^+ ions to an activated N_2 ligand bound to Fe may not only facilitate electron transfer to N but additionally direct subsequent protonation from activated H_2; this chemistry may be considered to mimic the Haber-Bosch process in which K(I) oxide is used as a co-catalyst. To explore this, ^{31}P NMR spectroscopic analysis was performed on a THF solution of **6** prior to and after addition of $KBArF_{24}$ (1:2) and H_2 (1 bar). Upon admittance of H_2 to the dark red **6**/$KBArF_{24}$ mixture, the solution immediately changed colour to a pale yellow. The ^{31}P NMR spectrum (Figure 3.87) of the resulting solution revealed formation of *cis*-$Fe(H)_2(dmpe)_2$ in ca. 66% yield from **6**, along with a small quantity of [*trans*-$Fe(H)(N_2)(dmpe)_2$][$BArF_{24}$] (< 4%); no further change in the ^{31}P NMR spectrum was observed upon leaving the solution under H_2 for a further 24 h. Thus, approximately one third of the ^{31}P NMR intensity is unaccounted for, indicating formation of a paramagnetic species. X-band CW EPR measurements were unable to resolve any Kramer's ions corresponding to Fe(I) or Fe(III) species (S = 1/2, 3/2, or 5/2) which would appear to implicate a HS Fe(II) non-Kramer's ion (S = 1, 2) unobservable at the X-band frequency.

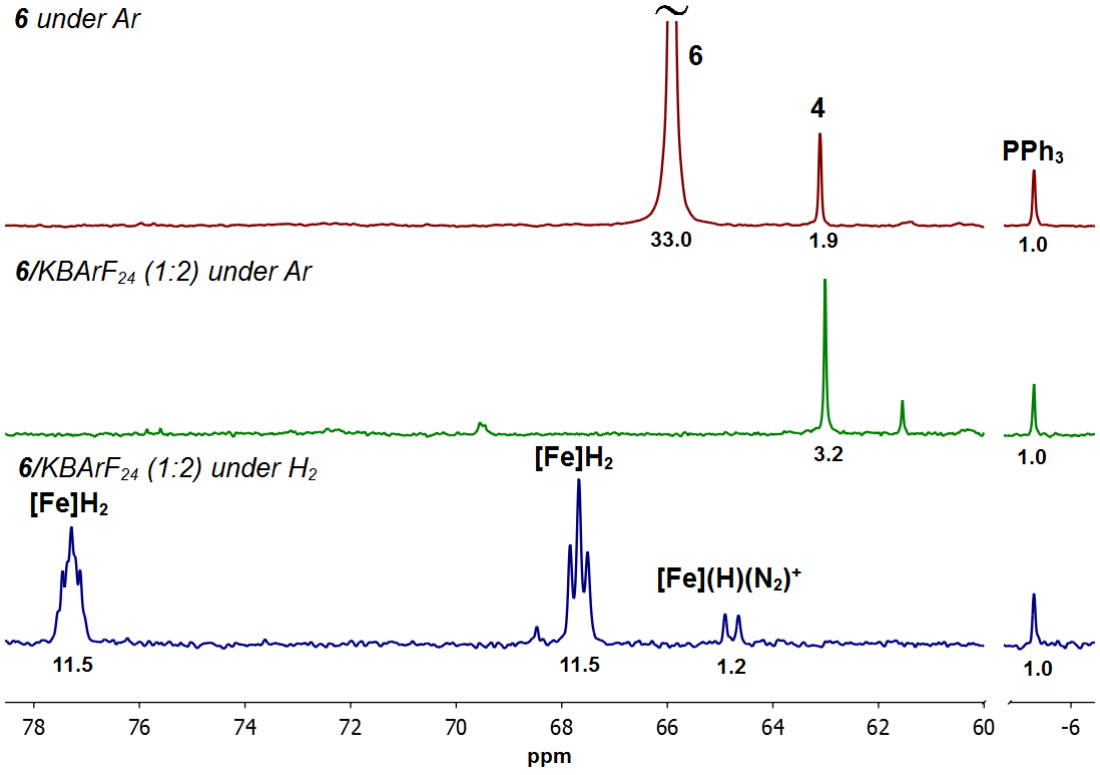


Figure 3.87 ^{31}P NMR spectrum of the reaction of **6** with $KBArF_{24}$ (1:2) under Ar (1 bar) and H_2 (1 bar) in THF; integrated relative to PPh_3 within a capillary insert; [Fe] = [$Fe(dmpe)_2$].

UV-vis spectroscopy performed on this solution provided a highly broadened absorbance spectrum which did not resolve any characteristic features besides CT bands corresponding

to $KBArF_{24}$ (Figure 3.88). Whilst *cis*-$Fe(H)_2(dmpe)_2$ by-product and regenerated $KBArF_{24}$ are separable due to the insolubility of the latter in hydrocarbons, attempts to selectively crystallize from the two fractions have only yielded crystalline $KBArF_{24}$. Together with the lack of a spectroscopic handle, this unfortunately limits understanding of this reaction. However, it is significant that *cis*-$Fe(H)_2(dmpe)_2$ accounts for almost all of the remaining diamagnetic two thirds, since **7** generated from the reaction of **6** with $KBArF_{24}$ is expected to produce an equal amount of *cis*-$Fe(H)_2(dmpe)_2$ and [*trans*-$Fe(H)(\eta^2\text{-}H_2)(dmpe)_2$][$BArF_{24}$], of which the latter was not detected. Alternatively, if H_2 reacts faster with **6** than the products of the reversible reaction with $KBArF_{24}$, full conversion to *cis*-$Fe(H)_2(dmpe)_2$ would be expected.

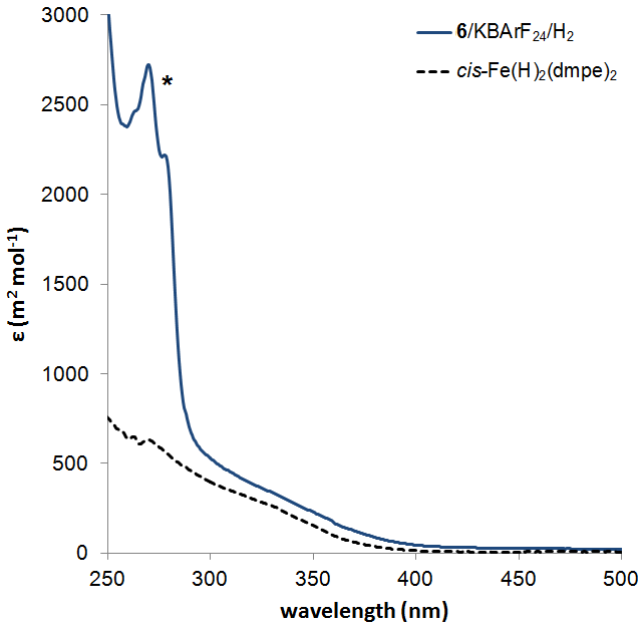


Figure 3.88 UV-vis spectra of **6** with $KBArF_{24}$ (1:4) under 1 bar H_2 (Et_2O, blue), and *cis*-$Fe(H)_2(dmpe)_2$ (Et_2O, dashed black); *CT features between 250–290 nm correspond to $KBArF_{24}$.

Thus, the $KBArF_{24}$ additive has clearly influenced the reactivity with H_2, increasing both the rate of the reaction and decreasing the resultant ^{31}P NMR balance by one third. Whilst these results remain inconclusive, the absence of [*trans*-$Fe(H)(\eta^2\text{-}H_2)(dmpe)_2$][$BArF_{24}$] would appear to indicate a proton transfer has occurred, which may be coupled to prior reduction of a N_2 ligand to a basic $[N_2]K_x$ fragment. Accordingly, a mechanism consistent with the ^{31}P NMR balance is tentatively proposed in Figure 3.89, in which K^+ ions perform a catalytic role in directing sequential electron and proton transfer to N_2 coordinated to both Fe and K^+; the overall process thus involves K^+-coupled electron transfer, followed by H_2-mediated protonation. It is hoped that greater understanding, particularly of the unknown intermediates, will be elucidated through the use of more niche and advanced spectroscopic

techniques such as high field/frequency EPR and Mössbauer spectroscopy, which are currently being pursued within the group.

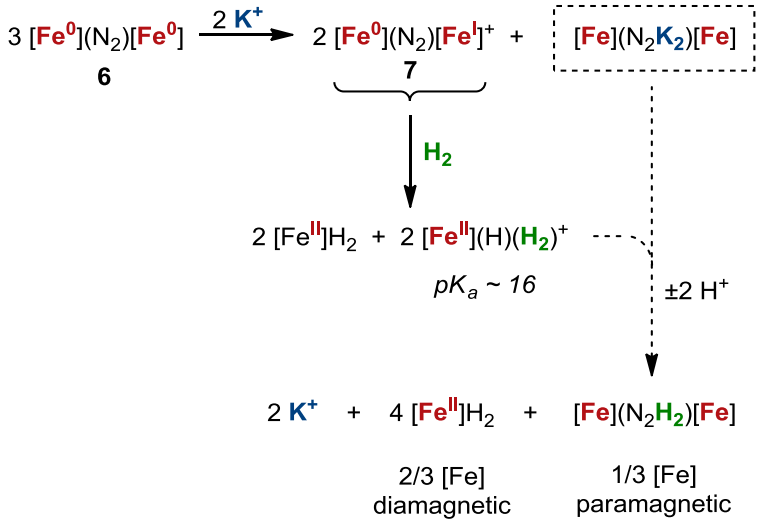


Figure 3.89 Hypothesised mechanism for the reaction of **6** with $KBArF_{24}$ under H_2; [Fe] = $[Fe(dmpe)_2]$.

Part 2: Fe complexes of depe

3.2.1 Introduction

The reactivity of analogous complexes of dmpe and depe are often very similar owing to the comparable electron donating ability of these two chelating σ-donor ligands. As a ligand depe is generally considered to be slightly less electron donating than dmpe, for instance as manifested in the trend in hydride donor ability of Group 12 metal hydrides ($[Pt(H)(dmpe)]^+$ > $[Pt(H)(depe)]^+$ > $[Ni(H)(dmpe)]^+$ > $[Ni(H)(depe)]^+$), reflecting reduced electron density at the metal.[56] Perhaps more significant is the greater steric shielding of the depe ligand due to the increased bulk of the Et substituents. Notably, although not discussed in detail, Leigh *et al.* have reported that the analogous deprotonation/reprotonation reaction of [*trans*-$Fe(H)(N_2)(depe)_2][BPh_4]$ produces NH_3 in comparable yields to the archetypal dmpe system - up to 20% based on maximum oxidation of Fe(0) up to Fe(II) (or 13% per Fe).[1, 4] However, as discussed in section 3.0, the major component of the deprotonation reaction, the Fe(0) complex $Fe(N_2)(depe)_2$ (**12**), has been independently synthesised and shown not to liberate any NH_3 upon acidification with HCl.[10, 12] Thus, as in the case for dmpe, interaction with the other components of the deprotonation mixture was anticipated to be crucial for NH_3 production, and parallel reactivity studies were undertaken.

3.2.2 Synthesis of Fe(0)

12 was first isolated and crystallographically characterised by Komiya *et al.* by Na naphthalenide reduction of $FeCl_2(depe)_2$ under a N_2 atmosphere (Figure 3.90).[12] This Fe(0) complex is an orange diamagnetic (S = 0) solid which exhibits a single ^{31}P NMR resonance (δ = 84.7 ppm, Et_2O) indicating rapid fluxional exchange of axial and equatorial phosphorus in solution. Dissociation of the N_2 ligand in **12** is not observed at RT *in vacuo*, suggesting an increased binding affinity of N_2 compared to **4**; furthermore, the 16 VE species $[Fe(depe)_2]$, which is prepared analogously under an Ar atmosphere, is stabilised *via* a reversible intramolecular cyclometallation reaction and readily converts under N_2 to form **12** (Figure 3.90(b)).[9, 10] Nonetheless, displacement of N_2 with various two electron donor ligands occurs to afford complexes of the general formula $Fe(L)(depe)_2$ (L = CO, CO_2, CS_2, C_2H_4, CN-2,6-$(Me)_2C_6H_3$).[10, 57] Jones *et al.* showed that the rate of ligand displacement was dependent on the identity and concentration of the incoming ligand and independent of N_2 pressure, indicating a bimolecular reaction rather than prior dissociation of N_2 (Figure 3.91). The *cis*-dihydride species *cis*-$Fe(H)_2(depe)_2$ was formed irreversibly by sparging a benzene solution of **12** with H_2 gas (*vide infra*).[10]

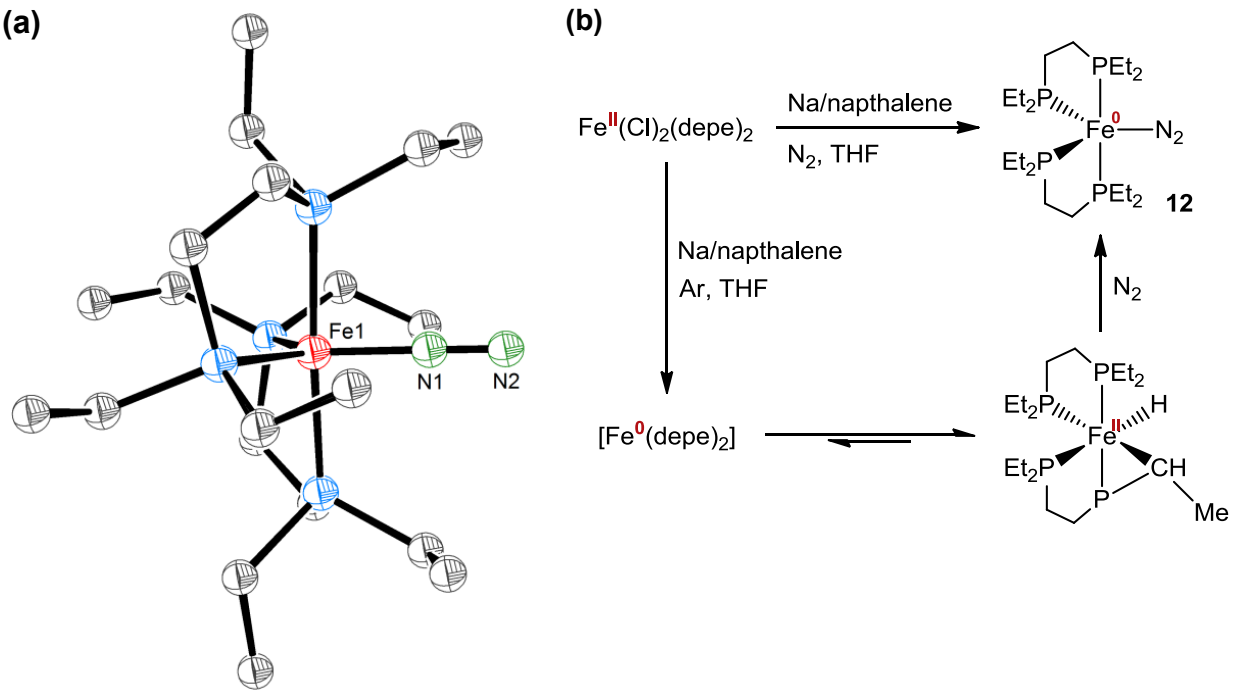


Figure 3.90 (a) Solid-state structure of $Fe(N_2)(depe)_2$ (**12**) taken from ref. 57; H atoms omitted for clarity, C atoms grey, Fe atom red, N atoms green, P atoms blue; ellipsoids shown at 50% probability; selected bond lengths (Å) and bond angles (deg): Fe1–N1 1.753(5), N1–N2 1.142(7), $[Fe1–P_{eq}]_{av}$ 2.187(2), $[Fe1–P_{ax}]_{av}$ 2.210(2); Fe1–N1–N2 179.1(6); (b) Synthesis of $Fe(N_2)(depe)_2$, reported by Komiya *et al.*.[12]

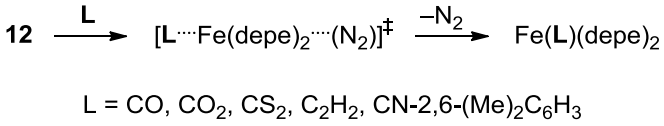


Figure 3.91 Ligand substituition reactions of **12** with various 2-electron donor ligands, reported by Jones *et al.*.[57]

In following the method of Komiya *et al.* to prepare **12**, separation issues were encountered due to the similar solubilities of **12** and the naphthalene by-product. Hence, activated Mg powder in THF solvent was substituted as the reductant, using 1,4-dioxane to precipitate $MgCl_2$ by-product (Figure 3.92). Thus **12** could be conveniently isolated in 80-90% yield following filtration and recrystallisation with pentane. In contrast to **4**, removal of N_2 from solutions of **12** *via* freeze-pump-thaw degassing showed no evidence of dimerisation by ^{31}P NMR, although trace amounts (< 2%) of free depe were often observed indicating some degree of dissociation, which would appear to be reversible since solutions are almost indefinitely stable at RT. Although still extremely air and moisture sensitive, the increased stability of **12** relative to **4** and **6** has enabled more convenient manipulation of this important complex.

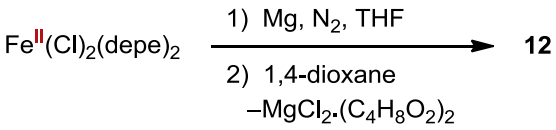


Figure 3.92 Alternative synthesis of **12** using activated Mg reductant; subsequent addition of 1,4-dioxane enables facile separation of $MgCl_2$ by-product as the THF insoluble 1,4-dioxane adduct.

3.2.3 Diamagnetic-paramagnetic transition in the Leigh deprotonation step

In parallel with the previous investigation of the dmpe system, NMR studies of the deprotonation reaction of [*trans*-Fe(H)(N_2)(depe)$_2$][BPh_4] revealed a similar decrease in the overall ^{31}P NMR intensity, in addition to the appearance of a broad resonance at –2.22 ppm in the ^{1}H NMR spectrum (Figure 3.93). The formation of a paramagnetic Fe species was confirmed by the presence of a pseudo axial Fe(I) signal in the X-band CW-EPR spectrum obtained for this mixture (Figure 3.94(a)). Thus, it appeared that a similar diamagnetic to paramagnetic transition was also occurring for the depe system and hence the influence of K^+ salts on **12** was investigated.

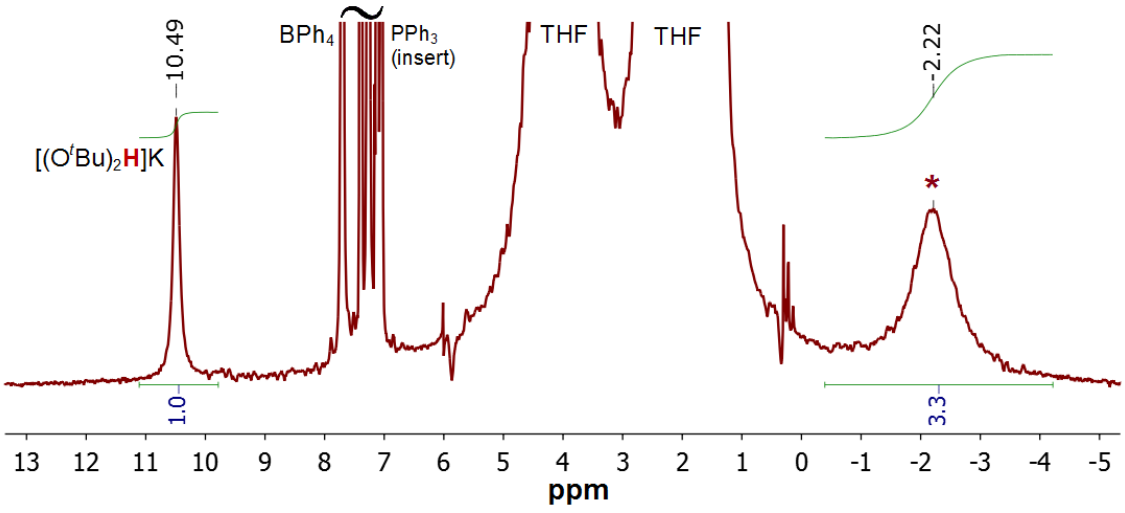


Figure 3.93 ^{1}H NMR spectrum of the deprotonation of [*trans*-Fe(H)(N_2)(depe)$_2$][BPh_4] with KO^{t}Bu (1:2, THF, N_2); resonances for **12** , [(^{t}BuO)$_2$H]K, and the THF solvent overlap; *marks broad paramagnetic resonance.

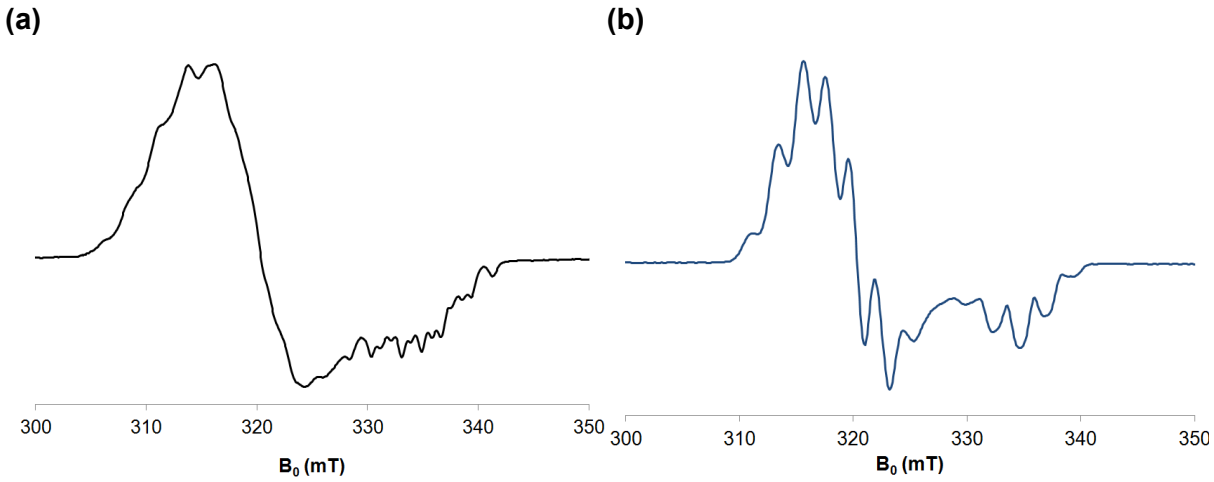


Figure 3.94 X-band CW EPR spectra of (a) the deprotonation of [*trans*-Fe(H)(N_2)(depe)$_2$][BPh_4] with KO^{t}Bu (1:2, THF, N_2); (b) **12** with $KBArF_{24}$ (1:2, TBME, N_2); recorded as glasses at 40 K.

The addition of two equivalents of $KBArF_{24}$ to an orange Et_2O solution of **12** under N_2 results in a slight darkening of the solution and a dramatic shift and broadening of the ^{31}P NMR resonance of **12** (Figure 3.95), whilst degassing this solution or performing the reaction under an Ar atmosphere results in a green solution, which is ^{31}P NMR silent. The formation of Fe(I) species was confirmed by X-band CW-EPR spectroscopy, which revealed an axial signal (Figure 3.94(b)) distinct from that observed previously for the Leigh deprotonation reaction. Under an Ar atmosphere, slow diffusion of pentane into this mixture yielded deep blue crystals, which were suitable for X-ray diffraction measurements; these solved as a tetrahedrally distorted square planar Fe(I) complex [Fe(depe)$_2$][$BArF_{24}$] (**13**, Figure 3.96).

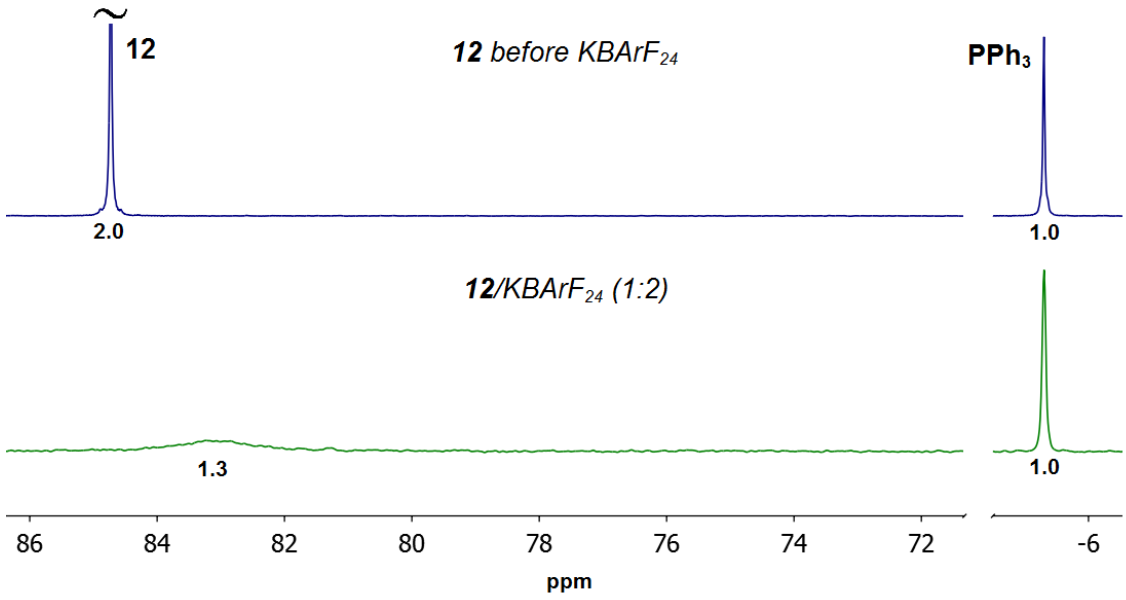
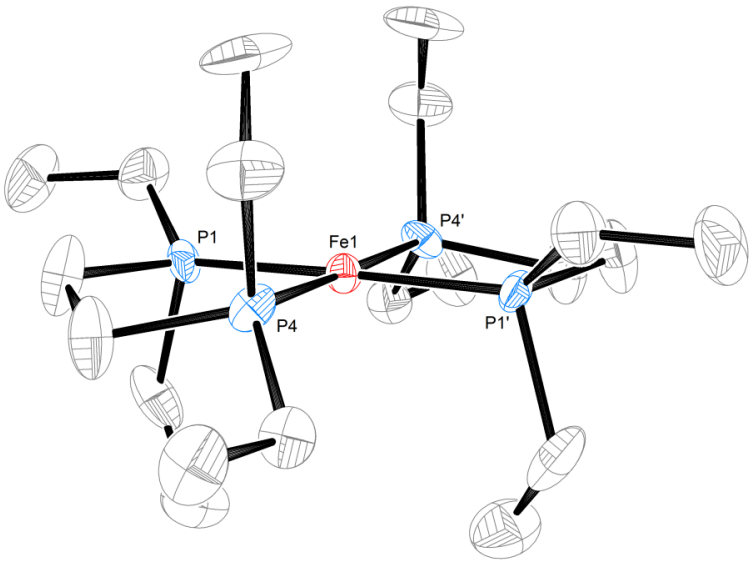
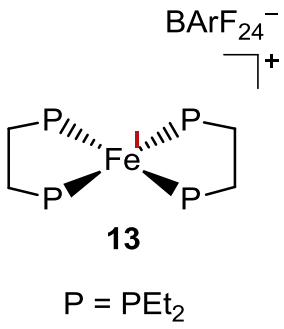


Figure 3.95 ^{31}P NMR spectra of the reaction of **12** with $KBArF_{24}$ (1:2, Et_2O, N_2).

Thus, similar to the dmpe system, addition of K^+ ions would appear to trigger a one electron oxidation of the Fe(0) precursor, which for the depe system results in a monomeric Fe(I) species and dissociation of N_2; likewise, a concomitant reduction process is also expected to have occurred, which will be discussed in section 3.2.6.





13

P = PEt_2

θ_{bite} (P1-Fe-P4) = 87.1(5)°

$\theta_{dihedral}$ (P_2Fe/P'_2Fe) = 12.4(6)°

d(Fe1–P1) = 2.203(10) Å

d(Fe1–P4) = 2.237(8) Å

Figure 3.96 Solid-state structure of $[Fe(depe)_2][BArF_{24}]$ (**13**); $BArF_{24}^-$ counteranion and H atoms omitted for clarity, C atoms grey, Fe atom red, P atoms blue; ellipsoids shown at 30% probability and C and P occupancies are 0.5 as a consequence of a second symmetry generated orientation of the two depe ligands, which has been omitted for clarity.

3.2.4 Isolating Fe(I) species

13 was independently synthesised *via* addition of $[Cp_2Fe][BArF_{24}]$ to a Et_2O solution of **12** (1:1); Cp_2Fe by-product was removed by washing with pentane, and the crude product was recrystallised from Et_2O/pentane (Figure 3.97). X-ray diffraction measurements on single crystals of **13** thus prepared gave an identical unit cell to that of the solved structure.

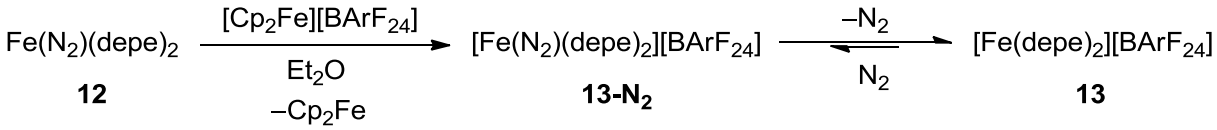


Figure 3.97 Synthesis of $[Fe(depe)_2][BArF_{24}]$ (**13**) via oxidation of $Fe(N_2)(depe)_2$.

Subsequent characterisation of **13** was performed on crystalline samples which provided combustion analysis consistent with this formulation. **13** is poorly soluble in hydrocarbon and ethereal solvents but dissolves well in the very polar, non-coordinating solvent 1,2-DFB (ε_r = 13.8 at 28 °C). Solutions under Ar are an intense blue colour, arising from electronic transitions at ~378 nm, ~414 nm, 496 nm, and 618 nm (Figure 3.98; Table 3.5).

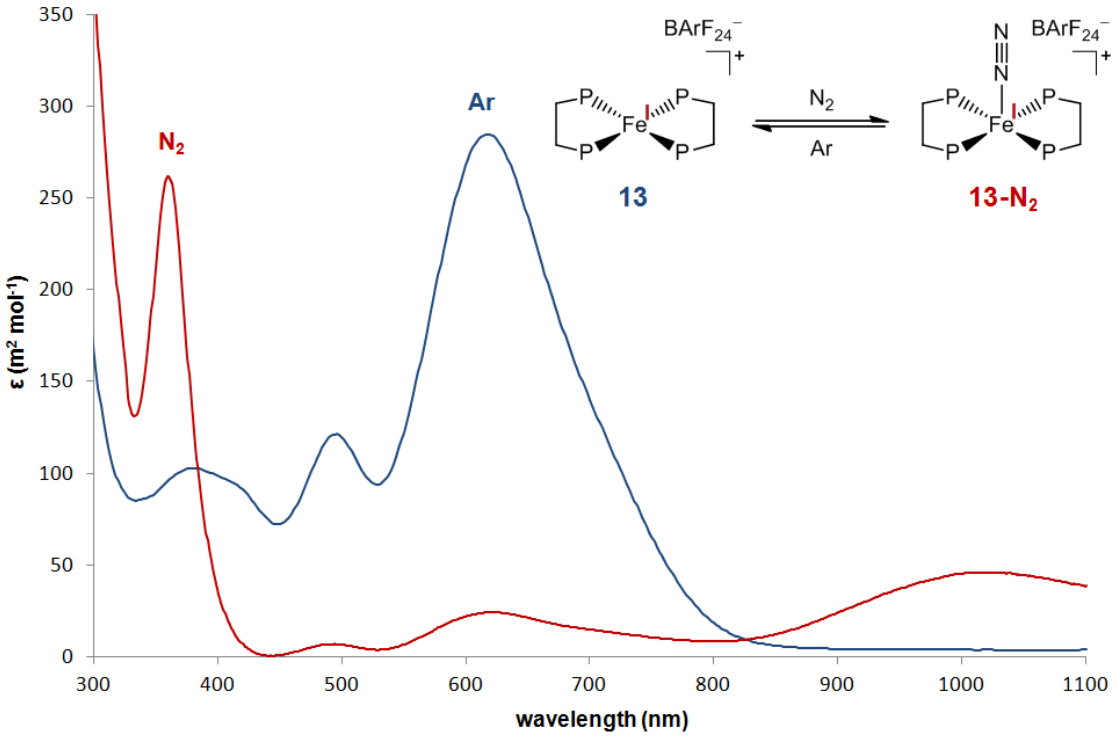


Figure 3.98 UV-vis spectra of 1,2-DFB solutions of **13** under Ar (blue), and N_2 (red) atmospheres (1 bar); recorded at 298 K; P = PEt_2.

Conversely, solutions under a N_2 atmosphere appear less intensely blue at RT and undergo a colour change to a pale yellow upon cooling (–15 °C) attendant with the appearance of two new absorptions in the UV-vis spectra at 359 nm and 1018 nm (Figure 3.98; Table 3.5). The latter may be an IVCT band, although no evidence for dimerisation has been observed by EPR spectroscopy (*vide infra*); herein, this species is proposed to be $[Fe(N_2)(depe)_2][BArF_{24}]$ (**13-N_2**). The blue solution is regenerated upon warming above RT or applying a partial vacuum, indicating reversible coordination of N_2. This is corroborated by an IR active *ν*(N-N) stretch at 2067 cm^{-1} (Et_2O, N_2), which is intermediate between **12** and $[Fe(H)(N_2)(depe)_2][BArF_{24}]$, formally Fe(0) and Fe(II), respectively (Figure 3.99). The reversible binding of both N_2 and H_2 to **13** will be discussed further in Chapter 4.

Table 3.5 Electronic absorption (UV-vis) features of **13** and **13-N_2**, and related Fe(I) complexes reported by Tyler *et al.*.[20]

Complex	λ_{max} (nm)	ε_{max} (m^2 mol^{-1})
$[Fe(depe)_2][BArF_{24}]$ (**13**)	378[a]	~103
	414[a]	~94
	496	121
	618	285
$[Fe(N_2)(depe)_2][BArF_{24}]$ (**13-N_2**)	359	316
	1018	55
$[\{Fe(DMeOPrPE)_2\}_2(\mu\text{-}N_2)][BPh_4]_2$	350[b]	c
	480	c
	580	c
$[Fe(N_2)(DMeOPrPE)_2][BPh_4]$	354[b]	c
	1010	c

[a] these bands overlap; [b] extracted visually from ref. 20; [c] not reported; DMeOPrPE = $[MeOCH_2CH_2CH_2)_2PCH_2]_2$.

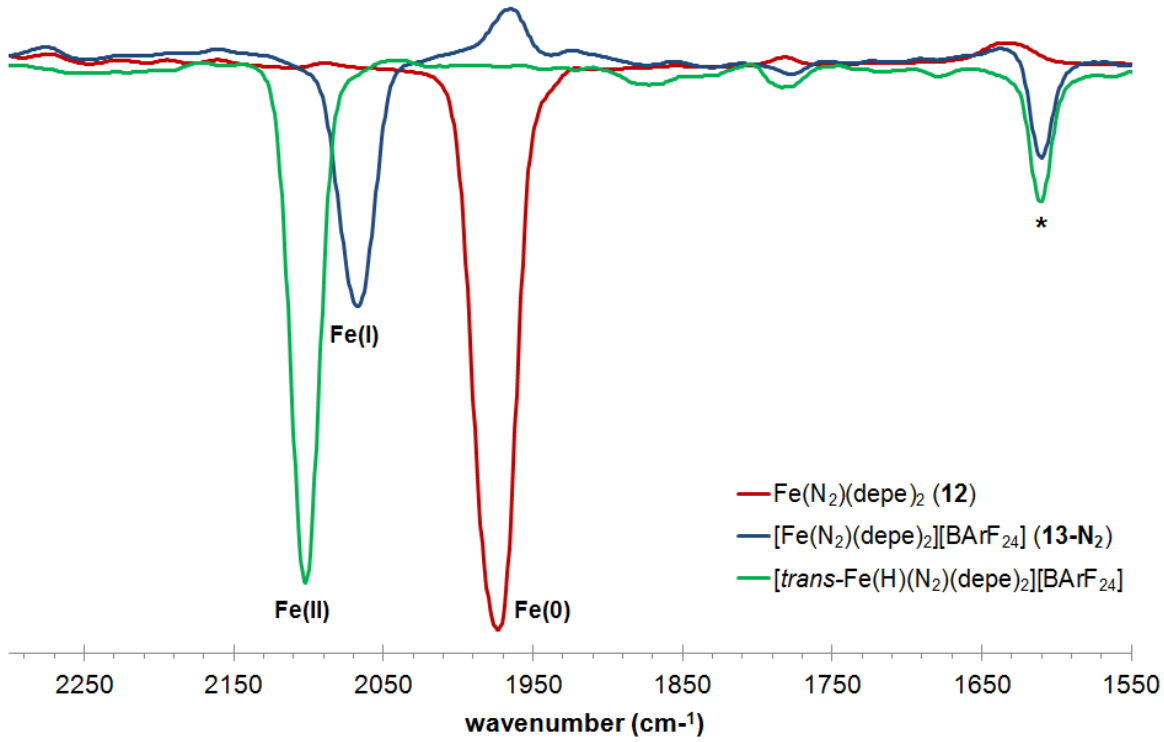


Figure 3.99 N_2 stretching region of the solution IR spectra (Et_2O, N_2) for $Fe(N_2)(depe)_2$ (**12**, red), **13-N_2** (blue), and $[Fe(H)(N_2)(depe)_2][BArF_{24}]$ (green); *signal due to $BArF_{24}^-$ counteranion.

Tyler *et al.* have reported a related Fe(I) dimeric complex $[\{Fe(DMeOPrPE)_2\}_2(\mu\text{-}N_2)][BPh_4]_2$, which they propose to undergo dissociation under an N_2 atmosphere to form $[Fe(N_2)(DMeOPrPE)_2][BPh_4]$ (Figure 3.100).[20] The latter monomeric complex exhibits a

comparable *v*(N-N) stretch (2054 cm^{-1}) to **13-N_2**, along with a similar UV-vis absorption feature at 1010 nm (see Table 3.5). However, under an Ar atmosphere, bands at 480 and 580 nm, which resemble those of monomeric **13**, were assigned to the dimeric species $[\{Fe(DMeOPrPE)_2\}_2(\mu\text{-}N_2)][BPh_4]_2$. The authors were unable to obtain a crystal structure or a Raman *v*(N-N) stretch for this species, whereas **13** has been crystallographically characterised and its assignment as a monomer verified by pulsed EPR experiments, *inter alia* (see Chapter 4). The propensity for complexes of dmpe to dimerise *via* a bridging N_2 ligand (e.g. **6**, **7**, **8**) is contrasted markedly by the lack of evidence to support similar dimerisation processes for related complexes of depe. It therefore seems possible that the dimeric complex reported by Tyler *et al.*, which incorporates substantially bulkier substituents on the P donor groups, is actually the monomeric species $[Fe(DMeOPrPE)_2][BPh_4]$; this may similarly be expected to exist in equilibrium with $[Fe(N_2)(DMeOPrPE)_2][BPh_4]$ as per **13**/**13-N_2** under N_2 atmosphere.

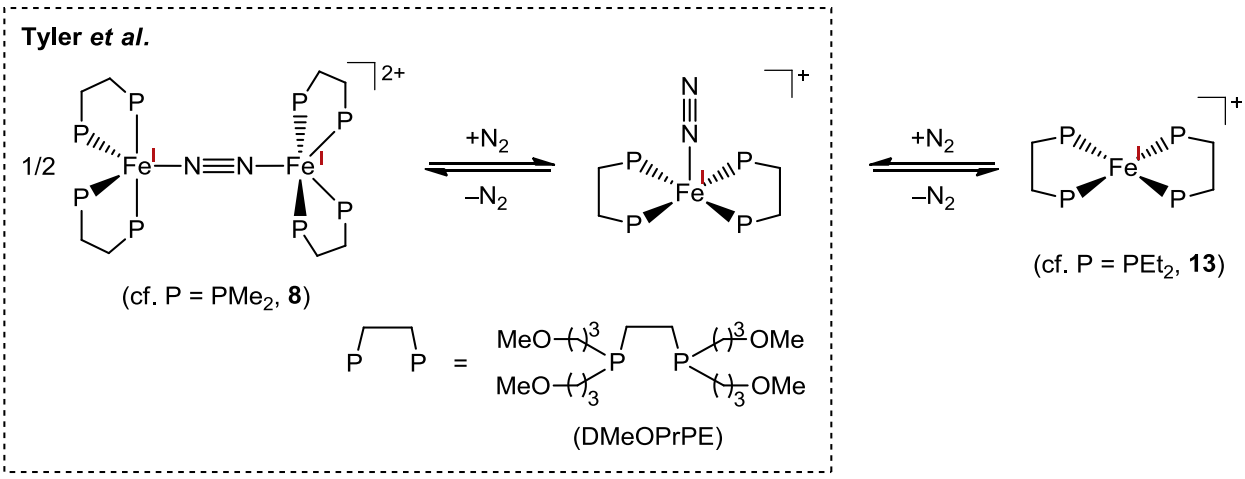


Figure 3.100 Related Fe(I) complexes reported by Tyler *et al.*.[20]

X-band CW-EPR spectroscopy performed on a 1,2-DFB glass of **13** under an Ar atmosphere resolved a rhombic signal with an average g-value of 1.94 (simulated spectra are presented in Chapter 4; simulated g = [1.98996, 2.2352, 2.47676]; $g_{av} = \{(g_x^2 + g_y^2 + g_z^2)/3\}^{½}$) consistent with a LS Fe(I) (S = ½) metal-based radical (Figure 3.101). Under a N_2 atmosphere, a pseudo axial signal was observed (g_{av} = 2.07; simulated g = [2.0014, 2.0922, 2.125]), in which the hyperfine coupling to the four ^{31}P nuclei could be resolved by measuring the sample as a THF glass (Figure 3.102). The absence of a half-field triplet dimer signal indicates that **13** remains monomeric upon coordination of N_2 to form **13-N_2**.

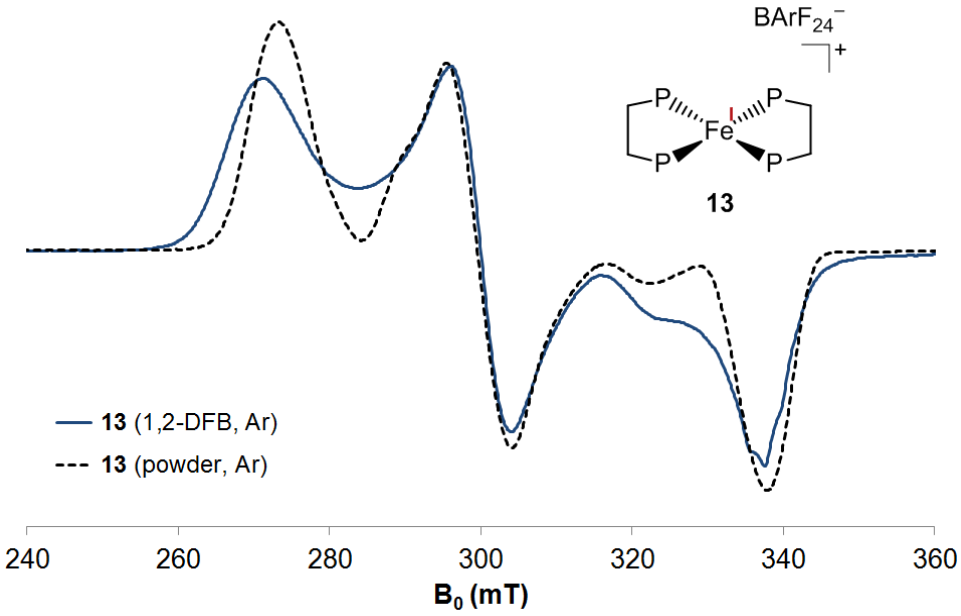


Figure 3.101 X-band CW EPR spectra of **13** recorded under Ar as a 1,2-DFB glass and as a powder at 40 K; P = PEt_2.

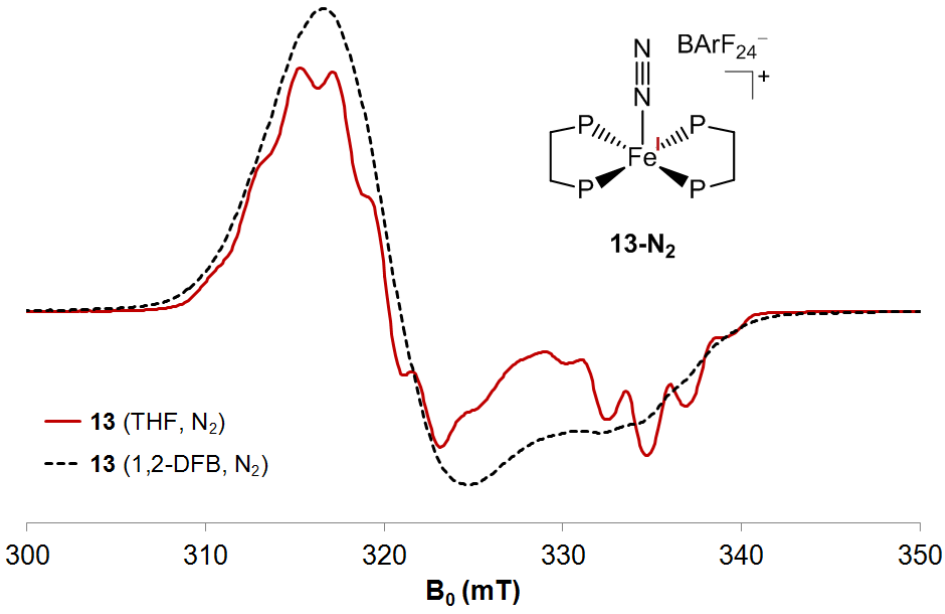


Figure 3.102 X-band CW EPR spectra of **13** under N_2 in THF (red) and 1,2-DFB (dashed black); recorded as glasses at 40 K; P = PEt_2.

1,2-DFB solutions of **13** are ^{31}P NMR silent; whilst the ^{1}H NMR spectrum of concentrated solutions under Ar exhibit three broad resonances (δ = {–0.54, –1.77, overlapped} and –21.30 ppm; Figure 3.103(top)) and a single resonance under N_2 (δ = –0.94; Figure 3.103(bottom)).

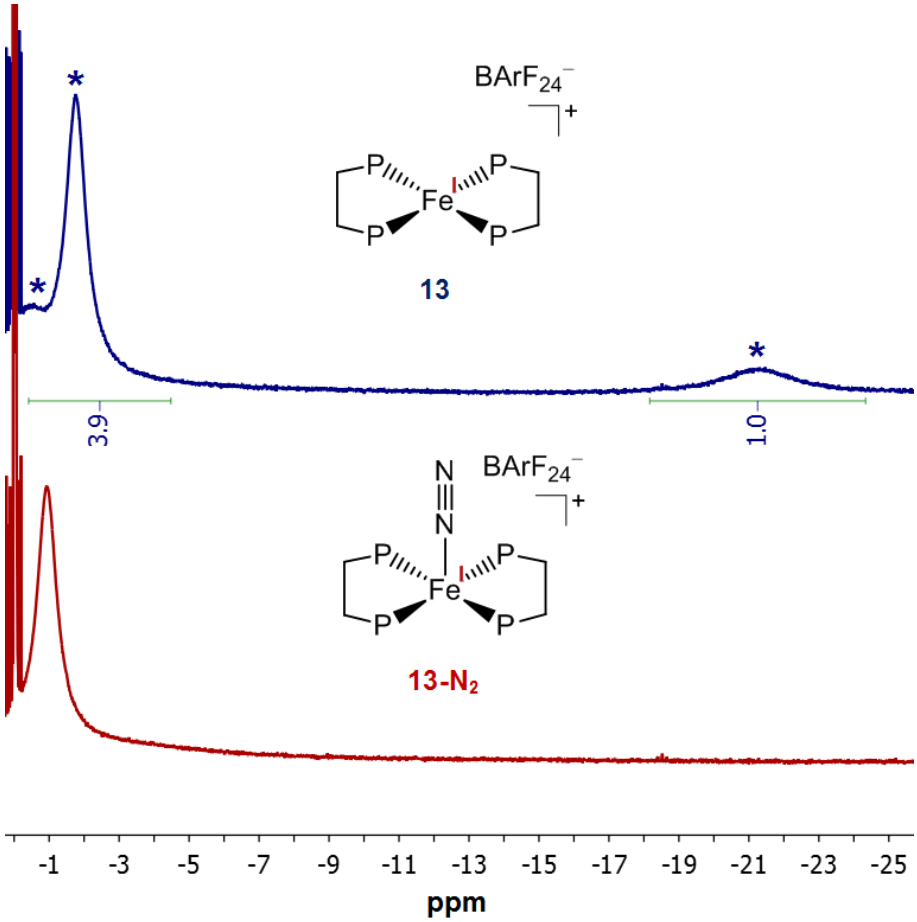


Figure 3.103 High field region of the ^{1}H NMR spectra of 1,2-DFB solutions of **13** under Ar (1 bar, top), and N_2 (4 bar, bottom) atmospheres, referenced to $SiMe_4$ (δ = 0) in the capillary insert; P = PEt_2.

Using the Evans NMR method,[32] a 1,2-DFB solution magnetic moment of **13** was calculated to be 1.95 μ_B (298 K). This value is higher than the spin-only value of 1.73 μ_B for an S = ½ spin state ($\mu_{so} = g_e\{S(S+1)\}^{½}$) due to an additional orbital contribution to μ_{eff}. This may arise if the d_{xz} or d_{yz} orbital is partially occupied (an E ground state); the relative orbital energies are currently under investigation by DFT. If this is the case, the total spin plus orbital contribution to μ_{eff} can be estimated using the following formula:[58]

$$\mu_{eff} = \mu_{so}\left[1-\left(\frac{\alpha\lambda}{\Delta}\right)\right]$$

α is a constant (α = 2 for an E state)

λ=+/–(ξ/2S) is positive for d^1-d^4 and negative for d^6–d^9

ξ is the spin orbit coupling constant for an Fe(I) ion (ξ = 345 cm^{-1})

S is the total spin value (S = ½)

Δ is the crystal-field splitting parameter in cm^{-1}

Extracting a value of Δ = 618 nm (16181 cm^{-1}) from the lowest d-d transition measured by UV-vis spectroscopy predicts a μ_{eff} of 1.81 μ_B; this may indicate an additional higher spin-state contribution to μ_{eff}.

The temperature dependence of the solid-state magnetic susceptibility of **13** was studied by SQUID magnetrometry; diamagnetic corrections from Pascal's constants were applied.[31] Curie-Weiss paramagnetism is demonstrated approximately within the range 30-300 K by a near linear relationship between the inverse molar susceptibility (χ_m^{-1}) and temperature (C = 1.40 emu K mol^{-1}; θ = –13.93 K; Figure 3.105)), whilst the drop in paramagnetism at very low temperature is typical and due to intermolecular exchange phenomena.[59] The gradual increase in μ_{eff} of 2.11-2.35 μ_B between the temperature range 30-300 K is likely due to increasing population of higher spin states, giving rise to an unquenched orbital contribution as well as an increased spin paramagnetic contribution. Variable field measurements were also carried out up to 50000 Oe at 5, 140 and 300K; an absence of any hysteresis in the isothermal plots of field versus χ_m^{-1} preclude the presence of ferromagnetic impurities in the sample.

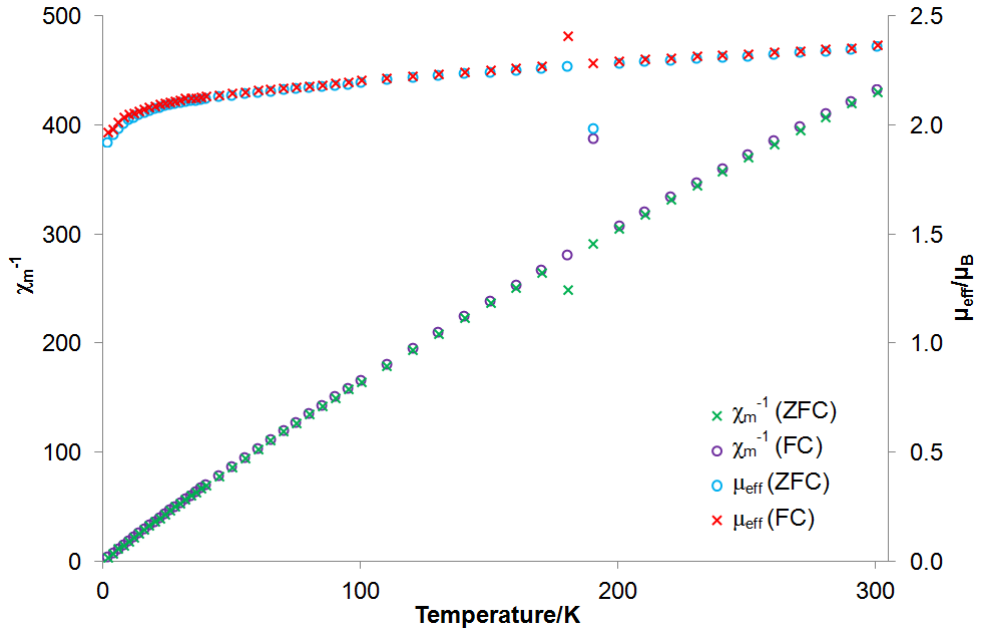


Figure 3.105 SQUID measured temperature dependence of μ_{eff} and χ_m^{-1} for **13**; zero-field cooled (ZFC) and field cooled (FC) measurements were recorded with an applied field of 1000 Oe.

Mössbauer spectroscopy has been performed on a powdered sample of **13** which provided consistent combustion analysis; the measurement was carried out at RT and zero-field over the course of 314 hours. The resultant absorption spectrum has been simulated as a Lorentzian doublet (92.2%) and a Lorentzian singlet (7.8%) with isomer shifts (δ, relative to α-Fe) and quadrupole splitting (E_Q) listed in Figure 3.106. The electronic configuration and

electron charge density of the ^{57}Fe nuclei measured has a pronounced effect on δ and E_Q and is a powerful tool for assessing oxidation states of Fe in a sample.[60] The δ of the doublet is within the range of known Fe(I) compounds, whereas the extremely low δ of the minor singlet component is representative of the much higher oxidation state of Fe(VI). However, given the unlikely event that a contaminant would be oxidised to this degree, it is perhaps more likely that the quadrupole doublet exhibits asymmetry, which is known to result from the presence of low lying higher spin states.[61] To explore this possibility it would be necessary to perform low-temperature and field-dependent measurements; access to this equipment is extremely limited.

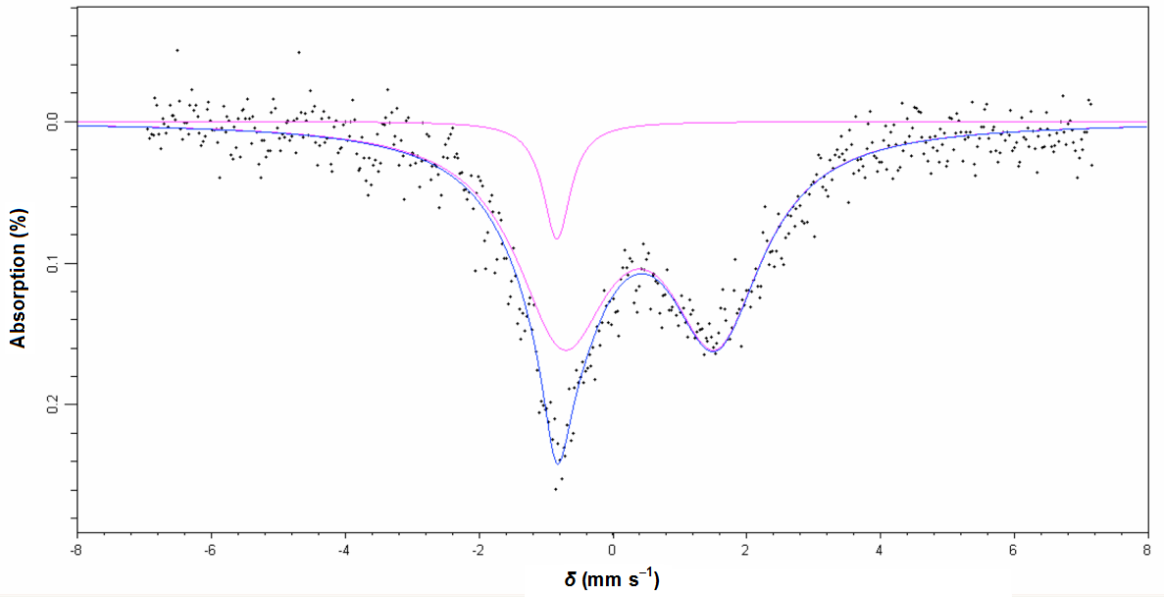


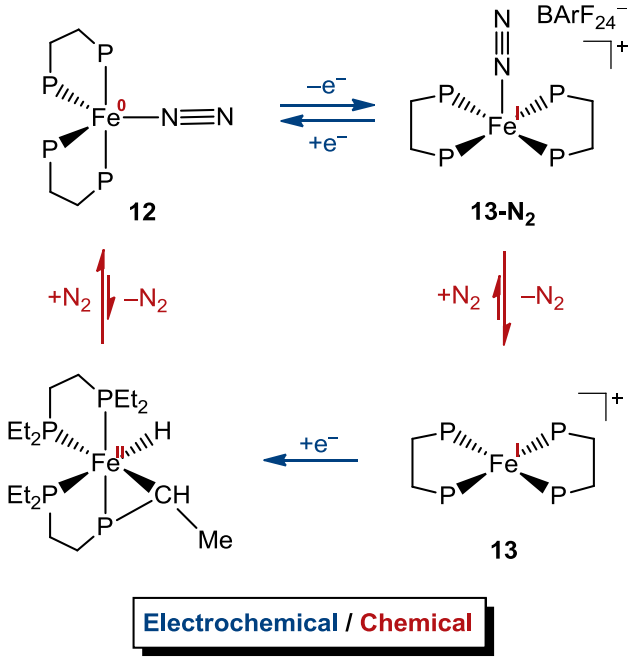
Figure 3.106 Mössbauer spectra of **13** recorded over 314 h. Simulated values: Lorentzian doublet, δ = +0.4 mm s^{-1}, E_Q = 2.25 mm s^{-1}, HWHM = 0.86 mm s^{-1}, 92.2%; Lorentzian singlet, δ = –0.84 mm s^{-1}, HWHM = 0.25 mm s^{-1}, 7.8%.

3.2.5 Electrochemistry of Fe(0) and Fe(I) species

Cyclic voltammetry (CV) measurements performed on **12** and **13** in Et_2O solutions with [^{n}Bu$_4$N][BArF$_{24}$] electrolyte show a dependence on the availability of N_2, as outlined in Figure 3.107(a). A reversible electrochemical process centred at –2.0 V was observed at all scan rates for solutions of **12** (oxidative sweep under N_2 or Ar) and **13** (reductive sweep under N_2), which can be assigned to the redox interconversion of **12** and **13** (Figure 3.107(b)-3.108(a)). In contrast, the CV plot of **13** under Ar (Figure 3.108(b)) shows an irreversible reduction since in the absence of N_2 the coordinatively unsaturated Fe(0) complex [Fe(depe)$_2$] is known to undergo cyclometalation *via* oxidative addition of a methylene C–H

bond on one of the depe ligands (*vide supra*).[9] A second reversible wave is observed for **13** (under N_2) centred at –0.6 V and likely corresponds to the Fe(I)/Fe(II) redox couple (Figure 3.109). Sweeping reductively from –0.6 V reveals the corresponding reduction on the second scan only, consistent with prior electrochemical oxidation of **13**. This Fe(I)/Fe(II) redox couple is also observed for **12** under either N_2 or Ar.

(a)



(b)

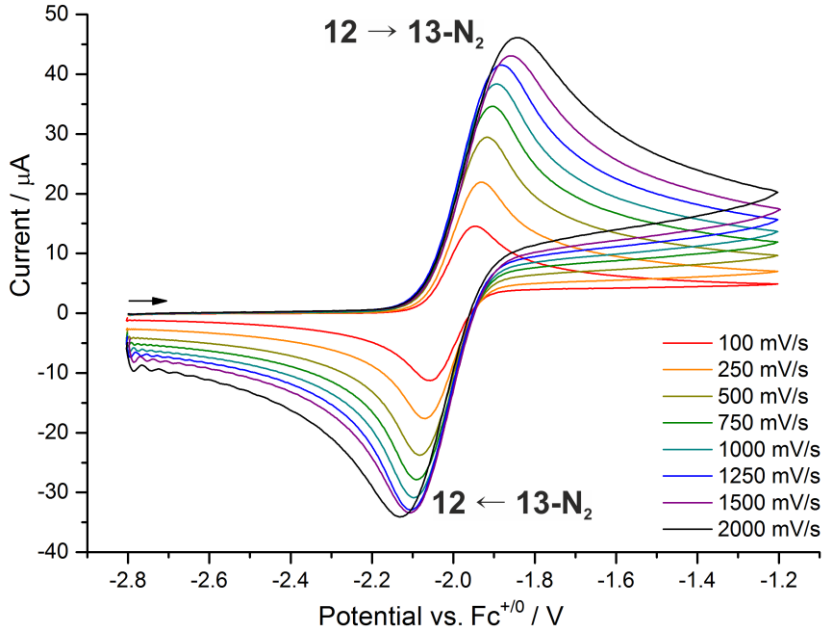


Figure 3.107 (a) Chemical and electrochemical transformations of **12**, **13**, **13-N_2**, and [Fe(depe)$_2$]; P = PEt_2; (b) Cyclic voltammogram of **12** (Et_2O, N_2, [^{n}Bu$_4$N][BArF$_{24}$] electrolyte); potential plotted relative to the Cp_2Fe/Cp_2Fe^+ couple; arrow indicates direction of scan.

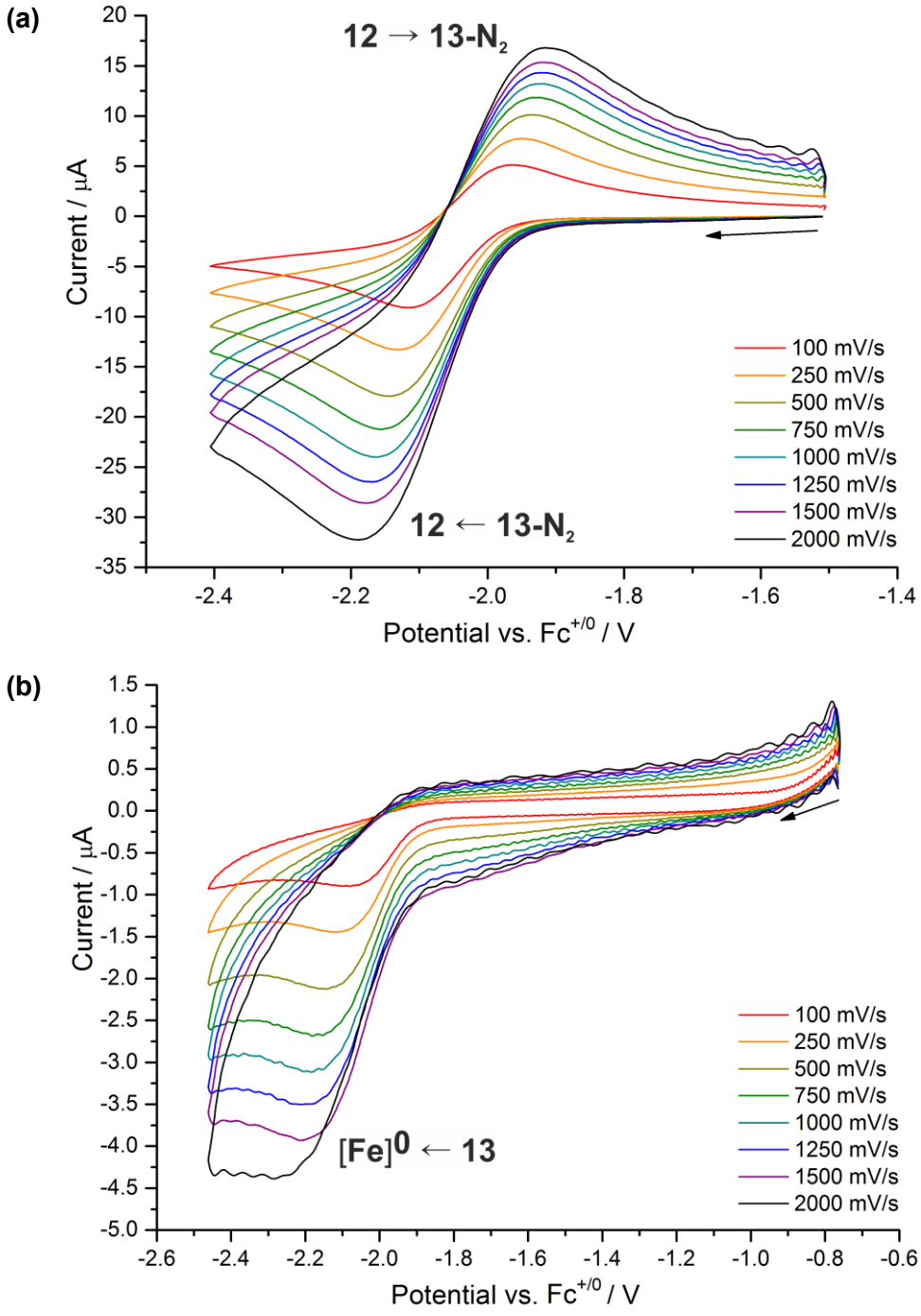


Figure 3.108 Cyclic voltammetry measurements of **13** in Et_2O with [^{n}Bu$_4$N][BArF$_{24}$] electrolyte; potential plotted relative to the Cp_2Fe/Cp_2Fe^+ couple; (a) **13** under N_2; (b) **13** under Ar; arrow indicates direction of scan.

Evidently, **12** is a powerful reductant, almost as strong as the related Fe(0) dmpe complex **6** (–2.2 V vs $Cp_2Fe^{+/0}$ in Et_2O); a direct comparison between **12** and **4** is obscured by the irreversibility of the [**4**]$^+$/**4** couple (ca. –1.9 V vs $Cp_2Fe^{+/0}$ in Et_2O), due to formation of **7**.

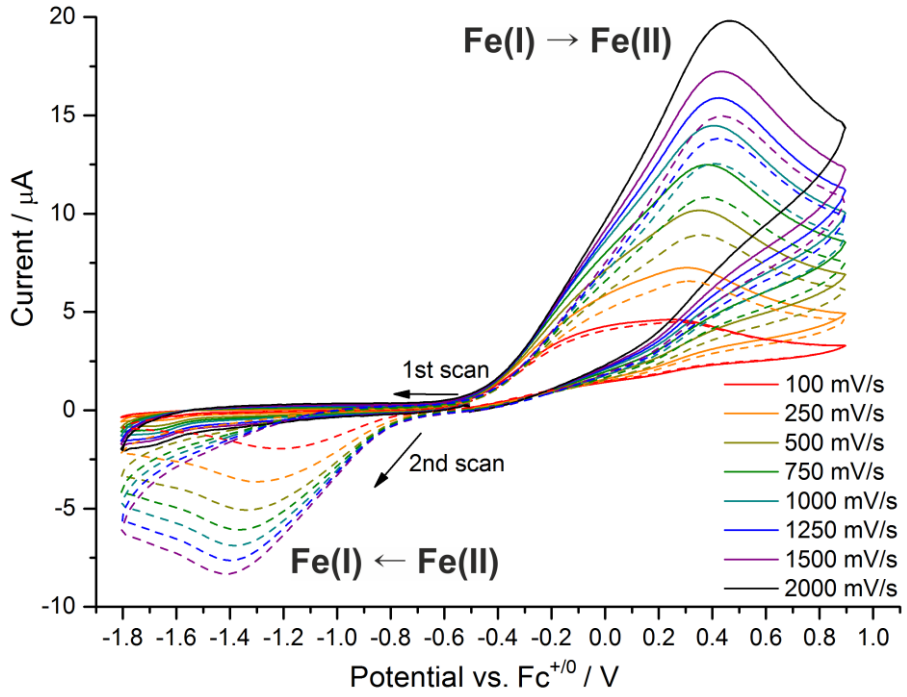


Figure 3.109 Cyclic voltammetry measurements of **13** (Et_2O, N_2, [$^nBu_4N$][$BArF_{24}$] electrolyte); potential plotted relative to the Cp_2Fe/Cp_2Fe^+ couple; arrow indicates direction of scan.

3.2.6 Cooperative activation of N_2 with Fe(0) and K^+ salts

The Fe(I) (S = ½) EPR signal generated from the addition of $KBArF_{24}$ to **12** is reproduced in the EPR spectra recorded for **13** under N_2 (Figure 3.111), and can therefore be assigned to the N_2 coordinated complex **13-N_2**. Thus, it appears that this reaction mimics the related oxidation chemistry of **4** and **6** in the presence of $KBArF_{24}$ (without additional dimerisation processes), and similarly a concomitant reduction process is expected (Figure 3.110).

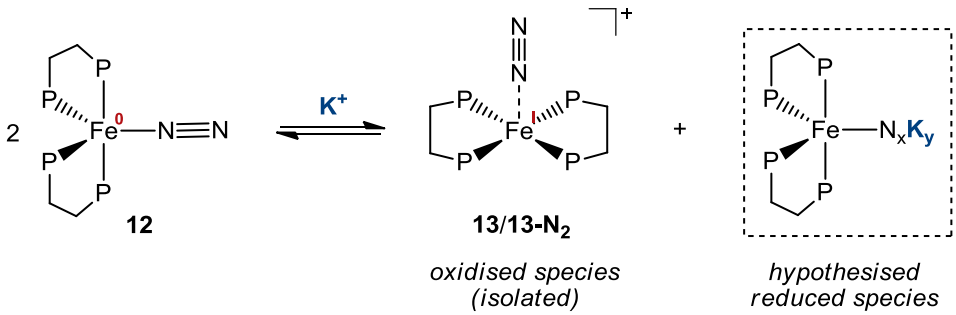


Figure 3.110 Hypothesised reactivity of **12** with $KBArF_{24}$ wherein K^+ ions facilitate concomitant oxidation and reduction of **12** *via* an electron transfer; P = PEt_2.

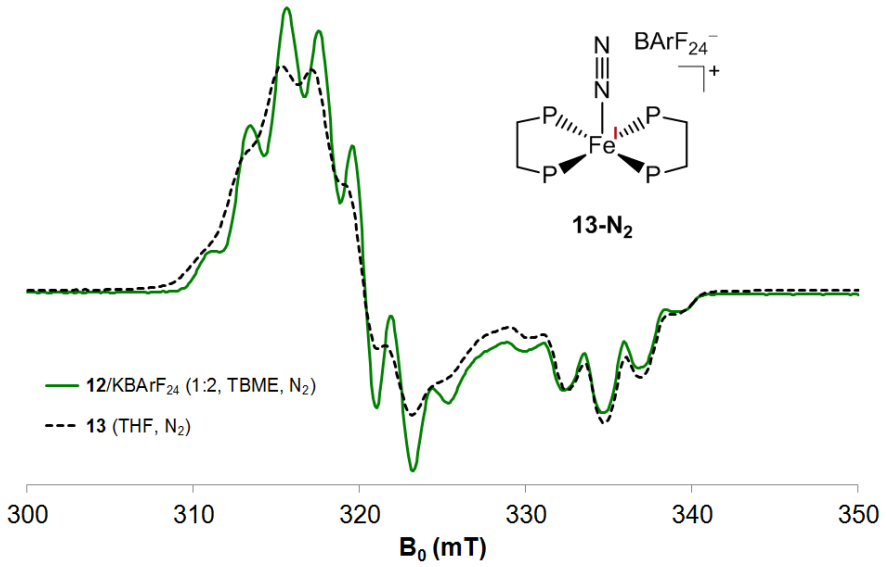


Figure 3.111 X-band CW EPR spectra of **12** with $KBArF_{24}$ (1:2, TBME, N_2, green) and **13** (THF, N_2, dashed black); recorded as glasses at 40 K; P = PEt_2.

Corroborating these EPR experiments, formation of **13** in the reaction of **12** with $KBArF_{24}$ was confirmed by the characteristic band at 618 nm in the UV-vis spectrum, albeit in low concentration (ca. 10%, Figure 3.112); the extreme dilution required for UV-vis may inhibit the effect of $KBArF_{24}$ by reducing its concentration.

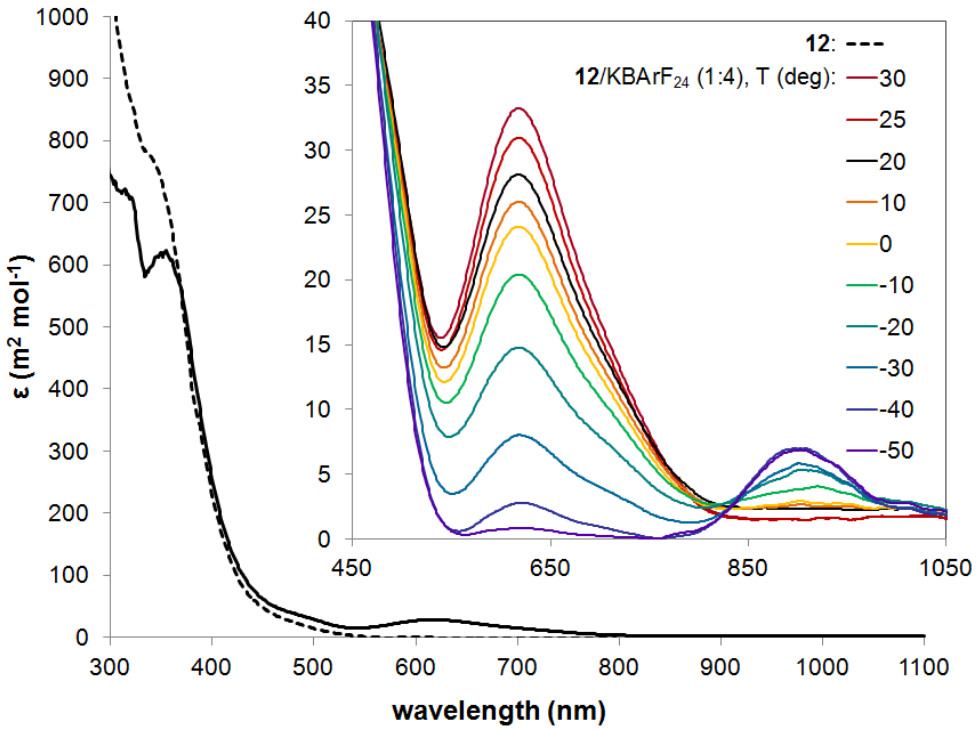
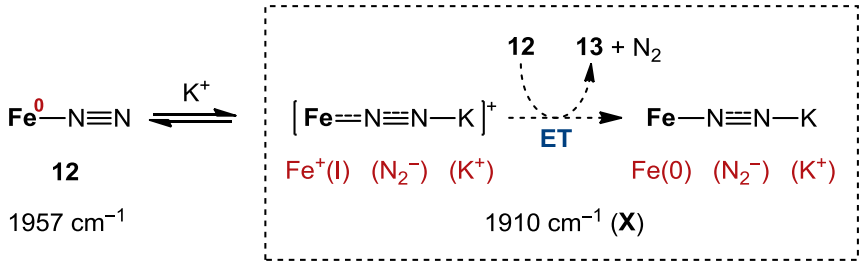


Figure 3.112 UV-vis spectra of **12** (RT, dashed black) and **12** with $KBArF_{24}$ (1:4, RT, solid black); inset: subsequent measurements between 30 and –50 °C; recorded in Et_2O under Ar.

Since N_2 is labile in **13-N_2**, the UV-vis experiment was performed under an Ar atmosphere to liberate N_2 and thereby shift the equilibrium in favour of the products by inhibiting reformation of **12**. However, VT experiments performed on **13** under N_2 indicate that the N_2 binding affinity of **13** is favoured at low temperature (see Chapter 4); thus the displacement of the band at 618 nm to 905 nm as the temperature is decreased (Figure 3.112 (inset)) likely corresponds to formation of **13-N_2**, which in isolation exhibits a broad band at 1018 nm. Unfortunately, since **12** remains the major Fe component of this mixture, the UV-vis spectrum is effectively masked below 450 nm; consequently, only the 618 nm band of **13** is discernible, whilst no other new absorption features could be resolved.

Solution IR spectroscopy was also performed on mixtures of **12** and $KBArF_{24}$ (1:2) in Et_2O (Figure 3.113).

(a)



(b)

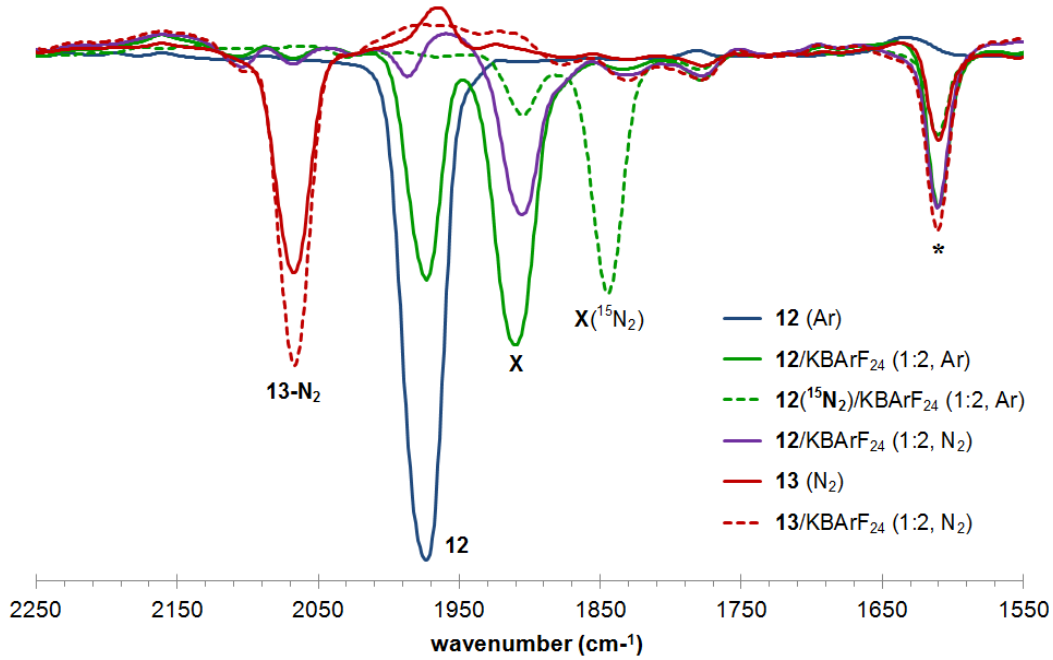


Figure 3.113 (a) proposed activation of N_2 from addition of K^+; Fe = [Fe(depe)$_2$]; ET = electron transfer; (b) N_2 stretching region of Et_2O solution IR spectra of Fe(N_2)(depe)$_2$ (**12**, Ar, blue); Fe($^{14}N_2$)(depe)$_2$/Fe($^{15}N_2$)(depe)$_2$ with $KBArF_{24}$ (1:2, under Ar, solid green/dashed green; and under N_2, purple); [Fe(N_2)(depe)$_2$][$BArF_{24}$] (**13-N_2**, N_2, solid red); and [Fe(N_2)(depe)$_2$][$BArF_{24}$] with $KBArF_{24}$ (1:2, N_2, dashed red); *signal due to $BArF_{24}^-$ counteranion.

Under both Ar and N_2 atmospheres, the *v*(N–N) stretch of **12** (1957 cm^{-1}) reduced in intensity or disappeared completely and a new stretch was observed 47 cm^{-1} lower (1910 cm^{-1}), which was confirmed to be a *v*(N–N) stretch through isotopic labelling with $^{15}N_2$. **13-N_2** (IR(Et_2O): 2067 cm^{-1}) is not clearly resolved in either case, which is suspected to be due to a combination of limiting concentration of N_2, weak N_2 binding affinity of **13**, and low concentration of **13**; $KBArF_{24}$ was independently confirmed not to influence the *v*(N–N) stretch of **13-N_2**. The *v*(N–N) stretch at 1910 cm^{-1} corresponds to a significantly activated N_2 ligand, which may arise from coordination of K^+ to the N_2 ligand in **12** (Figure 3.113(a)). The resultant cationic complex may subsequently be reduced by **12** to form the neutral species and **13**/N_2. Additional complexity is suggested by the reaction performed under N_2, for which the strong *v*(N–N) stretch of **12** is absent; since formation of Fe(I) in the reversible electron transfer may be driven by subsequent dissociation of N_2, an N_2 atmosphere is therefore expected to disfavour this reaction. Interestingly, the activation of Fe(0)-bound N_2 by a hypothetical cationic Fe(I) fragment in the Fe(0)/Fe(I) complex **7** (*vide supra*) may be viewed analogously to the proposed coordination of monomeric **12** by a K^+ ion, which is corroborated by the comparable *v*(N–N) stretch of **7** (IR(Et_2O): 1885 cm^{-1}).

Cyclic volatemmetry measurements performed on the reaction of **12** with 0.5 equivalents of $KBArF_{24}$ revealed the **13-N_2**/**12** couple centred at –2.0 V, along with an additional quasi-reversible wave also centred at –2.0 V (Figure 3.114). Increasing the amount of $KBArF_{24}$ resulted in poor resolution, as encountered for the dmpe system, preventing further analysis.

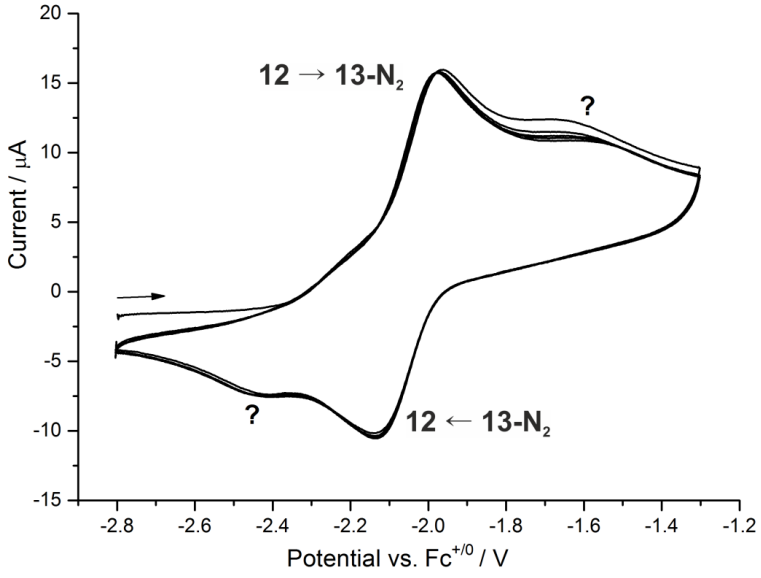


Figure 3.114 Cyclic voltammetry measurement of **12**/$KBArF_{24}$ (1:0.5) under Ar in Et_2O with [$^nBu_4$][$BArF_{24}$] electrolyte; potential plotted relative to the Cp_2Fe/Cp_2Fe^+ couple; arrow indicates direction of scan.

Spectroscopic distinction and isolation of this hypothesised additional component from the remaining mixture of **12**, **13** and $KBArF_{24}$, proved to be non-trivial, mirroring the situation for the dmpe system. Therefore, a similar approach was adopted wherein an Fe-ligated reduced nitrogen fragment would be targeted directly. Addition of K reducing agent to the **12**/$KBArF_{24}$ mixture was anticipated to regenerate **12** from **13**, whilst simultaneously providing additional K^+ ions to drive the reaction. However, K metal remained unreactive until the mixture was heated to 35 °C, wherein decomposition resulted in formation of the known ethylene complex $Fe(\eta^2\text{-}C_2H_4)(depe)_2$ (^{31}P NMR, δ = 83.9 and 73.5 ppm, Figure 3.115), presumably from activation of the Et_2O solvent.[62] This species was also formed at RT using the related K electron-carrier reductants, potassium naphthalenide (KNap) or K with substoichiometric di-*tert*-butylbiphenyl (DBB).

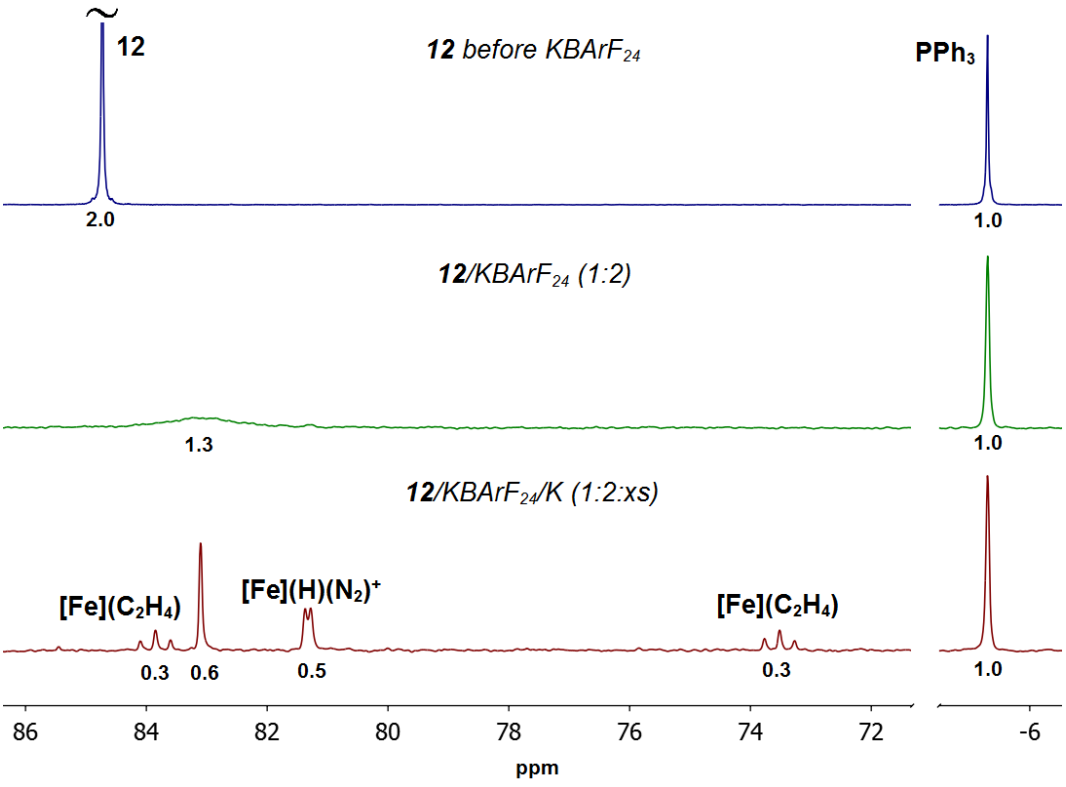


Figure 3.115 ^{31}P NMR spectra of the reaction of **12** with $KBArF_{24}$ (1:2, Et_2O, N_2) followed by subsequent addition of K with heating to 35 °C.

The Fe(II) hydrido azide complex *trans*-$Fe(H)(N_3)(depe)_2$ (**14**), which is the depe analogue of **9**, was also investigated as a possible precursor to a nitrido or amido complex through loss of N_2 (Figure 3.116). **14** was prepared from the Fe(II) hydrido dinitrogen complex by the same method as **9**; the crystal structure (Figure 3.117) and IR spectrum (Figure 3.67) of **14** closely resemble **9**, and given the now established reduction chemistry of the latter to form **10** and **11** with loss of azide rather than N_2, **14** can be expected to undergo similar

chemistry. Evidence for this was provided spectroscopically by the separate reactions of the Fe(II) hydrido complexes **14**, *trans*-Fe(H)(Cl)(depe)$_2$, and [*trans*-Fe(H)(N_2)(depe)$_2$][X] (X = BPh_4^- or $BArF_{24}^-$) with K or KC_8 reductant, which appear to all produce the same yellow Fe(I) product, irrespective of the anion (N_3^-, Cl^-, BPh_4^-, $BArF_{24}^-$).

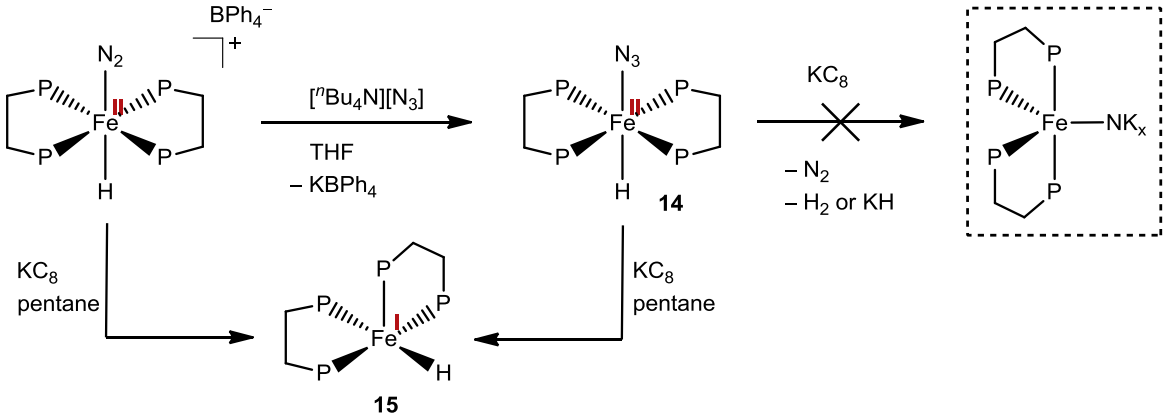
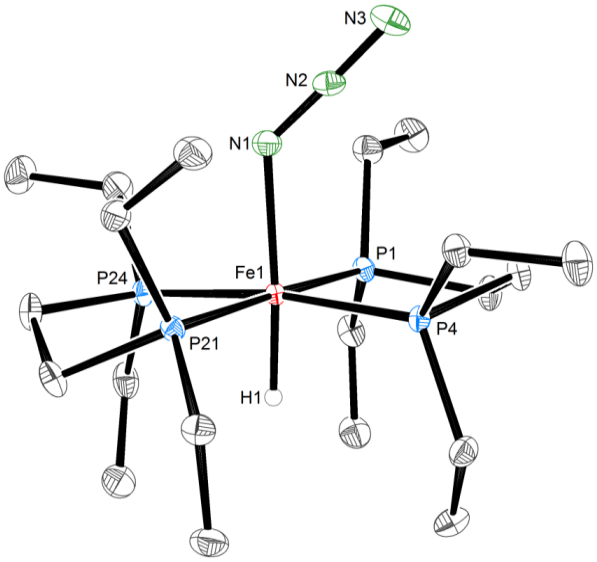


Figure 3.116 Attempted synthesis of a K-stabilised reduced N fragment *via* reduction of *trans*-Fe(H)(N_3)(depe)$_2$ (**14**), and the synthesis of Fe(H)(depe)$_2$ (**15**); P = PEt_2.



Bond lengths (Å):

Fe1–N1	2.0669(12)
N1–N2	1.1812(17)
N2–N3	1.1754(18)
Fe1–H1	1.47(3)
$[Fe1–P]_{av}$	2.2174(9)

Bond Angles (deg):

Fe1 N1 N2	131.07(10)
N1 N2 N3	178.12(16)

Figure 3.117 Solid-state structure of *trans*-Fe(H)(N_3)(depe)$_2$ (**14**); H1 atom white, all other H atoms omitted for clarity, C atoms grey, Fe atom red, N atoms green, P atoms blue; anisotropic displacement ellipsoids shown at 30% probability.

A comparison of the ^{1}H NMR spectra of the KC_8 reduction and Leigh deprotonation (KO^tBu) of [*trans*-Fe(H)(N_2)(depe)$_2$]$^+$ (Figure 3.118) strongly indicates generation of the same paramagnetic species in both cases. Gratifyingly, the corresponding X-band CW-EPR spectra (Figure 3.119) also revealed the same Fe(I) (S=½) signal as that observed for the Leigh deprotonation reaction, for which HYSCORE measurements indicated a strong hyperfine coupling interaction to a metal bound hydride (*vide supra*). A pentane solution magnetic moment was calculated by the Evans NMR method to be 1.64 μ_B (298 K), also

consistent with LS Fe(I) (S = ½). Therefore, it appears likely that this species is Fe(H)(depe)$_2$ (**15**), the depe analogue of the previously identified Fe(I) hydride, **10**, which exhibits a similar X-band CW-EPR spectrum (Figure 3.120).

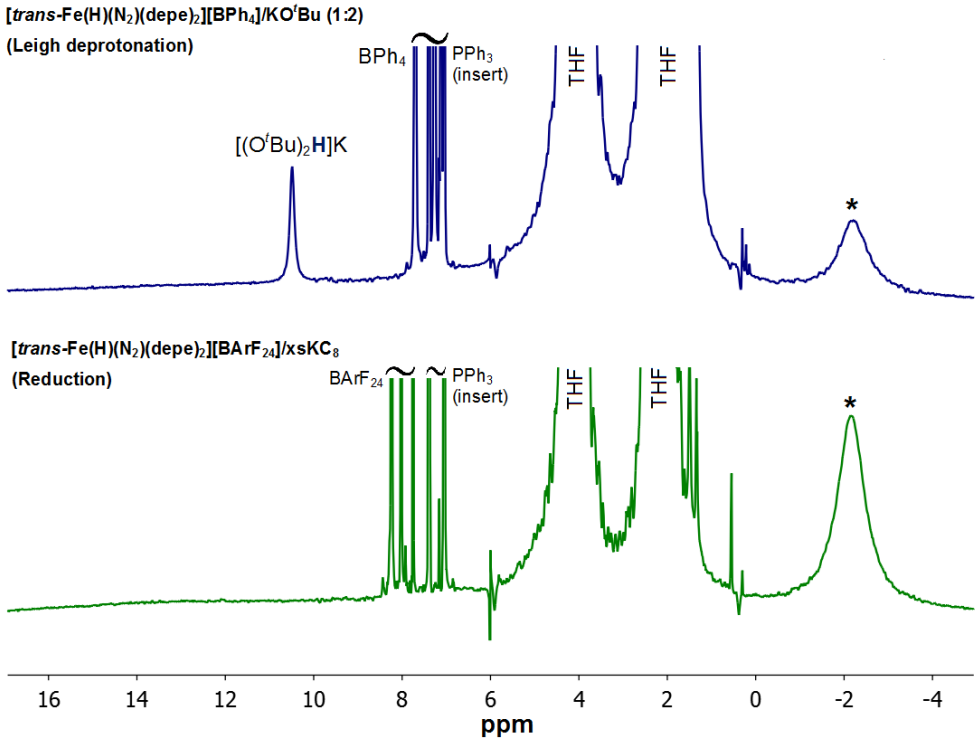


Figure 3.118 ^{1}H NMR spectrum of the deprotonation of [*trans*-Fe(H)(N$_2$)(depe)$_2$][BPh$_4$] with KO^{t}Bu (1:2, THF, N$_2$, top), and the reduction of [*trans*-Fe(H)(N$_2$)(depe)$_2$][BArF$_{24}$] with excess KC$_8$ (THF, N$_2$, bottom); *marks broad resonance corresponding to **15**.

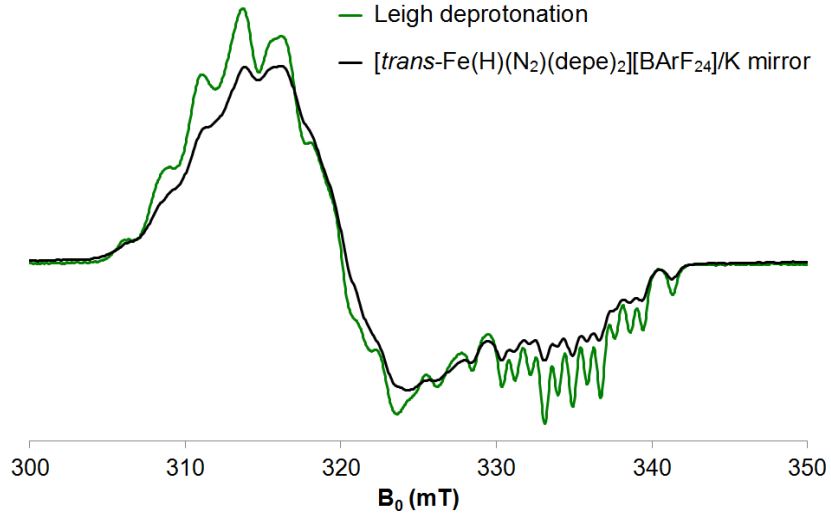


Figure 3.119 X-band CW-EPR spectra of the deprotonation of [*trans*-Fe(H)(N$_2$)(depe)$_2$][BPh$_4$] with KO^{t}Bu (1:2, THF, N$_2$, black); the K metal reduction of [*trans*-Fe(H)(N$_2$)(depe)$_2$][BArF$_{24}$] (THF, N$_2$); recorded as glasses at 40 K.

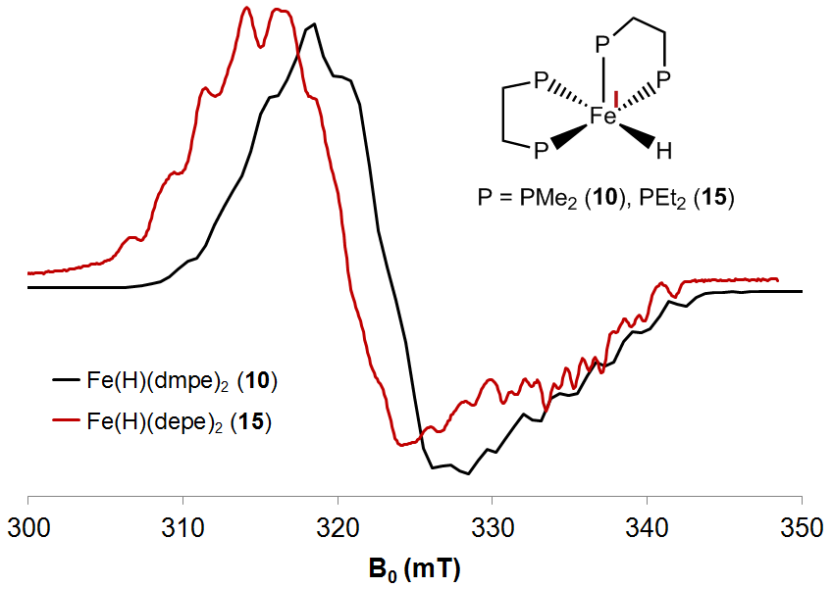


Figure 3.120 X-band CW-EPR spectra of isolated **15** (hexane, Ar, red) and **10** (hexane, Ar, black); recorded as glasses at 40 K.

Fortunately, this species can be prepared from *trans*-Fe(H)(Cl)(depe)$_2$ without forming Fe(II) hydride contaminant as was encountered for **10**. However, **15** is an oily solid and is extremely soluble in all common organic solvents; consequently it has not yet been possible to obtain a crystalline sample for X-ray diffraction measurements. No further reaction of **15** with excess KC_8 was observed in pentane solvent; however, substituting with Et_2O results in a deep red solution reminiscent of the Fe(–I) complex, **11**, with a corresponding UV-vis absorption spectrum that differs significantly from either **15** or *cis*-Fe(H)$_2$(depe)$_2$ (Figure 3.121).

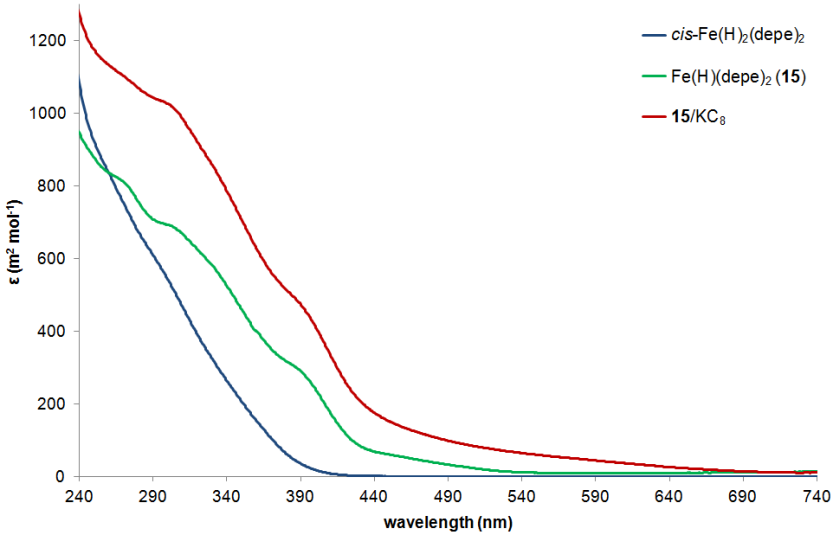


Figure 3.121 UV-vis spectra of *cis*-Fe(H)$_2$(depe)$_2$ (pentane, blue), Fe(H)(depe)$_2$ (**15**, pentane, green), and the reaction of **15** with xs KC_8 (Et_2O, red); recorded as 0.125 mM solutions under Ar.

Additionally, the broad ^{1}H NMR features of **15** disappeared, whilst a broad resonance was observed in the ^{31}P NMR spectrum (87.8 ppm, $v_{1/2}$ = 506 Hz, Figure 3.122). However, whilst this chemistry appears to follow that established for the analogous dmpe complexes, only the Fe(I) hydride of depe (**15**) is observed in the related Leigh deprotonation reaction by EPR spectroscopy (Figure 3.123), and evidently in considerable concentration to also be resolved in the ^{1}H NMR spectrum (Figure 3.118). This may reflect a greater susceptibility of [*trans*-Fe(H)(N_2)(depe)$_2$]$^+$ towards reduction from **12**, the Fe(0) product of the deprotonation, to form **15**. Alternatively, as hypothesised for the dmpe system, disproportionation of **12** to **13** and an Fe(–I) species may result in protonation of the latter to form **15** (Figure 3.124). However, whilst these mechanisms suggest **13** and **15** should be formed concurrently, only the latter Fe(I) species is accounted for. Furthermore, monitoring by ^{1}H NMR spectroscopy, formation of **15** was not observed for any combination of **12** with [*trans*-Fe(H)(N_2)(depe)$_2$][$BArF_{24}$], $KBArF_{24}$, and/or ^{t}BuOH (the conjugate acid of the KO^{t}Bu base). Thus, **15** has been conclusively shown to be formed in the deprotonation reaction but it is not yet fully understood how it is generated.

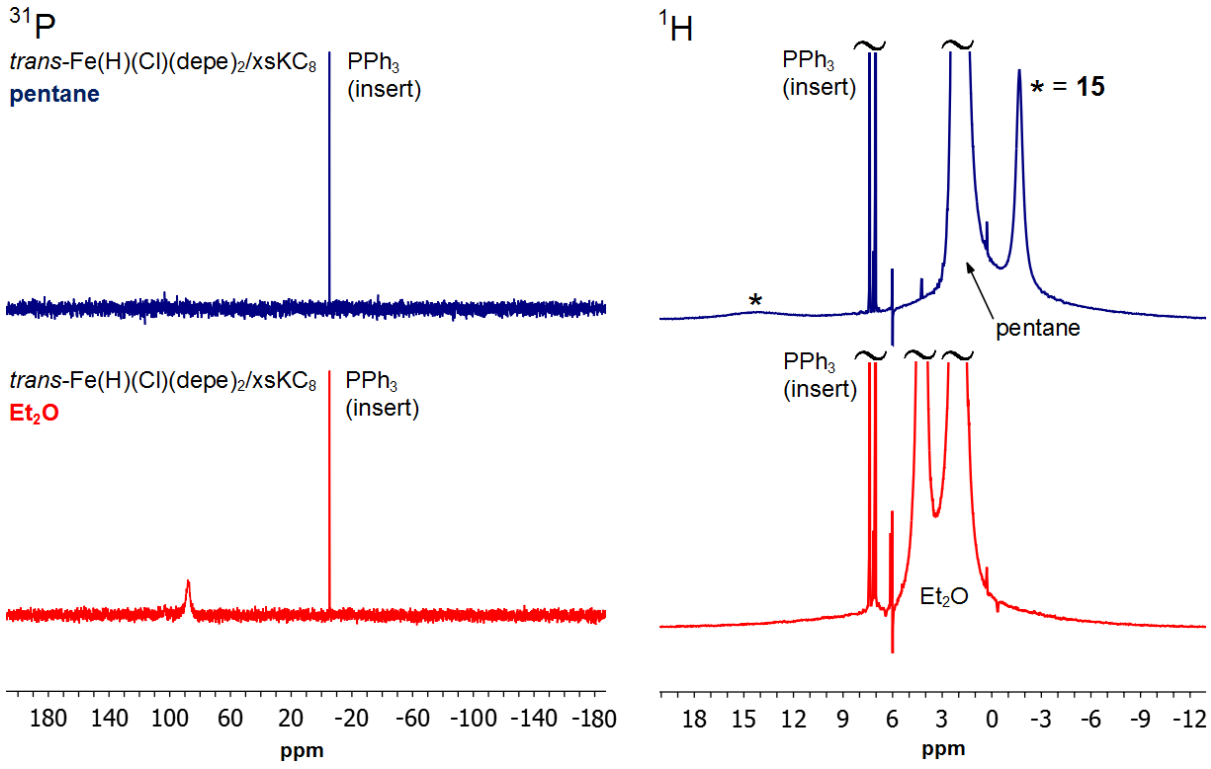


Figure 3.122 ^{31}P (left) and ^{1}H (right) NMR spectra for the reduction of *trans*-Fe(H)(Cl)(depe)$_2$ with excess KC_8 performed in pentane (blue) and Et_2O (red) under Ar.

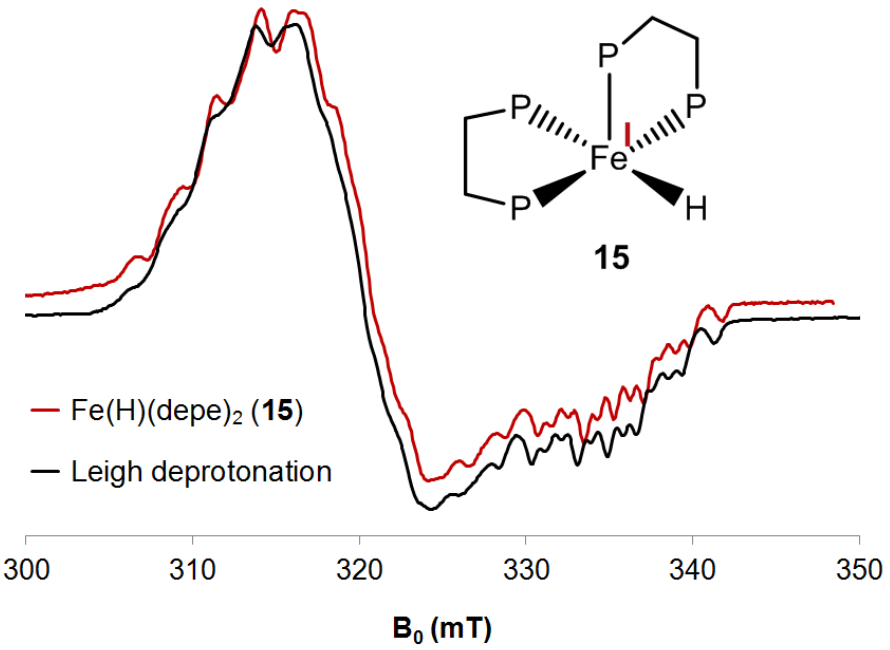


Figure 3.123 X-band CW EPR spectra of isolated **15** (hexane, Ar, red) and the Leigh deprotonation ([*trans*-Fe(H)(N_2)(depe)$_2$][BPh_4]/KO^{t}Bu (1:2) THF, N_2, black); recorded as glasses at 40 K; P = PEt_2.

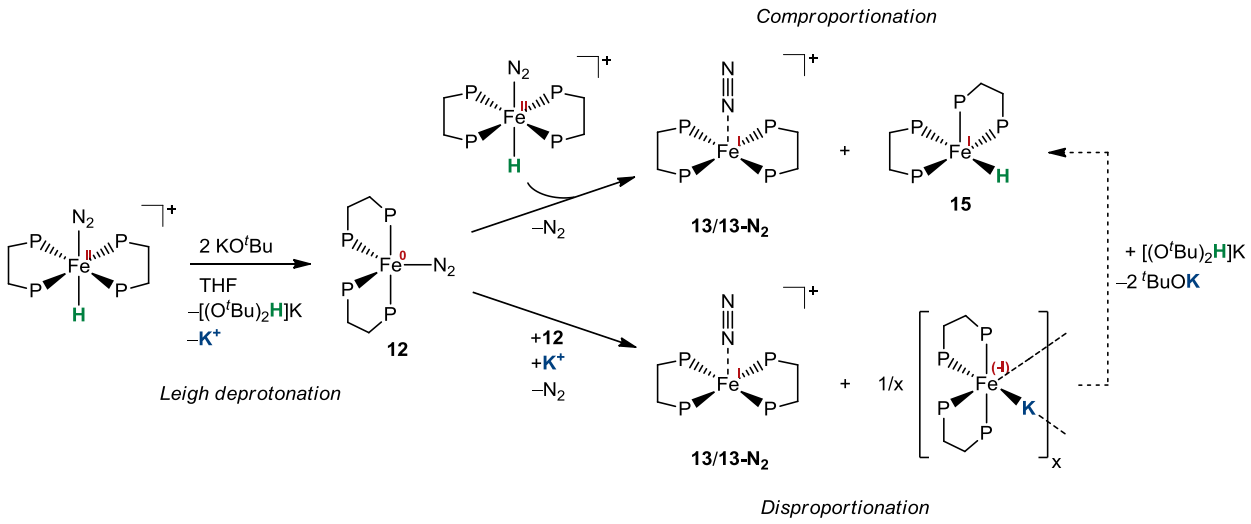


Figure 3.124 Hypothetical involvement of Fe(H)(depe)$_2$ (**15**) and a possible Fe(–1) species in the Leigh deprotonation reaction; P = PEt_2.

3.2.7 H_2 experiments

A THF solution of **12** reacted slowly with H_2 (1 bar) to form the oxidative addition product *cis*-Fe(H)$_2$(depe)$_2$[62] over the course of several days (Figure 3.125-3.126). In contrast, **13** reacts fairly rapidly with H_2 to form [*trans*-Fe(H)(η^2-H_2)(depe)$_2$][$BArF_{24}$][63] (Figure 3.127). This is

thought to proceed *via* initial formation of a non-classical paramagnetic H_2 complex $[Fe(\eta^2\text{-}H_2)(depe)_2][BArF_{24}]$ (**13-H$_2$**), which subsequently undergoes sequential solvent mediated proton transfer and disproportionation steps (Figure 3.128). Conversely, when the reaction is performed in the non-donor solvent 1,2-DFB, **13-H$_2$** is the resultant product (see Chapter 4).

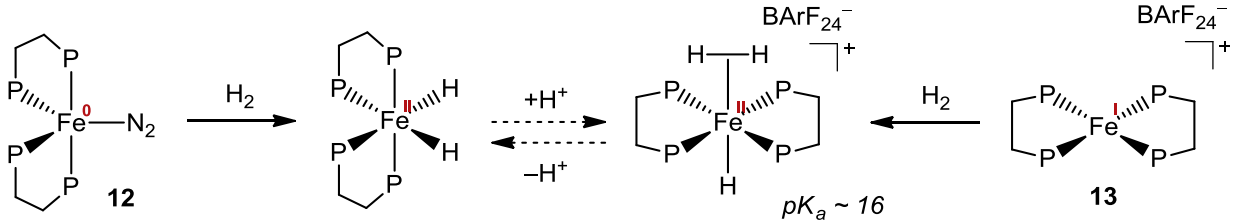


Figure 3.125 Reactions of **12** and **13** with H_2; P = PEt_2.

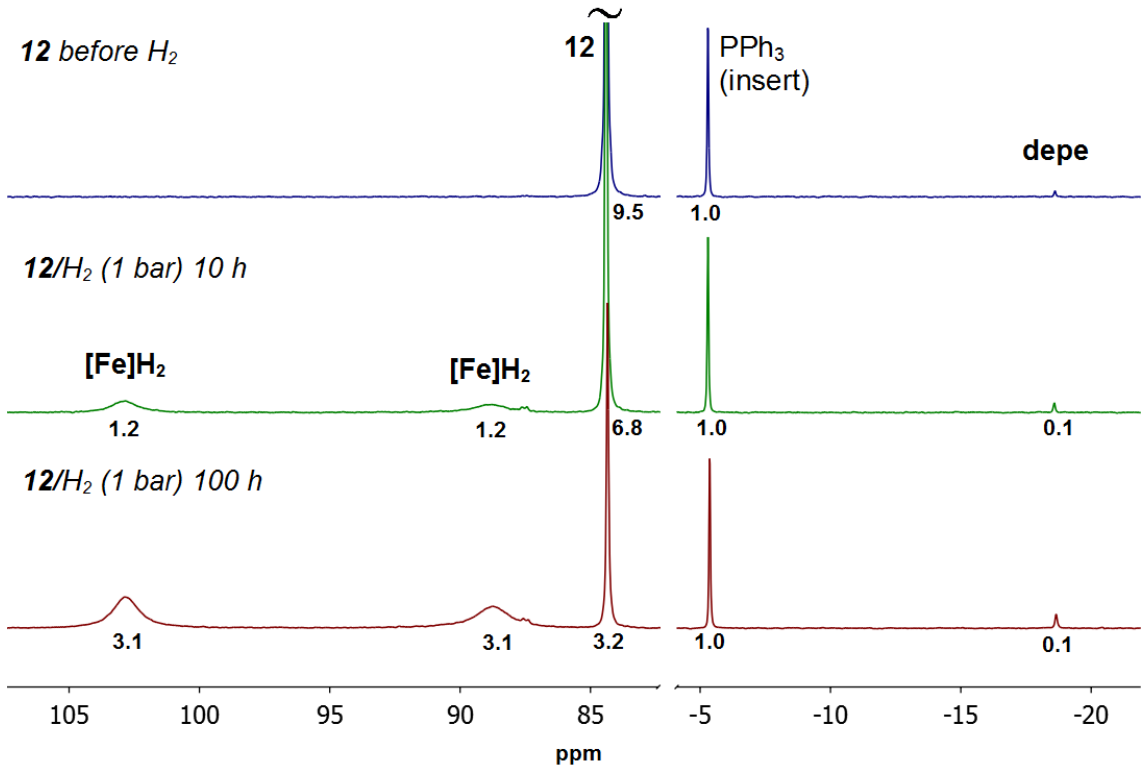


Figure 3.126 ^{31}P NMR spectra of the reaction of **12** with H_2 (1 bar) performed in THF.

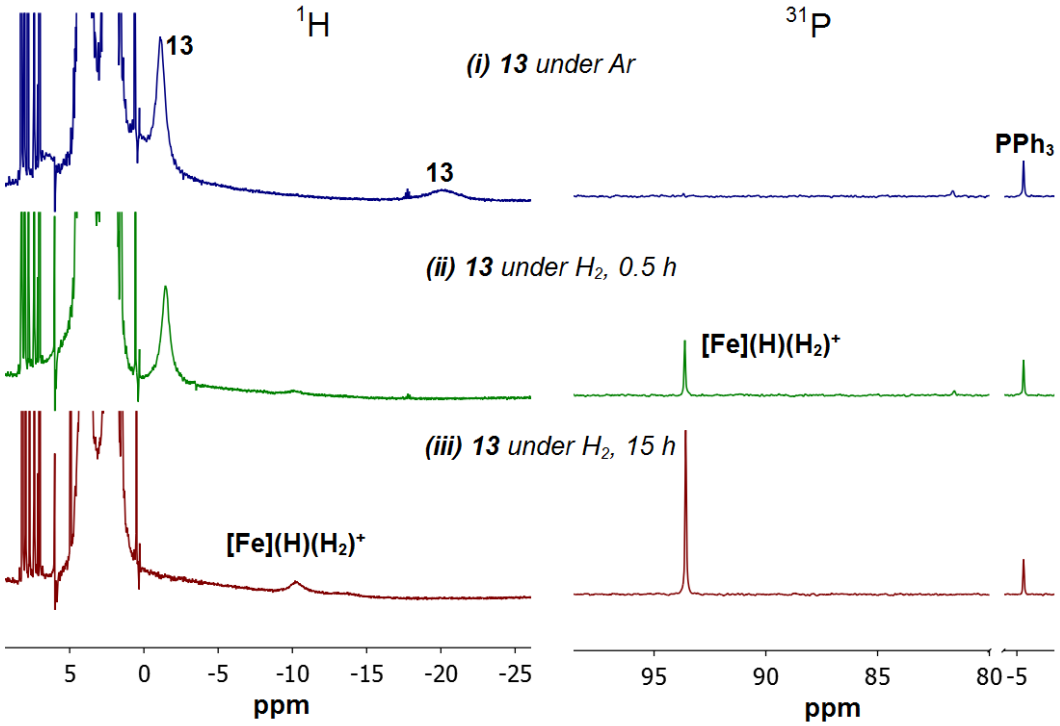


Figure 3.127 ^{1}H (left) and ^{31}P (right) NMR spectra of the reaction of **13** with H_2 (1 bar) performed in THF.



S = donor solvent (THF, Et_2O, TBME)



Figure 3.128 Proposed mechanism for the reaction of **13** with H_2.

Thus, in the reaction of **12** with $KBArF_{24}$, the reactivity of the two known Fe components, **12** and **13**, with H_2 was established; furthermore, any **13** present can be expected to activate H_2 to produce an acidic proton. At RT, admittance of H_2 (1 bar) to a THF solution of **12** and $KBArF_{24}$ (1:1) resulted in rapid formation of *cis*-Fe(H)$_2$(depe)$_2$ (48%) and a trace amount of [*trans*-Fe(H)(N$_2$)(depe)$_2$][$BArF_{24}$]. Over the course of 15 h under H_2 the overall ^{31}P balance remained at ca. 50%, and the trace amount of [*trans*-Fe(H)(N$_2$)(depe)$_2$][$BArF_{24}$] converted to [*trans*-Fe(H)(η^2-H$_2$)(depe)$_2$][$BArF_{24}$] (Figure 3.129). Thus, the products of the reversible reaction of **12** with $KBArF_{24}$ would appear to react much faster with H_2 than **12** only. Again, this mirrors the dmpe system, albeit without complication from dimerisation processes, and therefore a similar mechanism is suggested in Figure 3.130 to account for the outcome of

the ^{31}P NMR experiment. Similarly, K^+ ions are hypothesised to perform a catalytic role in directing sequential electron and proton transfer to N_2 coordinated to both Fe and K^+.

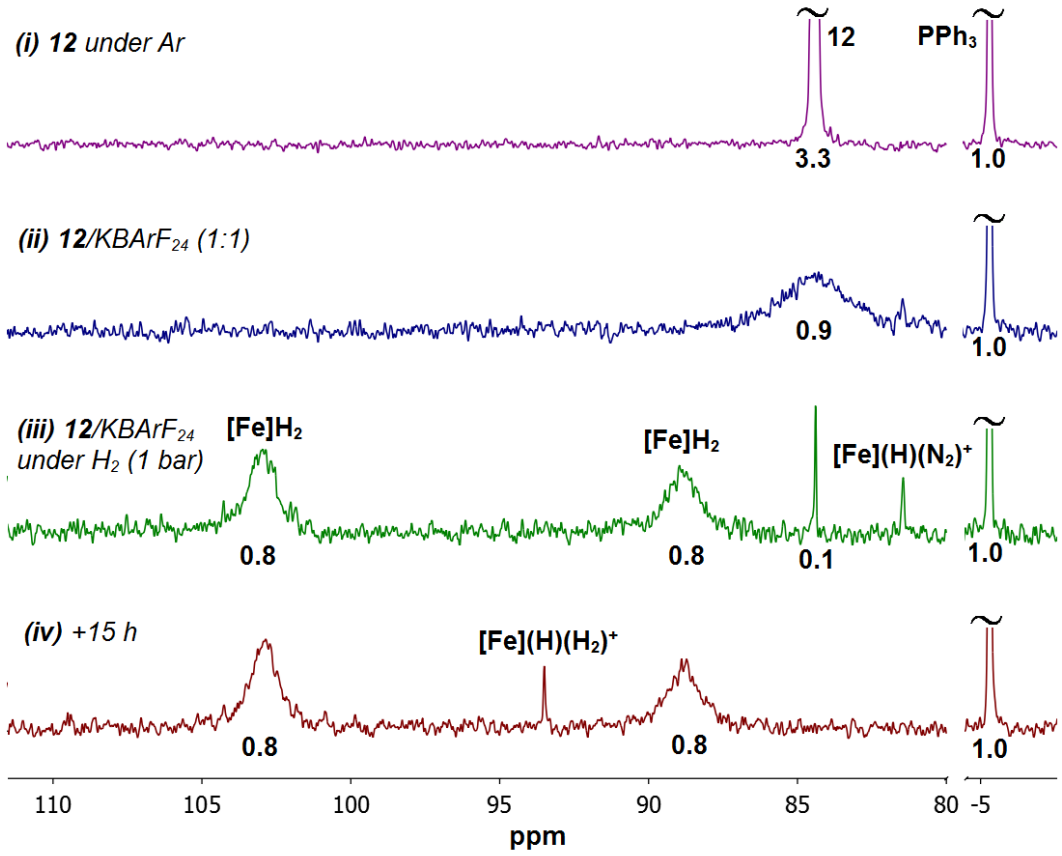


Figure 3.129 ^{31}P NMR spectra of the reaction of **12** with $KBArF_{24}$ (1:1) with subsequent addition of H_2 (1 bar) performed in THF at RT; [Fe] = $[Fe(depe)_2]$.

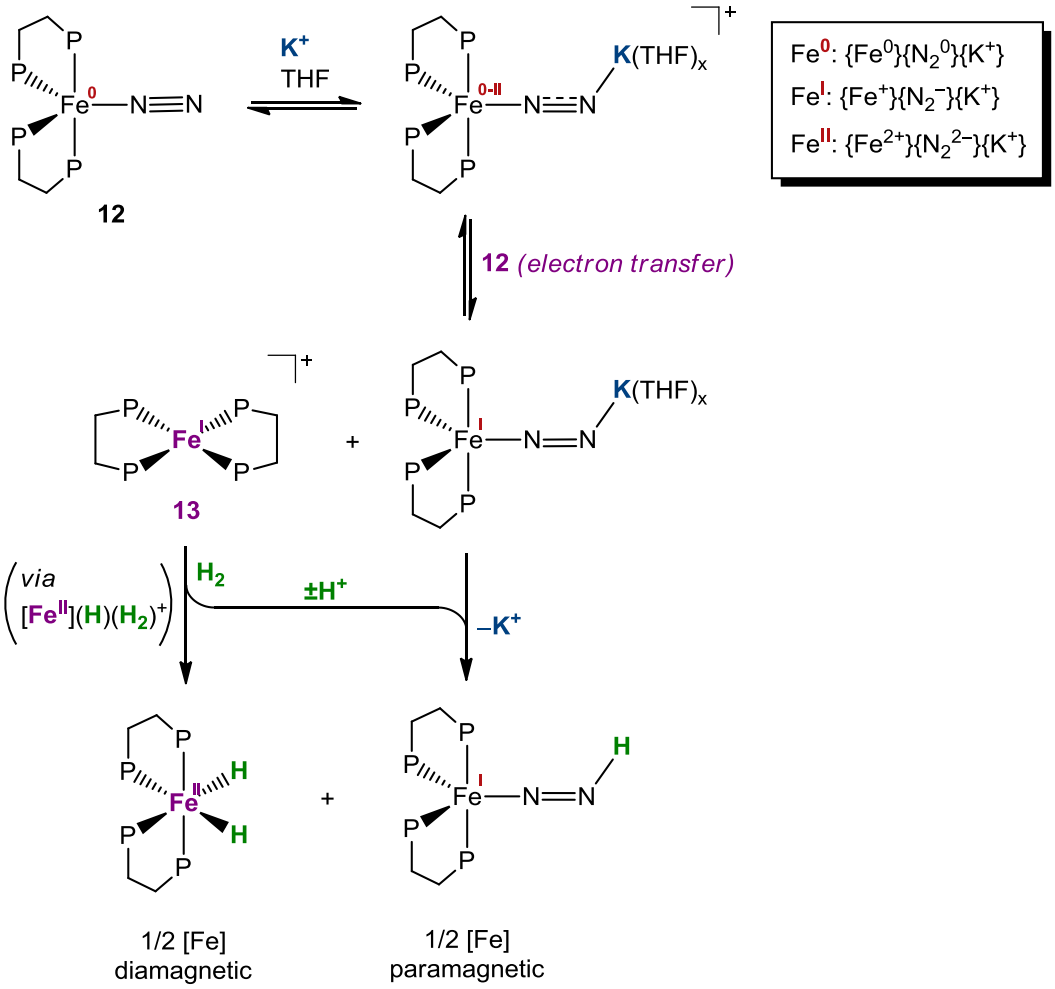


Figure 3.130 Proposed mechanism for the reaction of **12** with $KBArF_{24}$ and H_2; P = PEt_2.

Part 3: Quantification of NH_3 and N_2H_4 from acidification experiments

3.3.1 Introduction

The aim of this work has been to gain a greater understanding of the complex processes involved in the Leigh cycle and related reactivity of Fe(0) dinitrogen species with K^+ ions. Hence, we have focussed on the isolation and spectroscopic mapping of reactive intermediates generated in this chemistry. An alternative approach involving screening of various reaction conditions has been avoided due to numerous issues related to quantitatively assessing the resultant fixed nitrogen species, which will be discussed presently. However, in an attempt to appraise our understanding, acidification experiments for select species and reaction mixtures have been explored.

The standard literature method for quantifying yields of NH_3 is a spectrophotometric (UV-vis) test known as the indophenol method, which analyses for indophenol dye (λ_{max} = 634 nm) formed in the presence of NH_3 or NH_4^+ ions (Figure 3.131-3.132).[64] A similar spectrophotometric test is used to detect N_2H_4 by its reaction with *p*-(dimethylamino)benzaldehyde (pdmab) to form a yellow azine dye (λ_{max} = 458 nm, Figure 3.133-3.134).[65] Both tests are extremely sensitive, able to detect micro-gram quantities of NH_3 or N_2H_4, thus enabling acidification experiments to be performed on a small (0.008-0.032 mmol) scale.

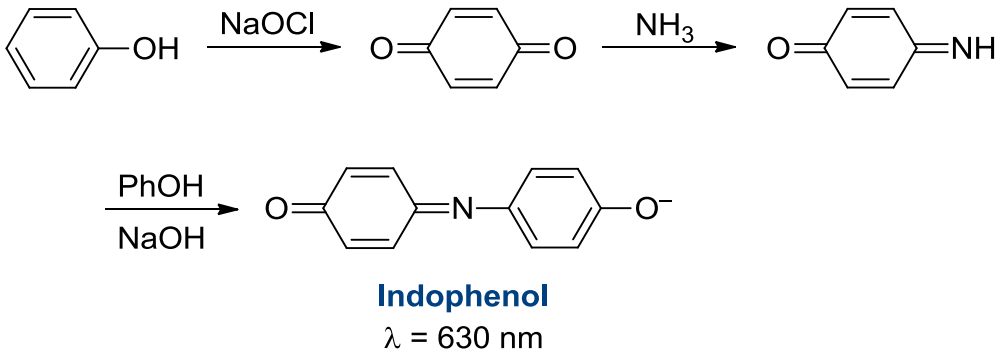


Figure 3.131 Formation of blue indophenol dye in the spectrophotometric indophenol test which analyses for NH_3; the reaction is catalysed by $Na_2[Fe(CN)_5(NO)]$.[64]

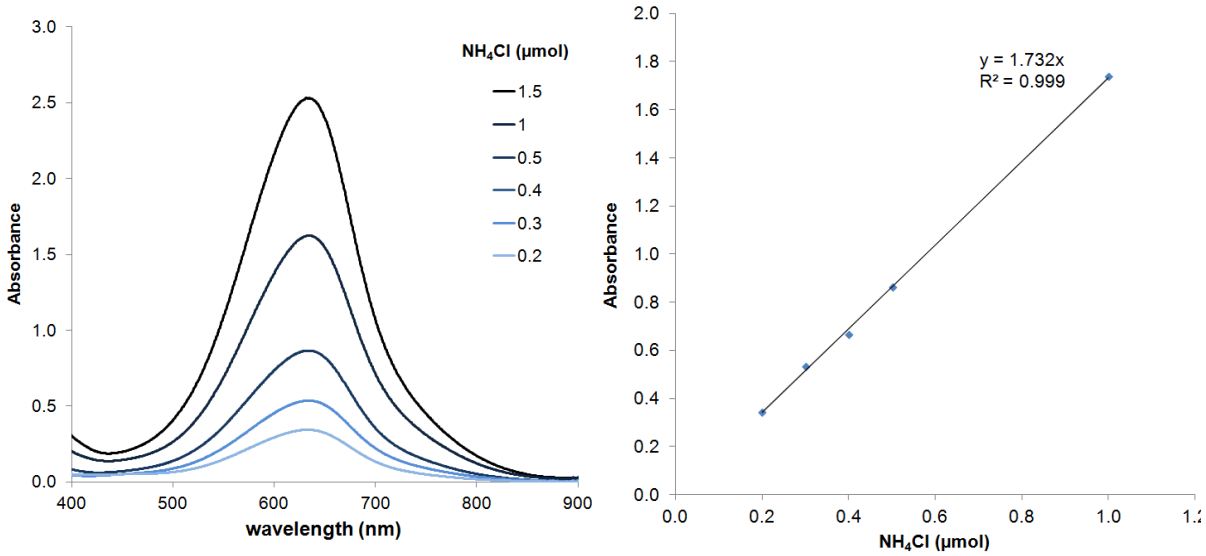


Figure 3.132 UV-vis calibration curves for the indophenol test generated from solutions of $[NH_4]Cl$ of known concentrations; λ_{max} = 634 nm.

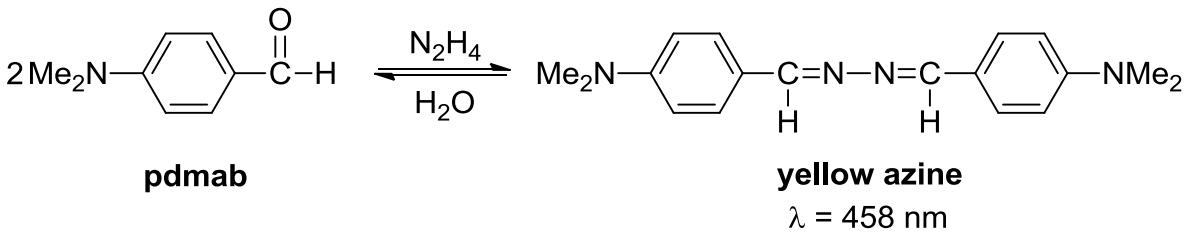


Figure 3.133 Formation of a yellow azine dye in the *p*-(dimethylamino)benzaldehyde (pdmab) test which analyses for N_2H_4.[65]

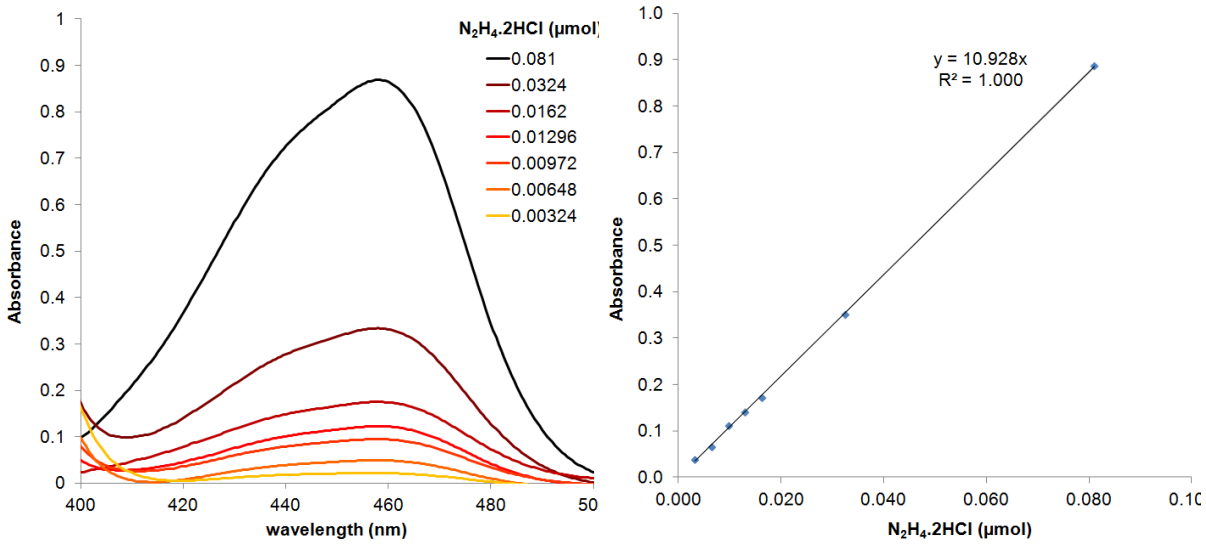


Figure 3.134 UV-vis calibration curves for the pdmab test generated from solutions of N_2H_4·2HCl of known concentrations; λ_{max} = 458 nm.

3.3.2 Comparison of literature procedures

Leigh *et al.* employed several acids for the acidification reaction (HCl, H_2SO_4, $HBF_4.Et_2O$) but since HCl afforded the highest yields of NH_3 and is required to regenerate $Fe(Cl)_2(dmpe)_2$ in the Leigh cycle, we chose to focus only on this proton source.[1, 4] Following their procedure, $[NH_4]Cl$ is isolated from the reaction mixture *via* an aqueous KOH base-distillation to liberate NH_3 which is vacuum transferred onto HCl, regenerating $[NH_4]Cl$ for subsequent indophenol analysis. Accordingly, we obtained a yield of NH_4^+ from acidification of the mixture resulting from deprotonation of $[Fe(H)(N_2)(dmpe)_2][BPh_4]$ of 19% (±4% –78 °C) per Fe, which is slightly higher than the yield reported by Leigh *et al.* (per Fe: 9% (RT), 13% (–40 °C)); this may reflect the lower temperature at which the acidification was performed, consistent with a kinetic preference for protonation at the N_2 ligand (N_β) rather than the Fe centre (*vide supra*). The same yield was obtained from analogous deprotonation/reprotonation of the $BArF_{24}^-$ salt, indicating no appreciable interference from the counteranion. Unfortunately, quantitative transfer of NH_3 in the base distillation requires that solvating H_2O must also be distilled, which can be a lengthy process. Thus we decided to explore more convenient procedures used by the groups of Patrick Holland and Jonas Peters in their acidification studies and apply them to the Leigh system; this work was jointly undertaken with the MSci student Caroline Wood.

The acidification studies performed by Holland *et al.* on Fe β-diketiminate ($\{(2,6\text{-}(R)_2C_6H_3)NC(R')\}_2CH$; R, R' = alkyl/aryl) complexes, have employed a phosphate buffer solution to moderate the pH of their acidified reaction mixtures; as such, an aliquot could be used directly for the indophenol test, circumventing the base-distillation procedure.[36] Crucially, other species present in the mixture must not affect the concentration of indophenol nor interfere with the absorbance band at λ_{max} = 634 nm by which this is measured. Hence, a control test was performed whereby a known quantity of $[NH_4]Cl$ was analysed for in the presence of HCl and $Fe(Cl)_2(dmpe)_2$ (the expected by-product of the acidification reaction). After addition of the buffer solution, analysis of a known volume fraction indicated NH_4^+ was fully accounted for (101% (±4%)). However, attempts to reproduce the yields reported by Leigh *et al.* using this method were unsuccessful (<3% NH_4^+ per Fe), possibly due to interference from uncoordinated phosphines or Fe-species other than $Fe(Cl)_2(dmpe)_2$; presumably this was not an issue with the β-diketiminate ligands used by Holland *et al.*.

Thus, it appears that isolation of NH_4^+ *via* a base distillation procedure is necessary. In the N_2 fixation studies of various Fe complexes with tripodal ligand frameworks, Peters *et al.* have reported a non-aqueous NaO^tBu base distillation procedure.[3] In contrast to KOH,

NaO^tBu is soluble in organic solvents such that the more volatile 1,2-dimethoxyethane (DME) solvent could be employed. To test the compatibility of this more convenient non-aqueous base distillation procedure another control experiment ($[NH_4]Cl/HCl/Fe(Cl)_2(dmpe)_2$) was performed; THF solvent was used in place of DME since this solvent was employed for the deprotonation reaction and has very similar solvent properties to DME. Accordingly, the distilled volatiles were analysed to contain 4% (±4%) of the initial NH_4^+ quantity, whilst the non-volatiles contained the remaining 96% (±4%). Crucially, Peters *et al.* used $HBArF_{24}{\cdot}(Et_2O)_2$ (Brookhart's acid) rather than HCl as their source of protons, generating $[NH_4]BArF_{24}$ which is much more soluble in organic solvents than $[NH_4]Cl$. Thus, it was rationalised that the poor solubility of $[NH_4]Cl$ in THF prevented reaction with NaO^tBu base to liberate NH_3; this was confirmed by substituting MeOH as the solvent, which resulted in complete recovery of NH_4^+ (104% (±4%)). However, despite this, attempts to reproduce yields reported by Leigh *et al.* were again unsuccessful (< 2% NH_4^+ per Fe). Field *et al.* have reported the reaction of $Fe(Cl)_2(dmpe)_2$ with NH_3 in THF to precipitate purple $[Fe(Cl)(NH_3)(dmpe)_2]^+$.[16] If this species is indeed generated in the acidification step or upon generation of NH_3 with base, it is possible that attack from a non-nucleophilic base such as NaO^tBu could result in deprotonation of the NH_3 ligand rather than ligand substitution (Figure 3.135). In contrast, OH^- ions are both strongly basic and nucleophilic such that an S_N1CB (conjugate base) mechanism - as documented for hydrolysis of $[Co(NH_3)_5Br]^{2+}$ and related octahedral amine complexes[66] - may account for the difference in quantified NH_3 liberated with these two different bases.

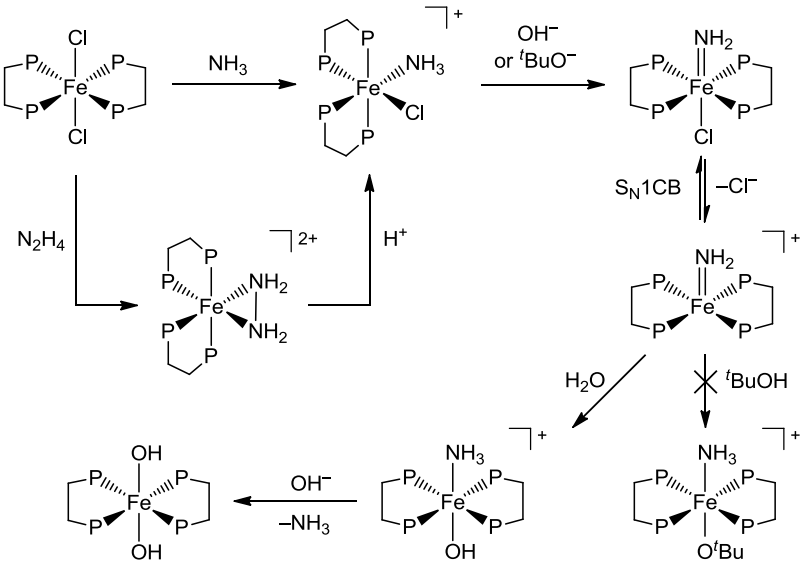


Figure 3.135 Reaction of $Fe(Cl)_2(dmpe)_2$ with NH_3 and N_2H_4 reported by Field *et al.*;[16] subsequent proposed reactivity with KOH (H_2O) or NaO^tBu (THF or MeOH) base. $[Fe(Cl)(NH_3)(dmpe)_2]^+$ precipitates in THF which alternatively may prevent further reaction with NaO^tBu in this solvent.

Thus, we returned to the original procedure reported by Leigh *et al.* for all subsequent NH_3 quantification experiments. In assaying for N_2H_4, N_2H_4·2HCl was base distilled along with $[NH_4]Cl$ in view of the previous findings and since Fe species in the reaction mixture were anticipated to interfere with the reference absorption band of the pdmab test (λ_{max} = 458 nm). However, this presented further complication due to the low volatility of N_2H_4 (bp. 114 °C) and its disproportionation to NH_3 and N_2, or N_2 and H_2, which is known to be catalysed by a variety of metal complexes including Fe.[15, 67] A control test was performed whereby known quantities of both N_2H_4·2HCl and $[NH_4]Cl$ were analysed in the presence of $Fe(Cl)_2(dmpe)_2$; addition of aqueous KOH liberates N_2H_4 and NH_3 which were vacuum transferred (10^{-3} mbar; < 50 °C) onto HCl. Subsequent analysis accounted for NH_3 and N_2H_4 in 102% (±3%) and 58% (±3%) yield, respectively, indicating the low yield of N_2H_4 was due to incomplete vacuum transfer rather than disproportionation; applying more intense heat to the distillation flask increased the yield of N_2H_4 (73% ±3%) but resulted in significant disproportionation to NH_3 (116% ±3%). It is possible that this issue could be resolved through the use of other acids with more solubilising anions, however, as previously discussed we wished to limit the choice of acid to HCl. Hence, subsequent distillations have been performed with minimal heating to limit disproportionation at the expense of N_2H_4 transfer. As a result, yields of N_2H_4 are likely underestimated.

It would be highly desirable to quantitatively analyse NH_3 and N_2H_4 (and even N_2H_2) production from acidification reactions performed under controlled conditions of various acids, solvents, temperatures, concentrations, etc. However, as has hopefully been demonstrated, experimental complications abound. Thus, without attempting an exhaustive exploration of the many factors involved in the acidification step, quantification experiments cannot be entirely conclusive; nevertheless, the following experiments were performed in the hope that they might be informative.

3.3.3 Acidification experiments

4 and **6** were acidified in THF by the same protocol used by Leigh *et al.* (HCl/KOH base distillation) and were determined to produce NH_4^+ in 7% (±3%, 2 runs) and 8% (±3%, 2 runs) yields, respectively; **4** was generated *in situ* from **6** under N_2, whilst **6** was acidified under Ar. No N_2H_4 was detected in either case. Although these yields are significantly lower than those obtained for the deprotonation mixture (19% (±3%)), it provides the first direct evidence that an Fe(0) dinitrogen complex in this system is capable of producing NH_4^+ with HCl acid. The similar yields of NH_4^+ obtained for **4** and **6** may indicate a shared intermediate, with the possibility of either dimerisation or dissociation occurring prior to or after protonation.

Acidification experiments performed on mixtures of **6** and $KBArF_{24}$ (1:3, THF, Ar) produced NH_4^+ in 14% (±3%, 2 runs) yield; no N_2H_4 was detected. Thus it would appear that $KBArF_{24}$ additive improves the NH_4^+ yield, although not up to the yield obtained for the deprotonation mixture. Fe(0) may be required to act as a sacrificial reductant after initial protonation steps, as proposed by Tyler *et al.* in their theoretical study of the acidification reaction (see section 3.0.1);[14] therefore, an optimal ratio of **4** or **6** to $KBArF_{24}$ may be required in order to ensure activation of coordinated N_2 without reducing the availability of Fe(0) below a threshold. Addition of H_2 prior to acidification did not yield any NH_4^+ or N_2H_4, which may be accounted for by the full conversion of Fe(0) in the presence of K^+ ions under H_2.

Consistent with the findings of Komiya *et al.*,[10, 12] acidification of **12** did not produce NH_4^+ or N_2H_4. However, with $KBArF_{24}$ additive (2 equivalents), NH_4^+ and N_2H_4 were detected in 4 and 8% (±2%, 2 runs) yield, respectively. Thus, it appears that $KBArF_{24}$ additive also promotes N_2H_4 production, which is not detected for the deprotonation mixture. The incomplete reduction of N_2 may similarly reflect that activation with $KBArF_{24}$ promotes initial protonation but reduces availability of Fe(0) for subsequent electron transfer at these ratios. As for the dmpe system, neither NH_4^+ or N_2H_4 were detected for the reaction with $KBArF_{24}$ and H_2. It is also perhaps surprising that N_2H_4 is only encountered for the depe and not the dmpe system in which dimerisation processes appear to occur more readily and might be expected to promote N_2H_4 production through protonation of bridging N_2. However, the degree of reduction may have a complex dependence; for instance, incomplete reduction may alternatively reflect a lower availability of reducing electrons. Although the reduction potentials of the Fe(0) complexes are very similar (**4**, ca. –1.9 V; **6**, –2.2 V; **12**, –2.0 V vs $Cp_2Fe^{+/0}$), the concentration of Fe(0) or other available reductants during acidification may vary.

An alternative NMR spectroscopic method has also been used to qualitatively assess for NH_4^+ production. Accordingly, protonation of **11** was performed with excess triflic acid (TfOH), which when conducted in hexane under a N_2 atmosphere provided a 1:1:1 triplet (δ = 7.05 ppm, $^1J_{NH}$ = 51.5 Hz) in the ^{1}H NMR spectrum of the redissolved mixture in DMSO-d_6 (Figure 3.136). As a formally Fe(–I) species, **11** is expected to be highly reducing, although this likely also prohibits involvement in either Leigh-type chemistry or the more controlled Fe(0)/$KBArF_{24}$ reactions. Unfortunately, broad underlying resonances in this region from unknown by-products prevent accurate integration of the NH_4^+ resonance and thus quantification. Analogous TfOH acidifications of **4**, **6** and **12** (with and without $KBArF_{24}$) yielded NH_4^+ by ^{1}H NMR for **12** (with and without $KBArF_{24}$) only, contrasting with the previous HCl experiments. Conversely, NH_4^+ was observed in the acidification of the Leigh

deprotonation mixture for the dmpe system only; therefore, this method cannot unambiguously assess for NH_4^+.

A comprehensive acidification study of these Leigh-type systems is long overdue; the identity and concentration of the acid, rate of addition, solvent choice, temperature, concentration of substrate, and addition of promoters (e.g. K^+ salts, ^{t}BuOH), may all influence NH_3 production. Obtaining a reliable method for NH_3 and N_2H_4 quantification will be crucial for establishing the viability of this system and related chemistry; many of the well-known N_2 fixation systems discussed in Chapter 1 have also shown a delicate dependence on reaction conditions. In a related Leigh-type system, Tyler *et al.* have investigated the effect of altering the anion of the acid employed for the acidification of $Fe(N_2)(DMeOPrPE)_2$.[20] They hypothesised that protonation of the N_2 ligand could be blocked by the anion, which agreed with the observed decrease in the yield of NH_4^+ with increased coordinating and/or ion-pairing ability (TfOH (17%) > HBF_4 (7%) > HCl (4%)). However, their KO^{t}Bu base distillation procedure was performed in THF solvent, and it is possible that their low yield for HCl reflects the poor solubility of $[NH_4]Cl$ in this solvent, as we have encountered (*vide supra*).

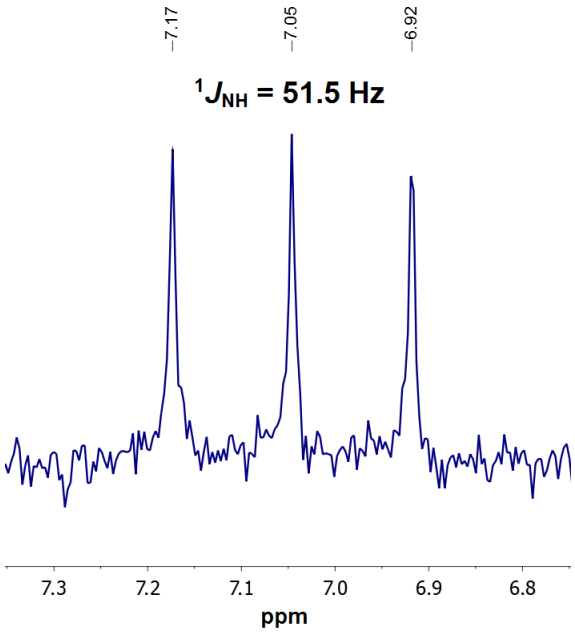


Figure 3.136 ^{1}H NMR spectrum in DMSO-d_6 of the redissolved mixture resulting from addition of excess TfOH to **11** (hexane, N_2).

Furthermore, the use of the indophenol method has received criticism, most recently highlighted by Kanatzidis *et al.*:[68]

"...this method employs a complex chemical reaction toolkit, it is susceptible to interference from many sources and requires elaborate handling of the reaction products that can introduce losses and errors. It is time-consuming, cumbersome, subject to interference, and thus inadequate for an accurate quantification of the amount of ammonia for our aliquots."

As an alternative, they advocate assaying NH_4^+ directly using ion chromatography, which it is hoped may provide a more viable method to be explored in future work.

Part 4: Concluding remarks

The Fe(0) N_2 complexes **4** and **12** are key intermediates in Leigh's seminal homogeneous N_2 fixation cycle using Fe. In the archetypal dmpe system, **4** was proposed to be the active species responsible for NH_3 production, although its instability under reduced N_2 pressure hindered further mechanistic insight; the depe analogue **12** was known to produce only N_2 and H_2 upon acidification casting further uncertainty on both systems. **6**, a stable solid-state analogue of **4**, has now been isolated and crystallographically characterised; in solution, **6** and **4** are in equilibrium, and the latter can be readily accessed under a N_2 atmosphere. Along with **12**, these Fe(0) complexes have been shown to be strong reductants, which may partly explain their unusual propensity to undergo redox processes in the presence of alkali metal salts ($KBArF_{24}$, $NaBArF_{24}$, $LiBArF_{20}$). The formation of Fe(I) generated by single electron oxidation of the Fe(0) species has been spectroscopically confirmed, and the corresponding Fe(I) and mixed valent Fe(0)/Fe(I) complexes (**7**, **8**, **13**) have been isolated and crystallographically characterised. A concomitant reduction process is therefore proposed involving a K^+-coupled electron transfer onto an activated N_2 ligand. This cooperative activation and reduction of N_2 bound to Fe(0) is thought to also occur in the Leigh cycle, in which K^+ ions are generated in the deprotonation step. The proposed reduced species are likely responsible for NH_3 production upon acidification in the Leigh cycle; preliminary acidification studies using HCl reveal that **12** produces NH_3 (and N_2H_4) in the presence of $KBArF_{24}$ promoter only, whilst **4** and **6** produce NH_3 in improved yields with $KBArF_{24}$. Almost all well-known N_2 fixation systems have shown considerable variability with reaction conditions, indicating a finely balanced dependence on multiple factors. Although the spectrophotometric indophenol test is the standard method for quantifying yields of NH_3, it has proven to be unreliable, inaccurate, and poorly suited to these Leigh-type systems; thus for future acidification studies, it is recommended that a more experimentally robust alternative be sought.

An external reductant is not employed in the reactions of these isolated Fe(0) complexes with $KBArF_{24}$, therefore in order to reduce N_2, all of the required electrons must come from Fe(0). This bears similarity to the Mittasch Fe catalyst used in the Haber Bosch process, in which K(I) oxide is used as a promoter to improve the catalytic activity of the predominantly Fe(0) surface, and multi-metallic cooperation is thought to be crucial for homolytic cleavage of adsorbed N_2. The Fe(0)/$KBArF_{24}$ mixtures also react rapidly with H_2, at room temperature and atmospheric pressure, which appears consistent with the involvement of reactive Fe(I) intermediates, shown separately to convert H_2 into proton and hydride equivalents;

subsequent protonation of a K^+-stabilised reduced N_2 moiety may provide a viable mechanism for using H_2 to directly fix activated N_2.

This work has mostly focussed on the influence of K^+ ions, in the form of $KBArF_{24}$, on the isolated Fe(0) species **4**, **6**, and **12**. Both Li^+ and Na^+ salts have also been shown to have a similar effect, which is thought to be more pronounced for Na^+ in particular, and warrants further investigation. Although the Fe(I) species generated in these reactions have been thoroughly characterised and interconversion processes occurring in solution are now well understood, the corresponding reduced species remain spectroscopically elusive. Further investigation will require an arsenal of advanced spectroscopic techniques, including high field/frequency EPR and Mössbauer spectroscopy. Chemical trapping of these reactive intermediates remains relatively unexplored and should also be a focus.

The Fe(I) monohydride **10** and Fe(–I) complex **11** are not thought to be involved in Leigh-type chemistry due to their extreme instability, however these complexes are interesting in their own right as rare examples of a paramagentic Fe hydride and an Fe(–I) complex, respectively. Reactivity studies of **10** have unfortunately been limited by the challenging synthesis of this species, which readily decomposes to the stable Fe(II) dihydride. However, in contrast to the latter, **10** reacts rapidly with azobenzene to generate an unusual end-on bound azobenzene complex, which appears to be formed as an intermediate to the known Fe(0) azobenzene π-complex. In contrast, the Fe(I) monohydride of depe (**15**) has been shown to be generated in the Leigh deprotonation reaction; investigation into its reactivity and the potential role it may play in the subsequent acidification step will be pursued in future work.

The cycle that Leigh proposed almost 25 years ago provides a rudimentary description of the N_2 fixation chemistry performed by these simple Fe diphosphine complexes.[1] A much more complex system has been illustrated in this work involving additional dimerisation and one-electron redox processes, and a possible cooperative activation of N_2 by Fe and K^+ salts (Figure 3.137). The ability of K^+ ions to promote reactivity of the Fe(0) complexes towards both N_2 and H_2 may be pertinent to related systems, as well as for developing a homogeneous mimic of the Haber-Bosch process which utilises H_2 as a mild and economically viable reductant for N_2 fixation.

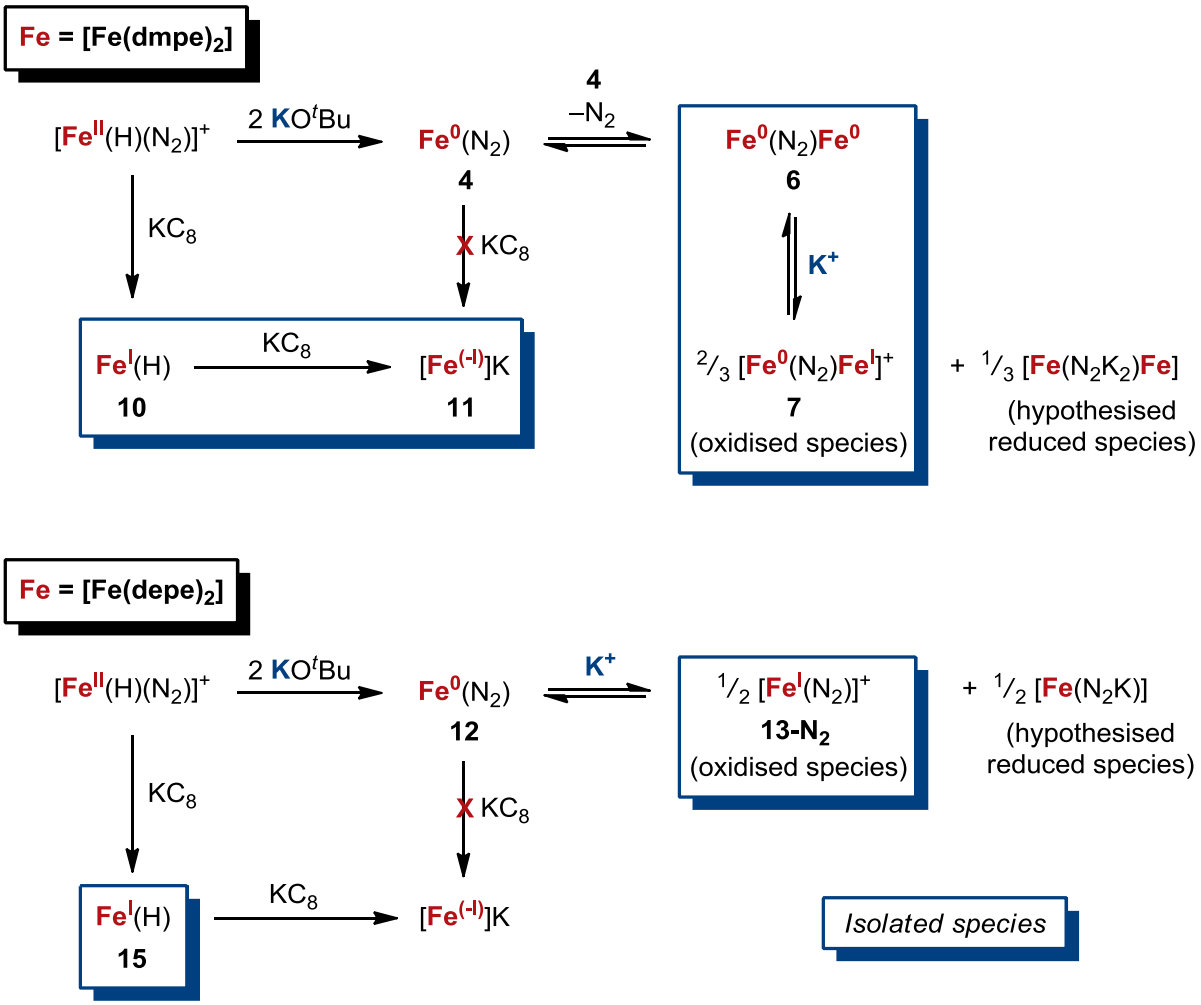


Figure 3.137 A summary of the reduction and disproportionation processes related to the deprotonation step of the Leigh cycle, which have been explored in this work.

References

1. Leigh, G. J.; Jimenez-Tenorio, M., *J. Am. Chem. Soc.*, **1991**, *113* (15), 5862-5863.
2. Yandulov, D. V.; Schrock, R. R., *Science*, **2003**, *301* (5629), 76-78.
3. Anderson, J. S.; Rittle, J.; Peters, J. C., *Nature*, **2013**, *501* (7465), 84-87.
4. Hall, D. A.; Leigh, G. J., *J. Chem. Soc., Dalton Trans.*, **1996**, (17), 3539-3541.
5. Hazari, N., *Chem. Soc. Rev.*, **2010**, *39* (11), 4044-4056.
6. Tolman, C. A.; Ittel, S. D.; English, A. D.; Jesson, J. P., *J. Am. Chem. Soc.*, **1978**, *100* (13), 4080-4089.
7. Hills, A.; Hughes, D. L.; Jimenez-Tenorio, M.; Leigh, G. J.; Rowley, A. T., *J. Chem. Soc., Dalton Trans.*, **1993**, (20), 3041-3049.
8. Whittlesey, M. K.; Mawby, R. J.; Osman, R.; Perutz, R. N.; Field, L. D.; Wilkinson, M. P.; George, M. W., *J. Am. Chem. Soc.*, **1993**, *115* (19), 8627-8637.
9. Baker, M. V.; Field, L. D., *Organometallics*, **1986**, *5* (4), 821-823.

10. Hirano, M.; Akita, M.; Morikita, T.; Kubo, H.; Fukuoka, A.; Komiya, S., *J. Chem. Soc., Dalton Trans.*, **1997**, (19), 3453-3458.
11. Gilbertson, J. D.; Szymczak, N. K.; Tyler, D. R., *J. Am. Chem. Soc.*, **2005**, *127* (29), 10184-10185.
12. Komiya, S.; Akita, M.; Yoza, A.; Kasuga, N.; Fukuoka, A.; Kai, Y., *J. Chem. Soc., Chem. Commun.*, **1993**, (9), 787-788.
13. George, T. A.; Rose, D. J.; Chang, Y. D.; Chen, Q.; Zubieta, J., *Inorg. Chem.*, **1995**, *34* (5), 1295-1298.
14. Yelle, R. B.; Crossland, J. L.; Szymczak, N. K.; Tyler, D. R., *Inorg. Chem.*, **2009**, *48* (3), 861-871.
15. Crossland, J. L.; Zakharov, L. N.; Tyler, D. R., *Inorg. Chem.*, **2007**, *46* (25), 10476-10478.
16. Field, L. D.; Li, H. L.; Magill, A. M., *Inorg. Chem.*, **2009**, *48* (1), 5-7.
17. Field, L. D.; Li, H. L.; Dalgarno, S. J.; Turner, P., *Chem. Commun.*, **2008**, (14), 1680-1682.
18. Crossland, J. L.; Tyler, D. R., *Coord. Chem. Rev.*, **2010**, *254* (17-18), 1883-1894.
19. Crossland, J. L.; Balesdent, C. G.; Tyler, D. R., *J. Chem. Soc., Dalton Trans.*, **2009**, (23), 4420-4422.
20. Balesdent, C. G.; Crossland, J. L.; Regan, D. T.; López, C. T.; Tyler, D. R., *Inorg. Chem.*, **2013**, *52* (24), 14178-14187.
21. a) Oscroft, L., MSci thesis, Imperial College, London, 2011; b) Driver, M., MSci thesis, Imperial College London, 2012; c) Briault-Hutter, C., MSci thesis, Imperial College London, 2013.
22. Nishida, H.; Takada, N.; Yoshimura, M.; Sonoda, T.; Kobayashi, H., *Bull. Chem. Soc. Jpn.*, **1984**, *57* (9), 2600-2604.
23. Olmstead, W. N.; Margolin, Z.; Bordwell, F. G., *J. Org. Chem.*, **1980**, *45* (16), 3295-3299.
24. Bordwell, F. G.; Algrim, D.; Vanier, N. R., *J. Org. Chem.*, **1977**, *42* (10), 1817-1819.
25. Addison, A. W.; Rao, T. N.; Reedijk, J.; van Rijn, J.; Verschoor, G. C., *J. Chem. Soc., Dalton Trans.*, **1984**, (7), 1349-1356.
26. a) Day, P.; Hush, N. S.; Clark, R. J. H., *Philos. Trans. R. Soc. London, Ser. A*, **2008**, *366* (1862), 5-14; b) Hush, N. S., *Coord. Chem. Rev.*, **1985**, *64* (0), 135-157.
27. Wood, C., MSci thesis, Imperial College London, 2014.
28. Pfennig, B. W.; Cohen, J. L.; Sosnowski, I.; Novotny, N. M.; Ho, D. M., *Inorg. Chem.*, **1999**, *38* (3), 606-612.
29. Robin, M. B., Day, P., *Adv. Inorg. Chem. Radiochem.*, **1967**, *10*, 248.
30. Arumugam, K.; Shaw, M. C.; Mague, J. T.; Bill, E.; Sproules, S.; Donahue, J. P., *Inorg. Chem.,* **2011**, *50* (7), 2995-3002.
31. Bain, G. A.; Berry, J. F., *J. Chem. Edu.*, **2008**, *85* (4), 532.
32. Evans, D. F., *J. Chem. Soc.*, **1959**, (0), 2003-2005.
33. Fryzuk, M. D.; Johnson, S. A., *Coord. Chem. Rev.*, **2000**, *200*, 379-409.
34. Aranzaes, J. R.; Daniel, M.-C.; Astruc, D., *Can. J. Chem.*, **2006**, *84* (2), 288-299.
35. Strong, H.; Krusic, P. J.; Filippo, J. S.; Keenan, S.; Finke, R. G., *Inorganic Syntheses*, **1990**, 203-207.
36. Rodriguez, M. M.; Bill, E.; Brennessel, W. W.; Holland, P. L., *Science*, **2011**, *334* (6057), 780-783.
37. Figg, T. M.; Holland, P. L.; Cundari, T. R., *Inorg. Chem.*, **2012**, *51* (14), 7546-7550.

38. Köhler, F. H., *Paramagnetic Complexes in Solution: The NMR Approach, eMagRes*, John Wiley & Sons, Ltd, **2007**.
39. Ozarowski, A.; Zvyagin, S. A.; Reiff, W. M.; Telser, J.; Brunel, L-C.; Krzystek, J., *J. Am. Chem. Soc.*, **2004**, *126* (21), 6574-6575.
40. Field, L. D.; George, A. V.; Pike, S. R.; Buys, I. E.; Hambley, T. W., *Polyhedron*, **1995**, *14* (20-21), 3133-3137.
41. Lieber, E.; Rao, C. N. R.; Chao, T. S.; Hoffman, C. W. W., *Anal. Chem.*, **1957**, *29* (6), 916-918.
42. a) Sklenak, S.; Gatial, A.; Biskupic, S., *J. Mol. Struct.-Theochem.*, **1997**, *397*, 249-262; b) Eyster, E. H.; Gillette, R. H., *J. Chem. Phys.*, **1940**, *8* (5), 369-377.
43. a) Zhang, Y.; Hallows, W. A.; Ryan, W. J.; Jones, J. G.; Carpenter, G. B.; Sweigart, D. A., *Inorg. Chem.*, **1994**, *33* (15), 3306-3312; b) Summerville, D. A.; Cohen, I. A., *J. Am. Chem. Soc.*, **1976**, *98* (7), 1747-1752.
44. a) Chiang, K. P.; Scarborough, C. C.; Horitani, M.; Lees, N. S.; Ding, K.; Dugan, T. R.; Brennessel, W. W.; Bill, E.; Hoffman, B. M.; Holland, P. L., *Angew. Chem. Int. Ed.*, **2012**, *51* (15), 3658-3662; b) Hounjet, L. J.; Adhikari, D.; Pink, M.; Carroll, P. J.; Mindiola, D. J., *Z. Anorg. Allg. Chem.* **2015**, *641* (1), 45-48.
45. Gargano, M.; Giannocc.P; Rossi, M.; Sacco, A., *J. Chem. Soc., Chem. Commun.*, **1973**, (7), 233-234.
46. Cordero, B.; Gomez, V.; Platero-Prats, A. E.; Reves, M.; Echeverria, J.; Cremades, E.; Barragan, F.; Alvarez, S., *J. Chem. Soc., Dalton Trans.*, **2008**, (21), 2832-2838.
47. Hu, S-Z.; Zhou, Z-H.; Robertson, B. E., *Z. Kristallogr.* **2009**, *224* (8), 375-383.
48. Gargano, M.; Giannoccaro, P.; Rossi, M.; Vasapollo, G.; Sacco, A., *J. Chem. Soc., Dalton Trans.*, **1975**, (1), 9-12.
49. Sadique, A. R.; Gregory, E. A.; Brennessel, W. W.; Holland, P. L., *J. Am. Chem. Soc.*, **2007**, *129* (26), 8112-8121.
50. a) Hansert, B.; Vahrenkamp, H., *J. Organomet. Chem.*, **1993**, *459* (1–2), 265-269; b) Bazhenova, T. A.; Emelyanova, N. S.; Shestakov, A. F.; Shilov, A. E.; Antipin, M. Y.; Lyssenko, K. A., *Inorg. Chim. Acta*, **1998**, *280* (1–2), 288-294.
51. Bouwstra, J. A.; Schouten, A.; Kroon, J., *Acta Crystallogr., Sect. C: Cryst. Struct. Commun.*, **1983**, *39*, 1121-1123.
52. Mostad, A.; Romming, C., *Acta Chem. Scand.*, **1971**, *25* (10), 3561-3568.
53. Hills, A.; Hughes, D. L.; Jimenez-Tenorio, M.; Leigh, G. J., *J. Organomet. Chem.*, **1990**, *391* (3), C41-C44.
54. Baker, M. V.; Field, L. D.; Young, D. J., *J. Chem. Soc., Chem. Commun.*, **1988**, (8), 546-548.
55. a) Morris, R. H., *Recent Advances in Hydride Chemistry*, Poli, M. P., Ed. Elsevier, Amsterdam, **2001**, 1-38; b) Crabtree, R. H., *The Organometallic Chemistry of the Transition Metals*, John Wiley & Sons, Inc., **2005**, 53-85.
56. Berning, D. E.; Noll, B. C.; DuBois, D. L., *J. Am. Chem. Soc.*, **1999**, *121* (49), 11432-11447.
57. Perthuisot, C.; Jones, W. D., *New J. Chem.*, **1994**, *18* (5), 621-628.
58. a) Cole, G. M.; Garrett, B. B., *Inorg. Chem.*, **1970**, *9* (8), 1898-1902; b) Figgis, B. N.; Lewis, J., *Progress in Inorganic Chemistry*, John Wiley & Sons, Inc., **1964**, 37-239.
59. Jenkins, D. M.; Di Bilio, A. J.; Allen, M. J.; Betley, T. A.; Peters, J. C., *J. Am. Chem. Soc.*, **2002**, *124* (51), 15336-15350.
60. Maddock, A., *Mössbauer Spectroscopy*, Maddock, A., Ed., Woodhead Publishing, **1997**, 104-140.

61. Kaczmarzyk, T.; Jackowski, T.; Dzilinski, K.; Sinyakov, G. N., *Nukleonika*, **2007**, *52*, S93-S98.
62. Baker, M. V.; Field, L. D., *J. Am. Chem. Soc.*, **1986**, *108* (23), 7436-7438.
63. Bautista, M.; Earl, K. A.; Morris, R. H.; Sella, A., *J. Am. Chem. Soc.*, **1987**, *109* (12), 3780-3782.
64. Weatherburn, M. W., *Anal. Chem.*, **1967**, *39* (8), 971-974.
65. Watt, G. W.; Chrisp, J. D., *Anal. Chem.*, **1952**, *24* (12), 2006-2008.
66. Tobe, M. L., *Acc. Chem. Res.*, **1970**, *3* (11), 377-385.
67. a) Block, E.; Ofori-Okai, G.; Kang, H.; Zubieta, J., *J. Am. Chem. Soc.*, **1992**, *114* (2), 758-759; b) Takei, I.; Dohki, K.; Kobayashi, K.; Suzuki, T.; Hidai, M., *Inorg. Chem.*, **2005**, *44* (11), 3768-3770; c) B. Hitchcock, P.; L. Hughes, D.; J. Maguire, M.; Marjani, K.; L. Richards, R., *J. Chem. Soc., Dalton Trans.*, **1997**, (24), 4747-4752.
68. Banerjee, A.; Yuhas, B. D.; Margulies, E. A.; Zhang, Y.; Shim, Y.; Wasielewski, M. R.; Kanatzidis, M. G., *J. Am. Chem. Soc.*, **2015**, *137* (5), 2030-2034.

Chapter 4: N_2 and H_2 binding to the S = ½ Fe(I) complex [Fe(depe)$_2$][BArF$_{24}$]

4.1 Introduction

The coordination of N_2 and H_2 to low valent Fe has received considerable attention as fundamental processes in the transformations of these basic molecules performed by nitrogenase and hydrogenase enzymes.[1] Historically, the greater accessibility of Fe(0) and Fe(II) model complexes has directed focus onto these systems, which are also typically more amenable to spectroscopic analysis than paramagnetic and often unstable Fe(I) species. However, Fe(I) is increasingly being recognised to play a pivotal role in the chemistry of the hydrogenase enzyme; furthermore, Fe(I) has also been shown to be pervasive in the N_2 fixation chemistry explored in the previous chapter. Peters *et al.* have recently demonstrated reduction of an Fe(II) ammonia complex to Fe(I) triggers N_2 uptake and quantitative release of NH_3 (Figure 4.1) which is a key transformation in a viable catalytic N_2 fixation cycle.[2] Thus, a greater understanding of the ability of Fe(I) to bind N_2 and H_2 is highly desirable.

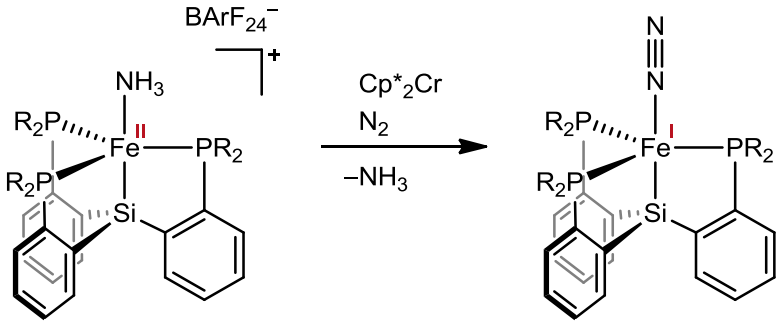


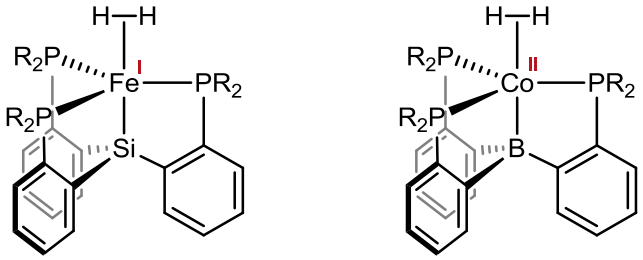
Figure 4.1 N_2 uptake and NH_3 release of an Fe(II) complex upon reduction to Fe(I), reported by Peters *et al.*.[2]

An important area that remains relatively unexplored, is the coordination of H_2 to open-shell transition metal complexes; only a handful of such complexes have been reported, and thoroughly characterised examples are extremely rare.[3-6] For closed-shell H_2 complexes, structural characterisation is typically provided by NMR spectroscopy on the basis of ^{1}H relaxation times (T_1) and $J_{H–D}$ coupling constants, whereby rapid dipole-dipole relaxation (T_1 ca. <150 ms) and $J_{H–D}$ values of between 10-35 Hz are typical of a σ-H_2 adduct.[7] However, this approach is not amenable to paramagnetic complexes due to the extreme line broadening expected for resonances of directly bound H.[4] Furthermore, it is often not

possible to resolve metal bound H_2 by single crystal X-ray diffraction due to its proximity to the metal, whilst fluxionality and rotation along the Fe–(η^2-H_2) bond axis can be expected to further obscure the electron density map.

Hoffman *et al.* have recently demonstrated the use of electron-nuclear double resonance (ENDOR) for measuring the hyperfine coupling to the H nuclei in proposed paramagnetic (S = ½) σ-H_2 complexes of Fe(I) and Co(II) (Figure 4.2(a)).[4, 6] The extent of H_2 activation is manifested in an increased H–H separation and a greater angle between Fe–H vectors and the g_1 principal axis (β), with oxidative addition leading to two Fe–H bonds in the extreme case (Figure 4.2(b)). By comparing simulated spectra of differing β with experimental data they confirmed a relatively weak hyperfine coupling to H in both cases, consistent with a small β and thus a σ-H_2 ligand.

(a)



(b)

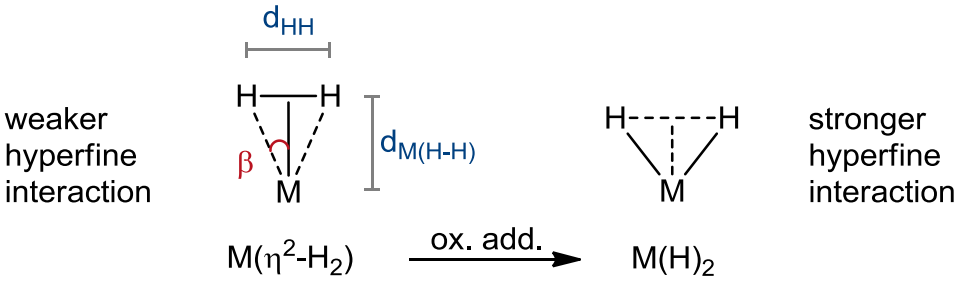


Figure 4.2 (a) Proposed σ-H_2 complexes of Fe(I) and Co(II), reported by Hoffman *et al.*;[4, 5] (b) the increase in H–H separation and the angle between Fe–H vectors and the g_1 principal axis (β) as an indication of H_2 activation.

The Fe(I) complex [Fe(depe)$_2$][BArF$_{24}$] (**13**) may be expected to demonstrate interesting coordination chemistry in view of its open-shell 15 VE configuration, low coordination number, and low oxidation state of Fe(I). As discussed in Chapter 3, solutions of **13** *in vacuo* or under Ar are an intense blue colour, whereas under N_2 these solutions appear less intense and change colour to yellow upon cooling. Admittance of H_2 to **13** dissolved in the aprotic, non-coordinating solvent 1,2-DFB, results in a green solution. These interconversions are conveniently discerned by UV-vis and ^{1}H NMR spectroscopy (Figure

4.3-4.4), and are proposed to involve formation of the σ-coordinated N_2 and H_2 complexes of **13**, $[Fe(N_2)(depe)_2][BArF_{24}]$ (**13-N_2**) and $[Fe(\eta^2\text{-}H_2)(depe)_2][BArF_{24}]$ (**13-H_2**).

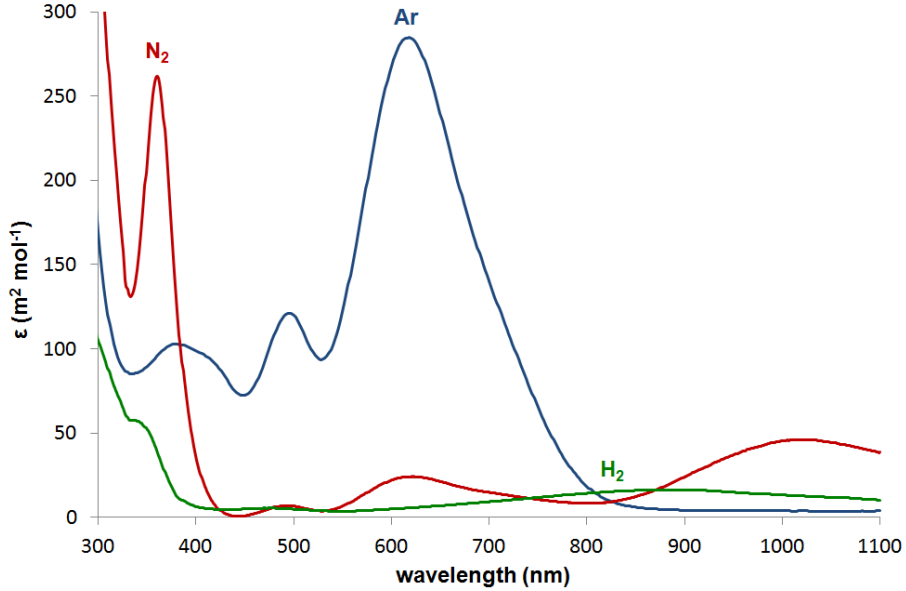


Figure 4.3 UV-vis spectra of **13** under Ar (blue), N_2 (red), and H_2 (green) atmosphere in 1,2-DFB at 293 K.

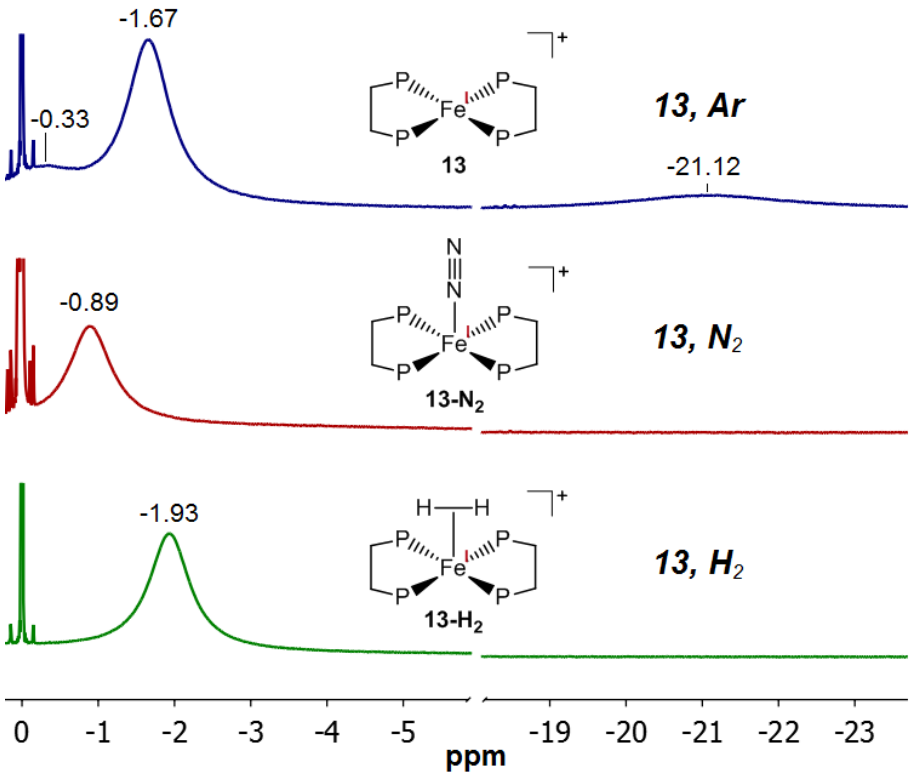


Figure 4.4 High field region of the ^{1}H NMR spectra of **13** in 1,2-DFB under Ar (1 bar, blue), N_2 (4 bar, red), and H_2 (4 bar, green); referenced to $SiMe_4$ (δ = 0) in the insert capillary.

4.2 Reversible N_2 binding to 13

13 was prepared by oxidation of **12** wherein N_2 coordinated to Fe(0) is labilised upon oxidation to Fe(I) and readily dissociates upon removal of solvent *in vacuo*. To elucidate the energetics of N_2 binding, variable temperature (VT) UV-vis spectroscopy was used to monitor the concentration of **13** under a N_2 atmosphere in the range 25-75 °C (THF, 1 bar N_2, Figure 4.5). This enabled a Van't Hoff analysis of K to obtain the thermodynamic parameters: K_{298} = 3934.1 M^{-1}, ΔH^{o} = –12.8 kcal mol^{-1}, and ΔS^{o} = –26.6 cal K^{-1} mol^{-1}. As expected, N_2 binding is exothermic and associated with a negative entropy; the values obtained are similar to those recently reported for N_2 coordination in Fe(II) and Co(II) complexes.[5, 8]

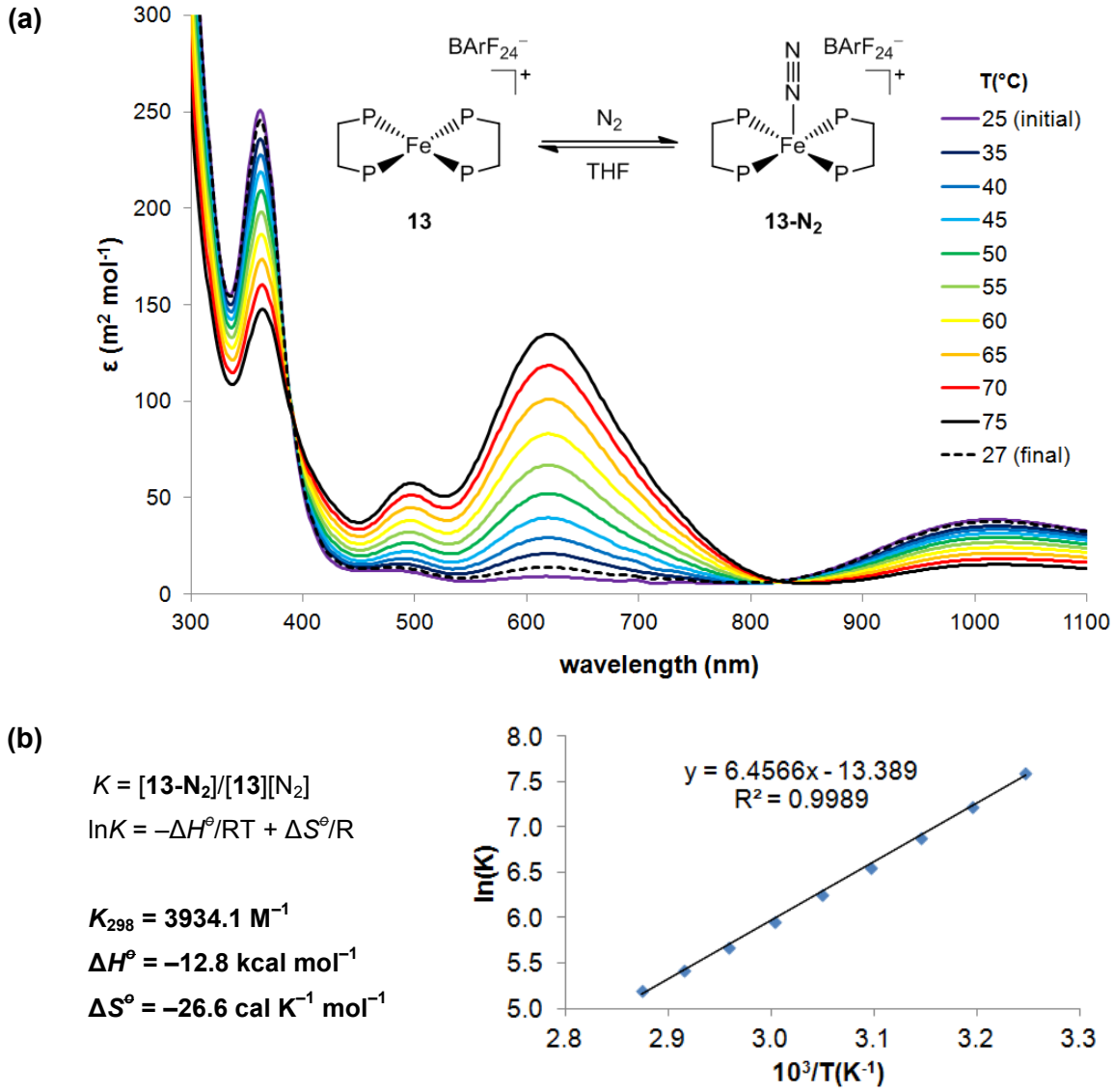


Figure 4.5 (a) Variable-temperature UV-vis spectra of **13** in THF under 1 bar N_2; (b) Van't Hoff plot derived from changes in the absorbance at 618 nm between 35-75 °C; the concentration of N_2 in THF was taken to be 6.4 mM using solubility data from ref. 9.

X-band CW-EPR spectroscopy performed on a 1,2-DFB glass of **13** under an Ar atmosphere produced a rhombic signal with an average g-value of 1.94 (g = [1.9900, 2.2352, 2.4768], g_{av} = $\{(g_x^2 + g_y^2 + g_z^2)/3\}^{½}$) consistent with a low-spin Fe(I) (S = ½) metal-based radical (Figure 4.6(a)). Under N_2 atmosphere, an almost axial signal is observed (g = [2.0014, 2.0922, 2.1250], g_{av} = 2.07) in which some hyperfine coupling to the four ^{31}P nuclei is resolved (Figure 4.6(b)). Although use of 1,2-DFB is ideal as an innocent, non-donor solvent, it leads to spin aggregation and corresponding broad linewidths from fast relaxation; whereas in THF glass the N_2-adduct was much better resolved (Figure 4.7). The absence of a corresponding half-field triplet dimer signal (see section 3.1.4) for this axial signal is consistent with the assignment of **13-N$_2$** as a monomeric N_2 complex.

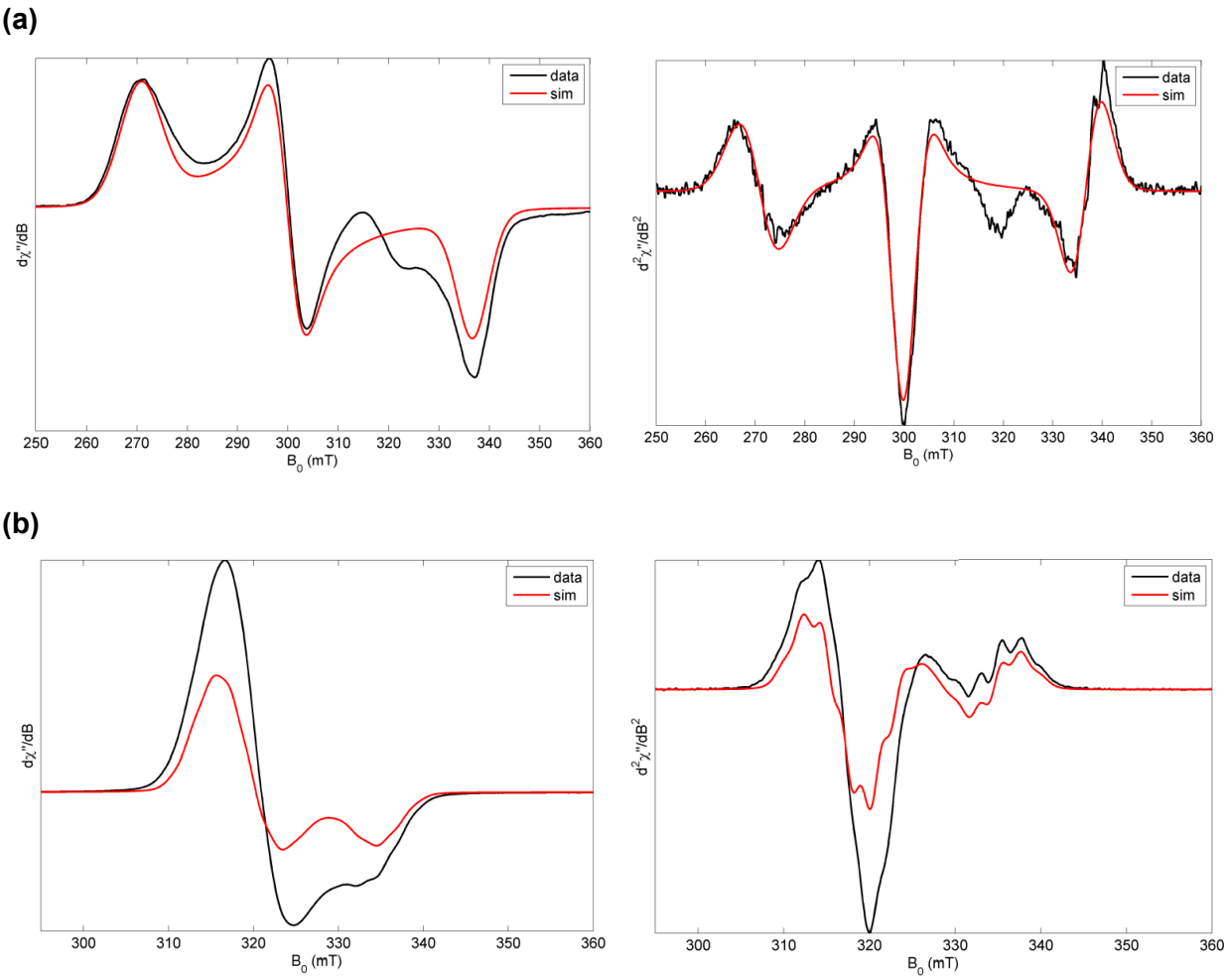


Figure 4.6 X-band CW-EPR spectra of (a) **13** (1,2-DFB, Ar); and (b) **13-N$_2$** (1,2-DFB, N_2); recorded as glasses at 40 K; first (LHS) and second (RHS) derivative spectra; black traces: experiment; red traces: simulation.

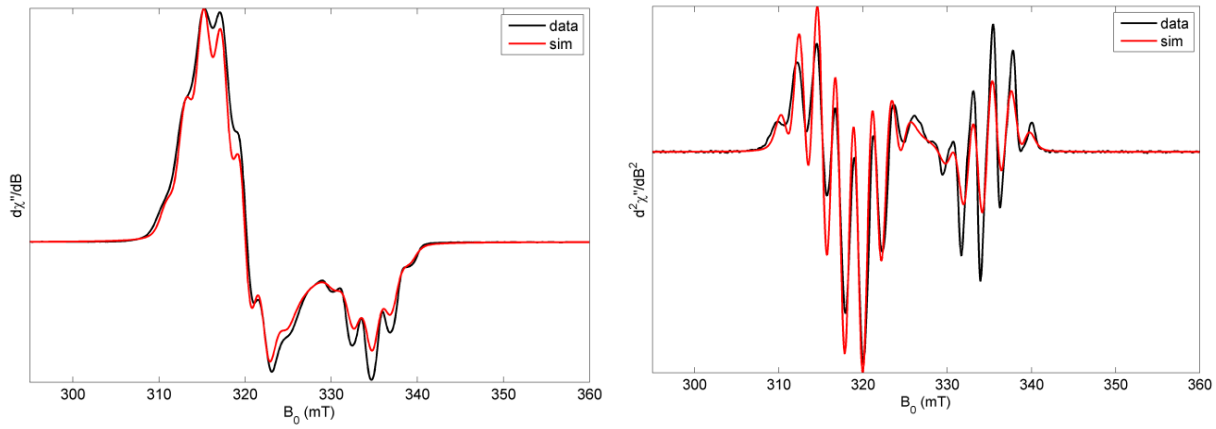


Figure 4.7 X-band CW-EPR spectra of **13-N$_2$** (**13**, THF, N_2) recorded as glasses at 40 K; first (LHS) and second (RHS) derivative spectra; black traces: experiment; red traces: simulation.

Greater understanding of these weak ligand interactions was sought using pulsed EPR spectroscopy, for which it was found that a toluene/1,2-DFB (7:1) glass mixture gave a much improved echo response than neat 1,2-DFB. For the adduct-free complex **13**, the apparent positioning of two of the ligand ethyl groups towards the axial sites of the Fe coordination sphere in the crystal structure was thought to be a possible indication of a favourable C–H agostic or anagostic interaction, rather than for steric reasons alone (Figure 4.8).[10] An average of the four shortest Fe–H$_\beta$ distances estimated by crystallography of 3.099 Å approaches that of an anagostic bond, which is characterised by a largely electrostatic interaction, as opposed to an agostic, 3-centre-2-electron bond.

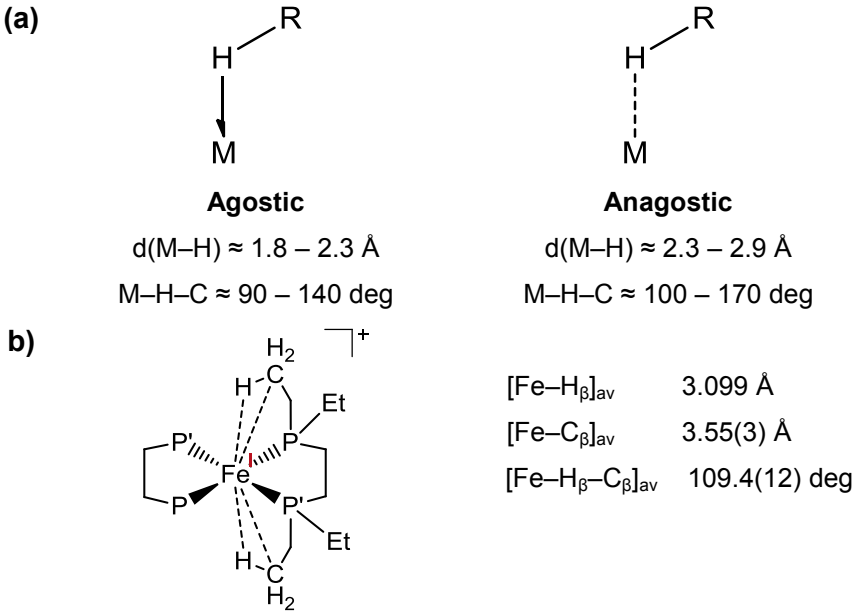


Figure 4.8 (a) Agostic and anagostic interactions, adapted from ref. 10; (b) possible anagostic interaction in **13** between Fe and a H$_\beta$ on each of the four P donor groups; experimental values determined by single crystal X-ray diffraction.

The DFT-optimized structure of **13** (Figure 4.9(a)) in a non-coordinating gas provides a similar bond distance of 3.104 Å, which can be estimated to provide a hyperfine splitting of 2.64 MHz between the Fe-centred radical and the $^1H_\beta$ nuclei (assuming a purely dipolar interaction). The two broad shoulders in the Mims ENDOR spectra of **13** under Ar (Figure 4.9(b)) thus appear to be consistent with a weak hyperfine interaction with the "over-hanging" β-protons on the ligand. Simulation of these varied field measurements are currently being pursued in order to further establish the coordination environment at the Fe centre.

(a) **(b)**

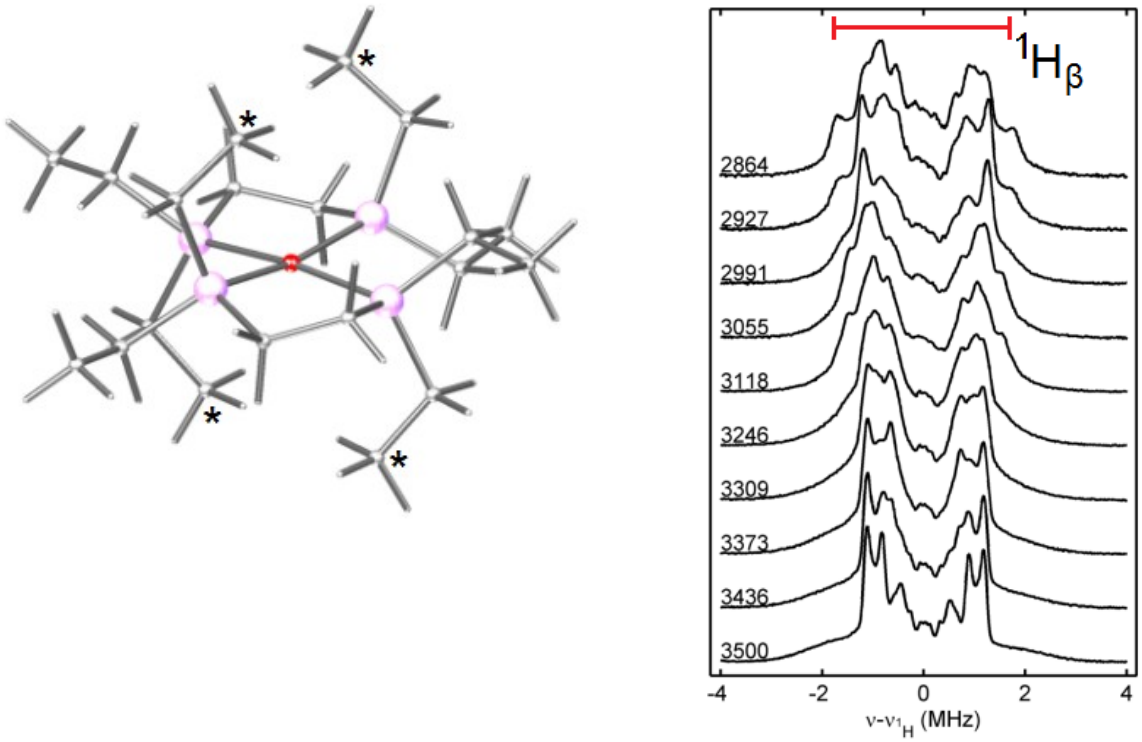


Figure 4.9 (a) The DFT-optimized structure of **13** in a non-coordinating gas; * marks the beta-C of the four Et groups pivoted towards the apical sites; (b) Mims ENDOR of **13** (toluene/1,2-DFB (7:1), Ar (1 bar)); recorded at 20 K, with field values as indicated; the microwave frequency was 9.7464 GHz.

Coordination of N_2 to **13** was further corroborated through HYSCORE experiments performed on equivalent solutions under $^{14}N_2$ and $^{15}N_2$ atmosphere (Figure 4.10(a)). A strong isotropic hyperfine coupling of 14.2 MHz in the intense double quantum dq,dq correlation peaks in the (-,+) quadrant corresponds to the ^{14}N directly bound to Fe(I), whilst the HYSCORE of the sample under $^{15}N_2$ displays the corresponding hyperfine coupling to ^{15}N (Figure 4.10(b)).

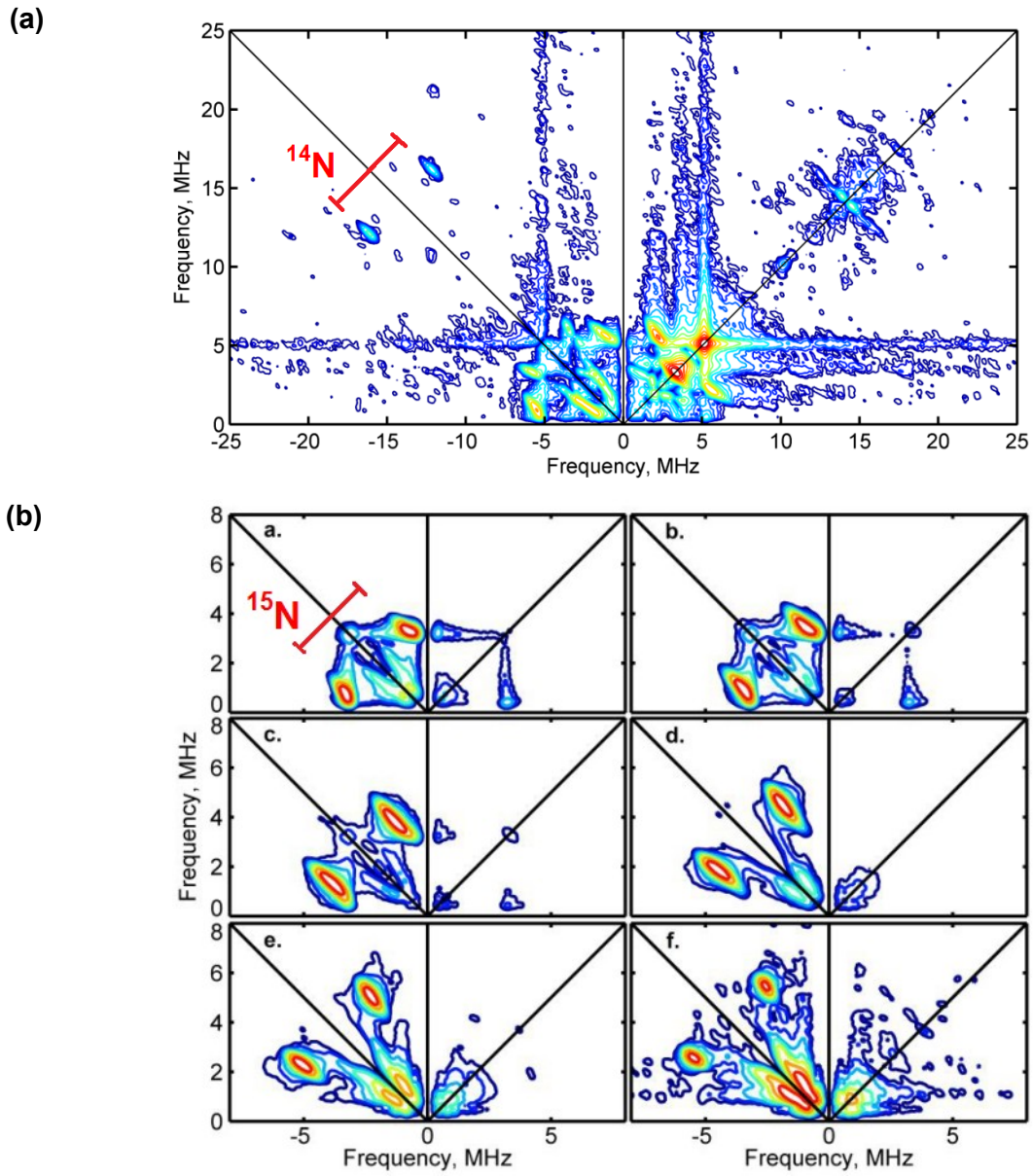


Figure 4.10 Pulsed EPR measurements of **13-$^{14/15}$N$_2$** (toluene:1,2-DFB (7:1), under $^{14/15}N_2$) as a glass at 40 K. (a) HYSCORE of **13-^{14}N$_2$**, at 3309 G with a microwave frequency of 9.7469 GHz (b) HYSCORE of **13-^{15}N$_2$** at several field positions: a. 3261 G, b. 3304 G, c. 3348 G, d. 3392 G, e. 3436 G, and f. 3480 G, with a microwave frequency of 9.7615 GHz.

4.3 Reversible H_2 binding to 13

Coordination of H_2 to a transition metal complex typically results in oxidative addition to form a classical dihydride complex; in the absence of homolytic H–H bond scission, a "non-classical" dihydrogen adduct results.[11] Notably, for the dihydride species *cis*-Fe(H)$_2$(PP)$_2$ (PP = dmpe and depe), protonation yields the Fe(II) complex *trans*-Fe(H)(η^2-H$_2$)(PP)$_2$ in which two hydrides can undergo reductive elimination to form a σ-H_2 ligand, which is reversible and

leads to chemical equivalence between all three hydrides (Figure 4.11).[12] As discussed in Chapter 3, a marked increase in the acidity of the hydride ligand is conferred upon σ-coordination of H_2 and π-backbonding from the metal into σ*(H–H). In addition, σ-H_2 is labile and may be displaced by N_2, as utilised in the Leigh cycle.[13] In contrast, Fe(0) is presumably too π-basic to stabilise Fe(η^2-H_2)(PP)$_2$ and thus displacement of N_2 in **4** or **12** with H_2 irreversibly forms the dihydride oxidative addition product.

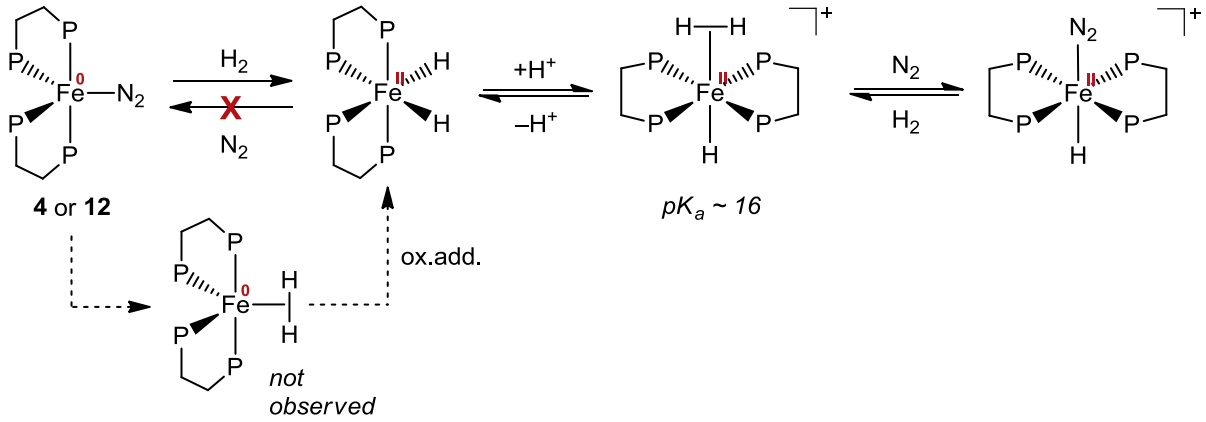


Figure 4.11 Interconversions of N_2 and hydride complexes of Fe(0) and Fe(II); P = PMe_2, PEt_2.

The solid-state structure of *trans*-Fe(H)(η^2-H_2)(dmpe)$_2$ has been solved by X-ray diffraction, although the H atom positions could not be located.[14] However, NMR spectroscopic analysis of T_1 values and $J_{H–D}$ coupling constants for this LS Fe(II) diamagnetic complex has provided an adequate description of the σ-H_2 bonding mode.[14] Whilst this approach is not amenable to studying the interaction between H_2 and paramagnetic **13**, a combination of EPR, ENDOR, IR, and UV-vis spectroscopy has been employed to investigate the binding affinity and coordination mode of H_2 in this system.

The addition of H_2 (1–4 bar) to degassed 1,2-DFB solutions of **13** resulted in an immediate colour change from blue to pale green, concurrent with the disappearance of one of the broad resonances in the ^{1}H NMR spectrum and a shift of the other to –1.93 ppm (Figure 4.4); the solution remains ^{31}P NMR silent and no further changes are observed after 15 h at RT. The blue solution of **13** is reformed upon degassing indicating reversible coordination of a labile σ-H_2 ligand in **13-H$_2$**, which is in equilibrium with **13** (Figure 4.12(a)); although reversible oxidative addition to form a hypothetical Fe(III) complex [Fe(H)$_2$(depe)$_2$][BArF$_{24}$] is a possibility, pulsed EPR measurements indicate the H–H bond remains intact (*vide infra*).

13-H$_2$ is characterised by a weak, broad electronic absorption at 850 nm (19 m^2 mol^{-1}) in 1,2-DFB; by heating the solution, it was possible to regenerate the absorption bands of **13** through dissociation of H_2 (Figure 4.12(b)). Although **13-H$_2$** was reformed upon subsequent

re-cooling to 20 °C, indicating reversibility, it was not possible to perform a Van't Hoff analysis due to experimental difficulties related to quantifying the H_2 concentration within the quartz UV-vis cuvette.

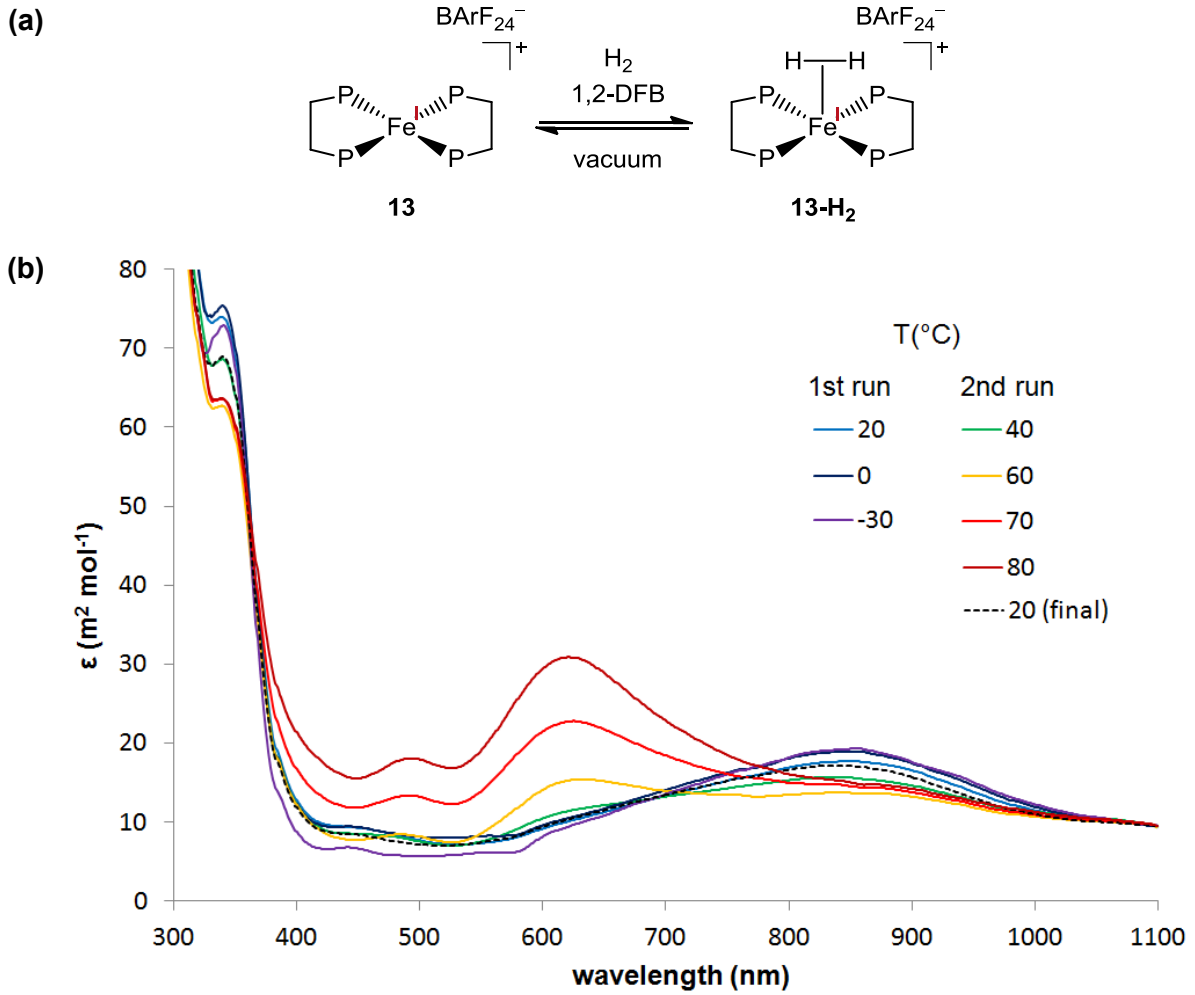


Figure 4.12 (a) Reversible H_2 binding to **13**. (b) Variable-temperature UV-vis spectra of **13** in 1,2-DFB under an Ar/H_2 mixture from 20 to –30 °C, then up to 80 °C.

In contrast, in THF or Et_2O solvent, the initially formed green solution converts rapidly to the known diamagnetic Fe(II) species [*trans*-Fe(H)(η^2-H_2)(depe)$_2$]$^+$ (see section 3.2.7), which exhibits a characteristically broad ^{1}H NMR resonance at –11 ppm resulting from fluxionality of H^-/H_2 ligands, and a sharp signal at 93 ppm in the ^{31}P NMR.[12] The difference in reactivity may be explained by the increased acidity of H_2 as a consequence of σ-donation to Fe(I); a weakly basic donor solvent may thus abstract H^+ inducing H_2 heterolysis to form a strong Fe–H bond and protonated solvent (Figure 4.13). The resultant Fe(I) species Fe(H)(depe)$_2$ (**15**) may convert under H_2 to *cis*-Fe(H)$_2$(depe)$_2$ (analogous to Fe(H)(dmpe)$_2$ (**10**)), which is susceptible to acidification by protonated solvent to form [*trans*-Fe(H)(η^2-H_2)(depe)$_2$]$^+$ (pK_a ~ 19). Importantly, it appears that in donor solvents, H_2 is converted to hydride and proton equivalents, whereas in non-donor 1,2-DFB no basic species are present to perform proton

transfer chemistry. However, in some cases, slow decomposition to [*trans*-Fe(H)(η^2-H_2)(depe)$_2$]$^+$ was observed in 1,2-DFB solvent, which is thought to be catalysed by trace amounts of H_2O in the H_2 gas that could similarly enable proton transfer.

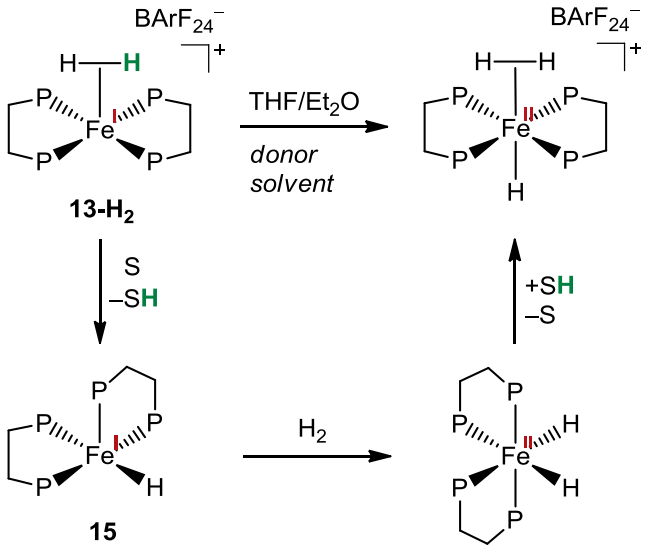


Figure 4.13 Reactions of **13** with H_2 in donor THF or Et_2O solvents.

The X-band CW-EPR spectra of **13-H$_2$** was measured in both the solid state (*vide infra*) and as a toluene/1,2-DFB (7:1) frozen glass. Prior to freezing, addition of H_2 (1 bar) to a degassed solution of **13** resulted in complete conversion to a new S = ½, near axial signal (g = [2.000, 2.085, 2.160], g_{av} = 2.08; Figure 4.14) with slightly more pronounced splitting of g_2 and g_3 than for **13-N$_2$**. The reversibility of H_2 and N_2 binding was further demonstrated by the interconversion of **13**, **13-N$_2$** and **13-H$_2$** through alteration of the atmosphere (Ar, N_2, or H_2, all 1 bar) in the head space of the EPR tube and subsequent thawing/re-freezing of the solution. The observable similarity in the CW-EPR spectra of **13-N$_2$** and **13-H$_2$** indicates a similar 5-coordinate environment for both complexes, consistent with the H_2 moiety being a σ-donor type ligand rather than two terminal hydrides.

Preliminary ^{1}H Davies ENDOR and HYSCORE experiments performed on **13-H$_2$** (Figure 4.15) reveal a hyperfine splitting of 17 MHz, consistent with an electron-^{1}H coupling interaction. This is a weaker interaction than that measured by Hoffman *et al.* for the proposed σ-H_2 complexes {Si(*o*-$C_6H_4P^iPr_2)_3$}Fe(η^2-H_2) and {B(*o*-$C_6H_4P^iPr_2)_3$}Co(η^2-H_2) (37.8 MHz and 20.8 MHz, respectively; Figure 4.2),[4, 6] which strongly supports the assignment of **13-H$_2$** as a σ-H_2 complex, rather than a dihydride species. Simulations of the experimental Davies ENDOR spectra are in progress, which will provide a more detailed understanding of the Fe–(σ-H_2) interaction.

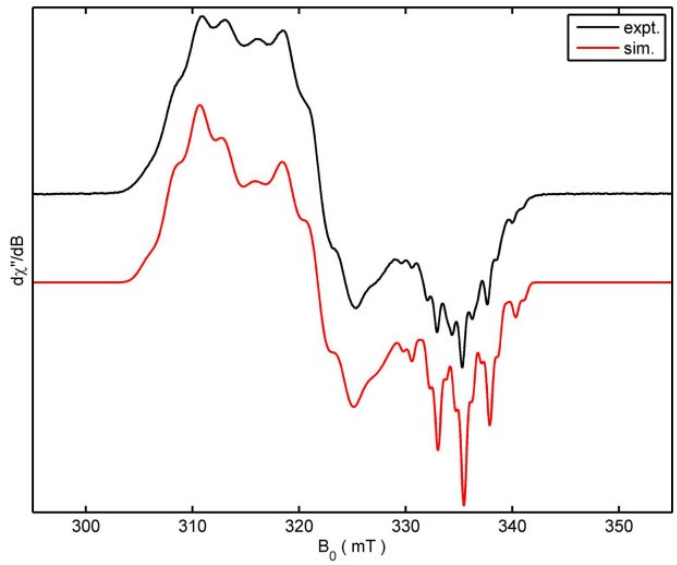


Figure 4.14 X-band CW-EPR spectra of **13-H_2** (**13**, toluene/1,2-DFB (7:1), H_2 (1 bar)); recorded at 40 K. Black trace: experiment; red trace: simulation.

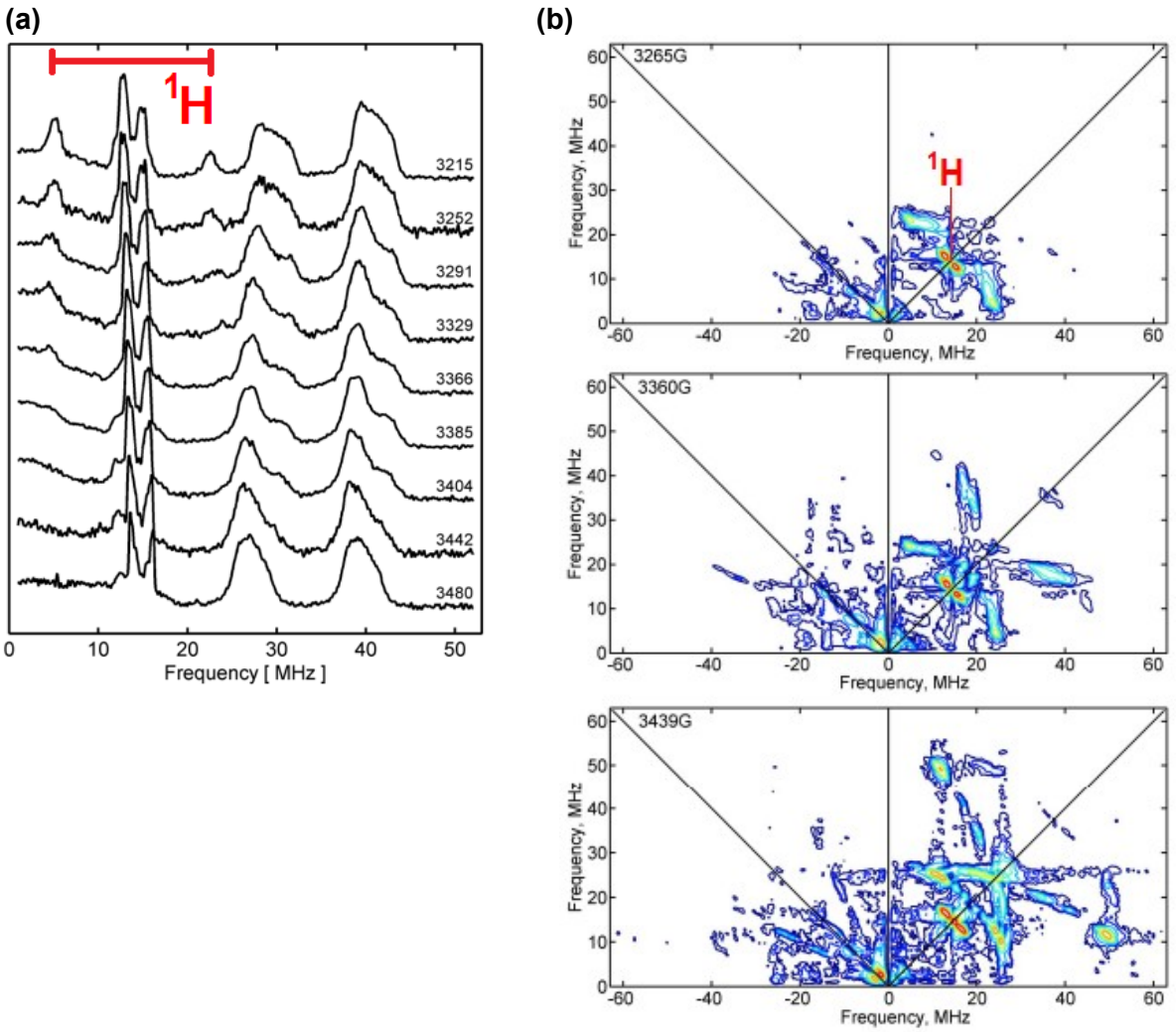


Figure 4.15 (a) Field-dependent X-band Davies ENDOR spectra of **13-H_2** (**13**, toluene/1,2-DFB (7:1), H_2 (1 bar)); recorded at 20 K, with field values as indicated; (b) X-band HYSCORE of **13-H_2** (toluene:1,2-DFB (7:1) glass, H_2) collected at 20 K, with field values as indicated.

4.4 Solid-state reactions of 13 with H_2

Heterogeneous reactions of **13** with H_2 have also been performed with **13** in both powder and crystalline forms; reversibility was confirmed by solid-state EPR and UV-vis spectroscopy.

Solid-state UV-vis spectroscopy was performed on a microcrystalline sample of **13** under both Ar and H_2 atmospheres (ca. 1 bar) between 200 and 700 nm utilising a diffuse reflectance accessory. Under an Ar atmosphere, broad absorption features were resolved at 270, 414, 493 and 594 nm, which appear shifted from the corresponding solution (300 nm cut-off) bands at 378, 414, 496, and 618 nm (1,2-DFB), possibly due to scattering effects. Subsequent evacuation and admittance of H_2 (ca. 1 bar) resulted in a new spectrum with absorption bands at 270 and 472 nm along with broad unresolved features between 300-400 nm (Figure 3.16); a final spectrum was recorded *in vacuo* after removal of H_2, which appears to closely resemble the initial spectrum under Ar atmosphere (absorbance may vary as a result of sample displacement during gas transfer). The reversibility of these measurements is consistent with the formation of a σ-H_2 complex (**13-H_2**), incorporating labile H_2.

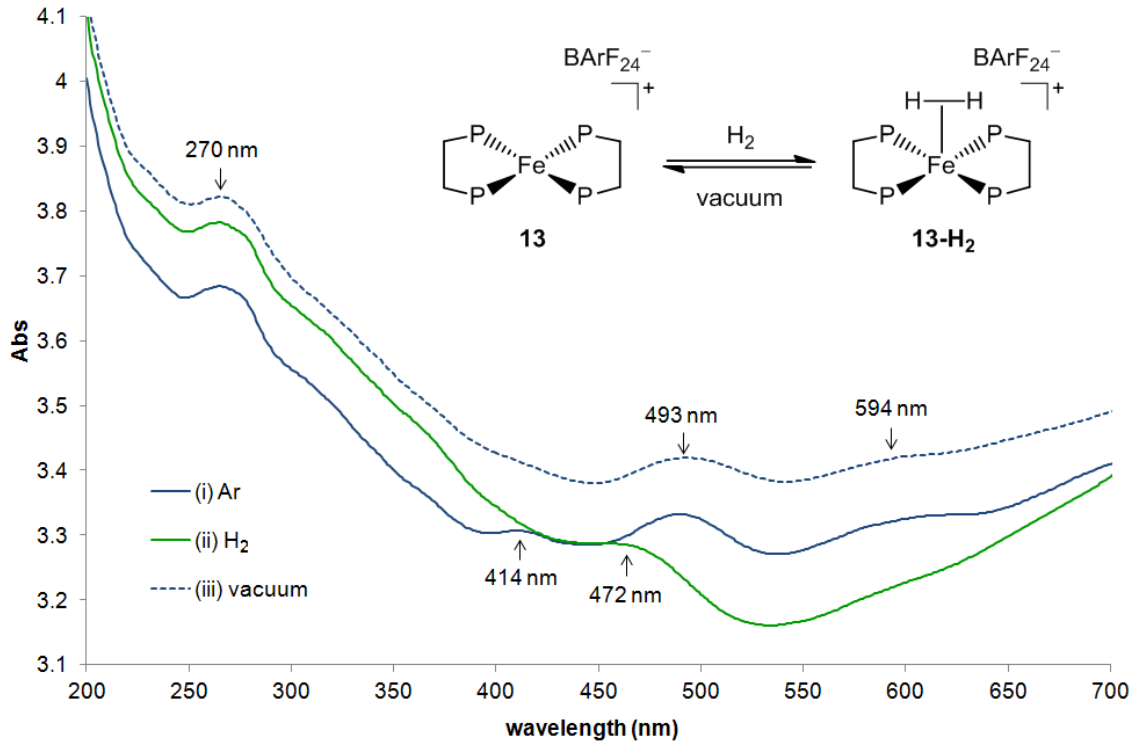


Figure 4.16 Solid-state UV-vis spectra of **13** under Ar (blue), under H_2 (green) and *in vacuo* after H_2 addition (dotted blue).

X-band CW-EPR spectroscopy was performed on a powdered sample of **13** under Ar (1 bar), which was subsequently evacuated and replaced by H_2 (1 bar), resulting in a colour

change from blue to pale green. The resultant spectra resemble the corresponding solution measurements with an expected signal broadening and a slight field shift (Figure 3.17). Integration of the Fe(I) absorption signals prior to and after addition of H_2 gave a ratio of 1:0.91, indicating almost quantitative conversion of **13** to **13-H$_2$**; the small loss of Fe(I) is thought to be due to protonation from adventitious moisture introduced by the H_2 gas. Since the reaction of **13** with H_2 proceeds reversibly in the solid state, in which significant bond displacement is not possible, the coordination geometry of the depe ligands in **13** can thus be expected to remain pseudo square planar upon coordination of H_2. Furthermore, the close resemblance between solid and solution spectra indicates this to also be the case *in situ*.

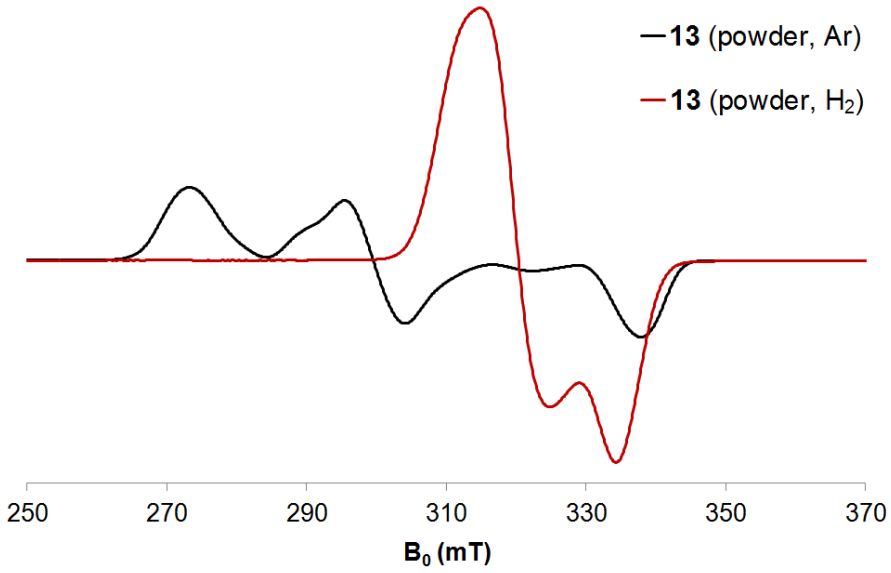


Figure 4.17 X-band CW-EPR spectra of a powdered sample of **13** under Ar (1 bar, black) and H_2 (1 bar, red) atmosphere, recorded at 40 K.

Crystalline samples of **13** also undergo a blue to pale green colour change upon admission of H_2, prompting us to attempt single crystal solid-state transformations, and thus obtain a crystallographic structural solution of **13-H$_2$**. Unfortunately, incorporation of H_2 into the crystal lattice was found to introduce significant disorder, which coupled with the poor X-ray diffracting ability of a σ-H_2 ligand proximal to Fe, has prevented adequate solution refinement. Attempts to obtain larger crystals suitable for neutron diffraction measurements are underway. Similarly, admittance of N_2 to single crystals of **13** results in a colour change from blue to yellow, although significant disorder within the unit cell has thus far prevented a satisfactory structural solution.

4.5 Concluding remarks

13 is a coordinatively unsaturated 15 VE Fe(I) complex, which has been demonstrated to reversibly bind both N_2 and H_2; the resultant σ–L type complexes are among very few well-characterised paramagnetic $M(N_2)$ and $M(H_2)$ species. Related Fe(I) fragments of the type $[Fe(diphosphine)_2]^+$ are prevalent in the chemistry discussed in Chapter 3; an understanding of the N_2 and H_2 coordination chemistry of **13** has therefore been crucial in spectroscopically analysing the complex reaction mixtures in which they are formed.

The N_2 binding affinity of **13** has been calculated to be exothermic and associated with a negative entropy, consistent with the observed dissociation of N_2 upon warming. This contrasts with the much stronger binding affinity of the Fe(0) N_2 complex **12**, in which N_2 is non-labile. A theoretical DFT treatment of these two complexes is being sought in order to elucidate the influence of the coordination geometry and electronic configuration of the Fe centre on the strength of the Fe–N interaction, as well as the extent of N_2 activation.

Under a H_2 atmosphere, the Fe(I) σ–H_2 complex **13-H_2** is stable in non-donor 1,2-DFB solvent, reflecting the lower π-basic character of **13** relative to $[Fe^0(depe)_2]$ in **12**, for which displacement of N_2 with H_2 results in H–H bond homolysis (oxidative addition) and oxidation of Fe(0) to Fe(II). Deprotonation of the acidic σ–H_2 ligand in **13-H_2** is thought to occur in the presence of weak Lewis bases, resulting in the formation of a known Fe(II) *tris*-hydride species. In this manner, H_2 is converted into hydride and proton equivalents, which is being explored for related N_2 fixation chemistry.

4.6 References

1. a) Tard, C.; Pickett, C. J., *Chem. Rev.*, **2009**, *109* (6), 2245-2274; b) Gloaguen, F.; Rauchfuss, T. B., *Chem. Soc. Rev.*, **2009**, *38* (1), 100-108; c) Vincent, K. A.; Parkin, A.; Armstrong, F. A., *Chem. Rev.*, **2007**, *107* (10), 4366-4413; d) Smith, J. M.; Sadique, A. R.; Cundari, T. R.; Rodgers, K. R.; Lukat-Rodgers, G.; Lachicotte, R. J.; Flaschenriem, C. J.; Vela, J.; Holland, P. L., *J. Am. Chem. Soc.*, **2006**, *128* (3), 756-769; e) Holland, P. L., *Can. J. Chem.*, **2005**, *83* (4), 296-301; f) Betley, T. A.; Peters, J. C., *J. Am. Chem. Soc.*, **2004**, *126* (20), 6252-6254; g) Mankad, N. P.; Whited, M. T.; Peters, J. C., *Angew. Chem. Int. Ed.*, **2007**, *46* (30), 5768-5771; h) Brown, S. D.; Betley, T. A.; Peters, J. C., *J. Am. Chem. Soc.*, **2003**, *125* (2), 322-323.
2. Lee, Y.; Mankad, N. P.; Peters, J. C., *Nature Chem.*, **2010**, *2* (7), 558-565.
3. a) Kubas, G. J., *Chem. Rev.*, **2007**, *107* (10), 4152-4205; b) Bart, S. C.; Lobkovsky, E.; Chirik, P. J., *J. Am. Chem. Soc.*, **2004**, *126* (42), 13794-13807; c) Baya, M.; Houghton, J.; Daran, J.-C.; Poli, R.; Male, L.; Albinati, A.; Gutman, M., *Chem. Eur. J.*, **2007**, *13* (19), 5347-5359; d) Hetterscheid, D. G. H.; Hanna, B. S.; Schrock, R. R., *Inorg. Chem.*, **2009**, *48* (17), 8569-8577; e) Kinney, R. A.; Hetterscheid, D. G. H.;

Hanna, B. S.; Schrock, R. R.; Hoffman, B. M., *Inorg. Chem.*, **2010**, *49* (2), 704-713.

4. Lee, Y.; Kinney, R. A.; Hoffman, B. M.; Peters, J. C., *J. Am. Chem. Soc.*, **2011**, *133* (41), 16366-16369.
5. Suess, D. L. M.; Tsay, C.; Peters, J. C., *J. Am. Chem. Soc.*, **2012**, *134* (34), 14158-14164.
6. Gunderson, W. A.; Suess, D. L. M.; Fong, H.; Wang, X.; Hoffmann, C. M.; Cutsail, G. E., III; Peters, J. C.; Hoffman, B. M., *J. Am. Chem. Soc.*, **2014**, *136* (42), 14998-15009.
7. Jessop, P. G.; Morris, R. H., *Coord. Chem. Rev.*, **1992**, *121*, 155-284.
8. Rittle, J.; McCrory, C. C. L.; Peters, J. C., *J. Am. Chem. Soc.*, **2014**, *136* (39), 13853-13862.
9. Battino, R.; Rettich, T. R.; Tominaga, T., *J. Phys. Chem. Ref. Data*, **1984**, *13* (2), 563-600.
10. Brookhart, M.; Green, M. L. H.; Parkin, G., *Proc. Natl. Acad. Sci. U.S.A.*, **2007**, *104* (17), 6908-6914.
11. a) Morris, R. H., *Recent Advances in Hydride Chemistry*, Poli, M. P., Ed., Elsevier, Amsterdam, **2001**, 1-38; b) Crabtree, R. H., *The Organometallic Chemistry of the Transition Metals*, John Wiley & Sons, Inc., **2005**, 53-85.
12. Baker, M. V.; Field, L. D.; Young, D. J., *J. Chem. Soc., Chem. Commun.*, **1988**, (8), 546-548.
13. Leigh, G. J.; Jimenez-Tenorio, M., *J. Am. Chem. Soc.*, **1991**, *113* (15), 5862-5863.
14. Hills, A.; Hughes, D. L.; Jimenez-Tenorio, M.; Leigh, G. J.; Rowley, A. T., *J. Chem. Soc., Dalton Trans.*, **1993**, (20), 3041-3049.

Chapter 5: Experimental

5.1 General procedures

All chemical manipulations were performed under a N_2 atmosphere either using standard Schlenk-line techniques or a MBraun Labmaster DP glovebox, unless stated otherwise. Solvents were purchased from VWR: pentane, hexane, heptane, toluene, CH_2Cl_2, and $CHCl_3$ were dried using an Innovative Technology Pure Solv™ SPS-400; THF and Et_2O were distilled from dark green Na/fluorenone indicator. Solvents were degassed by thorough sparging with N_2 or Ar gas and stored in gas-tight ampoules over suitable drying agents: CH_2Cl_2, $CHCl_3$, 1,4-dioxane (4 Å molecular sieves); 2-butanol (3 Å molecular sieves); Et_2O, aliphatics, aromatics (K mirror). Deuterated solvents were freeze-thaw degassed, dried, and stored in gas-tight ampoules over suitable drying agents: C_6D_6 (Sigma-Aldrich, 99.6% D; K mirror); $CDCl_3$ (Merck, 99.8% D; 4 Å molecular sieves); DMSO-d^6 (VWR, 99.5%; 4 Å molecular sieves). H_2 (BOC, 5.5 Research Grade) was dried by passage through a NANOCHEM® WA-500 OMX™ purifying column. $^{15}N_2$ (Cambridge Isotope Laboratories, 98% ^{15}N) was transferred from a breakseal flask using a Toepler pump (see Appendix).

NMR spectra were recorded using Bruker AV-400 (400.4 MHz) spectrometers. Chemical shifts, δ, are reported in parts per million (ppm). ^1H and $^{13}C\{^1H\}$ chemical shifts are given relative to Me_4Si and referenced internally to the residual proton shift of the deuterated solvent employed. ^{27}Al, ^{31}P and ^{15}N chemical shifts were referenced (δ = 0) externally to 1 M $AlCl_3$ (aq), 85% H_3PO_4 (aq), and neat nitromethane, respectively. ^1H and ^{31}P NMR spectra of solutions prepared in non-deuterated solvents incorporate an internal reference capillary containing a solution of ca. 0.1 M PPh_3 in C_6D_6 and are referenced to residual C_6H_6 and PPh_3 resonances, respectively. Air or moisture sensitive samples were prepared inside the glovebox using NMR tubes fitted with J. Young valves.

Infrared (IR) spectra were recorded using a Perkin Elmer FT-IR Spectrum GX spectrometer either as Nujol mulls, KBr pellets, or solutions. To form KBr pellets, the sample was combined with KBr (Sigma, FT-IR grade) and ground to a powder, which was transfered into an air-tight Specac® die inside the glovebox. A Specac® manual hydraulic press was then used outside the glovebox to press the pellet, which was then immediately measured to minimise sample decomposition. Solutions were recorded using an air tight Specac® Omni Cell™ loaded with ca. 0.01 M solutions *via* syringe inside the glovebox. Raman spectra were recorded using a LabRAM Infinity instrument with a 633 nm He-Ne laser. Samples were measured as fine powders deposited on the wall of a quartz UV-cuvette with a fitted J.

Young valve. $^{14}N_2$ stretches were confirmed through comparison with the shifted $^{15}N_2$ stretch of the corresponding ^{15}N isotopically labelled sample, prepared in each case from either $[\{Fe(dmpe)_2\}_2(\mu\text{-}^{15}N_2)]$ or $Fe(^{15}N_2)(depe)_2$ precursors.

Raman spectra were recorded on a LabRAM Infinity instrument (Horiba Jobin-Yvon Ltd., Middlesex, UK) using a He-Ne (red) 633 nm laser, calibrated by reference to the 520.7 nm band of a silicon wafer. Samples were prepared inside an Ar glovebox and deposited as a fine powder on the wall of a sealable quartz cuvette.

Electronic spectra were recorded using either a Perkin Elmer Lambda 20 or 25, or a Shimadzu UV-2101PC UV-visible spectrophotometers. Samples were prepared inside the glovebox using a quartz cuvette with an optical path length of 1 cm and fitted with a J. Young valve. Solid-state UV-vis spectra were recorded by Dr F. Mark Chadwick (Oxford) on an Agilent Cary series 4000, utilising a Pike instruments DiffusIR accessory. Cell loading was performed in an Ar glovebox prior to installing on the instrument, and connected to a vacuum pump and a H_2 gas inlet *via* a swagelock fitting.

CW-EPR spectra were collected by Dr Jeffrey Harmer or Dr William K. Myers in the Center for Advanced ESR (CAESR) in the Inorganic Chemistry Laboratory at the University of Oxford. X-band measurements performed with a Bruker-Biospin Micro EMX^{plus} spectrometer equipped with a PremiumX microwave bridge, a cylindrical TE011 resonator (SHQE-W), an ESR-900 liquid helium cryostat, and an Oxford Instruments ITC-503s temperature controller. Custom simulation scripts for matrix diagonalization were written in MatLab^{TM}.

Single crystal X-ray diffraction data were collected and refined by either Dr. Andrew J. P. White or the author; structures were solved by direct methods using SHELXL.[1] Crystals were mounted on a glass fibre using perfluoropolyether oil and recorded in a stream of N_2 at 173 K with an Oxford Diffraction Xcalibur unit.

Electrochemical experiments were carried out with assistance from Dr Gregory G. Wildgoose (University of East Anglia) using an AutoLab potentiostat controlled by Nova. Measurements were performed inside an Ar or N_2 glovebox on RT Et_2O solutions containing the sample (2 mM) and $[^nBu_4N][BArF_{24}]$ electrolyte (50 mM). A three-electrode configuration was employed: a Pt working electrode (PWE) (BASi, Indiana, USA); a Pt wire counter electrode (99.99 %; GoodFellow, Cambridge, UK); and an Ag wire pseudo-reference electrode (99.99 %; GoodFellow, Cambridge, UK). The PWE and Ag wire were polished using alumina/H_2O, and all electrodes rinsed with Et_2O and dried in a 100 °C oven prior to each measurement. Measurements were calibrated to the ferrocene/ferrocenium couple in

Et_2O at the end of each run, and iR-compensated to within 80 ± 5 % of the solution uncompensated resistance.

A Quantum Design MPMS XL Superconducting Quantum Interference Device (SQUID) magnetometer was used to perform solid-state magnetic measurements, with assistance from Samantha Binding (Oxford). Zero-field-cooled (ZFC) and field-cooled (FC) measurements were recorded between 2 and 300 K in a 1000 Oe field.

High resolution mass spectrometry samples (HRMS; EI & ESI) were recorded using either a Micromass Autospec Premier or a Micromass LCT Premier spectrometer.

Elemental analysis was performed by Mr. S. Boyer of the London Metropolitan University.

5.2 Experimental details for Chapter 2

Diethylphosphite (Sigma-Aldrich, 98%) and 1,2-dichloroethane (Sigma-Aldrich, ≥99.0%) were degassed by thorough sparging with N_2 and stored over 4 Å molecular sieves. Oxalyl chloride (Sigma-Aldrich, 98%), $NaAlH_4$ (Sigma-Aldrich, hydrogen-storage grade) and NaH (60 wt% dispersion in oil) were used as supplied. MeMgCl (3.0 M in THF), EtMgCl (2.0 M in THF), ^{i}PrMgCl (2.0 M in THF), ^{i}BuMgCl (2.0 M in THF), and ^{t}BuLi (1.7 M in pentane) were purchased from Sigma-Aldrich and freshly titrated against *sec*-butanol/1,10-phenanthroline indicator prior to use. 2,6-bis(chloromethyl)pyridine was prepared according to a literature procedure.[2]

1,2-*Bis*(dimethylphosphoryl)ethane (1a). Diethyl phosphite (51.5 mL, 0.40 mol) was added dropwise *via* a dropping funnel to a 3.01 M THF solution of MeMgCl (400 mL, 1.20 mol) at 0 °C. CH_4 gas was evolved during addition and the excess pressure vented *via* a paraffin oil bubbler. The mixture was stirred at 0 °C for 30 min followed by 6 h at RT. The resulting grey suspension was cooled to 0 °C and 1,2-dichloroethane (15.8 mL, 0.201 mol) was added slowly. The mixture was heated to reflux for 12 h yielding a viscous grey suspension which was poured into aqueous K_2CO_3 (166 g, 1.20 mol, 200 mL) and the THF/H_2O mixture removed by decanting. The remaining white precipitate was washed with hot MeOH (6 × 300 mL) and the combined MeOH washings were concentrated *in vacuo*. The oily solid obtained was dissolved in $CHCl_3$ (300 mL) and the solution dried over Na_2SO_4, filtered and evaporated. The resulting solids were dried *in vacuo* at 80°C to yield **1a** as a hygroscopic white powder (30.2 g, 84%).

^{1}H NMR (400.4 MHz, $CDCl_3$) δ: 1.98 (d, $^{2}J_{PH}$ = 2.6 Hz, 4H, CH_2), 1.54-1.51 (m, 12H, CH_3).
$^{13}C\{^{1}H\}$ NMR (100 MHz, $CDCl_3$) δ: 24.3-23.1 (m), 16.8-15.7 (m).
$^{31}P\{^{1}H\}$ NMR (162 MHz, $CDCl_3$) δ: 42.1 (s).
HRMS (ESI, m/z): for $C_6H_{17}O_2P_2$ Calcd: 183.0704. Found: 183.0704.
IR (Nujol, cm^{-1}): 1156 (s, ν_{PO}).
Anal. Calcd. for $C_6H_{16}O_2P_2$: C, 39.57; H, 8.85. Found: C, 39.66; H, 8.78.

1,2-*Bis*(diethylphosphoryl)ethane (1b). Following the procedure described for **1a**, with a 1.98 M THF solution of EtMgCl (200 mL, 396 mmol), addition of diethyl phosphite (17.0 mL, 132 mmol) at 0 °C resulted in a pale grey white suspension after 6 h stirring at RT. Subsequent addition of 1,2-dichloroethane (5.2 mL, 66.0 mmol) and refluxing for 12 h yielded a grey white suspension. A similar workup as for **1a** yielded crude **1b** as a pale yellow oily solid. Hot toluene (70 mL) was added with stirring and cooled. An equal volume of pentane was added to complete precipitation and the suspension was filtered and washed with cold pentane-toluene (1:1) to yield **1b** as a hygroscopic white powder (12.3 g, 78%).

^{1}H NMR (400.4 MHz, $CDCl_3$) δ: 1.91 (d, $^{2}J_{PH}$ = 2.5 Hz, 4H, CH_2), 1.83-1.66 (m, 8H, CH_2CH_3) 1.16 (dt, $^{2}J_{PH}$ = 16.8 Hz, $^{3}J_{HH}$ = 7.8 Hz, 12H, CH_3).
$^{13}C\{^{1}H\}$ NMR (100 MHz, $CDCl_3$) δ: 20.9-19.8 (m), 19.4-18.3 (m), 5.99 (s).
$^{31}P\{^{1}H\}$ NMR (162 MHz, $CDCl_3$) δ: 51.2 (s).
HRMS (ESI, m/z): for $C_{10}H_{25}O_2P_2$ Calcd: 239.1330. Found: 239.1340.
IR (Nujol, cm^{-1}): 1153 (s, ν_{PO}).
Anal. Calcd. for $C_{10}H_{24}O_2P_2$: C, 50.41; H, 10.15. Found: C, 50.32; H, 9.98.

1,2-*Bis*(di-*iso*-propylphosphoryl)ethane (1c). Following a similar procedure as described for **1a**, with 1.29 M THF solution of ^{i}PrMgCl (184 mL, 237 mmol), addition of diethyl phosphite (10.2 mL, 79.2 mmol) at 0 °C resulted in a grey suspension after 5 h stirring at RT followed by 1 h of reflux. Subsequent addition of 1,2-dichloroethane (3.15 mL, 40.0 mmol) and refluxing for 12 h yielded a viscous grey suspension. The warm suspension was poured into aqueous K_2CO_3 (32.8 g, 237 mmol) in 60 mL H_2O and the THF/H_2O mixture was decanted and extracted with $CHCl_3$ (200 mL). The remaining white precipitate was washed with hot MeOH (4 × 60 mL) and the combined MeOH washings were concentrated *in vacuo*. The oily solid obtained was combined with the $CHCl_3$ extract and dried over Na_2SO_4. The solution was filtered and evaporated *in vacuo*, and the resulting pale yellow oily solid washed with cold pentane to yield **1c** as a hygroscopic white powder (8.82 g, 76%).

^{1}H NMR (400.4 MHz, $CDCl_3$) δ: 2.09-1.99 (m, 4H, CH), 1.94 (d, $^{2}J_{PH}$ = 1.5 Hz, 4H, CH_2) 1.26-1.17 (m, 12H, CH_3).

$^{13}C\{^1H\}$ NMR (100 MHz, $CDCl_3$) δ: 26.4-25.6 (m), 16.0-15.9 (d, J = 14 Hz), 15.7-14.9 (m).
$^{31}P\{^1H\}$ NMR (162 MHz, $CDCl_3$) δ: 56.1 (s).
HRMS (ESI, m/z): for $C_{14}H_{33}O_2P_2$ Calcd: 295.1956. Found: 295.1969.
IR (Nujol, cm^{-1}): 1145 (s, ν_{PO}).
Anal. Calcd. for $C_{14}H_{32}O_2P_2$: C, 57.13; H, 10.96. Found: C, 57.03; H, 10.90.

1,2-*Bis*(di-*iso*-butylphosphoryl)ethane (1d). Following the procedure described for **1c**, with a 2.03 M THF solution of ^{i}BuMgCl (100 mL, 203 mmol), addition of diethyl phosphite (8.72 mL, 67.7 mmol) at 0 °C resulted in a pale grey white suspension after 12 h stirring at RT. Subsequent addition of 1,2-dichloroethane (2.67 mL, 33.9 mmol) and refluxing for 12 h yielded a grey white suspension. A similar workup as for **1c** yielded **1d** as a slightly hygroscopic white powder (10.9 g, 92%).

^1H NMR (400.4 MHz, $CDCl_3$) δ: 2.16-2.04 (m, 4H, CH), 1.92 (d, $^2J_{PH}$ = 2.7 Hz, 4H, CH_2CH_2) 1.66-1.62 (m, 8H, CH_2C(H)$(CH_3)_2$), 1.09 (dd, $^3J_{HH}$ = 6.7 Hz, $^2J_{PH}$ = 2.2 Hz, 24H, CH_3).
$^{13}C\{^1H\}$ NMR (100 MHz, $CDCl_3$) δ: 38.6-37.6 (m), 25.0-24.9 (m), 23.8 (s), 22.6-21.5 (m).
$^{31}P\{^1H\}$ NMR (162 MHz, $CDCl_3$) δ: 46.4 (s).
HRMS (ESI, m/z): for $C_{18}H_{41}O_2P_2$ Calcd: 351.2582. Found: 351.2583.
IR (Nujol, cm^{-1}): 1158 (s, ν_{PO}).
Anal. Calcd. for $C_{18}H_{40}O_2P_2$: C, 61.69; H, 11.50. Found: C, 61.62; H, 11.43.

1,2-*Bis*(di-*tert*-butylphosphoryl)ethane (1e). To a 1.71 M pentane solution of ^{t}BuLi (100 mL, 171 mmol) cooled to -40 °C was added Et_2O (80 mL) and diethyl phosphite (7.34 mL, 57.0 mmol) dropwise. The solution was stirred at -40 °C for 1 h with the formation of a white suspension and then warmed slowly to RT. After stirring for an additional 18 h, the reaction was cooled to 0 °C followed by the addition of THF (80 mL) and 1,2-dichloroethane (2.30 mL, 29.2 mmol). The reaction was subsequently heated to reflux for 24 h. After cooling to RT, 1 M HCl (30 mL) was added followed by $CHCl_3$ to dissolve the remaining white precipitate. The aqueous layer was extracted with $CHCl_3$ (3 × 150 mL) and the combined organic extracts dried over Na_2SO_4. The solution was filtered and evaporated *in vacuo*, and the resulting white solid washed with cold pentane to yield **1e** as a hygroscopic white powder (8.53 g, 85%).

^1H NMR (400.4 MHz, $CDCl_3$) δ: 2.00 (s, 4H, CH_2), 1.26 (d, $^3J_{PH}$ = 13.2 Hz, 36H, CH_3).
$^{13}C\{^1H\}$ NMR (100 MHz, $CDCl_3$) δ: 36.4-35.6 (m), 26.6 (s), 14.5-13.7 (m).
$^{31}P\{^1H\}$ NMR (162 MHz, $CDCl_3$) δ: 60.1 (s).
HRMS (ESI, m/z): for $C_{18}H_{41}O_2P_2$ Calcd: 351.2582. Found: 351.2576.
IR (Nujol, cm^{-1}): 1136 (s, ν_{PO}).
Anal. Calcd. for $C_{18}H_{40}O_2P_2$: C, 61.69; H, 11.50. Found: C, 61.56; H, 11.47.

Ethylene*bis*(dimethylchlorophosphonium) dichloride (2a). To a stirred solution of **1a** (20 g, 110 mmol) in CH_2Cl_2 cooled to 0°C, was added dropwise $(COCl)_2$ (19.5 mL, 230 mmol) (caution: gas evolution) resulting in precipitation. The reaction was allowed to stir for 1 h at RT after which the suspension was filtered , washed with Et_2O, and dried *in vacuo* to yield **2a** as a white powder (30.7 g, 96%).

Anal. Calcd. for $C_6H_{16}Cl_4P_2$: C, 24.68; H, 5.52. Found: C, 24.76; H, 5.46.

Ethylene*bis*(diethylchlorophosphonium) dichloride (2b). Following the procedure for **2a** starting with **1b** (3.4 g, 14.3 mmol) yielded **2b** as a pale yellow powder (4.81 g, 97%).

$^{31}P\{^1H\}$ NMR (162 MHz, $CDCl_3$) δ: 107.2 (s).
Anal. Calcd. for $C_{10}H_{24}Cl_4P_2$: C, 34.51; H, 6.95. Found: C, 34.44; H, 7.08.

Ethylene*bis*(di-*iso*-propylchlorophosphonium) dichloride (2c). **2c** was prepared following a similar procedure as described for **2a** starting with **1c** (3.0 g, 10.2 mmol). The reaction mixture was stirred for 1 h at RT after which CH_2Cl_2 and $(COCl)_2$ were removed by distillation and the remaining oily solid was dried *in vacuo* overnight yielding **2c** as a light brown solid (3.86g, 94%).

^1H NMR (400.4 MHz, $CDCl_3$) δ: 4.18 (d, $^2J_{PH}$ = 2.14 Hz, 4H, CH_2), 4.16-4.08 (m, 4H, CH), 1.58-1.51 (m, 24H, CH_3).
$^{13}C\{^1H\}$ NMR (100 MHz, $CDCl_3$) δ: 28.3 (t, J = 18 Hz), 19.3 (t, J = 18 Hz), 16.5 (s).
$^{31}P\{^1H\}$ NMR (162 MHz, $CDCl_3$) δ: 114.5 (s).
Anal. Calcd. for $C_{14}H_{32}Cl_4P_2$: C, 41.61; H, 7.98. Found: C, 41.54; H, 7.88.

Ethylene*bis*(di-*iso*-butylchlorophosphonium) dichloride (2d). Following the procedure for **2c** starting with **1d** (5.0 g, 14.3 mmol) yielded **2d** as a light brown solid (6.29 g, 96%).

^1H NMR (400.4 MHz, $CDCl_3$) δ: 4.18 (br s, 4H, CH_2CH_2), 3.30-3.26 (m, 8H, CH_2C(H)$(CH_3)_2$), 2.38-2.24 (m, 4H, CH), 1.19 (d, $^3J_{HH}$ = 6.7 Hz, 24H, CH_3).
$^{13}C\{^1H\}$ NMR (100 MHz, $CDCl_3$) δ: 36.1 (t, J = 19 Hz), 24.7 (t, J = 3 Hz), 24.2 (t, J = 5 Hz), 23.2 (t, J = 21 Hz).
$^{31}P\{^1H\}$ NMR (162 MHz, $CDCl_3$) δ: 99.0 (s).
Anal. Calcd. for $C_{18}H_{40}Cl_4P_2$: C, 46.97; H, 8.76. Found: C, 46.86; H, 8.68.

Ethylene*bis*(di-*tert*-butylchlorophosphonium) dichloride (2e). Following the procedure for **2c** starting with **1e** (7.0 g, 20.0 mmol) and 3.84 mL of $(COCl)_2$ (44.0 mmol), yielded **2e** as a pale yellow solid (8.82 g, 96%).

^{1}H NMR (400.4 MHz, $CDCl_3$) δ: 4.23 (d, $^{2}J_{PH}$ = 2.3 Hz, 4H, CH_2CH_2), 1.76 (d, $^{3}J_{PH}$ = 19.2 Hz, 36H, CH_3).
^{13}C{^{1}H} NMR (100 MHz, $CDCl_3$) δ: 42.0 (t, J = 12 Hz), 27.3 (s), 19.0 (t, J = 11.5 Hz).
^{31}P{^{1}H} NMR (162 MHz, $CDCl_3$) δ: 120.0 (s).
Anal. Calcd. for $C_{18}H_{40}Cl_4P_2$: C, 46.97; H, 8.76. Found: C, 46.88; H, 8.90.

1,2-*Bis*(dimethylphosphino)ethane (3a). NaH (60 wt% in mineral oil, 11.52 g, 288 mmol) was placed in a Schlenk tube and washed with THF (2 x 50 ml) to remove mineral oil. Subsequent activation[3] of NaH was achieved by stirring with a 1 M solution of $LiAlH_4$ in THF (30 mL, 30 mmol) for 2 hours, which was then removed by cannula filtration and the solid rinsed with a further 2 x 20 mL portions of THF. 100 mL of fresh THF was then added and the suspension cooled to –78 °C before addition of $NaAlH_4$ (8.14 g, 151 mmol) as a solid under a flush of N_2. **2a** (20 g, 68.5 mmol) was then added as a suspension in 150 mL of THF at –78 °C *via* a wide Teflon cannula. Reaction proceeded immediately with accompanying gas evolution (caution). The mixture was allowed to warm to room temperature, stirred for a further 1 h, and then filtered through a glass frit with a pad of Celite® and washed with THF (2 x 50 mL). THF was removed under reduced pressure (20 mmHg) and the resulting white solids extracted with pentane (4 x 150 mL); remaining solid $NaAlH_4$ was washed with cold Et_2O and reused in further reactions (7.7 g; 95%). The pentane was then removed under reduced pressure (20 mmHg), leaving behind a colourless oil which was vacuum distilled at 58 °C (5 mmHg) to yield **3a** as a colourless oil (7.44 g; 72%).

^{1}H NMR (400.4 MHz, C_6D_6) δ: 1.31-1.29 (m, 4H, CH_2), 0.81 (vt, $^{2}J_{PH}$ = 1.5 Hz, 12H, CH_3).
^{13}C{^{1}H} NMR (100 MHz, C_6D_6) δ: 28.2 (s), 13.9-14.1 (m).
^{31}P{^{1}H} NMR (162 MHz, C_6D_6) δ: –48.8 (s).
HRMS (EI, m/z): for $C_6H_{16}P_2$ Calcd: 150.0727. Found: 150.0726.
Anal. Calcd. for $C_6H_{16}P_2$: C, 48.00; H, 10.74. Found: C, 48.23; H, 10.64.

1,2-*Bis*(diethylphosphino)ethane (3b). Following the procedure for **3a** starting with **2b** (5.0 g, 14.4 mmol) yielded a colourless oil which was vacuum distilled at 60°C (0.045 mmHg) to obtain **3b** as a colourless oil (2.49 g; 84%).

^{1}H NMR (400.4 MHz, C_6D_6) δ: 1.44-1.42 (m, 4H, CH_2CH_2), 1.29-1.18 (m, 8H, CH_2CH_3), 0.98 (dt, $^{3}J_{PH}$ = 13.9 Hz, $^{3}J_{HH}$ = 7.6 Hz, 12H, CH_3).
^{13}C{^{1}H} NMR (100 MHz, C_6D_6) δ: 22.5-22.0 (m), 19.1 (t, J = 7 Hz), 9.8 (t, J = 7 Hz).
^{31}P{^{1}H} NMR (162 MHz, C_6D_6) δ: –18.8 (s).
HRMS (EI, m/z): for $C_{10}H_{24}P_2$ Calcd: 206.1353. Found: 206.1357.
Anal. Calcd. for $C_{10}H_{24}P_2$: C, 58.24; H, 11.73. Found: C, 58.09; H, 11.60.

1,2-*Bis*(di-*iso*-propylphosphino)ethane (3c). Following the procedure for **3a** starting with **2c** (6.0 g, 14.8 mmol) yielded a colourless oil which was vacuum distilled at 70 °C (0.045 mmHg) to obtain **3c** as a colourless oil (3.31 g; 85%).

^{1}H NMR (400.4 MHz, C_6D_6) *δ*: 1.66-1.55 (m, overlap, 8H, C*H*$_2$C*H*$_2$, CH), 1.08-1.01 (m, 24H, CH_3).
^{13}C{^{1}H} NMR (100 MHz, C_6D_6) *δ*: 23.9-23.7 (m), 21.0-20.9 (m), 20.4 (t, *J* = 8 Hz), 19.3 (t, *J* = 5 Hz).
^{31}P{^{1}H} NMR (162 MHz, C_6D_6) *δ*: 9.1 (s).
HRMS (EI, m/z): for $C_{14}H_{32}P_2$ Calcd: 262.1979. Found: 262.1977.
Anal. Calcd. for $C_{14}H_{32}P_2$: C, 64.09; H, 12.29. Found: C, 63.82; H, 12.04.

1,2-*Bis*(di-*iso*-butylphosphino)ethane (3d). Following the procedure for **3a** starting with **2d** (5.0 g, 10.9 mmol) yielded a colourless oil which was vacuum distilled at 100 °C (0.008 mmHg) to obtain **3d** as a colourless oil (2.54 g; 73%).

^{1}H NMR (400.4 MHz, C_6D_6) *δ*: 1.77-1.66 (m, 4H, CH), 1.55-1.53 (m, 4H, C*H*$_2$C*H*$_2$) 1.34-1.19 (m, 8H, C*H*$_2$C(H)(CH$_3$)$_2$), 1.04 (d, $^{3}J_{HH}$ = 6.5 Hz, 24H, CH_3).
^{13}C{^{1}H} NMR (100 MHz, C_6D_6) *δ*: 39.7-39.3 (m), 27.2-26.8 (m), 25.3-24.8 (m), 24.8-24.4 (m).
^{31}P{^{1}H} NMR (162 MHz, C_6D_6) *δ*: –36.0 (s).
HRMS (EI, m/z): for $C_{18}H_{40}P_2$ Calcd: 318.2605. Found: 318.2594.
Anal. Calcd. for $C_{18}H_{40}P_2$: C, 67.89; H, 12.66. Found: C, 67.65; H, 12.52.

1,2-*Bis*(di-*tert*-butylphosphino)ethane (3e). Following the procedure for **3a** starting with **2e** (6.0 g, 13.0 mmol) yielded a white solid which was sublimed *in vacuo* at 50 °C (0.065 mmHg) to obtain **3e** as a white crystalline solid (3.52 g; 85%).

^{1}H NMR (400.4 MHz, C_6D_6) *δ*: 1.76 (m, 4H, C*H*$_2$C*H*$_2$), 1.15-1.13 (m, 36H, CH_3).
^{13}C{^{1}H} NMR (100 MHz, C_6D_6) *δ*: 31.6-31.4 (m), 30.0 (t, *J* = 7.0 Hz), 23.2 (d, *J*=5 Hz).
^{31}P{^{1}H} NMR (162 MHz, C_6D_6) *δ*: 35.7 (s).
HRMS (EI, m/z): for $C_{18}H_{40}P_2$ Calcd: 318.2605. Found: 318.2603.
Anal. Calcd. for $C_{18}H_{40}P_2$: C, 67.89; H, 12.66. Found: C, 67.69; H, 12.40.

2,6-*Bis*[(di-*tert*-butylphosphino)methyl]pyridine P,P′-Dioxide ($^{t\mathrm{Bu}}$PNP(O)$_2$). To a 1.70 M pentane solution of ^{t}BuLi (80 mL, 136 mmol) cooled to –40 °C was added Et_2O (60 mL) and diethyl phosphite (5.84 mL, 45.3 mmol) dropwise. The solution was stirred at –40 °C for 1 h with the formation of a white suspension and then warmed slowly to RT and left to stir for an additional 18 h. Volatiles were mostly removed by distillation and 60 mL of cold THF was added to the remaining residue. The resulting suspension was cooled to –78 °C and 2,6-

bis(chloromethyl)pyridine (3.99 g, 22.7 mmol) dissolved in THF (40 mL) was added dropwise. Upon warming to RT, a yellow suspension formed which was left stirring for 15 h before volatiles were removed *in vacuo*. The resulting yellow residue was treated with 1 M $HCl_{(aq)}$ (45.3 mL, 45.3 mmol) forming a white suspension which was removed by filtration. The aqueous layer was extracted with CH_2Cl_2 (4 × 60 mL) and the combined organic extracts dried over Na_2SO_4. The solution was filtered and evaporated *in vacuo*, and the resulting white solid washed with cold Et_2O to yield **^{tBu}PNP(O)$_2$** as a hygroscopic white powder (7.0 g, 72%).

^{1}H NMR (400.4 MHz, $CDCl_3$): δ = 7.58-7.51 (m, 3H, Py), 3.33 (d, $^2J_{PH}$ = 10.8 Hz, 4H, CH_2), 1.23 (d, $^3J_{PH}$ = 13.4 Hz, 36H, CH_3).
^{13}C{^{1}H} NMR (100 MHz, $CDCl_3$): δ = 123.4 (s), 94.4 (s), 36.5 (d, J = 59 Hz), 32.6 (d, J = 49 Hz), 27.1 (s).
^{31}P{^{1}H} NMR (162 MHz, $CDCl_3$): δ = 58.2 (s).
HRMS (ESI, m/z): for $C_{23}H_{44}NO_2P_2$ Calcd: 428.2847. Found: 428.2853.
IR (Nujol, cm^{-1}): 1160 (s, ν_{PO}).
Anal. Calcd. for $C_{23}H_{43}NO_2P_2$: C, 64.61; H, 10.14; N, 3.28. Found: C, 64.51; H, 10.25; N, 3.22.

2,6-*Bis*[(di-*tert*-butylchlorophosphonium)methyl]pyridine dichloride (*^{tBu}*PNP(Cl)$_4$). **^{tBu}PNP(Cl)$_4$** was prepared following a similar procedure as described for **2a** starting with **^{tBu}PNP(O)$_2$** (6.0 g, 14.0 mmol). The reaction mixture was stirred for 30 min at RT then heated to 35 °C for 3 h forming an intensely purple coloured solution. CH_2Cl_2 and $(COCl)_2$ were removed by distillation and the remaining oily solid dried *in vacuo* overnight, washed with Et_2O followed by pentane, and then dried again *in vacuo* yielding **^{tBu}PNP(Cl)$_4$** as a purple solid (7.32 g, 97%).

^{1}H NMR (400.4 MHz, $CDCl_3$): δ = 7.95 (d, $^3J_{HH}$ = 7.5 Hz, 2H, Py), 7.81 (t, $^3J_{HH}$ = 7.2 Hz, 1H, Py), 5.40 (br s, 4H, CH_2), 1.65 (d, $^3J_{PH}$ = 18.9 Hz, 36H, CH_3).
^{13}C{^{1}H} NMR (100 MHz, $CDCl_3$): δ = 150.2 (d, J = 13 Hz), 139.5 (s), 127.1 (s), 41.7 (d, J = 24 Hz), 31.2 (d, J = 27 Hz), 27.1 (s).
^{31}P{^{1}H} NMR (162 MHz, CD_2Cl_2): δ = 114.8 (s).
Anal. Calcd. for $C_{23}H_{43}NCl_4P_2$: C, 51.41; H, 8.07; N, 2.61. Found: C, 51.54; H, 7.96; N, 2.72.

2,6-Bis[(di-*tert*-butylphosphino)methyl]pyridine (*^{tBu}*PNP). **^{tBu}PNP** was prepared following a similar procedure as described for **3a** starting with **^{tBu}PNP(Cl)$_4$** (10.0 g, 18.6 mmol). Extraction of **^{tBu}PNP** with pentane results in an intensely orange coloured solution, which was filtered through silica and eluted with additional CH_2Cl_2. Pentane and CH_2Cl_2 were subsequently removed *in vacuo* yielding **^{tBu}PNP** as a white crystalline solid (5.95 g; 81%).

^{1}H NMR (400.4 MHz, C_6D_6): δ = 7.25 (d, $^{3}J_{HH}$ = 7.5 Hz, 2H, Py), 7.16 (t, $^{3}J_{HH}$ = 7.6 Hz, 1H, Py), 3.09 (d, $^{2}J_{PH}$ = 2.8 Hz, 4H, CH_2), 1.12 (d, $^{3}J_{PH}$ = 10.7 Hz, 36H, CH_3).
$^{13}C\{^{1}H\}$ NMR (100 MHz, C_6D_6): δ = 161.6 (d, J = 15 Hz), 32.4 (d, J = 26 Hz), 31.9 (d, J = 24 Hz), 29.9 (d, J = 14 Hz).
$^{31}P\{^{1}H\}$ NMR (162 MHz, C_6D_6): δ = 35.1 (s).
Anal. Calcd. for $C_{23}H_{43}NCl_4P_2$: C, 69.84; H, 10.96; N, 3.54. Found: C, 69.74; H, 11.02; N, 3.66.

2,6-*Bis*[(dimethylphosphino)methyl]pyridine P,P′-Dioxide (^{Me}PNP(O)$_2$). To a stirred solution of 3 M MeMgCl in THF (60 mL, 180.0 mmol) cooled to 0 °C was added dropwise diethyl phosphite (7.73 mL, 60.0 mmol). A grey precipitate was formed immediately and the mixture was allowed to warm to RT. After stirring for a further 15 h the mixture was cooled to –78 °C and a solution of 2,6-bis(chloromethyl)pyridine (5.28 g, 30.0 mmol) in 40 mL of THF was added dropwise. A yellow suspension formed upon leaving the mixture to warm to RT, which was left stirring for a further 15 hours before volatiles were removed *in vacuo*. The resulting yellow residue was treated in air with saturated $K_2CO_{3(aq)}$ (24.88 g, 180.0 mmol). After filtering to remove $MgCO_3$, H_2O was distilled by rotary evaporation yielding a pale yellow oil, which was dissolved in 50 mL of $CHCl_3$, filtered, dried over Na_2SO_4, and rotary evaporated. The resulting residue was washed with cold Et_2O yielding a white solid, which was dried *in vacuo* (6.59 g, 85%).

^{1}H NMR (400.4 MHz, $CDCl_3$): δ = 7.63 (t, 1H, $^{3}J_{HH}$ = 15.5 Hz, Py), 7.22 (d, 2H, $^{3}J_{HH}$ = 7.8 Hz, Py), 3.35 (d, 4H, $^{2}J_{PH}$ = 15.4 Hz, CH_2), 1.51 (d, 12H, $^{2}J_{PH}$ = 12.8 Hz, CH_3).
$^{13}C\{^{1}H\}$ NMR (100 MHz, $CDCl_3$): δ = 153.54 (d, J = 7.8 Hz, Py), 137.83 (s, Py), 122.68 (t, J = 6.9 Hz, Py), 42.49 (d, J = 61.6 Hz, CH$_2$), 16.51 (d, J = 69.8 Hz, CH_3).
$^{31}P\{^{1}H\}$ NMR (162 MHz, $CDCl_3$): δ = 40.57 (s).

2,6-*Bis*[(dimethylchlorophosphonium)methyl]pyridine dichloride (^{Me}PNP(Cl)$_4$). **^{Me}PNP(Cl)$_4$** was prepared following a similar procedure as described for **2c** starting with **^{Me}PNP(O)$_2$** (2.5 g, 9.64 mmol). The reaction mixture was stirred for 1 h at RT forming an intensely purple coloured precipitate, which was worked-up as described for **^{tBu}PNP(Cl)$_4$** yielding **^{Me}PNP(Cl)$_4$** as a purple solid (3.44g, 97%).

Anal. Calcd. for $C_{11}H_{19}NCl_4P_2$: C, 35.80; H, 5.19; N, 3.80. Found: C, 35.54; H, 4.86; N, 3.37.

2,6-Bis[(dimethylphosphino)methyl]pyridine (^{Me}PNP). **^{Me}PNP** was prepared following a similar procedure as described for **3a** starting with **^{Me}PNP(Cl)$_4$** (2.5 g, 6.77 mmol), using NaH and $NaAlH_4$ in the ratio: 1:4.2:4. After the reaction mixture was filtered and THF removed *in vacuo*, **^{Me}PNP** was extracted with toluene as a yellow solution, which was filtered through

silica, evaporated *in vacuo* and the remaining residue extracted with pentane. Subsequently removal of pentane *in vacuo* yielded **^{Me}PNP** as a yellow oil (647 mg; 37%).

^{1}H NMR (400.4 MHz, C_6D_6): δ = 7.05 (t, $^3J_{HH}$ = 7.6 Hz, 1H, Py), 6.64 (t, $^3J_{HH}$ = 7.7 Hz, 2H, Py), 2.80 (d, $^2J_{PH}$ = 0.9 Hz, 4H, CH_2), 0.91 (d, $^2J_{PH}$ = 3.6 Hz, 12H, CH_3).
^{31}P{^{1}H} NMR (162 MHz, C_6D_6): δ = –44.9 (s).

2,6-*Bis*[(diethylphosphino)methyl]pyridine P,P′-Dioxide (^{Et}PNP(O)$_2$). To a stirred solution of 2 M EtMgCl in THF (40 mL, 80.0 mmol) cooled to 0 °C was added dropwise diethyl phosphite (3.44 mL, 26.7 mmol). The mixture was allowed to warm to RT, stirred for a further 15 h and then refluxed for an additional 1h. A solution of 2,6-bis(chloromethyl)pyridine (2.347 g, 13.3 mmol) in 20 mL of THF was then added at RT dropwise and the mixture refluxed for 5 h before volatiles were removed *in vacuo*. The resulting yellow residue was treated in air with saturated $K_2CO_{3(aq)}$ (11.06 g, 80.0 mmol), extracted with hot $CHCl_3$ (5 x 50 mL), dried over Na_2SO_4, and rotary evaporated. The resulting residue was washed with cold Et_2O yielding a white solid, which was dried *in vacuo* (3.19 g, 76%).

^{1}H NMR (400.4 MHz, $CDCl_3$): δ = 7.59 (t, $^3J_{HH}$ = 7.7 Hz, 1H, Py), 7.22 (d, $^3J_{HH}$ = 7.7 Hz, 2H, Py), 3.30 (d, $^2J_{PH}$ = 14.6 Hz, 4H, PyCH_2P), 1.76-1.67 (m, 8H, PCH_2CH$_3$), 1.22-1.14 (m, 12H, PCH$_2$CH_3).
^{31}P{^{1}H} NMR (162 MHz, $CDCl_3$): δ = 49.5 (s).

2,6-*Bis*[(diethylchlorophosphonium)methyl]pyridine dichloride (^{Et}PNP(Cl)$_4$). **^{Et}PNP(Cl)$_4$** was prepared following a similar procedure as described for **^{Me}PNP(Cl)$_4$** starting with **^{Et}PNP(O)$_2$** (2.5 g, 7.93 mmol) yielding **^{Et}PNP(Cl)$_4$** as a purple solid (3.32 g, 98%).

^{1}H NMR (400.4 MHz, $CDCl_3$): δ = 7.85 (t, $^3J_{HH}$ = 7.6 Hz, 1H, Py), 7.64 (d, $^3J_{HH}$ = 7.7 Hz, 2H, Py), 5.28 (d, $^2J_{PH}$ = 13.6 Hz, 4H, PyCH_2P), 3.47-3.39 (m, 8H, PCH_2CH$_3$), 1.43 (dt, $^3J_{PH}$ = 23.4 Hz, $^3J_{HH}$ = 7.5 Hz, 12H, PCH$_2$CH_3).
^{31}P{^{1}H} NMR (162 MHz, $CDCl_3$): δ = 105.3 (s).

2,6-Bis[(diethylphosphino)methyl]pyridine (^{Et}PNP). **^{Et}PNP** was prepared following a similar procedure as described for **^{Me}PNP** starting with **^{Et}PNP(Cl)$_4$** (3 g, 7.06 mmol) yielding **^{Et}PNP** as a yellow oil (570 mg; 29%).

^{1}H NMR (400.4 MHz, C_6D_6): δ = 7.06 (t, $^3J_{HH}$ = 7.7 Hz, 1H, Py), 6.73 (t, $^3J_{HH}$ = 7.7 Hz, 1H, Py), 2.89 (s, 4H, PyCH_2P), 1.44-1.24 (m, 8H, PCH_2CH$_3$), 1.03 (t, $^3J_{HH}$ = 7.6 Hz, 12H, PCH$_2$CH_3).
^{13}C{^{1}H} NMR (100 MHz, C_6D_6): δ = 159.0 (d, J = 3 Hz), 36.4 (d, J = 20.4 Hz), 19.33 (d, J = 14.8 Hz), 10.02 (d, J = 14.5 Hz).

$^{31}P\{^{1}H\}$ NMR (162 MHz, C_6D_6): δ = –15.7 (s).

5.3.1 Experimental details for Chapter 3, Part 1

KO^{t}Bu (Sigma-Aldrich, ≥98%) was purified by sublimation prior to use. KCH_2Ph,[4] $NaBArF_{24}$,[5] $KBArF_{24}$,[5] $FcBArF_{24}$,[6] and KC_8[7] were prepared according to published methods. $FeCl_2(dmpe)_2$,[8] *cis*-$Fe(H)_2(dmpe)_2$,[9] *trans*-$Fe(H)(Cl)(dmpe)_2$,[10] and [*trans*-$Fe(H)(N_2)(dmpe)_2][BPh_4]$[11] were prepared by modification of literature procedures.

$FeCl_2(dmpe)_2$.[8] Dmpe (7 g, 46.6mmol) in 5 mL of toluene was added slowly to a suspension of anhydrous $FeCl_2$ (2.95 g, 23.3 mmol) in 40 mL of toluene cooled to 0 °C, immediately forming a green solution. After stirring for a further hour at RT, the mixture was warmed to 50 °C and filtered. The remaining residue was extracted with further hot toluene (3 x 25 mL) and combined with the filtrate before concentrating *in vacuo*. Slow cooling of the saturated solution formed green crystals which were collected by filtration, washed with pentane, and dried *in vacuo* (8.64 g, 87%).

^{31}P NMR (162 MHz, THF) δ: 59.8 (s).

***cis*-$Fe(H)_2(dmpe)_2$.**[9] $FeCl_2dmpe_2$ (3.5 g, 8.20 mmol) in 40 mL of THF was added to a suspension of NaH (492 mg, 20.5 mmol) and $NaAlH_4$ (88.5 mg, 1.64 mmol) in 25 mL of THF cooled to 0 °C. The mixture was stirred at RT overnight resulting in a yellow solution which was subsequently filtered through a pad of Celite® on a sintered glass frit and rinsed with further THF (3 x 15 mL). THF was removed *in vacuo* and the remaining solid extracted with pentane (4 x 40 mL). After removal of pentane *in vacuo*, the crude *cis*-$Fe(H)_2(dmpe)_2$ was sublimed at 60 °C under 10^{-5} mbar pressure, yielding a pale yellow solid (2.49 g, 85%).

^{31}P NMR (162 MHz, THF) δ: 77.4 (tt, $^{2}J_{PP}$ = 26.8 Hz, $^{2}J_{PH}$ = 11.5 Hz 2P), 67.8 (t, $^{2}J_{PP}$ = 26.7 Hz, 2P).
^{1}H NMR (400.4 MHz, THF, hydride region) δ: –14.20-14.71 (m, FeH_2).

***trans*-$Fe(H)(Cl)(dmpe)_2$.**[10] LiCl (805 mg, 19.0 mmol) was added as a solid to a solution of *cis*-$Fe(H)_2(dmpe)_2$ (1.7 g, 4.75 mmol) in 30 mL of EtOH and the mixture stirred for 12 h at RT. The resulting orange solution was filtered and combined with additional EtOH washings (3 x 10 mL). EtOH was subsequently removed *in vacuo* and the remaining solid extracted with toluene (5 x 40 mL). After concentrating the combined toluene extracts *in vacuo*, orange crystals were grown by slow cooling, which were collected by filtration, rinsed with pentane, and dried *in vacuo* (1.75 g, 94%).

^{31}P NMR (162 MHz, THF) δ: 71.3 (d, $^{2}J_{PH}$ = 30.6 Hz, 4P).
^{1}H NMR (400.4 Hz, THF, hydride region) δ: –31.98 (quintet, $^{2}J_{PH}$ = 49.4 Hz, Fe-H).

[*trans*-Fe(H)(N_2)(dmpe)$_2$][BPh_4].[11] *trans*-Fe(H)(Cl)(dmpe)$_2$ (1.5 g, 3.82 mmol) and $NaBPh_4$ (1.308 g, 3.82 mmol) were added to a Schlenk followed by 30 mL of EtOH under a N_2 atmosphere. The mixture was stirred for 4 h at RT forming a cream precipitate which was collected by filtration and washed with further EtOH (3 x 10 mL). The solid was extracted with acetone (3 x 10 mL) and the combined extracts were layered with Et_2O. Slow diffusion of Et_2O into the acetone solution led to formation of off-white crystals which were collected by filtration, washed with further Et_2O, and dried *in vacuo* (2.21 g, 82%).

^{31}P NMR (162 MHz, THF) δ: 64.6 (d, $^2J_{PH}$ = 41.2 Hz, 4P).
^{1}H NMR (400.4 Hz, THF, hydride region) δ: –19.09 (quintet, $^2J_{PH}$ = 51.2 Hz, Fe-H).

[*trans*-Fe(H)(N_2)(dmpe)$_2$][$BArF_{24}$]. *trans*-Fe(H)(Cl)(dmpe)$_2$ (1 g, 2.55 mmol) and $NaBArF_{24}$ (2.212 g, 2.496 mmol) were added to a Schlenk followed by 30 mL of Et_2O. The mixture was stirred under a N_2 atmosphere for 4 h at RT before being filtered and extracted with additional Et_2O (3 x 10 mL). The combined filtrate and extracts were concentrated *in vacuo* and then layered with pentane. Slow diffusion of pentane into the Et_2O solution resulted in the formation of off-white crystals which were collected by filtration, washed with further pentane, and dried *in vacuo* (2.21 g, 82%).

^{31}P NMR (162 MHz, THF) δ: 64.8 (d, $^2J_{PH}$ = 46.9Hz, 4P).
^{1}H NMR (400.4 Hz, THF, hydride region) δ: –19.07 (quintet, $^2J_{PH}$ = 51.0 Hz, Fe-H).

Deprotonation of [*trans*-Fe(H)(N_2)(dmpe)$_2$][X], (X = BPh_4, $BArF_{24}$). [*trans*-Fe(H)(N_2)(dmpe)$_2$][X], (X = BPh_4, $BArF_{24}$) and the selected base (KO^{t}Bu *or* KCH_2Ph, 2 equiv.) were combined in THF or Et_2O and stirred for 3 h under N_2 or Ar atmosphere. Where X = BPh_4, precipitates are subsequently removed by filtration through Celite®.

FeN_2(dmpe)$_2$ (4). Solutions of FeN_2(dmpe)$_2$ can be obtained by dissolving [{Fe(dmpe)$_2$}$_2$(μ-N_2)] (**6**) under N_2. Attempts to grow single crystals of FeN_2(dmpe)$_2$ suitable for X-ray crystallography have yielded only [{Fe(dmpe)$_2$}$_2$(μ-N_2)].

^{31}P NMR (162 MHz, hexane) δ: 63.3 (s).
^{15}N NMR (40.55 MHz, hexane) δ: –47.1 (d, $^1J_{NN}$ = 6 Hz, 1N, N_β), –48.9 (d, $^1J_{NN}$ = 6 Hz, 1N, N_α).
IR (KBr, cm^{-1}): 1979 ($^{14}N_2$).
IR (Et_2O, cm^{-1}): 1996 ($^{14}N_2$).
UV-vis (Et_2O, nm {m^2 mol^{-1}}: 271 {2919}; ~340, br {~1708}.

[*trans*-Fe(H)(dmpe)$_2$(μ-N$_2$)Fe(dmpe)$_2$][BArF$_{24}$] (5).[12] A solution of [{Fe(dmpe)$_2$}$_2$(μ-N$_2$)]BArF$_{24}$ was prepared for solution IR by combining [{Fe(dmpe)$_2$}$_2$(μ-N$_2$)] and [*trans*-Fe(H)(N$_2$)(dmpe)$_2$][BArF$_{24}$] (1:2) in Et$_2$O under an Ar atmosphere.

^{31}P NMR (162 MHz, hexane) *δ*: 69.4 (s, 4P, Fe(H)P$_4$), 61.7 (s, 4P, FeP$_4$).
^{1}H NMR (400.4 Hz, THF, hydride region) *δ*: –26.89 (quintet, $^{2}J_{PH}$ = 52.4 Hz, Fe-H).
IR (Et$_2$O, cm^{-1}): 1914 (^{14}N$_2$), 1841 (Fe–H).

[{Fe(dmpe)$_2$}$_2$(μ-N$_2$)] (6). FeCl$_2$dmpe$_2$ (4 g, 9.37 mmol) and KC$_8$ (5.065 g, 37.5 mmol) were transferred into a Rotaflo® ampoule and sealed. With the ampoule submerged in a liquid N$_2$ bath, 40 mL of hexane was slowly added under a 1 bar N$_2$ pressure and the ampoule resealed. After removal of the liquid N$_2$ bath and allowing the ampoule to thaw behind a blast shield, a N$_2$ pressure of ca. 4 bar was obtained. The mixture was subsequently sonicated for 20 min and left to stir for 5 days with periodic sonication. After carefully releasing the pressure, the mixture was filtered through a pad of Celite® on a sintered glass frit and the remaining solids extracted with additional hexane (4 x 40 mL). The filtrate and extracts were combined and the hexane removed *in vacuo* to yield a red solid consisting of mainly FeN$_2$(dmpe)$_2$ with some [{Fe(dmpe)$_2$}$_2$(μ-N$_2$)]. Suspending this solid in 1-2 mL of hexane under an Ar atmosphere with minimal stirring for 7 days results in almost complete conversion to [{Fe(dmpe)$_2$}$_2$(μ-N$_2$)]. Minor impurities FeN$_2$(dmpe)$_2$, [{Fe(dmpe)$_2$}$_2$(μ-dmpe)], and *cis*-Fe(H)$_2$(dmpe)$_2$ can be removed by recrystalisation from hexane under Ar to yield red crystals of [{Fe(dmpe)$_2$}$_2$(μ-N$_2$)] in >98% purity by ^{31}P NMR (3.21 g, 93%).

Anal. Calcd. for C$_{24}$H$_{64}$N$_2$Fe$_2$P$_8$: C, 38.94; H, 8.71; N, 3.78. Found: C, 38.93; H, 8.85; N, 3.89.
^{31}P NMR (162 MHz, hexane) *δ*: 66.0 (s).
^{15}N NMR (40.55 MHz, hexane) *δ*: –54.9 (s).
Raman (solid, cm^{-1}): 1933 (^{14}N$_2$), 1870 (^{15}N$_2$).
UV-vis (Et$_2$O, nm {m^2 mol^{-1}}: 271 {2537}; 357 {3442}.

[{Fe(dmpe)$_2$}$_2$(μ-^{15}N$_2$)] 6(^{15}N$_2$). FeCl$_2$dmpe$_2$ (400 mg, mmol) and KC$_8$ (633 mg, mmol) were transferred into a Rotaflo® ampoule and sealed. With the ampoule submerged in a liquid N$_2$/pentane (–131 °C) bath, 10 mL of hexane was added under an Ar atmosphere and the mixture degassed and left under static vacuum. With the mixture still frozen, ^{15}N$_2$ (1.5 equiv) was delivered into the ampoule *via* Toepler pump (see Appendix). After thawing, the mixture was sonicated for 20 min and subsequently stirred for 5 days with periodic sonication. The reaction was worked up as above, under an Ar atmosphere (240 mg, 69%).

[{Fe(dmpe)$_2$}$_2$(μ-N$_2$)][BArF$_{24}$] (7). Under an Ar atmosphere, [Cp$_2$Fe][BArF$_{24}$] (430mg, 0.410 mmol) was dissolved in 5 mL of Et$_2$O and slowly added to a stirring solution of [{Fe(dmpe)$_2$}$_2$(μ-N$_2$)] (315 mg, 0.426 mmol) in 5 mL of Et$_2$O. The resulting dark yellow/green mixture was stirred for 2 h at RT before volatiles were removed *in vacuo*. The remaining solid was rinsed with hexane (4 x 10 mL) and subsequently extracted into Et$_2$O, concentrated, and then layered with hexane. Slow diffusion of hexane into the Et$_2$O solution resulted in dark yellow/green crystals which were collected by filtration, then rinsed with cold TBME (2 x 2 mL) followed by pentane (2 x 2 mL), before being dried *in vacuo* (588 mg, 86%).

Anal. Calcd. for $C_{56}H_{76}N_2BF_{24}Fe_2P_8$: C, 41.95; H, 4.78; N, 1.75. Found: C, 42.14; H, 4.76; N, 1.67.
^{1}H NMR (400.4 MHz, THF) *δ*: 24.00 (v br s), 13.42 (br s), 0.34 (br s), and –9.42 (br s).
IR (KBr, cm^{-1}): 1894 ($^{14}N_2$), 1833 ($^{15}N_2$).
IR (Et$_2$O, cm^{-1}): 1885 ($^{14}N_2$), 1827 ($^{15}N_2$).
UV-vis (Et$_2$O, nm {m^2 mol^{-1}}: 300 {2566}, 330-430 (v br), 470 {404}, 810 {274}.

[{Fe(dmpe)$_2$}$_2$(μ-N$_2$)][BArF$_{24}$]$_2$ (8). Under an Ar atmosphere, [Cp$_2$Fe][BArF$_{24}$] (425 mg, 0.405 mmol) was dissolved in 5 mL of Et$_2$O and slowly added to a stirring solution of [{Fe(dmpe)$_2$}$_2$(μ-N$_2$)] (150 mg, 0.203 mmol) in 5 mL of Et$_2$O. The mixture changed colour from green to blue over the course of 3 h stirring at RT, after which the volatiles were removed *in vacuo*. The remaining solid was rinsed with hexane (4 x 10 mL) and subsequently extracted into Et$_2$O, concentrated, and then layered with hexane. Slow diffusion of hexane into the Et$_2$O solution resulted in green crystals which were collected by filtration, then rinsed with cold TBME (2 x 2 mL) followed by pentane (2 x 2 mL), before being dried *in vacuo* (410 mg, 82%).

Anal. Calcd. for $C_{88}H_{88}N_2B_2F_{48}Fe_2P_8$: C, 42.85; H, 3.60; N, 1.14. Found: C, 42.78; H, 3.73; N, 0.98.
Raman (solid, cm^{-1}): 1929 ($^{14}N_2$), 1946 ($^{14}N_2$), 1963 ($^{14}N_2$), 1868 ($^{15}N_2$), 1880 ($^{15}N_2$), 1903 ($^{15}N_2$).
IR (Et$_2$O, cm^{-1}): 2081 ($^{14}N_2$), 2002 ($^{15}N_2$).
UV-vis (Et$_2$O, nm {m^2 mol^{-1}}: 358 {416}, 488 {234}, 598 {408}.

Fe(H)(N$_3$)(dmpe)$_2$ (9). *(Caution: metal azide complexes are potentially explosive. Exercise caution when handling: avoid physical stress on solid mixtures/samples, i.e., manipulate with a plastic spatula, avoid excessive scraping, and do not grind. Syntheses were limited to preparation of <200 mg of the azide complex.)* Method (a). Fe(H)(N$_2$)(dmpe)$_2$][BPh$_4$] (250 mg, 0.355 mmol), [Bu$_4$N][N$_3$] (101 mg, 0.355 mmol) and 5 mL of THF were transferred into a

thick walled vial containing a stirrer bar, inside the glovebox. The mixture was stirred at RT for 12 h before volatiles were removed *in vacuo*. The remaining solid was extracted with Et_2O, concentrated, and then layered with pentane. Slow diffusion of pentane into the Et_2O solution formed orange crystals which were collected by filtration, washed with pentane, and dried *in vacuo* (110 mg, 78%). Method (b). *cis*-$Fe(H)_2(dmpe)_2$ (112.4 mg, 0.314 mmol) and NaN_3 (20.4 mg, 0.314 mmol) were transferred into a thick walled vial containing a stirrer bar, inside the glovebox. Addition of 5 mL of MeOH resulted in an orange solution which was stirred at RT for 2 h before volatiles were removed *in vacuo*. The remaining solid was washed with pentane (3 x 3 mL), and subsequently extracted with Et_2O, concentrated, and then layered with pentane. Slow diffusion of pentane into the Et_2O solution formed orange crystals which were collected by filtration, washed with pentane, and dried *in vacuo* (92.7 mg, 74%).

^{31}P NMR (162 MHz, THF) δ: 73.1 (d, $^2J_{PH}$ = 30.2).
^{1}H NMR (400.4 Hz, THF, hydride region) δ: –30.76 (quintet, $^2J_{PH}$ = 48.4 Hz, Fe-H).
IR (KBr, cm^{-1}): 2026 ($N{=}N{=}N_{asymm}$).

$Fe(H)(dmpe)_2$ (10). Inside an Ar glovebox, KC_8 (34 mg, 0.252 mmol) was added to a pentane solution of $Fe(H)(N_3)(dmpe)_2$ (50 mg, 0.125 mmol) and the resulting mixture was stirred for 1 h, then filtered through Celite® to afford an orange solution. Upon addition of ^{t}BuOH (1-2 drops), the solution turned yellow and was filtered once more through Celite®. Removal of the solvent *in vacuo* yielding an orange solid (32.7 mg, 73%). Single crystal X-ray diffraction measurements were performed on a crystal grown from a $SiMe_4$ solution of **10** cooled to –30 °C.

Anal. Calcd. for $C_4H_9FeP_4$: C, 40.36; H, 9.31. Found: C, 40.50; H, 9.17.
UV-vis (Et_2O, nm {m^2 mol^{-1}}: ~400 {~258}.

$[Fe(dmpe)_2][K]$ (11). Inside an Ar glovebox, KC_8 (85 mg, 0.629 mmol) was added to a pentane solution of $Fe(H)(N_3)(dmpe)_2$ (50 mg, 0.125 mmol) and the resulting mixture was stirred for 1 h, then filtered through Celite® to afford a dark red solution. Concentration *in vacuo* and slow cooling to –30 °C yielded dark red crystals, which were collected by decanting away the supernatant and drying *in vacuo* (21.7 mg, 44%). A satisfactory elemental analysis could not be obtained, presumed to be due to the extreme sensitivity of this compound. Single crystal X-ray diffraction measurements were performed on a crystal grown from a cyclopentane solution of **11** cooled to –30 °C.

UV-vis (pentane, nm {m^2 mol^{-1}}: ~410 {~191}, ~555 {~40}.

Crystallisation of *trans*-Fe(H)$_x$(NPhNPh)(dmpe)$_2$; x = 0-1. Inside an Ar glove box, pentane was added to a vial containing **11** and azobenzene (1:1, 0.016 mmol). The resultant dark green solution was filtered through Celite® and cooled to –30 °C to yield dark green crystals.

5.3.2 Experimental details for Chapter 3, Part 2

KO^{t}Bu (Sigma-Aldrich, ≥98%) was purified by sublimation prior to use. KCH_2Ph,[4] $NaBArF_{24}$,[5] $KBArF_{24}$,[5] $FcBArF_{24}$,[6] and KC_8[7] were prepared according to published methods. $FeCl_2(depe)_2$,[8] *cis*-$Fe(H)_2(depe)_2$,[9] *trans*-Fe(H)(Cl)$(depe)_2$,[10] and [*trans*-$Fe(H)(N_2)(depe)_2][BPh_4]$[11] were prepared by modification of literature procedures.

$FeCl_2(depe)_2$.[8] Depe (3 g, 14.5 mmol) in 5 mL of DCM was added slowly to a suspension of anhydrous $FeCl_2$ (922 mg, 7.27 mmol) in 30 mL of DCM cooled to 0 °C. The mixture was stirred for 2 h at RT forming a green solution, which was filtered and the remaining residue extracted with additional DCM (3 x 20 mL). DCM was subsequently removed *in vacuo* and the remaining solid washed with cold EtOH (2 x 5 mL, 0 °C), followed by hexane (2 x 10 mL), before being dried *in vacuo* (3.52 g, 90%).

^{31}P NMR (162 MHz, THF) *δ*: 73.9 (vbr s).

***cis*-Fe(H)$_2$(depe)$_2$.**[9] A 1 M solution of $NaBEt_3H$ in toluene (3 mL, 3 mmol) was added to a stirring suspension of $FeCl_2depe_2$ (800 mg, 1.48 mmol) in Et_2O (20 mL) cooled to –78 °C, which was then allowed to warm to RT over the course of 3 h. The resultant yellow solution was filtered and the volatiles subsequently removed *in vacuo* to produce an oily solid, which was further dried for 15 h at 10^{-3} mbar to remove any residual BEt_3. The remaining crude *cis*-$Fe(H)_2(depe)_2$ was either used in subsequent reactions or purified by recrystallisation from cold pentane (576 mg, 83%).

^{31}P NMR (162 MHz, pentane) *δ*: 103.0 (br s, 2P), 88.9 (br s, 2P).
^{1}H NMR (400.4 MHz, pentane, hydride region) *δ*: –14.13-14.49 (m, FeH_2).

***trans*-Fe(H)(Cl)(depe)$_2$.**[10] LiCl (225 mg, 5.3 mmol) was added as a solid to a solution of *cis*-$Fe(H)_2(dmpe)_2$ (500 mg, 1.06 mmol) in 10 mL of EtOH and the mixture stirred for 15 h at RT. The resulting orange solution was filtered and combined with additional EtOH washings (3 x 5 mL). EtOH was subsequently removed *in vacuo* and the remaining solid extracted with toluene (5 x 20 mL). After concentrating the combined toluene extracts *in vacuo*, orange crystals were grown by slow cooling, which were collected by filtration, rinsed with pentane, and dried *in vacuo* (459 mg, 86%).

^{31}P NMR (162 MHz, Et_2O) δ: 87.8 (d, $^2J_{PH}$ = 29.4 Hz).
^{1}H NMR (400.4 Hz, Et_2O, hydride region) δ: –30.92 (quintet, $^2J_{PH}$ = 48.1 Hz, Fe-H).

[*trans*-Fe(H)(N_2)(depe)$_2$][BPh_4].[11] *trans*-Fe(H)(Cl)(depe)$_2$ (500 mg, 0.99 mmol) and $NaBPh_4$ (339 mg, 0.99 mmol) were added to a Schlenk followed by 20 mL of EtOH under a N_2 atmosphere. The mixture was stirred for 12 h at RT forming a cream precipitate which was collected by filtration and washed with additional EtOH (3 x 5 mL). The solid was extracted with acetone (3 x 10 mL) and the combined extracts layered with Et_2O. Slow diffusion of Et_2O into the acetone solution produced off-white crystals which were collected by filtration, washed with further Et_2O, and dried *in vacuo* (657 mg, 81%).

^{31}P NMR (162 MHz, THF) δ: 81.42 (d, $^2J_{PH}$ = 11.4 Hz).
^{1}H NMR (400.4 Hz, THF, hydride region) δ: –17.93 (quintet, $^2J_{PH}$ = 49.1 Hz, Fe-H).

[*trans*-Fe(H)(N_2)(depe)$_2$][$BArF_{24}$]. *trans*-Fe(H)(Cl)(depe)$_2$ (250 mg, 0.495 mmol) and $NaBArF_{24}$ (461 mg, 0.520 mmol) were dissolved in 10 mL of Et_2O under a N_2 atmosphere and stirred for 12 h at RT. After filtration, the solution was concentrated *in vacuo* and then layered with pentane. Slow diffusion of pentane into the Et_2O solution yielded off-white crystals which were collected by filtration, washed with further pentane, and dried *in vacuo* (598 mg, 89%).

^{31}P NMR (162 MHz, THF) δ: 81.5 (br s).
^{1}H NMR (400.4 Hz, THF, hydride region) δ: –17.89 (quintet, $^2J_{PH}$ = 48.9 Hz, Fe-H).

Deprotonation of [*trans*-Fe(H)(N_2)(depe)$_2$][X], (X = BPh_4, $BArF_{24}$). [*trans*-Fe(H)(N_2)(depe)$_2$][X], (X = BPh_4, $BArF_{24}$) and the base (KO^{t}Bu *or* KCH_2Ph, 2 equiv.) were combined in THF or Et_2O and stirred for 12 h under N_2 or Ar atmosphere. Where X = BPh_4, precipitates are subsequently removed by filtration through Celite®.

FeN_2(depe)$_2$ (12). *(N.B. this reaction requires a N_2 atmosphere.)* To a stirred suspension of Mg powder (564mg, 23.2 mmol) in 15 mL of THF was added 1,2-dibromoethane (0.2 mL, 2.31 mmol). The mixture was heated to 40 °C for 30 min to activate the Mg, evolving C_2H_4 gas. After allowing the mixture to cool to RT, a solution of $FeCl_2depe_2$ (2.5 g, 4.64 mmol) in 30 mL of THF was slowly added and the mixture subsequently sonicated for 20 min. The reaction is typically complete after 2 days of stirring under N_2 with periodic sonication. The resulting orange solution was filtered before addition of 1,4-dioxane (3.95 mL, 46.3 mmol), precipitating a fine white solid. After stirring for 12h, the mixture was filtered through a pad of Celite® on a sintered glass frit and rinsed through with additional THF (3 x 20 mL). THF was subsequently removed *in vacuo* and the remaining solid extracted with pentane (3 x 40

mL). Concentration of the pentane solution and slow cooling to –78 °C yielded orange crystals which were collected by filtration, washed with cold pentane, and then dried in vacuo (2.1 g, 91%).

^{31}P NMR (162 MHz, hexane) *δ*: 84.4 (s).
IR (KBr, cm^{-1}): 1956 ($^{14}N_2$), 1889 ($^{15}N_2$).
IR (Et_2O, cm^{-1}): 1973 ($^{14}N_2$).

Fe^{15}N$_2$(depe)$_2$ (12(^{15}N$_2$)). In a Rotaflo® ampoule under an Ar atmosphere, Mg powder (113 mg, 4.65 mmol) was activated with 1,2-dibromoethane in THF as above. THF was then removed by decanting and the mixture submerged in a liquid N_2/pentane bath (–131 °C). A solution of $FeCl_2depe_2$ (500 mg, 0.927 mmol) in 10 mL of THF was added under Ar and the mixture degassed and left under static vacuum. With the mixture still frozen, $^{15}N_2$ (2 equiv.; see Appendix) was delivered into the ampoule *via* a Toepler pump (see Appendix). After thawing, the mixture was sonicated for 20 min and subsequently stirred for 2 days with periodic sonication. The reaction was worked up as above, under an Ar atmosphere (350 mg, 76%).

[Fe(depe)$_2$][BArF$_{24}$] (13). Under an Ar atmosphere, [Cp_2Fe][$BArF_{24}$] (803 mg, 0.765 mmol) was dissolved in 5 mL of Et_2O and slowly added to a stirring solution of $Fe(N_2)(depe)_2$ (400 mg, 0.806 mmol) in 5 mL of Et_2O. The resulting blue solution was stirred for 2 h at RT before volatiles were removed *in vacuo*. The remaining solid was rinsed with hexane (4 x 5 mL) and subsequently extracted into 1,2-DFB, concentrated, and then layered with hexane. Slow diffusion of hexane into the 1,2-DFB solution resulted in blue crystals which were collected by filtration, then rinsed with cold TBME (2 x 2 mL) followed by pentane (2 x 2 mL), before being dried *in vacuo* (935 mg, 87%).

Anal. Calcd. for $C_{52}H_{60}BF_{24}FeP_4$: C, 46.90; H, 4.54. Found: C, 46.82; H, 4.64.
^{1}H NMR (400.4 MHz, THF) *δ*: –1.77 (br s), –21.30 (vbr s).
IR (KBr, under N_2, cm^{-1}): 2076 (**13-^{14}N$_2$**).
IR (Et_2O, under N_2, cm^{-1}): 2067 (**13-^{14}N$_2$**).
UV-vis (1,2-DFB, under Ar, 20 °C, nm {m^2 mol^{-1}}: ~378 (overlap) {~103}, ~414 (overlap) {~94}, 496 {121}, 618 {285}.
UV-vis (1,2-DFB, under N_2, –15 °C, nm {m^2 mol^{-1}}: 359 {316}, 1018 {55}.

Fe(H)(N$_3$)(depe)$_2$ (14). *(Caution: metal azide complexes are potentially explosive. Exercise caution when handling: avoid physical stress on solid mixtures/samples, i.e., manipulate with a plastic spatula, avoid excessive scraping, and do not grind. Syntheses were limited to preparation of <200 mg of the azide complex.)* $Fe(H)(N_2)(depe)_2$][BPh_4] (250 mg, 0.306

mmol), $[Bu_4N][N_3]$ (87.1 mg, 0.306 mmol) and 5 mL of THF were transferred into a thick walled vial containing a stirrer bar, inside the glovebox. The mixture was stirred at RT for 12 h before volatiles were removed *in vacuo*. The remaining solid was extracted with Et_2O, concentrated, and then layered with pentane. Slow diffusion of pentane into the Et_2O solution formed orange crystals which were collected by filtration, washed with pentane, and dried *in vacuo* (134 mg, 86%).

^{31}P NMR (162 MHz, THF) δ: 90.1 (d, $^2J_{PH}$ = 22.2).
^1H NMR (400.4 Hz, THF, hydride region) δ: –30.08 (quintet, $^2J_{PH}$ = 47.3 Hz, Fe-H).
IR (KBr, cm^{-1}): 2029 ($N{=}N{=}N_{asymm}$).

$Fe(H)(depe)_2$ (15). Inside an Ar glovebox, KC_8 (107 mg, 0.792 mmol) was added to a pentane solution of $Fe(H)(Cl)(depe)_2$ (100 mg, 0.198 mmol) and the resulting mixture was stirred for 1 h, then filtered through Celite® to afford a yellow solution. Removal of the solvent *in vacuo* yielding an oily yellow solid (76.0 mg, 82%).

^1H NMR (400.4 MHz, pentane) δ: 13.24 (vbr s), –2.58 (br s).
UV-vis (pentane, nm {m^2 mol^{-1}}: ~274 {~794}, ~290-370 (v br), ~396 {~264}.

5.3.3 Experimental details for Chapter 3, Part 3

Acidification and base distillation procedure

In a typical experiment, a ca. 0.016 M (1 mL, 0.016 mmol [Fe]) solution was cooled to –78 °C in a round bottom flask equipped with a J. Young tap (see Appendix). The tap was replaced by a rubber septum, and HCl (1 M in Et_2O, 10 equivalents per Fe) was quickly added *via* syringe. After replacing the J. Young tap, the mixture was stirred at –78 °C for a further 10 min before being allowed to warm to RT over the course of 20 min (*caution: the flask will be at ca. 2 bar pressure*). After removing the volatiles *in vacuo*, the flask was placed in a liquid N_2 bath prior to addition of 40% KOH (1 mL) and THF (1 mL) *via* syringe. The flask was then sealed and allowed to thaw under static vacuum (*caution: addition of KOH should be performed under a N_2 flow rather than Ar, which freezes at the temperature of liquid N_2*). The thawed mixture was stirred at RT for a further 1 h. During this time, a second flask was charged with HCl (1 M in Et_2O under N_2, 10 equivalents per Fe) and submerged in a liquid N_2 bath prior to degassing *in vacuo*. The volatiles in the first flask were then transferred into the second flask (submerged in liquid N_2) under a static vacuum (ca. 10^{-3} mbar) with the aid of gentle heating (< 50 °C). After sealing the second flask, the mixture was thawed under static vacuum and stirred for a further 30 min at RT. The volatiles

were subsequently removed *in vacuo* and the remaining residue was dissolved in H_2O up to 5 mL. Indophenol (NH_3) and pdmab (hydrazine) analyses were performed on 1 mL aliquots taken from this solution according to literature procedures.[13]

5.4 Experimental details for Chapter 4

Van't Hoff analysis of the N_2 binding affinity of 13

UV-vis measurements were recorded on a Perkin-Elmer Lambda 20 UV-vis spectrometer equipped with a UNISOKU CoolSpeK UV/CD cryostat. Solutions were measured in a specially adapted quartz cuvette fitted with a J. Young valve, and subsequently solvent subtracted using the same cuvette containing the pure solvent only. A 0.5 mM THF solution of **13** was prepared inside both an Ar and a N_2 glove box. The solution under N_2 was measured at RT and then at 5 °C intervals from 35-75 °C; a final measurement was recorded at RT to ensure reversibility. The concentration of **13** at each temperature was determined by reference to the 618 nm absorption measured at RT for the equivalent solution under Ar. The concentration of N_2 in THF was taken to be 6.4 mM using solubility data from ref. 14.

5.5 References

1. Sheldrick, G., *Acta Crystallogr., Sect. A*, **2008**, *64* (1), 112-122.
2. Sprakel, V. S. I.; Elemans, J. A. A. W.; Feiters, M. C.; Lucchese, B.; Karlin, K. D.; Nolte, R. J. M., *Eur. J. Org. Chem.*, **2006**, *2006* (10), 2281-2295.
3. Hubbard, J. L., *Tetrahedron Lett.*, **1988**, *29* (26), 3197-3200.
4. Bailey, P. J.; Coxall, R. A.; Dick, C. M.; Fabre, S.; Henderson, L. C.; Herber, C.; Liddle, S. T.; Loroño-González, D.; Parkin, A.; Parsons, S., *Chem. Eur. J.*, **2003**, *9* (19), 4820-4828.
5. Reger, D. L.; Little, C. A.; Lamba, J. J. S.; Brown, *Inorganic Syntheses*, John Wiley & Sons, Inc., **2004**, 1-48.
6. Le Bras, J.; Jiao, H.; Meyer, W. E.; Hampel, F.; Gladysz, J. A., *J. Organomet. Chem.*, **2000**, *616* (1–2), 54-66.
7. Weitz, I. S.; Rabinovitz, M., *J. Chem. Soc., Perkin Trans. 1*, **1993**, (1), 117-120.
8. Hughes, D. L.; Leigh, G. J.; Jimenez-Tenorio, M.; Rowley, A. T., *J. Chem. Soc., Dalton Trans.*, **1993**, (1), 75-82.
9. Whittlesey, M. K.; Mawby, R. J.; Osman, R.; Perutz, R. N.; Field, L. D.; Wilkinson, M. P.; George, M. W., *J. Am. Chem. Soc.*, **1993**, *115* (19), 8627-8637.
10. Chatt, J.; Hayter, R. G., *J. Chem. Soc.*, **1961**, (0), 5507-5511.
11. Hills, A.; Hughes, D. L.; Jimenez-Tenorio, M.; Leigh, G. J.; Rowley, A. T., *J. Chem. Soc., Dalton Trans.*, **1993**, (20), 3041-3049.

12. Briault-Hutter, C., MSci thesis, Imperial College London, 2013.
13. a) Weatherburn, M. W., *Anal. Chem.*, **1967**, *39* (8), 971-974; b) Watt, G. W.; Chrisp, J. D., *Anal. Chem.*, **1952**, *24* (12), 2006-2008.
14. Battino, R.; Rettich, T. R.; Tominaga, T., *J. Phys. Chem. Ref. Data*, **1984**, *13* (2), 563-600.

Appendix

Supporting information for Chapter 2 is published online at:

http://onlinelibrary.wiley.com/doi/10.1002/adsc.201300787/full

Quantitative gas transfer using a Toepler pump

A Toepler pump was used to quantitatively add $^{15}N_2$ in the synthesis of [{Fe(dmpe)$_2$}$_2$(μ-$^{15}N_2$)] and Fe$^{15}N_2$(depe)$_2$.

Calibration: In order to add gas quantitatively, the volumes in each of the segments must first be calculated. This is achieved by attaching gas (air) flasks of known volume (e.g. 15, 25, 50 cm^3; G), then evacuating the entire line up to the attached gas flask. By noting the change in pressure (M) as the gas is allowed to enter each of the segments, it is possible to determine their respective volumes using the ideal gas law (pV = nRT (fixed)). Accordingly, if gas is bled from G into a known volume (typically only the two segments leading to the manometer), then the number of moles of gas admitted into the line can be calculated by n = ΔpV/RT (R = 62.3637 cm^3 mmHg K^{-1} mmol^{-1}).

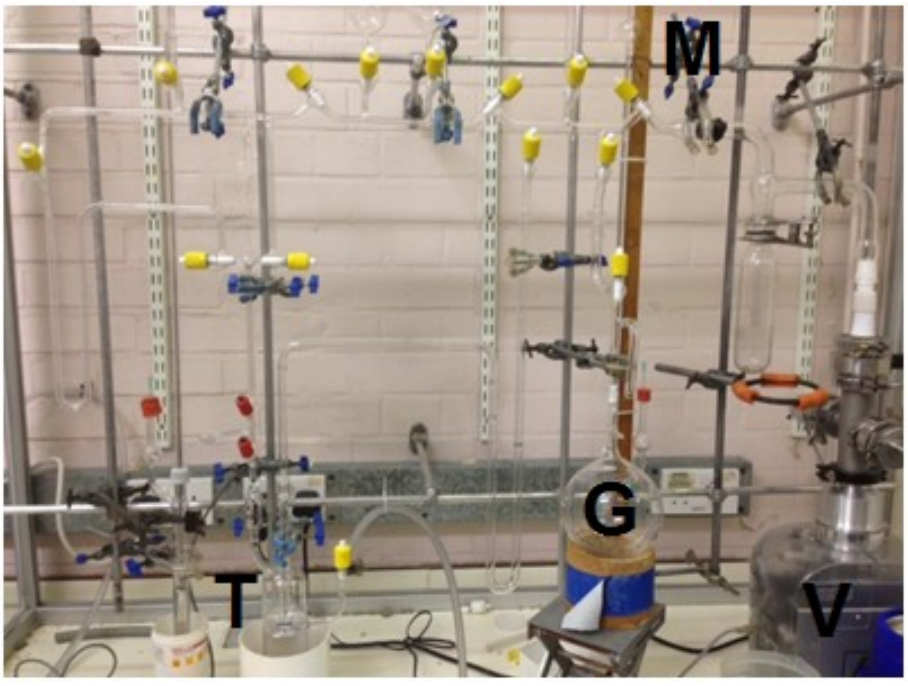
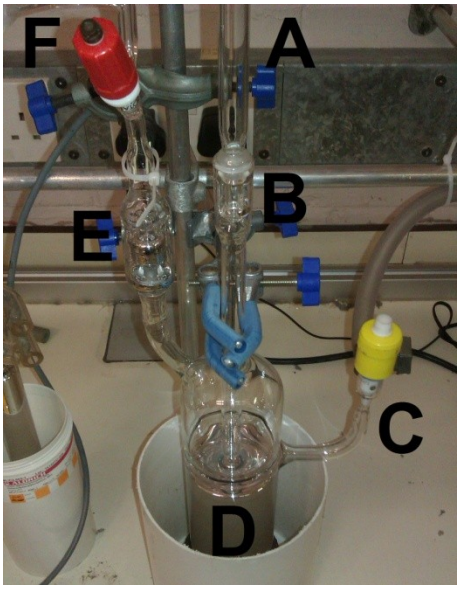
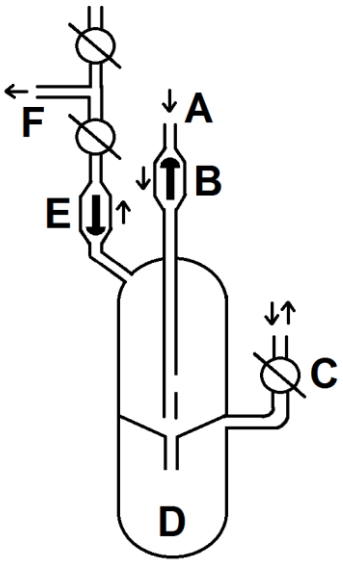


Figure (i) Toepler pump apparatus; (V) High vacuum pump; (G) gas ampoule; (T) Toepler pump; (M) Hg manometer.





A. Gas inlet

B. Hg valve

C. Air/vacuum inlet

D. Hg reservoir

E. Hg valve

F. Gas outlet

Figure (ii) Toepler pump.

Operation: With the output flask attached at side arm F, the line is fully evacuated to ca. 10^{-6} mbar; importantly the inlet valve C should either be under static vacuum or open to vacuum from a second pump. By noting the change in pressure (Δp) at the manometer (M), the desired amount of gas is carefully bled into the line. Unless the gas is condensable, a proportion of the gas will remain in the side arm leading to the output flask and should thus be compensated for in calculations. The gas is then allowed passage into the Toepler pump *via* A. The Toepler pump operates by forcing the gas into the output flask *via* a one-way Hg valve (E), which prevents backflow of the gas. This is achieved by carefully switching inlet valve C to air (the flow rate must be minimised using a needle valve), which provides a pressure differential that raises the Hg in the Hg reservoir (D). As the Hg rises, valve B is closed such that gas is forced through valve E. Once the Hg reaches beyond valve E, the inlet valve C is switched back to vacuum to lower the Hg and draw in more gas into the Toepler pump for the next cycle. In this manner, the gas initially bled into the line can be almost quantitatively transferred into the output flask.

Quantification of NH_3 and N_2H_4



Figure (iii) Distillation apparatus for NH_3 and N_2H_4 transfer.

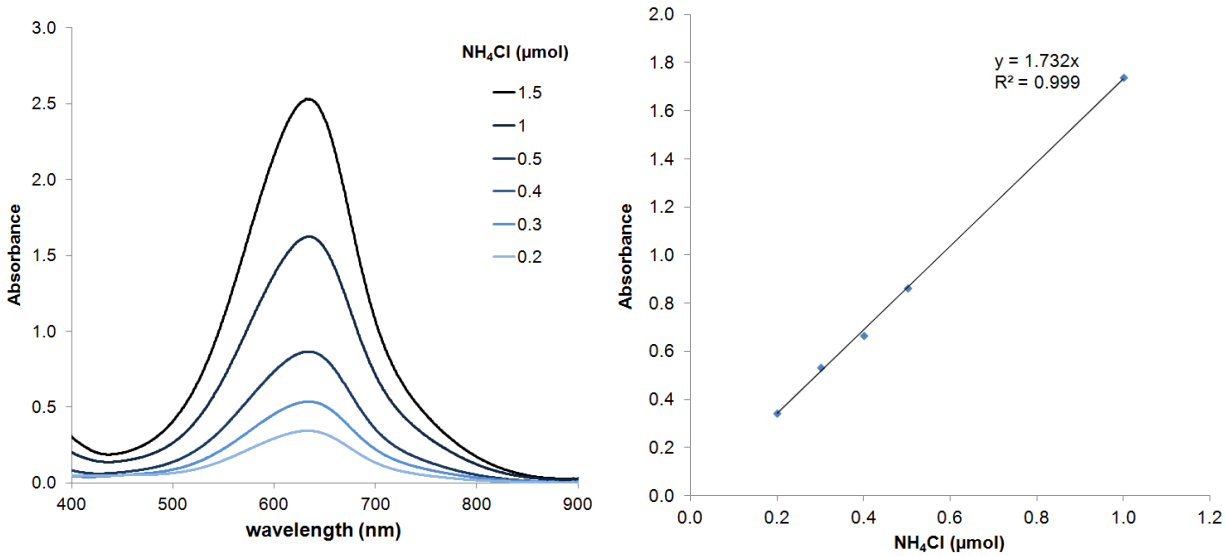


Figure (iv) UV-vis calibration curves for the indophenol test generated from solutions of $[NH_4]Cl$ of known concentrations; λ_{max} = 634 nm.

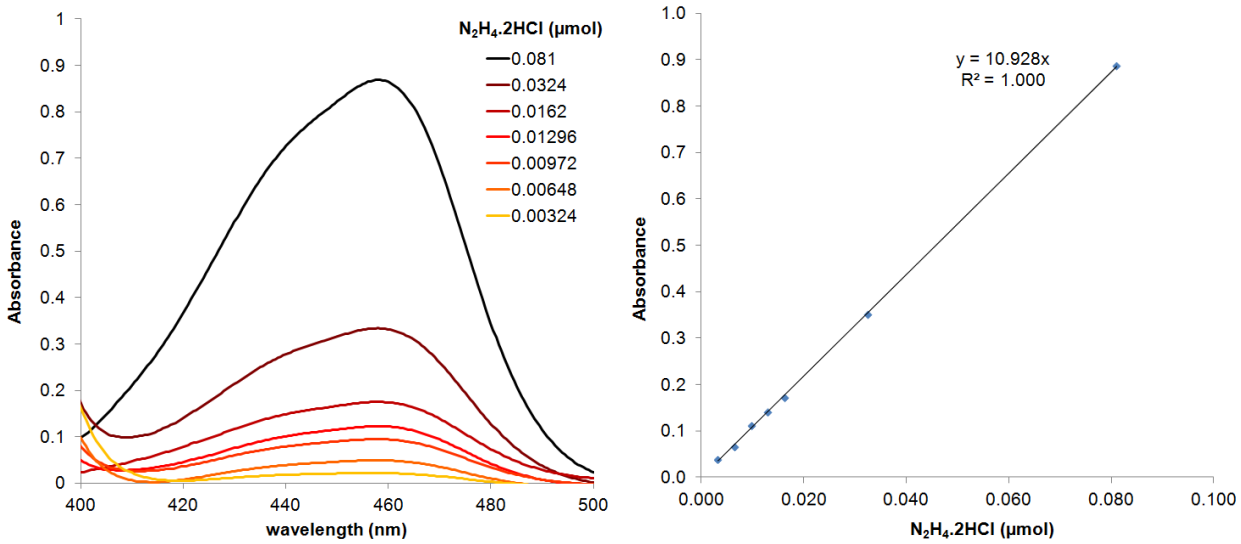


Figure (v) UV-vis calibration curves for the pdmab test generated from solutions of $N_2H_4 \cdot 2HCl$ of known concentrations; λ_{max} = 458 nm.

Mössbauer cell schematics

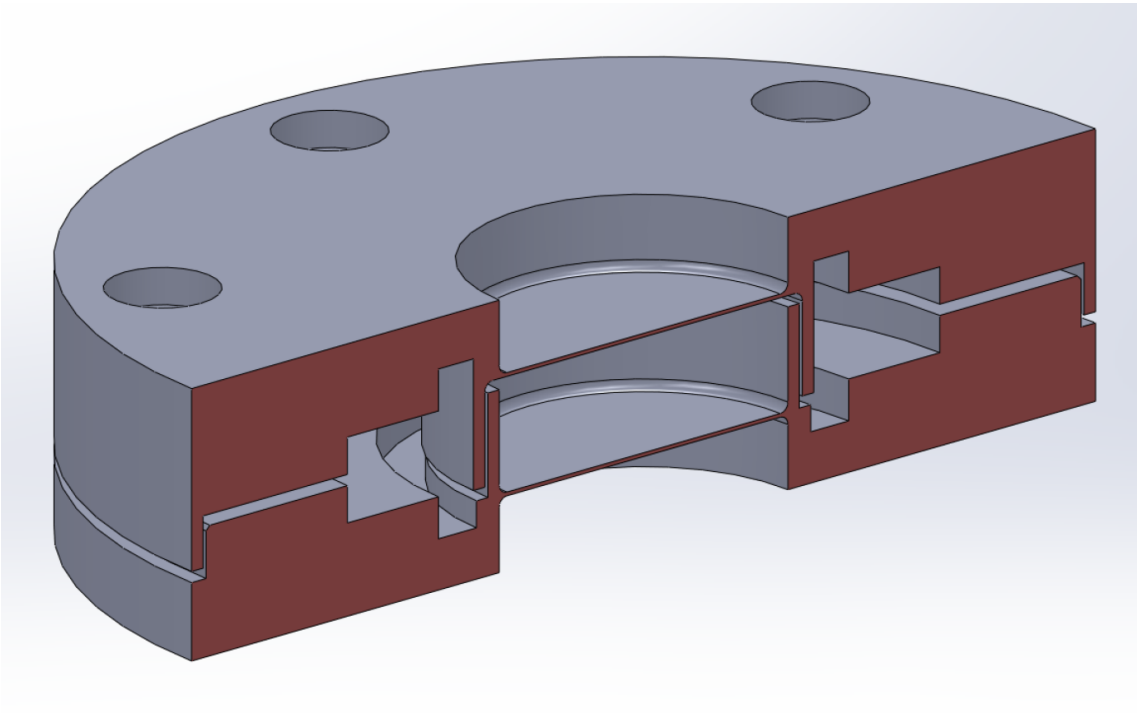
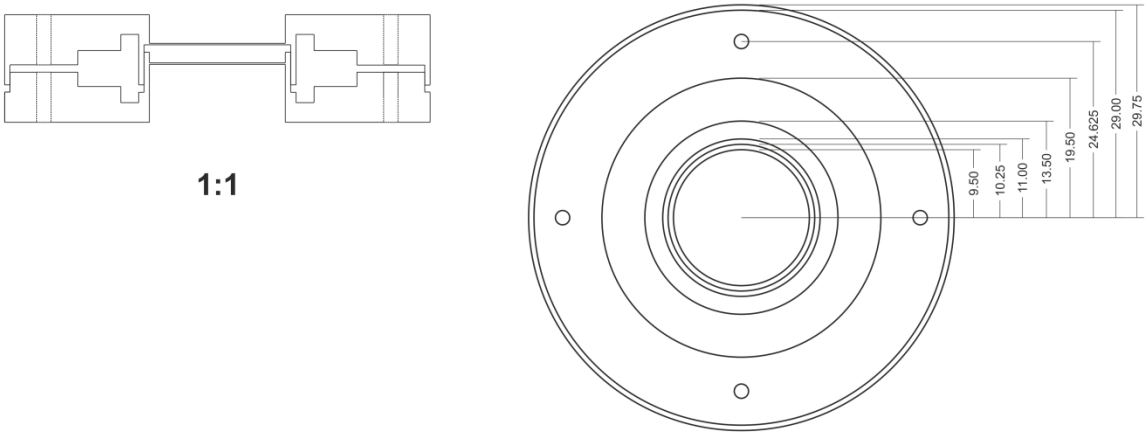
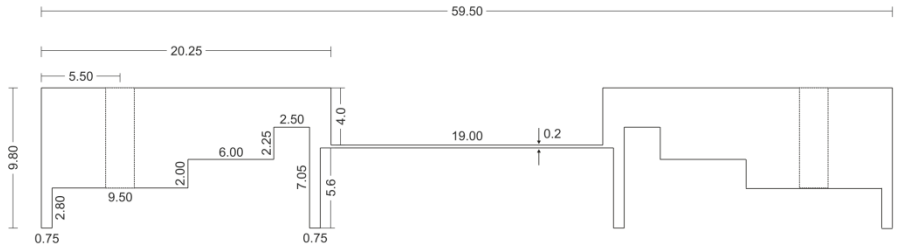


Figure (vi)



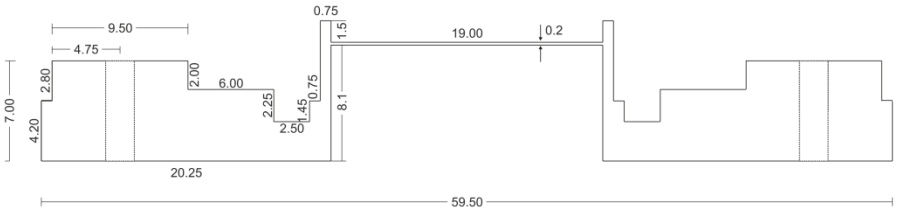
1:1

A/B

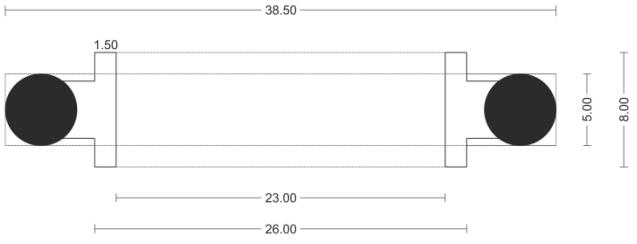


A

2:1



B



2:1



O-ring

Screw (example)

Figure (vii)

Crystallography data

[{Fe(dmpe)$_2$}$_2$(μ-N$_2$)] (6)

Crystal data and structure refinement for [{Fe(dmpe)$_2$}$_2$(μ-N$_2$)] (6).

Identification code	ASH1301
Empirical formula	$C_{24}H_{64}Fe_2N_2P_8$
Formula weight	740.23
Temperature/K	173
Crystal system	Triclinic
Space group	P-1
a/Å	9.3450(4)
b/Å	9.6733(3)
c/Å	23.4652(10)
α/°	90.674(3)
β/°	90.671(4)
γ/°	115.639(3)
Volume/Å^3	1911.86(14)
Z	2
ρ_{calc}g/cm^3	1.286
μ/mm^{-1}	1.110
F(000)	788.0
Crystal size/mm^3	0.41 × 0.35 × 0.06
Radiation	MoKα (λ = 0.71073)
2Θ range for data collection/°	5.88 to 58.64
Index ranges	-11 ≤ h ≤ 12, -13 ≤ k ≤ 13, -15 ≤ l ≤ 31
Reflections collected	15856
Independent reflections	8760 [R_{int} = 0.0202]
Data/restraints/parameters	8760/452/407
Goodness-of-fit on F^2	1.024
Final R indexes [I>=2σ (I)]	R_1 = 0.0431, wR_2 = 0.0900
Final R indexes [all data]	R_1 = 0.0556, wR_2 = 0.0984
Largest diff. peak/hole / e Å^{-3}	0.77/-0.64

Bond Lengths for [{Fe(dmpe)$_2$}$_2$(μ-N$_2$)] (6).

Atom	Atom	Length/Å	Atom	Atom	Length/Å
Fe1	N1	1.854(2)	C13	P14	1.855(3)
Fe1	P4	2.1556(8)	P14	C17	1.850(3)
Fe1	P14	2.1610(8)	P14	C18	1.855(3)
Fe1	P1	2.1806(8)	P21	C26	1.793(6)
Fe1	P11	2.1812(8)	P21	C25	1.816(5)
Fe2	N2	1.850(2)	P21	C22	1.887(6)
Fe2	P24'	2.121(3)	C22	C23	1.479(10)
Fe2	P34'	2.135(2)	C23	P24	1.879(7)
Fe2	P31	2.1655(17)	P24	C28	1.845(6)
Fe2	P21'	2.167(4)	P24	C27	1.852(6)
Fe2	P34	2.1671(14)	P31	C36	1.823(6)
Fe2	P24	2.1689(14)	P31	C35	1.836(6)
Fe2	P21	2.1867(17)	P31	C32	1.839(8)
Fe2	P31'	2.194(4)	C32	C33	1.415(12)
N1	N2	1.144(3)	C33	P34	1.867(7)

P1	C6'	1.800(8)	P34	C38	1.831(6)
P1	C5	1.810(5)	P34	C37	1.834(6)
P1	C6	1.844(5)	P21'	C25'	1.802(9)
P1	C2	1.849(5)	P21'	C26'	1.815(11)
P1	C2'	1.857(7)	P21'	C22'	1.913(11)
P1	C5'	1.874(8)	C22'	C23'	1.529(17)
C2	C3	1.543(8)	C23'	P24'	1.822(10)
C3	P4	1.871(6)	P24'	C27'	1.871(13)
C2'	C3'	1.595(11)	P24'	C28'	1.878(11)
C3'	P4	1.866(10)	P31'	C36'	1.789(10)
P4	C8	1.846(3)	P31'	C35'	1.840(12)
P4	C7	1.854(4)	P31'	C32'	1.849(10)
P11	C15	1.826(3)	C32'	C33'	1.647(13)
P11	C12	1.843(3)	C33'	P34'	1.786(8)
P11	C16	1.845(4)	P34'	C37'	1.882(11)
C12	C13	1.496(5)	P34'	C38'	1.896(11)

Bond Angles for [{Fe(dmpe)$_2$}$_2$(μ-N$_2$)] (6).

Atom	Atom	Atom	Angle/˚	Atom	Atom	Atom	Angle/˚
N1	Fe1	P4	121.43(7)	C12	C13	P14	108.8(2)
N1	Fe1	P14	118.62(7)	C17	P14	C13	99.72(17)
P4	Fe1	P14	119.94(3)	C17	P14	C18	97.57(17)
N1	Fe1	P1	89.18(7)	C13	P14	C18	98.12(18)
P4	Fe1	P1	84.81(3)	C17	P14	Fe1	120.21(12)
P14	Fe1	P1	95.54(3)	C13	P14	Fe1	111.48(11)
N1	Fe1	P11	90.53(7)	C18	P14	Fe1	125.05(12)
P4	Fe1	P11	94.67(3)	C26	P21	C25	102.4(3)
P14	Fe1	P11	85.29(3)	C26	P21	C22	100.9(4)
P1	Fe1	P11	179.17(3)	C25	P21	C22	97.4(3)
N2	Fe2	P24'	121.10(10)	C26	P21	Fe2	122.9(3)
N2	Fe2	P34'	120.54(9)	C25	P21	Fe2	117.63(19)
P24'	Fe2	P34'	118.33(10)	C22	P21	Fe2	111.6(2)
N2	Fe2	P31	90.08(8)	C23	C22	P21	105.6(5)
N2	Fe2	P21'	88.61(13)	C22	C23	P24	111.9(5)
P24'	Fe2	P21'	86.42(13)	C28	P24	C27	98.1(3)
P34'	Fe2	P21'	96.85(12)	C28	P24	C23	99.6(4)
N2	Fe2	P34	121.87(8)	C27	P24	C23	98.9(4)
P31	Fe2	P34	86.50(8)	C28	P24	Fe2	123.8(3)
N2	Fe2	P24	122.18(8)	C27	P24	Fe2	120.7(3)
P31	Fe2	P24	95.58(8)	C23	P24	Fe2	111.4(2)
P34	Fe2	P24	115.91(6)	C36	P31	C35	100.7(4)
N2	Fe2	P21	88.81(8)	C36	P31	C32	100.0(5)
P31	Fe2	P21	178.87(7)	C35	P31	C32	99.7(4)
P34	Fe2	P21	94.24(8)	C36	P31	Fe2	117.0(3)
P24	Fe2	P21	84.86(7)	C35	P31	Fe2	122.6(3)
N2	Fe2	P31'	87.43(13)	C32	P31	Fe2	113.2(3)
P24'	Fe2	P31'	95.29(13)	C33	C32	P31	111.7(6)
P34'	Fe2	P31'	85.52(11)	C32	C33	P34	116.9(5)
P21'	Fe2	P31'	176.02(16)	C38	P34	C37	99.7(4)
N2	N1	Fe1	178.7(2)	C38	P34	C33	96.9(4)
N1	N2	Fe2	179.1(2)	C37	P34	C33	97.6(4)

C5	P1	C6	99.9(3)	C38	P34	Fe2	123.7(2)
C5	P1	C2	100.1(3)	C37	P34	Fe2	123.2(3)
C6	P1	C2	99.3(3)	C33	P34	Fe2	110.0(3)
C6'	P1	C2'	101.1(4)	C25'	P21'	C26'	101.9(6)
C6'	P1	C5'	99.1(4)	C25'	P21'	C22'	96.1(6)
C2'	P1	C5'	97.3(4)	C26'	P21'	C22'	98.2(6)
C6'	P1	Fe1	119.0(3)	C25'	P21'	Fe2	123.9(5)
C5	P1	Fe1	126.38(19)	C26'	P21'	Fe2	121.3(5)
C6	P1	Fe1	117.51(19)	C22'	P21'	Fe2	109.8(4)
C2	P1	Fe1	109.30(18)	C23'	C22'	P21'	105.0(8)
C2'	P1	Fe1	111.2(3)	C22'	C23'	P24'	110.7(8)
C5'	P1	Fe1	124.8(3)	C23'	P24'	C27'	98.8(7)
C3	C2	P1	103.9(4)	C23'	P24'	C28'	100.5(5)
C2	C3	P4	106.1(4)	C27'	P24'	C28'	95.4(7)
C3'	C2'	P1	104.6(6)	C23'	P24'	Fe2	112.9(4)
C2'	C3'	P4	104.7(6)	C27'	P24'	Fe2	122.8(9)
C8	P4	C7	97.93(17)	C28'	P24'	Fe2	122.0(5)
C8	P4	C3'	104.4(4)	C36'	P31'	C35'	102.2(7)
C7	P4	C3'	91.9(3)	C36'	P31'	C32'	102.0(5)
C8	P4	C3	95.1(2)	C35'	P31'	C32'	98.9(7)
C7	P4	C3	102.6(3)	C36'	P31'	Fe2	124.0(5)
C8	P4	Fe1	121.56(12)	C35'	P31'	Fe2	115.1(8)
C7	P4	Fe1	123.37(12)	C32'	P31'	Fe2	111.2(4)
C3'	P4	Fe1	112.6(3)	C33'	C32'	P31'	106.8(6)
C3	P4	Fe1	111.4(2)	C32'	C33'	P34'	107.7(6)
C15	P11	C12	103.79(17)	C33'	P34'	C37'	103.5(5)
C15	P11	C16	97.11(19)	C33'	P34'	C38'	101.1(5)
C12	P11	C16	97.96(18)	C37'	P34'	C38'	93.4(6)
C15	P11	Fe1	115.90(12)	C33'	P34'	Fe2	115.9(3)
C12	P11	Fe1	111.20(11)	C37'	P34'	Fe2	117.3(5)
C16	P11	Fe1	127.36(13)	C38'	P34'	Fe2	121.9(5)
C13	C12	P11	108.4(2)				

$[\{Fe(dmpe)_2\}_2(\mu\text{-}N_2)][BArF_{24}]$ (7)

Crystal data and structure refinement for $[\{Fe(dmpe)_2\}_2(\mu\text{-}N_2)][BArF_{24}]$ (7).

Identification code	ASH1312b
Empirical formula	$C_{58.5}H_{82}BF_{24}Fe_2N_2O_{0.5}P_8$
Formula weight	1647.53
Temperature/K	173
Crystal system	tetragonal
Space group	I-4
a/Å	24.2660(2)
b/Å	24.2660(2)
c/Å	27.1965(4)
α/°	90
β/°	90
γ/°	90
Volume/Å^3	16014.4(4)
Z	8
ρ_{calc}g/cm^3	1.367

μ/mm^{-1}	0.614
F(000)	6752.0
Crystal size/mm^3	0.34 × 0.32 × 0.08
Radiation	MoKα (λ = 0.71073)
2Θ range for data collection/°	5.856 to 59.076
Index ranges	-21 ≤ h ≤ 31, -33 ≤ k ≤ 33, -34 ≤ l ≤ 35
Reflections collected	67627
Independent reflections	19279 [R_{int} = 0.0259, R_{sigma} = 0.0333]
Data/restraints/parameters	19279/301/909
Goodness-of-fit on F^2	1.067
Final R indexes [I>=2σ (I)]	R_1 = 0.0450, wR_2 = 0.1148
Final R indexes [all data]	R_1 = 0.0653, wR_2 = 0.1252
Largest diff. peak/hole / e Å^{-3}	0.61/-0.32
Flack parameter	-0.010(4)

Bond Lengths for [{Fe(dmpe)$_2$}$_2$(μ-N$_2$)][BArF$_{24}$] (7).

Atom	Atom	Length/Å	Atom	Atom	Length/Å
Fe1A	N1A	1.814(4)	C21	C22	1.386(5)
Fe1A	P1A	2.1933(10)	C21	C26	1.397(5)
Fe1A	P1A^1	2.1933(10)	C22	C23	1.402(5)
Fe1A	P4A^1	2.2072(10)	C23	C24	1.380(5)
Fe1A	P4A	2.2073(10)	C23	C27	1.488(6)
Fe2A	N2A	1.816(4)	C24	C25	1.394(6)
Fe2A	P11A^1	2.1913(12)	C25	C26	1.391(5)
Fe2A	P11A	2.1914(12)	C25	C28'	1.46(2)
Fe2A	P14A	2.2006(11)	C25	C28	1.500(6)
Fe2A	P14A^1	2.2006(11)	C27	F27C	1.325(6)
N1A	N2A	1.159(6)	C27	F27A	1.327(7)
P1A	C6A	1.840(4)	C27	F27B	1.329(7)
P1A	C5A	1.845(5)	C28	F28C	1.306(7)
P1A	C2A	1.852(5)	C28	F28B	1.314(7)
C2A	C3A	1.535(8)	C28	F28A	1.337(6)
C3A	P4A	1.830(5)	C28'	F28F	1.28(2)
P4A	C8A	1.829(5)	C28'	F28D	1.282(19)
P4A	C7A	1.851(5)	C28'	F28E	1.28(2)
P11A	C16A	1.832(5)	C29	C30	1.396(5)
P11A	C15A	1.837(6)	C29	C34	1.408(5)
P11A	C12A	1.857(6)	C30	C31	1.396(5)
C12A	C13A	1.490(10)	C31	C32	1.389(6)
C13A	P14A	1.839(6)	C31	C35	1.491(6)
P14A	C18A	1.817(5)	C32	C33	1.391(6)
P14A	C17A	1.855(6)	C33	C34	1.385(5)
Fe1B	N1B	1.827(4)	C33	C36'	1.47(2)
Fe1B	P1B^2	2.1915(11)	C33	C36	1.499(6)
Fe1B	P1B	2.1916(11)	C35	F35B	1.317(6)
Fe1B	P4B^2	2.2061(11)	C35	F35A	1.319(6)
Fe1B	P4B	2.2062(11)	C35	F35C	1.326(6)
Fe2B	N2B	1.816(4)	C36	F36C	1.295(7)
Fe2B	P14'^{2}	2.170(7)	C36	F36B	1.296(7)
Fe2B	P14'	2.170(7)	C36	F36A	1.324(7)

Fe2B	P11B[2]	2.190(3)	C36'	F36F	1.284(19)
Fe2B	P11B	2.190(3)	C36'	F36E	1.287(19)
Fe2B	P11'[2]	2.201(12)	C36'	F36D	1.293(19)
Fe2B	P11'	2.202(12)	C37	C38	1.391(5)
Fe2B	P14B	2.213(2)	C37	C42	1.403(5)
Fe2B	P14B[2]	2.213(2)	C38	C39	1.390(5)
N1B	N2B	1.149(6)	C39	C40	1.377(5)
P1B	C6B	1.843(4)	C39	C43	1.499(5)
P1B	C2B	1.846(6)	C40	C41	1.390(5)
P1B	C5B	1.854(5)	C41	C42	1.387(5)
C2B	C3B	1.500(9)	C41	C44	1.499(5)
C3B	P4B	1.824(5)	C43	F43C	1.337(5)
P4B	C8B	1.829(5)	C43	F43B	1.339(6)
P4B	C7B	1.831(5)	C43	F43A	1.345(5)
P11B	C15B	1.832(7)	C44	F44B	1.308(5)
P11B	C16B	1.834(6)	C44	F44C	1.329(5)
P11B	C12B	1.835(8)	C44	F44A	1.349(5)
C12B	C13B	1.420(15)	C45	C46	1.398(5)
C13B	P14B	1.811(8)	C45	C50	1.403(5)
P14B	C18B	1.777(7)	C46	C47	1.388(5)
P14B	C17B	1.820(8)	C47	C48	1.381(5)
P11'	C12'	1.806(19)	C47	C51	1.488(6)
P11'	C16'	1.816(19)	C48	C49	1.400(5)
P11'	C15'	1.834(18)	C49	C50	1.391(5)
C12'	C13'	1.39(2)	C49	C52	1.484(5)
C13'	P14'	1.813(17)	C51	F51C	1.317(5)
P14'	C17'	1.825(16)	C51	F51A	1.336(6)
P14'	C18'	1.837(18)	C51	F51B	1.355(7)
B20	C29	1.629(5)	C52	F52C	1.317(5)
B20	C45	1.632(5)	C52	F52B	1.321(5)
B20	C37	1.635(5)	C52	F52A	1.357(5)
B20	C21	1.641(5)			

[1]2-X,1-Y,+Z; [2]2-X,-Y,+Z

Bond Angles for [{Fe(dmpe)$_2$}$_2$(μ-N$_2$)][BArF$_{24}$] (7).

Atom	Atom	Atom	Angle/˚	Atom	Atom	Atom	Angle/˚
N1A	Fe1A	P1A	123.05(3)	C13'	P14'	Fe2B	109.8(7)
N1A	Fe1A	P1A[1]	123.05(3)	C17'	P14'	Fe2B	127.5(9)
P1A	Fe1A	P1A[1]	113.89(6)	C18'	P14'	Fe2B	115.1(12)
N1A	Fe1A	P4A[1]	91.69(3)	C29	B20	C45	101.9(3)
P1A	Fe1A	P4A[1]	93.54(4)	C29	B20	C37	113.2(3)
P1A[1]	Fe1A	P4A[1]	84.61(4)	C45	B20	C37	114.1(3)
N1A	Fe1A	P4A	91.70(3)	C29	B20	C21	112.7(3)
P1A	Fe1A	P4A	84.61(4)	C45	B20	C21	113.7(3)
P1A[1]	Fe1A	P4A	93.54(4)	C37	B20	C21	101.8(3)
P4A[1]	Fe1A	P4A	176.61(6)	C22	C21	C26	115.9(3)
N2A	Fe2A	P11A[1]	122.97(4)	C22	C21	B20	122.5(3)
N2A	Fe2A	P11A	122.97(4)	C26	C21	B20	120.9(3)
P11A[1]	Fe2A	P11A	114.06(7)	C21	C22	C23	122.6(3)
N2A	Fe2A	P14A	91.73(3)	C24	C23	C22	120.6(4)

P11A[1]	Fe2A	P14A	93.61(5)
P11A	Fe2A	P14A	84.50(5)
N2A	Fe2A	P14A[1]	91.72(3)
P11A[1]	Fe2A	P14A[1]	84.51(5)
P11A	Fe2A	P14A[1]	93.61(5)
P14A	Fe2A	P14A[1]	176.55(7)
N2A	N1A	Fe1A	180.0
N1A	N2A	Fe2A	180.0
C6A	P1A	C5A	99.8(2)
C6A	P1A	C2A	101.2(2)
C5A	P1A	C2A	98.9(3)
C6A	P1A	Fe1A	121.13(16)
C5A	P1A	Fe1A	120.33(16)
C2A	P1A	Fe1A	111.72(16)
C3A	C2A	P1A	109.1(3)
C2A	C3A	P4A	107.2(3)
C8A	P4A	C3A	102.4(2)
C8A	P4A	C7A	100.2(2)
C3A	P4A	C7A	99.7(2)
C8A	P4A	Fe1A	114.26(17)
C3A	P4A	Fe1A	110.37(16)
C7A	P4A	Fe1A	126.68(18)
C16A	P11A	C15A	100.5(3)
C16A	P11A	C12A	101.3(3)
C15A	P11A	C12A	97.9(4)
C16A	P11A	Fe2A	121.6(2)
C15A	P11A	Fe2A	120.7(2)
C12A	P11A	Fe2A	110.9(2)
C13A	C12A	P11A	110.3(4)
C12A	C13A	P14A	106.9(4)
C18A	P14A	C13A	102.5(3)
C18A	P14A	C17A	100.2(3)
C13A	P14A	C17A	101.1(3)
C18A	P14A	Fe2A	114.0(2)
C13A	P14A	Fe2A	110.41(19)
C17A	P14A	Fe2A	125.8(2)
N1B	Fe1B	P1B[2]	123.82(3)
N1B	Fe1B	P1B	123.82(3)
P1B[2]	Fe1B	P1B	112.36(6)
N1B	Fe1B	P4B[2]	91.49(3)
P1B[2]	Fe1B	P4B[2]	84.71(5)
P1B	Fe1B	P4B[2]	93.63(5)
N1B	Fe1B	P4B	91.49(3)
P1B[2]	Fe1B	P4B	93.63(5)
P1B	Fe1B	P4B	84.70(5)
P4B[2]	Fe1B	P4B	177.02(6)
N2B	Fe2B	P14'[2]	91.47(19)
N2B	Fe2B	P14'	91.47(19)
P14'[2]	Fe2B	P14'	177.1(4)
N2B	Fe2B	P11B[2]	123.10(7)
N2B	Fe2B	P11B	123.10(7)
P11B[2]	Fe2B	P11B	113.81(15)
N2B	Fe2B	P11'[2]	122.5(3)

C24	C23	C27	120.5(4)
C22	C23	C27	118.9(4)
C23	C24	C25	117.9(3)
C26	C25	C24	120.9(3)
C26	C25	C28'	120.5(13)
C24	C25	C28'	118.6(13)
C26	C25	C28	119.7(4)
C24	C25	C28	119.4(4)
C25	C26	C21	122.2(4)
F27C	C27	F27A	106.7(5)
F27C	C27	F27B	106.2(4)
F27A	C27	F27B	104.3(5)
F27C	C27	C23	113.8(4)
F27A	C27	C23	112.7(4)
F27B	C27	C23	112.4(5)
F28C	C28	F28B	106.4(5)
F28C	C28	F28A	104.8(5)
F28B	C28	F28A	104.8(5)
F28C	C28	C25	113.5(4)
F28B	C28	C25	114.2(4)
F28A	C28	C25	112.3(4)
F28F	C28'	F28D	109(2)
F28F	C28'	F28E	107(2)
F28D	C28'	F28E	110(2)
F28F	C28'	C25	108(3)
F28D	C28'	C25	113(3)
F28E	C28'	C25	108(3)
C30	C29	C34	115.7(3)
C30	C29	B20	122.6(3)
C34	C29	B20	120.8(3)
C29	C30	C31	122.4(3)
C32	C31	C30	120.5(4)
C32	C31	C35	120.5(4)
C30	C31	C35	119.0(4)
C31	C32	C33	118.2(3)
C34	C33	C32	120.8(4)
C34	C33	C36'	117.3(10)
C32	C33	C36'	121.9(10)
C34	C33	C36	120.2(4)
C32	C33	C36	119.0(4)
C33	C34	C29	122.3(3)
F35B	C35	F35A	104.2(5)
F35B	C35	F35C	107.0(4)
F35A	C35	F35C	106.0(4)
F35B	C35	C31	112.7(4)
F35A	C35	C31	112.9(4)
F35C	C35	C31	113.3(4)
F36C	C36	F36B	108.6(6)
F36C	C36	F36A	102.6(5)
F36B	C36	F36A	105.4(6)
F36C	C36	C33	113.0(5)
F36B	C36	C33	113.8(4)
F36A	C36	C33	112.6(4)

P14'[2]	Fe2B	P11'[2]	85.5(3)
P14'	Fe2B	P11'[2]	93.0(3)
N2B	Fe2B	P11'	122.5(3)
P14'[2]	Fe2B	P11'	92.9(3)
P14'	Fe2B	P11'	85.5(3)
P11'[2]	Fe2B	P11'	115.0(7)
N2B	Fe2B	P14B	90.49(5)
P11B[2]	Fe2B	P14B	94.86(12)
P11B	Fe2B	P14B	84.59(12)
N2B	Fe2B	P14B[2]	90.49(5)
P11B[2]	Fe2B	P14B[2]	84.60(12)
P11B	Fe2B	P14B[2]	94.86(12)
P14B	Fe2B	P14B[2]	179.01(11)
N2B	N1B	Fe1B	180.0
N1B	N2B	Fe2B	180.0
C6B	P1B	C2B	102.2(3)
C6B	P1B	C5B	99.4(2)
C2B	P1B	C5B	97.6(3)
C6B	P1B	Fe1B	121.12(16)
C2B	P1B	Fe1B	111.7(2)
C5B	P1B	Fe1B	120.98(17)
C3B	C2B	P1B	109.3(4)
C2B	C3B	P4B	109.0(4)
C3B	P4B	C8B	102.6(3)
C3B	P4B	C7B	100.4(3)
C8B	P4B	C7B	100.4(3)
C3B	P4B	Fe1B	109.62(19)
C8B	P4B	Fe1B	114.18(18)
C7B	P4B	Fe1B	126.5(2)
C15B	P11B	C16B	100.0(4)
C15B	P11B	C12B	98.4(5)
C16B	P11B	C12B	99.8(4)
C15B	P11B	Fe2B	121.2(3)
C16B	P11B	Fe2B	122.2(4)
C12B	P11B	Fe2B	111.0(3)
C13B	C12B	P11B	111.3(6)
C12B	C13B	P14B	111.9(6)
C18B	P14B	C13B	104.2(5)
C18B	P14B	C17B	100.5(5)
C13B	P14B	C17B	99.3(5)
C18B	P14B	Fe2B	114.5(3)
C13B	P14B	Fe2B	109.6(3)
C17B	P14B	Fe2B	125.9(4)
C12'	P11'	C16'	101.6(13)
C12'	P11'	C15'	99.7(11)
C16'	P11'	C15'	99.5(13)
C12'	P11'	Fe2B	110.7(8)
C16'	P11'	Fe2B	119.9(19)
C15'	P11'	Fe2B	122.1(13)
C13'	C12'	P11'	114.2(14)
C12'	C13'	P14'	114.9(13)
C13'	P14'	C17'	100.8(9)
C13'	P14'	C18'	101.5(11)
F36F	C36'	F36E	105.9(18)
F36F	C36'	F36D	104.6(18)
F36E	C36'	F36D	105.6(18)
F36F	C36'	C33	112.9(18)
F36E	C36'	C33	112(2)
F36D	C36'	C33	115(2)
C38	C37	C42	116.6(3)
C38	C37	B20	121.1(3)
C42	C37	B20	121.7(3)
C39	C38	C37	121.8(3)
C40	C39	C38	121.4(3)
C40	C39	C43	120.1(3)
C38	C39	C43	118.5(3)
C39	C40	C41	117.6(3)
C42	C41	C40	121.4(3)
C42	C41	C44	120.9(3)
C40	C41	C44	117.7(3)
C41	C42	C37	121.3(3)
F43C	C43	F43B	106.1(4)
F43C	C43	F43A	107.1(4)
F43B	C43	F43A	104.9(4)
F43C	C43	C39	113.3(3)
F43B	C43	C39	112.3(4)
F43A	C43	C39	112.6(3)
F44B	C44	F44C	107.3(4)
F44B	C44	F44A	107.1(4)
F44C	C44	F44A	103.4(4)
F44B	C44	C41	114.1(3)
F44C	C44	C41	112.2(4)
F44A	C44	C41	111.9(3)
C46	C45	C50	116.1(3)
C46	C45	B20	121.0(3)
C50	C45	B20	122.3(3)
C47	C46	C45	122.2(3)
C48	C47	C46	121.2(3)
C48	C47	C51	120.0(3)
C46	C47	C51	118.8(4)
C47	C48	C49	117.8(3)
C50	C49	C48	120.7(3)
C50	C49	C52	121.3(3)
C48	C49	C52	118.0(3)
C49	C50	C45	122.0(3)
F51C	C51	F51A	107.7(4)
F51C	C51	F51B	106.6(4)
F51A	C51	F51B	103.9(4)
F51C	C51	C47	114.0(4)
F51A	C51	C47	112.3(4)
F51B	C51	C47	111.7(4)
F52C	C52	F52B	107.0(4)
F52C	C52	F52A	105.2(4)
F52B	C52	F52A	105.7(4)
F52C	C52	C49	113.2(4)
F52B	C52	C49	113.3(4)

C17'	P14'	C18'	98.5(10)		F52A	C52	C49	111.9(3)

[1]2-X,1-Y,+Z; [2]2-X,-Y,+Z

[{Fe(dmpe)$_2$}$_2$(μ-N$_2$)][BArF$_{24}$]$_2$ (8)

Crystal data and structure refinement for [{Fe(dmpe)$_2$}$_2$(μ-N$_2$)][BArF$_{24}$]$_2$ (8).

Identification code	ASH1444
Empirical formula	$C_{44}H_{44}BF_{24}FeN_2P_4$
Formula weight	1247.35
Temperature/K	173.00(14)
Crystal system	triclinic
Space group	P-1
a/Å	13.2340(7)
b/Å	14.1440(8)
c/Å	14.8769(8)
α/°	106.989(5)
β/°	96.917(4)
γ/°	91.241(4)
Volume/Å^3	2639.0(3)
Z	2
ρ_{calc}g/cm^3	1.570
μ/mm^{-1}	0.526
F(000)	1258.0
Radiation	MoKα (λ = 0.71073)
2Θ range for data collection/°	4.458 to 56.516
Index ranges	-15 ≤ h ≤ 16, -17 ≤ k ≤ 18, -18 ≤ l ≤ 13
Reflections collected	15463
Independent reflections	10355 [R_{int} = 0.0245, R_{sigma} = 0.0733]
Data/restraints/parameters	10355/53/636
Goodness-of-fit on F^2	1.574
Final R indexes [I>=2σ (I)]	R_1 = 0.1542, wR_2 = 0.4111
Final R indexes [all data]	R_1 = 0.2130, wR_2 = 0.4580
Largest diff. peak/hole / e Å^{-3}	3.01/-1.45

Bond Lengths for [{Fe(dmpe)$_2$}$_2$(μ-N$_2$)][BArF$_{24}$]$_2$ (8).

Atom	Atom	Length/Å	Atom	Atom	Length/Å
Fe0A	P0AA	2.229(4)	C4BA	C0BA	1.3900
Fe0A	P	2.209(4)	C4BA	C7BA	1.505(12)
Fe0A	P1	2.207(4)	C0BA	C7AA	1.3900
Fe0A	P2	2.227(4)	C7AA	C3BA	1.3900
Fe0A	N1	1.949(6)	C7AA	C1CA	1.467(11)
P0AA	C7CA	1.825(14)	C2AA	C4	1.3900
P0AA	C0DA	1.807(16)	C2AA	C9AA	1.3900
P0AA	C9	1.800(15)	C2AA	B4AA	1.674(8)
P	C4CA	1.815(15)	C4	C7	1.3900
P	C10	1.787(15)	C7	C5	1.3900
P	C14	1.791(14)	C7	C8BA	1.487(9)
P1	C9CA	1.838(15)	C5	C0AA	1.3900
P1	C1DA	1.790(15)	C0AA	C9AA	1.3900

P1	C13	1.798(13)	C0AA	C6BA	1.464(10)
P2	C5CA	1.863(14)	F8BA	C2CA	1.243(12)
P2	C11	1.789(14)	C3AA	C1	1.3900
P2	C12	1.782(15)	C3AA	C4AA	1.3900
F0AA	C8	1.294(13)	C1	C2	1.3900
F1AA	C6BA	1.340(11)	C1	B4AA	1.673(10)
F2AA	C7BA	1.299(16)	C2	C2BA	1.3900
F3AA	C9BA	1.334(13)	C2BA	C6	1.3900
F4AA	C8BA	1.306(13)	C2BA	C2CA	1.466(11)
F5AA	C1CA	1.334(13)	C6	C4AA	1.3900
F6AA	C7BA	1.268(12)	C4AA	C9BA	1.492(10)
F7AA	C8BA	1.312(11)	C8AA	C1AA	1.3900
F8AA	C9BA	1.340(11)	C8AA	C5BA	1.3900
F9AA	C8	1.277(14)	C1AA	C5AA	1.3900
F0BA	C6BA	1.304(12)	C1AA	B4AA	1.679(9)
F1BA	C9BA	1.353(12)	C5AA	C6AA	1.3900
F1	C1CA	1.297(13)	C6AA	C3	1.3900
F2BA	C6BA	1.354(13)	C6AA	C0CA	1.501(11)
F3BA	C0CA	1.328(12)	C3	C5BA	1.3900
F4BA	C0CA	1.336(12)	C5BA	C8	1.525(11)
F5BA	C8	1.280(13)	F9BA	C7BA	1.317(17)
F6BA	C8BA	1.323(13)	F2	C2CA	1.333(14)
F7BA	C0CA	1.294(13)	C1CA	F3	1.230(14)
C	C1BA	1.3900	C2CA	F4	1.207(12)
C	C3BA	1.3900	C4CA	C9CA	1.44(2)
C	B4AA	1.719(9)	C5CA	C7CA	1.49(2)
C1BA	C4BA	1.3900	N1	N1[1]	1.072(12)

[1]2-X,-Y,-Z

Bond Angles for [{Fe(dmpe)$_2$}$_2$(μ-N$_2$)][BArF$_{24}$]$_2$ (8).

Atom	Atom	Atom	Angle/°	Atom	Atom	Atom	Angle/°
P	Fe0A	P0AA	163.03(18)	C8AA	C1AA	B4AA	118.8(4)
P	Fe0A	P2	92.6(2)	C5AA	C1AA	C8AA	120.0
P1	Fe0A	P0AA	94.3(2)	C5AA	C1AA	B4AA	121.2(4)
P1	Fe0A	P	84.9(2)	C1AA	C5AA	C6AA	120.0
P1	Fe0A	P2	161.32(17)	C5AA	C6AA	C3	120.0
P2	Fe0A	P0AA	82.8(2)	C5AA	C6AA	C0CA	119.6(5)
N1	Fe0A	P0AA	97.4(2)	C3	C6AA	C0CA	120.2(5)
N1	Fe0A	P	99.6(2)	C5BA	C3	C6AA	120.0
N1	Fe0A	P1	96.6(2)	C8AA	C5BA	C8	117.6(5)
N1	Fe0A	P2	102.1(2)	C3	C5BA	C8AA	120.0
C7CA	P0AA	Fe0A	115.2(7)	C3	C5BA	C8	122.2(5)
C0DA	P0AA	Fe0A	116.4(8)	C2AA	B4AA	C	109.5(5)
C0DA	P0AA	C7CA	95.7(16)	C2AA	B4AA	C1AA	114.6(5)
C9	P0AA	Fe0A	117.2(8)	C1	B4AA	C	115.6(5)
C9	P0AA	C7CA	118.6(17)	C1	B4AA	C2AA	104.9(5)
C9	P0AA	C0DA	88(2)	C1	B4AA	C1AA	110.9(5)
C4CA	P	Fe0A	113.1(8)	C1AA	B4AA	C	101.6(5)
C10	P	Fe0A	120.4(9)	F1AA	C6BA	F2BA	104.1(8)
C10	P	C4CA	105.6(16)	F1AA	C6BA	C0AA	114.1(7)

C10	P	C14	85(2)
C14	P	Fe0A	124.1(14)
C14	P	C4CA	104.3(13)
C9CA	P1	Fe0A	108.9(6)
C1DA	P1	Fe0A	121.0(9)
C1DA	P1	C9CA	99.4(14)
C1DA	P1	C13	96.3(14)
C13	P1	Fe0A	121.7(8)
C13	P1	C9CA	106.5(14)
C5CA	P2	Fe0A	107.7(6)
C11	P2	Fe0A	121.0(9)
C11	P2	C5CA	106.1(13)
C12	P2	Fe0A	122.1(8)
C12	P2	C5CA	101.5(15)
C12	P2	C11	96.1(16)
C1BA	C	C3BA	120.0
C1BA	C	B4AA	117.7(4)
C3BA	C	B4AA	122.2(4)
C	C1BA	C4BA	120.0
C1BA	C4BA	C7BA	118.8(6)
C0BA	C4BA	C1BA	120.0
C0BA	C4BA	C7BA	121.1(6)
C4BA	C0BA	C7AA	120.0
C0BA	C7AA	C1CA	120.5(6)
C3BA	C7AA	C0BA	120.0
C3BA	C7AA	C1CA	119.5(6)
C7AA	C3BA	C	120.0
C4	C2AA	C9AA	120.0
C4	C2AA	B4AA	117.5(4)
C9AA	C2AA	B4AA	122.2(4)
C2AA	C4	C7	120.0
C4	C7	C8BA	120.4(5)
C5	C7	C4	120.0
C5	C7	C8BA	119.6(5)
C0AA	C5	C7	120.0
C5	C0AA	C6BA	119.5(5)
C9AA	C0AA	C5	120.0
C9AA	C0AA	C6BA	120.5(5)
C0AA	C9AA	C2AA	120.0
C1	C3AA	C4AA	120.0
C3AA	C1	C2	120.0
C3AA	C1	B4AA	116.9(4)
C2	C1	B4AA	123.1(4)
C2BA	C2	C1	120.0
C2	C2BA	C6	120.0
C2	C2BA	C2CA	121.1(5)
C6	C2BA	C2CA	118.8(5)
C2BA	C6	C4AA	120.0
C3AA	C4AA	C9BA	119.8(6)
C6	C4AA	C3AA	120.0
C6	C4AA	C9BA	120.0(6)
C1AA	C8AA	C5BA	120.0
F0BA	C6BA	F1AA	103.9(9)
F0BA	C6BA	F2BA	106.7(9)
F0BA	C6BA	C0AA	114.9(7)
F2BA	C6BA	C0AA	112.2(10)
F2AA	C7BA	C4BA	109.5(11)
F2AA	C7BA	F9BA	107.7(12)
F6AA	C7BA	F2AA	107.2(10)
F6AA	C7BA	C4BA	114.2(9)
F6AA	C7BA	F9BA	106.8(14)
F9BA	C7BA	C4BA	111.2(9)
F4AA	C8BA	F7AA	105.8(9)
F4AA	C8BA	F6BA	106.2(8)
F4AA	C8BA	C7	113.9(8)
F7AA	C8BA	F6BA	105.5(10)
F7AA	C8BA	C7	112.9(6)
F6BA	C8BA	C7	111.9(9)
F3AA	C9BA	F8AA	105.5(9)
F3AA	C9BA	F1BA	106.6(8)
F3AA	C9BA	C4AA	113.7(8)
F8AA	C9BA	F1BA	106.1(9)
F8AA	C9BA	C4AA	111.4(7)
F1BA	C9BA	C4AA	113.0(8)
F3BA	C0CA	F4BA	103.3(9)
F3BA	C0CA	C6AA	113.0(8)
F4BA	C0CA	C6AA	111.4(7)
F7BA	C0CA	F3BA	109.9(9)
F7BA	C0CA	F4BA	105.3(9)
F7BA	C0CA	C6AA	113.2(9)
F5AA	C1CA	C7AA	112.9(10)
F1	C1CA	F5AA	102.3(9)
F1	C1CA	C7AA	112.9(9)
F3	C1CA	F5AA	105.5(12)
F3	C1CA	F1	107.9(14)
F3	C1CA	C7AA	114.4(9)
F8BA	C2CA	C2BA	115.3(9)
F8BA	C2CA	F2	91.2(11)
F2	C2CA	C2BA	112.4(9)
F4	C2CA	F8BA	113.7(12)
F4	C2CA	C2BA	116.1(8)
F4	C2CA	F2	104.7(13)
C9CA	C4CA	P	111.7(14)
C7CA	C5CA	P2	120.7(11)
C5CA	C7CA	P0AA	105.9(13)
C4CA	C9CA	P1	118.1(12)
F0AA	C8	C5BA	112.2(9)
F9AA	C8	F0AA	104.9(10)
F9AA	C8	F5BA	103.2(12)
F9AA	C8	C5BA	111.2(9)
F5BA	C8	F0AA	111.7(11)
F5BA	C8	C5BA	113.1(8)
N1[1]	N1	Fe0A	177.4(8)

[1]2-X,-Y,-Z

$Fe(H)(N_3)(dmpe)_2$ (9)

Crystal data and structure refinement for $Fe(H)(N_3)(dmpe)_2$ (9).

Identification code	ASH1440
Empirical formula	$C_{13}H_{32}FeN_2P_4$
Formula weight	396.13
Temperature/K	172.9(3)
Crystal system	monoclinic
Space group	$P2_1/c$
a/Å	9.0771(2)
b/Å	11.9630(2)
c/Å	18.3468(4)
α/°	90
β/°	97.386(2)
γ/°	90
Volume/Å^3	1975.74(7)
Z	4
ρ_{calc}g/cm^3	1.332
μ/mm^{-1}	1.081
F(000)	840.0
Radiation	MoKα (λ = 0.71073)
2Θ range for data collection/°	4.478 to 56.29
Index ranges	-10 ≤ h ≤ 12, -15 ≤ k ≤ 14, -23 ≤ l ≤ 13
Reflections collected	6955
Independent reflections	3978 [R_{int} = 0.0412, R_{sigma} = 0.0625]
Data/restraints/parameters	3978/0/193
Goodness-of-fit on F^2	1.060
Final R indexes [I>=2σ (I)]	R_1 = 0.0350, wR_2 = 0.0849
Final R indexes [all data]	R_1 = 0.0454, wR_2 = 0.1057
Largest diff. peak/hole / e Å^{-3}	0.47/-0.62

Bond Lengths for $Fe(H)(N_3)(dmpe)_2$ (9).

Atom	Atom	Length/Å	Atom	Atom	Length/Å
Fe1	P6	2.1865(8)	P14	C15	1.828(3)
Fe1	P3	2.1899(7)	P14	C13	1.842(3)
Fe1	P14	2.1916(8)	P14	C16	1.826(3)
Fe1	P11	2.1926(7)	P11	C12	1.837(3)
Fe1	N18	2.077(2)	P11	C10	1.824(3)
P6	C8	1.829(3)	P11	C17	1.829(3)
P6	C7	1.830(3)	N19	N18	1.169(3)
P6	C5	1.837(3)	N19	N20	1.185(3)
P3	C4	1.840(3)	C12	C13	1.521(4)
P3	C2	1.833(3)	C4	C5	1.521(4)
P3	C9	1.826(3)			

Bond Angles for $Fe(H)(N_3)(dmpe)_2$ (9).

Atom	Atom	Atom	Angle/°	Atom	Atom	Atom	Angle/°
P6	Fe1	P3	85.61(3)	C9	P3	C4	100.49(13)
P6	Fe1	P14	173.78(3)	C9	P3	C2	99.76(13)
P6	Fe1	P11	94.30(3)	C15	P14	Fe1	119.05(10)
P3	Fe1	P14	93.65(3)	C15	P14	C13	100.65(14)
P3	Fe1	P11	173.94(3)	C13	P14	Fe1	109.50(10)
P14	Fe1	P11	85.79(3)	C16	P14	Fe1	121.10(10)
N18	Fe1	P6	94.63(7)	C16	P14	C15	102.17(14)
N18	Fe1	P3	93.50(7)	C16	P14	C13	101.21(14)
N18	Fe1	P14	91.58(7)	C12	P11	Fe1	109.83(10)
N18	Fe1	P11	92.54(7)	C10	P11	Fe1	122.74(10)
C8	P6	Fe1	122.76(10)	C10	P11	C12	100.66(14)
C8	P6	C5	100.65(13)	C10	P11	C17	101.50(14)
C7	P6	Fe1	118.60(10)	C17	P11	Fe1	117.78(10)
C7	P6	C8	101.27(14)	C17	P11	C12	101.09(14)
C7	P6	C5	100.42(13)	N18	N19	N20	178.0(3)
C5	P6	Fe1	109.65(9)	N19	N18	Fe1	130.48(19)
C4	P3	Fe1	110.33(9)	C13	C12	P11	107.50(19)
C2	P3	Fe1	123.92(9)	C5	C4	P3	107.90(17)
C2	P3	C4	101.02(13)	C4	C5	P6	107.50(18)
C9	P3	Fe1	117.80(9)	C12	C13	P14	107.74(19)

$Fe(H)(dmpe)_2$ (10).

Crystal data and structure refinement for $Fe(H)(dmpe)_2$ (10).

Identification code	ASH1331
Empirical formula	$C_{12}H_{33}FeP_4$
Formula weight	357.11
Temperature/K	173
Crystal system	monoclinic
Space group	$P2_1/c$
a/Å	9.8349(3)
b/Å	10.5752(4)
c/Å	18.1387(7)
α/°	90
β/°	92.251(3)
γ/°	90
Volume/Å^3	1885.09(12)
Z	4
ρ_{calc}g/cm^3	1.258
μ/mm^{-1}	1.122
F(000)	764.0
Crystal size/mm^3	0.75 × 0.51 × 0.41
Radiation	MoKα (λ = 0.71073)
2Θ range for data collection/°	5.994 to 55.778
Index ranges	-12 ≤ h ≤ 12, -12 ≤ k ≤ 13, -22 ≤ l ≤ 10
Reflections collected	6166
Independent reflections	3704 [R_{int} = 0.0178, R_{sigma} = 0.0316]
Data/restraints/parameters	3704/0/159
Goodness-of-fit on F^2	1.068

Final R indexes [I>=2σ (I)]	R_1 = 0.0288, wR_2 = 0.0677
Final R indexes [all data]	R_1 = 0.0346, wR_2 = 0.0707
Largest diff. peak/hole / e Å^{-3}	0.32/-0.23

Bond Lengths for Fe(H)(dmpe)$_2$ (10).

Atom	Atom	Length/Å	Atom	Atom	Length/Å
Fe1	P11	2.1521(6)	P4	C8	1.828(2)
Fe1	P14	2.1611(6)	P4	C7	1.838(2)
Fe1	P4	2.1702(6)	P11	C15	1.835(2)
Fe1	P1	2.1750(6)	P11	C16	1.838(2)
P1	C5	1.841(2)	P11	C12	1.863(2)
P1	C6	1.842(2)	C12	C13	1.526(3)
P1	C2	1.848(2)	C13	P14	1.848(2)
C2	C3	1.523(3)	P14	C17	1.838(2)
C3	P4	1.854(2)	P14	C18	1.843(2)

Bond Angles for Fe(H)(dmpe)$_2$ (10).

Atom	Atom	Atom	Angle/˚	Atom	Atom	Atom	Angle/˚
P11	Fe1	P14	86.39(2)	C8	P4	Fe1	121.57(8)
P11	Fe1	P4	163.22(2)	C7	P4	Fe1	122.74(8)
P14	Fe1	P4	103.80(2)	C3	P4	Fe1	108.20(7)
P11	Fe1	P1	103.16(2)	C15	P11	C16	98.82(12)
P14	Fe1	P1	102.82(2)	C15	P11	C12	101.28(12)
P4	Fe1	P1	87.74(2)	C16	P11	C12	101.43(11)
C5	P1	C6	98.28(12)	C15	P11	Fe1	118.61(9)
C5	P1	C2	99.40(10)	C16	P11	Fe1	121.96(8)
C6	P1	C2	99.79(11)	C12	P11	Fe1	111.55(8)
C5	P1	Fe1	117.90(8)	C13	C12	P11	108.97(15)
C6	P1	Fe1	127.72(8)	C12	C13	P14	107.96(15)
C2	P1	Fe1	109.12(7)	C17	P14	C18	97.83(13)
C3	C2	P1	107.61(14)	C17	P14	C13	100.53(11)
C2	C3	P4	108.74(14)	C18	P14	C13	99.51(11)
C8	P4	C7	98.86(11)	C17	P14	Fe1	125.84(8)
C8	P4	C3	100.93(10)	C18	P14	Fe1	119.95(8)
C7	P4	C3	100.84(11)	C13	P14	Fe1	108.82(7)

[Fe(dmpe)$_2$][K] (11).

Crystal data and structure refinement for [Fe(dmpe)$_2$][K] (11).

Identification code	ASH1329
Empirical formula	$C_{68}H_{168}Fe_4K_4P_{16}$
Formula weight	1861.33
Temperature/K	173
Crystal system	monoclinic
Space group	C2/c
a/Å	23.6486(8)
b/Å	15.6165(4)

c/Å	28.5949(8)
α/°	90
β/°	105.480(3)
γ/°	90
Volume/Å^3	10177.3(5)
Z	4
ρ_{calc}g/cm^3	1.215
μ/mm^{-1}	8.564
F(000)	3984.0
Crystal size/mm^3	0.59 × 0.46 × 0.39
Radiation	CuKα (λ = 1.54184)
2Θ range for data collection/°	6.414 to 147.36
Index ranges	-28 ≤ h ≤ 28, -19 ≤ k ≤ 13, -33 ≤ l ≤ 35
Reflections collected	16184
Independent reflections	9786 [R_{int} = 0.0418, R_{sigma} = 0.0603]
Data/restraints/parameters	9786/443/520
Goodness-of-fit on F^2	1.034
Final R indexes [I>=2σ (I)]	R_1 = 0.0692, wR_2 = 0.1853
Final R indexes [all data]	R_1 = 0.0931, wR_2 = 0.2039
Largest diff. peak/hole / e Å^{-3}	0.65/-0.78

Bond Lengths for [Fe(dmpe)$_2$][K] (11).

Atom	Atom	Length/Å	Atom	Atom	Length/Å
Fe1	P1	2.1264(16)	P31	C36	1.864(9)
Fe1	P11	2.1267(15)	C32	C33	1.442(18)
Fe1	P4	2.1342(16)	C33	P34	1.832(11)
Fe1	P14	2.1348(16)	P34	C38	1.814(12)
Fe1	K1	3.4224(8)	P34	C37	1.856(13)
Fe1	K2	3.4562(15)	P21'	C22'	1.855(18)
Fe2	P34'	1.968(13)	P21'	C26'	1.857(19)
Fe2	P31'	2.054(12)	P21'	C25'	1.872(17)
Fe2	P34	2.099(3)	C22'	C23'	1.49(3)
Fe2	P21	2.1322(18)	C23'	P24'	1.86(2)
Fe2	P31	2.148(3)	P24'	C28'	1.85(2)
Fe2	P24	2.187(4)	P24'	C27'	1.89(2)
Fe2	P21'	2.208(6)	P31'	C32'	1.83(2)
Fe2	P24'	2.241(12)	P31'	C35'	1.862(19)
Fe2	K3	3.3576(9)	P31'	C36'	1.870(17)
Fe2	K2	3.4933(15)	C32'	C33'	1.43(2)
K1	Fe1^1	3.4223(8)	C33'	P34'	1.83(2)
K1	K2^1	4.870(2)	P34'	C38'	1.81(2)
K1	K2	4.870(2)	P34'	C37'	1.86(2)
K2	K3	4.907(2)	C41	C42	1.423(12)
K3	Fe2^1	3.3576(9)	C41	C45	1.463(13)
K3	K2^1	4.907(2)	C42	C43	1.468(12)
P1	C6	1.853(7)	C43	C44	1.442(12)
P1	C5	1.862(8)	C44	C45	1.449(12)
P1	C2	1.867(9)	C41'	C42'	1.447(14)
C2	C3	1.460(13)	C41'	C45'	1.464(15)
C3	P4	1.864(9)	C42'	C43'	1.455(14)
P4	C7	1.836(8)	C43'	C44'	1.447(14)
P4	C8	1.843(7)	C44'	C45'	1.468(14)

P11	C15	1.837(8)	C51	C55	1.474(14)
P11	C16	1.842(7)	C51	C52	1.493(14)
P11	C12	1.879(7)	C52	C53	1.509(15)
C12	C13	1.509(10)	C53	C54	1.489(15)
C13	P14	1.856(7)	C54	C55	1.476(15)
P14	C17	1.847(7)	C51'	C55'	1.469(14)
P14	C18	1.864(7)	C51'	C52'	1.480(14)
P21	C26	1.852(9)	C52'	C53'	1.491(14)
P21	C25	1.862(8)	C53'	C54'	1.465(14)
P21	C22	1.870(10)	C54'	C55'	1.464(14)
C22	C23	1.442(18)	C51"	C55"	1.470(14)
C23	P24	1.865(11)	C51"	C52"	1.494(15)
P24	C28	1.849(11)	C52"	C53"	1.498(16)
P24	C27	1.869(10)	C53"	C54"	1.485(15)
P31	C35	1.840(9)	C54"	C55"	1.474(14)
P31	C32	1.847(10)			

[1]1-X,+Y,1/2-Z

Bond Angles for [Fe(dmpe)$_2$][K] (11).

Atom	Atom	Atom	Angle/˚	Atom	Atom	Atom	Angle/˚
P1	Fe1	P11	107.92(7)	C13	P14	C18	98.8(4)
P1	Fe1	P4	86.60(7)	C17	P14	Fe1	124.4(3)
P11	Fe1	P4	100.28(7)	C13	P14	Fe1	111.1(2)
P1	Fe1	P14	97.50(7)	C18	P14	Fe1	119.6(3)
P11	Fe1	P14	84.90(6)	C26	P21	C25	94.6(5)
P4	Fe1	P14	172.12(7)	C26	P21	C22	97.4(6)
P1	Fe1	K1	164.99(5)	C25	P21	C22	97.4(5)
P11	Fe1	K1	82.22(6)	C26	P21	Fe2	122.9(4)
P4	Fe1	K1	80.58(5)	C25	P21	Fe2	127.3(3)
P14	Fe1	K1	94.36(5)	C22	P21	Fe2	111.0(3)
P1	Fe1	K2	81.50(6)	C23	C22	P21	109.5(7)
P11	Fe1	K2	167.90(6)	C22	C23	P24	109.9(8)
P4	Fe1	K2	87.61(6)	C28	P24	C23	100.4(6)
P14	Fe1	K2	86.36(6)	C28	P24	C27	95.9(6)
K1	Fe1	K2	90.14(5)	C23	P24	C27	99.0(6)
P34'	Fe2	P31'	89.3(5)	C28	P24	Fe2	122.6(4)
P34	Fe2	P21	102.20(12)	C23	P24	Fe2	110.4(4)
P34	Fe2	P31	84.78(16)	C27	P24	Fe2	123.9(4)
P21	Fe2	P31	108.08(10)	C35	P31	C32	98.6(6)
P34	Fe2	P24	169.46(15)	C35	P31	C36	92.1(5)
P21	Fe2	P24	85.84(12)	C32	P31	C36	101.4(6)
P31	Fe2	P24	99.31(14)	C35	P31	Fe2	124.0(4)
P34'	Fe2	P21'	103.6(4)	C32	P31	Fe2	109.8(4)
P31'	Fe2	P21'	106.9(4)	C36	P31	Fe2	125.9(4)
P34'	Fe2	P24'	164.5(5)	C33	C32	P31	110.1(8)
P31'	Fe2	P24'	103.2(4)	C32	C33	P34	106.4(8)
P21'	Fe2	P24'	81.8(3)	C38	P34	C33	99.8(7)
P34'	Fe2	K3	91.1(4)	C38	P34	C37	92.9(9)
P31'	Fe2	K3	177.0(3)	C33	P34	C37	100.9(7)
P34	Fe2	K3	83.22(12)	C38	P34	Fe2	123.4(5)

P21	Fe2	K3	78.82(7)
P31	Fe2	K3	167.23(11)
P24	Fe2	K3	91.80(10)
P21'	Fe2	K3	75.92(15)
P24'	Fe2	K3	76.0(3)
P34'	Fe2	K2	88.0(4)
P31'	Fe2	K2	85.6(3)
P34	Fe2	K2	90.54(11)
P21	Fe2	K2	162.82(7)
P31	Fe2	K2	84.28(8)
P24	Fe2	K2	80.28(11)
P21'	Fe2	K2	162.80(17)
P24'	Fe2	K2	83.8(3)
K3	Fe2	K2	91.47(5)
Fe1[1]	K1	Fe1	162.63(7)
Fe1[1]	K1	K2[1]	45.21(3)
Fe1	K1	K2[1]	117.93(5)
Fe1[1]	K1	K2	117.93(5)
Fe1	K1	K2	45.21(3)
K2[1]	K1	K2	77.14(5)
Fe1	K2	Fe2	169.97(6)
Fe1	K2	K1	44.65(3)
Fe2	K2	K1	131.09(5)
Fe1	K2	K3	141.33(5)
Fe2	K2	K3	43.16(2)
K1	K2	K3	103.21(4)
Fe2[1]	K3	Fe2	153.70(8)
Fe2[1]	K3	K2	110.18(5)
Fe2	K3	K2	45.37(3)
Fe2[1]	K3	K2[1]	45.37(3)
Fe2	K3	K2[1]	110.19(5)
K2	K3	K2[1]	76.45(5)
C6	P1	C5	94.7(4)
C6	P1	C2	100.2(4)
C5	P1	C2	97.7(5)
C6	P1	Fe1	122.7(3)
C5	P1	Fe1	125.7(3)
C2	P1	Fe1	110.7(3)
C3	C2	P1	109.1(6)
C2	C3	P4	111.1(6)
C7	P4	C8	96.1(4)
C7	P4	C3	101.0(6)
C8	P4	C3	96.1(5)
C7	P4	Fe1	124.6(3)
C8	P4	Fe1	122.4(3)
C3	P4	Fe1	111.5(3)
C15	P11	C16	95.4(4)
C15	P11	C12	96.8(4)
C16	P11	C12	98.7(4)
C15	P11	Fe1	126.8(3)
C16	P11	Fe1	120.9(3)
C12	P11	Fe1	112.7(2)
C13	C12	P11	110.6(5)
C33	P34	Fe2	113.9(4)
C37	P34	Fe2	121.3(5)
C22'	P21'	C26'	104.9(14)
C22'	P21'	C25'	95.9(12)
C26'	P21'	C25'	93.9(14)
C22'	P21'	Fe2	113.1(8)
C26'	P21'	Fe2	118.8(14)
C25'	P21'	Fe2	126.1(12)
C23'	C22'	P21'	105.5(18)
C22'	C23'	P24'	110.1(19)
C28'	P24'	C23'	103.0(16)
C28'	P24'	C27'	95.5(15)
C23'	P24'	C27'	99.8(17)
C28'	P24'	Fe2	123.5(15)
C23'	P24'	Fe2	112.2(11)
C27'	P24'	Fe2	119.0(13)
C32'	P31'	C35'	99.1(15)
C32'	P31'	C36'	105.3(17)
C35'	P31'	C36'	90.6(13)
C32'	P31'	Fe2	110.1(11)
C35'	P31'	Fe2	125.6(13)
C36'	P31'	Fe2	122.2(12)
C33'	C32'	P31'	113(2)
C32'	C33'	P34'	111.6(19)
C38'	P34'	C33'	101.6(15)
C38'	P34'	C37'	92.5(15)
C33'	P34'	C37'	99.6(15)
C38'	P34'	Fe2	125.0(15)
C33'	P34'	Fe2	113.7(11)
C37'	P34'	Fe2	119.7(14)
C42	C41	C45	108.9(7)
C41	C42	C43	107.0(7)
C44	C43	C42	107.6(7)
C43	C44	C45	107.3(7)
C44	C45	C41	106.8(7)
C42'	C41'	C45'	106.8(10)
C41'	C42'	C43'	107.7(8)
C44'	C43'	C42'	107.4(8)
C43'	C44'	C45'	106.3(10)
C41'	C45'	C44'	105.1(11)
C55	C51	C52	106.7(7)
C51	C52	C53	104.7(9)
C54	C53	C52	102.7(11)
C55	C54	C53	103.2(11)
C51	C55	C54	106.6(9)
C55'	C51'	C52'	107.7(8)
C51'	C52'	C53'	106.2(9)
C54'	C53'	C52'	105.9(9)
C55'	C54'	C53'	107.8(9)
C54'	C55'	C51'	107.5(8)
C55"	C51"	C52"	106.1(9)
C51"	C52"	C53"	103.6(12)
C54"	C53"	C52"	104.1(12)

C12	C13	P14	107.2(5)	C55"	C54"	C53"	106.4(9)
C17	P14	C13	99.9(4)	C51"	C55"	C54"	107.7(8)
C17	P14	C18	98.6(4)				

[1]1-X,+Y,1/2-Z

trans-Fe(H)$_x$(NPhNPh)(dmpe)$_2$; x = 0-1

Crystal data and structure refinement for *trans*-Fe(H)$_x$(NPhNPh)(dmpe)$_2$; x = 0-1.

Identification code	ASH1503
Empirical formula	$C_{24}H_{42}FeN_2P_4$
Formula weight	538.32
Temperature/K	173.05(10)
Crystal system	monoclinic
Space group	$P2_1/c$
a/Å	10.2914(3)
b/Å	15.1651(6)
c/Å	18.5928(6)
α/°	90
β/°	105.523(3)
γ/°	90
Volume/Å^3	2795.92(17)
Z	4
ρ_{calc}g/cm^3	1.279
μ/mm^{-1}	6.588
F(000)	1144.0
Radiation	CuKα (λ = 1.54184)
2Θ range for data collection/°	7.638 to 147.046
Index ranges	-12 ≤ h ≤ 12, -10 ≤ k ≤ 18, -20 ≤ l ≤ 22
Reflections collected	9309
Independent reflections	5356 [R_{int} = 0.0337, R_{sigma} = 0.0484]
Data/restraints/parameters	5356/169/343
Goodness-of-fit on F^2	1.056
Final R indexes [I>=2σ (I)]	R_1 = 0.0528, wR_2 = 0.1342
Final R indexes [all data]	R_1 = 0.0703, wR_2 = 0.1463
Largest diff. peak/hole / e Å^{-3}	1.53/-0.39

Bond Lengths for *trans*-Fe(H)$_x$(NPhNPh)(dmpe)$_2$; x = 0-1.

Atom	Atom	Length/Å	Atom	Atom	Length/Å
Fe1	P2	2.2014(10)	N2	C19'	1.430(10)
Fe1	P1	2.1991(11)	C13	C18	1.3900
Fe1	P3	2.1902(11)	C13	C14	1.3900
Fe1	P4	2.2103(10)	C18	C17	1.3900
Fe1	N1	2.079(3)	C17	C16	1.3900
P2	C6	1.824(5)	C16	C15	1.3900
P2	C1	1.860(4)	C15	C14	1.3900
P2	C5	1.839(4)	C24	C23	1.3900
P1	C10'	1.74(2)	C24	C19	1.3900
P1	C8	1.923(8)	C23	C22	1.3900
P1	C9	1.709(11)	C22	C21	1.3900

P1	C8'	1.828(10)	C21	C20	1.3900
P1	C9'	1.922(10)	C20	C19	1.3900
P1	C10	1.871(18)	C2	C1	1.510(7)
P3	C4	1.849(5)	C7	C8	1.447(11)
P3	C3	1.828(5)	C7	C8'	1.658(12)
P3	C2	1.851(4)	C19'	C20'	1.3900
P4	C11	1.808(5)	C19'	C24'	1.3900
P4	C12	1.830(5)	C20'	C21'	1.3900
P4	C7	1.872(5)	C21'	C22'	1.3900
N1	N2	1.368(4)	C22'	C23'	1.3900
N1	C13	1.437(3)	C23'	C24'	1.3900
N2	C19	1.400(9)			

Bond Angles for *trans*-Fe(H)$_x$(NPhNPh)(dmpe)$_2$; x = 0-1.

Atom	Atom	Atom	Angle/˚	Atom	Atom	Atom	Angle/˚
P2	Fe1	P4	160.62(5)	C12	P4	C7	98.6(3)
P1	Fe1	P2	93.90(4)	C7	P4	Fe1	110.71(16)
P1	Fe1	P4	85.04(4)	N2	N1	Fe1	111.0(2)
P3	Fe1	P2	85.44(4)	N2	N1	C13	115.9(3)
P3	Fe1	P1	173.33(5)	C13	N1	Fe1	129.99(19)
P3	Fe1	P4	93.38(5)	N1	N2	C19	126.1(7)
N1	Fe1	P2	106.42(8)	N1	N2	C19'	114.0(8)
N1	Fe1	P1	90.65(9)	C18	C13	N1	118.79(17)
N1	Fe1	P3	95.91(9)	C18	C13	C14	120.0
N1	Fe1	P4	92.94(8)	C14	C13	N1	121.17(17)
C6	P2	Fe1	114.98(17)	C17	C18	C13	120.0
C6	P2	C1	99.0(2)	C16	C17	C18	120.0
C6	P2	C5	99.2(2)	C17	C16	C15	120.0
C1	P2	Fe1	111.38(15)	C16	C15	C14	120.0
C5	P2	Fe1	126.73(16)	C15	C14	C13	120.0
C5	P2	C1	101.5(2)	C23	C24	C19	120.0
C10'	P1	Fe1	123.7(7)	C22	C23	C24	120.0
C10'	P1	C8	77.4(6)	C23	C22	C21	120.0
C8	P1	Fe1	108.6(3)	C20	C21	C22	120.0
C9	P1	Fe1	122.5(4)	C21	C20	C19	120.0
C9	P1	C10'	109.5(8)	C24	C19	N2	118.8(9)
C9	P1	C8	102.3(5)	C20	C19	N2	120.5(9)
C8'	P1	Fe1	111.9(4)	C20	C19	C24	120.0
C8'	P1	C9'	94.3(5)	C1	C2	P3	110.6(3)
C8'	P1	C10	120.2(7)	C2	C1	P2	108.3(3)
C9'	P1	Fe1	118.9(3)	C8	C7	P4	105.7(4)
C10	P1	Fe1	119.3(6)	C8'	C7	P4	112.7(4)
C10	P1	C9'	86.8(7)	C7	C8	P1	109.8(5)
C4	P3	Fe1	122.64(19)	C7	C8'	P1	105.2(6)
C4	P3	C2	98.2(2)	C20'	C19'	N2	129.6(11)
C3	P3	Fe1	117.85(16)	C20'	C19'	C24'	120.0
C3	P3	C4	100.1(3)	C24'	C19'	N2	110.3(11)
C3	P3	C2	103.6(2)	C19'	C20'	C21'	120.0
C2	P3	Fe1	111.28(17)	C22'	C21'	C20'	120.0
C11	P4	Fe1	127.01(18)	C23'	C22'	C21'	120.0
C11	P4	C12	98.9(3)	C24'	C23'	C22'	120.0

C11	P4	C7	101.9(3)	C23'	C24'	C19'	120.0
C12	P4	Fe1	115.39(18)				

$Fe(H)(dppe)_2$

Crystal data and structure refinement for $Fe(H)(dppe)_2$.

Identification code	ASH1102
Empirical formula	$C_{52}H_{49}FeP_4$
Formula weight	853.64
Temperature/K	173
Crystal system	Monoclinic
Space group	$P2_1/n$
a/Å	9.95356(12)
b/Å	20.7687(3)
c/Å	21.0948(2)
α/°	90.00
β/°	90.5288(10)
γ/°	90.00
Volume/Å^3	4360.58(9)
Z	4
ρ_{calc}g/cm^3	1.300
μ/mm^{-1}	0.528
F(000)	1788.0
Crystal size/mm^3	0.44 × 0.27 × 0.08
Radiation	MoKα (λ = 0.71073)
2Θ range for data collection/°	6.84 to 65.84
Index ranges	-9 ≤ h ≤ 14, -28 ≤ k ≤ 31, -29 ≤ l ≤ 31
Reflections collected	48551
Independent reflections	14984 [R_{int} = 0.0283]
Data/restraints/parameters	14984/0/518
Goodness-of-fit on F^2	1.051
Final R indexes [I>=2σ (I)]	R_1 = 0.0392, wR_2 = 0.0927
Final R indexes [all data]	R_1 = 0.0564, wR_2 = 0.0996
Largest diff. peak/hole / e Å^{-3}	0.43/-0.28

Bond Lengths for $Fe(H)(dppe)_2$.

Atom	Atom	Length/Å	Atom	Atom	Length/Å
Fe	P1	2.1788(4)	C26	C27	1.374(3)
Fe	P4	2.1824(4)	C27	C28	1.392(3)
Fe	P34	2.1844(4)	P31	C41	1.8405(15)
Fe	P31	2.1970(4)	P31	C35	1.8616(14)
P1	C11	1.8353(14)	P31	C32	1.8620(14)
P1	C5	1.8516(13)	C32	C33	1.536(2)
P1	C2	1.8597(14)	C33	P34	1.8498(14)
C2	C3	1.527(2)	P34	C53	1.8360(15)
C3	P4	1.8644(14)	P34	C47	1.8423(14)
P4	C17	1.8377(14)	C35	C36	1.394(2)
P4	C23	1.8427(14)	C35	C40	1.395(2)
C5	C6	1.391(2)	C36	C37	1.385(2)
C5	C10	1.394(2)	C37	C38	1.378(2)

C6	C7	1.392(2)	C38	C39	1.381(2)
C7	C8	1.383(3)	C39	C40	1.393(2)
C8	C9	1.372(3)	C41	C46	1.392(2)
C9	C10	1.388(2)	C41	C42	1.393(2)
C11	C12	1.390(2)	C42	C43	1.389(2)
C11	C16	1.392(2)	C43	C44	1.383(3)
C12	C13	1.388(2)	C44	C45	1.370(3)
C13	C14	1.387(3)	C45	C46	1.394(2)
C14	C15	1.375(3)	C47	C48	1.392(2)
C15	C16	1.394(2)	C47	C52	1.395(2)
C17	C18	1.384(2)	C48	C49	1.393(2)
C17	C22	1.3940(19)	C49	C50	1.382(3)
C18	C19	1.396(2)	C50	C51	1.381(3)
C19	C20	1.374(2)	C51	C52	1.386(2)
C20	C21	1.383(2)	C53	C58	1.393(2)
C21	C22	1.384(2)	C53	C54	1.395(2)
C23	C28	1.383(2)	C54	C55	1.391(2)
C23	C24	1.383(2)	C55	C56	1.373(3)
C24	C25	1.392(3)	C56	C57	1.384(3)
C25	C26	1.362(3)	C57	C58	1.397(2)

Bond Angles for Fe(H)(dppe)$_2$.

Atom	Atom	Atom	Angle/˚	Atom	Atom	Atom	Angle/˚
P1	Fe	P4	85.962(14)	C25	C26	C27	119.64(17)
P1	Fe	P34	108.467(15)	C26	C27	C28	120.08(19)
P4	Fe	P34	148.743(16)	C23	C28	C27	121.17(19)
P1	Fe	P31	100.938(15)	C41	P31	C35	99.53(6)
P4	Fe	P31	116.641(15)	C41	P31	C32	102.66(7)
P34	Fe	P31	88.414(14)	C35	P31	C32	98.60(6)
C11	P1	C5	99.66(6)	C41	P31	Fe	124.16(5)
C11	P1	C2	102.80(7)	C35	P31	Fe	120.71(5)
C5	P1	C2	99.56(6)	C32	P31	Fe	107.15(5)
C11	P1	Fe	124.75(5)	C33	C32	P31	107.97(10)
C5	P1	Fe	117.82(5)	C32	C33	P34	107.39(10)
C2	P1	Fe	108.64(5)	C53	P34	C47	98.52(6)
C3	C2	P1	107.12(9)	C53	P34	C33	103.96(7)
C2	C3	P4	107.74(9)	C47	P34	C33	102.62(7)
C17	P4	C23	99.53(6)	C53	P34	Fe	117.79(5)
C17	P4	C3	101.73(6)	C47	P34	Fe	124.26(5)
C23	P4	C3	103.30(7)	C33	P34	Fe	107.21(5)
C17	P4	Fe	124.38(5)	C36	C35	C40	117.87(13)
C23	P4	Fe	114.29(5)	C36	C35	P31	119.24(11)
C3	P4	Fe	110.99(5)	C40	C35	P31	122.86(11)
C6	C5	C10	118.28(13)	C37	C36	C35	121.15(14)
C6	C5	P1	118.78(11)	C38	C37	C36	120.29(15)
C10	C5	P1	122.95(11)	C37	C38	C39	119.71(15)
C5	C6	C7	120.61(15)	C38	C39	C40	120.11(15)
C8	C7	C6	120.07(16)	C39	C40	C35	120.83(15)
C9	C8	C7	119.90(15)	C46	C41	C42	117.76(15)
C8	C9	C10	120.19(17)	C46	C41	P31	124.49(13)
C9	C10	C5	120.91(16)	C42	C41	P31	117.73(12)

C12	C11	C16	118.71(14)	C43	C42	C41	121.56(17)
C12	C11	P1	117.04(11)	C44	C43	C42	119.52(19)
C16	C11	P1	124.25(12)	C45	C44	C43	119.91(17)
C13	C12	C11	120.84(16)	C44	C45	C46	120.58(18)
C14	C13	C12	120.06(18)	C41	C46	C45	120.63(18)
C15	C14	C13	119.53(16)	C48	C47	C52	118.23(14)
C14	C15	C16	120.63(17)	C48	C47	P34	124.46(12)
C11	C16	C15	120.22(16)	C52	C47	P34	117.09(11)
C18	C17	C22	118.53(13)	C47	C48	C49	120.95(16)
C18	C17	P4	119.97(11)	C50	C49	C48	119.96(17)
C22	C17	P4	121.49(11)	C51	C50	C49	119.65(15)
C17	C18	C19	120.78(14)	C50	C51	C52	120.47(16)
C20	C19	C18	119.94(15)	C51	C52	C47	120.73(15)
C19	C20	C21	119.88(15)	C58	C53	C54	118.61(14)
C20	C21	C22	120.26(15)	C58	C53	P34	119.15(11)
C21	C22	C17	120.60(14)	C54	C53	P34	122.24(12)
C28	C23	C24	117.55(15)	C55	C54	C53	120.29(18)
C28	C23	P4	125.07(13)	C56	C55	C54	120.60(18)
C24	C23	P4	117.37(12)	C55	C56	C57	120.07(16)
C23	C24	C25	121.23(17)	C56	C57	C58	119.69(18)
C26	C25	C24	120.30(19)	C53	C58	C57	120.73(16)

$[Fe(depe)_2][BArF_{24}]$ (13)

Crystal data and structure refinement for $[Fe(depe)_2][BArF_{24}]$ (13).

Identification code	ASH1322b
Empirical formula	$C_{52}H_{60}BF_{24}FeP_4$
Formula weight	1331.54
Temperature/K	173
Crystal system	tetragonal
Space group	I-4
a/Å	13.2989(3)
b/Å	13.2989(3)
c/Å	17.4417(6)
α/°	90
β/°	90
γ/°	90
Volume/Å^3	3084.75(18)
Z	2
ρ_{calc}g/cm^3	1.434
μ/mm^{-1}	0.454
F(000)	1358.0
Crystal size/mm^3	0.44 × 0.22 × 0.07
Radiation	MoKα (λ = 0.71073)
2Θ range for data collection/°	6.128 to 58.268
Index ranges	-15 ≤ h ≤ 16, -17 ≤ k ≤ 17, -23 ≤ l ≤ 20
Reflections collected	11440
Independent reflections	3536 [R_{int} = 0.0245, R_{sigma} = 0.0315]
Data/restraints/parameters	3536/127/265
Goodness-of-fit on F^2	1.039
Final R indexes [I>=2σ (I)]	R_1 = 0.0465, wR_2 = 0.0990

Final R indexes [all data]	R_1 = 0.0595, wR_2 = 0.1060
Largest diff. peak/hole / e Å^{-3}	0.29/-0.18
Flack parameter	0.029(8)

Bond Lengths for [Fe(depe)$_2$][BArF$_{24}$] (13).

Atom	Atom	Length/Å	Atom	Atom	Length/Å
Fe1	P4	2.203(10)	C22	C23	1.380(5)
Fe1	P1	2.237(8)	C23	C24	1.385(6)
P1	C7	1.811(11)	C23	C27	1.504(6)
P1	C5	1.819(13)	C24	C25	1.389(6)
P1	C2	1.885(12)	C25	C26	1.380(5)
C2	C3	1.528(13)	C25	C28	1.496(6)
C3	P4	1.865(12)	C27	F27F	1.261(16)
P4	C11	1.820(15)	C27	F27E	1.282(16)
P4	C9	1.856(12)	C27	F27A	1.288(6)
C5	C6	1.521(18)	C27	F27C	1.292(6)
C7	C8	1.538(12)	C27	F27D	1.292(16)
C9	C10	1.542(14)	C27	F27B	1.315(7)
C11	C12	1.519(19)	C28	F28F	1.239(16)
B20	C21	1.632(4)	C28	F28E	1.272(16)
B20	C21^1	1.632(4)	C28	F28A	1.284(6)
B20	C21^2	1.632(3)	C28	F28C	1.345(7)
B20	C21^3	1.632(4)	C28	F28B	1.359(7)
C21	C26	1.387(5)	C28	F28D	1.385(16)
C21	C22	1.403(5)			

^{1}1/2+Y,3/2-X,3/2-Z; ^{2}3/2-Y,-1/2+X,3/2-Z; ^{3}2-X,1-Y,+Z

Bond Angles for [Fe(depe)$_2$][BArF$_{24}$] (13).

Atom	Atom	Atom	Angle/°	Atom	Atom	Atom	Angle/°
P4	Fe1	P1	87.1(5)	C24	C23	C27	119.7(4)
C7	P1	C5	104.3(7)	C23	C24	C25	118.0(3)
C7	P1	C2	100.8(6)	C26	C25	C24	120.5(4)
C5	P1	C2	102.9(8)	C26	C25	C28	119.3(4)
C7	P1	Fe1	124.5(5)	C24	C25	C28	120.2(4)
C5	P1	Fe1	112.4(8)	C25	C26	C21	122.9(4)
C2	P1	Fe1	109.5(5)	F27F	C27	F27E	108.2(14)
C3	C2	P1	110.7(7)	F27A	C27	F27C	107.7(5)
C2	C3	P4	110.5(7)	F27F	C27	F27D	105.9(15)
C11	P4	C9	103.7(9)	F27E	C27	F27D	106.9(14)
C11	P4	C3	102.6(8)	F27A	C27	F27B	105.3(5)
C9	P4	C3	100.1(7)	F27C	C27	F27B	104.1(5)
C11	P4	Fe1	116.3(10)	F27F	C27	C23	112.6(14)
C9	P4	Fe1	121.1(6)	F27E	C27	C23	115.0(13)
C3	P4	Fe1	110.4(6)	F27A	C27	C23	113.0(4)
C6	C5	P1	114.1(14)	F27C	C27	C23	114.2(4)
C8	C7	P1	116.7(8)	F27D	C27	C23	107.7(14)
C10	C9	P4	115.6(10)	F27B	C27	C23	111.8(4)
C12	C11	P4	113.9(14)	F28F	C28	F28E	115.0(16)
C21	B20	C21^1	112.73(12)	F28A	C28	F28C	109.5(6)

C21	B20	C21[2]	112.72(12)	F28A	C28	F28B	106.6(6)
C21[1]	B20	C21[2]	103.1(2)	F28C	C28	F28B	100.9(5)
C21	B20	C21[3]	103.1(2)	F28F	C28	F28D	108.2(15)
C21[1]	B20	C21[3]	112.73(12)	F28E	C28	F28D	103.6(14)
C21[2]	B20	C21[3]	112.73(12)	F28F	C28	C25	117.3(16)
C26	C21	C22	115.4(3)	F28E	C28	C25	109.3(13)
C26	C21	B20	123.4(3)	F28A	C28	C25	114.7(5)
C22	C21	B20	120.8(3)	F28C	C28	C25	112.3(5)
C23	C22	C21	122.5(4)	F28B	C28	C25	111.8(4)
C22	C23	C24	120.6(4)	F28D	C28	C25	101.7(14)
C22	C23	C27	119.7(4)				

[1]1/2+Y,3/2-X,3/2-Z; [2]3/2-Y,-1/2+X,3/2-Z; [3]2-X,1-Y,+Z

$Fe(H)(N_3)(depe)_2$ (14)

Crystal data and structure refinement for $Fe(H)(N_3)(depe)_2$ (14).

Identification code	ASH1328
Empirical formula	$C_{20}H_{49}FeN_3P_4$
Formula weight	511.35
Temperature/K	173
Crystal system	orthorhombic
Space group	Pbca
a/Å	15.18959(9)
b/Å	14.71335(8)
c/Å	23.73390(14)
α/°	90
β/°	90
γ/°	90
Volume/Å^3	5304.28(5)
Z	8
ρ_{calc}g/cm^3	1.281
μ/mm^{-1}	6.918
F(000)	2208.0
Crystal size/mm^3	0.48 × 0.23 × 0.12
Radiation	CuKα (λ = 1.54184)
2Θ range for data collection/°	7.45 to 147.504
Index ranges	-16 ≤ h ≤ 18, -18 ≤ k ≤ 14, -29 ≤ l ≤ 28
Reflections collected	30586
Independent reflections	5330 [R_{int} = 0.0255, R_{sigma} = 0.0172]
Data/restraints/parameters	5330/96/311
Goodness-of-fit on F^2	1.042
Final R indexes [I>=2σ (I)]	R_1 = 0.0243, wR_2 = 0.0634
Final R indexes [all data]	R_1 = 0.0256, wR_2 = 0.0645
Largest diff. peak/hole / e Å^{-3}	0.32/-0.25

Bond Lengths for $Fe(H)(N_3)(depe)_2$ (14).

Atom	Atom	Length/Å	Atom	Atom	Length/Å
Fe1	N1	2.0669(12)	P1'	C5'	1.829(14)
Fe1	P4'	2.177(17)	P1'	C7'	1.851(17)
Fe1	P24	2.2091(4)	C2'	C3'	1.513(16)
Fe1	P1	2.2153(11)	C3'	P4'	1.842(16)
Fe1	P4	2.2158(14)	P4'	C9'	1.822(17)
Fe1	P21	2.2192(4)	P4'	C11'	1.850(17)
Fe1	P1'	2.290(13)	C5'	C6'	1.523(17)
N1	N2	1.1812(17)	C7'	C8'	1.522(17)
N2	N3	1.1754(18)	C9'	C10'	1.528(18)
P1	C7	1.847(2)	C11'	C12'	1.535(18)
P1	C2	1.8519(19)	P21	C27	1.8413(14)
P1	C5	1.855(2)	P21	C22	1.8434(15)
C2	C3	1.525(3)	P21	C25	1.8510(15)
C3	P4	1.8510(19)	C22	C23	1.521(2)
P4	C11	1.849(2)	C23	P24	1.8509(15)
P4	C9	1.855(3)	P24	C29	1.8251(16)
C5	C6	1.528(3)	P24	C31	1.8533(16)
C7	C8	1.524(3)	C25	C26	1.522(2)
C9	C10	1.535(3)	C27	C28	1.528(2)
C11	C12	1.519(3)	C29	C30	1.533(2)
P1'	C2'	1.817(14)	C31	C32	1.530(3)

Bond Angles for $Fe(H)(N_3)(depe)_2$ (14).

Atom	Atom	Atom	Angle/°	Atom	Atom	Atom	Angle/°
N1	Fe1	P4'	99.5(4)	C2'	P1'	C5'	103.9(9)
N1	Fe1	P24	92.48(4)	C2'	P1'	C7'	103.2(12)
P4'	Fe1	P24	167.5(4)	C5'	P1'	C7'	97.4(10)
N1	Fe1	P1	91.28(5)	C2'	P1'	Fe1	107.0(7)
P24	Fe1	P1	93.68(3)	C5'	P1'	Fe1	121.2(7)
N1	Fe1	P4	95.67(5)	C7'	P1'	Fe1	121.6(11)
P24	Fe1	P4	171.85(4)	C3'	C2'	P1'	109.8(11)
P1	Fe1	P4	85.93(4)	C2'	C3'	P4'	111.6(12)
N1	Fe1	P21	91.08(4)	C9'	P4'	C3'	103.0(13)
P4'	Fe1	P21	98.5(4)	C9'	P4'	C11'	99.9(13)
P24	Fe1	P21	84.770(14)	C3'	P4'	C11'	105.9(13)
P1	Fe1	P21	177.23(3)	C9'	P4'	Fe1	115.3(12)
P4	Fe1	P21	95.28(4)	C3'	P4'	Fe1	110.8(9)
N1	Fe1	P1'	85.7(3)	C11'	P4'	Fe1	120.1(14)
P4'	Fe1	P1'	86.0(5)	C6'	C5'	P1'	115.9(13)
P24	Fe1	P1'	91.3(3)	C8'	C7'	P1'	121.3(17)
P21	Fe1	P1'	174.8(3)	C10'	C9'	P4'	121(2)
N2	N1	Fe1	131.07(10)	C12'	C11'	P4'	114.0(18)
N3	N2	N1	178.12(16)	C27	P21	C22	100.49(7)
C7	P1	C2	99.04(13)	C27	P21	C25	101.02(7)
C7	P1	C5	102.03(11)	C22	P21	C25	98.51(7)
C2	P1	C5	101.32(10)	C27	P21	Fe1	124.85(5)
C7	P1	Fe1	124.92(10)	C22	P21	Fe1	109.02(5)
C2	P1	Fe1	110.96(7)	C25	P21	Fe1	118.62(5)
C5	P1	Fe1	115.13(8)	C23	C22	P21	107.12(10)

C3	C2	P1	109.33(12)	C22	C23	P24	108.63(10)
C2	C3	P4	109.92(13)	C29	P24	C23	103.13(8)
C11	P4	C3	102.02(16)	C29	P24	C31	101.26(9)
C11	P4	C9	100.12(13)	C23	P24	C31	100.08(8)
C3	P4	C9	99.49(12)	C29	P24	Fe1	117.82(6)
C11	P4	Fe1	120.17(14)	C23	P24	Fe1	110.95(5)
C3	P4	Fe1	109.54(8)	C31	P24	Fe1	120.87(5)
C9	P4	Fe1	122.04(11)	C26	C25	P21	116.65(11)
C6	C5	P1	118.40(18)	C28	C27	P21	113.52(10)
C8	C7	P1	114.75(17)	C30	C29	P24	118.06(13)
C10	C9	P4	116.7(2)	C32	C31	P24	115.00(12)
C12	C11	P4	116.2(2)				

Permissions

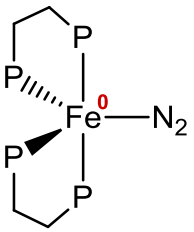
The following article is reproduced in Chapter 2 with permission from John Wiley and Sons:

L. R. Doyle, A. Heath, C. H. Low, A. E. Ashley, *Adv. Synth. Catal.*, **2014**, *356*, 603-608.

Licence number: 3594291180685 (March 22nd, 2015)

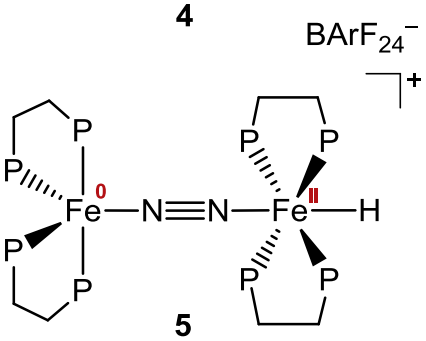
Abbreviations for Chapter 3 and 4

Complexes of dmpe ($Me_2PCH_2CH_2PMe_2$)



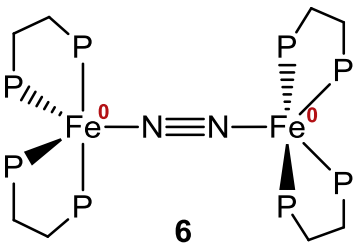
4

P = PMe_2

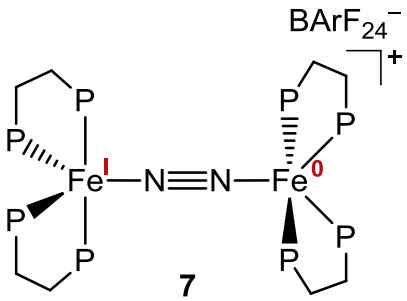


5

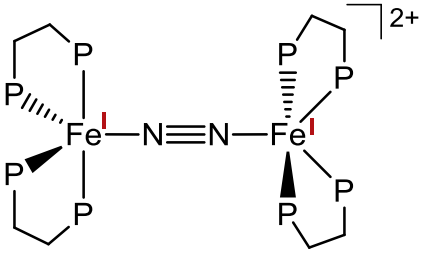
$BArF_{24}^- = \bar{B}(C_6H_3(CF_3)_2)_4$



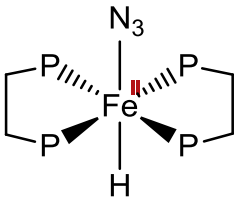
6



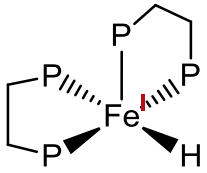
7



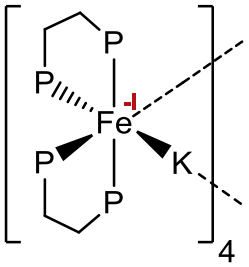
8



9

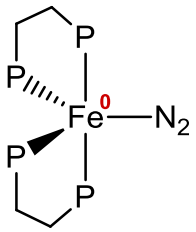


10



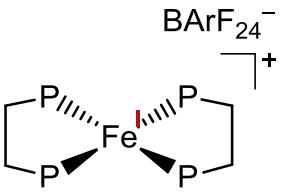
11

Complexes of depe ($Et_2PCH_2CH_2PEt_2$)

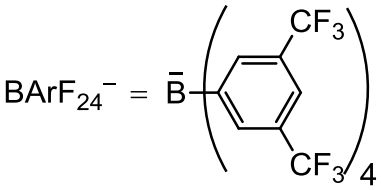


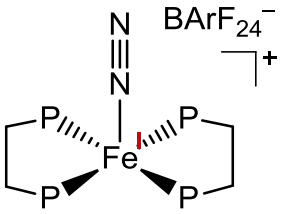
12

P = PEt_2

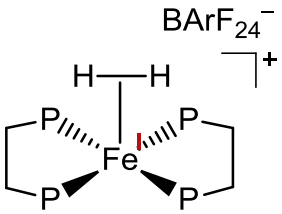


13

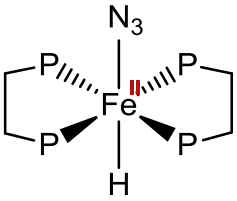




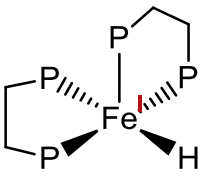
13-N_2



13-H_2



14



15